Selected Scientific Publications
in 2017
(Xinglong 2.16 m Telescope)

兴隆观测基地 2.16 米望远镜
科学产出论文集
(2017 年)

Preface

The Xinglong Observatory of the National Astronomical Observatories, Chinese Academy of Sciences (NAOC) was founded in 1968. As the largest optical astronomical observatory site in the continent of Asia, it has 9 telescopes with an effective aperture larger than 50 cm. Each year, more than 100 astronomers use the telescopes of Xinglong Observatory to perform the observations for the studies on stars, galaxies and solar system objects. In 2017, the observational researches of supernovae, galaxies and stars have been carried out by using the Xinglong 2.16 m telescope. Here we present the selected 14 publications, of which one is published in *NATURE*.

序 言

兴隆观测基地隶属于中国科学院国家天文台和中国科学院光学天文重点实验室，建于 1968 年。兴隆观测基地目前是亚洲大陆规模最大的光学天文观测基地，拥有口径 50 厘米以上的天文望远镜 9 台。每年有百余人次的国内外天文学家利用基地的天文望远镜从事恒星、星系和太阳系内天体的天文观测研究。2017 年，使用兴隆观测基地 2.16 米望远镜开展了超新星、星系、恒星等方面的观测研究，本论文集精选了发表的 14 篇学术论文，其中有一篇发表在《自然》学术期刊上。

Contents

LETTER

Energetic eruptions leading to a peculiar hydrogen–rich explosion of a massive star

Iair Arcavi[1,2,3], D. Andrew Howell[1,3], Daniel Kasen[4,5,6], Lars Bildsten[2,3], Griffin Hosseinzadeh[1,3], Curtis McCully[1,3], Zheng Chuen Wong[1,3], Sarah Rebekah Katz[1,3], Avishay Gal-Yam[7], Jesper Sollerman[8], Francesco Taddia[8], Giorgos Leloudas[7,9], Christoffer Fremling[8], Peter E. Nugent[6,10], Assaf Horesh[7,11], Kunal Mooley[12], Clare Rumsey[13], S. Bradley Cenko[14,15], Melissa L. Graham[6,16], Daniel A. Perley[9,17], Ehud Nakar[18], Nir J. Shaviv[11], Omer Bromberg[18], Ken J. Shen[6], Eran O. Ofek[7], Yi Cao[16,19], Xiaofeng Wang[20], Fang Huang[20], Liming Rui[20], Tianmeng Zhang[21,22], Wenxiong Li[20], Zhitong Li[20], Jujia Zhang[23,24], Stefano Valenti[25], David Guevel[1,3], Benjamin Shappee[26], Christopher S. Kochanek[27,28], Thomas W.-S. Holoien[27,28], Alexei V. Filippenko[6,29], Rob Fender[12], Anders Nyholm[8], Ofer Yaron[7], Mansi M. Kasliwal[30], Mark Sullivan[31], Nadja Blagorodnova[30], Richard S. Walters[30], Ragnhild Lunnan[30], Danny Khazov[7], Igor Andreoni[32,33,34], Russ R. Laher[35], Nick Konidaris[26], Przemek Wozniak[36] & Brian Bue[37]

Every supernova so far observed has been considered to be the terminal explosion of a star. Moreover, all supernovae with absorption lines in their spectra show those lines decreasing in velocity over time, as the ejecta expand and thin, revealing slower-moving material that was previously hidden. In addition, every supernova that exhibits the absorption lines of hydrogen has one main light-curve peak, or a plateau in luminosity, lasting approximately 100 days before declining[1]. Here we report observations of iPTF14hls, an event that has spectra identical to a hydrogen-rich core-collapse supernova, but characteristics that differ extensively from those of known supernovae. The light curve has at least five peaks and remains bright for more than 600 days; the absorption lines show little to no decrease in velocity; and the radius of the line-forming region is more than an order of magnitude bigger than the radius of the photosphere derived from the continuum emission. These characteristics are consistent with a shell of several tens of solar masses ejected by the progenitor star at supernova-level energies a few hundred days before a terminal explosion. Another possible eruption was recorded at the same position in 1954. Multiple energetic pre-supernova eruptions are expected to occur in stars of 95 to 130 solar masses, which experience the pulsational pair instability[2–5]. That model, however, does not account for the continued presence of hydrogen, or the energetics observed here. Another mechanism for the violent ejection of mass in massive stars may be required.

On 2014 September 22.53 UT (universal time dates are used throughout), the Intermediate Palomar Transient Factory (iPTF) wide-field camera survey[6,7] discovered iPTF14hls at right ascension $\alpha_{J2000} = 09\,h\,20\,min\,34.30\,s$ and declination $\delta_{J2000} = +50°\,41'\,46.8''$, at an R-band magnitude of 17.716 ± 0.033 (Extended Data Fig. 1). We have no observations of this position between 2014 May 28 and September 22, inducing an approximately 100-day uncertainty in the explosion time, so we use the discovery date as a reference epoch for all phases. We adopt a redshift of $z = 0.0344$, determined from narrow host-galaxy features, corresponding to a luminosity distance[9] of 156 Mpc.

On 2015 January 8, iPTF14hls was classified as a supernova of type II-P, on the basis of prominent, broad, Balmer series P Cygni lines in an optical spectrum[8]. So far, type II-P supernovae have been the only events ever observed to produce such spectra. In a type II-P supernova, the core of a massive star collapses to create a neutron star, sending a shock wave through the outer hydrogen-rich envelope and ejecting the envelope. The shock ionizes the ejecta, which later expand, cool and recombine. The photosphere follows the recombination front, which is at a roughly constant temperature ($T \approx 6,000\,K$) as it makes its way inward in mass through the expanding ejecta[10] (that is, the photosphere is moving from material that is further out from the exploding star towards material that is further in, but the material inside the photosphere is expanding in the meantime). This leads to the approximately 100-day 'plateau' phase of roughly constant luminosity in the light curve and prominent hydrogen P Cygni features in the spectrum.

iPTF14hls, although identical to type II-P supernovae in its spectroscopic features, has several properties never before seen in a supernova. Instead of a 100-day plateau, the light curve of iPTF14hls lasts over 600 days and has at least five distinct peaks during which the luminosity varies by as much as 50% (Fig. 1). Blackbody fits to the broad-band

[1]Las Cumbres Observatory, Goleta, California 93117, USA. [2]Kavli Institute for Theoretical Physics, University of California, Santa Barbara, California 93106, USA. [3]Department of Physics, University of California, Santa Barbara, California 93106, USA. [4]Nuclear Science Division, Lawrence Berkeley National Laboratory, Berkeley, California 94720, USA. [5]Department of Physics, University of California, Berkeley, California 94720, USA. [6]Department of Astronomy, University of California, Berkeley, California 94720-3411, USA. [7]Department of Particle Physics and Astrophysics, The Weizmann Institute of Science, Rehovot 76100, Israel. [8]The Oskar Klein Centre, Department of Astronomy, Stockholm University, AlbaNova, SE-10691 Stockholm, Sweden. [9]Dark Cosmology Centre, Niels Bohr Institute, University of Copenhagen, Juliane Maries vej 30, 2100 Copenhagen, Denmark. [10]Computational Research Division, Lawrence Berkeley National Laboratory, Berkeley, California 94720, USA. [11]Racah Institute of Physics, The Hebrew University of Jerusalem, Jerusalem 91904, Israel. [12]Department of Physics, Astrophysics, University of Oxford, Denys Wilkinson Building, Oxford OX1 3RH, UK. [13]Astrophysics Group, Cavendish Laboratory, 19 J. J. Thomson Avenue, Cambridge CB3 0HE, UK. [14]Astrophysics Science Division, NASA Goddard Space Flight Center, Code 661, Greenbelt, Maryland 20771, USA. [15]Joint Space-Science Institute, University of Maryland, College Park, Maryland 20742, USA. [16]Department of Astronomy, University of Washington, Box 351580, Seattle, Washington 98195-1580, USA. [17]Astrophysics Research Institute, Liverpool John Moores University, IC2, Liverpool Science Park, 146 Brownlow Hill, Liverpool L3 5RF, UK. [18]The Raymond and Beverly Sackler School of Physics and Astronomy, Tel Aviv University, Tel Aviv 69978, Israel. [19]eScience Institute, University of Washington, Box 351570, Seattle, Washington 98195-1580, USA. [20]Physics Department and Tsinghua Center for Astrophysics, Tsinghua University, Beijing 100084, China. [21]Key Laboratory of Optical Astronomy, National Astronomical Observatories of China, Chinese Academy of Sciences, Beijing 100012, China. [22]School of Astronomy and Space Science, University of Chinese Academy of Sciences, Beijing 101408, China. [23]Yunnan Observatories, Chinese Academy of Sciences, Kunming 650011, China. [24]Key Laboratory for the Structure and Evolution of Celestial Objects, Chinese Academy of Sciences, Phoenix Mountain, East District, Kunming, Yunnan 650216, China. [25]Department of Physics, University of California, 1 Shields Avenue, Davis, California 95616, USA. [26]Carnegie Observatories, 813 Santa Barbara Street, Pasadena, California 91101, USA. [27]Department of Astronomy, The Ohio State University, 140 West 18th Avenue, Columbus, Ohio 43210, USA. [28]Center for Cosmology and AstroParticle Physics (CCAPP), The Ohio State University, 191 W. Woodruff Avenue, Columbus, Ohio 43210, USA. [29]Miller Institute for Basic Research in Science, University of California, Berkeley, California 94720, USA. [30]Cahill Center for Astrophysics, California Institute of Technology, Pasadena, California 91125, USA. [31]Department of Physics and Astronomy, University of Southampton, Southampton SO17 1BJ, UK. [32]Centre for Astrophysics and Supercomputing, Swinburne University of Technology, PO Box 218, Victoria 3122, Australia. [33]ARC Centre of Excellence for All-sky Astrophysics (CAASTRO), Australia. [34]Australian Astronomical Observatory. PO Box 915, North Ryde, New South Wales 1670, Australia. [35]Spitzer Science Center, California Institute of Technology, MS 314-6, Pasadena, California 91125, USA. [36]Space and Atmospheric Sciences Group, Mail Stop D466, Los Alamos National Laboratory, Los Alamos, New Mexico 87545, USA. [37]Jet Propulsion Laboratory, California Institute of Technology, Pasadena, California 91109, USA.

1
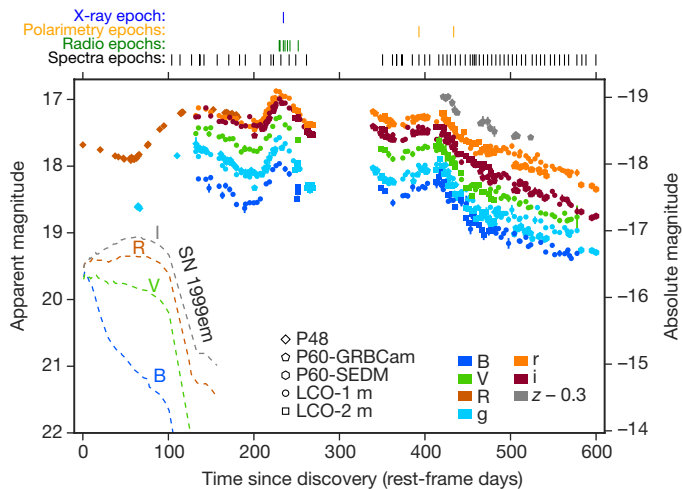
Figure 1 | Light curves of iPTF14hls. The type II-P supernova SN 1999em is shown in dashed lines[22], according to the ordinate axis at right. Data from the same day, instrument, and filter are averaged for clarity. The Spectral Energy Distribution Machine (SEDM) i-band data are shifted by $+0.3$ mag to compensate for filter differences. Unlike any known supernova, iPTF14hls has at least five distinct peaks in its light curve (at approximately 140 days, 220 days and 410 days after discovery, before discovery as indicated by the R-band light curve, and while it was behind the Sun between day 260 and day 340 after discovery). Error bars denote 1σ uncertainties.

optical $BVgi$ photometry of iPTF14hls (see Methods) indicate a roughly constant effective temperature of 5,000–6,000 K, the same as the hydrogen-recombination temperature typically seen in type II-P

supernovae. However, the inferred bolometric luminosity of a few times 10^{42} erg s^{-1} is at the high end of the range for typical type II-P supernovae[11], and the total radiated energy of $2.20^{+0.03}_{-0.05} \times 10^{50}$ erg emitted during the 450 days of our multi-band optical coverage is a few times larger than that of any known type II-P supernova. Given the uncertainty in the explosion time of iPTF14hls, the discrepancies with type II-P supernova timescales and energetics may be even larger.

The spectroscopic evolution of iPTF14hls is even harder to understand. It is a factor of approximately 10 slower than that of type II-P supernovae (Fig. 2); for example, the spectrum of iPTF14hls at 600 days looks like that of a normal type II-P supernova at 60 days (Extended Data Fig. 4). In all previously observed supernovae, the faster material is outside—spectra show a decrease of all measured velocities with time (by a factor of approximately 3 over 100 days) as the material expands and thins, and the photosphere moves inward in mass revealing deeper, slower-moving material. In iPTF14hls, velocities of hydrogen decline by only 25%, from 8,000 km s^{-1} to 6,000 km s^{-1} over 600 days, while the iron lines stay at a constant velocity of 4,000 km s^{-1} (Fig. 3).

It is usual to see hydrogen lines at higher velocities than iron lines owing to optical depth effects. But eventually, as the material expands and thins, hydrogen should be seen at lower velocity where the iron was previously seen (Extended Data Fig. 7). If the ejecta are expanding in size by a factor of approximately 6 between day 100 and day 600, in the absence of an additional energy source, an inward-moving photosphere scanning through the ejecta in velocity must occur.

An observation of constant velocity in a supernova can thus be caused by: (1) a central engine pushing material from the inside, sweeping the ejecta into a thin, dense shell[12,13], or (2) the spectral lines may correspond to ejecta that are far above the photosphere and detached from it. One-dimensional central-engine models compress
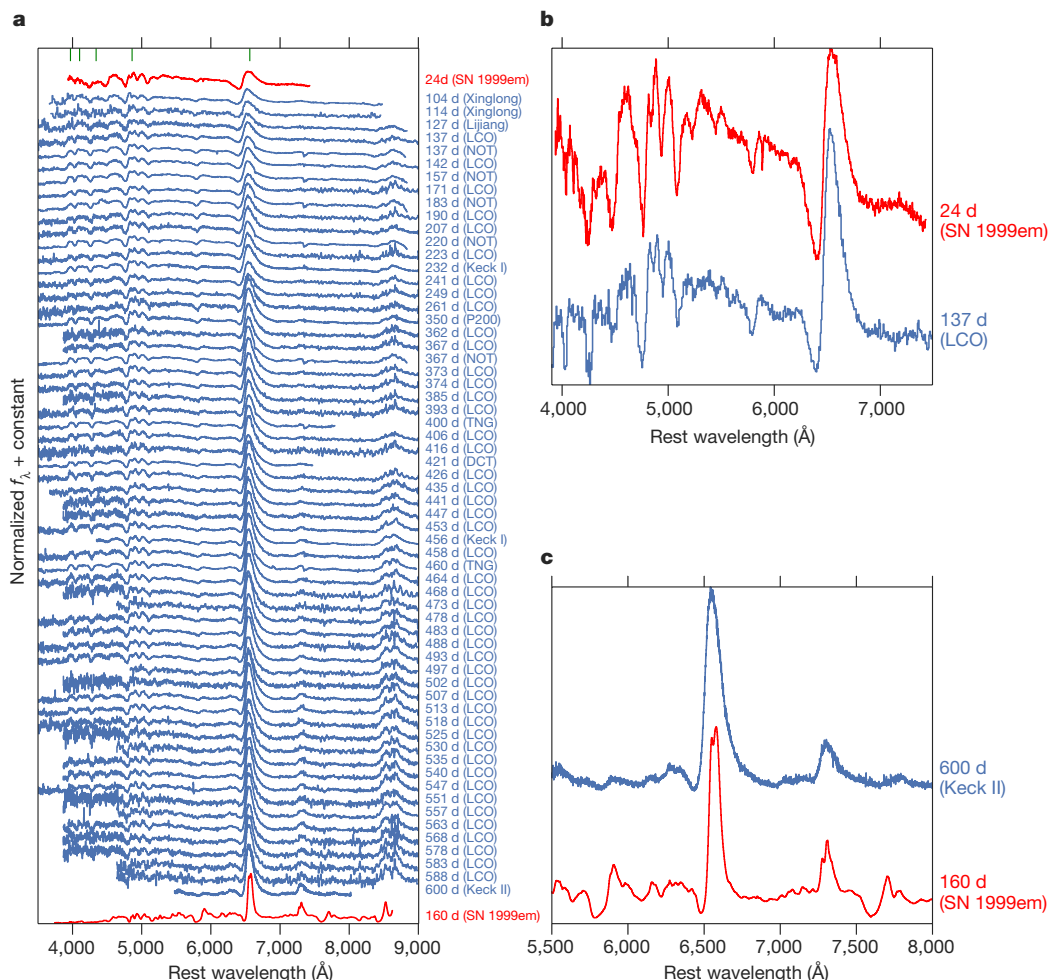
Figure 2 | Spectroscopic sequence of iPTF14hls. Our full sequence (**a**; blue) is shown with select spectra highlighted (**b**, **c**), in terms of normalized flux density as a function of rest-frame wavelength. The spectra are binned in wavelength and shifted in flux density for clarity. Phases are noted in rest-frame days since discovery, with the telescopes used in parentheses. Spectra of the type II-P supernova SN 1999em[22] (red) are shown with phases noted in rest-frame days since explosion. Balmer series hydrogen-line wavelengths are denoted in green (**a**). iPTF14hls is very similar spectroscopically to a type II-P supernova but evolves much more slowly. The spectral evolution is very smooth (**a**).
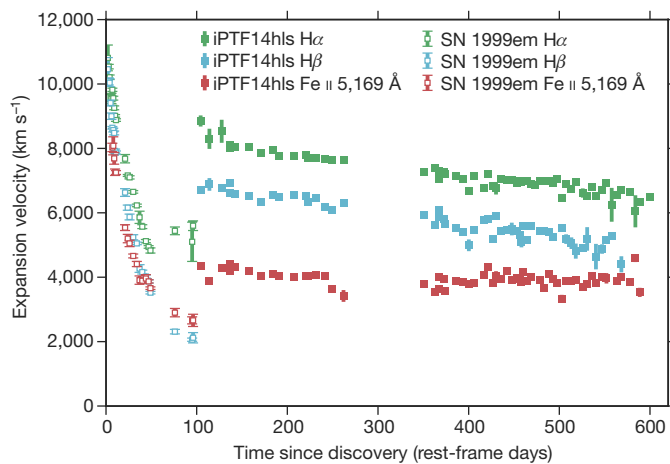
Figure 3 | Expansion velocities as a function of time. Velocities are measured from the P Cygni absorption component of three different spectral lines (see Methods) for iPTF14hls (filled symbols) and the prototypical type II-P supernova SN 1999em[22] (empty symbols). Error bars denote 1σ uncertainties for $n = 1,000$ samplings of the endpoints and are sometimes smaller than the marker size. The velocities seen for iPTF14hls evolve much more slowly compared with SN 1999em.

Figure 4 | The photospheric radius of iPTF14hls. The radius is estimated in two different ways: (1) using blackbody fits to the broad-band $BVgi$ photometry (blue) and (2) using the derived expansion velocities of Fe II $\lambda = 5,169$ Å times the elapsed rest-frame time (vt) since discovery (red). The same quantities are shown for the type II-P supernova SN 1999em (empty symbols; after correcting for the blackbody dilution factor)[22]. Error bars denote 1σ uncertainties and are sometimes smaller than the marker size. For SN 1999em the radii overlap as expected, but for iPTF14hls they diverge, indicating that the line-forming region may be detached from the photosphere.

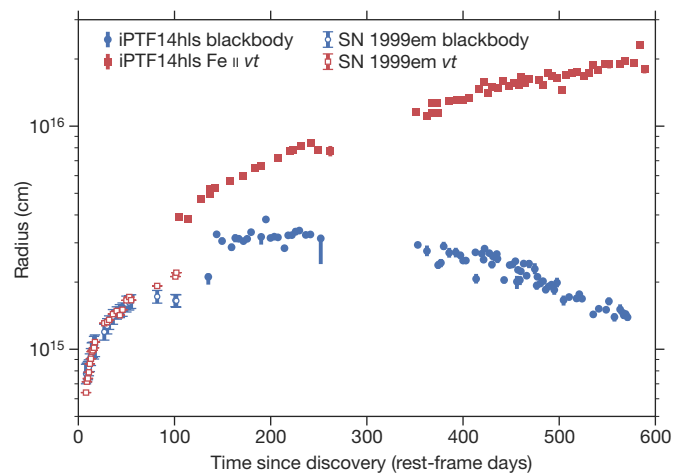the iron and hydrogen lines to the same velocity, which is not the case for iPTF14hls (though multi-dimensional effects could alter this prediction). The spectral line evolution can more readily be explained if the lines are formed by ejecta from a prior eruption (that happened a few years before the discovery of iPTF14hls) that are detached from the continuum-emitting photosphere, which was formed in the terminal explosion (see Methods).

We estimate the position of the line-forming region to be vt, where v is the observed expansion velocity of the material at time t. For type II-P supernovae, this radius, when using the iron line velocities, is the same as the photospheric radius obtained by blackbody fits to the continuum emission, up to an order-unity "blackbody dilution factor"[14–16]. For iPTF14hls, the vt-inferred radius is instead larger than the blackbody-inferred radius by an order of magnitude on day 600 (Fig. 4). The fact that the two radii are so different from each other indicates that the line-forming region in iPTF14hls is indeed spatially detached from the continuum-emitting photosphere, in contrast to what is observed in all known type II-P supernovae.

The observations are thus consistent with the line-forming material being ejected in a massive and very energetic pre-supernova outburst, specifically in a shell of the order of a few tens of solar masses (see Methods). However, this requires a kinetic energy of about 10^{52} erg, normally associated with (or even exceeding that of) a supernova. Further evidence for a third, even earlier, explosion comes from an outburst of R-band magnitude $M_R \approx -15.6$ detected at the position of iPTF14hls in 1954 (formally a 2.2σ detection, though this is probably an underestimate owing to photographic nonlinearity; see Methods).

It is also unknown what is powering the light curve of iPTF14hls. Strong asymmetry may induce a luminosity increase in a particular direction. However, we do not detect any substantial polarization that would be indicative of asymmetry in the explosion (see Methods). Another energy source in iPTF14hls compared to normal type II-P supernovae could come from the interaction of the ejecta with previously ejected shells. However, in cases of supernovae interacting with dense circumstellar material, the interaction dominates the spectra in the form of a strong continuum together with broad, intermediate and narrow components of the Balmer emission lines[17,18]. None of these features is seen in the spectra of iPTF14hls (Fig. 2; Extended Data Fig. 5). We find no evidence of X-ray or radio emission (which are possible additional indicators of strong interaction)[19] in observations taken during the brightest peak of the optical light curve (see Methods).

It is possible that any signs of interaction are being reprocessed by overlying, previously ejected material.

Either way, the progenitor of iPTF14hls probably experienced multiple energetic eruptions over the last decades of its life. Energetic eruptions are expected in stars with initial masses of about 95–130 solar masses, which undergo an instability arising from the production of electron–positron pairs[2]. Interactions between the different shells and/or the supernova ejecta and the shells can produce a variety of luminous long-lived transients with highly structured light curves[4,5] similar to that of iPTF14hls. Such pulsational pair instability supernovae are expected to occur in low-metallicity environments; indeed, iPTF14hls occurred on the outskirts of a low-mass, star-forming galaxy, possibly of low metal content (see Methods).

However, models of stars undergoing the pulsational pair instability eject most of the hydrogen envelope in the first eruption[5], whereas for iPTF14hls a few tens of solar masses of hydrogen were retained in the envelope after the 1954 outburst. Another problem is that pulsational pair instability models can account for up to about 4×10^{51} erg of kinetic energy in all eruptions together, while about 10^{52} erg are required just for the most recent eruption that ejected the line-forming region of iPTF14hls (see Methods).

iPTF14hls demonstrates that stars in the local Universe can undergo very massive eruptions in the decades leading to their collapse and yet, surprisingly, maintain a massive hydrogen-rich envelope for most of this period. Current models of massive star evolution and explosion need to be modified, or a completely new picture needs to be put forward, to account for the energetics of iPTF14hls, its lack of strong interaction signatures and the inferred amount of hydrogen it retained toward the end of its life.

1. Arcavi, I. Hydrogen-rich core-collapse supernova. In *Handbook of Supernovae* (eds Alsabti, A. W. & Murdin, P.) (in the press, Springer, 2016).
2. Barkat, Z., Rakavy, G. & Sack, N. Dynamics of supernova explosion resulting from pair formation. *Phys. Rev. Lett.* **18,** 379–381 (1967).
3. Heger, A. & Woosley, S. E. The nucleosynthetic signature of population III. *Astrophys. J.* **567,** 532–543 (2002).

3

4. Woosley, S. E., Blinnikov, S. & Heger, A. Pulsational pair instability as an explanation for the most luminous supernovae. *Nature* **450,** 390–392 (2007).
5. Woosley, S. E. Pulsational pair-instability supernovae. *Astrophys. J.* **836,** 244 (2017).
6. Law, N. M. *et al.* The Palomar Transient Factory: system overview, performance and first results. *Publ. Astron. Soc. Pacif.* **121,** 1395–1408 (2009).
7. Rau, A. *et al.* Exploring the optical transient sky with the Palomar Transient Factory. *Publ. Astron. Soc. Pacif.* **121,** 1334–1351 (2009).
8. Li, W., Wang, X. & Zhang, T. Spectroscopic classification of CSS141118:092034 +504148 as a type II-P supernova. *Astron. Telegr.* **6898** (2015).
9. The Planck Collaboration *et al.* Planck 2015 results. XIII. Cosmological parameters. *Astron. Astrophys.* **594,** A13 (2016).
10. Popov, D. V. An analytical model for the plateau stage of Type II supernovae. *Astrophys. J.* **414,** 712 (1993).
11. Bersten, M. C. & Hamuy, M. Bolometric light curves for 33 type II plateau supernovae. *Astrophys. J.* **701,** 200–208 (2009).
12. Kasen, D. & Bildsten, L. Supernova light curves powered by young magnetars. *Astrophys. J.* **717,** 245–249 (2010).
13. Dexter, J. & Kasen, D. Supernova light curves powered by fallback accretion. *Astrophys. J.* **772,** 30 (2013).
14. Kirshner, R. P. & Kwan, J. The envelopes of type II supernovae. *Astrophys. J.* **197,** 415 (1975).
15. Eastman, R. G., Schmidt, B. P. & Kirshner, R. The atmospheres of type II supernovae and the expanding photosphere method. *Astrophys. J.* **466,** 911 (1996).
16. Dessart, L. & Hillier, D. J. Distance determinations using type II supernovae and the expanding photosphere method. *Astron. Astrophys.* **439,** 671–685 (2005).
17. Schlegel, E. A new subclass of Type II supernovae? *Mon. Not. R. Astron. Soc.* **244,** 269–271 (1990).
18. Kiewe, M. *et al.* Caltech Core-Collapse Project (CCCP) observations of type IIn supernovae: typical properties and implications for their progenitor stars. *Astrophys. J.* **744,** 10 (2012).
19. Chevalier, R. A., Fransson, C. & Nymark, T. K. Radio and X-ray emission as probes of type IIP supernovae and red supergiant mass loss. *Astrophys. J.* **641,** 1029–1038 (2006).
20. Geha, M. *et al.* Variability-selected quasars in MACHO Project Magellanic cloud fields. *Astrophys. J.* **125,** 1–12 (2003).
21. Michel, F. C. Neutron star disk formation from supernova fall-back and possible observational consequences. *Nature* **333,** 644–645 (1988).
22. Leonard, D. C. *et al.* The distance to SN 1999em in NGC 1637 from the expanding photosphere method. *Publ. Astron. Soc. Pacif.* **114,** 35–64 (2002).

Supplementary Information is available in the online version of the paper.

Author Contributions I. Arcavi initiated the study, triggered follow-up observations, reduced data, performed the analysis and wrote the manuscript. D.A.H. is the Principal Investigator of the Las Cumbres Observatory (LCO) Supernova Key Project through which all of the LCO data were obtained; he also assisted with interpretation and the manuscript. D. Kasen and L.B. assisted with theoretical models, data interpretation, and with the manuscript. G.H. and C.McC. assisted with obtaining and reducing LCO data. Z.C.W. first flagged the supernova as interesting. S.R.K. performed the spectral expansion velocity measurements. A.G.-Y. is the Principal Investigator for core-collapse supernovae in iPTF and assisted with interpretation. J.S. and F.T. obtained the Nordic Optical Telescope spectra and polarimetry data and assisted with the manuscript. G.L. reduced the polarimetry data. C.F. reduced the Palomar 60-inch telescope (P60) data. P.E.N. discovered the 1954 eruption image of iPTF14hls, helped obtain the host-galaxy spectrum, and is a Co-Principal Investigator of the Keck proposal under which it and one of the supernova spectra were obtained. A.H. obtained and reduced the Very Large Array (VLA) data and is Principal Investigator of the programme through which the data were obtained. K.M. and C.R. obtained and reduced the Arcminute Microkelvin Imager Large Array (AMI-LA) data. S.B.C. obtained and reduced the Swift X-Ray Telescope (XRT) data. M.L.G. obtained and reduced Keck spectra. D.A.P. performed the host-galaxy analysis and assisted with the manuscript. E.N., O.B., N.J.S. and K.J.S. assisted with theoretical interpretation and the manuscript. E.O.O. helped with interpretation and the manuscript. Y.C. built the real-time iPTF image-subtraction pipeline and obtained Palomar 200-inch telescope (P200) observations. X.W., F.H., L.R., T.Z., W.L., Z.L. and J.Z. obtained and reduced the Xinglong, Lijiang, and Tsinghua University-NAOC telescope (TNT) data. S.V. built the LCO photometric and spectroscopic reduction pipelines and assisted with LCO observations, interpretation, and the manuscript. D.G. assisted with the Palomar Observatory Sky Survey (POSS) image analysis. B.S., C.S.K. and T.W.-S.H. obtained and reduced the All Sky Automated Survey for Supernovae (ASAS-SN) pre-discovery limits. A.V.F. is a Co-Principal Investigator of the Keck proposal under which the host-galaxy spectrum and one of the supernova spectra were obtained; he also helped with the manuscript. R.F. is Principal Investigator of the programme through which the AMI-LA data were obtained. A.N. helped scan for iPTF candidates and assisted with the manuscript. O.Y. is in charge of the iPTF candidate scanning effort. M.M.K. led the work for building iPTF. M.S. wrote the pipeline used to reduce Palomar 48-inch Oschin Schmidt telescope (P48) data. N.B. and R.S.W. obtained P60 SEDM photometry. R.L., D. Khazov, and I. Andreoni obtained P200 observations. R.R.L. contributed to building the P48 image-processing pipeline. N.K. was a main builder of the P60 SEDM. P.W. and B.B. helped build the machine-learning algorithms that identify iPTF supernova candidates.

4

METHODS

Discovery. The intermediate Palomar Transient Factory (iPTF) first detected iPTF14hls on 2014 September 22.53 (Extended Data Fig. 1) using the iPTF real-time image-subtraction pipeline[23]. No source was seen at that position when it was previously visited by iPTF and by the All Sky Automated Survey for Supernovae (ASAS-SN)[24] on 2014 May 6.19 and 2014 May 20–28 down to 3σ limiting magnitudes of $R < 20.95$ and $V < 18.7$, respectively. The source was observed by iPTF again on 2014 October 13, October 31, November 4 and November 10 before being saved and given a name as part of routine iPTF transient scanning. On 2014 November 18, iPTF14hls was independently discovered by the Catalina Real-Time Transient Survey[25] as CSS141118:092034+504148, and later the event was reported to the Transient Name Server as AT 2016bse and Gaia16aog. On 2015 February 3, upon routine Las Cumbres Observatory (LCO) rescanning of previously saved iPTF candidates, we noticed the peculiar decline and subsequent rise of the light curve, and began an extensive campaign of spectroscopic and multi-band photometric follow-up observations.

Follow-up imaging. Follow-up imaging was obtained with the Palomar 48-inch Oschin Schmidt telescope (P48), the Palomar 60-inch telescope (P60)[26] using both the GRBCam and the SEDM instruments, the LCO[27] network 1-m and 2-m telescopes, and the 0.8-m Tsinghua University-NAOC telescope (TNT)[28] at the Xinglong Observatory. The TNT photometry is presented, together with Catalina Sky Survey (CSS; http://nesssi.cacr.caltech.edu/catalina/20141118/1411181490344143272.html) and Gaia (http://gsaweb.ast.cam.ac.uk/alerts/alert/Gaia16aog/) photometry downloaded from their respective websites, in Extended Data Figure 2. P48 images were first pre-processed by the Infrared Processing and Analysis Center (IPAC)[29]. Image subtraction and point-spread-function fitting were then performed[30] using pre-explosion images as templates. Magnitudes were calibrated against observations of the same field by the Sloan Digital Sky Survey (SDSS) DR10[31]. P60 images were pre-processed using a PyRAF-based pipeline[26]. Image subtraction, photometry extraction and calibration were performed with the FPipe pipeline[32] using SDSS images as references. LCO images were pre-processed using the Observatory Reduction and Acquisition Control Data Reduction pipeline (ORAC-DR)[33] up to 2016 May 4, and using the custom Python-based BANZAI pipeline afterward. Photometry was then extracted using the PyRAF-based LCOGTSNPipe pipeline[34] to perform point-spread-function fitting and calibration to the AAVSO Photometric All-Sky Survey[35] for BV-band data and SDSS DR8[36] for gri-band data. TNT images were reduced with standard Image Reduction and Analysis Facility (IRAF) routines; point-spread-function fitting was performed using the SNOoPy package and calibrated to the SDSS DR9[37] transformed to the Johnson system[38]. We correct all photometry for Milky Way extinction[39] extracted via the NASA Extragalactic Database. Pre-explosion non-detection limits are presented in Extended Data Figure 3.

We fitted a blackbody spectral energy distribution to every epoch of LCO photometry containing at least three of the $BVgi$ filters obtained within 0.4 days of each other (we exclude r-band and R-band data from the fits owing to contamination from the $H\alpha$ line). For each epoch we perform a blackbody fit using Markov Chain Monte Carlo simulations through the Python emcee package[40] to estimate the blackbody temperature and radius at the measured distance to iPTF14hls of 156 Mpc.

Follow-up spectroscopy. Spectra of iPTF14hls were obtained with the Floyds instrument mounted on the northern LCO 2-m telescope[27], the Andalucia Faint Object Spectrograph and Camera (ALFOSC) mounted on the 2.5-m Nordic Optical Telescope (NOT), the Device Optimized for the LOw RESolution (DOLoRes) mounted on the 3.6-m Telescopio Nazionale Galileo (TNG), the Low Resolution Imaging Spectrometer (LRIS)[41] mounted on the Keck-I 10-m telescope, the DEep Imaging Multi-Object Spectrograph (DEIMOS)[42] mounted on the Keck-II 10-m telescope, the Double Beam Spectrograph (DBSP)[43] mounted on the Palomar 200-inch telescope (P200), the Beijing Faint Object Spectrograph and Camera (BFOSC) on the Xinglong 2.16-m telescope of the National Astronomical Observatories of China, the Yunnan Faint Object Spectrograph and Camera (YFOSC) on the Lijiang 2.4-m telescope of the Yunnan Observatories, and the DeVeny spectrograph mounted on the 4.3-m Discovery Channel Telescope (DCT). The Floyds spectra were reduced using the PyRAF-based floydsspec pipeline. The ALFOSC and DOLORES spectra were reduced using custom MATLAB pipelines. The LRIS spectra were reduced using the IDL LPipe pipeline. The DEIMOS spectrum was reduced using a modified version of the DEEP2 pipeline[44,45] combined with standard PyRAF and IDL routines for trace extraction, flux calibration and telluric correction. The DBSP spectrum was reduced using custom IRAF and IDL routines. The BFOSC, YFOSC and DeVeny spectra were reduced using standard IRAF procedures. No Na I D line absorption is seen at the redshift of the host galaxy, indicating very low host-galaxy extinction at the supernova position.

We fitted each iPTF14hls spectrum to a library of type II supernovae (which includes a full set of SN 1999em spectra[22]) using Superfit[47]. We then calculate the average best-fitting supernova phase, weighing all the possible fits by their corresponding fit scores. We repeat this process for cutouts of the iPTF14hls spectra centred around the $H\alpha$, $H\beta$ and Fe II $\lambda = 5,169$ Å features (separately). The weighted-average best-fit phases for each cutout are presented in Extended Data Figure 4. iPTF14hls can be seen to evolve more slowly than other type II supernovae by a factor of approximately 10 when considering the entire spectrum, as well as when considering the $H\beta$ and the Fe II $\lambda = 5,169$ features separately, and by a factor of 6–7 when considering the $H\alpha$ emission feature separately.

Expansion velocities for different elements in iPTF14hls were measured by fitting a parabola around the minimum of the absorption feature of their respective P Cygni profiles. The difference between the minimum of the best-fit parabola and the rest wavelength of the line was translated to an expansion velocity. The endpoints of each parabolic fit were chosen manually for each line, so that they would remain the same for all spectra. Uncertainties in the velocities were estimated by randomly varying these endpoints 1,000 times by ± 5 Å around their original values.

iPTF14hls is probably not powered by interaction. As mentioned in the main text, interaction between supernova ejecta and pre-existing, dense circumstellar material could cause an increase in luminosity. However, iPTF14hls does not display the spectral line profiles typically seen in such cases (Extended Data Fig. 5).

In some interaction models the collision of the supernova ejecta and the circumstellar material occurs outside the broad-line-forming region, diluting the line emission. Focusing on the approximately 50% luminosity increase of iPTF14hls between rest-frame day 207 and day 232 after discovery (Fig. 1), we find that the spectra taken on day 207 and day 232 are identical up to a global normalization factor. This indicates that the increase in luminosity is equal at all wavelengths, in contrast to the expected line dilution from interaction (Extended Data Fig. 6).

Additional possible indicators of interaction are strong X-ray and/or radio emission. We observed the location of iPTF14hls with the X-Ray Telescope (XRT)[48] onboard the Swift satellite[49] on 2015 May 23.05. A total of 4.9 ks of live exposure time was obtained on the source. We use online analysis tools[50,51] to search for X-ray emission at the location of iPTF14hls. No source is detected with an upper limit on the 0.3–10.0-keV count rate of $<2.3 \times 10^{-3}$ counts s^{-1}. Assuming a power-law spectrum with a photon index of $\Gamma = 2$ and a Galactic H column density[52] of 1.4×10^{20} cm^{-2}, this corresponds to an upper limit on the unabsorbed 0.3–10.0-keV flux of $f_X < 8.4 \times 10^{-14}$ erg cm^{-2} s^{-1}. At the luminosity distance of iPTF14hls this corresponds to a luminosity limit of $L_X < 2.5 \times 10^{41}$ erg s^{-1} (which is roughly 10^{-2} of the peak bolometric luminosity). The lack of X-ray emission disfavours strong interaction in iPTF14hls, though some interacting supernovae display X-ray emission fainter than the limit we deduce here[53].

We observed iPTF14hls also with the Arcminute Microkelvin Imager Large Array (AMI-LA)[54] at 15 GHz on 2015 May 18.59, May 19.77, May 23.63, May 25.65, May 28.66, and May 31.62. Quasars 3C48 and J2035+1056 were used as the flux/bandpass and phase calibrators, respectively. Radio frequency interference excision and calibration of the raw data were done with a fully automated pipeline AMI-REDUCE[55,56]. The calibrated data for the supernova were imported into CASA (Common Astronomy Software Applications) and imaged independently for each epoch into 512×512 pixel maps (4″ per pixel) using the clean task. A similar imaging scheme was used for the concatenated data from all the epochs as well. The supernova was not detected on any of the individual epochs, with 3σ upper limits of 60–120 μJy. The combined 3σ upper limit is 36 μJy. There is a 5%–10% absolute flux calibration uncertainty that we have not considered in these upper limits. On 2016 June 10, iPTF14hls was observed with the VLA at 6.1 GHz. The VLA data were reduced using standard CASA software routines where J0920+4441 and 3C286 were used as phase and flux calibrators. No radio emission was observed at the supernova position to a 3σ upper limit of 21.3 μJy. At the luminosity distance of iPTF14hls, this corresponds to 6.2×10^{26} erg s^{-1} Hz^{-1}, which is fainter than the radio emission of most interacting supernovae[53]. We conclude that iPTF14hls does not show any of the signatures normally seen in supernovae powered by interaction.

A possible central-engine power source for iPTF14hls. A central engine such as the spindown of a magnetar[12,57,58] or fallback accretion onto a black hole[13,59] created after core collapse (assuming the material falling back has sufficient angular momentum to form a disk) could inject power to the supernova, although (as noted in the main text) this may fail to reproduce the observed iron and hydrogen line velocity difference. A magnetar (with an initial spin period of about 5–10 ms and a magnetic field of about $(0.5–1) \times 10^{14}$ G) could produce the observed average luminosity and timescale of iPTF14hls[12]. However, the analytical magnetar light curve required to fit the late-time decline overpredicts the early-time emission of iPTF14hls (Extended Data Fig. 2) and produces a smooth rather than variable light curve[12,13].

For a black-hole central engine, on the other hand, instabilities in the accretion flow might produce strong light-curve variability, as seen in active galactic nuclei[20].

5

In this case, the light curve is expected to eventually settle onto a $t^{-5/3}$ decline rate[21] after the last instability. Such a decline rate is indeed observed for iPTF14hls starting around day 450 (Extended Data Fig. 2), supporting a black-hole power source. We conclude that iPTF14hls does not show the expected signatures of magnetar power (using available analytical models), but might be consistent with black-hole accretion power.

No signs of asymmetry in iPTF14hls. A possible explanation for the high luminosities and apparent emitted energy of iPTF14hls, as well as the discrepancy between its line-forming versus blackbody radii, is strong asymmetry in the explosion. Such asymmetry would be indicated by a polarization signal.

We observed iPTF14hls with the Andalucia Faint Object Spectrograph and Camera (ALFOSC) mounted on the 2.5-m Nordic Optical Telescope (NOT) in polarimetric mode on 2015 November 03 in the R band, and on December 15 in the V band (we also obtained observations on 2015 October 28 and November 14 but we discard them because of very poor observing conditions). We used a 1/2-wave plate in the FAPOL unit (the polarimeter unit in the Filter And Shutter Unit, FASU) and a calcite plate mounted in the aperture wheel, and observed at four different retarder angles (0°, 22.5°, 45°, 67.5°). The data were reduced in a standard manner, using bias frames and flat fields without the polarization units in the light path. The field of view contains one bright star that can be used for calibration and for determining the interstellar polarization in the Galaxy. The low Galactic extinction towards iPTF14hls implies an expected interstellar polarization value[60] of <0.13%.

To measure the fluxes we performed aperture photometry, and to compute the polarisation we followed standard procedures[61]. For our epoch with the best signal-to-noise (2015 November 03), we measure $P = 0.40\% \pm 0.27\%$ for iPTF14hls and $P = 0.17\% \pm 0.09\%$ for the comparison star, in agreement with the interstellar polarization prediction. These results suggest that iPTF14hls is close to spherically symmetric, similar to what is observed for type II-P supernovae during their plateau phase[62]. The 2015 December 15 epoch yields a lower precision ($P = 1.1\% \pm 0.7\%$ for iPTF14hls and $P = 0.80\% \pm 0.23\%$ for the comparison star), but is still consistent with very low asphericity.

Expansion velocities of iPTF14hls. In a supernova, the ejecta are in homologous expansion—that is, the radius of the ejecta at time t evolves as $r = vt$, with faster material at larger radii. Even for perfectly mixed ejecta, at any given time, spectral lines of different elements form in different regions. Specifically, the iron (Fe) lines are formed at smaller radii than the hydrogen (H) lines and therefore display a lower velocity. This is also the case in iPTF14hls. As time passes and the ejecta expand and recombine, the line-forming region of each element moves inward in mass to a region where the outflow is slower. This is why, normally, the velocity of all lines is observed to decrease with time. Thus, following the line velocity over a wide range of time (and hence mass coordinates) provides a 'scan' of the velocity profile over a large range of the ejecta. Although different lines are formed in different regions, all line-forming regions scan the velocity profile of the same ejecta. Therefore, if there is a large velocity gradient in the ejecta, we expect to see both a large velocity difference between the Fe and H lines as well as considerable evolution in the velocity of each line as the material expands. These two features are seen clearly in the typical case of SN 1999em (Extended Data Fig. 7). However, this is not the case in iPTF14hls. On the one hand, there is a large difference between the H and Fe line velocities, indicating a large velocity gradient in the ejecta. On the other hand, the velocity of each line shows almost no evolution in time between day 100 and day 600 after discovery. If the line-forming material were ejected at the time of discovery, then this time span corresponds to a change by a factor of about 6 in radius. In this case, the lack of observed velocity evolution indicates a very shallow velocity gradient in the ejecta, which is inconsistent with the large velocity difference between the lines. However, if the ejection of the line-forming material took place before discovery, then the relative change in radius during the observations is small, indicating that the position of the line-forming region does not change much, potentially solving the apparent contradiction.

The line-forming region of iPTF14hls. The nearly constant line velocities measured in iPTF14hls suggest that the lines form in a massive shell, perhaps ejected prior to the explosion. Here we estimate the mass and energetics required for such a shell to produce the observed line features.

Consider a uniform shell of mass M with a radius r and width Δr. The number density of hydrogen atoms in the shell is:

$$n_{\mathrm{H}} = \frac{Y_{\mathrm{H}} M}{\mu m_{\mathrm{p}} 4\pi r^2 \Delta r} \tag{1}$$

where $Y_{\mathrm{H}} \approx 0.9$ is the number fraction of hydrogen and $\mu \approx 1.34$ is the mean atomic mass for solar gas (m_{p} is the proton mass). In a rapidly expanding, homologous outflow ejected at a time t_{ej}, the strength of a spectral line is characterized by the Sobolev optical depth approximation:

$$\tau_{\mathrm{Sob}} = \frac{\pi e^2}{m_e c} n_1 f t_{\mathrm{ej}} \lambda_0 \tag{2}$$

where n_1 is the number density of atoms in the lower level, f is the line oscillation strength, t_{ej} is the time since explosion, m_e is the mass of the electron and λ_0 is the line rest wavelength. For a line to produce a noticeable absorption component in the spectra, it must have $\tau_{\mathrm{Sob}} \gtrsim 1$.

To estimate the populations in the lower level of the line transition (for the Balmer series this is the $n = 2$ level), we apply the nebular approximation[63], which assumes that the mean intensity of the radiation field at a radius above a nearly blackbody photosphere is $J_\nu(r) = W(r) B_\nu(T_{\mathrm{bb}})$, where B_ν is the Planck function, T_{bb} is the temperature of the photosphere, and $W(r)$ is the geometrical dilution factor of the radiation field:

$$W(r) = \frac{1}{2}\left[1 - \sqrt{1 - r_{\mathrm{p}}^2/r^2}\right] \approx \frac{r_{\mathrm{p}}^2}{4r^2} \tag{3}$$

Here, r_{p} is the photospheric radius and the last expression assumes $r \gg r_{\mathrm{p}}$. For a two-level atom subject to this radiation field, the number density in the $n = 2$ excited state is:

$$n_2 \approx n_1 W \frac{g_2}{g_1} e^{-\Delta E_{1,2}/kT} \tag{4}$$

where (n_1, n_2) and (g_1, g_2) are, respectively, the number density and statistical weights of the $n = 1$ and $n = 2$ levels, and $\Delta E_{1,2}$ is the energy difference between the levels.

Since essentially all of the hydrogen in the shell will be neutral and in the ground state, $n_1 \approx n_{\mathrm{H}}$. The Sobolev optical depth is then:

$$\tau_{\mathrm{H}\alpha} \approx \left[\frac{\pi e^2}{m_e c} f \lambda_0 t_{\mathrm{ej}}\right] \frac{Y_{\mathrm{H}} M}{\mu m_{\mathrm{p}}} \frac{r_{\mathrm{p}}^2}{16\pi r^4 \Delta r} \frac{g_2}{g_1} e^{-\Delta E_{1,2}/kT} \tag{5}$$

Using $g_1 = 2$, $g_2 = 8$, $\Delta E_{1,2} = 10.2\,\mathrm{eV}$, $\lambda_0 = 6,563\,\text{Å}$ (for the Hα transition), and $f = 0.64$, and taking $T = 6,500\,\mathrm{K}$, $\Delta r = \Delta v t_{\mathrm{ej}}$, and $r = v t_{\mathrm{ej}}$ gives

$$\tau_{\mathrm{H}\alpha} \approx 0.96 \left[\frac{M}{45 M_\odot}\right]\left[\frac{600\ \mathrm{days}}{t_{\mathrm{ej}}}\right]^4 \left[\frac{r_{\mathrm{p}}}{1.5 \times 10^{15}\ \mathrm{cm}}\right]^2$$
$$\left[\frac{6{,}000\ \mathrm{km\ s^{-1}}}{\nu}\right]^4 \left[\frac{1{,}000\ \mathrm{km\ s^{-1}}}{\Delta\nu}\right] \tag{6}$$

(where $M_\odot$ is the solar mass). Though approximate, this argument demonstrates that a shell with a mass of the order of a few tens of solar masses is probably required for producing Balmer absorption lines throughout the approximately 600-day duration of the iPTF14hls light curve. The corresponding kinetic energy of the outburst is about 10^{52} erg. In the case where the shell was ejected before the first iPTF14hls observations, the mass and energy required would increase. However, the mass required to associate the line-forming region with the 1954 eruption would be about $10^7 M_\odot$, and hence not reasonable, implying that the line-forming region was ejected in a separate, more recent, eruption.

For comparison, the electron-scattering optical depth of the shell is:

$$\tau_{\mathrm{es}} = n_{\mathrm{H}} x_{\mathrm{H\,II}}\ \sigma_{\mathrm{T}} \Delta r \approx 0.77 x_{\mathrm{H\,II}} \left[\frac{M}{45 M_\odot}\right]\left[\frac{600\ \mathrm{days}}{t_{\mathrm{ej}}}\right]^2 \left[\frac{6{,}000\ \mathrm{km\ s^{-1}}}{\nu}\right]^4 \tag{7}$$

where σ_{T} is the Thomson cross-section and $x_{\mathrm{H\,II}}$ is the fraction of ionized hydrogen. The shell will be largely neutral ($x_{\mathrm{H\,II}} \ll 1$), because the region where the radiation field is sufficient to ionize hydrogen occurs at the photosphere (r_{p}) where the recombination front forms. The shell radius is much larger than r_{p}, so the radiation field is strongly diluted. Thus, while the shell can form line features, it will be optically thin in the continuum and allow most of the pseudo-blackbody continuum from the photosphere to pass through.

The velocity of $6{,}000\,\mathrm{km\,s^{-1}}$ seen for Hα at day 600 after discovery is also seen for Hβ at day 200 after discovery. If we calculate the optical depth (see equation (5)) for Hβ (plugging in the parameters for day $200 + t_0$, where t_0 is the offset between the ejection of the shell and discovery) and equate it to that of Hα at day $600 + t_0$, then we can solve for the ejection time t_0, assuming that the optical depths for Hα and Hβ were the same when each was observed at $6{,}000\,\mathrm{km\,s^{-1}}$, and that the entire shell was ejected simultaneously. Using $\lambda_0 = 4{,}861\,\text{Å}$ and $f = 0.12$ for the Hβ transition, we find $t_0 \approx 100$–200 days (the main source of error is the uncertainty in the precise temperature difference between the two epochs), meaning that the line-forming shell was ejected 100–200 days before discovery. We have deep non-detection limits for part of this epoch (Extended Data Fig. 3), suggesting that the

6

ejection of the shell could have been a low-luminosity event. This estimation of the ejection time, however, relies on many simplifying assumptions, so it should be considered only as an approximation.

A historical outburst at the position of iPTF14hls. The Palomar Observatory Sky Survey (POSS)[64] observed the field of iPTF14hls on 1954 February 23 in the blue and red filters. POSS-II[65] then re-observed the field on 1993 January 2 in the blue filter and on 1995 March 30 in the red filter. We obtained these images through the STScI Digitized Sky Survey and we find a source at the position of iPTF14hls in the blue image from POSS that is not present in the blue image from POSS-II (Extended Data Fig. 8). We do not see this source in either of the red images, but they are not as deep as the blue images (the limiting magnitude is roughly 20 for the red images compared to 21.1 for the blue images)[64].

We register the POSS blue image to the POSS-II blue image using the IRAF task wregister. We then use the apphot package in PyRAF, with a 3-pixel aperture, to measure the flux in six stars in the field near the position of iPTF14hls to determine a zero-point offset for the two images. We find an offset of 0.132 ± 0.050 mag. We then perform the same measurement around the nucleus of the host galaxy of iPTF14hls and find an offset of 0.141 mag, consistent with the zero-point offset. Next we perform the same aperture photometry measurement at the position of iPTF14hls in both images. We find a magnitude difference of 0.31 ± 0.14 over the host-galaxy level confirming the presence of an outburst in the 1954 image at the position of iPTF14hls at a 2.2σ confidence level. Owing to the nonlinear nature of the photographic plates used in the two POSS surveys, as well as differences between the filters[65], we cannot perform meaningful image subtraction between the POSS epochs to obtain more accurate photometric measurements. We consider this confidence level to be a conservative estimate; the outburst can be seen clearly by eye in the images (Extended Data Fig. 8).

We calibrate the six stars used for the zero-point comparison to SDSS u-band plus g-band fluxes (the POSS blue filter roughly covers the SDSS u and g bands)[64] and find that the magnitude of the 1954 outburst (after removing the host-galaxy contribution) is $20.4 \pm 0.1\text{(stat)} \pm 0.8\text{(sys)}$. The first error is statistical and due to photometric measurement uncertainties, while the second error is systematic and caused by the calibration to SDSS (the large error value is probably produced by filter and detector differences between POSS and SDSS).

This corresponds to an absolute magnitude for the outburst of approximately -15.6 at the luminosity distance of iPTF14hls (this is only a lower limit on the peak luminosity of the eruption, as we have only one epoch of observations). Such an eruption may be produced by the pulsational pair instability[2–5]. Eruptions of similar luminosity (though probably caused by different instabilities) are inferred to be common in type IIn supernova progenitors in the last year prior to explosion[66]. Spectra and broad-band colours are available for three such possible outbursts—a precursor to PTF10bjb[66], PTF13efv (a precursor to SNHunt275)[67] and the first 2012 outburst of SN2009ip[68]—all of which display rather flat continuum emission, consistent with the limited colour information we have for the 1954 outburst of iPTF14hls (that is, the red nondetection limit being about 0.4 magnitudes brighter than the blue detection).

Given the host galaxy size of about 10–100 times the centroiding error of the outburst, and a typical supernova rate of about 1/100 per galaxy per year, there is a probability of a few per cent that the detected outburst is an unrelated supernova that happened to occur at the position of iPTF14hls.

The rate of iPTF14hls-like events. On 2014 November 18, iPTF14hls was independently discovered by the Catalina Real-Time Transient Survey[25] as CSS141118:092034+504148, and more recently the event was reported to the Transient Name Server as AT 2016bse and Gaia16aog. The fact that it was discovered multiple times, but dismissed as a run-of-the-mill type II-P supernova, suggests that similar events may have been missed in the past. We ourselves would not have noticed the unique properties of iPTF14hls had the iPTF survey scheduler not automatically continued to monitor the position of iPTF14hls. In addition, if iPTF14hls-like events are limited to low-mass galaxies, then targeted transient surveys would have missed them completely.

To our knowledge, iPTF14hls is the only supernova ever discovered to show such long-lived, slowly evolving type II-P-like emission. The PTF and iPTF surveys discovered 631 type II supernovae, indicating that iPTF14hls-like events could be about 10^{-3}–10^{-2} of the type II supernova rate. Since luminous, long-lived varying events could be easier to detect in transient surveys compared to normal supernovae, the true volumetric rate of iPTF14hls-like events could be much lower. On the other hand, we cannot rule out whether such events were discovered in the past but dismissed as normal type II-P supernovae after one spectrum with no subsequent follow-up observations or as possible active galactic nuclei owing to the light curve behaviour. It is therefore not possible to calculate a precise rate for iPTF14hls-like events based on this single discovery, but whatever the explosion channel, it is likely to be rare. Even so, the Large Synoptic Survey Telescope could find hundreds of

iPTF14hls-like events in its decade-long survey of the transient sky (and more if iPTF14hls-like events are more common in the early Universe, as is indicated by the possible low-metallicity environment of iPTF14hls).

The host galaxy of iPTF14hls. We obtained a spectrum of the host galaxy of iPTF14hls on 2015 December 11 with the Low Resolution Imaging Spectrometer (LRIS)[41] mounted on the Keck-I 10-m telescope. The spectrum was reduced using standard techniques optimized for Keck+LRIS by the CarPy package in PyRAF, and flux calibrated with spectrophotometric standard stars obtained on the night of our observations in the same instrument configuration. The host-galaxy spectrum, which is available for download via WISeREP[46], shows clear detections of Hα, Hβ, [O II] $\lambda = 3{,}727$ Å and [O III] $\lambda = 4{,}958$ Å and 5,007 Å, which we use to determine a redshift of 0.0344. A faint detection of [N II] $\lambda = 6{,}583$ Å is also possible, but the feature is difficult to confirm because the continuum is contaminated by broad Hα emission from the nearby supernova. All of the lines are weak (equivalent width <20 Å) and no other lines are strongly detected. We extracted the fluxes of all lines by fitting Gaussians to their profiles (Extended Data Table 1), and calculated the metallicity by fitting[69] the line-strength ratios using several different diagnostics and calibrations (Extended Data Table 2). We find a range of metallicity estimates of $12 + \log(\text{O/H}) = 8.3$–$8.6$, corresponding to about $(0.4$–$0.9)Z_\odot$ (where $Z_\odot$ is the solar metallicity)[70]. A low metallicity could help explain how the progenitor of iPTF14hls retained a very massive hydrogen envelope. Future, more direct environment studies will be able to better probe the metallicity at the explosion site.

We fitted the SDSS $ugriz$ photometry of the host galaxy[71] with standard spectral energy distribution fitting techniques[72] using the BC03[73] stellar population synthesis models. Assuming a metallicity of $0.5Z_\odot$, the best-fit total stellar mass is $(3.2 \pm 0.5) \times 10^8 M_\odot$, similar to that of the Small Magellanic Cloud.

Data availability. The photometric data that support the findings of this study are available in the Open Supernova Catalog[81], https://sne.space/sne/iPTF14hls/. The spectroscopic data that support the findings of this study are available on the Weizmann Interactive Supernova data REPository (WISeREP)[46], https://wiserep.weizmann.ac.il/, and on the Open Supernova Catalog. Source Data for Figs 1, 3 and 4, and for Extended Data Figures 2, 3 and 4 are provided with the online version of the paper.

23. Cao, Y., Nugent, P. E. & Ka sliwal, M. M. Intermediate Palomar Transient Factory: realtime image subtraction pipeline. *Publ. Astron. Soc. Pacif.* **128,** 114502 (2016).
24. Shappee, B. J. *et al.* The man behind the curtain: X-rays drive the UV through NIR variability in the 2013 active galactic nucleus outburst in NGC 2617. *Astrophys. J.* **788,** 48 (2014).
25. Drake, A. J. *et al.* First results from the Catalina Real-time Transient Survey. *Astrophys. J.* **696,** 870–884 (2009).
26. Cenko, S. B. *et al.* The Automated Palomar 60 Inch Telescope. *Publ. Astron. Soc. Pacif.* **118,** 1396–1406 (2006).
27. Brown, T. M. *et al.* Las Cumbres Observatory Global Telescope Network. *Publ. Astron. Soc. Pacif.* **125,** 1031–1055 (2013).
28. Huang, F. *et al.* The photometric system of the Tsinghua-NAOC 80-cm telescope at NAOC Xinglong Observatory. *Res. Astron. Astrophys.* **12,** 1585–1596 (2012).
29. Laher, R. R. *et al.* IPAC image processing and data archiving for the Palomar Transient Factory. *Publ. Astron. Soc. Pacif.* **126,** 674–710 (2014).
30. Sullivan, M. *et al.* Photometric selection of high-redshift type Ia supernova candidates. *Astron. J.* **131,** 960–972 (2006).
31. Ahn, C. P. *et al.* The tenth data release of the Sloan Digital Sky Survey: first spectroscopic data from the SDSS-III Apache Point Observatory Galactic Evolution Experiment. *Astrophys. J. Suppl. Ser.* **211,** 17 (2014).
32. Fremling, C. *et al.* PTF12os and iPTF13bvn. Two stripped-envelope supernovae from low-mass progenitors in NGC 5806. *Astron. Astrophys.* **593,** A68 (2016).
33. Jenness, T. & Economou, F. ORAC-DR: a generic data reduction pipeline infrastructure. *Astron. Comput.* **9,** 40–48 (2015).
34. Valenti, S. *et al.* The diversity of Type II supernova versus the similarity in their progenitors. *Mon. Not. R. Astron. Soc.* **459,** 3939–3962 (2016).
35. Henden, A. A., Welch, D. L., Terrell, D. & Levine, S. E. The AAVSO Photometric All-Sky Survey (APASS). *Am. Astron. Soc. Meet. Abstr.* **214,** 407.02 (2009).
36. Aihara, H. *et al.* The eighth data release of the Sloan Digital Sky Survey: first data from SDSS-III. *Astrophys. J. Suppl. Ser.* **193,** 29 (2011).
37. Ahn, C. P. *et al.* The ninth data release of the Sloan Digital Sky Survey: first spectroscopic data from the SDSS-III Baryon Oscillation Spectroscopic Survey. *Astrophys. J. Suppl. Ser.* **203,** 21 (2012).
38. Chonis, T. S. & Gaskell, C. M. Setting UBVRI photometric zero-points using Sloan Digital Sky Survey ugriz magnitudes. *Astron. J.* **135,** 264–267 (2008).
39. Schlafly, E. F. & Finkbeiner, D. P. Measuring reddening with SDSS stellar spectra and recalibrating SFD. *Astrophys. J.* **737,** 103 (2011).
40. Foreman-Mackey, D., Hogg, D. W., Lang, D. & Goodman, J. emcee: the MCMC hammer. *Publ. Astron. Soc. Pacif.* **125,** 306–312 (2013).
41. Oke, J. B. *et al.* The Keck Low-Resolution Imaging Spectrometer. *Publ. Astron. Soc. Pacif.* **107,** 375 (1995).
42. Faber, S. M. *et al.* in *Instrument Design and Performance for Optical/Infrared Ground-based Telescopes* (eds Iye, M. & Moorwood, A. F. M.) *Proc. SPIE* **4841,** 1657–1669 (2003).

43. Oke, J. B. & Gunn, J. E. An efficient low resolution and moderate resolution spectrograph for the Hale telescope. *Publ. Astron. Soc. Pacif.* **94,** 586 (1982).
44. Cooper, M. C., Newman, J. A., Davis, M., Finkbeiner, D. P., & Gerke, B. F. spec2d: DEEP2 DEIMOS Spectral Pipeline. *Astrophysics Source Code Library* ascl:1203.003 (2012).
45. Newman, J. A. *et al.* The DEEP2 galaxy redshift survey: design, observations, data reduction, and redshifts. *Astrophys. J.* **208,** 5 (2013).
46. Yaron, O. & Gal-Yam, A. WISeREP—an interactive supernova data repository. *Publ. Astron. Soc. Pacif.* **124,** 668–681 (2012).
47. Howell, D. A. *et al.* Gemini spectroscopy of supernovae from SNLS: improving high redshift SN selection and classification. *Astrophys. J.* **634,** 1190–1201 (2005).
48. Burrows, D. N. *et al.* The Swift X-ray telescope. *Space Sci. Rev.* **120,** 165–195 (2005).
49. Gehrels, N. *et al.* The Swift gamma-ray burst mission. *Astrophys. J.* **611,** 1005–1020 (2004).
50. Evans, P. A. *et al.* An online repository of Swift/XRT light curves of GRBs. *Astron. Astrophys.* **469,** 379–385 (2007).
51. Evans, P. A. *et al.* Methods and results of an automatic analysis of a complete sample of Swift-XRT observations of GRBs. *Mon. Not. R. Astron. Soc.* **397,** 1177–1201 (2009).
52. Willingale, R., Starling, R. L. C., Beardmore, A. P., Tanvir, N. R. & O'Brien, P. T. Calibration of X-ray absorption in our Galaxy. *Mon. Not. R. Astron. Soc.* **431,** 394–404 (2013).
53. Margutti, R. *et al.* Ejection of the massive hydrogen-rich envelope timed with the collapse of the stripped SN2014C. *Astrophys. J.* **835,** 140 (2017).
54. Zwart, J. T. L. *et al.* The Arcminute Microkelvin Imager. *Mon. Not. R. Astron. Soc.* **391,** 1545–1558 (2008).
55. Davies, M. L. *et al.* Follow-up observations at 16 and 33 GHz of extragalactic sources from WMAP 3-year data: I—spectral properties. *Mon. Not. R. Astron. Soc.* **400,** 984–994 (2009).
56. Perrott, Y. C. *et al.* AMI galactic plane survey at 16 GHz: I—observing, mapping and source extraction. *Mon. Not. R. Astron. Soc.* **429,** 3330–3340 (2013).
57. Ostriker, J. P. & Gunn, J. E. On the nature of pulsars. I. Theory. *Astrophys. J.* **157,** 1395 (1969).
58. Woosley, S. E. Bright supernovae from magnetar birth. *Astrophys. J.* **719,** L204–L207 (2010).
59. Colgate, S. A. Neutron-star formation, thermonuclear supernovae, and heavy-element reimplosion. *Astrophys. J.* **163,** 221 (1971).
60. Serkowski, K., Mathewson, D. L. & Ford, V. L. Wavelength dependence of interstellar polarization and ratio of total to selective extinction. *Astrophys. J.* **196,** 261 (1975).
61. Patat, F. & Romaniello, M. Error analysis for dual-beam optical linear polarimetry. *Publ. Astron. Soc. Pacif.* **118,** 146–161 (2006).
62. Leonard, D. C. & Filippenko, A. V. Spectropolarimetry of the type II supernovae 1997ds, 1998A, and 1999gi. *Publ. Astron. Soc. Pacif.* **113,** 920–936 (2001).
63. Abbott, D. C. & Lucy, L. B. Multiline transfer and the dynamics of stellar winds. *Astrophys. J.* **288,** 679 (1985).
64. Minkowski, R. L. & Abell, G. O. The National Geographic Society—Palomar Observatory Sky Survey. In *Basic Astronomical Data: Stars and Stellar Systems* (ed. Strand, K. A.) 481–487 (Univ. Chicago Press, 1963).
65. Reid, I. N. *et al.* The second Palomar Sky Survey. *Publ. Astron. Soc. Pacif.* **103,** 661 (1991).
66. Ofek, E. O. *et al.* Precursors prior to type IIn supernova explosions are common: precursor rates, properties, and correlations. *Astrophys. J.* **789,** 104 (2014).
67. Ofek, E. O. *et al.* PTF13efv: an outburst 500 days prior to the SNHunt 275 explosion and its radiative efficiency. *Astrophys. J.* **824,** 6 (2016).
68. Fraser, M. *et al.* SN 2009ip a la PESSTO: no evidence for core-collapse yet. *Mon. Not. R. Astron. Soc.* **433,** 1312–1337 (2013).
69. Bianco, F. B. *et al.* Monte Carlo method for calculating oxygen abundances and their uncertainties from strong-line flux measurements. *Astron. Comput.* **16,** 54–66 (2016).
70. Asplund, M., Grevesse, N., Sauval, A. J. & Scott, P. The chemical composition of the Sun. *Annu. Rev. Astron. Astrophys.* **47,** 481–522 (2009).
71. Alam, S. *et al.* The eleventh and twelfth data releases of the Sloan Digital Sky Survey: final data from SDSS-III. *Astrophys. J. Suppl. Ser.* **219,** 12 (2015).
72. Perley, D. A. *et al.* A population of massive, luminous galaxies hosting heavily dust-obscured gamma-ray bursts: implications for the use of GRBs as tracers of cosmic star formation. *Astrophys. J.* **778,** 128 (2013).
73. Bruzual, G. & Charlot, S. Stellar population synthesis at the resolution of 2003. *Mon. Not. R. Astron. Soc.* **344,** 1000–1028 (2003).
74. Nagao, T., Maiolino, R. & Marconi, A. Gas metallicity diagnostics in star-forming galaxies. *Astron. Astrophys.* **459,** 85–101 (2006).
75. Denicoló, G., Terlevich, R. & Terlevich, E. New light on the search for low metallicity galaxies I. The N$_2$ calibrator. *Mon. Not. R. Astron. Soc.* **330,** 69–74 (2002).
76. Pettini, M. & Pagel, B. E. J. [O III]/[N II] as an abundance indicator at high redshift. *Mon. Not. R. Astron. Soc.* **348,** L59–L63 (2004).
77. Maiolino, R. *et al.* AMAZE. I. The evolution of the mass-metallicity relation at $z > 3$. *Astron. Astrophys.* **488,** 463–479 (2008).
78. Marino, R. A. *et al.* The O$_3$N$_2$ and N$_2$ abundance indicators revisited: improved calibrations based on CALIFA and Te-based literature data. *Astron. Astrophys.* **559,** A114 (2013).
79. Kobulnicky, H. A. & Kewley, L. J. Metallicities of 0.3. *Astrophys. J.* **617,** 240–261 (2004).
80. Kewley, L. J. & Dopita, M. A. Using strong lines to estimate abundances in extragalactic H ii regions and starburst galaxies. *Astrophys. J. Suppl. Ser.* **142,** 35–52 (2002).
81. Guillochon, J. *et al.* An open catalog for supernova data. *Astrophys. J.* **835,** 64 (2017).

8
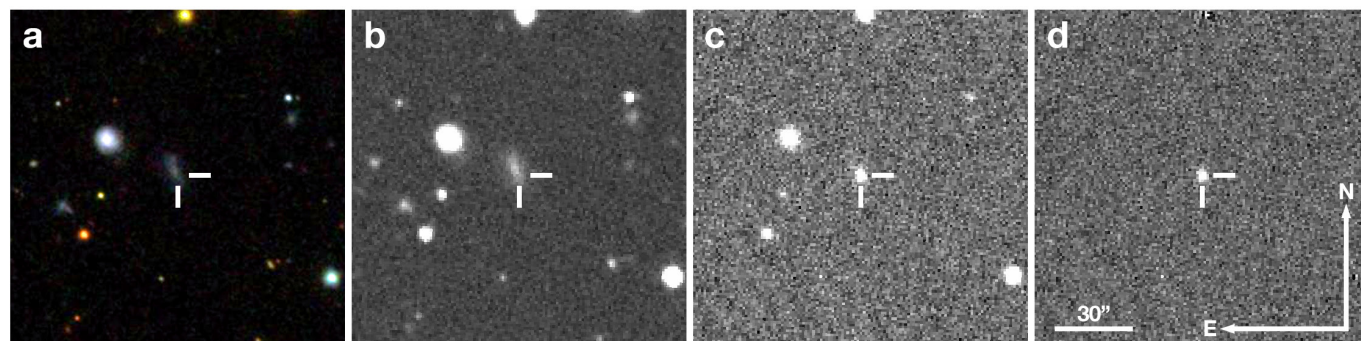
Extended Data Figure 1 | The discovery and environment of iPTF14hls. **a**, SDSS image centered at the position of iPTF14hls. **b**, Palomar 48-inch deep coadded pre-discovery reference image. **c**, Palomar 48-inch discovery image of iPTF14hls. **d**, The result of subtracting the reference image from the discovery image. The position of iPTF14hls is indicated by tick marks in each image.
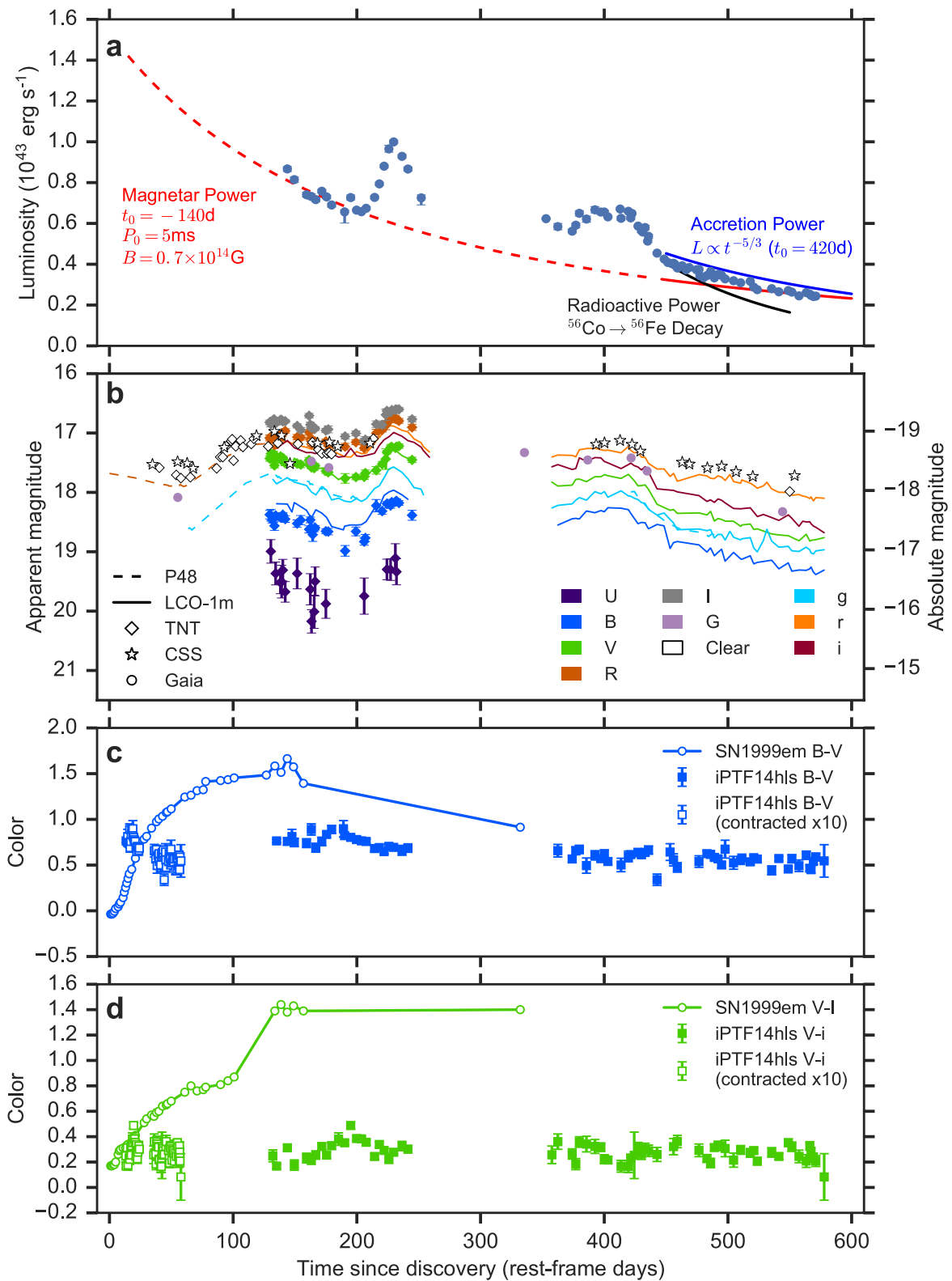
Extended Data Figure 2 | Additional photometry of iPTF14hls. The bolometric light curve of iPTF14hls (**a**) deduced from the blackbody fits shows a late-time decline rate that is slower than the radioactive decay of ^{56}Co (black), but consistent with both delayed accretion power (blue; t_0 is the onset of accretion at the last peak which could represent a final fallback event) and magnetar spindown power (red; t_0 is the formation time of the magnetar, P_0 is the initial spin period and B is the magnetic field in this simple analytic model). The magnetar model, however, is not consistent with the luminosity during the first 100 days, as implied by the P48, CSS and Gaia observations (**b**), unless the early-time magnetar emission is substantially adiabatically degraded. TNT photometry of

iPTF14hls and publicly available CSS photometry (retrieved from the CSS website) and Gaia photometry (retrieved from the Gaia Alerts website) not presented in Fig. 1 are shown in **b**. Data from the P48 (dashed lines) and the LCO 1-m telescope (solid lines) presented in Fig. 1 are shown for comparison. Photometric points from the same day, instrument and filter are averaged for clarity. The $B - V$ (**c**) and $V - I/i$ (**d**) colour evolution of iPTF14hls from the LCO 1-m data (filled squares) differs from that of the normal type II-P SN 1999em (empty circles)[22], even when contracting the iPTF14hls data by a factor of 10 in time (empty squares) to compensate for the slow evolution observed in its spectra compared to that of normal type II-P supernovae. All error bars, when available, denote 1σ uncertainties.

10
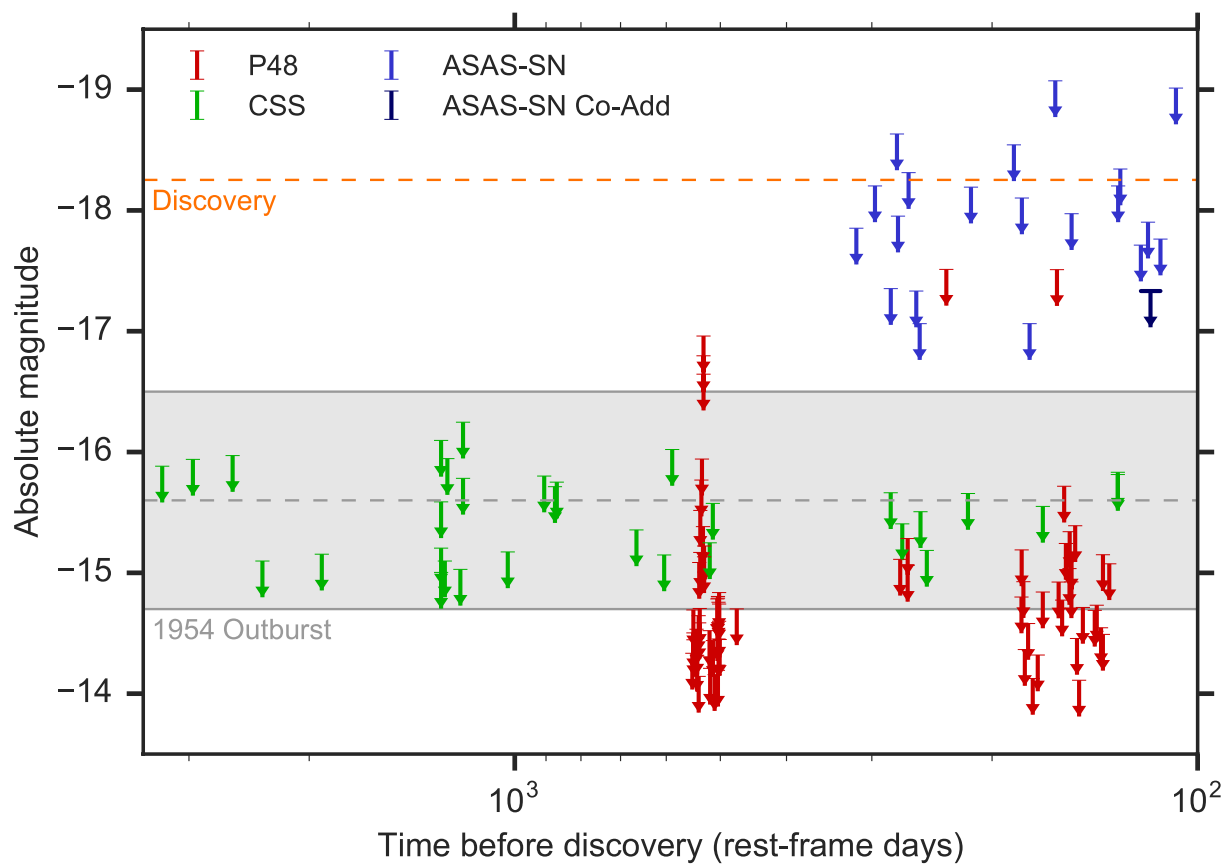
Extended Data Figure 3 | Pre-explosion nondetection limits for iPTF14hls. Data from P48 (*R* band, 3σ nondetections), CSS (unfiltered, obtained via the CSS website), and ASAS-SN (*V* band, 3σ nondetections—the dark-blue arrow is a deep coadd of the three images taken during the time range denoted by the horizontal line in the marker) are shown. The dashed line indicates the discovery magnitude and the shaded region shows the 1954 outburst magnitude and its uncertainty.
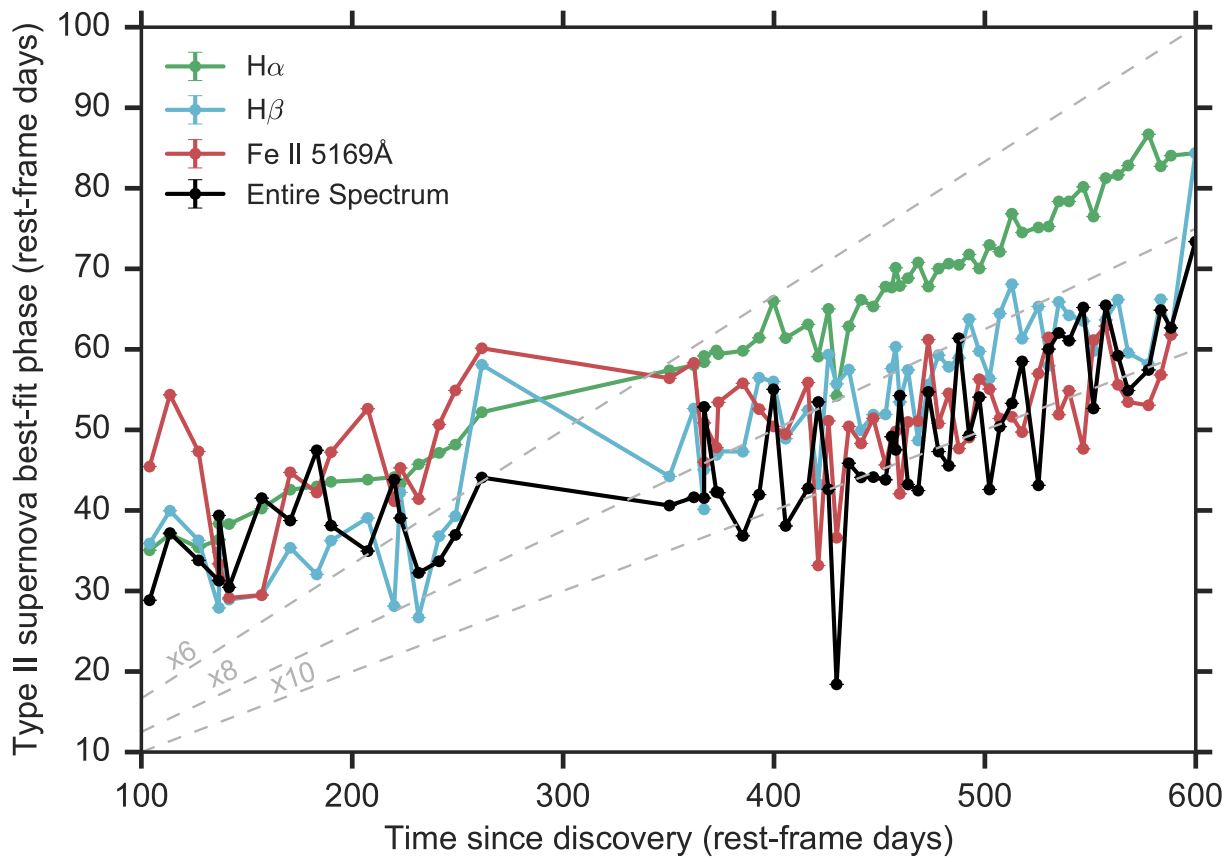
Extended Data Figure 4 | The slow spectral evolution of iPTF14hls compared to normal supernovae. Weighted average best-fit phase of iPTF14hls spectra from Superfit[47], compared to the true spectral phase are shown, when fitting the entire spectrum (black) or only certain line regions as noted. The dashed lines denote constant ratios between the observed and best-fit phases (assuming the explosion happened at discovery). The spectra of iPTF14hls evolve a factor of approximately 6–10 times slower than those of other type II supernovae.

12
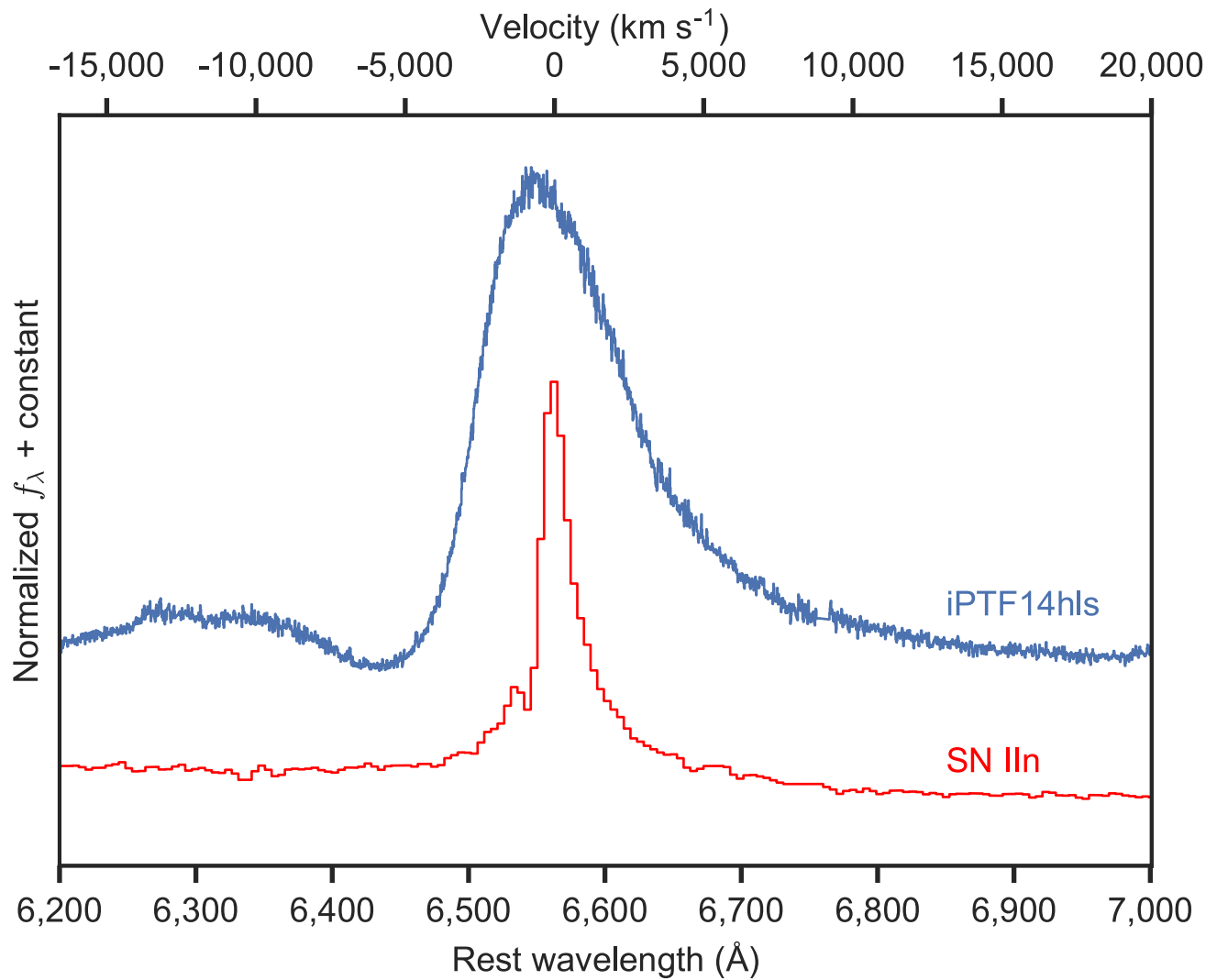
Extended Data Figure 5 | A lack of spectral interaction signatures in iPTF14hls. The Hα region in our highest-resolution spectrum of iPTF14hls taken on 2016 June 4 using DEIMOS on Keck II (blue), expressed in terms of normalized flux density as a function of rest-frame wavelength (bottom axis), compared to the interaction-powered type IIn SN2005cl[18] (red). The top axis is the corresponding velocity of Hα. iPTF14hls shows no signs of the narrow emission or narrow P Cygni features seen in interacting supernovae.
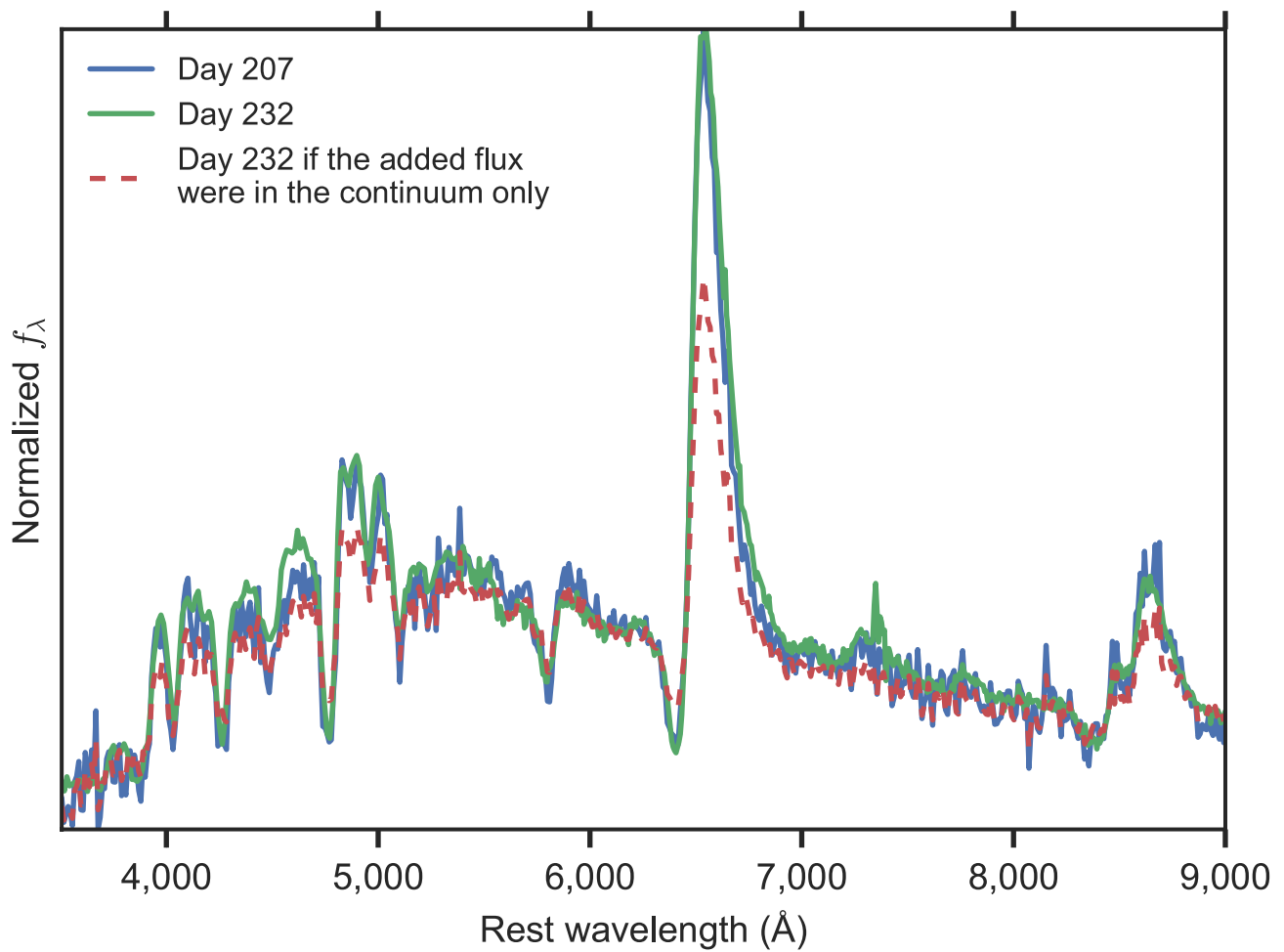
Extended Data Figure 6 | The nature of the increased flux during the brightest peak of iPTF14hls. Spectra of iPTF14hls expressed in terms of normalized flux density as a function of rest-frame wavelength taken on rest-frame day 207 (right before the rise to the brightest peak in the light curve) and day 232 (at the brightest peak in the light curve) after discovery (solid lines) are shown. The similarity of the spectra indicates that the increase of about 50% in luminosity observed in the light curve between the two epochs is equal at all wavelengths. If the increase were due only to the continuum flux, then the line emission on day 232 would have been diluted by the continuum (as simulated by the dashed line).

14
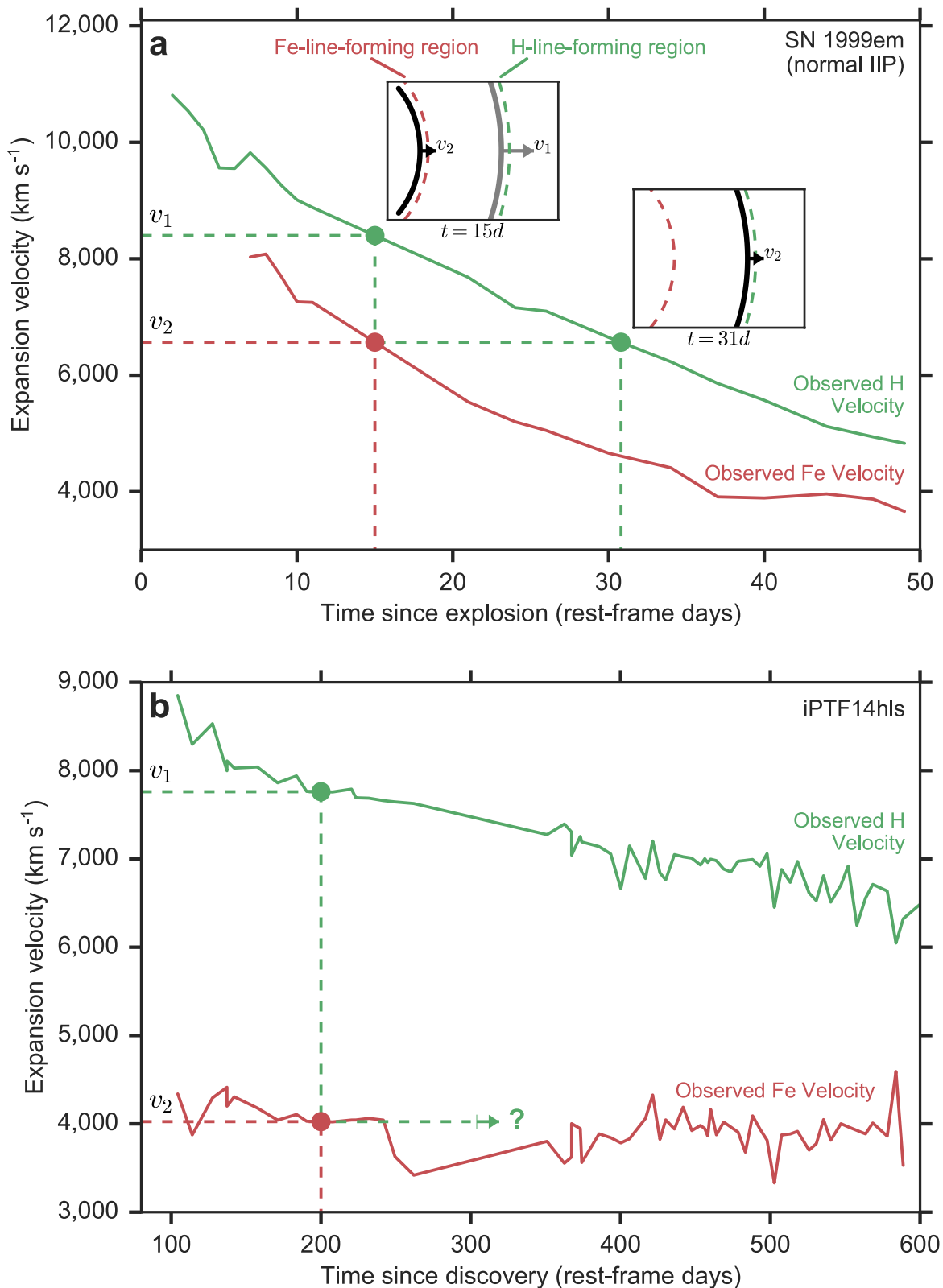
Extended Data Figure 7 | The perplexing velocity evolution of iPTF14hls. Evolution of the measured velocity gradient in the normal type II-P SN 1999em[22] (**a**) and in iPTF14hls (**b**) are shown. At a given time, the H-line-forming region is at material expanding with velocity v_1, while the Fe-line-forming region is at material expanding with lower velocity v_2 (top inset in **a**). For SN 1999em, the H-line-forming region soon reaches the material expanding at velocity v_2 as it moves inward in mass (bottom inset in **a**) and v_2 is measured in the H lines. For iPTF14hls, in contrast, the H-line-forming region does not reach the material expanding at v_2 even after the time since discovery increases by a factor of 6. If the material were ejected at the time of discovery, this would indicate an increase in the radius of the line-forming regions by a factor of about 6, which is unlikely given the observed velocity gradient between the H and Fe lines. If the material were ejected before discovery, on the other hand, the relative expansion in radius would be much smaller, thus offering one possible explanation for the constant velocity gradient observed in iPTF14hls.

15
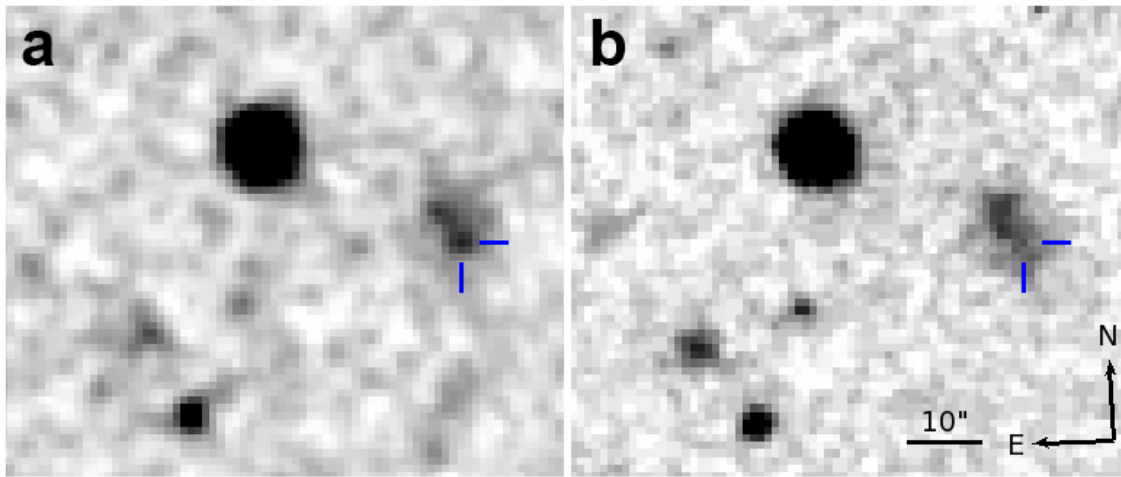
Extended Data Figure 8 | A historic eruption at the position of iPTF14hls. Blue-filter images of the position of iPTF14hls (marked by blue ticks) from 1954 February 23 (POSS; **a**) and 1993 January 2 (POSS-II; **b**) are shown. A source is visible at the position of iPTF14hls in the 1954 image, which is not there in the 1993 image. Using aperture photometry, we find that the 1954 source is 0.31 ± 0.14 mag brighter than the underlying host galaxy at that position, corresponding to a rough outburst magnitude of about -15.6 at the luminosity distance of iPTF14hls, after removing the host-galaxy contribution and calibrating the field to the SDSS $u+g$ bands.

Extended Data Table 1 | iPTF14hls host-galaxy line fluxes

Line	Flux	Flux Error
[O II] 3727 Å	2.050×10^{-16}	1.152×10^{-17}
Hβ	5.666×10^{-17}	6.349×10^{-18}
[O III] 4958 Å	1.742×10^{-17}	6.130×10^{-18}
[O III] 5007 Å	1.003×10^{-16}	6.171×10^{-18}
Hα	1.539×10^{-16}	4.089×10^{-18}
[N II] 6583 Å	1.361×10^{-17}	4.095×10^{-18}

Data are shown in erg s^{-1} cm^{-2}. Errors denote 1σ uncertainties.

Extended Data Table 2 | iPTF14hls host-galaxy metallicity values

Diagnostic	Metallicity	Lower Error	Upper Error
N06-N2[74]	8.339	-0.126	+0.098
N06-R23[74]	8.633	-0.166	+0.071
D02[75]	8.334	-0.166	+0.139
PP04-N2Ha[76]	8.250	-0.059	+0.044
PP04-O3N2[76]	8.309	-0.051	+0.037
M08-N2Ha[77]	8.458	-0.116	+0.076
M13-O3N2[78]	8.252	-0.035	+0.025
M13-N2[78]	8.249	-0.078	+0.060
KK04-N2Ha[79]	8.490	-0.127	+0.080
KD02comb[80]	8.386	-0.130	+0.055

Data are shown as $12 + \log(O/H)$ values under different diagnostics and calibrations from refs 74–80. Error ranges denote 1σ uncertainties.

18

New ZZ Ceti Stars from the LAMOST Survey

Jie Su[1,2,5] , Jianning Fu[1] , Guifang Lin[2,3,4] , Fangfang Chen[1], Pongsak Khokhuntod[1], and Chunqian Li[1]
[1] Department of Astronomy, Beijing Normal University, Beijing 100875, China; jnfu@bnu.edu.cn
[2] Key Laboratory for the Structure and Evolution of Celestial Objects, Chinese Academy of Sciences, Kunming 650216, China
[3] Yunnan Observatories, Chinese Academy of Sciences, Kunming 650216, China
[4] Center for Astronomical Mega-Science, Chinese Academy of Sciences, Beijing 100012, China

Abstract

The spectroscopic sky survey carried out by the Large Sky Area Multi-Object Fiber Spectroscopic Telescope (LAMOST) provides the largest stellar spectra library in the world to date. A large number of new DA white dwarfs had been identified based on the LAMOST spectra. The effective temperature ($T_{\rm eff}$) and surface gravity (log g) of most DA white dwarfs were determined and published in the catalogs. We selected ZZ Ceti candidates from the published catalogs by considering whether their $T_{\rm eff}$ are situated in the ZZ Ceti instability strip. The follow-up time-series photometric observations for the candidates were performed in 2015 and 2016. Four stars: LAMOST J004628.31+343319.90, LAMOST J062159.49+252335.9, LAMOST J010302.46+433756.2, and LAMOST J013033.90+273757.9 are finally confirmed to be new ZZ Ceti stars. They show dominant peaks with amplitudes rising above the 99.9% confidence level in the amplitude spectra. As LAMOST J004628.31+343319.90 has an estimated mass of $\sim 0.40\,M_\odot$, and LAMOST J013033.90+273757.9 has a mass of $\sim 0.45\,M_\odot$ derived from their log g values, these two stars are inferred to be potential helium-core white dwarfs.

Key words: stars: oscillations – surveys – white dwarfs

1. Introduction

White dwarfs are the final evolutionary stage of low- and medium-mass stars. They are stellar remnants composed mostly of electron degenerate matter. The vast majority ($\sim$98%) of stars in the universe are expected to evolve into white dwarfs. They thus present an important boundary condition for investigating the previous evolution of stars. White dwarfs are recognized to be reliable clocks for determining the cosmic chronology, due to the simplicity of their evolution. In particular, white dwarfs are ready-made laboratories for studying physical processes under extreme conditions (Winget & Kepler 2008; Althaus et al. 2010).

There are separate instability strips of white dwarfs that associate with their atmosphere composition. More than 80% of white dwarfs are classified under the spectral type of DA, which have hydrogen-rich atmospheres. The instability strip of DA white dwarfs is located in a narrow range of effective temperature ($T_{\rm eff}$) between $\sim$12,500 and $\sim$10,500 K for a typical mass of $\sim 0.6\,M_\odot$(Gianninas et al. 2011). As DA white dwarfs cool and pass through the corresponding instability strip, pulsations are thought to be excited by both the κ–γ mechanism due to the partial ionization of hydrogen (Dolez & Vauclair 1981; Winget et al. 1982) and by the convective driving mechanism (Brickhill 1991). The pulsations in DA white dwarfs result in brightness variations with typical periods between $\sim$100 and $\sim$1500 s. The pulsating DA white dwarfs are known as DAV or ZZ Ceti stars.

Pulsations observed in pulsating white dwarfs are non-radial g-modes, with buoyancy as the restoring force. Different pulsating modes propagate through different regions inside a white dwarf. By detecting the pulsating modes and matching them to those of theoretical models, one can probe the invisible interior of a white dwarf to get information about its composition and internal structure, and then determine its stellar parameters such as masses (total mass and masses of H/He layers), effective temperature, luminosity, rotation period, magnetic field strength, etc. This technique is called asteroseismology, somewhat similar to the technique that seismologists use to study the interior of the Earth using seismic waves.

Research on ZZ Ceti stars has been carried out for decades since the discovery of the first ZZ Ceti star, HL Tau 76, by Landolt (1968). Detailed asteroseismological analyses require precise identification of pulsating modes, which requires a long uninterrupted high-precision observation of the targets. Conventional ground-based observations have their limitations on obtaining long continuous data. However, the barriers have been overcome by multi-site campaigns, especially through the Whole Earth Telescope (Nather et al. 1990) or by space missions such as *Kepler* (Borucki et al. 2010). On the other hand, comprehensive asteroseismological research requires a large sample of pulsating white dwarfs. In order to enlarge the sample, the search for new pulsating white dwarfs is necessary.

The Large Sky Area Multi-Object Fiber Spectroscopic Telescope (LAMOST, also called Guoshoujing Telescope), as one of the National Major Scientific Projects undertaken by the Chinese Academy of Science, is located in the Xinglong Observatory of National Astronomical Observatories at the Chinese Academy of Sciences. It is a special quasi-meridian reflecting Schmidt telescope with 4000 fibers in a field of view (FOV) of $5° \times 5°$, which guarantees a high efficiency of acquiring spectra (Cui et al. 2012). The spectroscopic sky survey carried out by LAMOST has been running since 2011. The pilot survey was launched in 2011 October and ended in 2012 June (Zhao et al. 2012; Luo et al. 2012). A five-year regular survey, which was initiated in 2012 September, had been terminated in 2017 June. In the past five years of the survey, a total number of 7,664,073 spectra (the fourth data release, DR4, including 6,856,896 stars, 118,657 galaxies, 36,374 quasars, and 652,146 other unknown objects) have been
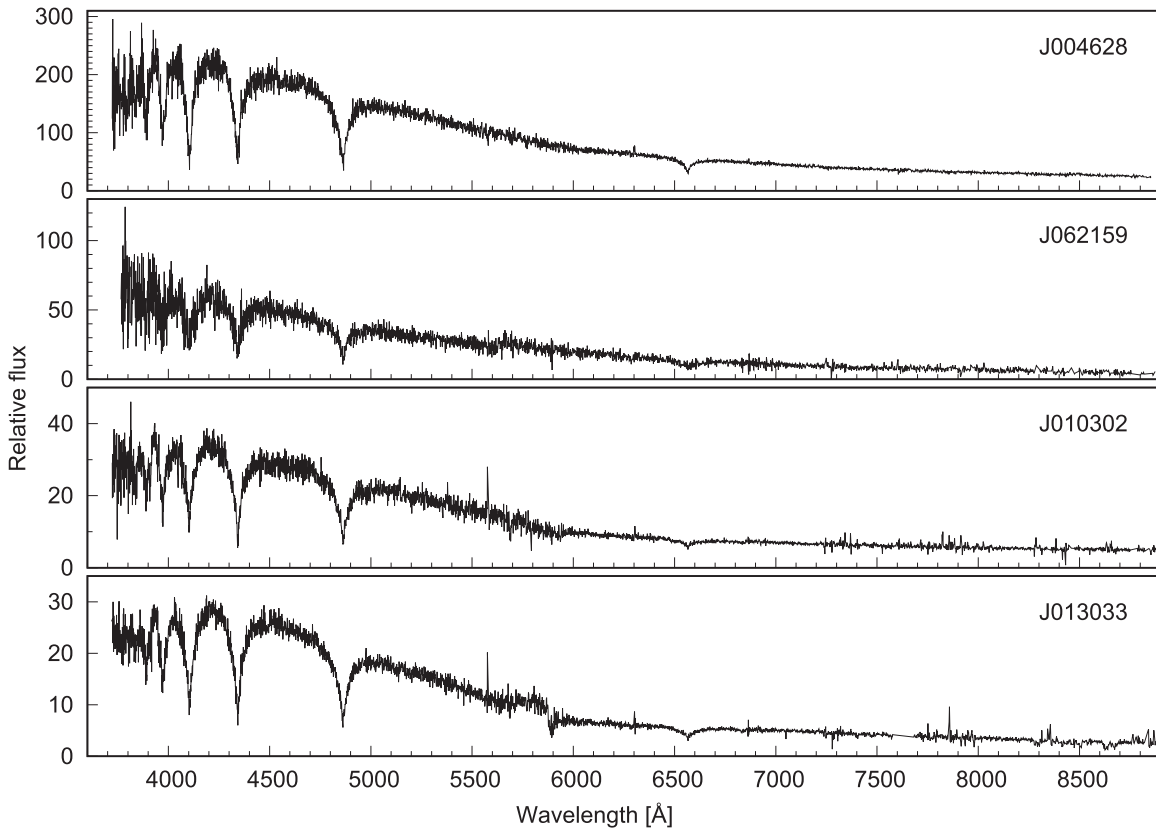
19

Figure 1. LAMOST spectra of the four white dwarfs.

Table 1
Summary of Information about the LAMOST Spectra

Object	R.A. (degree)	Decl. (degree)	Obs. Date	Plan ID	Sp. ID	Fiber ID	S/N_g
J004628	11.61796	+34.55553	2011 Dec 11	M31_007N34_B1	3	9	10.89
J062159	95.49792	+25.39331	2013 Jan 11	GAC094N27M1	7	21	6.76
J010302	15.76029	+43.63228	2013 Dec 29	M31016N43M1	3	154	8.36
J013033	22.64129	+27.63275	2014 Jan 01	M31023N28M1	3	245	12.63

obtained, which offer the largest stellar spectra library in the world to date.

A large number of white dwarfs including those of hydrogen-rich atmospheres, helium-rich atmospheres, and white dwarf-main sequence binaries had been spectroscopically identified based on the LAMOST spectra (see the catalogs published by Ren et al. 2013, 2014; Zhang et al. 2013; Zhao et al. 2013; Gentile Fusillo et al. 2015; Guo et al. 2015; Rebassa-Mansergas et al. 2015). Most of them are new sources, which further expand the number of known white dwarfs. This provides opportunities to search for new pulsating white dwarfs. The spectral types of the sources can be determined based on the spectra and the atmospheric parameters (T_{eff} and $\log g$) of most DA white dwarfs are derived and provided along with the catalogs.

We selected DA white dwarfs whose effective temperatures meet the condition of $10{,}000 \leqslant T_{eff} \pm \sigma \leqslant 14{,}000$ K as the ZZ Ceti candidates. Here σ is the error of T_{eff} given in the catalogs. The typical value (median) of σ is 458 K. Note that we had set a less rigorous criterion for selecting candidates concerning the errors of T_{eff} and to avoid missing some of the potential targets. The temperature range of the criterion is wider than that of the empirical ZZ Ceti instability strip, regardless of

$\log g$, although the instability strip position seems to be $\log g$ and T_{eff} dependent. We then perform a time-series photometry on an individual candidate to ascertain whether pulsations are detected.

In this paper, we report the progress of our search for new pulsating white dwarfs. Four new ZZ Ceti stars have been photometrically confirmed in 2015 and 2016, which are LAMOST J004628.31+343319.90 (hereafter J004628), LAMOST J062159.49+252335.9 (hereafter J062159), LAMOST J010302.46 +433756.2 (hereafter J010302), and LAMOST J013033.90 +273757.9 (hereafter J013033). The LAMOST spectra and stellar parameters of the four new ZZ Ceti stars are described in Section 2. In Section 3, we summarize the observations, data reduction, and pulsation analysis. In Section 4, the significance criteria are discussed. Discussion and conclusions are in Section 5.

2. LAMOST Spectra and Stellar Parameters

Figure 1 shows the flux- and wavelength-calibrated, sky-subtracted spectra of the four new ZZ Ceti stars, which are obtained from the LAMOST database.[6] The information about

---
[6] http://dr4.lamost.org/

Table 2
Apparent Magnitude and Stellar Parameters of the Four New ZZ Ceti Stars

Object	Apparent Magnitude					$T_{\rm eff}$ (K)	$\log g$ (cgs)	Mass ($M_\odot$)	References
	u	g	r	i	z				
J004628	16.83	16.33	16.40	16.53	16.75	14644 (808)	7.60 (0.18)	0.41 (0.08)	1
						11681 (199)	7.53 (0.15)	0.38 (0.05)	4
J062159	⋯	17.56	17.62	17.70	⋯	11728 (651)	8.25 (0.31)	0.76 (0.19)	2
J010302	18.84	18.33	18.43	18.57	18.72	11750 (492)	7.89 (0.33)	0.54 (0.21)	3
J013033	18.99	18.57	18.70	18.85	19.03	14127 (334)	7.69 (0.07)	0.45 (0.03)	4

References. (1) Zhao et al. (2013), (2) Rebassa-Mansergas et al. (2015), (3) Gentile Fusillo et al. (2015), (4) Guo et al. (2015).

Table 3
Journal of the Observations for the New ZZ Ceti Stars

Object	Obs. Date	Telescope	Start Time (HJD)	End Time (HJD)	Length (h)	Exp. Time (s)
J004628	2015 Jan 27	LJ 240	2457050.0347	2457050.1209	2.07	40
J062159	2016 Jan 17	⋯	2457404.9884	2457405.1627	4.18	50
J010302	2016 Nov 26	XL 216	2457718.9322	2457719.0453	2.71	60
J013033	2016 Nov 27	⋯	2457719.9357	2457720.0457	2.64	70

these spectra is summarized in Table 1. Columns 1–4 list the name, coordinates (J2000), and date of the observations of each star. Columns 5–7 list the identifiers of the plan, spectrograph, and fiber of the spectra. Column 8 lists the signal-to-noise ratio (S/N) in the g-band of each individual spectrum.

The apparent magnitudes and stellar parameters of the four new ZZ Ceti stars are listed in Table 2. Column 1 is the name of object. Columns 2–6 list the apparent magnitudes of each star. The atmospheric parameters $T_{\rm eff}$ and $\log g$ are listed in columns 7 and 8. The mass estimated according to the atmospheric parameters is listed in column 9. The last column indicates the source of the parameters.

We note that there are two sets of parameters of J004628, which are derived from catalogs of Zhao et al. (2013) and Guo et al. (2015), respectively. The values of $\log g$ from the two catalogs are compatible to each other, but the values of $T_{\rm eff}$ are quite different. However, both $T_{\rm eff}$ meet our selecting criterion (see Section 1). We note that there is a large uncertainty in the determination of the value of $T_{\rm eff}$ of this star.

3. Observations and Data Analysis

3.1. Observations

As the ZZ Ceti stars are relatively faint, the observations were performed with the two 2 m class telescopes in China: the 2.4 m telescope (LJ 240, Fan et al. 2015) at the Lijiang Observatory of Yunnan Observatories at the Chinese Academy of Sciences (YAO) and the 2.16 m telescope (XL 216, Fan et al. 2016) at the Xinglong Observatory of National Astronomical Observatories at the Chinese Academy of Sciences (NAOC). The journal of the observations is summarized in Table 3.

J004628 and J062159 were observed with LJ 240 on 2015 January 27 and 2016 January 17, respectively. Images of J004628 were taken with a Princeton Instruments VersArray: 1300B back-illuminated CCD Camera, which has the CCD size of 1300×1340 with the FOV of $4'\!.40 \times 4'\!.48$. The exposure time was set as 40 s for each image. Images of J062159 were obtained with another instrument, the Yunnan Faint Object Spectrograph and Camera (YFOSC), which has the CCD size

of 2048×2048 and the FOV of $9'\!.6 \times 9'\!.6$ under the direct imaging mode. The exposure time of each image was 50 s. No filter was used during the above observations in order to obtain as many photons as possible.

J010302 and J013033 were observed with XL 216 on 2016 November 26 and 27, respectively. The YFOSC's sister instrument, the Beijing Faint Object Spectrograph and Camera (BFOSC), was used, which has the CCD size of 2048×2048 and the FOV of $9'\!.36 \times 9'\!.36$ under the direct imaging mode. The exposure time of each image was 60 s for J010302 and 70 s for J013033, respectively. No filter was used during the observations.

3.2. Data Reduction

All of the observed data were reduced using the IRAF[7] packages. The instrumental magnitudes of stars on each image were calculated using the method of aperture photometry according to the standard procedure. The differential magnitude of the candidate star relative to the comparison star was calculated and plotted versus the time of the observation to produce the light curve. In order to get rid of the low-frequency variations of the atmospheric transparency during the night, the light curves were divided by a fourth order polynomial. The normalized light curves of the four stars are shown in the upper panels of Figures 2–5. Periodical variations are clearly visible in the light curves.

3.3. Fourier Analysis

In order to further verify the variability of these stars, we performed a discrete Fourier transform (DFT) of the light curves to search for periodical variations. The amplitude spectra of the light curves are shown in the bottom panels of Figures 2–5. The spectral window corresponding to each light curve is shown in the inset. The spectral window (or window function) is the DFT of a single period sinusoidal function

---
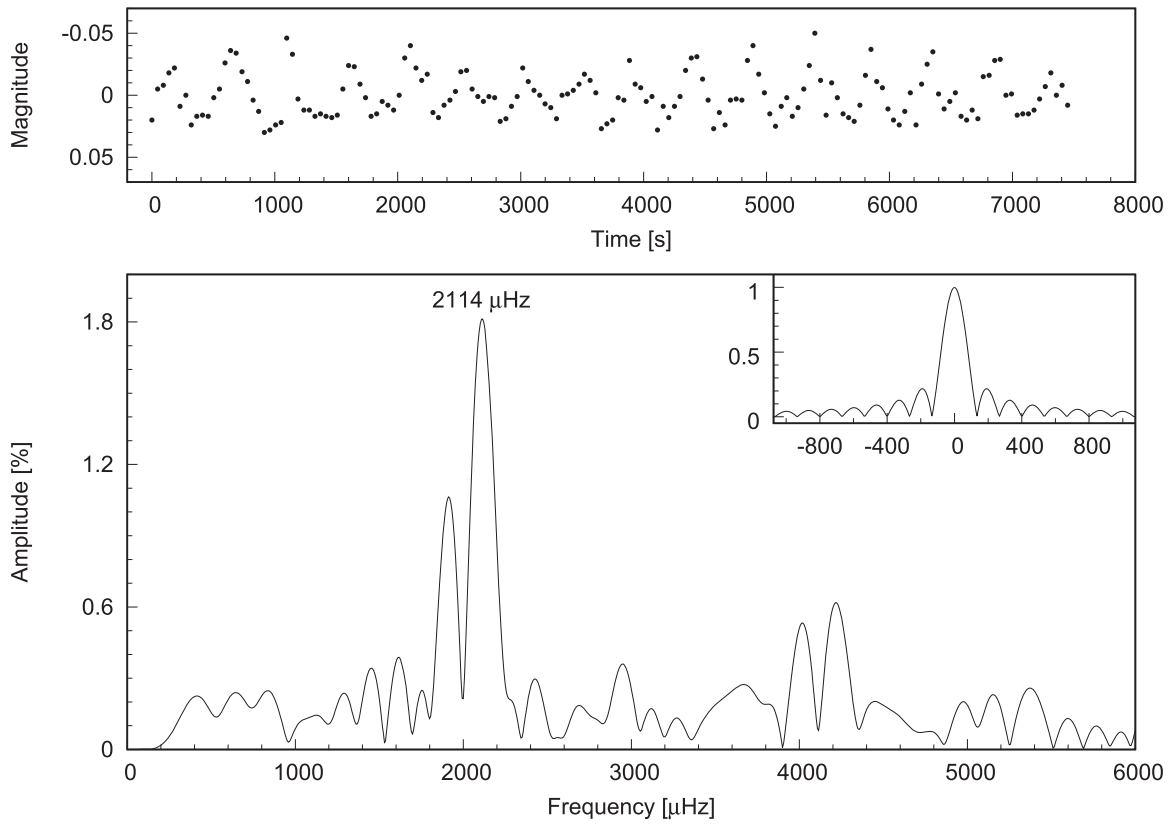
Figure 2. The upper panel shows the normalized light curve of J004628. The *x*-axis is the time in seconds and the *y*-axis is the differential magnitude of J004628 relative to the comparison star. The zero point is the average of the light curve. The bottom panel shows the amplitude spectrum of the light curve. The relative amplitude is plotted versus the frequency in the range from 0 to 6000 μHz. The inset shows the spectral window.
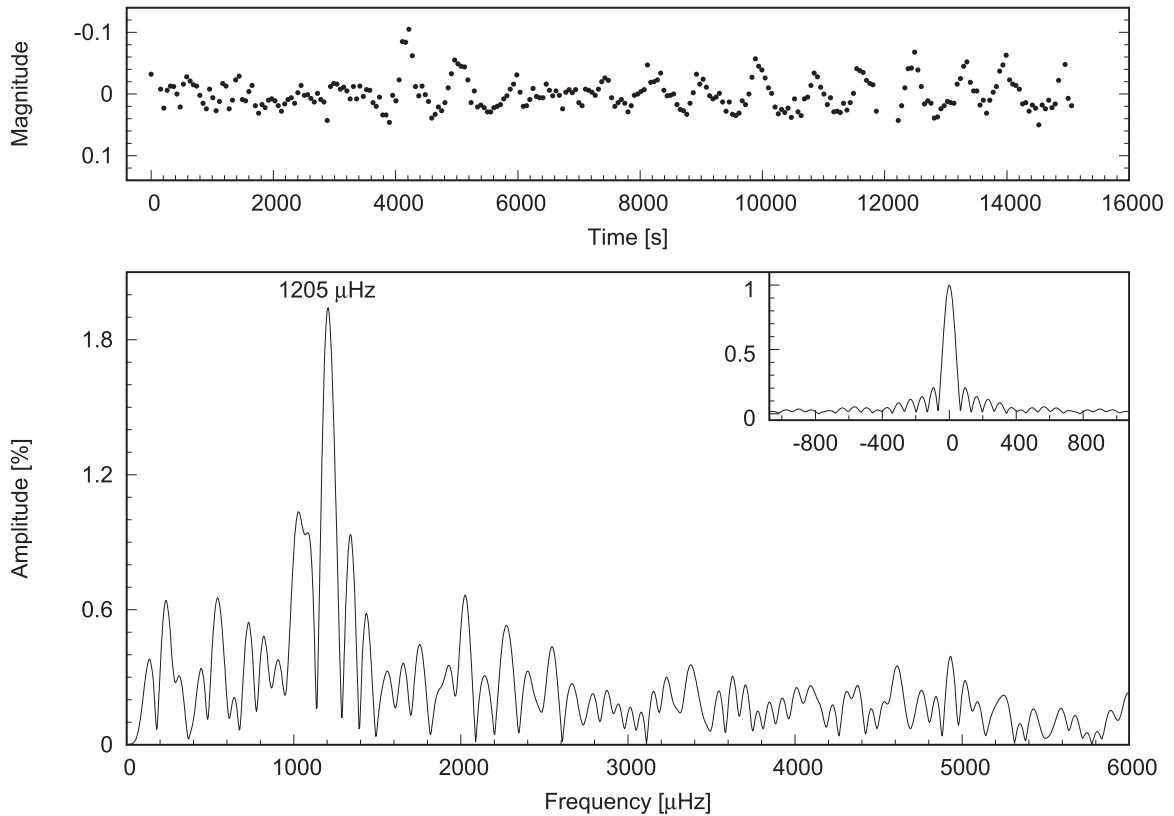
Figure 3. Same as Figure 2 but for J062159.
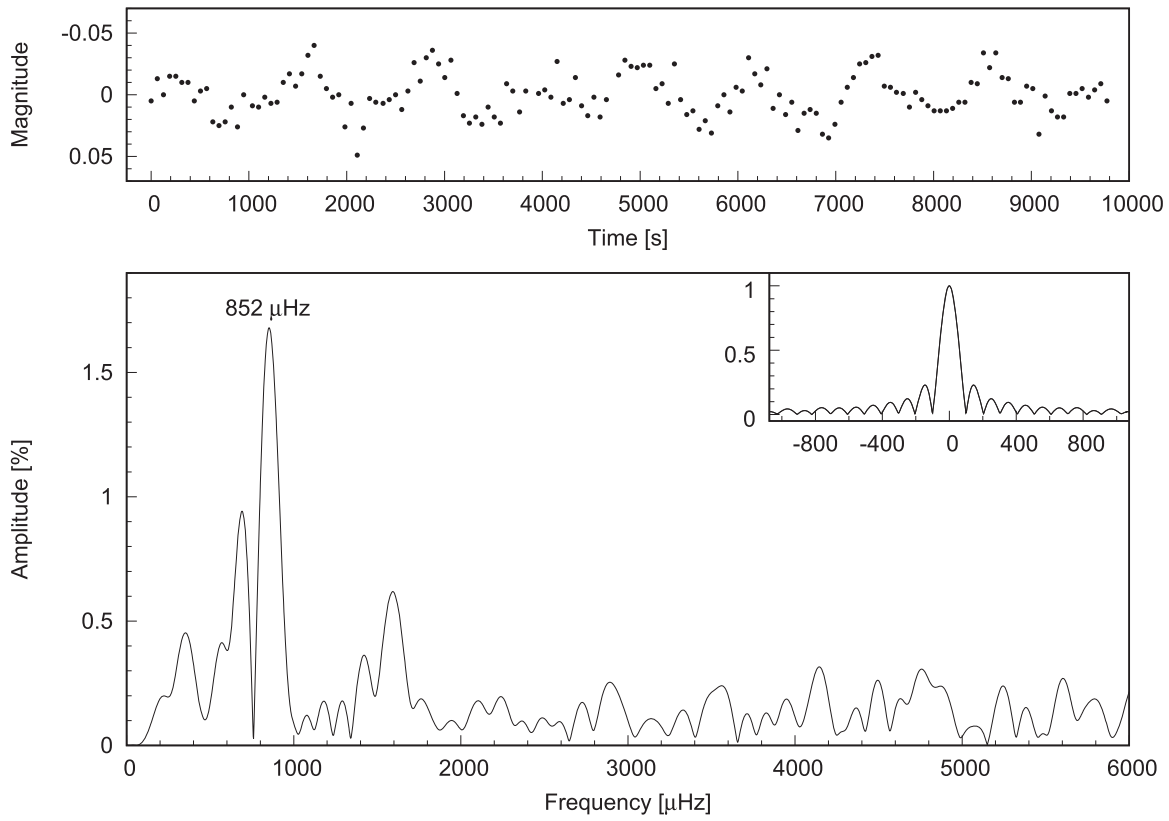
Figure 4. Same as Figure 2 but for J010302.
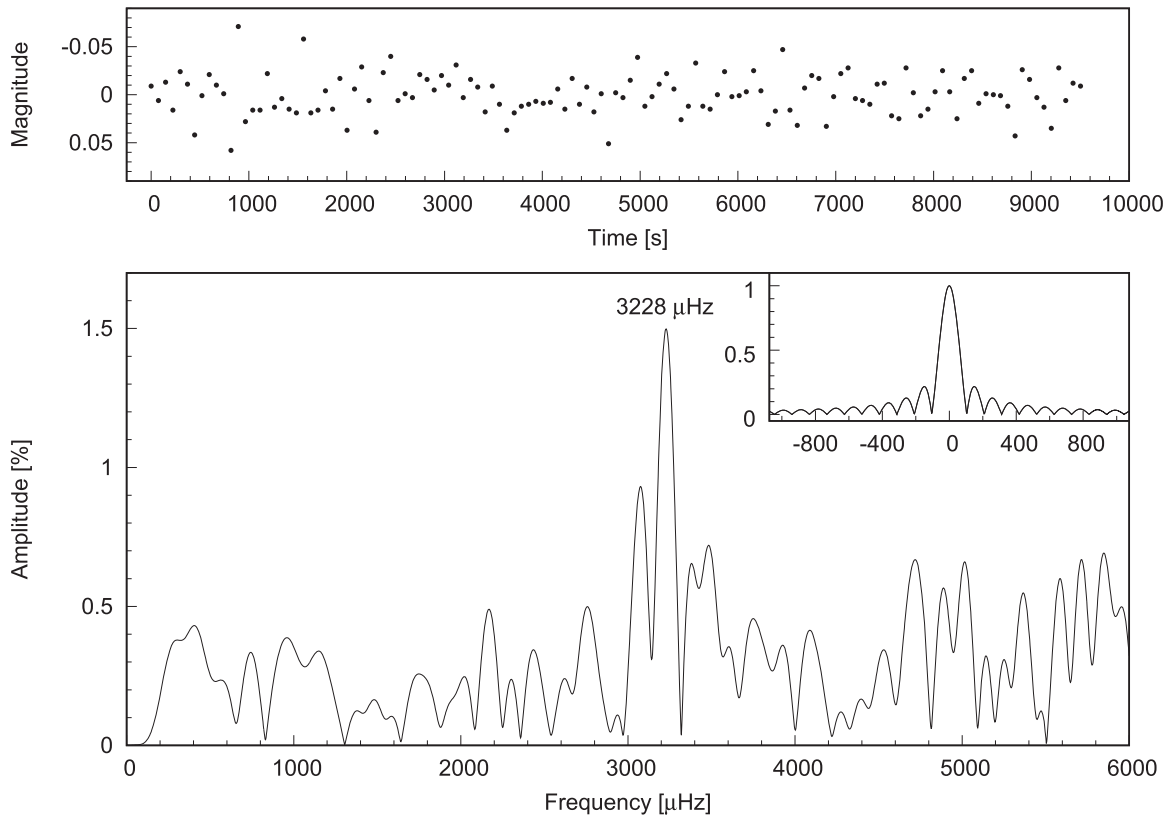
Figure 5. Same as Figure 2 but for J013033.

23
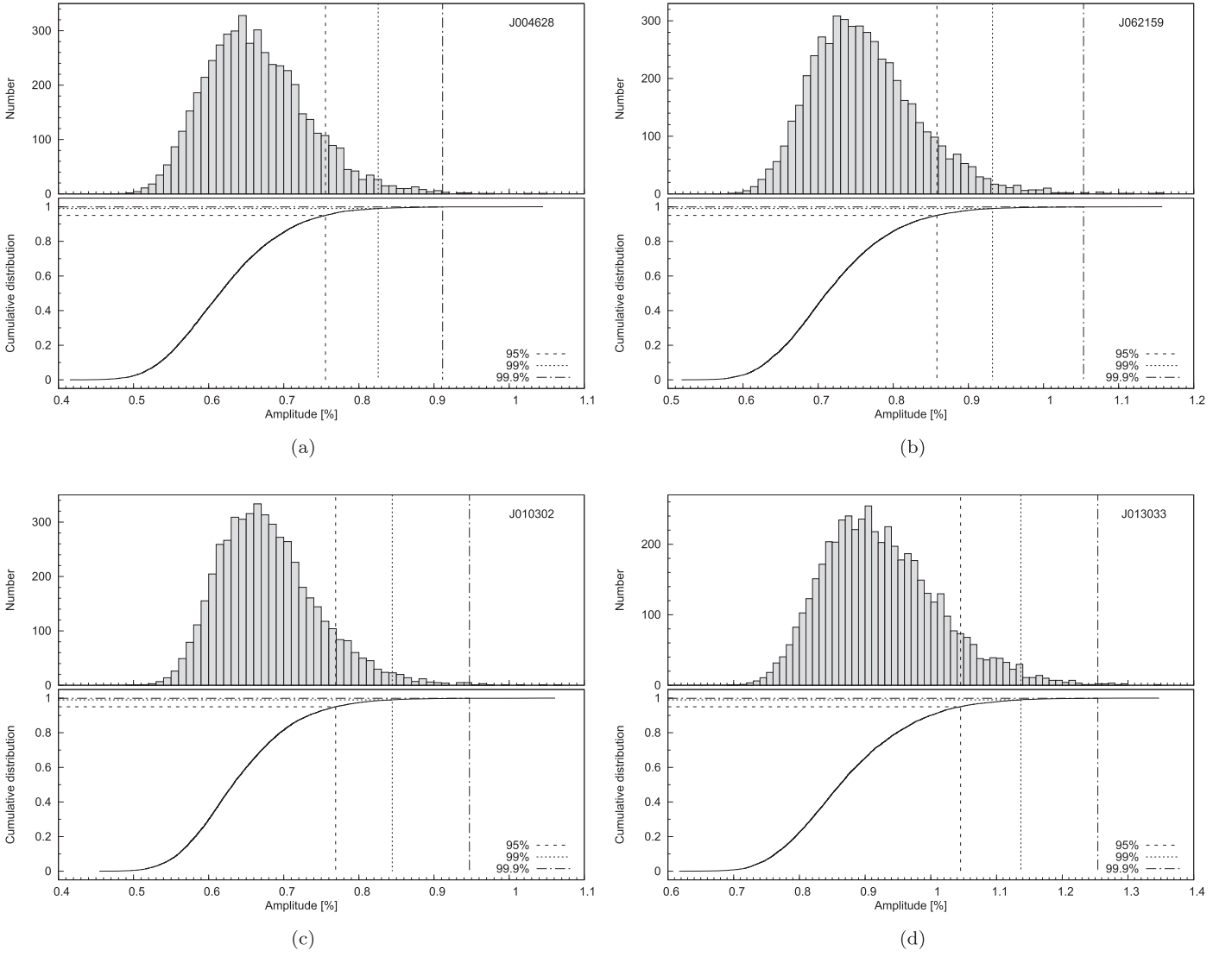
Figure 6. Simulation results for (a) J004628, (b) J062159, (c) J010302, and (d) J013033. The upper panel of each subfigure shows the distribution of the highest amplitudes in 10,000 simulations. The bottom panel shows the corresponding CDF. The locations of the 95%, 99%, and 99.9% confidence levels are marked with the dashed, dotted, and dashed–dotted lines, respectively.

sampled as the data, whose value equals to unity at each data point and zero elsewhere. It reflects the effect of spectral leakage due to the finite time duration and gaps in the light curve. In the ideal case (an infinite duration signal), it will be a δ function. In reality, it will be far from the δ function and will help us identify the actual modes from the aliases due to the imperfect sampling.

Figure 2 shows the amplitude spectrum of J004628. The highest peak with an amplitude of 1.8% is detected at the frequency of $2114 \pm 12 \, \mu$Hz (the period of 473 ± 3 s). Figure 3 shows the case of J062159. The highest peak is located at the frequency of $1205 \pm 6 \, \mu$Hz (the period of 830 ± 4 s) with an amplitude of 1.9%. The amplitude spectrum of J010302 is shown in Figure 4 with a dominant peak at the frequency of $852 \pm 10 \, \mu$Hz (the period of 1174 ± 14 s), which has an amplitude of 1.7%. In the amplitude spectrum of J013033 shown in Figure 5, a dominant peak with an amplitude of 1.5% is found at the frequency of $3228 \pm 14 \, \mu$Hz (the period of 310 ± 1 s). The uncertainties of the frequencies are estimated using the

Monte Carlo simulations as described in Fu et al. (2013) and applied in our previous work (Su et al. 2014a, 2014b).

4. Significance Criteria

In order to give quantitative criteria to determine whether the dominant peaks are significant or not, we simulated light curves to estimate the significance thresholds for each star. The simulations are based on the principle described in Greiss et al. (2014, 2016). In summary, we keep the time of the data points of the original light curve in place, but randomly permute brightness to create a simulated light curve. We then perform DFT on each simulated light curve and record the highest amplitude in the amplitude spectrum. This operation is repeated 10,000 times. All of the recorded highest amplitudes thus constitute a random sample. The cumulative distribution function (CDF) of the sample is calculated. The value of the CDF at any particular value of x, denoted by $F(x)$, is the fraction of the elements in the sample that are less than or equal to x. The values at the 95th, 99th, and 99.9th percentiles, which mean that 95%, 99%, and 99.9% of the simulated light

Figure 7. Amplitude spectra with confidence levels of the new ZZ Ceti stars: (a) J004628, (b) J062159, (c) J010302, (d) J013033, and (e) the case for J004628 after prewhitening with the highest peak. The 95%, 99%, and 99.9% confidence levels and the $4\langle A\rangle$ levels are marked with the dashed, dotted, dashed–dotted, and solid lines, respectively.
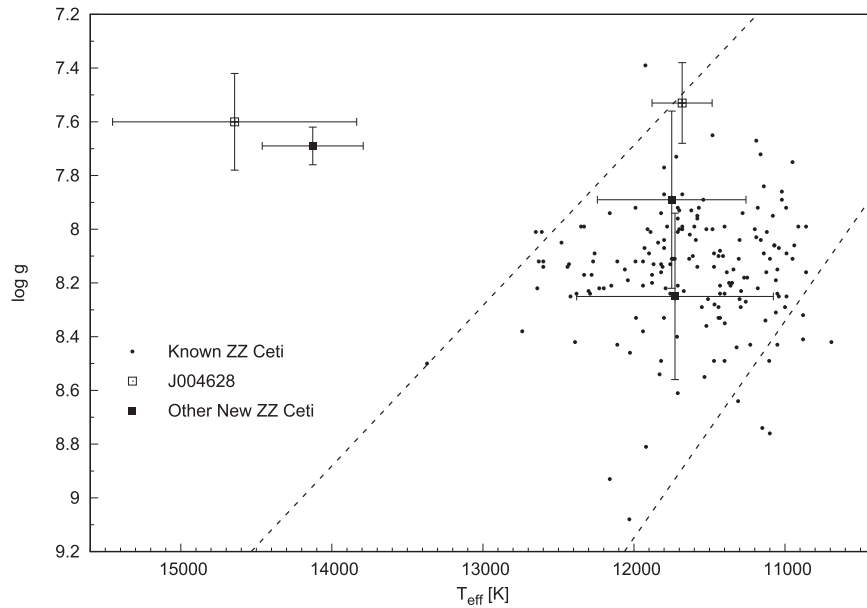
Figure 8. $T_{\rm eff}$–$\log g$ diagram of the ZZ Ceti stars. The black points correspond to the 172 known ZZ Ceti stars with determined atmospheric parameters. The open squares with error bars mark the two positions of J004628 with different atmospheric parameters and the filled squares with error bars correspond to the three new ZZ Ceti stars. The empirical boundaries of the ZZ Ceti instability strip are marked with the dashed lines.

curves that have the highest amplitudes fall below those values, are determined from the CDF and taken as significance criteria (confidence levels).

We generate 10,000 simulated light curves for each star. Our previous experience showed that the results converged well using 10,000 simulated light curves. The distribution of the recorded highest amplitudes in the simulated sample of each star is shown as a histogram in the upper panel of each subfigure of Figure 6. To construct the histogram, the entire range of each sample is divided into a series of intervals (bins), where the bin width is 0.01%. The y-axis indicates the number of values that fall into each bin. The bottom panel of each subfigure shows the CDF calculated based on the distribution. The locations of the 95%, 99%, and 99.9% confidence levels are marked with the dashed, dotted, and dashed–dotted lines, respectively.
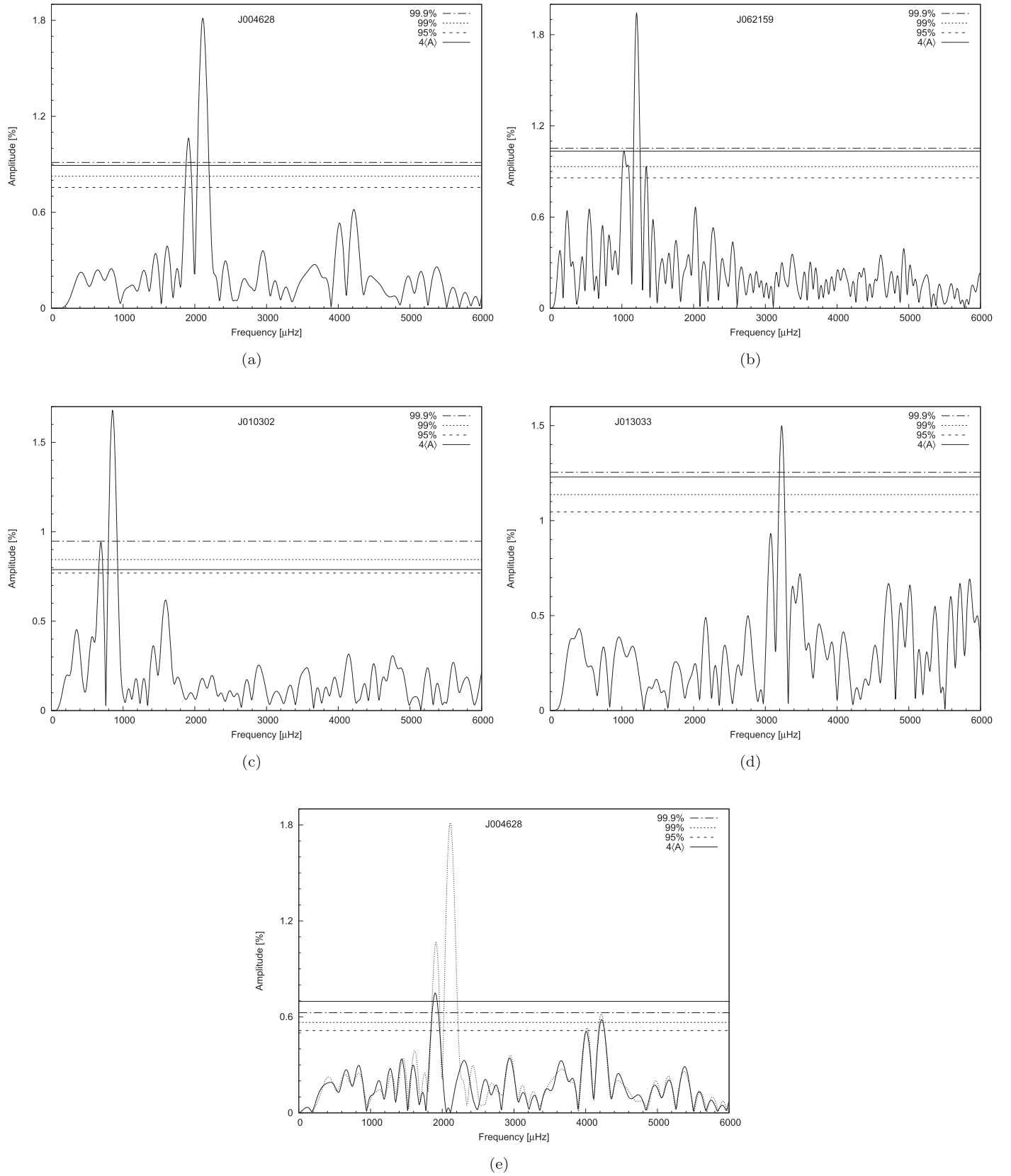
Figure 7 shows amplitude spectra with the confidence levels of the four stars. The 95%, 99%, and 99.9% confidence levels are marked with the dashed, dotted, and dashed–dotted lines, respectively in each amplitude spectrum. The $4\langle A\rangle$ level, which is a widely used significance criterion (Breger et al. 1993; Kuschnig et al. 1997), is also marked with the solid line for comparison. Here, we take the average amplitude ($\langle A\rangle$) of the amplitude spectrum as an estimate of the noise level.

The 99.9% confidence level corresponds to a more strict significance threshold than that of the 3σ level. All the highest peaks in the four amplitude spectra rise above the 99.9% confidence levels. They are thus considered significant. In addition, another significant peak at a frequency of $\approx 1913\,\mu$Hz (period ≈ 523 s) is found in the amplitude spectrum of J004628. In order to check the significance of the second peak, we prewhiten the original light curve of J004628 with the highest peak and perform simulations based on the residual light curve to estimate the confidence levels. The residual amplitude spectrum and confidence levels are shown in Figure 7(e). The original amplitude spectrum is plotted with the dotted lines for comparison. The second peak is still significant.

Meanwhile, we note that the $4\langle A\rangle$ levels in all amplitude spectra are above the 95% confidence levels. If we roughly take the $4\langle A\rangle$ level as the significance threshold, any peak whose amplitude exceeds that threshold can be considered significant in a sufficient confidence level higher than 95%.

5. Discussion and Conclusions

Four new ZZ Ceti stars have been identified. All of them are selected from the LAMOST spectroscopic survey data set and are confirmed by the follow-up photometric observations. Figure 8 shows the $T_{\rm eff}$–$\log g$ diagram of 172 known ZZ Ceti stars with determined atmospheric parameters. These known objects were collected from the literature (14 from Kepler et al. (2005), 41 from Mukadam et al. (2006), 5 from Voss et al. (2006, 2007), 34 from Castanheira et al. (2006, 2007, 2010, 2013), 56 from Gianninas et al. (2011), 6 from Green et al. (2015), 11 in the *Kepler* field (Hermes et al. 2011; Greiss et al. 2014, 2016), and 5 massive or ultramassive ZZ Ceti stars discovered by Hermes et al. (2013) and Curd et al. (2017)). The positions of our new ZZ Ceti stars are marked in the diagram with the squares with the error bars. The empirical boundaries of the ZZ Ceti instability strip determined by Tremblay et al. (2015) are marked with the dashed lines. J004628 had been given two different sets of atmospheric parameters, which correspond to different positions marked with the open squares in the $T_{\rm eff}$–$\log g$ diagram. Obviously, the $T_{\rm eff}$ and $\log g$ provided by Zhao et al. (2013) place the object well outside the instability strip, while the parameters given by Guo et al. (2015) place it within the instability strip. We therefore believe that the atmospheric parameters given by the latter are more reliable. The positions of the three new ZZ Ceti stars in the $T_{\rm eff}$–$\log g$ diagram are marked with the filled squares. J013033 has been determined with a relatively high $T_{\rm eff}$ and low $\log g$, which makes its position seriously deviate from the instability strip. However, J013033 has the smallest error of $\log g$ among the four ZZ Ceti stars. It seems that the determination of $T_{\rm eff}$ about J013033 is probably not correct, but the $\log g$ value would be reliable. For J062159 and

26

J010302, their positions in the $T_{\rm eff}$–$\log g$ diagram are consistent with that of the ZZ Ceti stars.

Both of the parameter estimates for J004628 imply relatively low $\log g$ and hence an estimated mass of $\sim 0.40\, M_\odot$. The theory of stellar evolution shows that a white dwarfs whose mass is $\lesssim 0.5\, M_\odot$ cannot have a carbon-oxygen core, since the core mass is lower than that of the critical value for igniting helium. J004628 is hence inferred to be a white dwarf with a helium core. If we believe the $\log g$ estimate of J013033, the mass of J013033 is $\sim 0.45\, M_\odot$. Owing to the low mass of J013033, it is also inferred to be another potential helium-core white dwarf. The formation of low-mass helium-core white dwarfs requires a mechanism different from the normal single star evolution, since a single star with such low mass would take longer than the age of the universe to evolve into a white dwarf. It is widely accepted that low-mass white dwarfs should originate from the evolution of close binary systems. The interaction between binary stars removes most of the outer envelope of one component before helium ignition. The remnant of the component with a helium core would not go through the asymptotic giant branch phase and would directly contract toward a white dwarf. On the other hand, the existence of single low-mass white dwarfs and the potential formation channels for them are discussed by Brown et al. (2011). The existing observations, both light curves and spectra, temporarily cannot reveal whether either J004628 or J013033 has a companion. It is still debatable whether or not the two white dwarfs are singles. Perhaps some objects might benefit from higher S/N spectra.

Further time-series photometric observations are needed to detect additional pulsating modes for the asteroseismological analysis, which would allow the essential parameters of the new ZZ Ceti stars to be refined. Our work for the search of new pulsating white dwarfs will continue.

ORCID iDs

Jie Su ⬤ https://orcid.org/0000-0001-7566-9436
Jianning Fu ⬤ https://orcid.org/0000-0001-8241-1740
Guifang Lin ⬤ https://orcid.org/0000-0001-6725-8207

References

Althaus, L. G., Córsico, A. H., Isern, J., & García-Berro, E. 2010, A&ARv, 18, 471
Borucki, W. J., Koch, D., Basri, G., et al. 2010, Sci, 327, 977
Breger, M., Stich, J., Garrido, R., et al. 1993, A&A, 271, 482
Brickhill, A. J. 1991, MNRAS, 251, 673
Brown, J. M., Kilic, M., Brown, W. R., & Kenyon, S. J. 2011, ApJ, 730, 67
Castanheira, B. G., Kepler, S. O., Costa, A. F. M., et al. 2007, A&A, 462, 989
Castanheira, B. G., Kepler, S. O., Kleinman, S. J., Nitta, A., & Fraga, L. 2010, MNRAS, 405, 2561
Castanheira, B. G., Kepler, S. O., Kleinman, S. J., Nitta, A., & Fraga, L. 2013, MNRAS, 430, 50
Castanheira, B. G., Kepler, S. O., Mullally, F., et al. 2006, A&A, 450, 227
Cui, X.-Q., Zhao, Y.-H., Chu, Y.-Q., et al. 2012, RAA, 12, 1197
Curd, B., Gianninas, A., Bell, K. J., et al. 2017, MNRAS, 468, 239
Dolez, N., & Vauclair, G. 1981, A&A, 102, 375
Fan, Y.-F., Bai, J.-M., Zhang, J.-J., et al. 2015, RAA, 15, 918
Fan, Z., Wang, H., Jiang, X., et al. 2016, PASP, 128, 115005
Fu, J.-N., Dolez, N., Vauclair, G., et al. 2013, MNRAS, 429, 1585
Gentile Fusillo, N. P., Rebassa-Mansergas, A., Gänsicke, B. T., et al. 2015, MNRAS, 452, 765
Gianninas, A., Bergeron, P., & Ruiz, M. T. 2011, ApJ, 743, 138
Green, E. M., Limoges, M.-M., Gianninas, A., et al. 2015, in ASP Conf. Ser. 493, 19th European Workshop on White Dwarfs, ed. P. Dufour, P. Bergeron, & G. Fontaine (San Francisco, CA: ASP), 237
Greiss, S., Gänsicke, B. T., Hermes, J. J., et al. 2014, MNRAS, 438, 3086
Greiss, S., Hermes, J. J., Gänsicke, B. T., et al. 2016, MNRAS, 457, 2855
Guo, J., Zhao, J., Tziamtzis, A., et al. 2015, MNRAS, 454, 2787
Hermes, J. J., Kepler, S. O., Castanheira, B. G., et al. 2013, ApJL, 771, L2
Hermes, J. J., Mullally, F., Østensen, R. H., et al. 2011, ApJL, 741, L16
Kepler, S. O., Castanheira, B. G., Saraiva, M. F. O., et al. 2005, A&A, 442, 629
Kuschnig, R., Weiss, W. W., Gruber, R., Bely, P. Y., & Jenkner, H. 1997, A&A, 328, 544
Landolt, A. U. 1968, ApJ, 153, 151
Luo, A.-L., Zhang, H.-T., Zhao, Y.-H., et al. 2012, RAA, 12, 1243
Mukadam, A. S., Montgomery, M. H., Winget, D. E., Kepler, S. O., & Clemens, J. C. 2006, ApJ, 640, 956
Nather, R. E., Winget, D. E., Clemens, J. C., Hansen, C. J., & Hine, B. P. 1990, ApJ, 361, 309
Rebassa-Mansergas, A., Liu, X.-W., Cojocaru, R., et al. 2015, MNRAS, 450, 743
Ren, J., Luo, A., Li, Y., et al. 2013, AJ, 146, 82
Ren, J. J., Rebassa-Mansergas, A., Luo, A. L., et al. 2014, A&A, 570, A107
Su, J., Li, Y., & Fu, J.-N. 2014a, NewA, 33, 52
Su, J., Li, Y., Fu, J.-N., & Li, C. 2014b, MNRAS, 437, 2566
Tremblay, P.-E., Gianninas, A., Kilic, M., et al. 2015, ApJ, 809, 148
Voss, B., Koester, D., Østensen, R., et al. 2006, A&A, 450, 1061
Voss, B., Koester, D., Østensen, R., et al. 2007, in ASP Conf. Ser. 372, 15th European Workshop on White Dwarfs, ed. R. Napiwotzki & M. R. Burleigh (San Francisco, CA: ASP), 583
Winget, D. E., & Kepler, S. O. 2008, ARA&A, 46, 157
Winget, D. E., van Horn, H. M., Tassoul, M., et al. 1982, ApJL, 252, L65
Zhang, Y.-Y., Deng, L.-C., Liu, C., et al. 2013, AJ, 146, 34
Zhao, G., Zhao, Y.-H., Chu, Y.-Q., Jing, Y.-P., & Deng, L.-C. 2012, RAA, 12, 723
Zhao, J. K., Luo, A. L., Oswalt, T. D., & Zhao, G. 2013, AJ, 145, 169

NLTE ANALYSIS OF HIGH-RESOLUTION H-BAND SPECTRA. II. NEUTRAL MAGNESIUM[*]

JUNBO ZHANG[1,2], JIANRONG SHI[1,2], KAIKE PAN[3], CARLOS ALLENDE PRIETO[4,5], AND CHAO LIU[1]

[1] Key Laboratory of Optical Astronomy, National Astronomical Observatories, Chinese Academy of Sciences, A20 Datun Road,
Chaoyang District, Beijing 100012, China; sjr@bao.ac.cn
[2] University of Chinese Academy of Sciences, Beijing 100049, China
[3] Apache Point Observatory and New Mexico State University, P.O. Box 59, Sunspot, NM 88349-0059, USA
[4] Instituto de Astrofísica de Canarias, E-38205 La Laguna, Tenerife, Spain
[5] Departamento de Astrofísica, Universidad de La Laguna, E-38206 La Laguna, Tenerife, Spain

ABSTRACT

Aiming at testing the validity of our magnesium atomic model and investigating the effects of non-local thermodynamical equilibrium (NLTE) on the formation of the H-band neutral magnesium lines, we derive the differential Mg abundances from selected transitions for 13 stars either adopting or relaxing the assumption of local thermodynamical equilibrium (LTE). Our analysis is based on high-resolution and high signal-to-noise ratio H-band spectra from the Apache Point Observatory Galactic Evolution Experiment (APOGEE) and optical spectra from several instruments. The absolute differences between the Mg abundances derived from the two wavelength bands are always less than 0.1 dex in the NLTE analysis, while they are slightly larger for the LTE case. This suggests that our Mg atomic model is appropriate for investigating the NLTE formation of the H-band Mg lines. The NLTE corrections for the Mg I H-band lines are sensitive to the surface gravity, becoming larger for smaller $\log g$ values, and strong lines are more susceptible to departures from LTE. For cool giants, NLTE corrections tend to be negative, and for the strong line at 15765 Å they reach -0.14 dex in our sample, and up to -0.22 dex for other APOGEE stars. Our results suggest that it is important to include NLTE corrections in determining Mg abundances from the H-band Mg I transitions, especially when strong lines are used.

Key words: line: formation – line: profiles – stars: abundances – stars: atmospheres

1. INTRODUCTION

Magnesium is a key element in the universe, and plays a significant part in various astrophysical applications. As a typical α-element, magnesium is mostly produced by SNe II (Woosley & Weaver 1995). Thus, it is a good tracer to study α-process nucleosynthesis. Unlike Fe, which is prone to be affected by Type-Ia SNae nucleosynthesis, Mg is a reliable reference element for the early evolution of the Milky Way (Zhao et al. 1998). Shigeyama & Tsujimoto (1998) and Andrievsky et al. (2010) recommended Mg instead of iron as a reference element to investigate the evolution of different abundance ratios, while Si and Ca are more easily influenced by mixing and fallback episodes and possible contributions. Fuhrmann (1998, 2004) applied [Mg/Fe] as a reference to explore thick- and thin-disk stars, and found that there is a distinct behavior between the two populations. Next to Fe, Mg is an important donor of free electrons in relatively cool turnoff stellar atmospheres, and contributes significant ultraviolet (UV) opacity (Kurucz 1979; Mashonkina 2013). Furthermore, it is one of the best observed elements, inasmuch as several strong Mg lines are easily observed in visible and infrared regions in A- to late-type stars.

In recent decades, many studies have determined local thermodynamical equilibrium (LTE) Mg abundances and have used this element as a tracer to probe the chemical evolution history of our Galaxy, e.g., Lambert & Luck (1978), Tomkin et al. (1985), Chen et al. (2000), Reddy et al. (2006),

and Bensby et al. (2014). However, it is known that Mg abundances may be impacted by non-local thermodynamical equilibrium (NLTE) effects. At the end of the 1960s, Athay & Canfield (1969) first included NLTE effects in the analysis of Mg I b lines in the Sun based on a small atomic model. Many subsequent studies have focused on investigating the NLTE effects on Mg I line formation, e.g., Lemke & Holweger (1987), Mauas et al. (1988), Gigas (1988), Chang et al. (1991), and Carlsson et al. (1992). Zhao et al. (1998) and Zhao & Gehren (2000) carefully investigated NLTE effects for Mg I lines in the Sun and 10 cool stars, and found the abundance corrections in the Sun to be negligible, while they can reach ~0.1 dex in metal-deficient stars. They found that the corrections increase with decreasing metallicity, which was confirmed by Gehren et al. (2006). The latter authors derived NLTE abundances of Na, Mg, and Al for a sample of 55 nearby metal-poor stars, and concluded that the ratio of [Al/Mg] is a promising discriminant between thick-disk and halo stellar populations. For extremely metal-poor stars, Andrievsky et al. (2010) studied the NLTE line formation for Mg, and they argued that NLTE effects could, at least partly, explain the unexpected scatter of [X/Mg] found by Cayrel et al. (2004) and Bonifacio et al. (2009), and the different behaviors between dwarfs and giants described in Bonifacio et al. (2009).

Recently, Mashonkina (2013) improved the Mg atomic model by introducing the newly calculated inelastic collisions with neutral hydrogen from Barklem et al. (2012), which were based on quantum mechanical computations, and verified that the updated atomic data can improve the determinations of Mg abundances for late-type stars. Her results were confirmed by Osorio et al. (2015), who produced a novel model atom of Mg and tested its validity for spectral line formation in late-type stars. They predicted that NLTE effects for solar-type and

28

metal-poor dwarfs are even smaller than those found in previous studies. However, NLTE corrections can reach up to 0.4 dex for giants. Bergemann et al. (2015) carried out a NLTE analysis of near-infrared J-band Mg I lines for red supergiants. Their results show that NLTE corrections are substantial in the atmospheres of red supergiants, and vary smoothly between -0.4 and -0.1 dex as a function of the effective temperature.

The Apache Point Observatory Galactic Evolution Experiment (APOGEE) survey[6], part of the Sloan Digital Sky Survey III (SDSS-III;[7] Eisenstein et al. 2011), has observed $\sim$150,000 predominantly red giants covering the full range of Galactic bulge, bar, disk, and halo (Majewski et al. 2016) since 2011, and APOGEE-2, an on-going extension of the project in SDSS-IV will significantly enlarge this database. APOGEE infrared H-band spectra have already been publicly released as part of the SDSS Data Release 10 (DR10; Ahn et al. 2014) and Data Release 12 (DR12; Alam et al. 2015). These observations provide a promising way to trace and to explore the formation history of the Milky Way.

The APOGEE Stellar Parameters and Chemical Abundances Pipeline (ASPCAP; García Pérez et al. 2016) is designed to derive the stellar parameters (effective temperature, surface gravity, metallicity) and chemical abundances of 15 different elements. As pointed out by Mészáros et al. (2013), NLTE effects may have an impact on the APOGEE derived stellar parameters and chemical abundances due to low densities present in the atmospheres of giants. Thus, as an extension of our previous work (hereinafter Paper I), which is confined to H-band Si lines, this paper focuses on NLTE line formation of Mg I H-band transitions for the 13 sample stars from Paper I. The main purpose of this work is to validate the applied Mg atomic model, and to investigate the influence of departures from LTE. This will help us to improve the accuracy of stellar parameters determined by the APOGEE pipeline and help to explore the chemical enrichment history of the Galaxy based on large samples of APOGEE H-band spectra.

This paper is organized as follows. In Section 2, we introduce the Mg model atom and the NLTE calculations. The data and the determination of stellar parameters for our sample stars are briefly described in Section 3. Section 4 derives the Mg abundances from both H-band and optical lines for our sample stars under LTE and NLTE analyses, respectively, and compares derived Mg abundances from the two bands, discussing the implications. In the last section, we summarize our results.

2. METHOD OF NLTE CALCULATIONS

2.1. Model Atom of Magnesium

We utilized the updated model atom for Mg from Mashonkina (2013), which was based on the model produced by Zhao et al. (1998) and Zhao & Gehren (2000). This comprehensive model atom contains the first three ionization stages of Mg, including 85 terms of Mg I, two levels of Mg II, and the ground state of Mg III. Here, we briefly introduce the atomic data. For electron impact excitation, the collisional rates were taken from Mauas et al. (1988) when available, while from Zhao et al. (1998) for the rest of the transitions. Ionization cross-sections were computed from the formula by Seaton (1962). For hydrogen-impact excitation and

Table 1
Atomic Data of the Optical and H-Band Magnesium Lines

λ (Å)	Transition[a]	χ (eV)	log gf	log C_6
4571.096	$3s^2\ ^1S_0 - 3p\ ^3P^o_1$	0.000	-5.49	-31.799[b]
4702.991	$3p\ ^1P^o_1 - 5d\ ^1D_2$	4.346	-0.36	-29.849[b]
5172.684	$3p\ ^3P^o_1 - 4s\ ^3S_1$	2.712	-0.44	-30.549[b]
5183.604	$3p\ ^3P^o_2 - 4s\ ^3S_1$	2.717	-0.21	-30.549[b]
5528.405	$3p\ ^1P^o_1 - 4d\ ^1D_2$	4.346	-0.40	-30.324[b]
5711.088	$3p\ ^1P^o_1 - 5s\ ^1S_0$	4.346	-1.70	-29.890[c]
15740.716	$4p\ ^3P^o_0 - 4d\ ^3D_1$	5.932	-0.36	-29.658[d]
15748.886	$4p\ ^3P^o_1 - 4d\ ^3D_1$	5.932	-0.54	-29.658[d]
15748.988	$4p\ ^3P^o_1 - 4d\ ^3D_2$	5.932	0.02	-29.658[d]
15765.645	$4p\ ^3P^o_2 - 4d\ ^3D_1$	5.933	-1.54	-29.658[d]
15765.747	$4p\ ^3P^o_2 - 4d\ ^3D_2$	5.933	-0.55	-29.658[d]
15765.842	$4p\ ^3P^o_2 - 4d\ ^3D_3$	5.933	0.30	-29.658[d]
15886.183	$3d\ ^3D_2 - 5p\ ^3P^o_1$	5.946	-1.71	-29.569[d]
15886.261	$3d\ ^3D_1 - 5p\ ^3P^o_1$	5.946	-2.07	-29.569[d]

Notes.
[a] Transition information is from NIST Atomic Spectra Database.
[b] Mashonkina (2013).
[c] The damping constant was determined by fitting the line wings of the solar spectrum.
[d] Meléndez & Barbuy (1999).
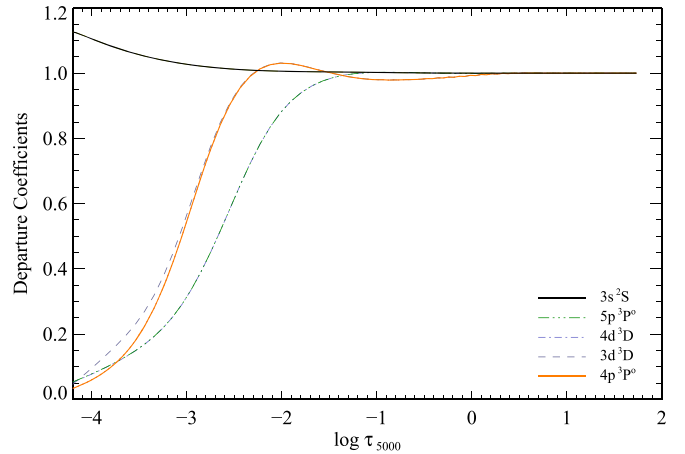
Figure 1. Departure coefficients $b_i = n_i^{NLTE}/n_i^{LTE}$ as a function of the standard optical depth for HD 58367. $4p\ ^3P^o$ (the red solid line) and $3d\ ^3D$ (the dashed line) couple with each other.

charge transfer, the rate coefficients of the transitions between the seven lowest levels of Mg and the ionic state (Mg +H and Mg$^+$ +H$^-$) were adopted from Barklem et al. (2012; see Mashonkina 2013 for details).

2.2. Model Atmospheres

In this study, we adopted the widely used grid of MARCS atmosphere models[8] (Gustafsson et al. 2008). These LTE models are divided into two groups: models with $3.0 \leqslant \log g \leqslant 5.5$ were computed with a plane-parallel geometry, while those with relatively low surface gravities ($-1.0 \leqslant \log g \leqslant 3.5$) were calculated in spherical geometry. As in Paper I, according to the suggestions by Gustafsson et al. (2008) and Heiter & Eriksson (2006), spherical models were adopted for stars with

Table 2
Magnesium Abundances Relative to Iron for the Individual Mg I H-band Lines under LTE and NLTE Analysis

Star	15740(Å)		15748(Å)		15765 (Å)		15886 (Å)	
	LTE	NLTE	LTE	NLTE	LTE	NLTE	LTE	NLTE
Arcturus[a]	0.39	0.35	0.38	0.32	0.38	0.32	0.37	0.39
Arcturus[b]	0.40	0.35	0.37	0.31	0.38	0.32	0.31	0.32
HD 87	0.08	0.06	0.07	0.03	0.06	0.03	−0.04	−0.04
HD 6582	0.35	0.36	0.35	0.36	0.35	0.35	⋯	⋯
HD 6920	0.02	0.05	0.06	0.05	0.09	0.08	⋯	⋯
HD 22675	0.08	0.07	⋯	⋯	0.06	0.03	⋯	⋯
HD 31501	0.28	0.28	0.21	0.21	0.23	0.23	⋯	⋯
HD 58367	0.23	0.16	0.20	0.09	0.29	0.15	⋯	⋯
HD 67447	0.13	0.08	⋯	⋯	0.10	0.03	⋯	⋯
HD 102870	−0.08	−0.06	⋯	⋯	−0.10	−0.10	⋯	⋯
HD 103095	0.42	0.42	0.30	0.30	0.31	0.31	⋯	⋯
HD 121370	0.02	0.03	⋯	⋯	0.00	−0.01	⋯	⋯
HD 148816	0.32	0.35	0.28	0.30	0.28	0.30	⋯	⋯
HD 177249	0.13	0.10	⋯	⋯	0.15	0.08	⋯	⋯

Notes.
[a] The *H*-band spectrum of Arcturus is from Hinkle et al. (1995).
[b] The *H*-band spectrum of Arcturus is the 1 m +APOGEE one.

log $g \leqslant 3.5$ and plane-parallel model atmospheres for the rest. The final models were derived by interpolating with a FORTRAN routine coded by Thomas Masseron.[9] MARCS model atmospheres (Gustafsson et al. 2008) adopt a solar chemical composition from Grevesse et al. (2007). An α-enhancement is considered, and the mixing-length parameter is set to $l/H_P = 1.5$.

2.3. Statistical Equilibrium Codes

As in Paper I, we adopted a revised version of the DETAIL code (Butler & Giddings 1985), to solve the coupled statistical equilibrium and the radiative transfer equations. This statistical equilibrium code is based on the accelerated lambda iteration algorithm described by Rybicki & Hummer (1991, 1992), which has been widely applied in previous studies, e.g., Gehren et al. (2004), Shi et al. (2008), Mashonkina et al. (2011), Mashonkina (2013), Bergemann et al. (2012), and Sitnova et al. (2015). We calculated the departure coefficients using DETAIL, and then input these coefficients to SIU (Reetz 1991) to calculate the synthetic NLTE line profiles.

3. THE SAMPLE STARS AND STELLAR PARAMETERS

3.1. Sample Selection

We selected 13 stars with both IR *H*-band and optical high-resolution and high S/N spectra available as sample stars. The *H*-band spectra are mainly from APOGEE DR12 except those for the Sun and Arcturus, which will be described below. These APOGEE data were acquired with the NMSU (New Mexico State University) 1 m telescope coupled to the APOGEE instrument: a bundle of 10 fibers connects the APOGEE spectrograph and the NMSU 1 m telescope. In each observation, one fiber is assigned to the science target while the rest are used as sky fibers. (See Feuillet et al. 2016 for more details.) The wavelength range of APOGEE spectra spans from 15100 to 16900 Å, and the resolving power is ~22,500. A high-resolution and high S/N *H*-band spectrum of the Sun was taken

with the McMath–Pierce solar telescope on Kitt Peak (Wallace et al. 1996), and corresponds to the disk center region ($\mu = 1$). A high-quality IR spectrum of Arcturus was obtained from the NOAO data archives[10] (see Hinkle et al. 1995 for more observational information). The resolving power is around 300,000 and 100,000, respectively, for the Sun and Arcturus. The high-resolution optical spectra of the 13 sample stars are from several different telescopes, and their characteristics have been described in detail in Paper I.

3.2. Stellar Parameters

We determined the stellar parameters $T_{\rm eff}$, log g, [Fe/H], and ξ_t using a spectroscopic approach from the analysis of Fe I and Fe II lines. The final parameters satisfy the Fe I excitation equilibrium ($T_{\rm eff}$), the ionization equilibrium between Fe I and Fe II (log g), and [Fe/H] does not depend on equivalent width (ξ_t). NLTE effects on Fe I lines have been considered as in Sitnova et al. (2015). We estimated the typical uncertainties of $T_{\rm eff}$, log g, [Fe/H], and ξ_t as ±80 K, ±0.1 dex, ±0.08 dex, and 0.2 km s^{-1}, respectively. The determination of the stellar parameters and the comparison with previous work have been discussed in Paper I.

4. NLTE CALCULATIONS FOR SAMPLE STARS

4.1. Line Data

4.1.1. Infrared Atomic Line Data in the H-band

Magnesium abundances were derived from eight *H*-band Mg I lines, and the characteristics of these transitions are listed in Table 1. The damping constants, log C_6, are adopted from Meléndez & Barbuy (1999), which were calculated according to the *ABO* theory (Anstee & O'Mara 1995; Barklem & O'Mara 1997). The rest of the line data was adopted from the NIST atomic spectra database.[11] The values of oscillator strengths, log gf, were rescaled with respect to the solar NLTE results (adopting log $\varepsilon_\odot$(Mg) = 7.53 dex measured from

---

[9] http://marcs.astro.uu.se/software.php

[10] http://ast.noao.edu/data/
[11] http://www.nist.gov/pml/data/asd.cfm
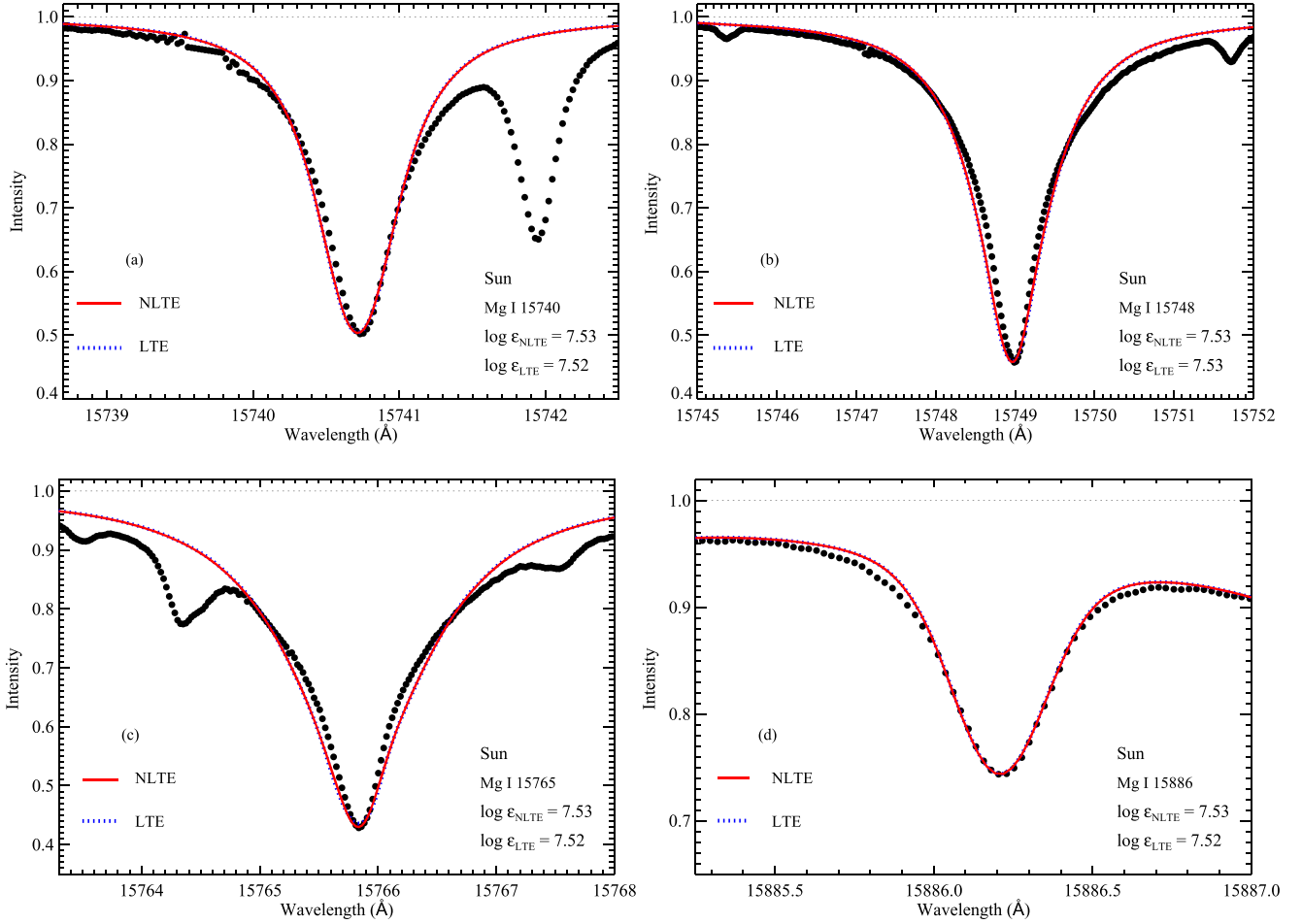
Figure 2. Best NLTE (continuous curve) and LTE (dotted curve) fits of the four *H*-band Mg I lines in comparison with the observed solar spectrum (filled circles).
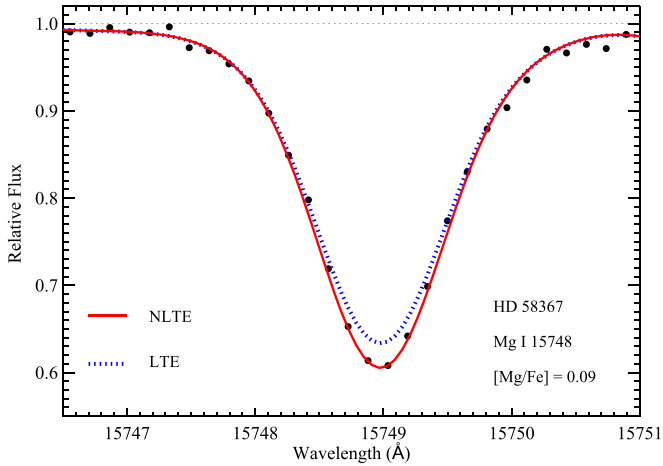
Figure 3. LTE and NLTE synthetic spectra of Mg I 15748 Å line with the same [Mg/Fe] for HD 58367. The filled circles represent the observed spectrum.

meteorites according to Grevesse et al. 2007 as the absolute solar Mg abundance). Among these eight lines, two transitions at 15748.886 and 15748.988 Å, three transitions at 15765.645, 15765.747, and 15765.842 Å, and transitions at 15886.183 and 15886.261 Å are blended, and they cannot be resolved at the resolution that the APOGEE instrument provides. However, it is worthwhile noting that each of the three blended lines is due

to transitions between the same lower (or higher) energy level and fine structure splitting of the higher (or lower) level, we therefore fit all lines in a blended feature together via spectrum synthesis in a small wavelength interval. As a result, only four values for the Mg abundances from the eight lines are actually derived for each star from the infrared spectra.

4.1.2. Optical Atomic Line Data

There are six optical Mg I lines included in our analysis, and their main characteristics are presented in Table 1. Similar to the *H*-band lines, the oscillator strengths have been scaled in order to have the NLTE computed profiles matching the observations with $\log \varepsilon_\odot(\mathrm{Mg}) = 7.53$ dex. We calculated the van der Waals damping constants for the 4571, 5172, and 5183 Å lines according to Table 1 of Mashonkina (2013), who presented van der Waals broadening constants Γ_6 based on the *ABO* theory. Following her suggestion, we reduced Γ_6 by 0.3 and 0.2 dex for the Mg I 4703 and 5528 Å lines, respectively. For the 5711 Å line, the C_6 value was determined by fitting the wings of the lines in the solar spectrum (Gehren et al. 2004). Actually these three optical Mg I lines' C6 values (4703, 5528, 5711) were determined by fitting the solar spectrum, because the values from the ABO theory enhance the abundance discrepancy among the different solar Mg lines.

31

Figure 5. LTE and NLTE synthetic spectra of the Mg I 15765 Å line with different values of [Mg/Fe] and the same parameters of T_{eff} = 5000 K, log g = 0.5 dex, and [Fe/H] = 0.0 dex, ξ_t = 2.0 km s^{-1}. [Mg/Fe] = 0.00, 0.10, 0.22 dex under LTE, respectively, while [Mg/Fe] = 0.00 dex under NLTE.

depths near unity. This reduction in the level population is the result of the large photoionization rate, which is known to dominate the near-UV spectra of cool stars. The other two higher excitation levels (4d ^{3}D, 5p ^{3}P°) are underpopulated due to photon loss at optical depths around −2 (see Figure 1 for details).

The Mg abundances were estimated through spectrum synthesis, and the NLTE effects can be assessed by comparing NLTE and LTE results ($\Delta = \log \varepsilon_{NLTE} - \log \varepsilon_{LTE}$). For each star, spectral synthesis calculations were required to fit the observed line profiles by changing the elemental abundance in the NLTE and LTE cases, respectively. The Mg abundances relative to iron for our four-group H-band lines are presented in Table 2. The adopted solar stellar parameters are T_{eff} = 5777 K, [Fe/H] = 0.0 dex, log g = 4.44 dex, and ξ_t = 0.9 km s^{-1}. The H-band solar Mg I line profiles are computed for μ = 1, and the comparison of the best-fit NLTE synthetic profiles (solid line) and LTE (dotted line) with the observed solar ones (open circles) for the four Mg I lines is illustrated in Figure 2. We noted that the synthesized line profiles are slightly broad in the central part compared to the observed ones for strong lines, especially for lines at 15748 Å and 15765 Å, as is apparent in Figure 2, while the weak line at 15886 Å is reproduced much better. The systematic deviations between model and observed line profiles for the transitions 15748 and 15765 Å are apparent both in LTE and NLTE, since NLTE corrections are very small. In addition, the observations for these lines exhibit significant asymmetries between the blue and red wings. We have tested the influence of micro-turbulence and scattering and they have only a minor impact on the computed profiles. These strong lines are sampling a very large range in optical depth, and the noted discrepancies are likely reflecting modeling shortcomings such as atmospheric inhomogeneities in temperature and velocity, or systematic errors in the line formation associated to them. This also possibly results from an imperfectness of the line broadening theory. As mentioned above, the NLTE corrections for the four solar H-band lines are very small, within 0.01 dex. Figure 3 shows the synthetic flux profiles under LTE (dotted curve) and NLTE (solid curve) assumptions with the same Mg abundance for the line at 15748 Å in the spectrum of HD 58367, and the difference is obvious.

Figure 4. NLTE corrections for Mg 15765 Å as functions of [Fe/H], T_{eff}, and log g, respectively (from top to bottom).

4.2. NLTE Effects

4.2.1. Departures form LTE for Mg I H-band Lines

We present the departure coefficients (b_i) for the relevant Mg I levels, including Mg II ground state, as a function of the optical depth at 5000 Å (τ_{5000}) for a model atmosphere for HD 58367 in Figure 1. The departure coefficient is defined as $b_i = n_i^{NLTE}/n_i^{LTE}$, while n_i^{NLTE} and n_i^{LTE}, respectively, indicate NLTE and LTE atomic level number densities. We noted that the populations of the two relative low levels 4p ^{3}P° and 3d ^{3}D slightly deviate from their LTE values at optical

Table 3
Stellar Magnesium LTE and NLTE Abundances

Star	$T_{\rm eff}$	$\log g$	[Fe/H]	ξ_t	[Mg I$_{\rm LTE}$/Fe](IR)	[Mg I$_{\rm NLTE}$/Fe](IR)	$\Delta_{\rm IR}$	[Mg I$_{\rm LTE}$/Fe](OPT)	[Mg I$_{\rm NLTE}$/Fe](OPT)	$\Delta_{\rm OPT}$
Arcturus[a]	4275	1.67	−0.58	1.60	0.38 ± 0.01	0.35 ± 0.03	−0.03	0.38 ± 0.07	0.35 ± 0.03	−0.03
Arcturus[b]	4275	1.67	−0.58	1.60	0.36 ± 0.04	0.32 ± 0.02	−0.04	⋯	⋯	⋯
HD 87	5053	2.71	−0.10	1.35	0.04 ± 0.06	0.02 ± 0.04	−0.02	0.07 ± 0.06	0.06 ± 0.03	−0.01
HD 6582	5390	4.42	−0.81	0.90	0.35 ± 0.00	0.36 ± 0.01	0.01	0.40 ± 0.02	0.41 ± 0.02	0.01
HD 6920	5845	3.45	−0.06	1.40	0.06 ± 0.04	0.06 ± 0.02	0.00	0.06 ± 0.06	0.06 ± 0.07	0.00
HD 22675	4901	2.76	−0.05	1.30	0.07 ± 0.01	0.05 ± 0.03	−0.02	0.08 ± 0.05	0.06 ± 0.03	−0.02
HD 31501[c]	5320	4.45	−0.40	1.00	0.24 ± 0.04	0.24 ± 0.04	0.00	0.22 ± 0.00	0.22 ± 0.00	0.00
HD 58367	4932	1.79	−0.18	2.00	0.24 ± 0.05	0.13 ± 0.04	−0.11	0.13 ± 0.10	0.08 ± 0.03	−0.05
HD 67447	4933	2.17	−0.05	2.12	0.12 ± 0.02	0.06 ± 0.04	−0.06	0.07 ± 0.04	0.02 ± 0.01	−0.05
HD 102870	6070	4.08	0.20	1.20	−0.09 ± 0.01	−0.08 ± 0.03	0.01	−0.08 ± 0.06	−0.07 ± 0.06	0.01
HD 103095	5085	4.65	−1.35	0.80	0.34 ± 0.07	0.34 ± 0.07	0.00	0.30 ± 0.05	0.30 ± 0.05	0.00
HD 121370	6020	3.80	0.28	1.40	0.01 ± 0.01	0.01 ± 0.03	0.00	0.00 ± 0.04	0.00 ± 0.05	0.00
HD 148816	5830	4.10	−0.73	1.40	0.29 ± 0.02	0.32 ± 0.03	0.03	0.25 ± 0.05	0.27 ± 0.05	0.02
HD 177249	5273	2.66	0.03	1.65	0.14 ± 0.01	0.09 ± 0.01	−0.05	0.07 ± 0.10	0.04 ± 0.05	−0.03

Notes. $\Delta_{\rm ir}$ and $\Delta_{\rm opt}$ stand for the NLTE effects ($\Delta = \log \varepsilon_{\rm NLTE} - \log \varepsilon_{\rm LTE}$) derived from IR and optical spectra respectively.
[a] The *H*-band spectrum of Arcturus is from Hinkle et al. (1995).
[b] The *H*-band spectrum of Arcturus is the 1 m +APOGEE one.
[c] Only one line is calculated, so the error is zero.

As shown in Table 2, the NLTE effects differ from line to line. Among our four-group *H*-band lines, the three strong Mg I lines at 15740, 15748, and 15765 Å present relatively strong NLTE effects, while the weak one at 15886 Å shows smaller effects. We plotted the difference of the [Mg/Fe] ratios under NLTE and LTE assumptions for the strong magnesium line at 15765 Å as a function of metallicity, effective temperature, and surface gravity in Figure 4. It is clear that the NLTE effects depend mainly on surface gravity, similar to our findings for Si (Paper I), namely the corrections increase with decreasing surface gravity, reaching 0.14 dex for HD 58367. The stellar parameters of this object are $T_{\rm eff} = 4932$ K, [Fe/H] = −0.18 dex, and $\log g = 1.79$ dex.

It is also interesting to check how large the NLTE corrections can get in the extreme cases for APOGEE. We calculated the NLTE line profile for the Mg I line at 15765 Å for a giant with $T_{\rm eff} = 5000$ K, [Fe/H] = 0.0 dex, $\log g = 0.5$ dex, and [Mg/Fe] = 0.0 dex (see open circle curve in Figure 5). The LTE profile computed with the corresponding NLTE abundance is presented with a dashed curve for comparison. When [Mg/Fe] under LTE and NLTE share the same value of 0.0 dex, the two profiles are quite different from each other, and the line core in the LTE calculations becomes deeper for increasing values of [Mg/Fe]. The calculated LTE profile obviously deviates from the NLTE one until [Mg/Fe] is increased by 0.22 dex. This indicates that, in this extreme case, the NLTE abundance correction could reach approximately −0.22 dex.

The mean Mg abundances based on the *H*-band spectra under NLTE and LTE cases, respectively, are listed in Table 3, along with statistical uncertainties and the mean NLTE corrections. We noted that the value and sign of the NLTE Mg abundance correction are determined by a relative contribution of the core and the wings to the overall line strength. It can be seen that the NLTE corrections range from −0.11 to 0.03 dex.

We derived the Mg abundance of Arcturus for both the spectrum from Hinkle et al. (1995; $R \sim 100,000$) and from the 1 m+APOGEE ($R \sim 22,500$), and the best NLTE fitting line profiles are compared with observations in Figure 6. In this figure, the left panel is for the spectrum of Arcturus from

Hinkle et al. (1995) and the right panel for the 1 m+APOGEE spectrum. We also listed the determined Mg abundance in Table 2 (values for individual lines) and Table 3 (mean values). A consistent mean Mg abundance is derived from these two spectra with a negligible difference of 0.03 dex.

4.2.2. Departures from LTE for the Mg I Optical Lines

We used six Mg I optical lines, which are described in Section 4.1.2, to derive the Mg abundance, and to investigate the NLTE effects for lines in this wavelength band. The mean Mg abundances from the optical spectra under both LTE and NLTE assumptions are separately given in Table 3. The standard deviation is small, less than 0.07 dex under NLTE. The [Mg/Fe] ratios for individual lines are also presented in Table 4.

4.2.3. Comparisons with the Optical Results and Discussions

We present the average Mg abundances based on the IR and optical spectra under the LTE and NLTE assumptions, respectively, as well as the stellar parameters adopted for our sample stars in Table 3. In Figure 7, the differences of the mean Mg abundances between *H*-band and optical lines are plotted against the metallicity for our target stars, where the open circles represent the LTE abundances, while filled circles stand for NLTE results. It can clearly be seen that a better consistent result can be derived when the NLTE effects considered, though the differences are small (~0.1 dex) both in LTE and NLTE.

5. CONCLUSIONS

We verified the reliability of our Mg atomic model for the *H*-band line formation based on the high-quality *H*-band spectra, and investigated NLTE effects on Mg I *H*-band lines for 13 FGK sample stars. A detailed analysis based on a line-to-line differential analysis relative to the Sun both under LTE and NLTE allows us to obtain accurate Mg abundances. Our conclusions can be summarized as follows.

33
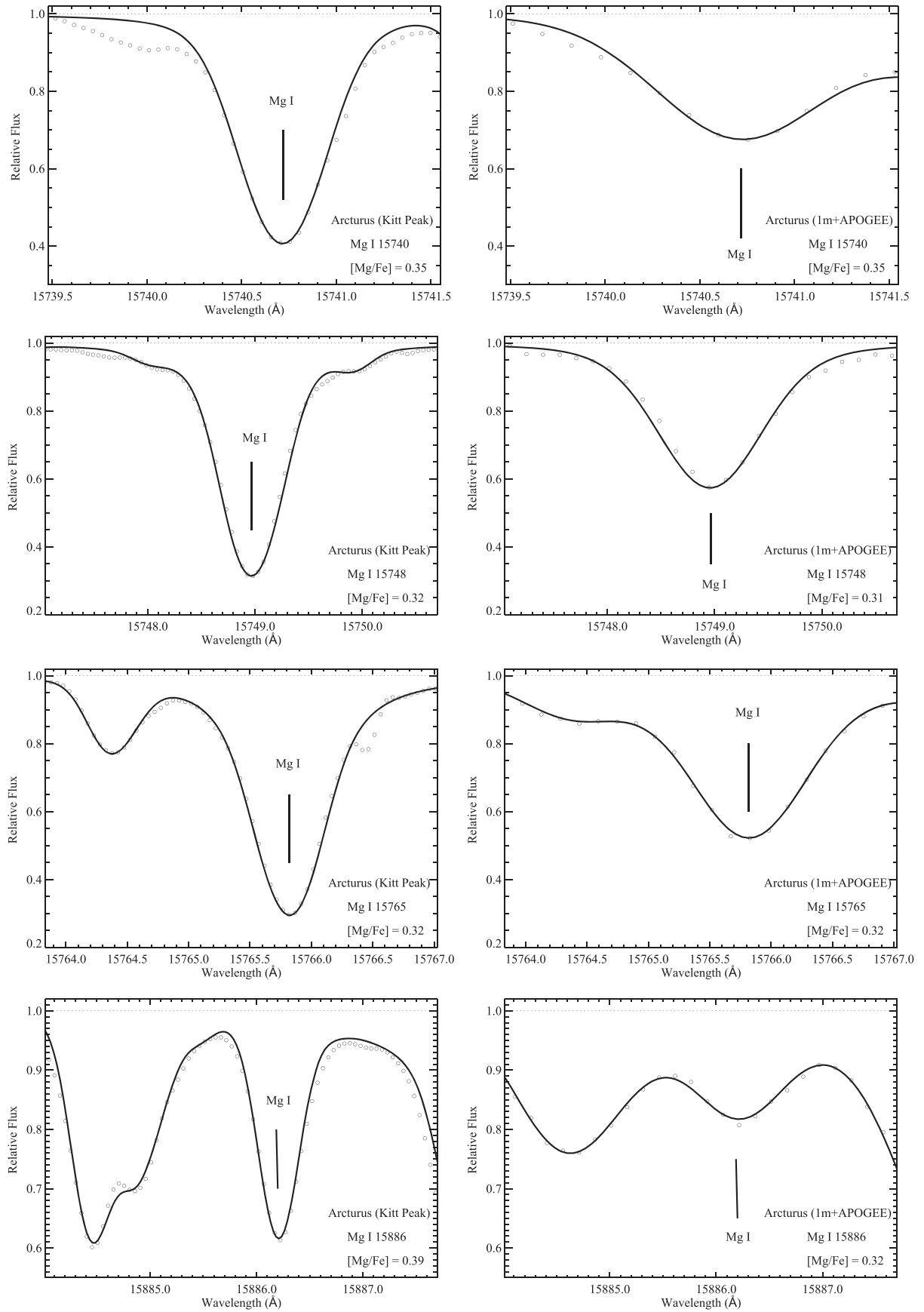
Figure 6. NLTE best fitting profiles (solid line) of the four investigated Mg I lines for Kitt Peak (Hinkle et al. 1995) and 1 m+APOGEE observed spectra (open circles) of Arcturus. The left column is for the spectrum of Arcturus from Hinkle et al. (1995) while the right column is for the 1 m+APOGEE spectrum.

34

Table 4
Magnesium Abundances Relative to Iron Based on Optical Mg I Lines under LTE and NLTE Analysis

Star	4571 (Å)		4702 (Å)		5172 (Å)		5183 (Å)		5528 (Å)		5711 (Å)	
	LTE	NLTE	LTE	NLTE	LTE	NLTE	LTE	NLTE	LTE	NLTE	LTE	NLTE
Arcturus	0.37	0.38	⋯	⋯	0.32	0.33	0.30	0.31	0.43	0.38	0.46	0.34
HD 87	⋯	⋯	⋯	⋯	0.02	0.04	0.02	0.03	0.13	0.08	0.11	0.08
HD 6582	⋯	⋯	0.42	0.42	⋯	⋯	⋯	⋯	0.39	0.38	0.40	0.42
HD 6920	⋯	⋯	0.15	0.16	−0.01	0.00	0.02	0.03	0.06	0.02	0.06	0.10
HD 22675	⋯	⋯	⋯	⋯	0.05	0.05	0.03	0.04	0.11	0.07	0.14	0.10
HD 31501	⋯	⋯	⋯	⋯	⋯	⋯	⋯	⋯	⋯	⋯	0.22	0.22
HD 58367	⋯	⋯	⋯	⋯	0.06	0.08	0.04	0.06	0.25	0.12	0.15	0.08
HD 67447	⋯	⋯	0.03	0.03	⋯	⋯	⋯	⋯	0.11	0.01	0.07	0.02
HD 102870	−0.13	−0.10	0.02	0.03	−0.11	−0.11	−0.13	−0.13	−0.06	−0.09	−0.04	−0.01
HD 103095	0.22	0.22	0.32	0.32	0.32	0.32	0.30	0.30	0.27	0.26	0.36	0.37
HD 121370	⋯	⋯	⋯	⋯	−0.03	−0.02	−0.03	−0.03	0.00	−0.02	0.06	0.08
HD 148816	0.21	0.24	0.33	0.35	0.23	0.24	0.19	0.21	0.30	0.30	0.26	0.31
HD 177249	⋯	⋯	⋯	⋯	0.00	0.01	0.00	0.01	0.21	0.11	0.07	0.04
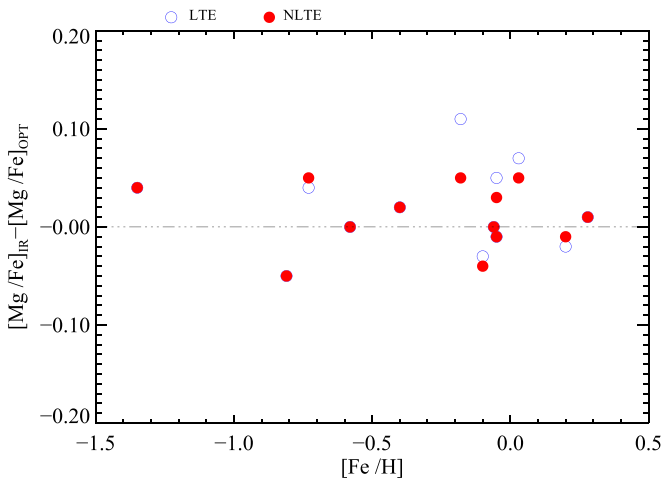
Figure 7. Difference between the mean Mg abundances derived from IR and Optical spectra for our sample stars.

1. The mean Mg abundance differences between the *H*-band and optical lines are within 0.05 dex for all our sample stars when NLTE effects are included, which suggests that our Mg atomic model can be applied to study the formation of *H*-band Mg I lines.

2. It is shown that the NLTE effects tend to be large for strong Mg I lines at 15740, 15748, and 15765 Å, and smaller for the relatively weak line at 15886 Å. The NLTE correction is as large as approximately −0.14 dex for the strong Mg I line in our sample stars, and for the extreme case in APOGEE it reaches up to approximately −0.22 dex. Thus, departures from LTE need to be considered in the Mg abundance analysis, especially when only strong lines are available.

3. The NLTE effects in *H*-band Mg lines are very sensitive to surface gravity, increasing for lower gravities. Therefore, they need to be considered for APOGEE since most of their sample are giant, RGB stars. The corrections are always negative for cool stars, and therefore LTE Mg abundances will be overestimated.

We conclude that it is important to consider NLTE effects in the calculations of *H*-band Mg lines.

REFERENCES

Ahn, C. P., Alexandroff, R., Allende Prieto, C., et al. 2014, ApJS, 211, 17
Alam, S., Albareti, F. D., Allende Prieto, C., et al. 2015, ApJS, 219, 12
Andrievsky, S. M., Spite, M., Korotin, S. A., et al. 2010, A&A, 509, A88
Anstee, S. D., & O'Mara, B. J. 1995, MNRAS, 276, 859
Athay, R. G., & Canfield, R. C. 1969, ApJ, 156, 695
Barklem, P. S., Belyaev, A. K., Spielfiedel, A., et al. 2012, A&A, 541, A80
Barklem, P. S., & O'Mara, B. J. 1997, MNRAS, 290, 102
Bensby, T., Feltzing, S., & Oey, M. S. 2014, A&A, 562, A71
Bergemann, M., Kudritzki, R. P., Gazak, Z., et al. 2015, ApJ, 804, 113
Bergemann, M., Kudritzki, R. P., Plez, B., et al. 2012, ApJ, 751, 156
Bonifacio, P., Spite, M., Cayrel, R., et al. 2009, A&A, 501, 519

Butler, K., & Giddings, J. 1985, Newsletter on the Analysis of Astronomical Spectra (Univ. London)
Carlsson, M., Rutten, R. J., & Shchukina, N. G. 1992, A&A, 253, 567
Cayrel, R., Depagne, E., Spite, M., et al. 2004, A&A, 416, 1117
Chang, E. S., Avrett, E. H., Noyes, R. W., et al. 1991, ApJL, 379, L79
Chen, Y. Q., Nissen, P. E., Zhao, G., et al. 2000, A&A, 141, 491
Eisenstein, D. J., Weinberg, D. H., Agol, E., et al. 2011, AJ, 142, 72
Feuillet, D. K., Bovy, J., Holtzman, J., et al. 2016, ApJ, 817, 40
Fuhrmann, K. 1998, A&A, 338, 161
Fuhrmann, K. 2004, AN, 325, 3
García Pérez, A. E., Allende Prieto, C., Holtzman, J. A., et al. 2016, AJ, 151, 144
Gehren, T., Liang, Y. C., Shi, J. R., et al. 2004, A&A, 413, 1045
Gehren, T., Shi, J. R., Zhang, H. W., et al. 2006, A&A, 451, 1065
Gigas, D. 1988, A&A, 192, 264
Grevesse, N., Asplund, M., & Sauval, A. J. 2007, SSRv, 130, 105
Gustafsson, B., Edvardsson, B., Eriksson, K., et al. 2008, A&A, 486, 951
Heiter, U., & Eriksson, K. 2006, A&A, 452, 1039
Hinkle, K., Wallace, L., & Livingston, W. 1995, PASP, 107, 1042
Kurucz, R. L. 1979, ApJS, 40, 1
Lambert, D. L., & Luck, R. E. 1978, MNRAS, 183, 79
Lemke, M., & Holweger, H. 1987, A&A, 173, 375

Majewski, S. R., Schiavon, R. P., Allende Prieto, C., et al. 2016, AN, 337, 863
Mashonkina, L. 2013, A&A, 550, A28
Mashonkina, L., Gehren, T., Shi, J. R., et al. 2011, A&A, 528, A87
Mauas, P. J., Avrett, E. H., & Loeser, R. 1988, ApJ, 330, 1008
Meléndez, J., & Barbuy, B. 1999, ApJS, 124, 527
Mészáros, S., Holtzman, J., García Pérez, A. E., et al. 2013, AJ, 146, 133
Osorio, Y., Barklem, P. S., Lind, K., et al. 2015, A&A, 579, A53
Reddy, B. E., Lambert, D. L., & Allende Prieto, C. 2006, MNRAS, 367, 1329
Reetz, J. K. 1991, Diploma thesis, Univ. München
Rybicki, G. B., & Hummer, D. G. 1991, A&A, 245, 171
Rybicki, G. B., & Hummer, D. G. 1992, A&A, 262, 209
Seaton, M. J. 1962, Atomic and Molecular Processes (New York: Academic)
Shi, J. R., Gehren, T., Butler, K., et al. 2008, A&A, 486, 303
Shigeyama, T., & Tsujimoto, T. 1998, ApJL, 507, L135
Sitnova, T., Zhao, G., Mashonkina, L., et al. 2015, ApJ, 808, 148
Tomkin, J., Lambert, D. L., & Balachandran, S. 1985, ApJ, 290, 289
Wallace, L., Livingston, W., & Hinkle, K. 1996, ApJS, 106, 165
Woosley, S. E., & Weaver, T. A. 1995, ApJS, 101, 181
Zhang, J. B., Shi, J. R., Pan, K. K., et al. 2016, ApJ, 833, 137
Zhao, G., Butler, K., & Gehren, T. 1998, A&A, 333, 219
Zhao, G., & Gehren, T. 2000, A&A, 362, 1077

Discovery and Follow-up Observations of the Young Type Ia Supernova 2016coj

WeiKang Zheng[1], Alexei V. Filippenko[1], Jon Mauerhan[1], Melissa L. Graham[1,2], Heechan Yuk[1], Griffin Hosseinzadeh[3,4],
Jeffrey M. Silverman[5,18], Liming Rui[6], Ron Arbour[7], Ryan J. Foley[8], Bela Abolfathi[9], Louis E. Abramson[10], Iair Arcavi[3,4,19],
Aaron J. Barth[9], Vardha N. Bennert[11], Andrew P. Brandel[9], Michael C. Cooper[9], Maren Cosens[11], Sean P. Fillingham[9],
Benjamin J. Fulton[12], Goni Halevi[1], D. Andrew Howell[3,4], Tiffany Hsyu[8], Patrick L. Kelly[1], Sahana Kumar[1], Linyi Li[6],
Wenxiong Li[6], Matthew A. Malkan[10], Christina Manzano-King[13], Curtis McCully[3,4], Peter E. Nugent[1,14], Yen-Chen Pan[8],
Liuyi Pei[9], Bryan Scott[13], Remington Oliver Sexton[13], Isaac Shivvers[1], Benjamin Stahl[15], Tommaso Treu[10], Stefano Valenti[16],
H. Alexander Vogler[9], Jonelle L. Walsh[17], and Xiaofeng Wang[6]
[1] Department of Astronomy, University of California, Berkeley, CA 94720-3411, USA; zwk@astro.berkeley.edu
[2] Department of Astronomy, University of Washington, Box 351580, U.W., Seattle, WA 98195-1580, USA
[3] Las Cumbres Observatory Global Telescope Network, 6740 Cortona Drive, Ste. 102, Goleta, CA 93117-5575, USA
[4] Department of Physics, University of California, Santa Barbara, CA 93106-9530, USA
[5] Department of Astronomy, University of Texas, Austin, TX 78712, USA
[6] Physics Department and Tsinghua Center for Astrophysics, Tsinghua University, Beijing, 100084, China
[7] Pennel Observatory, 29 Wrights Way, South Wonston, Hants S021 3He, UK
[8] Department of Astronomy and Astrophysics, University of California, Santa Cruz, CA 95064, USA
[9] Department of Physics and Astronomy, University of California, 4129 Frederick Reines Hall, Irvine, CA 92697, USA
[10] Department of Physics and Astronomy, University of California, 430 Portola Plaza, Los Angeles, CA 90095, USA
[11] Physics Department, California Polytechnic State University, San Luis Obispo, CA 93407, USA
[12] Institute for Astronomy, University of Hawaii, 2680 Woodlawn Drive, Honolulu, HI 96822, USA
[13] Department of Physics and Astronomy, University of California, 900 University Avenue, Riverside, CA 92521, USA
[14] Lawrence Berkeley National Laboratory, Berkeley, California 94720, USA
[15] Department of Physics, University of California, Berkeley, 94720, USA
[16] Department of Physics, University of California, Davis, 1 Shields Avenue, Davis, CA 95616-5270, USA
[17] George P. and Cynthia Woods Mitchell Institute for Fundamental Physics and Astronomy, Department of Physics and Astronomy,
Texas A&M University, College Station, TX 77843, USA

Abstract

The Type Ia supernova (SN Ia) 2016coj in NGC 4125 (redshift $z = 0.00452 \pm 0.00006$) was discovered by the Lick Observatory Supernova Search 4.9 days after the fitted first-light time (FFLT; 11.1 days before B-band maximum). Our first detection (prediscovery) is merely 0.6 ± 0.5 days after the FFLT, making SN 2016coj one of the earliest known detections of an SN Ia. A spectrum was taken only 3.7 hr after discovery (5.0 days after the FFLT) and classified as a normal SN Ia. We performed high-quality photometry, low- and high-resolution spectroscopy, and spectropolarimetry, finding that SN 2016coj is a spectroscopically normal SN Ia, but the velocity of Si II λ6355 around peak brightness ($\sim$12,600 km s^{-1}) is a bit higher than that of typical normal SNe. The Si II λ6355 velocity evolution can be well fit by a broken-power-law function for up to a month after the FFLT. SN 2016coj has a normal peak luminosity ($M_B \approx -18.9 \pm 0.2$ mag), and it reaches a B-band maximum $\sim$16.0 days after the FFLT. We estimate there to be low host-galaxy extinction based on the absence of Na I D absorption lines in our low- and high-resolution spectra. The spectropolarimetric data exhibit weak polarization in the continuum, but the Si II line polarization is quite strong ($\sim$0.9% $\pm$ 0.1%) at peak brightness.

Key words: supernovae: general – supernovae: individual (SN 2016coj)

Supporting material: data behind figure

1. Introduction

Type Ia supernovae (SNe Ia; see Filippenko 1997 for a review of supernova classification) are the thermonuclear runaway explosions of carbon/oxygen white dwarfs (see, e.g., Hillebrandt & Niemeyer 2000 for a review). They can be used as standardizable candles with many important applications, including measurements of the expansion rate of the universe (Riess et al. 1998; Perlmutter et al. 1999). Two general scenarios are favored as the progenitor system for SNe Ia. One is the single-degenerate model (Hoyle & Fowler 1960; Hachisu et al. 1996; Meng et al. 2009; Röpke et al. 2012), which consists of a single white dwarf accreting material from a companion. The other is the double-degenerate

scenario involving the merger of two white dwarfs (Iben & Tutukov 1984; Webbink 1984; Pakmor et al. 2012; Röpke et al. 2012). However, our understanding of their progenitor systems and explosion mechanisms remains substantially incomplete.

Very early discovery and detailed follow-up observations are essential for understanding those problems. For example, Bloom et al. (2012) were able to constrain the companion-star radius to be $\lesssim$0.1 $R_\odot$ from an optical nondetection just 4 hr after the explosion of SN 2011fe (Nugent et al. 2011). Cao et al. (2015) found strong but declining ultraviolet emission in SN Ia iPTF14atg in early-time *Swift* observations, consistent with theoretical expectations of the collision between supernova (SN) ejecta and a companion star (Kasen 2010). Im et al. (2015) found evidence of a "dark phase" in SN 2015F, which can last for a few hours to days between the moment of

37

explosion and the first observed light (e.g., Rabinak et al. 2012; Piro & Nakar 2013, 2014); see also Cao et al. (2016) for the case of iPTF14pdk. Differences in the duration of the "dark phase" could be caused by a varying distribution of ^{56}Ni near the surface of an SN Ia. For example, Piro & Morozova (2016) show that it is short (with a steep rise) when the ^{56}Ni is shallow, and longer (with a more gradual rise) when the ^{56}Ni is deeper (see their Figure 7).

Spectra of SNe Ia not only reveal the ejecta composition from nuclear burning, but also provide a way to measure the ejecta expansion velocity. Benetti et al. (2005) separated SN Ia samples into different groups according to their velocity gradient and found that high-velocity-gradient objects tend to have a higher velocity of the Si II $\lambda6355$ line near maximum light. Note that the higher velocity discussed in this paragraph is not the high-velocity feature described in Section 3.2. Nugent et al. (1995) quantified the spectral diversity using line-strength ratios, finding a good correlation between the absorption-depth ratio of Si II $\lambda5972$ to Si II $\lambda6355$) and the brightness decline rate. Wang et al. (2009, 2013) and Foley & Kasen (2011) separated SNe Ia into high-velocity and normal-velocity groups with a boundary at 11,800 km s^{-1} at peak brightness, and found that the former are ~0.1 mag (on average) redder in $B - V$ than the latter.

Meanwhile, high-resolution spectral observations provide a powerful way to study absorption along the line of sight, both from the interstellar medium and circumstellar material. Patat et al. (2007) found a complex of Na I D lines that showed evolution in SN 2006X (Wang et al. 2008). Two additional cases of time-variable Na absorption are provided by Blondin et al. (2009) and Simon et al. (2009). Sternberg et al. (2014) found that in their sample with high-resolution spectra, $\sim18\%$ of SNe Ia exhibit time-variable Na, indicating the presence of circumstellar material and suggesting that it may be more common than expected in SNe Ia, though some objects do not show evolution (e.g., SN 2014J; Graham et al. 2015).

Spectropolarimetry can be used to probe the geometry of SNe Ia (see Wang & Wheeler 2008 for a review). The continuum polarization, an indication of the photosphere's shape, was found to be quite low in SNe Ia, on the order of a few tenths of a percent (Höflich 1991; Wang et al. 1997). However, for individual SNe Ia, significant line polarization is sometimes observed (e.g., Kasen et al. 2003; Wang et al. 2003). Wang et al. (2007) also found a correlation between the degree of polarization of Si II $\lambda6355$ and the brightness decline rate.

Observationally, there are numerous efforts to discover SNe Ia at very early times, which can benefit follow-up observations in many ways. Recent examples of early-observed and well-studied SNe Ia include SN 2009ig (Foley et al. 2012), SN 2011fe (Li et al. 2011; Nugent et al. 2011), SN 2012cg (Silverman et al. 2012b), SN 2013dy (Zheng et al. 2013), iPTF13ebh (Hsiao et al. 2015), SN 2014J (Goobar et al. 2014; Zheng et al. 2014; Graham et al. 2015), and ASASSN-14lp (Shappee et al. 2016); like SN 2016coj discussed here, they were either discovered or detected shortly after exploding.

In 2011, the observing strategy for our Lick Observatory Supernova Search (LOSS; Filippenko et al. 2001; Filippenko 2005; Leaman et al. 2011) with the 0.76 m Katzman Automatic Imaging Telescope (KAIT) was modified to monitor fewer galaxies but at a more rapid cadence, with the objective of promptly identifying very young SNe (hours to days after explosion). In the past few years, this strategy has led to

discoveries of all types of young SNe, where we define an SN to be "young" if there was a KAIT nondetection one to three days before the first detection or if it was spectroscopically confirmed to be within a few days after explosion. SN 2012cg (Silverman et al. 2012b) was the first case, followed by more than a dozen others (e.g., SN 2012ck, Kandrashoff et al. 2012; SN 2012ea, Cenko et al. 2012; SN 2013ab, Blanchard et al. 2013; SN 2013dy, Zheng et al. 2013; SN 2013ej, Dhungana et al. 2016; SN 2013gh, Hayakawa et al. 2013; SN 2013fv, Kim et al. 2013a; SN 2013gd, Casper et al. 2013; SN 2013gy, Kim et al. 2013b; SN 2014C, Kim et al. 2014b; SN 2014J, though not discovered by KAIT, but with KAIT early detections, see Zheng et al. 2014; SN 2014ce, Kim et al. 2014a; SN 2014eh, Kumar et al. 2014; SN 2015N, Stegman et al. 2015a; SN 2015U, Shivvers et al. 2016; SN 2015X, Hughes et al. 2015; SN 2015O, Ross et al. 2015; SN 2015be, Stegman et al. 2015b; and SN 2016esw, discovered by Halevi et al.[20]).

SN 2016coj was another SN discovered by KAIT when very young, merely 0.6 ± 0.5 days after the fitted first-light time (FFLT). Here we present the first 40 days of our optical photometric, low- and high-resolution spectroscopic, and spectropolarimetric follow-up observations and analysis of it.

2. Discovery and Observations

SN 2016coj was discovered in an 18 s unfiltered KAIT image taken at 04:39:05 on 2016 May 28 (UT dates are used throughout this paper), at 14.98 ± 0.03 mag (close to the R band; see Li et al. 2003). It was reported to the Transient Name Server (TNS) shortly after discovery by Yuk, Zheng, & Filippenko[21] (see also Zheng et al. 2016). We measure its J2000.0 coordinates to be $\alpha = 12^{\rm h}08^{\rm m}06''80$, $\delta = +65°10'38''2$, with an uncertainty of $0''5$ in each coordinate. SN 2016coj is $5''0$ east and $10''8$ north of the nucleus of the host galaxy NGC 4125, which has redshift $z = 0.00452 \pm 0.00006$ (de Vaucouleurs et al. 1991), an early-type peculiar elliptical morphology (E6 pec; de Vaucouleurs et al. 1991), and a stellar mass of $2.4 \times 10^{11} M_\odot$ from its 3.6 μm flux (Wilson et al. 2013).

KAIT performed photometric follow-up observations of SN 2016coj with nearly daily cadence after discovery. The data were reduced using our image-reduction pipeline (Ganeshalingam et al. 2010). We applied an image-subtraction procedure to remove host-galaxy light, and point-spread-function photometry was then obtained using DAOPHOT (Stetson 1987) from the IDL Astronomy User's Library.[22] The unfiltered instrumental magnitudes, which are found to be close to the R band (Li et al. 2003), are calibrated to local SDSS standards (see Figure 1) transformed into Landolt R-band magnitudes.[23] Here we publish our unfiltered photometry (Table 1). We have also obtained a filtered data sequence, but we are still awaiting high-quality galaxy template images in those bands.

Interestingly, we find that SN 2016coj was detected in a KAIT prediscovery image taken at 04:30:35 on May 24 (see middle panels of Figure 2) with an unfiltered mag of

---

[20] https://wis-tns.weizmann.ac.il//object/2016esw
[21] https://wis-tns.weizmann.ac.il//object/2016coj
[22] http://idlastro.gsfc.nasa.gov/
[23] http://www.sdss.org/dr7/algorithms/sdssUBVRITransform.html#Lupton2005
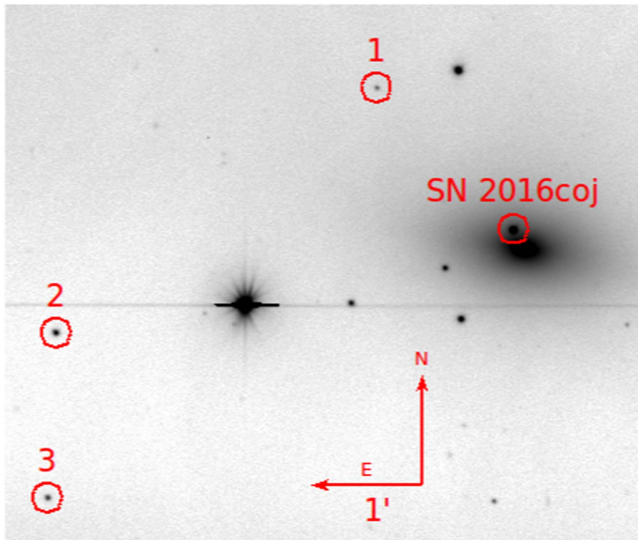
Figure 1. KAIT unfiltered image showing the location of SN 2016coj. Three reference stars are also marked with circles.

Figure 2. Left panels: Arbour's image taken on May 23. Middle panels: KAIT unfiltered image taken on May 24. Right panels: KAIT unfiltered image taken on May 28. Upper panels show the original image and lower panels show the residual after subtraction; SN 2016coj is marked.

Table 1
Unfiltered Photometry of SN 2016coj

MJD	UT	Mag	Error	From
57520.2370	May 12.2370	>19.6	…	KAIT
57522.2513	May 14.2513	>19.4	…	KAIT
57524.2240	May 16.2240	>19.4	…	KAIT
57525.2479	May 17.2479	>19.3	…	KAIT
57527.2708	May 18.2708	>19.2	…	KAIT
57531.9092	May 23.9092	18.06	0.42	R. Arbour
57532.1877	May 24.1877	18.02	0.22	KAIT
57536.2694	May 28.2694	14.98	0.03	KAIT
57537.2196	May 29.2196	14.50	0.04	KAIT
57538.1827	May 30.1827	14.11	0.03	KAIT
57539.1814	May 31.1814	13.85	0.03	KAIT
57540.2518	June 01.2518	13.54	0.04	KAIT
57541.2022	June 02.2022	13.39	0.06	KAIT
57542.2075	June 03.2075	13.18	0.03	KAIT
57543.2120	June 04.2120	13.16	0.03	KAIT
57544.1995	June 05.1995	13.02	0.03	KAIT
57545.2245	June 06.2245	13.00	0.03	KAIT
57546.2200	June 07.2200	12.95	0.03	KAIT
57547.2051	June 08.2051	12.93	0.03	KAIT
57548.2197	June 09.2197	12.94	0.04	KAIT
57549.2162	June 10.2162	12.99	0.05	KAIT
57550.2638	June 11.2638	12.97	0.02	KAIT
57551.2201	June 12.2201	13.01	0.03	KAIT
57552.2516	June 13.2516	13.03	0.03	KAIT
57553.2115	June 14.2115	13.15	0.03	KAIT
57555.2189	June 16.2189	13.27	0.03	KAIT
57556.2284	June 17.2284	13.30	0.03	KAIT
57558.2110	June 19.2110	13.52	0.02	KAIT
57559.2229	June 20.2229	13.61	0.04	KAIT
57560.2189	June 21.2189	13.66	0.04	KAIT
57561.2097	June 22.2097	13.70	0.04	KAIT

18.02 ± 0.22, which means the SN had brightened ~3.0 mag in the following four days until it was discovered. In addition, an unfiltered prediscovery detection was obtained at 21:48:57 on May 23, 6.7 hr earlier than KAIT's first detection, by R. Arbour with a 0.35 m $f/6$ Schmidt–Cassegrain reflector (see the left panels of Figure 2). Using a template image taken on 2016 April 5, we performed the same subtraction and

calibration methods as for the KAIT unfiltered images. We find an SN unfiltered brightness of 18.06 ± 0.42 mag, consistent with KAIT's first detection. A ~5 mag detection before peak magnitude, along with our analysis in the following section, confirms that SN 2016coj is one of the youngest SNe Ia ever detected.

Two classification spectra of SN 2016coj were obtained shortly (~3.7 hr) after the SN was discovered (~5.0 days after the FFLT). The spectra were taken with the Kast double spectrograph (Miller & Stone 1993) on the Shane 3 m telescope at Lick Observatory and the FLOYDS robotic spectrograph on the Las Cumbres Observatory Global Telescope Network (LCOGT; Brown et al. 2013) 2.0 m Faulkes Telescope North on Haleakala, Hawaii. We obtained nearly daily spectra of SN 2016coj with different instruments including Kast, FLOYDS, the BFOSC spectrograph on the 2.16 m telescope at Xinglong station of NAOC (China), the Low Resolution Imaging Spectrometer (LRIS; Oke et al. 1995) on the 10 m Keck I telescope, and the Kitt Peak Ohio State Multi-Object Spectrograph (KOSMOS; Martini et al. 2014) on the KPNO Mayall 4 m telescope. Data were reduced following standard techniques for CCD processing and spectrum extraction using IRAF. The spectra were flux calibrated through observations of appropriate spectrophotometric standard stars. All Kast and LRIS spectra were taken at or near the parallactic angle (Filippenko 1982) to minimize differential light losses caused by atmospheric dispersion. Low-order polynomial fits to calibration-lamp spectra were used to calibrate the wavelength scale, and small adjustments derived from night-sky lines in the target frames were applied. Flux calibration and telluric-band removal were done with our own IDL routines; details are described by Silverman et al. (2012a).

We also obtained four epochs of Lick/Shane spectropolarimetry using the polarimetry mode of the Kast spectrograph on May 30, June 8, June 16, and July 6. The spectra were observed at each of four waveplate angles (0°, 45°, 22°.5, and 67°.5) with several waveplate sequences coadded to improve the signal-to-noise ratio (S/N). Each night, both low- and high-polarization standard stars were also observed in order to calibrate the data. All of the spectropolarimetric reductions and calculations follow the method described by Mauerhan et al. (2015).
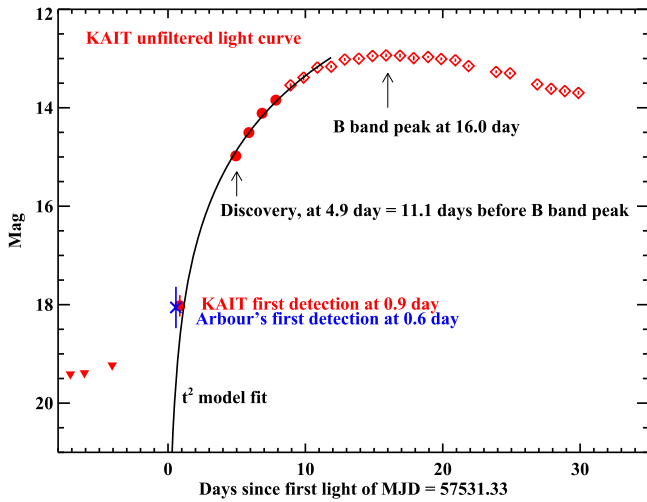
Figure 3. KAIT unfiltered (red) light curve of SN 2016coj. The solid black line is the $t^{2.0}$ model fit to the red solid circles. The blue cross marks the earliest detection at 0.6 ± 0.5 days after the fitted first light observed by R. Arbour. Red triangles show the KAIT upper limits before explosion.

In addition, we observed SN 2016coj on May 31, June 2, 4, and 6 with the 2.4 m Automated Planet Finder (APF) telescope at the Lick Observatory. The APF hosts the Levy Spectrograph, a high-resolution optical echelle spectrograph with resolution R (5500 Å) $\approx 110{,}000$ with a slit width of $1''$ (Vogt et al. 2014). At each epoch, we obtained three 1800 s spectra with the M decker ($1''0$ wide, $8''0$ long to allow for background subtraction), reduced the data with a custom pipeline, and corrected for the redshift of the host galaxy ($z = 0.004523$) and for the barycentric velocity (approximately $-15 \, \mathrm{km \, s^{-1}}$). Because the apparent magnitude (peaking at ~ 13 mag) of SN 2016coj is a bit faint for APF, the S/N of our spectra was $\lesssim 10$ at best, significantly lower than that obtained with APF spectra of the bright (peak ~ 10 mag), nearby SN Ia 2014J (Graham et al. 2015).

3. Analysis and Results

3.1. Light Curve

Figure 3 shows our unfiltered light curve of SN 2016coj. In order to determine the first-light time t_0 (note that the SN may exhibit a "dark phase"), one can assume that the SN luminosity scales as the surface area of the expanding fireball, and therefore increases quadratically with time ($L \propto t^2$, commonly known as the t^2 model; Arnett 1982; Riess et al. 1999). The t^2 model fits well for several SNe Ia with early-time observations (e.g., SN 2011fe, Nugent et al. 2011 SN 2012ht, Yamanaka et al. 2014). Some studies also adopt a t^n model (n varies from ~ 1.5 to ~ 3.0; e.g., Conley et al. 2006; Ganeshalingam et al. 2011; Firth et al. 2015). Interestingly, Zheng et al. (2013, 2014) use a broken-power-law model to estimate the first-light time of SN 2013dy and SN 2014J. However, since our early-time photometric coverage of SN 2016coj is not as good as that of SN 2013dy and SN 2014J, we simply apply the t^2 model to fit the KAIT unfiltered data for the first few days (red solid circles in Figure 3); thereafter, the light curve starts deviating from the t^2 model. We also exclude Arbour's unfiltered detection (blue cross), considering the different response curve compared to the KAIT unfiltered data: Arbour's unfiltered band is closer to V (see Botticella et al. 2009), while KAIT's is closer to R (see Li et al. 2003).

We find that the best t^2 model fit gives the first-light time to be MJD $= 57531.33 \pm 0.50$, around May 23.33. Here the uncertainty (not including the "dark phase") is estimated by calculating the reduced χ^2 ratio with the minimum reduced χ^2 at a 90% confidence level, when t_0 changes around the best-fitted value while all the other parameters are fixed with the best-fitted value. Note that the uncertainty does not include any systematic error caused by the t^2 model fitting. For example, if we include (or exclude) one data point before and after the data set we used, the best-fit first-light time deviates -0.4 to 1.0 days from the above first-light time. Therefore, there could be a systematic error of up to 1.0 day from this method, which we did not include in the following analysis. Our results show that the first detection (from an image by R. Arbour) was merely 0.6 ± 0.5 days after first light, or 0.9 days from KAIT's first detection on May 24. This makes SN 2016coj one of the earliest detected SNe Ia—slightly later than SN 2013dy (~ 2.4 hr after first light; Zheng et al. 2013) and SN 2011fe (~ 11.0 hr after first light; Nugent et al. 2011), but similar to SN 2009ig (~ 17 hr after first light; Foley et al. 2012).

Applying a low-order polynomial fit, we find that SN 2016coj reached a peak magnitude of 12.91 ± 0.03 at MJD $= 57547.31$ in KAIT unfiltered data. Although we do not present B-band data because no B-band template image is currently available, the fit allows us to determine the B-band peak time: MJD $= 57547.35$, similar to the result with unfiltered data. This means SN 2016coj was discovered only 4.9 days after the fitted first light, or 11.1 days before maximum light.

The distance modulus of the host galaxy NGC 4125 is quite uncertain (with a range of 30.04–32.80 mag) owing to different measurements (e.g., de Vaucouleurs & Olson 1984; Tully 1988; Willick et al. 1997; Blakeslee et al. 2001; Tonry et al. 2001; Humphrey 2009; Tully et al. 2013). However, some of them are outdated, or adopted an inappropriate H_0 value. The one with the smallest uncertainty (and also the latest estimate) is 31.90 ± 0.14 mag (Tully et al. 2013), which was based on $H_0 = 74.4 \, \mathrm{km \, s^{-1} \, Mpc^{-1}}$, quite close to the current widely accepted value of $H_0 \approx 70$. We therefore adopt this distance for the following ananlysis. With $E(B - V)_{\mathrm{MW}} = 0.02$ mag (Schlafly & Finkbeiner 2011) and very small (even negligible) host-galaxy extinction (see Sections 3.2 and 3.5), this implies that SN 2016coj has $M_R = -19.0 \pm 0.2$ mag at peak brightness. Our preliminary measurement of B-band data, assuming the host background contamination is small, shows that the B-band peak is $\sim 13.1 \pm 0.1$ mag and $\Delta m_{15}(B) = 1.25 \pm 0.12$ mag. This gives $M_B \approx -18.9 \pm 0.2$ mag, but we expect $M_B \approx -19.1$ mag from the Phillips (1993) relation with the above value of $\Delta m_{15}(B)$; thus, SN 2016coj is a normal-brightness SN Ia. Its $\Delta m_{15}(B) = 1.25 \pm 0.12$ mag is also typical of normal SNe Ia (see also Section 3.3 for the spectral classification).

3.2. Optical Spectra

We obtained optical spectra of SN 2016coj nearly daily for a month (Figure 4), sometimes obtaining multiple spectra in a given night.

We first examine the Na I D absorption feature in several of our high-S/N spectra. The Na I D absorption feature is often converted into reddening, but with large scatter over the empirical relationship according to Poznanski et al. (2011); they estimated a systematic scatter of 0.3 mag (1σ) in $E(B - V)$ with the relation of the Na I D absorption equivalent

Zheng et al.
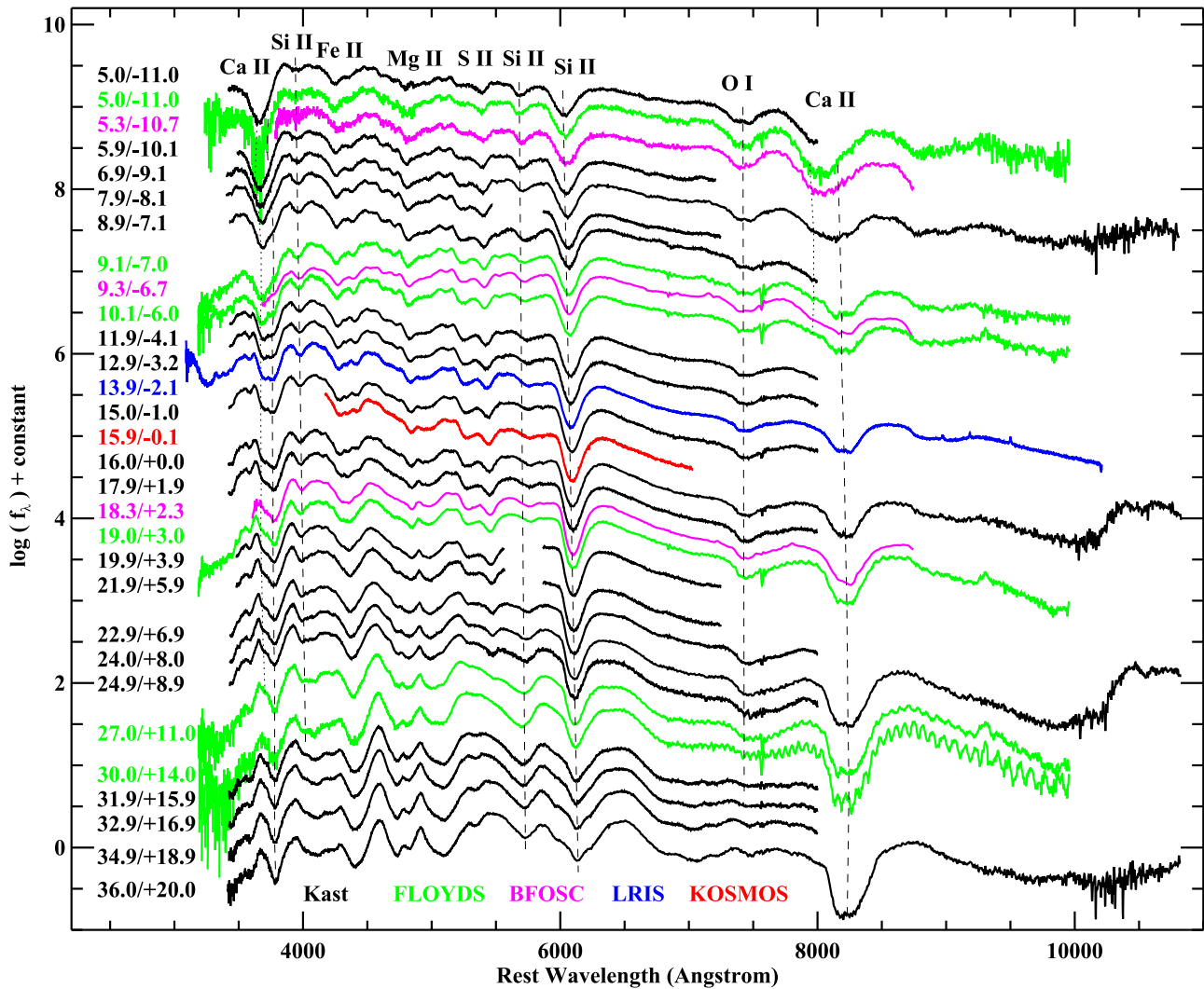
Figure 4. Spectral sequence of SN 2016coj over the first month after discovery. Each spectrum is labeled with its age relative to both the fitted first light and to the B-band maximum light. Some major spectral features are labeled at the top. Spectra taken by different instruments are shown in different colors. Three Lick/Kast spectra have no coverage around 5500–5900 Å; those sections are left blank. Dashed lines are meant to help guide the eye when examining absorption features, while the dotted lines mark the high-velocity components of Ca II H&K and the Ca II NIR triplet. The data used to create this figure are available.

width. The absorption is not clearly detected at the Na I D wavelength for both the Milky Way component and the host-galaxy component. However, there appears to be a weak absorption feature consistent with the Milky Way Na I D wavelength. If real, this could be associated with the Milky Way extinction, which has $E(B - V)_{MW} = 0.02$ mag according to Schlafly & Finkbeiner (2011). Since we do not detect similar absorption at the host-galaxy wavelength of Na I D, we can put an upper limit of $E(B - V) \lesssim 0.02$ mag on host-galaxy extinction. However, if the weak absorption feature is caused by noise instead of Milky Way gas, we can determine an upper limit on $E(B - V)$ through comparison with our spectra of SN 2013dy (Zheng et al. 2013), where we clearly detect the Na I D absorption with the same instrument setting. For SN 2013dy, the equivalent width (W_λ) is ~0.5 Å from both the Milky Way and host galaxy, giving $E(B - V) = 0.15$ mag. Our similar-quality data on SN 2016coj should allow a detection of 1/3 (or less) of Na I D absorption if it exists, yielding an upper limit of $E(B - V) \lesssim 0.05$ mag of host-galaxy extinction. Lastly, we also estimate a 3σ upper limit on the W_λ of an undetected

feature in a spectrum using the equation presented by Leonard (2007): $W_\lambda(3\sigma) = 3\Delta\lambda\Delta I\sqrt{W_{line}/\Delta\lambda}\sqrt{1/B}$, where $\Delta\lambda$ is the spectral resolution element (in Å), ΔI is the 1σ root-mean-square fluctuation of the flux around a normalized continuum level, W_{line} is the full-width at half-maximum intensity (FWHM) of the expected line feature, and B is the number of bins per resolution element. For our high-S/N Kast spectra, we measure $\Delta\lambda \approx 4.0$ Å, $\Delta \approx 0.015$, $W_{line} \approx 12.0$ Å, and $B = 1$, which gives $W_\lambda(3\sigma) \approx 0.3$ Å, and $E(B - V) \lesssim 0.09$ mag of host-galaxy extinction.

All of the above suggests that the host-galaxy extinction of SN 2016coj is likely to be very small, consistent with the nondetection of Na I D absorption in our high-resolution spectra (see Section 3.5). However, note that since the Na I D versus extinction relation has large scatter, even a nondetection of Na I D does not fully exclude the possibility that there may be some dust along the SN line of sight.

The spectra show absorption features from ions typically seen in SNe Ia including Ca II, Si II, Fe II, Mg II, S II, and O I. We do not find a clear C II feature (e.g., Zheng et al. 2013),
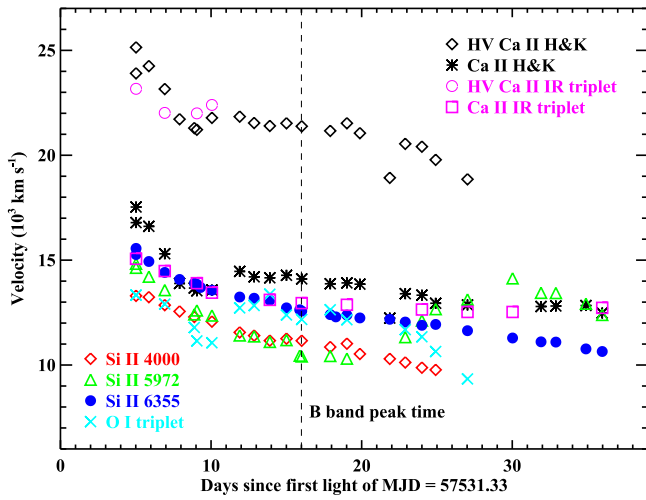
Figure 5. Expansion velocity evolution of different lines measured from the spectra of SN 2016coj. The black dashed line marks the time of *B*-band maximum light.

which is found in over one-fourth of all SNe Ia (e.g., Parrent et al. 2011; Thomas et al. 2011; Folatelli et al. 2012; Silverman & Filippenko 2012). Strong absorption features of Si II, including Si II λ4000, Si II λ5972, and Si II λ6355, are clearly seen in all spectra. The Si II λ5972 feature in SN 2016coj is quite strong relative to those in SN 2012cg and SN 2013dy, though it is relatively small if compared with a large SN Ia sample (see Silverman et al. 2012c).

We measure the individual line velocities from the minimum of the absorption features (see Silverman et al. 2012c for details) and show them in Figure 5. The velocities of all Si II features decrease from ~13,000–15,000 km s^{-1} at discovery to ~11,000–13,000 km s^{-1} around maximum light, and they continue to decrease thereafter.

In addition to the usual photospheric-velocity feature (PVF) of Ca II H&K, SN 2016coj exhibits a high-velocity feature (HVF; e.g., Mazzali et al. 2005; Maguire et al. 2012, 2014; Folatelli et al. 2013; Childress et al. 2014; Silverman et al. 2015) in nearly all of the early-time spectra. This HVF appears to be detached from the rest of the photosphere, with a velocity of ~25,000 km s^{-1} at discovery and slowing down to ~20,000 km s^{-1} at ~8 days after the fitted first-light time. The HVF feature of Ca II H&K stays for a long time, being distinct until roughly age +11 days; thereafter, it is a high-velocity shoulder of the Ca II H&K absorption.

A Ca II near-infrared (NIR) triplet HVF is also found in the first few spectra that covered the wavelength range before maximum light, and the velocity of ≳22,000 km s^{-1} is in good agreement with that of the Ca II H&K HVF at early times, though it is slightly smaller in the first-epoch spectrum. Such HVFs are seen in a few other well-observed SNe Ia, including SN 2005cf (Wang et al. 2009) and SN 2012fr (e.g., Childress et al. 2013; Maund et al. 2013; Zhang et al. 2014). However, in SN 2016coj, the Ca II NIR triplet HVF becomes weaker around peak brightness, and it completely disappears ~8 days later and thereafter. This is different from the Ca II H&K HVF, which is seen for a much longer time. It is not obvious why the HVF of the Ca II NIR triplet goes away after peak brightness while the HVF of Ca II H&K persists. One possibility is that the apparent HVF of Ca II H&K after peak could actually be Si II λ3858 (e.g., Foley 2013). In fact, it is possible that the early-time

apparent HVF of Ca II H&K could be a mixture of Si II λ3858 (including both the HVF and PVF) plus the true HVF of Ca II H&K. If so, the velocity of the Ca II H&K HVF could be smaller than that shown in Figure 5, and thus more consistent with the velocity of the Ca II NIR triplet HVF, but this case is too complicated to verify.

One note about the O I triplet feature is that we adopted only one component in our fit. However, our early-time spectra before peak brightness reveal that the O I triplet has a double absorption profile. Following the Zhao et al. (2016) method to fit the O I triplet with both HVF and PVH (Zhao et al. also adopted a second, faster HVF, but that is not clear in SN 2016coj), we find an HVF O I triplet velocity of ~16,000 km s^{-1} and a PVF O I triplet velocity of ~12,000 km s^{-1}. The HVF velocity is smaller than that of both Ca II H&K and the Ca II NIR triplet. If the HVF really exists in the O I triplet, it suggests that the oxygen in the outer layers is not completely burned (see Zhao et al. 2016).

The strong absorption of Si II λ6355 is commonly used to estimate the photospheric velocity. As shown in Figure 5, the Si II λ6355 velocity of SN 2016coj decreases rapidly from ~15,500 km s^{-1} at discovery to ~12,600 km s^{-1} around peak brightness, and then slowly decreases to ~11,600 km s^{-1} at +11.0 days after peak. A velocity of ~12,600 km s^{-1} at peak brightness is ~1500 km s^{-1} higher than average in SNe Ia (e.g., Wang et al. 2013 >2.5σ away from the mean of their SN Ia velocity distribution fitted with a Gaussian).

Since the optical emission of SNe Ia comes mainly from the photosphere, the photospheric velocity evolution could be directly related to the optical light curves of SNe Ia (see Zheng & Filippenko 2017); therefore, it is important to understand the photospheric velocity evolution of SNe Ia. Here, we compare the photospheric velocity measurement of SN 2016coj with the three well-observed SNe Ia 2009ig (Foley et al. 2012; Marion et al. 2013), 2012cg (Silverman et al. 2012b), and 2013dy (Zheng et al. 2013). Note that while both SN 2012cg and SN 2009ig have an HVF identified for Si II λ6355, we consider only the photospheric component.

Figure 6 displays the photospheric velocity evolution over time for the four SNe Ia. Overall, the photospheric velocity evolution is similar to the evolution seen in most SNe Ia (e.g., Benetti et al. 2005; Foley et al. 2011; Silverman et al. 2012c): the velocity drops rapidly at early times (within the first week after explosion), and then slowly but steadily decreases thereafter. For each of these four SNe, we consequently try to fit the early-time velocities (typically within 10 days after first light) with a power-law function, $v = C_1 t'^\alpha$, where t' is the time after first light (t_0); the results are shown in the top panel of Figure 6 for each SN. This is very similar to the method that of Silverman et al. (2015, Figure 12) adopted, but they used a natural exponential function to fit the velocities before +5 days after peak brightness and also obtained reasonable fitting results. In fact, Piro & Nakar (2013, Equation (13)) mathematically show that the photospheric velocity could decay as a power law at early times. For the later velocities (typically >10 days after first light), we then fit them with a linear function, $v = at' + C_2$ (results shown in the middle-top panel); Silverman et al. (2012c, Figure 5) also use the same method to fit their data around peak brightness. As seen in Figure 6, both the power-law function and the linear function can fit the corresponding data well, but only in their respective regimes—early-time data for the power-law function and later-time data for the linear function.
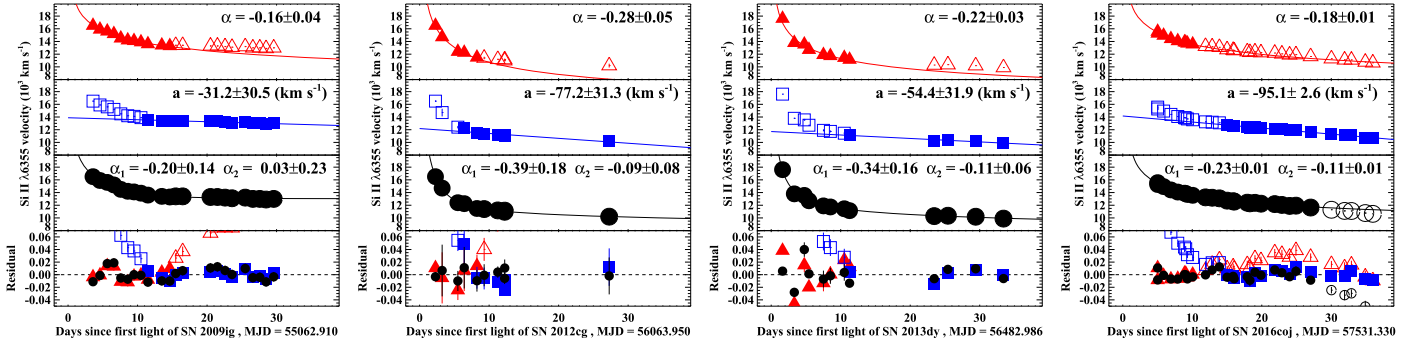
Figure 6. Photospheric velocity (measured from the strong Si II λ6355 absorption) evolution of SN 2016coj (right panel), compared to those of the well-observed SN 2009ig (left panel), SN 2012cg (middle-left panel), and SN 2013dy (middle-right panel). For all SNe Ia, the top panels show the result of a power-law function fit to the early-time data, the middle-top panels display the result of a linear function fit to the later-time data, the middle-bottom panels give the result of a broken-power-law function fit to all the data, and the bottom panels show the residuals for each fit. Solid points are included in the fitting while open points are not.

Table 2
Photospheric Velocity Fitting Results

SN	α	a	α_1	α_2	Reduced χ^2
	Power Law	Linear[a]	Broken Power Law[b]		
SN 2009ig	-0.16 ± 0.04	-32 ± 31	-0.20 ± 0.14	0.03 ± 0.23	0.04
SN 2012cg	-0.28 ± 0.05	-77 ± 32	-0.39 ± 0.18	-0.09 ± 0.08	0.04
SN 2013dy	-0.22 ± 0.03	-54 ± 32	-0.34 ± 0.16	-0.11 ± 0.06	0.14
SN 2016coj	-0.18 ± 0.01	-95 ± 3	-0.23 ± 0.01	-0.11 ± 0.01	1.72

Notes.
[a] In units of km s^{-1} day^{-1}.
[b] The smoothing parameter s was fixed to -10 during fitting, and the very small reduced χ^2 for some SNe is largely caused by overestimating the velocity uncertainty.

As with the early-time light curve (Zheng et al. 2013, 2014), we find that a broken-power-law function is useful for fitting the photospheric velocity evolution; a low-index power-law function approximates the linear function found at late times. Specifically,

$$v = A \left(\frac{t'}{t_b} \right)^{\alpha_1} \left[1 + \left(\frac{t'}{t_b} \right)^{s(\alpha_1 - \alpha_2)} \right]^{-1/s}, \qquad (1)$$

where v is the photospheric velocity, A is a scaling constant, t' is the time after first light (t_0), t_b is the break time, α_1 and α_2 are the two power-law indices before and after the break (respectively), and s is a smoothing parameter. We apply this broken-power-law function to the entire data set of photospheric velocities for all four SNe until about a month after the explosion. Our fitting results (we fixed s to be -10) are listed in Table 2 and shown in the middle-bottom panels in Figure 6.

The power-law indices from both the power-law fitting (α) and broken-power-law fitting (α_1) at early times are consistent with the value of -0.22 adopted by Piro & Nakar (2014) when fitting three SNe Ia (SNe 2009ig, 2011fe, and 2012cg), and are also the value adopted by Shappee et al. (2016) when fitting ASASSN-14lp. The index from the broken power law (α_1) is slightly steeper than that from the power law (α). At late times (around maximum light) with linear fitting, the rate of velocity decrease from the fitting is slightly larger than the average rate of -38 km s^{-1} day^{-1} found by Silverman et al. (2012c) for a large sample of SNe Ia.

Overall, the broken-power-law function can fit the photospheric velocity evolution well for all four SNe until a month after explosion (see the small residuals at the bottom panel of Figure 6 and the reduced χ^2 given in Table 2). This function

also has the potential to fit the photospheric velocity evolution of most other SNe Ia as well, given that most SNe Ia have very similar velocity evolution (e.g., Silverman & Filippenko 2012; Silverman et al. 2012c). High-cadence spectroscopy is required to verify this, especially at early times. However, it currently remains unclear whether there is a good physical explanation behind the fitting; Piro & Nakar (2013) show that the photospheric velocity could decay as a power law at early times, but our broken-power-law function fitting extends to a much later time.

3.3. Classification

We use the SuperNova IDentification code (SNID; Blondin & Tonry 2007) to spectroscopically classify SN 2016coj. For nearly all of the spectra presented here, we find that SN 2016coj is spectroscopically similar to many normal SNe Ia. Compared to SN 1992A ($M_B = -18.79$ mag and $\Delta m_{15}(B) = 1.47$ mag; Della Valle et al. 1998) and SN 2002er ($M_B = -19.35$ mag and $\Delta m_{15}(B) = 1.33$ mag; Pignata et al. 2004), for example, SN 2016coj has similar spectra, absolute magnitude, and $\Delta m_{15}(B)$. Another spectroscopic comparison is the so-called Si II ratio, $\mathfrak{R}(\text{Si II})$ (the ratio of Si II λ5972 to Si II λ6355), defined by Nugent et al. (1995) using the depths of spectral features and later by Hachinger et al. (2006) using their pseudo-equivalent widths. Hachinger et al. (2006) found a good correlation between the $\mathfrak{R}(\text{Si II})$ and $\Delta m_{15}(B)$ (see their Figure 13). We measure SN 2016coj to have $\mathfrak{R}(\text{Si II}) = 0.11 \pm 0.4$, with $\Delta m_{15}(B) = 1.25$ mag, placing SN 2016coj in the normal SN Ia region in Figure 13 of Hachinger et al. (2006), very close to SN 2002er. Thus, we conclude that SN 2016coj is a

43

Table 3
Polarization of SN 2016coj

Epoch	$P_V{}^a$(%)	θ_V(deg)	$P_{\rm cont}$	$\theta_{\rm cont}$(deg)
6.9	0.27(0.01)	54.3(0.8)	0.51(0.01)	55.4(0.9)
16.0	0.20(0.01)	52.6(0.8)	0.38(0.01)	53.4(0.8)
24.0	0.16(0.01)	39.2(1.6)	0.06(0.02)	09.0(4.3)
44.0	0.39(0.04)	41.0(1.3)	0.28(0.03)	30.0(2.2)

Note.
[a] V-band and continuum integrated over wavelength ranges of 5050–5950 Å and 6700–7150 Å, respectively. Uncertainties are statistical.

spectroscopically normal SN Ia, consistent with the photometric analysis given in Section 3.1.

3.4. Spectropolarimetry

Linear polarization is expressed as the quadratic sum of the Q and U Stokes vectors, $P = \sqrt{Q^2 + U^2}$. The position angle on the sky is given by $\theta = (1/2)\tan^{-1}(U/Q)$, taking into account the quadrant in the Q–U plane where the inverse tangent angle is located. Since P is a positive-definite quantity, it is overestimated in situations where the S/N is low. It is thus typical to express the "debiased" (or bias-corrected) form of P as $P_{\rm db} = \sqrt{(Q^2 + U^2) - (\sigma_Q^2 + \sigma_U^2)}$, where σ_Q and σ_U are the uncertainties in the Q and U Stokes parameters. Note, however, that at low S/N, $P_{\rm db}$ is also not a fully reliable function because it has a peculiar probability distribution (Miller et al. 1988). Thus, for extracting statistically reliable values of polarization within a particular waveband, we have binned the calibrated Q and U Stokes spectra separately over the wavelength range of interest before calculating P and θ. All quoted and listed values in Table 3 were determined in this manner, while Figure 7 displays $P_{\rm db}$. For θ, if $(\sigma_Q^2 + \sigma_U^2) > (Q^2 + U^2)$, then we set a 1σ upper limit on P of $\sqrt{\sigma_Q^2 + \sigma_U^2}$. In cases where $P/\sigma_P < 1.5$, θ is essentially undetermined and is not graphically displayed.

3.4.1. Interstellar and Instrumental Polarization

The interstellar polarization (ISP) appears to be low in the direction of SN 2016coj. Indeed, the estimated value of $E(B - V) = 0.02$ mag indicates that the extinction from the Milky Way and host galaxy are not substantial; a small contribution from ISP is thus to be expected. According to Serkowski et al. (1975), an upper limit to the ISP is given by $9 \times E(B - V)$, which implies $P_{\rm ISP} < 0.18\%$ for SN 2016coj. To obtain a direct estimate of the Galactic component of ISP, we observed three Galactic stars in the vicinity of the SN position: HD 104436 (A3 V), HD 106998 (A5 V), and HD 108907 (M3 III). We measure respective V-band polarization and θ values of $P = (0.12\%, 0.09\%, 0.09\%)$ and $\theta = (36°, 34°, 30°)$. Under the reasonable assumption of low intrinsic polarization for these stars, the resulting average values of $P \approx 0.1\%$, $\theta \approx 33°$ confirm the low Galactic polarization. Furthermore, the lack of Na I D absorption lines in our low- and high-resolution spectra (see Sections 3.2 and 3.5) indicates low extinction from the early-type host galaxy, and thus implies that the host ISP is probably even lower than the small Galactic value.

The instrumental polarization of the Kast instrument is also low. Measurements of the low-polarization standard star BD
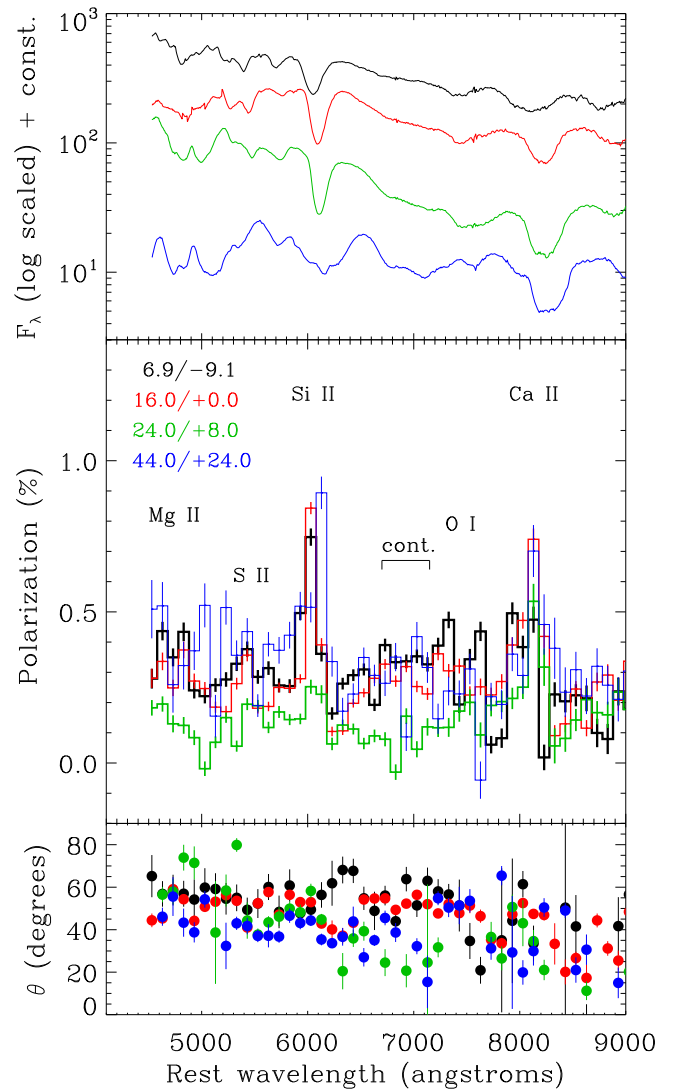
Figure 7. Four epochs of spectropolarimetry of SN 2016coj. Top panel: observed total-flux spectrum, color coded for each epoch. Middle panel: debiased polarization ($P_{\rm db}$), with several major features labeled. Bottom panel: position angle (θ) for the corresponding epochs. The value of θ is undetermined where $P/\sigma_P < 1.5$; those points are omitted.

+33 2642 at each epoch indicate an average V-band polarization of $\sim 0.15\%$, with a standard deviation of 0.05% between all four epochs; the average value is consistent with that reported by Schmidt et al. (1992) for this star, which indicates that the low level is intrinsic to the source and that Kast contributes an insignificant amount of instrumental polarization to the measurements. The standard deviation is near the systematic uncertainty level we typically experience using the spectropolarimetry mode of Kast. Our observations therefore constrain the average instrumental polarization to <0.05%. Based on the low values of ISP and instrumental polarization, we move forward without attempting to subtract their minor contributions from the data.

3.4.2. Intrinsic Polarization

Our spectropolarimetry results are shown in Figure 7 and the integrated broadband measurements are listed in Table 3. On day 6.9, the source exhibits weak polarization in the continuum at a level of $\sim 0.3\%$, integrated over the wavelength range

of 6700–7150 Å. This is consistent with the weak levels of continuum polarization that are typically associated with SNe Ia (Wang & Wheeler 2008), though we note that some fraction of the polarization, perhaps half, could potentially be contributed by ISP. Strong polarization is exhibited across prominent line features, particularly Si II λ6355 and the Ca II NIR triplet, at levels of ∼0.9% and ∼0.6%, respectively. The Ca II polarization feature appears to exhibit two peaks, perhaps associated with the high- and low-velocity components. The position angles across the polarized line features, particularly Si II, are close to that of the continuum, which suggests an axisymmetric configuration for the SN.

By day 16.0, the continuum polarization is consistent with having no change relative to day 6.9, while Si II has increased in strength slightly to peak at this epoch. A Gaussian fit to the Si II feature indicates a line polarization of $0.9 \pm 0.1\%$ with respect to the continuum level. For Ca II polarization, the enhancement of the high-velocity component from day 6.9 has disappeared and the peak of the lower-velocity component has increased by ∼0.3%.

By day 24.0, the continuum and Si II line polarization appears to have dropped substantially for wavelengths shortward of 7000 Å, with no significant change apparent at longer wavelengths; polarization in the continuum region is undetected at this epoch. If real, such a continuum polarization drop roughly one week after peak would be reminiscent of the evolution of SN 2001el (Wang et al. 2003). However, by day 44.0 the continuum polarization appears to have regained the strength exhibited on day 16.0 and earlier. Si II has restrengthened as well, while declining in radial velocity along with the minimum of the weakening absorption profile. Based on this unexpected restrengthening, we exercise caution regarding the temporarily weakened polarization on day 24.0 because we are concerned that this could be the result of a systematic error. The drop in polarization appears to have only affected the Stokes q parameter (derived from exposures with polarimeter waveplate angles at 0° and 45°). Each of our three q sequences of the SN are consistent, and we see no such change in the q parameter of our standard-star observations from the same night. Thus, if the change on day 24.0 is the result of systematic error (e.g., some unknown temporary source of instrumental polarization above our typical limit of <0.05%), then it must have occurred over an hourly timescale. Alternatively, a subsequent rise in continuum polarization on day 44.0 could result from the appearance of weak line features in the chosen continuum region (6700–7150 Å), but, in this case, we would not expect the simultaneous rise in the Si II feature. As a final possibility, the temporary influence of a separate light-echo component, possibly associated with dust in the host ISM, could result in the observed fluctuation; this possibility has the advantage of accounting for the brief change in the continuum and line polarization simultaneously, and it would also explain why the reddest wavelengths are not significantly affected.

Overall, the spectropolarimetric character of SN 2016coj is consistent with the trends exhibited by "normal" SNe Ia. For example, Maund et al. (2010) reported a correlation between the polarization of the Si II λ6355 feature, measured near or before peak luminosity, and the radial-velocity decline rate of the absorption minimum (also see Leonard et al. 2006), physically interpreted as evidence for a single geometric configuration for normal SNe Ia. At peak brightness on day 16.0, the line polarization of $0.9 \pm 0.1\%$ combined with our

measured value of $-95\,\mathrm{km\,s^{-1}\,day^{-1}}$ for the velocity evolution, shows that SN 2016coj falls where expected on the correlated distribution of SNe Ia reported by Maund et al. (2010), and within the range of high-velocity explosions.

3.5. High-resolution Spectra

We examine the APF high-resolution spectra for narrow absorption features, such as those that were identified in APF spectra of SN 2014J (Graham et al. 2015). We began spectral monitoring with the APF based on an early classification and the assumption of a host-galaxy distance smaller than that adopted here. The object's peak apparent brightness ended up being ∼3 mag fainter than that of SN 2014J, and fainter than the projected minimum we typically require for triggering the APF. For this reason, the S/N of our SN 2016coj APF spectra is quite low. Instead of ceasing our APF monitoring, we obtained multiple observations over several nights in order to stack our spectra, but ultimately we do not identify any absorption features of Na I D λλ5889.95, 5895.92, Ca II H&K λλ3933.7, 3968.5, K I λλ7664.90, 7698.96, Hα λ6562.801, Hβ λ4861.363, or the diffuse interstellar bands (λ ≈ 5780, 5797, 6196, 6283, 6613 Å).

Since the Na I D feature is most useful for constraining the presence of circumstellar material and line-of-sight host-galaxy dust extinction, and owing to grating blaze is in a region of relatively higher S/N (∼10), we estimate an upper limit on its W_λ in the following way. The flux of the continuum-normalized stacked APF spectra in the region of Na I D, shown in black in Figure 8, has a standard deviation of $\sigma \approx 0.038$. As an upper limit on the depth of an absorption feature that we could have detected, we use $3\sigma \approx 0.11$. Our instrumental configuration for the Levy spectrograph results in a spectral resolution of $\Delta\lambda \approx 0.03$ Å, from which we estimate that the minimum FWHM of a detected feature is $3\Delta\lambda \approx 0.1$ Å. Assuming a Gaussian profile for this hypothetical absorption, we constrain the Na I D feature to have $W_\lambda \lesssim 0.56$ Å. Based on Figure 9 of Phillips et al. (2013), this puts an upper limit on host-galaxy extinction of $A_V \lesssim 0.2$ mag (with $E(B - V) = 0.07$ mag assuming $R_V = 3.1$). Although this is a rather large upper limit, it is consistent with the small host-galaxy extinction constrained from our low-resolution spectra (see Section 3.2) and also with the low extinction expected given the early type of the host, NGC 4125.

4. Conclusions

In this paper, we have presented optical photometric, low- and high-resolution spectroscopic, and spectropolarimetric observations of SN 2016coj, one of the youngest discovered and best-observed SNe Ia. Our clear-band light curve shows that our first detection is merely 0.6 ± 0.5 days after the FFLT, making it one of the earliest detected SNe Ia. We estimate that SN 2016coj took ∼16.0 days after the fitted first-light time to reach B-band maximum. Its maximum brightness has a normal luminosity, $B = -18.9 \pm 0.2$ mag. An estimated $\Delta m_{15}(B)$ value of 1.25 mag along with spectral information support its normal SN Ia classification. In the well-observed low-resolution spectral sequence, we identify a high-velocity feature from both Ca II H&K and the Ca II NIR triplet, and also possibly from the O I triplet. SN 2016coj has a Si II λ6355 velocity of ∼12,600 km s^{-1} at peak brightness, ∼1500 km s^{-1} higher than that of typical SNe Ia. We find that the Si II λ6355 velocity
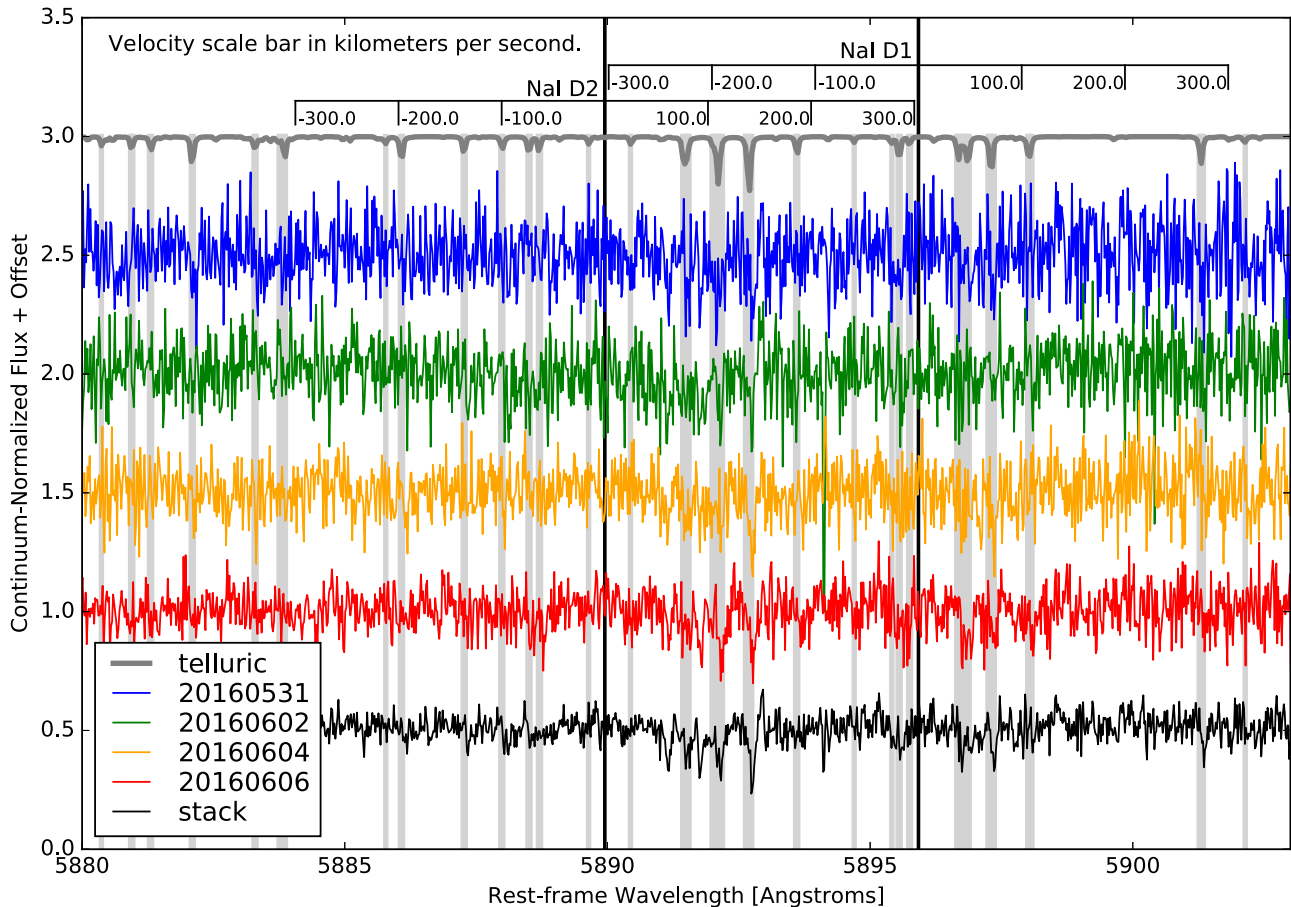
Figure 8. High-resolution spectra of SN 2016coj in the region of Na I D absorption from the APF obtained at four epochs (2016 May 31, blue; 2016 Jun 02, green; 2016 Jun 04, orange; 2016 Jun 06, red). The bottom (black) shows the stacked spectrum from the data of these epochs. A mean barycentric velocity of ~15 km s^{-1} has been applied for all epochs of SN 2016coj spectra. The atmospheric absorption lines are shown in gray, which has been redshifted into the frame of SN 2016coj. The most significant features are highlighted with vertical bars in order to identify their presence in the spectra of SN 2016coj. A rest-frame velocity scale bar is provided for each Na I D feature along the top of the plot.

decreases rapidly during the first few days and then slowly decreases after peak brightness, very similar to that of other SNe Ia. A broken-power-law function can well fit the Si II $\lambda6355$ velocity for up to about a month after first light. We estimate there to be very small host-galaxy extinction based on the lack of Na I D lines from the host galaxy in our low- and high-resolution spectra. Our four epochs of spectropolarimetry show that SN 2016coj exhibits weak polarization in the continuum, but the Si II line polarization is quite strong (~0.9% ± 0.1%) at peak brightness.

Although SN 2016coj appears to be a normal SN Ia in many respects, it was detected very early (with the first detection merely 0.6 ± 0.5 days after the FFLT). So far, there are only a handful of SNe Ia that have been observed so soon after the explosion, making them very valuable at this stage to build up a bigger sample for studying SNe Ia at very early times. With new facilities coming online in the near future (e.g., the Zwicky Transient Facility; the Large Synoptic Survey Telescope), one can expect the number of such events to increase significantly, providing more opportunities for studying individual SNe Ia in greater detail shortly after explosion and also for performing statistical analyses.

46

References

Arnett, W. D. 1982, ApJ, 253, 785
Benetti, S., Cappellaro, E., Mazzali, P. A., et al. 2005, ApJ, 623, 1011
Blakeslee, J. P., Lucey, J. R., Barris, B. J., et al. 2001, MNRAS, 327, 1004
Blanchard, P., Zheng, W., Cenko, S. B., et al. 2013, CBET, 3422, 1
Blondin, S., Prieto, J. L., Patat, F., et al. 2009, ApJ, 693, 207
Blondin, S., & Tonry, J. L. 2007, ApJ, 666, 1024
Bloom, J., Kasen, D., Shen, K., et al. 2012, ApJL, 744, L17
Botticella, M. T., Pastorello, A., Smartt, S. J., et al. 2009, MNRAS, 398, 1041
Brown, T. M., Baliber, N., Bianco, F. B., et al. 2013, PASP, 125, 1031
Cao, Y., Kulkarni, S. R., Gal-Yam, A., et al. 2016, ApJ, 832, 86
Cao, Y., Kulkarni, S. R., Howell, D. A., et al. 2015, Natur, 521, 328
Casper, C., Fuller, K. L., Zheng, W., et al. 2013, CBET, 3700, 1
Cenko, S. B., Li, W., Filippenko, A. V., et al. 2012, CBET, 3199, 1
Childress, M., Filippenko, A. V., Ganeshalingam, M., & Schmidt, B. P. 2014, MNRAS, 437, 338
Childress, M., Scalzo, R. A., Sim, S. A., et al. 2013, ApJ, 770, 29
Conley, A., Howell, D. A., Howes, A., et al. 2006, ApJ, 132, 1707
de Vaucouleurs, G., de Vaucouleurs, A., Corwin, H. G., Jr., et al. 1991, RC3.9, Third Reference Catalogue of Bright Galaxies, version 3.9 (New York: Springer)
de Vaucouleurs, G., & Olson, D. W. 1984, ApJS, 56, 91
Della Valle, M., Kissler-Patig, M., Danziger, J., & Storm, J. 1998, MNRAS, 299, 267
Dhungana, G., Kehoe, R., Vinko, J., et al. 2016, ApJ, 822, 6
Filippenko, A. V. 1982, PASP, 94, 715
Filippenko, A. V. 1997, ARA&A, 35, 309
Filippenko, A. V. 2005, in ASP Conf. Ser. 342, 1604–2004, Supernovae as Cosmological Lighthouses, ed. M. Turatto et al. (San Francisco, CA: ASP), 87
Filippenko, A. V., Li, W. D., Treffers, R. R., & Modjaz, M. 2001, in ASP Conf. Ser. 246, Small-Telescope Astronomy on Global Scales, ed. B. Paczyński, W. P. Chen, & C. Lemme (San Francisco, CA: ASP), 121
Firth, R. E., Sullivan, M., Gal-Yam, A., et al. 2015, MNRAS, 446, 3895
Folatelli, G., Morrell, N., Phillips, M. M., et al. 2013, ApJ, 773, 53
Folatelli, G., Phillips, M. M., Morrell, N., et al. 2012, ApJ, 745, 74
Foley, R. J. 2013, MNRAS, 435, 273
Foley, R. J., Challis, P. J., Filippenko, A. V., et al. 2012, ApJ, 744, 38
Foley, R. J., & Kasen, D. 2011, ApJ, 729, 55
Foley, R. J., Sanders, N. E., & Kirshner, R. P. 2011, ApJ, 742, 89
Ganeshalingam, M., Li, W., & Filippenko, A. V. 2011, MNRAS, 416, 2607
Ganeshalingam, M., Li, W., Filippenko, A. V., et al. 2010, ApJS, 190, 418
Goobar, A., Johansson, J., Amanullah, R., et al. 2014, ApJL, 784, L12
Graham, M., Valenti, S., Fulton, B. J., et al. 2015, ApJ, 801, 136
Hachinger, S., Mazzali, P. A., & Benetti, S. 2006, MNRAS, 370, 299
Hachisu, I., Kato, M., & Nomoto, K. 1996, ApJL, 470, L97
Hayakawa, K., Cenko, S. B., Zheng, W., et al. 2013, CBET, 3706, 1
Hillebrandt, W., & Niemeyer, J. C. 2000, ARA&A, 38, 191
Höflich, P. 1991, A&A, 246, 481
Hoyle, F., & Fowler, W. A. 1960, ApJ, 132, 565
Hsiao, E. Y., Burns, C. R., Contreras, C., et al. 2015, A&A, 578, 9
Hughes, A., Zheng, W., & Filippenko, A. V. 2015, CBET, 4169, 1
Humphrey, P. J. 2009, ApJ, 690, 512
Iben, I., Jr., & Tutukov, A. V. 1984, ApJS, 54, 335
Im, M., Choi, C., Yoon, S., et al. 2015, ApJS, 221, 22
Kandrashoff, M., Fuller, K., Cenko, S. B., et al. 2012, CBET, 3121, 1
Kasen, D. 2010, ApJ, 708, 1025
Kasen, D., Nugent, P. E., Wang, L., et al. 2003, ApJ, 593, 788
Kim, H., Casper, C., Zheng, W., et al. 2013a, CBET, 3678, 1
Kim, H., Zheng, W., Filippenko, A. V., et al. 2014a, CBET, 3942, 1
Kim, H., Zheng, W., Li, W., et al. 2013b, CBET, 3743, 1
Kim, M., Zheng, W., Li, W., & Filippenko, A. V. 2014b, CBET, 3777, 1
Kumar, S., Yuk, H., Zheng, W., et al. 2014, CBET, 4165, 1
Leaman, J., Li, W., Chornock, R., & Filippenko, A. V. 2011, MNRAS, 412, 1419
Leonard, D. 2007, ApJ, 670, 1275
Leonard, D. C., Filippenko, A. V., Ganeshalingam, M., et al. 2006, Natur, 440, 505
Li, W., Bloom, J. S., Podsiadlowski, P., et al. 2011, Natur, 480, 348
Li, W., Filippenko, A. V., Chornock, R., & Jha, S. 2003, PASP, 115, 844
Maguire, K., Sullivan, M., Ellis, R. S., et al. 2012, MNRAS, 426, 2359
Maguire, K., Sullivan, M., Pan, Y., et al. 2014, MNRAS, 444, 3258
Marion, G. H., Vinko, J., Wheeler, J. C., et al. 2013, ApJ, 777, 40
Martini, P., Elias, J., Points, S., et al. 2014, Proc. SPIE, 9147, 91470Z
Mauerhan, J. C., Williams, G. G., Leonard, D., et al. 2015, MNRAS, 453, 4467
Maund, J. R., Höflich, P., Patat, F., et al. 2010, ApJL, 725, L167
Maund, J. R., Spyromilio, J., Höflich, P. A., et al. 2013, MNRAS, 433, L20
Mazzali, P. A., Benetti, S., Altavilla, G., et al. 2005, ApJL, 623, L37
Meng, X., Chen, X., Han, Z., et al. 2009, MNRAS, 395, 2103
Miller, J. S., Robinson, L. B., & Goodrich, R. W. 1988, in Instrumentation for Ground-Based Optical Astronomy, ed. L. B. Robinson (New York: Springer), 157
Miller, J. S., & Stone, R. P. S. 1993, Lick Obs. Tech. Rep. 66 (Santa Cruz: Lick Obs)
Nugent, P. E., Phillips, M. M., Baron, E., Branch, D., & Hauschildt, P. 1995, ApJL, 455, L147
Nugent, P. E., Sullivan, M., Cenko, S. B., et al. 2011, Natur, 480, 344
Oke, J. B., Cohen, J. G., Carr, M., et al. 1995, PASP, 107, 375
Pakmor, R., Kromer, M., Taubenberger, S., et al. 2012, ApJL, 747, L10
Parrent, J. T., Thomas, R. C., Fesen, R. A., et al. 2011, ApJ, 732, 30
Patat, F., Chandra, P., Chevalier, R., et al. 2007, Sci, 317, 924
Perlmutter, S., Aldering, G., Goldhaber, G., et al. 1999, ApJ, 517, 565
Phillips, M. M. 1993, ApJL, 413, L105
Phillips, M. M., Simon, J. D., Morrell, N., et al. 2013, ApJ, 779, 38
Pignata, G., Patat, F., Benetti, S., et al. 2004, MNRAS, 355, 178
Piro, A. L., & Morozova, V. S. 2016, ApJ, 826, 96
Piro, A. L., & Nakar, E. 2013, ApJ, 769, 67
Piro, A. L., & Nakar, E. 2014, ApJ, 784, 85
Poznanski, D., Ganeshalingam, M., Silverman, J. M., & Filippenko, A. V. 2011, MNRAS, 415, L81
Rabinak, I., Livne, E., & Waxman, E. 2012, ApJ, 757, 35
Riess, A. G., Filippenko, A. V., Challis, P., et al. 1998, AJ, 116, 1009
Riess, A. G., Filippenko, A. V., Li, W., et al. 1999, AJ, 118, 2675
Röpke, F. K., Kromer, M., Seitenzahl, I. R., et al. 2012, ApJL, 750, L19
Ross, T. W., Zheng, W., Filippenko, A. V., et al. 2015, CBET, 4125, 1
Schlafly, E. F., & Finkbeiner, D. P. 2011, ApJ, 737, 103
Schmidt, G. D., Elston, R., & Lupie, O. L. 1992, AJ, 104, 1563
Serkowski, K., Mathewson, D. S., & Ford, V. L. 1975, ApJ, 196, 261
Shappee, B. J., Piro, A. L., Holoien, T. W., et al. 2016, ApJ, 826, 144
Shivvers, I., Zheng, W., Mauerhan, J., et al. 2016, MNRAS, 461, 3057
Silverman, J. M., & Filippenko, A. V. 2012, MNRAS, 425, 1917
Silverman, J. M., Foley, R., Filippenko, A. V., et al. 2012a, MNRAS, 425, 1789
Silverman, J. M., Ganeshalingam, M., Cenko, S. B., et al. 2012b, ApJL, 756, L7
Silverman, J. M., Kong, J. J., & Filippenko, A. V. 2012c, MNRAS, 425, 1819
Silverman, J. M., Vinkó, J., Marion, G. H., et al. 2015, MNRAS, 451, 1973
Simon, J. D., Gal-Yam, A., Gnat, O., et al. 2009, ApJ, 702, 1157
Stegman, S., Zheng, W., & Filippenko, A. V. 2015a, CBET, 4124, 1
Stegman, S., Zheng, W., & Filippenko, A. V. 2015b, CBET, 4128, 1
Sternberg, A., Gal-Yam, A., Simon, J. D., et al. 2014, MNRAS, 443, 1849
Stetson, P. B. 1987, PASP, 99, 191
Thomas, R. C., Aldering, G., Antilogus, P., et al. 2011, ApJ, 743, 27
Tonry, J. L., Dressler, A., Blakeslee, J. P., et al. 2001, ApJ, 546, 681
Tully, R. B. 1988, Nearby Galaxy Catalog (Cambridge: Cambridge Univ. Press)

Tully, R. B., Courtois, H. M., Dolphin, A. E., et al. 2013, AJ, 146, 86
Vogt, S., Radovan, M., Kibrick, R., et al. 2014, PASP, 126, 359
Wang, L., Baade, D., Höflich, P., et al. 2003, ApJ, 591, 1110
Wang, L., Baade, D., & Patat, F. 2007, Sci, 315, 212
Wang, L., & Wheeler, J. C. 2008, ARA&A, 46, 433
Wang, L., Wheeler, J. C., & Höflich, P. 1997, ApJL, 476, L27
Wang, X., Li, W., Filippenko, A. V., et al. 2008, ApJ, 675, 626
Wang, X., Li, W., Filippenko, A. V., et al. 2009, ApJ, 697, 380
Wang, X., Wang, L., Filippenko, A. V., Zhang, T., & Zhao, X. 2013, Sci,
    340, 170

Webbink, R. F. 1984, ApJ, 277, 355
Willick, J. A., Courteau, S., Faber, S. M., et al. 1997, ApJS, 109, 333
Wilson, C. D., Cridland, A., Foyle, K., et al. 2013, ApJ, 776, 30
Yamanaka, M., Maeda, K., Kawabata, M., et al. 2014, ApJL, 782, L35
Zhang, J., Wang, X., Bai, J., et al. 2014, AJ, 148, 1
Zhao, X. L., Maeda, K., Wang, X., et al. 2016, ApJ, 826, 211
Zheng, W., & Filippenko, A. V. 2017, ApJL, 838, L4
Zheng, W., Shivvers, I., Filippenko, A. V., et al. 2014, ApJL, 783, L24
Zheng, W., Silverman, J. M., Filippenko, A. V., et al. 2013, ApJL, 778, L15
Zheng, W., Yuk, H., Manzano-King, C., et al. 2016, ATel, 9095, 1

M101: SPECTRAL OBSERVATIONS OF H II REGIONS AND THEIR PHYSICAL PROPERTIES

Ning Hu,[1,2] Enci Wang,[1,2] Zesen Lin,[1,2] Xu Kong,[1,2] Fuzhen Cheng,[1,2] Zou Fan,[3] Guangwen Fang,[4] Lin Lin,[5] Yewei Mao,[6] Jing Wang,[7] Xu Zhou,[8] Zhiming Zhou,[8] Yinan Zhu,[3] and Hu Zou[8]

[1] *CAS Key Laboratory for Research in Galaxies and Cosmology, Department of Astronomy, University of Science and Technology of China, Hefei 230026, China*
[2] *School of Astronomy and Space Sciences, University of Science and Technology of China, Hefei 230026, China*
[3] *Key Laboratory of Optical Astronomy, National Astronomical Observatories, Chinese Academy of Sciences, 20A Datun Road, Chaoyang District, Beijing 100012, China*
[4] *Institute for Astronomy and History of Science and Technology, Dali University, Dali 671003, China*
[5] *Shanghai Astronomical Observatory, Chinese Academy of Science, 80 Nandan Road, Shanghai, 200030, China*
[6] *Purple Mountain Observatory, Chinese Academy of Sciences, Nanjing 210008, China*
[7] *CSIRO Astronomy & Space Science, Australia Telescope National Facility, P.O. Box 76, Epping, NSW 1710, Australia*
[8] *Key Laboratory of Optical Astronomy, National Astronomical Observatories, Chinese Academy of Sciences, Beijing 100012, China*

ABSTRACT

By using the Hectospec 6.5 m Multiple Mirror Telescope (MMT) and the 2.16 m telescope of National Astronomical Observatories, Chinese Academy of Sciences (NAOC), we obtained 188 high signal-to-noise ratio (S/N) spectra of H II regions in the nearby galaxy M101, which are the largest spectroscopic sample of H II regions for this galaxy so far. These spectra cover a wide range of regions on M101, which enables us to analyze two dimensional distributions of its physical properties. The physical parameters are derived from emission lines or stellar continuum, including stellar population age, electron temperature, oxygen abundance and etc. The oxygen abundances are derived using two empirical methods based on O3N2 and R_{23} indicators, as well as the direct T_e method when [O III]$\lambda4363$ is available. By applying the harmonic decomposition analysis to the velocity field, we obtained line-of-sight rotation velocity of 71 km s^{-1} and a position angle of 36 degree. The stellar age profile shows an old stellar population in galaxy center and a relative young stellar population in outer regions, suggesting an old bulge and a young disk. Oxygen abundance profile exhibits a clear break at $\sim$18 kpc, with a gradient of -0.0364 dex kpc^{-1} in the inner region and -0.00686 dex kpc^{-1} in the outer region. Our results agree with the "inside-out" disk growth scenario of M101.

Keywords: galaxies: evolution – galaxies: fundamental parameters – galaxies: stellar content – individual(M101): galaxies

huning@mail.ustc.edu.cn

1. INTRODUCTION

H II regions are the sites of strong star formation in galaxies, which make H II regions perfect probes of star formation processes, evolution of massive stars and the surrounding interstellar medium. Plenty of information can be obtained by analyzing the emission lines and underlying stellar continuum of their spectra. The gas-phase metallicity, defined as the number ratio of oxygen to hydrogen atom, is one of the key properties in galaxy formation and evolution. The oxygen is synthesized in high-mass stars ($>8M_\odot$) and then released to the inter-stellar medium through stellar winds or supernova explosion. The spatial distributions of the oxygen abundance in galaxies are affected by a variety of processes, such as enriched outflows (Tremonti et al. 2004), accretion (Dalcanton et al. 2004), and mergers (Kewley et al. 2006; Rupke et al. 2010; Kewley et al. 2010; Rich et al. 2012; Torrey et al. 2012; Sánchez et al. 2014). Thus studying the metallicity and its relation with other properties would provide clues on the galaxy formation and evolution.

Researches on the metallicity of H II regions are booming in the last two decades. Zaritsky et al. (1994) and van Zee et al. (1998) found that H II regions have an average metallicity gradient of -0.05 dex kpc^{-1}, i.e. the inner regions of galaxies are more metal-rich than the outskirts. The negative gradients are found to be universal, as reviewed by many following researches (**Bresolin 2007; Scarano & Lépine 2013; Li et al. 2013; Sánchez et al. 2014; Ho et al. 2015; Sánchez et al. 2016b**), suggesting inner-to-out transportation of metals. Observations also show breaks in the oxygen abundance gradients in a number of galaxies (Zaritsky 1992; Roy & Walsh 1997). Pilyugin (2003) claimed that such breaks are due to the systematic error involving the excitation parameter, while others attribute it to the barrier effect of corotation, which isolates the inner and outer regions of the disk one from the other due to opposite directions of gas flow (Lépine et al. 2011; Scarano & Lépine 2013). **More recently, several studies focusing on gas content have found that the metallicity gradients flatten to a constant value beyond the isophotal radii R$_{25}$ or 2R$_e$ (Rosales-Ortega et al. 2011; Marino et al. 2012; Sánchez et al. 2012, 2014; López-Sánchez et al. 2015; Sánchez et al. 2016b), and several scenarios are proposed to explain the nature of this flattening, such as the bar induced radial gas flows (Cavichia et al. 2014), minor mergers and perturbations from satellite galaxies (Bird et al. 2012; López-Sánchez et al. 2015), the varying star formation efficiency over a large galacentric distances (Bresolin et al. 2012; Esteban et al. 2013), and the balance between outflows and inflows with the intergalactic medium (Oppenheimer & Davé 2008; Oppenheimer et al. 2010; Davé et al. 2011, 2012).**

Recently, the Integral Field Unit (IFU) spectrograph is becoming a most important and powerful tool for spatial-resolved spectroscopic observations, which has greatly increased the progress of the two-dimensional research on galaxies. Many surveys using IFU technology are carried out, such as SAURON (Bacon et al. 2001), PINGS (Rosales-Ortega et al. 2010), CALIFA (Sánchez et al. 2012) and MaNGA (Bundy et al. 2015) survey. **According to their different observational strategies, MaNGA is mapping a large number of galaxies with limited spatial resolution (1-3 kpc) and field of view ($\sim$70 acrsec), while PIGNS provides a better spatial resolution and larger field of view but with limited number of galaxies, and CALIFA is a compromise between the two.** Sánchez et al. (2014) found a common metallicity gradient of -0.10 ± 0.09 dex R$_e^{-1}$ for 193 CALIFA galaxies, and the metallicity gradients do not exhibit the dependence on other properties of galaxies, such as morphology, mass, and

the presence or absence of bars (Sánchez et al. 2016b). **By studying 49 local field star-forming galaxies, Ho et al. (2015) proposed a local benchmark of metallicity gradients of -0.39 ± 0.18 dex R_{25}^{-1}. More recently, Belfiore et al. (2017) analyzed 550 nearby galaxies from MaNGA survey and confirm that metallicity gradient is flat for low mass galaxies ($M_* < 10^{9.0} M_\odot$), steepens for more massive galaxies until $M_* \sim 10^{10.5} M_\odot$ and flattens lightly again for even more massive galaxies.** These researches provided strong constraints on galactic chemical composition of nearby galaxies (Chiappini et al. 2001; Fu et al. 2009; Ho et al. 2015; Sánchez et al. 2016b; Belfiore et al. 2017).

Kong et al. (2014) proposed the "Spectroscopic Observations of the H II Regions In Nearby Galaxies (H2ING)" Project, which performs spectroscopic observations on H II regions in 20 nearby large galaxies since 2008. As the third paper of this project, we report the spectroscopic observation of H II regions in nearby galaxy M101, with the MMT 6.5 m telescope (Fabricant et al. 2005) and the NAOC 2.16 m telescope (Fan et al. 2016). M101 (also known as NGC 5457, $\alpha = 14^h 03^m 12^s.5$, $\delta = +54°20'56''$) is a large face-on Scd galaxy containing plenty of H II regions (Hodge et al. 1990; Kennicutt et al. 2003; Gordon et al. 2008; Bresolin 2007; Croxall et al. 2016). It has a distance of about 7.4 Mpc and an apparent scale of about 36 pc arcsec^{-1}, which enables us to observe its H II regions to a scale of a few hundred pc with our 1.5″ fiber and 2.5″ slit observations. A major-axis position angle of 39° and an inclination angle of 18° (Bosma et al. 1981) allow us to perform detailed studies of its stellar populations and ionized nebulae. Observations of the M101 H II regions have been carried out since 1970s (Searle 1971; Smith 1975; McCall et al. 1985; Kennicutt & Garnett 1996; Bresolin 2007). Recently, Li et al. (2013) presented a catalog containing 79 H II regions from their observations and several previous works since 1996. Croxall et al. (2016) have enlarged the sample of H II regions by using the Large Binocular Telescope (LBT), and obtained 109 spectra of H II regions in M101. In this paper, we have obtained 188 H II region with high S/N from our observations, which is the largest spectroscopic sample of H II regions for M101.

With the spectra of numerous H II regions, we have derived the physical properties of H II regions, and presented a detailed study of the spatial distribution of these properties. This paper is structured as follows. In Section 2, we describe the observation, data reduction and emission line measurements. In Section 3, we present the measurements and analysis of physical properties of the H II region sample. Metallicities are derived with three methods and the gradient is also calculated and discussed. We summarize our results in Section 4.

2. DATA

2.1. *Observations*

The H II region candidates are selected from the continuum-subtracted Hα image (Hoopes et al. 2001). Candidates are primarily selected with preference for large regions, using SExtractor (Bertin & Arnouts 1996) with irregular area filter with at least 25-pixel (1 pixel = 2.028″). The foreground stars are excluded from the H II catalog by matching with the 2MASS all-sky Point Source Catalog (PSC; Cutri et al. 2003). Then candidates are observed with the Hectospec multi-fiber positioner and spectrograph on the 6.5 m MMT telescope and the NAOC 2.16 m telescope.

The usable field of the MMT 6.5 m telescope is 1° in diameter, and the instrument deployed three hundred 1.5″-diameter fibers on the field, corresponding to ~ 54 pc at the distance of M101. We used Hectospecs 270 gpm grating that provided a dispersion of 1.2 Å pixel^{-1} and a resolution of

$\sim$ 5 Å. The spectral wavelength coverage is from 3650 to 9200 Å. The Hectospec fiber assignment software *xfitfibs*[1] allows the user to assign rankings to targets. If we ignored the spatial positions of our targets, fiber collisions would prevent many objects in the center portion of the center of M101 from being observed. We therefore assigned priority to H II regions based on their Hα fluxes. We observed two fields at the night on 2012 February 10 with 3600 s exposure times and one field on 2013 March 15 with 5400 s exposure times. Weather conditions are clear on both nights, and seeings are about 1.2″, 0.8″ and 0.6″ for each field, respectively.

The NAOC 2.16 m telescope worked with an OMR (Optomechanics Research Inc.) spectrograph providing a dispersion of 4.8 Å pixel $^{-1}$ and a resolution of 10 Å. The observed spectra cover the wavelength range of 3500 to 8100 Å. Slits of 2.5″ are placed manually to cover as many candidates as possible and to avoid those observed by MMT. Observations are carried out over 9 nights between 2012 and 2014 with 20 slits, and exposure times varied between 3600 s and 5400 s depending on weather conditions. Typical seeing is $\sim$ 2.5″, corresponding to an spatial resolution of $\sim$300 pc.

2.2. Data reduction

2.2.1. MMT spectra

We obtained over 300 spectra from MMT observations, and these spectra are reduced in an uniform manner with the publicly available HSRED[2] software. The frames are first de-biased and flat-fielded. Individual spectra are then extracted and wavelength calibrated. Sky subtraction is achieved with Hectospec by averaging spectra from "blank sky" fibers from the same exposures. Three spectra of the same target are reduced and combined into one final spectrum. Standard stars are obtained intermittently and are used to calibrate spectra using IRAF ONEDSPEC package. These relative flux corrections are carefully applied to ensure that the relative line flux ratios are accurate. We have checked the spectra by visually inspection to exclude spectra with problematic continuum shape, or missing Hα and Hβ emission lines. Finally, we obtained a sample of 164 H II region spectra for analysis. The 164 spectra have a median S/N of 35 at 5000Å, and over 50 spectra have S/N higher than 60.

2.2.2. NAOC 2.16 m Spectra

The spectroscopic data from NAOC 2.16 m observations are reduced following standard procedures using IRAF software package. The CCD reduction includes bias and flat-field correction, as well as cosmic-ray removal. Wavelength calibration is performed based on helium/argon lamps exposed at both the beginning and the end of each slit during the observation. Flux calibration is performed based on observations of the KPNO spectral standard stars (Massey et al. 1988) observed at the end of each slit observation. The atmospheric extinction is corrected by using the mean extinction co-efficients measured for Xinglong by the Beijing-Arizona-Taiwan-Connecticut (BATC) multicolor sky survey (H. J. Yan 1995, priv. comm.). Similar to MMT spectra, those with problematic continuum shape or missing Hα and Hβ emission lines are excluded. Finally we extracted 41 spectra, among which 17 spectra are also observed by MMT 6.5 m telescope. Considering the higher S/Ns and better resolution of MMT spectra, we use MMT spectra for these 17 candidates, and NAOC observations provide 24 additional spectra.

---

[1] https://www.cfa.harvard.edu/john/xfitfibs
[2] http://mmto.org/ rcool/hsred/index.html

Finally we have 188 spectra in total (164 from MMT 6.5 m and 24 from NAOC 2.16 m). Locations of these H II regions are shown in Figure 1 and their coordinates are listed in Table 1. Velocities are measured using the SAO xcsao package with IRAF (see Figure 2). We have carefully checked the velocities and corrected a few bad results manually. Spectra are corrected for Galactic reddening (Schlegel et al. 1998), and then shifted to rest frame for further measurements.

2.3. *Spectral Fitting*

To measure the emission lines of each individual spectra, the underlying stellar continuum must be subtracted. We perform a modeling of stellar continuum using advanced ICA algorithm, mean field approach to Bayesian independent component analysis (MF-ICA), which is comparatively precise and efficient (Højen-Sørensen et al. 2001, 2002). The MF-ICA approach extracts 12 independent components (ICs) from BC03[3] (Bruzual & Charlot 2003). The 12 ICs contain full information of BC03 library and excellently recover the library, **which spans a stellar age range from** 1.0×10^5 **to** 2.0×10^{10} **yr, and an initial chemical composition metallicity from** 0.0001 **to** 0.1. **The star formation histories (SFHs) are parameterized in terms of an underlying continuous model superimposed with random bursts on it (Kauffmann et al. 2003). The intrinsic starlight reddening is modeled by the extinction law of Charlot & Fall (2000). The velocity dispersion is set to vary between 50** $\mathrm{km\,s^{-1}}$ **and 450** $\mathrm{km\,s^{-1}}$. MF-ICA provides reliable modeling of stellar continuum and estimates physical parameters accurately with a large improvement in efficiency. More detailed informations about MF-ICA algorithm are described in Hu et al. (2016). Figure 3 shows two typical fitting results. For each spectrum, emission lines [O II]$\lambda 3727$, Hβ+ [O III]$\lambda\lambda 4959, 5007$, H$\alpha$+ [N II]$\lambda\lambda 6548, 6583$ and [S II]$\lambda\lambda 6717, 6731$ are enlarged in four small panels below the spectrum.

2.4. *Line Flux Measurement*

After subtracting the stellar continuum, we perform the non-linear least-squares fit to emission lines using MPFIT package implemented in IDL (Markwardt 2009). Each emission line is modeled with one Gaussian profile, and we constrain the ratios [N II]$\lambda 6583$/[N II]$\lambda 6548$ and [O III]$\lambda 4959$/[O III]$\lambda 5007$ to their theoretical values given by quantum mechanics. The emission line fluxes are measured by integration of the flux based on the fitted profiles.

The interstellar reddening is corrected by comparing the observed Hα/Hβ Balmer decrement to the theoretical value, since intrinsic value of Hα/Hβ is not very sensitive to the physical conditions of the gas. Assuming Hα/Hβ = 2.86 and R_V = 3.1 with Cardelli et al. (1989) extinction curve under the case-B recombination, the extinction in the V band is given by:

$$A_V = 6.77 \log \frac{F(\mathrm{H}\alpha)/F(\mathrm{H}\beta)}{2.86}. \tag{1}$$

negative color excesses are all set to be zero. The reddening-corrected line flux measurements are listed in Table 1, with values normalized to Hβ flux. All spectra have strong Hα and Hβ emission lines, and 14 of them have [O III]$\lambda 4363$ emission line.

In Figure 4, we examine the excitation properties of our sample by plotting [O III]$\lambda 5007$/Hβ versus [N II]$\lambda 6583$/Hα diagnostic diagrams (BPT, Baldwin et al. 1981). The color-code indicates the de-projected distance to the galaxy center. We plot the boundaries between different photoionization

---

[3] http://www.bruzual.org

sources (star-forming regions and active galactic nuclei) by Kewley et al. (2001) and Kauffmann et al. (2003). As shown in Figure 4, almost all targets in our sample are located in the pure star forming region with only 5 exceptions. Further, the H II regions show a radially changing sequence on the BPT diagram: the inner regions have higher [N II]λ6583/Hα and lower [O III]λ5007/Hβ than outer regions, suggesting a negative gradient of metallicity. **This is well consistent with the results from Sánchez et al. (2015), that the inner H II regions of the galaxies appear to have higher [N II]λ6583/Hα and lower [O III]λ5007/Hβ than outer regions, using over 5000 H II regions from 306 galaxies.**

More detailed information will be discussed in section 3.3.

2.5. *Oxygen Abundance determination*
2.5.1. *The direct method*

The direct method to derive oxygen abundance is to measure the ratio of a higher excitation line to a lower excitation line, in which case [O III]λ4363/[O III]$\lambda\lambda$4959, 5007 is the most commonly used. This ratio together with a model of two excitation zone structure for the H II regions provides an estimation of the electron temperature of the gas, and then the electron temperatures are converted to oxygen abundances with corrections for unseen stage of ionization.

To calculate the total oxygen abundances, we make the usual assumption: O/H = (O$^+$ + O^{2+})/H$^+$. Electron temperatures are derived based on the emission line intensity ratio [O III]λ4363/[O III]$\lambda\lambda$4959, 5007, and electron densities (n_e) are derived based on the intensity ratio [S II]λ6717/[S II]λ6731. Among the spectra of H II regions, 14 of them have [O III]λ4363 detections with well-defined line profiles and the S/Ns larger than 3. The electron temperatures of them for the O^{2+}-emitting region (T[O III]) are derived with the PYNEB package (Luridiana et al. 2015). PYNEB is a python package for analyzing emission lines, which includes the Fortran code FIVEL (De Robertis et al. 1987) and the IRAF nebular package (Shaw & Dufour 1995). We adopted the transition probabilities of Wiese et al. (1996) and Storey & Zeippen (2000) for O^{2+}, Podobedova et al. (2009) for S$^+$, the collision strengths of Aggarwal & Keenan (1999) for O^{2+}, Tayal & Zatsarinny (2010) for S^+. Electron temperatures and electron densities are calculated simultaneously to obtain self-consistent estimates by PYNEB. Then the electron temperatures of [O II] (T[O II]) are obtained with applying the relation from Garnett (1992): T[O II] = 0.7 × T[O III] + 3000K. With giving T[O II], T[O III] and n_e, metallicities are finally calculated from the line intensities of [O II]λ3727 and [O III]$\lambda\lambda$4959, 5007 with PYNEB.

Errors are estimated with Monte Carlo algorithm by repeating the calculation 2000 times. In each calculation, the input flux of each emission line is generated from a Gaussian distribution with mean value equaling to measured emission line flux and standard deviation equaling to its error. We use the median value of 2000 results as the final value, and the half of 16% − 84% range of this distribution as the corresponding error. The electron temperatures and densities are listed in Table 2.

Although the direct method is considered to be **one of the most reliable methods** to derive gas-phase oxygen abundances, the [O III]λ4363 line is weak, especially in meta-rich environments. Since most of our H II regions do not have [O III]λ4363 detections, we applied two strong-line methods to determine the oxygen abundance.

2.5.2. *O3N2 index*

The O3N2 index, defined as O3N2 = log{([O III]λ5007/Hβ)/([N II]λ6583/Hα)}, is firstly introduced by Alloin et al. (1979). It is widely used to diagnose oxygen abundances in the literature. The four

lines involved in the index are easily detected, and the close wavelength between the two pairs of lines make the index nearly free from extinction. By using 137 extragalactic H II regions, Pettini & Pagel (2004) empirically calibrated the O3N2 vs oxygen abundance determined by T_e method **and photoionization models**. **More recently, Marino et al. (2013) provide a new calibration with** T_e **based metallicities of 603 H II regions, which is adopted here:**

$$12 + \log (O/H) = 8.533 - 0.214 \times O3N2, \tag{2}$$

However, O3N2 calibrations do not consider the variations of ionization parameter (q), which may cause systematic errors. More will be discussed in the next subsection.

2.5.3. *KK04 method*

Kobulnicky & Kewley (2004, hereafter KK04) adopted the stellar evolution and photoionization from Kewley & Dopita (2002) to produce a modified R_{23} calibration. R_{23} index, defined as $R_{23} = ([O II]\lambda 3727 + [O III]\lambda\lambda 4959, 5007)/H\beta$, is sensitive to the ionization parameter of the gas, which is defined as the ratio between the number of hydrogen ionizing photons passing through a unit area per second and the hydrogen density of the gas. The ionization parameter is typically derived based on the line ratio $O_{32} = [O III]\lambda 5007/[O II]\lambda 3727$, and it is also sensitive to oxygen abundance, therefore KK04 applied an iterative process to derive a consistent ionization parameter and oxygen abundance. First we determined whether the H II regions lie on the upper or lower R_{23} branch with ratio N2O2 $= [N II]\lambda 6583/[O II]\lambda 3727$, then we calculated an initial ionization parameter by assuming a starting oxygen abundance 8.0 for lower branch and 9.0 for upper branch. The initial ionization parameter is used to calculate an initial oxygen abundance. These processes are iterated until oxygen abundance converges. Errors are generated with the same Monte Carlo algorithm used in direct T_e method, i.e. repeating the calculation 2000 times.

The results of three calibrations, electron temperatures $T[O III]$, electron densities n_e and ionization parameter q are listed in Table 2. To test the reliability of the oxygen abundance, we compare the three calibrations in Figure 6. In Figure 6 we plot O3N2 calibrations and T_e calibrations vs KK04 calibrations, with different colors indicating different ionization parameter (see Figure 6 for details). As shown in this figure, good linear correlations are seen with systematic offsets as whole. O3N2 calibration is systematically ~ 0.4 dex lower than KK04 calibration, and it flattens when KK04 calibration is lower than 8.5 due to the limited range of O3N2 index. T_e calibrations agree well with O3N2 calibrations if we ignore the values near the lower limit of O3N2 calibration. The systematic biases of different methods are expected, which are investigated by Kewley & Ellison (2008) in detail. The systemic 0.4 dex bias could be caused by temperature fluctuations or gradients within high-metallicity H II regions. In the presence of temperature fluctuations or gradients, [O III] is emitted predominantly in high-temperature zones where O^{2+} is present only in small amounts. Thus the high electron temperatures estimated from the [O III]$\lambda 4363$ line do not reflect the true electron temperature in the H II region, leading to a systematic lower estimation of metallicity by as much as 0.4 dex (Stasińska et al. 2002; Stasińska 2005; Kewley & Ellison 2008). Moreover, the scattering between O3N2 calibrations and KK04 calibrations is not random. It correlates with ionization parameter q: samples with lower $\log(q)$ tend to have larger measured metallicity. Considering all the discussion above, we use KK04 calibrations in the following analysis.

3. RESULTS

3.1. *Velocity field*

M101 is a giant and nearly face-on spiral galaxy (Sandage & Tammann 1974; Bosma et al. 1981). The velocity field of M101 have been studied based on the kinematics of HI gas (Bosma et al. 1981) and Hα-data (Comte et al. 1979). In this paper, the H II regions cover a wide range of regions on M101, which enables us to acquire the velocity map for M101. The left panel of Figure 2 shows the line of sight velocities of H II regions in M101, which are good tracers of gas movements. The velocities are measured using the SAO xcsao package with IRAF.

As seen in this panel, a rotating disk is clearly shown. We then apply the harmonic decomposition method (Krajnović et al. 2006) to model the velocity field. This method has been widely used to analyze the gas and stellar kinematics in both late-type (Franx et al. 1994; Wong et al. 2004) and early-type galaxies (Emsellem et al. 2007; Krajnović et al. 2008). This method is able to decompose the line of sight velocity map into a series of Fourier components, which are kinematic components with different azimuthal symmetry. In this work, we broadly expand the Fourier terms to the third order:

$$V(a, \psi) = A_0(a) + \sum_{n=1}^{3} A_n(a) \sin n\psi + B_n(a) \cos(n\psi) \qquad (3)$$

where ψ is the eccentric anomaly, and a is the length of the semimajor axis of the elliptical ring. Using this model, we obtained the kinematic position angle of 36 degree, the inclination of 26 degree, the systemic velocity of 242 km/s and the line of sight rotation velocity of 71 km/s, corresponding to a maximum rotation velocity of 168 km/s. These values agree well with the previous modeling of velocity field from Comte et al. (1979), who found the position angle of 35 degree, the inclination of 27 degree and the systemic velocity of 238 km/s. However, the inclination measured in this work is slightly larger than the result from Bosma et al. (1981), who found a inclination of 18 degree based on the HI velocity map. This discrepancy may due to the larger HI disks than optical disk and interactions with close companions in outskirts (Bosma et al. 1981; Waller et al. 1997; Mihos et al. 2012). The modeled velocity map is shown in the right panel of Figure 2 with the same color-coding of the left panel.

3.2. *Stellar population ages*

The light-weighted mean stellar age is a good tracer to the star formation history. Low stellar age indicates the young stellar population and recent strong star formation activities in the galaxy, while high stellar age means old stellar populations with few recent star formation activities. The equivalent width (EW) of Hα emission line is sensitive to the ratio of present to past star formation rate, therefore it is expected to be correlated with stellar age, with the higher values the younger populations.

From the MF-ICA fits, we have estimated the stellar population age by computing light-weighed mean age of different stellar population components. The left panel of Figure 5 shows the two dimensional distribution of the mean stellar age. As shown in this figure, the stellar ages of the inner region are generally older than the outskirts in M101. We also present the EW(Hα) of each H II region in the right panel of Figure 5. The results in both of panels are broadly consistent, with older stellar population in the inner regions and younger stellar population in outer regions. This negative stellar age gradient in M101 agrees with the "inside-out" disk growth scenario (Pérez et al. 2013; Bezanson et al. 2009; Tacchella et al. 2015).

We note that it appears to have a younger stellar population component at the very center of the bulge (see Figure 5). This is also discovered in Lin et al. (2013) by using SED modelings of resolved multi-band photometric images from ultraviolet and optical to infrared of M101. They found a resolved bar at the center of M101, and proposed that the bulge of M101 is a disk-like pseudobulge, likely induced by secular evolution of the small bar (Hawarden et al. 1986; Ho et al. 1997; Wang et al. 2012; Cole et al. 2014; Lin et al. 2017a).

3.3. *Radial Abundance Gradient*

The measurements of radial abundance gradient from H II regions are firstly carried out by Searle (1971) and Smith (1975), after that series of works showed up (McCall et al. 1985; Kennicutt & Garnett 1996; Bresolin 2007; Lin et al. 2013; Sánchez et al. 2012, 2014, 2016b, 2017; Pilyugin et al. 2014; Belfiore et al. 2017).

There are 173 out of 188 H II regions whose oxygen abundances are computed by the KK04 calibration. The distribution of oxygen abundance (left panel) and its radial gradient (right panel) are presented in Figure 7. Some other works are also shown in different symbols. As the figure shows, the oxygen abundances from the KK04 calibration are 0.5 dex higher than Bresolin (2007) and Kennicutt et al. (2003), because their calibrations are based on the T_e method. However, the metallicity gradients are consistent based on different calibrations and works. In addition, our result also shows a break in the gradient at around 18 kpc radius, so we use two linear least-squares fits:

$$12 + \log(O/H) = 9.24 - 0.0364 \times R \tag{4}$$

for R<18 kpc, and

$$12 + \log(O/H) = 8.64 - 0.00686 \times R \tag{5}$$

for R>18 kpc. The gradient of the inner regions is -0.0364 dex kpc^{-1}, which is slightly steeper than the results from Bresolin (2007), **Li et al. (2013) and Pilyugin et al. (2014)(-0.0278, -0.0268 and -0.0293 dex kpc^{-1}). However, the metallicity gradient becomes flat at the radius greater than 20 kpc. To compare with the characteristic gradient provided by Ho et al. (2015)(-0.39 ± 0.18 dex R$_{25}^{-1}$), we convert the derived gradient to same scale. For inner regions, the gradient is -1.18 ± 0.017 dex R$_{25}^{-1}$, which is steeper than characteristic gradients. However, the gradient of the outer region is -0.221 ± 0.038 dex R$_{25}^{-1}$, which is flatter.**

Rosales-Ortega et al. (2012) found that gas metallicity increases with stellar mass surface density, which plays a role in determining the mass-metallicity relation and radial metallicity gradients in spirals. This has been confirmed by several researches (e.g.,Sánchez et al. 2013, Barrera-Ballesteros et al. 2016). Chemical evolution models with most important parameters varying smoothly with radius can easily reproduce negative gradients, which show that the maxima of both neutral and molecular gas move from the center to outskirts through the disk as the galaxy evolves. Thus the star formation is strong in the central regions at early times and spread outward through disks as the gas is efficiently consumed. This shapes present galaxies with high metallicity, low specific star formation rate in the center and negative radial metallicity gradients that flatten with time. This is knew as the "inside-out" disk growth.

**Several studies have found that metallicity gradients flatten to a constant value be-
yond the isophotal radii R$_{25}$ or 2R$_e$**(Rosales-Ortega et al. 2011; Marino et al. 2012;
Sánchez et al. 2012, 2014; López-Sánchez et al. 2015; Sánchez et al. 2016b). **The mecha-
nism of this gradient flattening is under debate. One possible mechanism is a slow radial
dependence of the star formation efficiency across over a large galactocentric distances**
(Bresolin et al. 2012; Esteban et al. 2013). **Cosmological simulations that introduce a
balance between outflows and inflows with the intergalactic medium may also contribute
to shaping the metal content** (Oppenheimer & Davé 2008; Oppenheimer et al. 2010;
Davé et al. 2011, 2012). **Interactions with satellite galaxies are suggested to enhance
the metallicity in the outer regions of galaxies, which may also flatten the metallicity
gradient** (Bird et al. 2012; López-Sánchez et al. 2015). **The real senario is likely to be
the mixture of several mechanisms. We note that the turning point of the gradient in
M101 is at $\sim$ 18 kpc, which is much smaller than R$_{25}$($\sim$ 31 kpc). An alternative expla-
nation is proposed** Lépine et al. (2011), **that** the break in the gradient is the "pumping out"
effect of corotation, which produces gas flows in opposite directions on the two sides of the radius.
The corotation radius of M101 is 16.7 kpc (Scarano & Lépine 2013), which is very close to the break
radius we find in this work. This suggests that the radial break of metallicity in M101 probably
caused by the result of corotation.

There are 7 outliers far below the fit line with oxygen abundance lower than 8.2. These H II
regions are located to the east of M101. M101 is not the isolated galaxy, and two close companions
(NGC5474 in the east and NGC5477 in the southeast) are found. Kewley et al. (2006) presented
some evidence that galaxy pairs have systematically lower oxygen abundance than field galaxies, and
mergers may also flatten the oxygen abundance gradient. More recently, Sánchez et al. (2014) found
that the metallicity gradients are independent of morphology, incidence of bars, absolute magnitude
and mass, and that the only clear correlation is between merger stage and metallicity gradient,
where merger progresses flatten the slope of gradients (see also Torrey et al. 2012; Rich et al. 2012;
Kewley et al. 2010; Rupke et al. 2010) . M101 might be interacting with NGC5474 and NGC 5477,
as suggested by Waller et al. (1997); Mihos et al. (2012, 2013), who analyzed deep neutral hydrogen
observation and deep optical images and concluded that M101 is in an ongoing interactions with
lower mass companions. These interactions may dilute the oxygen abundance of these H II regions
in gas mixing processes, making the 7 outliers relatively meta-poor.

4. SUMMARY

We have investigated the distributions of physical properties of H II regions in nearby galaxy M101
using spectra obtained from the 6.5 m MMT telescope and the NAOC 2.16 m telescope during 2012
to 2014. We present the observations, data reductions, and measurements of emission lines. This is
the largest spectroscopic sample of H II regions in M101 by now.

We estimated the stellar population ages by fit the continuum with MF-ICA approach, and the
stellar age profile shows an older stellar population in the inner regions and a younger in the outer
regions. There is a younger component at the center of the galaxy, which indicates that a recent
star formation occurred at the center. This might be caused by gas falling into the center due to the
nonaxisymmetric gravity of the bar.

We calculated the electron temperatures T[O III], electron densities n_e, and measured oxygen abun-
dances with three methods. O3N2 calibrations are consistent with direct T_e calibrations when ignore

the limitation effect of O3N2 calibration, and both calibrations are systemically $\sim$0.4 dex lower than KK04 calibration, due to temperature fluctuations or gradients within high-metallicity H$\,$II regions. O3N2 calibrations do not consider ionization parameters, which may cause systemic errors.

The oxygen abundance profile shows a negative gradient with a clear break at 20 kpc radius. The gradient is -0.0364 dex kpc^{-1} in the inner region and -0.00686 dex kpc^{-1} in the outer region. **This is likely to be the mixture of several mechanisms, such as radial dependence of SFE over large a large galactocentric distances, a balance between outflows and inflows with the intergalactic medium and interactions with satellite galaxies.** Since the break radius is comparable to the corotation radius (16.7 kpc), the break in the gradient could be the "pumping out" effect of corotation. If this is the case, gas flows play an important role in chemical evolutions of galaxies and should not be regarded as minor effects in evolution models. There are several H$\,$II regions with oxygen abundance lower than 8.2, which locate far from major distribution, and we find they are all located in the east of M101, close to its companions, NGC5474 and NGC5477. These low metallicities may be the result of interactions with close companions.

Both stellar population age distribution and oxygen abundance gradient support the "inside-out" disk growth scenario: the early gas infall or collapse made the inner region more metal-rich and older, while the outer disk is enriched more slowly and younger. In order to learn more about the formation and evolution of nearby galaxies, we intend to combine the spectra of H$\,$II regions with multi-wavelength photometry data (especially UV to IR) to investigate the nature of dispersions of IRX-β relation. Due to the relatively simple star formation history and structure of H$\,$II regions, it would be helpful to find a second parameter to reduce the scatter of IRX-β relation. This will help us understand further in the interaction between dust and interstellar radiation field, as well as the formation and evolution of nearby galaxies.

Facilities: MMT, Beijing:2.16m

Software: SExtractor (Bertin & Arnouts 1996), xfitfibs, HSRED, MF-ICA (Hu et al. 2016), MP-FIT (Markwardt 2009), PyNeb (Luridiana et al. 2015)

REFERENCES

Aggarwal, K. M., & Keenan, F. P. 1999, ApJS, 123, 311

Bacon, R., Copin, Y., Monnet, G., et al. 2001, MNRAS, 326, 23

Baldwin, J. A., Phillips, M. M., & Terlevich, R. 1981, PASP, 93, 5

Barrera-Ballesteros, J. K., Heckman, T. M., Zhu, G. B., et al. 2016, MNRAS, 463, 2513

Belfiore, F., Maiolino, R., Tremonti, C., et al.
    2017, MNRAS, 469, 151

Bertin, E., & Arnouts, S. 1996, A&AS, 117, 393

Berg, D. A., Skillman, E. D., Garnett, D. R., et
    al. 2013, ApJ, 775, 128

Bezanson, R., van Dokkum, P. G., Tal, T., et al.
    2009, ApJ, 697, 1290

Bird, J. C., Kazantzidis, S., & Weinberg, D. H.
    2012, MNRAS, 420, 913

Bosma, A., Goss, W. M., & Allen, R. J. 1981,
    A&A, 93, 106

Bresolin, F. 2007, ApJ, 656, 186

Bresolin, F. 2011, ApJ, 730, 129

Bresolin, F., Kennicutt, R. C., & Ryan-Weber, E.
    2012, ApJ, 750, 122

Bruzual, G., & Charlot, S. 2003, MNRAS, 344,
    1000

Bundy, K., Bershady, M. A., Law, D. R., et al.
    2015, ApJ, 798, 7

Caldwell, N., Harding, P., Morrison, H., et al.
    2009, AJ, 137, 94

Cardelli, J. A., Clayton, G. C., & Mathis, J. S.
    1989, ApJ, 345, 245

Carollo, C. M., Scarlata, C., Stiavelli, M., Wyse,
    R. F. G., & Mayer, L. 2007, ApJ, 658, 960

Cavichia, O., Mollá, M., Costa, R. D. D., &
    Maciel, W. J. 2014, MNRAS, 437, 3688

Cid Fernandes, R., Mateus, A., Sodré, L.,
    Stasińska, G., & Gomes, J. M. 2005, MNRAS,
    358, 363

Charlot, S., & Fall, S. M. 2000, ApJ, 539, 718

Chiappini, C., Matteucci, F., & Romano, D. 2001,
    ApJ, 554, 1044

Cole, D. R., Debattista, V. P., Erwin, P., Earp,
    S. W. F., & Roškar, R. 2014, MNRAS, 445, 3352

Crockett, N. R., Garnett, D. R., Massey, P., &
    Jacoby, G. 2006, ApJ, 637, 741

Croxall, K. V., Pogge, R. W., Berg, D. A.,
    Skillman, E. D., & Moustakas, J. 2016, ApJ,
    830, 4

Comte, G., Monnet, G., & Rosado, M. 1979,
    A&A, 72, 73

Cutri, R. M., Skrutskie, M. F., van Dyk, S., et al.
    2003, VizieR Online Data Catalog, 2246,

Daddi, E., Renzini, A., Pirzkal, N., et al. 2005,
    ApJ, 626, 680

Dalcanton, J. J., Yoachim, P., & Bernstein, R. A.
    2004, ApJ, 608, 189

Davé, R., Finlator, K., & Oppenheimer, B. D.
    2011, MNRAS, 416, 1354

Davé, R., Finlator, K., & Oppenheimer, B. D.
    2012, MNRAS, 421, 98

De Robertis, M. M., Dufour, R. J., & Hunt, R. W.
    1987, JRASC, 81, 195

Emsellem, E., Cappellari, M., Krajnović, D., et al.
    2007, MNRAS, 379, 401

Esteban, C., Carigi, L., Copetti, M. V. F., et al.
    2013, MNRAS, 433, 382

Fabricant, D., Fata, R., Roll, J., et al. 2005,
    PASP, 117, 1411

Fan, Z., Wang, H., Jiang, X., et al. 2016, PASP,
    128, 5005

Franx, M., van Gorkom, J. H., & de Zeeuw, T.
    1994, ApJ, 436, 642

Fu, J., Hou, J. L., Yin, J., & Chang, R. X. 2009,
    ApJ, 696, 668

Ganda, K., Peletier, R. F., McDermid, R. M., et
    al. 2007, MNRAS, 380, 506

Garnett, D. R. 1992, AJ, 103, 1330

Gordon, K. D., Engelbracht, C. W., Rieke, G. H.,
    et al. 2008, ApJ, 682, 336-354

Hawarden, T. G., Mountain, C. M., Leggett,
    S. K., & Puxley, P. J. 1986, MNRAS, 221, 41

Henry, R. B. C., & Howard, J. W. 1995, ApJ, 438,
    170

Ho, L. C., Filippenko, A. V., & Sargent, W. L. W.
    1997, ApJ, 487, 591

Ho, I.-T., Kudritzki, R.-P., Kewley, L. J., et al.
    2015, MNRAS, 448, 2030

Hodge, P. W., Gurwell, M., Goldader, J. D., &
    Kennicutt, R. C., Jr. 1990, ApJS, 73, 661

Hoopes, C. G., Walterbos, R. A. M., & Bothun,
    G. D. 2001, ApJ, 559, 878

Højen-Sørensen, P. A. D. F. R., Winther, O. &
    Hansen, L. K. 2001, Advances in Neural
    Information Processing Systems, Vol. 13, MIT
    Press, Cambridge, MA, 542

Højen-Sørensen, P. A. D. F. R., Winther, O. &
    Hansen, L. K. 2002, Neural Comput, 14, 889

Hu, N., Su, S.-S., & Kong, X. 2016, RAA, 16, 42

Kauffmann, G., Heckman, T. M., Tremonti, C., et
    al. 2003, MNRAS, 346, 1055

Kewley, L. J., Dopita, M. A., Sutherland, R. S.,
    Heisler, C. A., & Trevena, J. 2001, ApJ, 556,
    121

Kewley, L. J., & Dopita, M. A. 2002, ApJS, 142,
    35

Kewley, L. J., Geller, M. J., & Barton, E. J. 2006,
    AJ, 131, 2004

Kewley, L. J., & Ellison, S. L. 2008, ApJ, 681, 1183

Kewley, L. J., Rupke, D., Zahid, H. J., Geller, M. J., & Barton, E. J. 2010, ApJL, 721, L48

Kennicutt, R. C., Jr., & Garnett, D. R. 1996, ApJ, 456, 504

Kennicutt, R. C., Jr., Bresolin, F., & Garnett, D. R. 2003, ApJ, 591, 801

Kobulnicky, H. A., & Kewley, L. J. 2004, ApJ, 617, 240

Kong, X., Lin, L., Li, J.-r., et al. 2014, ChA&A, 38, 427

Kormendy, J., & Kennicutt, R. C., Jr. 2004, ARA&A, 42, 603

Krajnović, D., Bacon, R., Cappellari, M., et al. 2008, MNRAS, 390, 93

Krajnović, D., Cappellari, M., de Zeeuw, P. T., & Copin, Y. 2006, MNRAS, 366, 787

Lépine, J. R. D., Cruz, P., Scarano, S., Jr., et al. 2011, MNRAS, 417, 698

Li, Y., Bresolin, F., & Kennicutt, R. C., Jr. 2013, ApJ, 766, 17

Lin, L., Li, C., He, Y., Xiao, T., & Wang, E. 2017, ApJ, 838, 105

Lin, L., Zou, H., Kong, X., et al. 2013, ApJ, 769, 127

Lin, Z., Hu, N., Kong, X., et al. 2017, arXiv:1704.06935

López-Sánchez, Á. R., Westmeier, T., Esteban, C., & Koribalski, B. S. 2015, MNRAS, 450, 3381

Luridiana, V., Morisset, C., & Shaw, R. A. 2015, A&A, 573, A42

Magrini, L., Stanghellini, L., Corbelli, E., Galli, D., & Villaver, E. 2010, A&A, 512, A63

Markwardt C. B., 2009, in Bohlender D. A., Durand D., Dowler P., eds, ASP Conf. Ser. Vol. 411, Astronomical Data Analysis Softwar and Systems XVIII. Astron. Soc. Pac., San Francisco, p. 251

Marino, R. A., Gil de Paz, A., Castillo-Morales, A., et al. 2012, ApJ, 754, 61

Marino, R. A., Rosales-Ortega, F. F., Sánchez, S. F., et al. 2013, A&A, 559, A114

Massey, P., Strobel, K., Barnes, J. V., & Anderson, E. 1988, ApJ, 328, 315

McCall, M. L., Rybski, P. M., & Shields, G. A. 1985, ApJS, 57, 1

Mihos, J. C., Harding, P., Spengler, C. E., Rudick, C. S., & Feldmeier, J. J. 2013, ApJ, 762, 82

Mihos, J. C., Keating, K. M., Holley-Bockelmann, K., Pisano, D. J., & Kassim, N. E. 2012, ApJ, 761, 186

Moustakas, J., Kennicutt, R. C., Jr., Tremonti, C. A., et al. 2010, ApJS, 190, 233-266

Oppenheimer, B. D., & Davé, R. 2008, MNRAS, 387, 577

Oppenheimer, B. D., Davé, R., Kereš, D., et al. 2010, MNRAS, 406, 2325

Peletier, R. F., Davies, R. L., Illingworth, G. D., Davis, L. E., & Cawson, M. 1990, AJ, 100, 1091

Pettini, M., & Pagel, B. E. J. 2004, MNRAS, 348, L59

Pérez, E., Cid Fernandes, R., González Delgado, R. M., et al. 2013, ApJL, 764, L1

Pilyugin, L. S. 2003, A&A, 397, 109

Pilyugin, L. S., Vílchez, J. M., & Contini, T. 2004, A&A, 425, 849

Pilyugin, L. S., Grebel, E. K., & Kniazev, A. Y. 2014, AJ, 147, 131

Podobedova, L. I., Kelleher, D. E., & Wiese, W. L. 2009, Journal of Physical and Chemical Reference Data, 38, 171

Rosales-Ortega, F. F., Kennicutt, R. C., Sánchez, S. F., et al. 2010, MNRAS, 405, 735

Rich, J. A., Torrey, P., Kewley, L. J., Dopita, M. A., & Rupke, D. S. N. 2012, ApJ, 753, 5

Rosales-Ortega, F. F., Sánchez, S. F., Iglesias-Páramo, J., et al. 2012, ApJL, 756, L31

Roškar, R., Debattista, V. P., Stinson, G. S., et al. 2008, ApJL, 675, L65

Roy, J.-R., & Walsh, J. R. 1997, MNRAS, 288, 715

Rosales-Ortega, F. F., Díaz, A. I., Kennicutt, R. C., & Sánchez, S. F. 2011, MNRAS, 415, 2439

Rosolowsky, E., & Simon, J. D. 2008, ApJ, 675, 1213-1222

Rupke, D. S. N., Kewley, L. J., & Barnes, J. E. 2010, ApJL, 710, L156

Scarano, S., & Lépine, J. R. D. 2013, MNRAS, 428, 625

Schlegel, D. J., Finkbeiner, D. P., & Davis, M. 1998, ApJ, 500, 525

Scowen, P. A., Dufour, R. J., & Hester, J. J. 1992, AJ, 104, 92

Sánchez, S. F., Kennicutt, R. C., Gil de Paz, A., et al. 2012a, A&A, 538, A8

Sánchez, S. F., Rosales-Ortega, F. F., Marino, R. A., et al. 2012b, A&A, 546, A2

Sánchez, S. F., Rosales-Ortega, F. F., Jungwiert, B., et al. 2013, A&A, 554, A58

Sánchez, S. F., Rosales-Ortega, F. F., Iglesias-Páramo, J., et al. 2014, A&A, 563, A49

Sánchez, S. F., Pérez, E., Rosales-Ortega, F. F., et al. 2015, A&A, 574, A47

Sánchez-Menguiano, L., Sánchez, S. F., Kawata, D., et al. 2016a, ApJL, 830, L40

Sánchez-Menguiano, L., Sánchez, S. F., Pérez, I., et al. 2016b, A&A, 587, A70

Sánchez-Menguiano, L., Sánchez, S. F., Pérez, I., et al. 2017, A&A, 603, A113

Sandage, A., & Tammann, G. A. 1974, ApJ, 194, 223

Searle, L. 1971, ApJ, 168, 327

Shaw, R. A., & Dufour, R. J. 1995, PASP, 107, 896

Smith, H. E. 1975, ApJ, 199, 591

Tacchella, S., Carollo, C. M., Renzini, A., et al. 2015, Science, 348, 314

Stasińska G., 2002, Rev. Mex AA Conf. Ser., 12, 62

Stasińska, G., Mateus, A., Jr., Sodré, L., Jr., & Szczerba, R. 2004, A&A, 420, 475

Stasińska, G. 2005, A&A, 434, 507

Storey, P. J., & Zeippen, C. J. 2000, MNRAS, 312, 813

Tamura, N., & Ohta, K. 2003, AJ, 126, 596

Tayal, S. S., & Zatsarinny, O. 2010, ApJS, 188, 32

Torrey, P., Cox, T. J., Kewley, L., & Hernquist, L. 2012, ApJ, 746, 108

Tremonti, C. A., Heckman, T. M., Kauffmann, G., et al. 2004, ApJ, 613, 898

Trujillo, I., Förster Schreiber, N. M., Rudnick, G., et al. 2006, ApJ, 650, 18

van Zee, L., Salzer, J. J., Haynes, M. P., O'Donoghue, A. A., & Balonek, T. J. 1998, AJ, 116, 2805

Waller, W. H., Bohlin, R. C., Cornett, R. H., et al. 1997, ApJ, 481, 169

Wang, Y., Zhao, H., Mao, S., & Rich, R. M. 2012, MNRAS, 427, 1429

Wiese, W. L., Fuhr, J. R., & Deters, T. M. 1996, Atomic transition probabilities of carbon, nitrogen, and oxygen: a critical data compilation

Wong, T., Blitz, L., & Bosma, A. 2004, ApJ, 605, 183

Wyse, R. F. G., Gilmore, G., Norris, J. E., et al. 2006, ApJL, 639, L13

Zaritsky, D. 1992, ApJL, 390, L73

Zaritsky, D., Kennicutt, R. C., Jr., & Huchra, J. P. 1994, ApJ, 420, 87
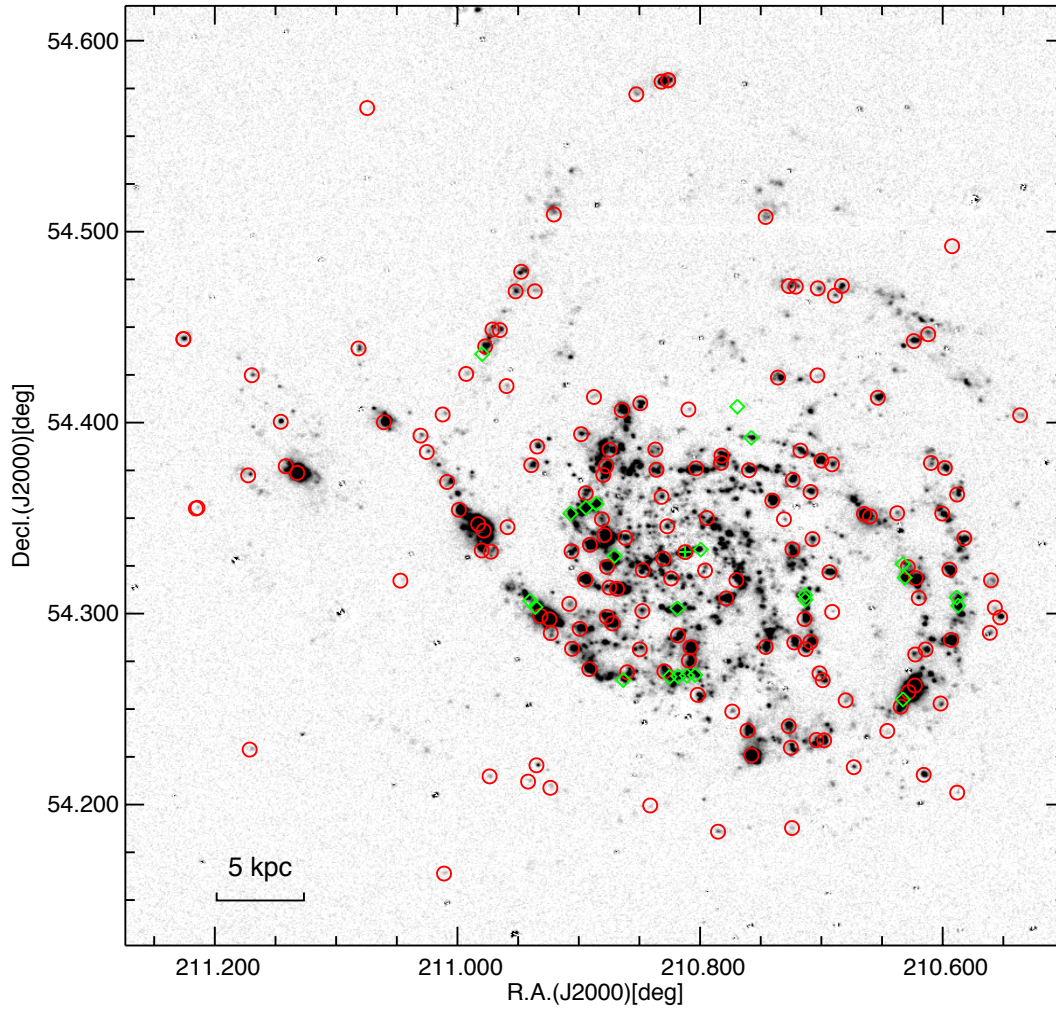
Figure 1. Location of H II regions of final 188 samples on the narrow-band Hα image of M101 observed with KPNO Schmidt telescope (Hoopes et al. 2001). Two symbols represent spectra from two telescop: red circles from MMT and green diamonds from NAOC. The green cross marks the center of the galaxy.
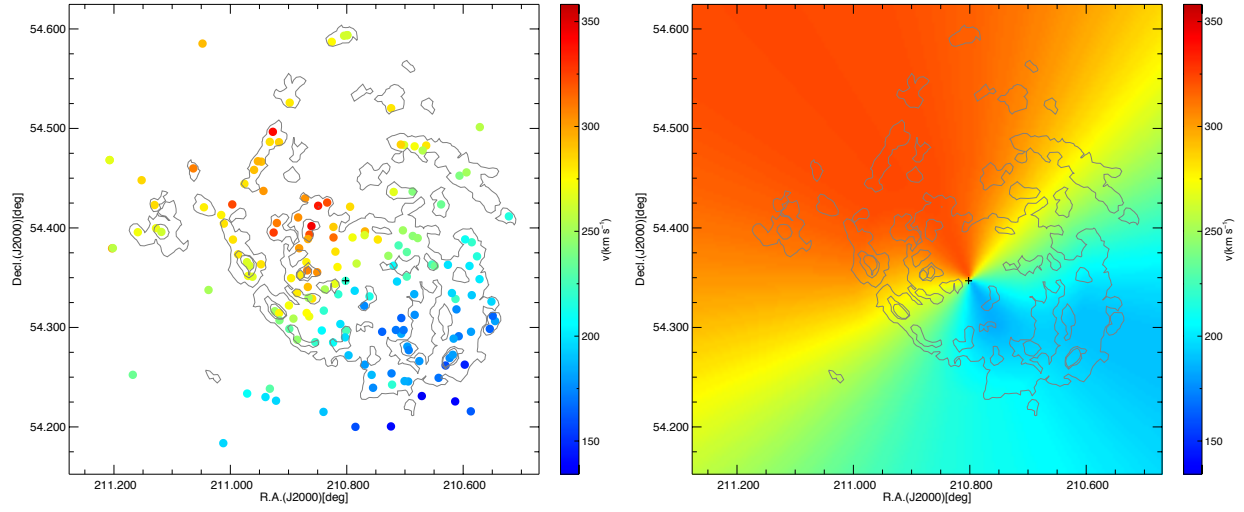
Figure 2. Velocity field of M101. Left: the line of sight velocities of H II regions; Right: modeled velocity map using the method from Krajnović et al. (2006). Contours show the shape of M101 in Hα image, and the center of the galaxy is marked with a black cross.
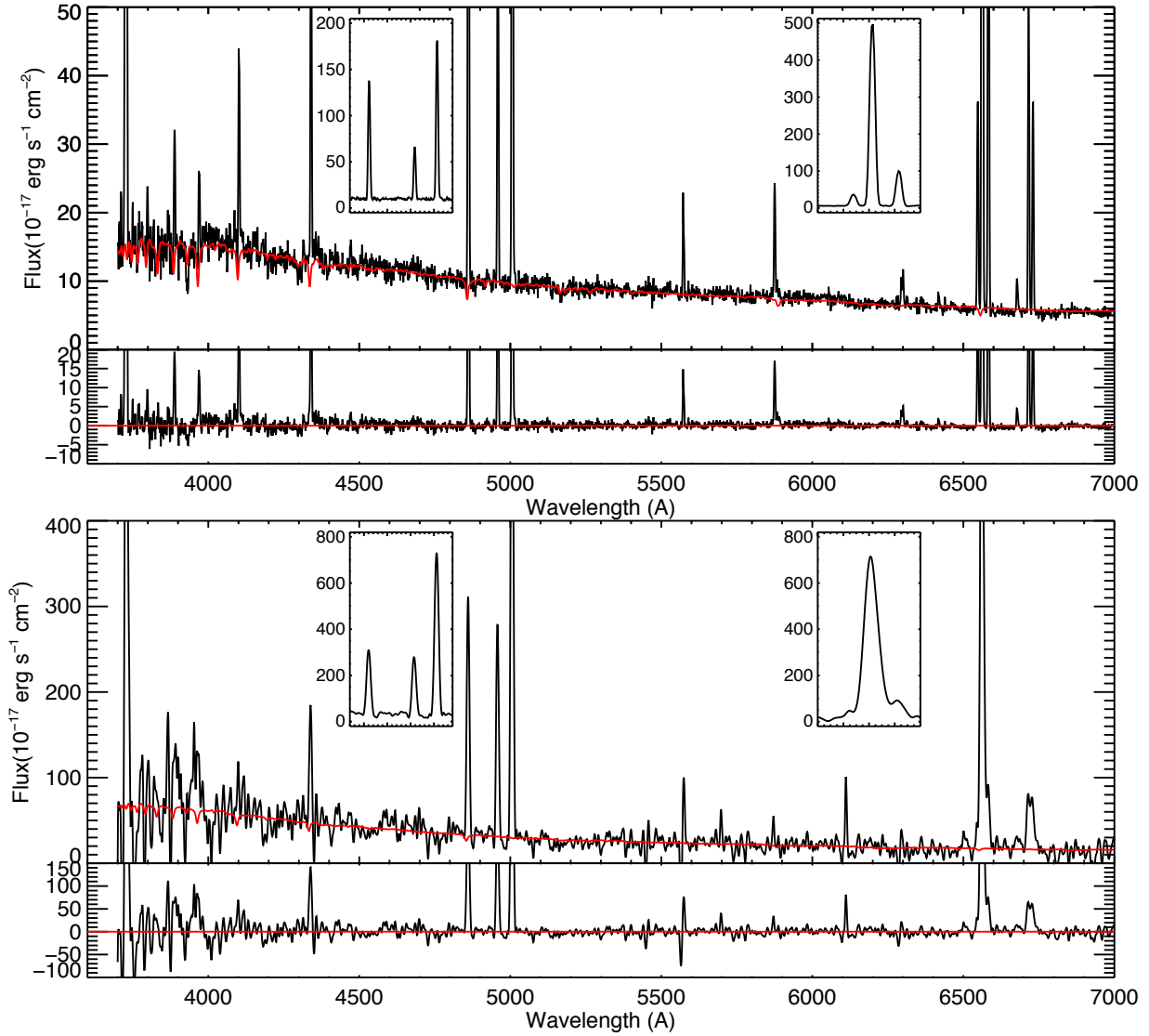
Figure 3. Typical spectrum of H II regions in M101 observed by MMT (upper panel) and NAOC 2.16m (lower panel). Panels show the observed spectra (black line) and MF-ICA continuum fit (red line), and the two small insets of each spectrum zoom in several strong emission lines: Hβ+ [O III]λλ4959,5007, Hα+ [N II]λλ6548,6583.
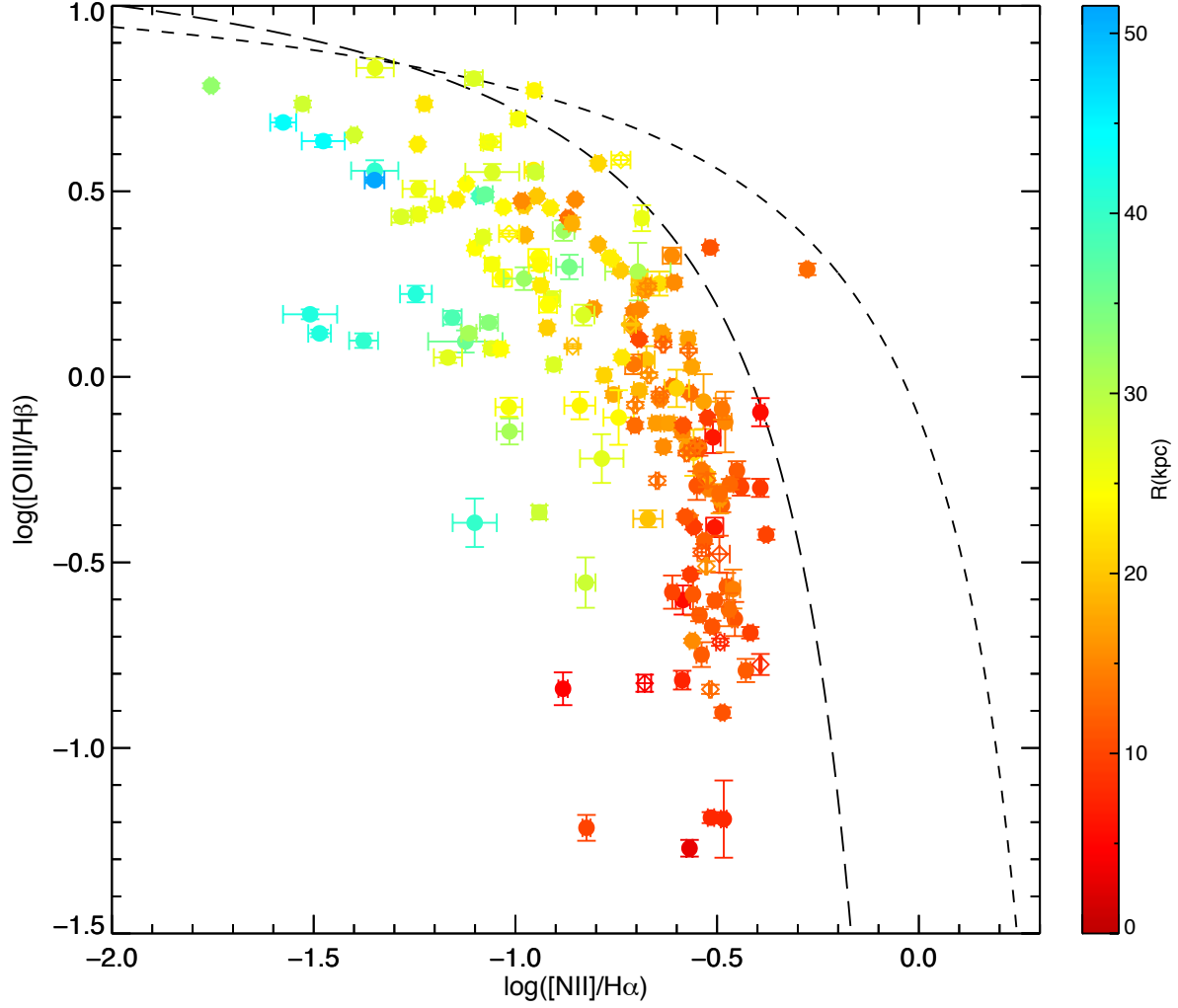
Figure 4. BPT diagram showing the excitation properties of our H II regions. The boundaries are taken from Kewley et al. (2001, short-dashed line) and Kauffmann et al. (2003, long-dashed line). Filled points are from MMT and diamonds are from NAOC, and colors indicate the de-projected distance to the galaxy center. Almost all targets in our sample are located in the pure star forming region of the diagram with a clear profile against the de-projected distances to the galaxy center.
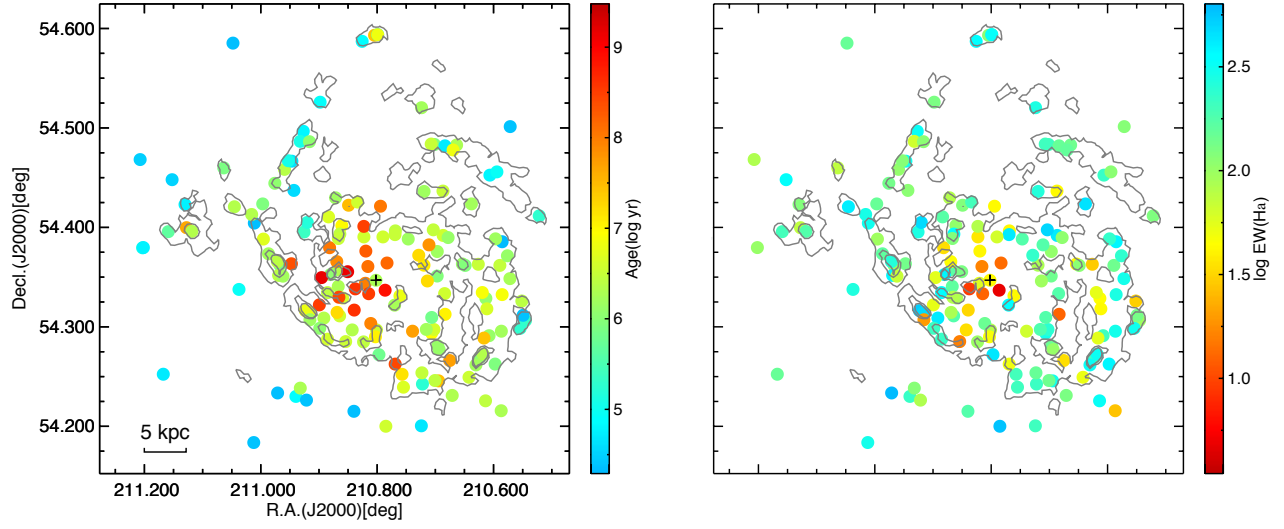
Figure 5. The two dimensional distrbution of stellar population age and EW(Hα). Contours show the shape of M101 in Hα image, and center of the galaxy is marked with a black cross.
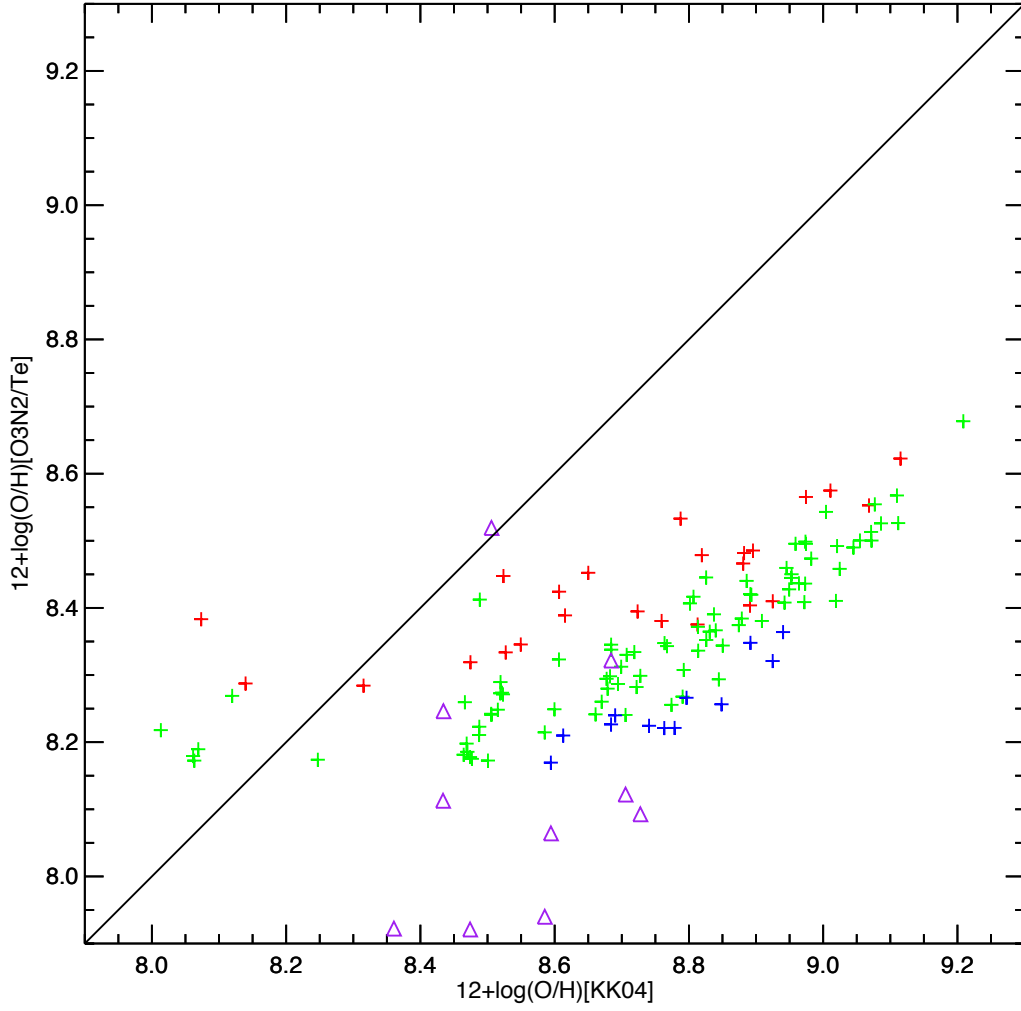
Figure 6. Comparation of the three abundance calibrations. Solid line is the y=x line. Triangle points represent direct T_e calibration, and cross points represent O3N2 calibration. Different colors of cross ponits indicate different ionization parameter q: red, $\log(q)<7.2$; green, $7.2<\log(q)<7.7$; blue, $\log(q)>7.7$. Error bar shows the typical error of the measurements.
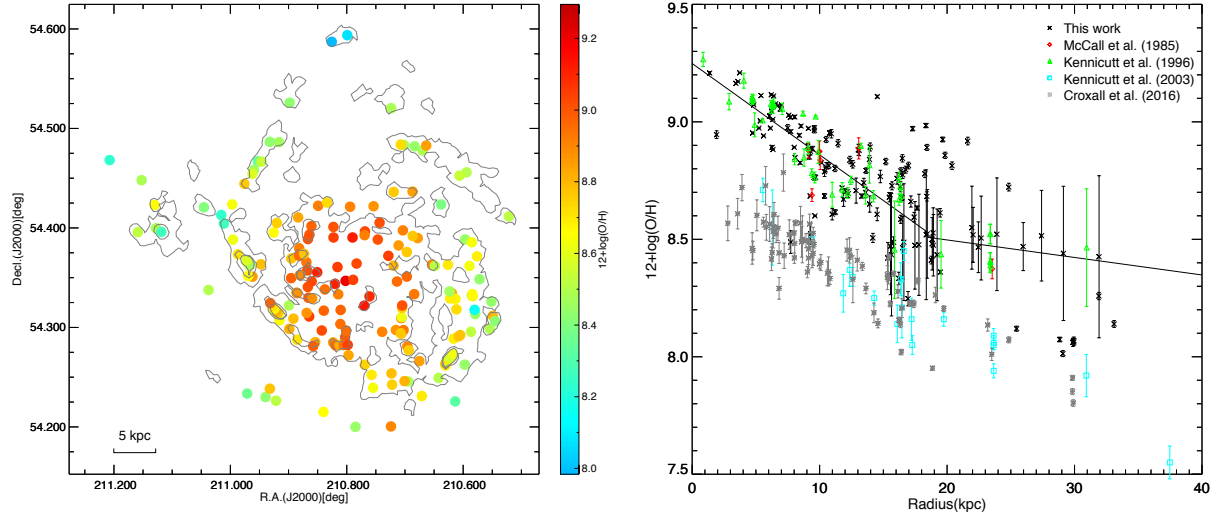
Figure 7. Left: distributions of metallicities of H II regions in M101. Right: Radial metallicity gradient for H II regions. Metallicities are determined from KKO4 calibration for this plot.

Table 1. Coordinates and Dereddened Line Fluxes of H II Regions in M101

ID	R.A.	Decl.	[O II] λ3727	[Ne III] λ3869	Hδ λ4102	Hγ λ4340	[O III] λ4363	[O III] λ4959	[O III] λ5007	[He I] λ5876	[O I] λ6300	[N II] λ6548	Hα λ6563	[N II] λ6583	[S II] λ6717	[S II] λ6731	Hβ λ4861
1	14:03:01.15	54:14:27.0	276.4	19.5	26.5	48.1	82.44	99.4	294.7	10.9	6.5	9.9	285.9	28.4	22.4	16.5	3611.51
			0.6	0.2	0.1	0.3	0.09	0.01	0.8	0.03	0.04	0.07	1.1	0.1	0.11	0.09	12.85
2	14:02:44.66	54:23:36.1	344.0	...	30.2	51.6	...	43.7	128.5	8.9	...	15.6	228.7	44.6	20.3	14.3	3478.57
			0.2	...	0.1	0.2	...	0.09	0.2	0.1	...	0.06	0.6	0.1	0.11	0.09	7.04
3	14:02:49.49	54:17:42.5	294.0	...	28.3	48.1	...	49.7	148.8	11.3	...	19.0	286.0	54.4	35.0	24.1	276.81
			1.9	...	0.6	0.4	...	0.05	1.3	0.4	...	0.01	2.4	0.4	0.66	0.32	2.37
4	14:02:20.22	54:23:12.8	434.4	...	40.7	46.6	...	51.2	152.7	11.9	...	11.1	286.9	31.9	41.5	28.1	131.22
			5.0	...	1.2	3.5	...	0.07	1.2	0.6	...	0.02	1.9	0.9	0.95	0.92	2.77
5	14:02:20.65	54:17:48.9	389.9	27.1	26.2	46.4	23.73	94.7	283.2	10.3	8.1	8.9	275.3	25.6	29.3	21.3	510.45
			2.4	0.9	0.5	0.4	0.35	0.01	1.2	0.3	0.2	0.05	1.3	0.2	0.07	0.18	6.79
6	14:03:45.54	54:13:53.3	482.9	43.4	...	77.8	...	103.1	304.0	...	...	4.8	236.9	13.6	16.9	16.6	174.60
			3.3	1.3	...	1.8	...	0.09	1.0	...	...	0.01	0.8	0.4	0.51	0.24	1.69
7	14:03:41.73	54:19: 4.0	374.0	21.2	36.3	56.6	...	94.3	275.3	9.6	3.9	10.5	286.0	29.9	14.1	11.2	23703.82
			0.1	0.01	0.02	0.1	...	0.04	0.2	0.01	0.1	0.02	0.4	0.02	0.03	0.02	24.11
8	14:03:34.05	54:18:37.1	174.1	12.1	30.0	50.7	...	86.3	256.0	12.6	2.6	11.9	252.0	34.0	9.1	7.5	18061.50
			0.3	0.1	0.2	0.3	...	0.03	0.6	0.1	0.1	0.01	1.2	0.1	0.04	0.05	63.28
9	14:02:46.64	54:14:49.7	334.0	40.9	29.5	56.4	7.29	125.1	374.6	8.6	12.7	15.9	286.0	45.5	44.6	32.2	354.90
			2.2	0.9	0.8	0.4	0.38	0.02	2.4	0.2	0.5	0.01	2.2	0.5	0.50	0.27	2.75
10	14:03:27.54	54:18:45.0	153.5	...	31.9	52.3	...	7.0	20.8	8.6	3.3	28.8	269.0	82.6	43.5	28.3	442.82
			1.2	...	0.5	0.5	...	0.01	0.4	0.2	0.2	0.01	0.9	0.5	0.51	0.25	1.80
11	14:02:29.51	54:16:14.1	295.0	15.8	25.6	46.4	...	92.9	275.6	10.9	6.6	10.7	251.7	30.7	26.3	18.0	1471.36
			0.8	0.2	0.3	0.4	...	0.01	0.5	0.1	0.2	0.02	1.0	0.2	0.12	0.15	6.10
12	14:02:46.97	54:16:56.1	280.2	...	33.0	36.7	...	21.6	64.7	...	8.8	26.1	286.0	74.9	40.1	23.5	110.45
			4.0	...	2.1	1.3	...	0.02	1.9	...	0.7	0.01	3.0	0.7	0.95	0.62	1.72
13	14:03:12.28	54:17:54.2	222.8	...	14.0	49.0	...	21.2	63.6	11.6	...	27.8	279.3	79.8	44.1	30.3	164.75
			2.8	...	0.8	2.2	...	0.01	1.6	0.6	...	0.03	1.6	0.8	1.06	0.22	2.31
14	14:02:20.29	54:20: 1.4	275.7	21.6	28.6	47.3	...	100.1	300.4	11.0	6.2	7.0	286.2	20.2	18.6	13.5	576.54
			2.5	0.6	0.8	0.8	...	0.02	1.7	0.2	0.2	0.04	2.1	0.2	0.17	0.22	5.98
15	14:02:12.15	54:19:37.9	175.2	78.7	...	...	...	227.3	681.8	...	...	...	237.9	...	...	...	34.70
			11.6	6.4	...	...	...	0.04	6.5	...	...	...	2.3	...	...	...	1.69

Note— Line fluxes are normalized to Hβline, after correcting for reddening. Hβλ 4861 is the measured Hβ flux in units of $\times 10^{-17}$ erg s^{-1} cm^{-2}, corrected for extinction.

Table 2. Gas Conditions and Oxygen Abundance Measurements

ID	$T[\text{O\,{\sc iii}}]$	n_e	$\log q$	12 + log(O/H)		
	(K)	(cm^{-3})	(log cm s^{-1})	O3N2	KK04	T_e
1	10120 ± 1134	76 ± 12	7.77 ± 0.153	8.27 ± 0.023	8.68 ± 0.009	8.32 ± 0.933
2	...	29 ± 7	7.47 ± 0.019	8.46 ± 0.013	8.83 ± 0.002	...
3	...	...	7.60 ± 0.654	8.45 ± 0.070	8.85 ± 0.009	...
4	...	...	7.37 ± 1.145	8.37 ± 0.096	8.68 ± 0.012	...
5	13696 ± 1415	62 ± 11	7.57 ± 0.388	8.25 ± 0.036	8.59 ± 0.017	7.94 ± 0.820
6	...	539 ± 30	7.55 ± 3.646	8.17 ± 0.036	8.63 ± 0.009	...
7	...	170 ± 29	7.58 ± 0.056	8.31 ± 0.006	8.60 ± 0.002	...
8	...	215 ± 37	8.05 ± 0.394	8.32 ± 0.021	8.85 ± 0.004	...
9	9519 ± 2096	53 ± 20	7.68 ± 0.343	8.29 ± 0.057	8.51 ± 0.020	8.52 ± 1.876
10	...	...	7.33 ± 0.773	8.78 ± 0.078	9.11 ± 0.003	...
11	...	...	7.72 ± 0.283	8.29 ± 0.017	8.69 ± 0.008	...
12	...	...	7.39 ± 1.443	8.61 ± 0.165	8.95 ± 0.010	...
13	...	...	7.53 ± 1.244	8.62 ± 0.147	9.02 ± 0.010	...
14	...	62 ± 15	7.65 ± 0.572	8.21 ± 0.050	8.47 ± 0.206	...
16	...	59 ± 16	...	...	9.16 ± 0.004	...
17	...	...	7.96 ± 1.300	8.45 ± 0.039	8.89 ± 0.008	...
18	15259 ± 764	69 ± 27	7.65 ± 0.539	8.20 ± 0.043	8.46 ± 0.133	7.79 ± 0.390
19	...	20 ± 7	...	...	9.03 ± 0.004	...
20	...	...	7.44 ± 2.586	8.57 ± 0.114	8.95 ± 0.018	...
21	...	113 ± 34	7.48 ± 0.211	8.68 ± 0.023	9.07 ± 0.002	...
22	...	...	7.76 ± 2.431	8.25 ± 0.088	8.61 ± 0.018	...
23	...	164 ± 35	...	...	......	...
24	...	25 ± 9	7.42 ± 0.569	8.59 ± 0.115	8.96 ± 0.011	...
25	...	...	7.69 ± 2.493	8.55 ± 0.101	9.02 ± 0.006	...
26	...	55 ± 12	7.43 ± 0.433	8.44 ± 0.038	8.68 ± 0.010	...
27	...	...	...	...	8.86 ± 0.013	...
28	...	498 ± 22	7.42 ± 0.453	8.29 ± 0.089	8.66 ± 0.024	...
29	...	923 ± 83	7.39 ± 0.445	8.30 ± 0.255	8.51 ± 0.179	...
30	...	182 ± 15	7.56 ± 3.270	8.33 ± 0.144	8.79 ± 0.014	...

AE Ursae Majoris – a δ Scuti star in the Hertzsprung Gap

Jia-Shu Niu,[1,2,3] Jian-Ning Fu,[1]★ Yan Li,[4] Xiao-Hu Yang,[1,5] Weikai Zong,[1,6,7]
Hui-Fang Xue,[1] Yan-Ping Zhang,[1] Nian Liu,[1] Bing Du[5] and Fang Zuo[5]

[1]*Astronomy Department, Beijing Normal University, Beijing 100875, P.R. China*
[2]*CAS Key Laboratory of Theoretical Physics and Kavli Institute for Theoretical Physics China (KITPC), Institute of Theoretical Physics,*
Chinese Academy of Sciences, Beijing 100190, P.R. China
[3]*School of Physical Sciences, University of Chinese Academy of Sciences, No. 19A Yuquan Road, Beijing 100049, P.R. China*
[4]*National Astronomical Observatories/Yunnan Observatory, Chinese Academy of Sciences, PO Box 110, Kunming 650011, P.R. China*
[5]*National Astronomical Observatories, Chinese Academy of Sciences, Beijing 100012, P.R. China*
[6]*Université de Toulouse, UPS-OMP, IRAP, Toulouse F-31400, France*
[7]*CNRS, IRAP, 14 avenue Edouard Belin, F-31400 Toulouse, France*

ABSTRACT

We analyse the photometric data and spectroscopic data collected on the δ Scuti star AE Ursae Majoris (AE UMa). The fundamental and the first overtone frequencies are confirmed as $f_0 = 11.62560$ c d^{-1} and $f_1 = 15.03124$ c d^{-1}, respectively, from the frequency content by analysing light curves over 40 nights, spanning from 2009 to 2012. Additionally, another 37 frequencies are identified as either the harmonics or the linear combinations of the fundamental and the first overtone frequencies, among which 25 are newly detected. The rate of period change of the fundamental mode is determined as $(1/P_0)(dP_0/dt) = 5.4(\pm 1.9) \times 10^{-9}$ yr^{-1} as revealed from the O $-$ C diagram based on the 84 newly determined times of maximum light combined with those derived from the literature. The spectroscopic data suggest that AE UMa is a Population I δ Scuti star. With these physical properties, we perform theoretical explorations based on the stellar evolution code MESA on this target, considering that the variation of pulsation period is caused by secular evolutionary effects. We finally constrain AE UMa with physical parameters as follows: mass of 1.805 ± 0.055 M$_\odot$, radius of $1.647 \pm 0.032 \times 10^{11}$ cm, luminosity of $1.381 \pm 0.048(\log L/L_\odot)$ and age of $1.055 \pm 0.095 \times 10^9$ yr. AE UMa can be the (Population I) δ Scuti star that locates just after the second turn-off of its evolutional track leaving the main sequence, a star in the phase of the Hertzsprung Gap with a helium core and a hydrogen-burning shell.

Key words: techniques: photometric – techniques: spectroscopic – stars: individual: AE UMa – stars: oscillations – stars: variables: δ Scuti.

1 INTRODUCTION

δ Scuti stars are a class of pulsating variable stars that lie in the classical instability strip crossing the main sequence (MS) on the Hertzsprung–Russell diagram. Their pulsations are driven by the κ-mechanism, which drives both the Cepheids and the RR Lyrae stars as well. The amplitudes of pulsations in δ Scuti stars are from mmag up to tenths of a magnitude, periods between 0.03 and 0.3 d (see, e.g. Niu, Fu & Zong 2013; Zong et al. 2015). These stars are found with masses between 1.5 and 2.5 M$_\odot$, and luminosities between 10 and 50 L$_\odot$. The general consensus shows that most (possibly all) δ Scuti stars are normal stars that evolve in the

MS or the immediate post-MS stages, according to standard stellar-evolution theory (see, e.g. Baglin et al. 1973; Breger 1979, 1980). Nevertheless, an observational proof of the validity of this hypothesis has not been found yet (Petersen & Christensen-Dalsgaard 1996).

The high-amplitude δ Scuti stars (hereafter HADS) are traditionally found with slow rotation, with one or two dominant radial modes with amplitudes larger than 0.1 mag, although some of them may have low-amplitude non-radial modes (e.g. Poretti 2003). SX Phoenicis (SX Phe) stars is a subgroup of HADS with low metallicity and large spatial motion (see e.g. Fu et al. 2008b). They are old Population II stars and found to be members of globular clusters (Rodríguez & López-González 2000). However, some of them have been discovered in the general star fields (Rodríguez & Breger 2001). Interestingly, pulsations in the majority of the field SX Phe variables display simple frequency spectra with short periods
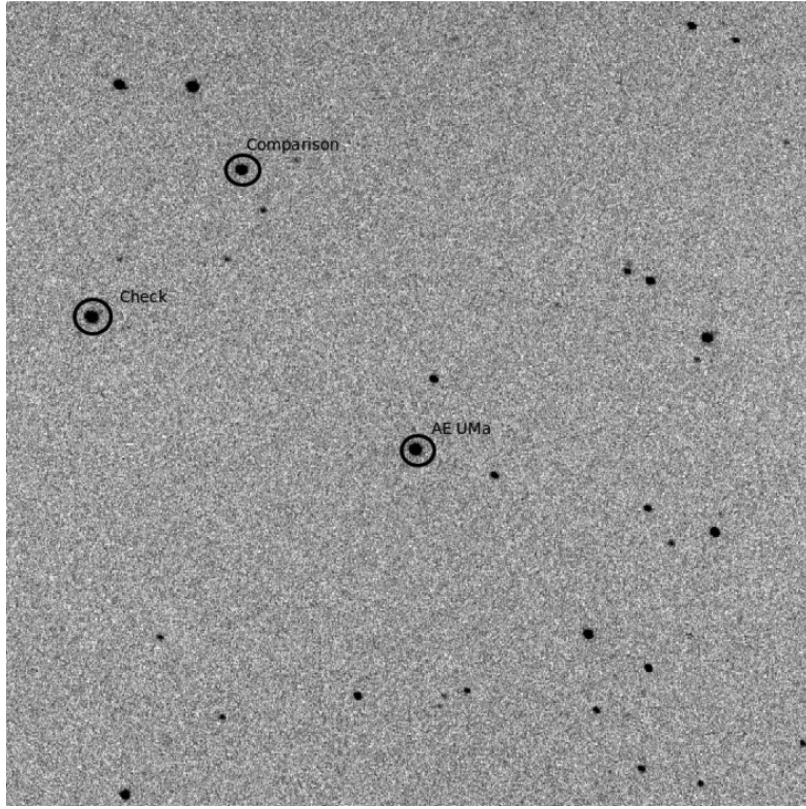
Figure 1. A CCD image (16.5×16.5 arcmin^2) of AE UMa ($\alpha_{2000} = 09^h 36^m 53^s$, $\delta_{2000} = +44°04'00''$) taken with the 85-cm telescope at the Xinglong station. North is down and east is to the right. AE UMa, the comparison star and the check star are marked.

Table 1. Journal of photometric observations in *V* for AE UMa with the 85-cm telescope.

CCD	Year	Month	Nights	Frames
PI BFT1024	2009	March	5	4055
	2009	May	3	516
	2010	February	2	1385
	2011	January	5	1275
	2011	February	8	4759
	2012	January	1	328
	2012	February	6	1887
PI BFT512	2012	March	5	2516
	2012	April	5	556

(≤ 0.08 d) and large visual peak-to-peak amplitudes (≥ 0.1 mag; e.g. Fu et al. 2008a). The period changes of pulsations can be determined based on long-term and high-precision photometric observations of such stars, which can constrain the stellar evolutionary phase of the star (e.g. Yang, Fu & Zha 2012).

The star AE Ursae Majoris (hereafter AE UMa = HIP 47181, $\alpha_{2000} = 09^h 36^m 53^s$, $\delta_{2000} = 44°04'01''$, $\langle V \rangle = 11\overset{m}{.}27$ mag, $P_0 = 0\overset{d}{.}0860$ d, $\Delta V = 0.10$ mag) was discovered to be a variable star by Geyer, Kippenhahn & Strohmeier (1955). The spectral type of AE UMa was classified in accordance with the type of variability by Götz & Wenzel (1961) as A9. The period of light variations was determined by Tsesevich (1973), and they classified it as a dwarf Cepheid. The beat phenomenon of the pulsations of this star was found by Szeidl (1974). AE UMa was listed as an SX Phe star

by Garcia et al. (1995). However, Hintz, Hintz & Joner (1997b) showed strong evidence against this classification and reclassified it as a normal Population I HADS. According to the measurement of Breger & Pamyatnykh (1998), AE UMa had a fast period decreasing rate of 4.8×10^{-7} yr^{-1}; hence, it should be a pre-MS star. However, there is no other evidence for this star to be a pre-MS star. Recently, both Pócs & Szeidl (2001) and Zhou (2001) analysed pulsations of the star with high-precision and longer photometric data. Their results are consistent with the outcomes of Hintz et al. (1997b): AE UMa is a Population I, post-MS δ Scuti star, but with a stable fundamental frequency and the first overtone decreasing with a rate of $\sim 10^{-8}$ yr^{-1}.

In this paper, we present a detailed study of the pulsations and the period changes of AE UMa, mainly based on both photometric observations and spectroscopic observations. Based on the observational results, we perform theoretical explorations using the stellar code MESA and constrain the physical parameters on this star. The organization of the paper is as follows: Section 2 describes the photometry and data reduction, as well as spectral results; we present the pulsation analysis of the new data in Section 3; in Section 4, the rate of period change of the fundamental pulsations is determined before we conduct calculations of the stellar models with the constraints of the stellar parameters, the frequencies and their variations in Section 5. The conclusions of this study is given in the final section.

2 OBSERVATIONS AND DATA REDUCTION

Photometric observations for AE UMa were made with the 85-cm telescope located at the Xinglong Station of NAOC between 2009

Table 2. The comparison star and the check star used in the photometry of AE UMa.

Star name	α(2000)	δ(2000)	V	B	$B - V$
Object = AE Ursae Majoris	$09^h36^m53^s.155$	$+44°04'00''.39$	11.35 ± 0.08	11.54 ± 0.06	0.19 ± 0.14
Comparison = TYC 2998-1249-1	$09^h37^m28^s.5826$	$+44°01'16''.854$	11.32 ± 0.08	11.82 ± 0.08	0.50 ± 0.16
Check = TYC 2998-1166-1	$09^h37^m12^s.058$	$+43°58'20''.12$	12.21 ± 0.18	13.10 ± 0.30	0.89 ± 0.48
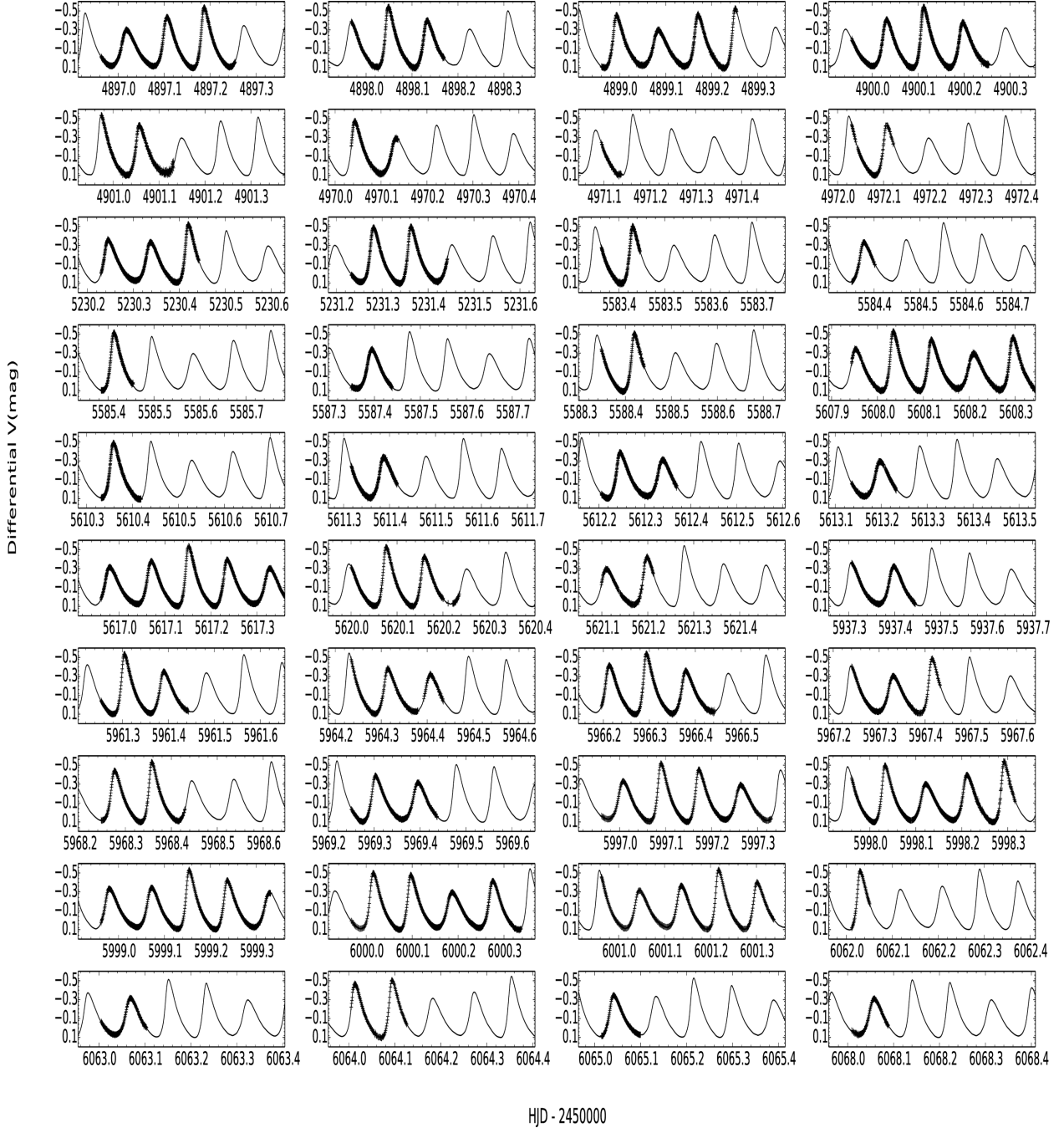
Figure 2. Light curves of AE UMa relative to the comparison star in the *V* band from 2009 to 2012, observed with the 85-cm telescope. The solid curves represent the fitting with a solution up to 18 frequencies listed in Table 3.

March and 2012 May. The 85-cm telescope was equipped with a standard Johnson–Cousin–Bessel multicolour filter system and a PI1024 BFT CCD camera mounted on the primary focus (Zhou et al. 2009). The CCD had 1024 × 1024 pixels, corresponding

to a field of view of 16.5 × 16.5 arcmin². Since 2012 March, the CCD camera has been replaced by a PI512 BFT with a larger size of pixels, which has 512 × 512 pixels corresponding to a field of view of 15 × 15 arcmin². The observations were made through a
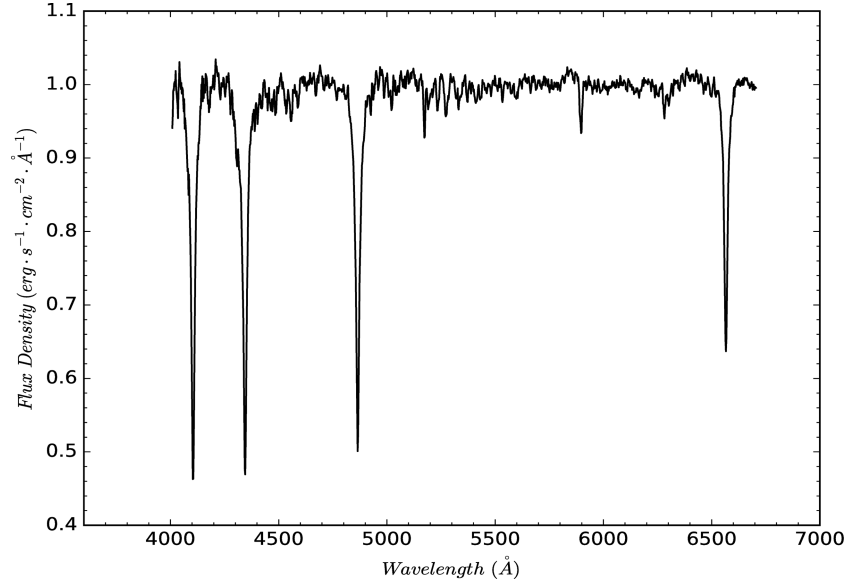
Figure 3. Spectroscopic observation results of AE UMa.

Table 3. Parameters of AE UMa derived from spectroscopic observations.

Parameters	Values	σ
T_{eff} (K)	7600	180
$\log g$	4.1	0.2
[Fe/H]	-0.32	0.23
RV (km s^{-1})	150	27

standard Johnson *V* filter with the exposure time ranging from 15 to 120 s, depending on the atmospheric conditions. A journal of the new observations is listed in Table 1.

In total, 17 277 CCD frames were collected for AE UMa during 40 nights. Fig. 1 shows an image of AE UMa taken with the 85-cm telescope, where the comparison star (TYC 2998-1249-1) and the check star (TYC 2998-1166-1) are marked as well. The details of the three stars from SIMBAD (Wenger et al. 2000) are listed in Table 2.

The preliminary processing of the CCD frames (bias, dark subtraction and flat-field correction) was performed with the standard routines of CCDPROC from the IRAF software. After that, we employed the IRAF DAOPHOT package to perform aperture photometry. In order to optimize the size of the aperture, we used 12 different sizes of apertures for the data in each night and adopted the aperture that brought the minimum variance of the magnitude differences between the check star and the comparison star. The data reduction was carried out with the standard process of aperture photometry.

The light curves were then produced by computing the magnitude differences between AE UMa and the comparison star. The standard deviations of the magnitude differences between the check star and the comparison star yielded an estimation of photometry precisions, with a typical value of 0.003 mag in good observation conditions and 0.011 mag in poor cases from night to night. As there were slight zero-point shifts, we adjusted it with the fitted light curves for every month by assuming that the pulsations were stable in one month.

Fig. 2 shows the light curves of AE UMa in the Johnson *V* band observed with the 85-cm telescope in 2009–2012, which was used

to conduct pulsation analysis, and determination of new times of maximum light.

Spectroscopic observations of AE UMa were made with the 2.16-m telescope, which is located at the Xinglong station of NAOC, on 2016 May 21. The BFOSC low-dispersion spectrometer was employed for the observations. The used grating was G7 with a slit width of 1.8 arcsec and a line dispersion of 95 Å mm^{-1}. The centre wavelength was at 530 nm with the wavelength range of 380–680 nm.

The data were reduced with IRAF, and the obtained low-resolution spectrum is shown in Fig. 3. With the results from spectroscopic observations, we used the automated 1D parametrization pipeline LASP, which is based on the stellar spectral template library (Wu et al. 2011), to get the stellar atmospheric parameters (see Table 3). We note that T_{eff} and $\log g$ correspond to a fixed phase since we had acquired only one spectrum. These values may vary differently from phase to phase during the pulsations of AE UMa. However, the metal-to-hydrogen ratio [Fe/H] is not sensitive to the pulsations. The value of [Fe/H] is $-0.32(\pm 0.23)$, which indicates that AE UMa is possibly a Population I δ Scuti star. This is consistent with the classification of the results obtained from Hintz et al. (1997b), Pócs & Szeidl (2001) and Zhou (2001) without spectroscopic data. Hence, AE UMa can be modelled as a single star in Section 5.

3 PULSATION ANALYSIS

Pulsation analysis was performed with the light curves of AE UMa in the years 2009–2012, respectively, with the software PERIOD04 (Lenz & Breger 2005), which provides Fourier transformations of the light curves to search for significant peaks in the amplitude spectra until 150 c d^{-1}, since there are no significant peaks above this frequency limit. Then, the light curves are fitted with the following formula:

$$m = m_0 + \Sigma A_i \sin(2\pi(f_i t + \phi_i)). \tag{1}$$

Table 4 lists the solutions of 37 frequencies whose signal-to-noise ratios (S/N) are higher than 4.0 (Breger et al. 1993), and the averaged noise level is calculated over the whole frequency range of 0–150 c d^{-1} (e.g. Kepler et al. 2005). The solid curves in Fig. 2

Table 4. Multifrequency solutions of the light curves of AE UMa in the *V* band in 2009–2012. Fre: Frequency in c d^{-1}. Amp: Amplitude in mmag. S/N: signal-to-noise ratio.

NO.	Marks	Fre	Amp	SN	Fre	Amp	SN	Fre	Amp	SN	Fre	Amp	SN
			2009			2010			2011			2012	
1	f_0	11.625 25	220.45	1078.98	11.629 44	216.36	2343.67	11.625 49	218.93	1360.27	11.625 58	218.26	1652.90
2	$2f_0$	23.250 14	74.36	373.67	23.258 88	73.25	727.33	23.250 36	73.77	467.10	23.251 08	73.57	565.07
3	f_1	15.031 09	45.29	223.73	15.011 05	43.95	464.85	15.032 01	45.00	278.92	15.031 17	45.11	343.71
4	$3f_0$	34.878 73	28.48	147.81	34.888 32	29.66	299.18	34.876 20	27.70	175.13	34.876 80	27.99	216.03
5	$f_0 + f_1$	26.658 47	29.39	148.03	26.640 49	28.76	294.84	26.656 20	29.27	184.42	26.656 65	29.72	228.20
6	$f_1 - f_0$	3.405 80	25.47	123.84	3.422 85	27.36	282.12	3.406 60	24.36	153.48	3.405 72	25.44	192.97
7	$2f_0 + f_1$	38.282 17	16.24	84.60	39.342 15	15.07	150.52	38.282 80	16.11	101.50	38.282 16	15.97	123.94
8	$4f_0$	46.512 74	12.80	67.53	46.559 00	13.02	126.33	46.501 60	12.91	82.28	46.502 33	12.99	100.78
9	$3f_0 + f_1$	49.907 05	9.31	49.30	49.940 62	10.26	97.83	49.908 20	9.14	57.64	49.907 96	9.11	71.07
10	$5f_0$	58.134 93	6.23	33.19	57.157 47	4.19	37.35	58.127 00	5.89	36.99	58.127 68	5.99	47.29
11	$2f_0 - f_1$	8.227 89	6.16	29.75	9.155 09	6.12	66.30	8.222 57	6.44	40.27	8.218 96	6.21	46.75
12	$4f_0 + f_1$	61.541 23	4.99	26.63	60.332 88	5.85	50.38	61.533 60	5.15	31.85	61.534 27	4.92	38.89
13	$f_0 + 2f_1$	41.703 15	4.33	22.78	41.775 26	3.15	31.22	41.689 40	4.16	26.42	41.688 53	4.22	32.67
14	$2f_1$	30.080 96	3.77	19.17	30.063 34	5.03	50.90	30.064 00	3.32	20.86	30.061 74	4.00	30.82
15	$6f_0$	69.769 12	3.68	19.56	69.859 13	3.51	28.13	69.752 40	3.74	23.61	69.753 22	3.29	26.59
16	$2f_1 - f_0$	19.814 09	3.45	17.17	18.227 71	3.46	36.34	19.844 20	3.04	19.00	19.845 74	3.16	24.26
17	$5f_0 + f_1$	73.163 42	3.27	17.40	74.230 48	3.31	25.21	73.159 00	3.31	20.83	73.159 80	3.42	27.88
18	$6f_0 + f_1$	84.763 12	2.15	11.31	84.773 68	2.83	19.70	84.782 67	2.21	14.30	84.785 66	2.19	18.38
19	$2f_0 + 2f_1$	53.349 33	2.07	11.00	53.693 38	1.82	16.55	53.314 80	1.66	10.51	53.312 82	2.26	17.81
20	$7f_0$	81.392 80	2.00	10.53	80.567 29	1.80	12.95	81.379 84	1.90	12.21	81.380 32	1.93	15.96
21	$7f_0 + f_1$	96.397 30	1.45	7.94	96.361 88	1.51	9.96	96.408 07	1.60	10.48	96.411 20	1.62	14.13
22	$3f_0 + 2f_1$	64.935 53	1.60	8.59	63.838 21	3.22	26.65	64.943 97	1.64	10.21	64.938 35	1.59	12.67
23	$4f_0 - f_1$	31.448 28	1.76	9.02	31.547 95	1.18	11.96	32.242 12	1.34	8.43	31.470 03	1.56	12.05
24	$2f_1 - 2f_0$	6.776 61	1.41	6.81	7.794 20	3.97	42.67	6.025 61	2.05	12.85	7.788 61	1.07	8.06
25	$2f_1 - f_0$	18.458 77	1.40	6.98	18.227 71	3.46	36.34	18.442 37	2.04	12.70	18.437 45	1.93	14.83
26	$4f_0 + 2f_1$	76.547 23	1.32	7.07	–	–	–	75.798 89	1.16	7.32	76.562 96	1.18	9.64
27	$8f_0 + f_1$	108.007 50	1.06	5.94	109.104 78	1.26	7.68	108.033 47	1.25	8.15	108.035 49	0.99	8.77
28	$8f_0$	93.038 98	1.22	6.65	–	–	–	93.012 78	0.88	5.75	93.005 86	1.18	10.13
29	$5f_0 + 2f_1$	88.205 40	1.05	5.55	–	–	–	88.185 50	1.06	6.91	88.189 75	1.05	8.95
30	$6f_0 - f_1$	54.692 65	1.20	6.36	–	–	–	53.314 80	1.66	10.51	54.724 85	0.98	7.74
31	$3f_1$	44.053 97	1.03	5.45	–	–	–	43.098 77	1.13	7.24	43.096 81	1.00	7.75
32	$10f_0 + f_1$	131.287 86	0.91	5.43	–	–	–	–	–	–	–	–	–
33	$9f_0 + f_1$	119.629 69	0.82	4.78	118.713 50	0.97	5.63	119.655 10	0.72	4.76	118.655 64	0.57	4.97
34	$6f_0 + 2f_1$	100.823 09	0.78	4.35	100.774 47	0.99	6.34	99.814 67	1.01	6.64	99.815 28	0.77	6.75
35	$7f_0 + 2f_1$	110.502 25	0.73	4.16	110.995 41	0.78	7.68	111.439 57	0.69	5.19	–	–	–
36	$9f_0$	103.665 67	0.71	4.01	104.898 39	0.90	5.74	104.864 28	0.69	4.48	103.653 46	0.67	5.94
37	$8f_0 + 2f_1$	–	–	–	–	–	–	–	–	–	123.067 60	0.54	4.82

show the fits with the frequency solutions in different years. From Table 4, one notes that the 37 frequencies are composed of the fundamental and the first overtone frequencies, their harmonics and linear combinations. As can be noted, no significant signals are detected in addition to these frequencies.

Figs 4 and 5 show, respectively, the window function and the amplitude spectra of the frequency pre-whitening process for the light curves in *V* in 2009.

As can be seen from Fig. 2, the constructed curves fit well the light curves observed in 2009–2012, respectively, which shows that the fundamental and the first overtone frequencies, together with their harmonics and linear combinations, can explain the pulsation behaviour of AE UMa.

To show the variations of the frequencies and amplitudes of pulsations of the star, we compare our results with those from Zhou (2001), who analysed the data for AE UMa from 1974 to 2001. By dividing the data into four segments of data sets following Zhou (2001), we resolved the pulsation parameters of the fundamental and the first overtone frequencies of AE UMa and listed them in Table 5.

4 THE O − C DIAGRAM

With the new observations from 2009 to 2012, the light curves around the light maxima were fitted with a fourth polynomial by the non-linear least-squares method. The errors in polynomial fitting are consistent with the uncertainties estimated from Monte Carlo simulations of 100 iterations for each maximum. We obtained 84 times of maximum light in the *V* band, as listed in Table 6.

In order to conduct an O − C analysis for the period change of AE UMa, we combined the new times of maximum light with those provided from the previous literature.[1] We finally obtained 461 times of maximum light, which are listed in Table 7. We discarded 17 times of maximum light, which were collected with either photograph

[1] Agerer, Dahm & Hubscher (1999a), Pócs & Szeidl (2001), Pejcha, Havlik & Kral (2001), Zhou (2001), Agerer & Hubscher (2003), Hubscher (2005), Hubscher, Paschke & Walter (2005), Klingenberg, Dvorak & Robertson (2006), Hubscher, Paschke & Walter (2006), Hubscher & Walter (2007), Samolyk (2010), Hubscher (2007), Hubscher, Steinbach & Walter (2009), Hubscher et al. (2010) and Huebscher & Monninger (2011).
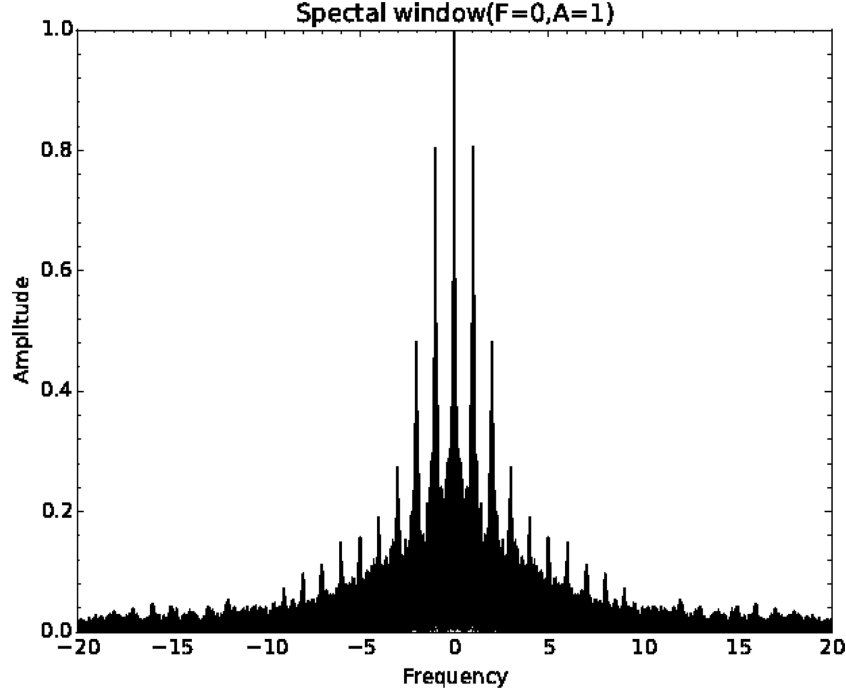
Figure 4. Spectral window of the light curves in *V* for AE UMa in 2009.

(pg) or visual (vis), with large uncertainties, compared to those collected with the CCD or photoelectric photometer (pe). We finally used 444 data points to construct the O − C (the Observed minus Calculated values) diagram. The used linear ephemeris formula is

$$\mathrm{HJD}_{\mathrm{max}} = 2442062.5824 + 0\overset{\mathrm{d}}{.}08601707\,E \qquad (2)$$

following Pócs & Szeidl (2001).

A linear fit to the 444 times of maximum light yields the ephemeris formula

$$\mathrm{HJD}_{\mathrm{max}} = 2442062.5818(\pm0.0002)$$
$$+ 0\overset{\mathrm{d}}{.}086017078(\pm0.000000002)E \qquad (3)$$

with a standard deviation of $\sigma_0 = 0.002\,46$ d. The O − C values are listed in Table 7 as well. The O − C diagram is shown in Fig. 6.

In addition, we made a quadratic fit with a second-order polynomial:

$$\mathrm{HJD}_{\mathrm{max}} = 2442062.5822(\pm0.0002)$$
$$+ 0.086017060(\pm0.000000006)E$$
$$+ 0.5 \times 1.09(\pm0.38) \times 10^{-13}E^2 \qquad (4)$$

with the standard deviation of $\sigma_1 = 0.002\,44$ d. The quadratic terms differ from zero by a factor of 2.87σ with a significance of ∼99.5 per cent, and the statistic test proposed by Pringle (1975) suggests that the small improvement in period deviation gives the quadratic term in the fit with a significance of ∼99.3 per cent. From the values in equation (4), we take the period change rate of AE UMa as $(1/P_0)(\mathrm{d}P_0/\mathrm{d}t) = 5.4(\pm1.9) \times 10^{-9}$ yr^{-1}, which is different from the result of -0.35×10^{-10} yr^{-1} provided by Zhou (2001). This value will be used in our model calculations in the next section. However, the data may not be distributed as Gaussian random noise, and more data points need to be collected to confirm this period change.

Since the modulation frequency $f_{\mathrm{m}} = f_1 - f_0$ has not been varying significantly compared with f_1 (Pócs & Szeidl 2001), one may take

the method that is used in Pócs & Szeidl (2001) and Zhou (2001) to calculate the rate of changes of the first overtone frequency. But the result shows large uncertainties. Hence, we do not consider it a credible result from our observations.

5 CONSTRAINTS FROM THE THEORETICAL MODELS

Because the order of the period change of the fundamental mode is the same as the result from our calculation in Section 4 in the post-MS phase (about 10^{-8} yr^{-1}), we assume that the result is completely from the evolutionary effects.

In this section, we describe the details of the calculation of the theoretical models of AE UMa to constrain the physical parameters for the target. Section 5.1 presents the initial input physical parameters of AE UMa for the theoretical models; Section 5.2 uses the two frequencies f_0 and f_1 to constrain the initial parameters and determines some parameters for the subsequent calculation; Section 5.3 uses two independent ways to calculate the period changes of the fundamental mode of AE UMa induced by the stellar evolutionary effects.

5.1 Physical parameters

Rodriguez et al. (1992) conducted $uvby\beta$ photoelectric photometry for AE UMa. Intrinsic values of $b - y$, m_1 and c_1 were derived and the stellar physical parameters were determined. The effective temperature of AE UMa varied from 8320 to 7150 K. The surface gravity $\log g$ varied from 4.16 to 3.77. The mean values obtained along the cycle were $\langle T_{\mathrm{eff}} \rangle = 7560$ K and $\langle \log g \rangle = 3.90$, respectively. The metal abundance was estimated from δm_1 at the minimum light as [Fe/H] = −0.3. By using the $\log g$–$\log P$ relation derived by Claret et al. (1990), Rodriguez et al. (1992) obtained the values of $M = 1.80\,\mathrm{M}_\odot$, age = 1.3×10^9 yr and $M_{\mathrm{bol}} = 1.76$ mag. Hintz et al. (1997b) provided the value of [Fe/H] = −0.1 according
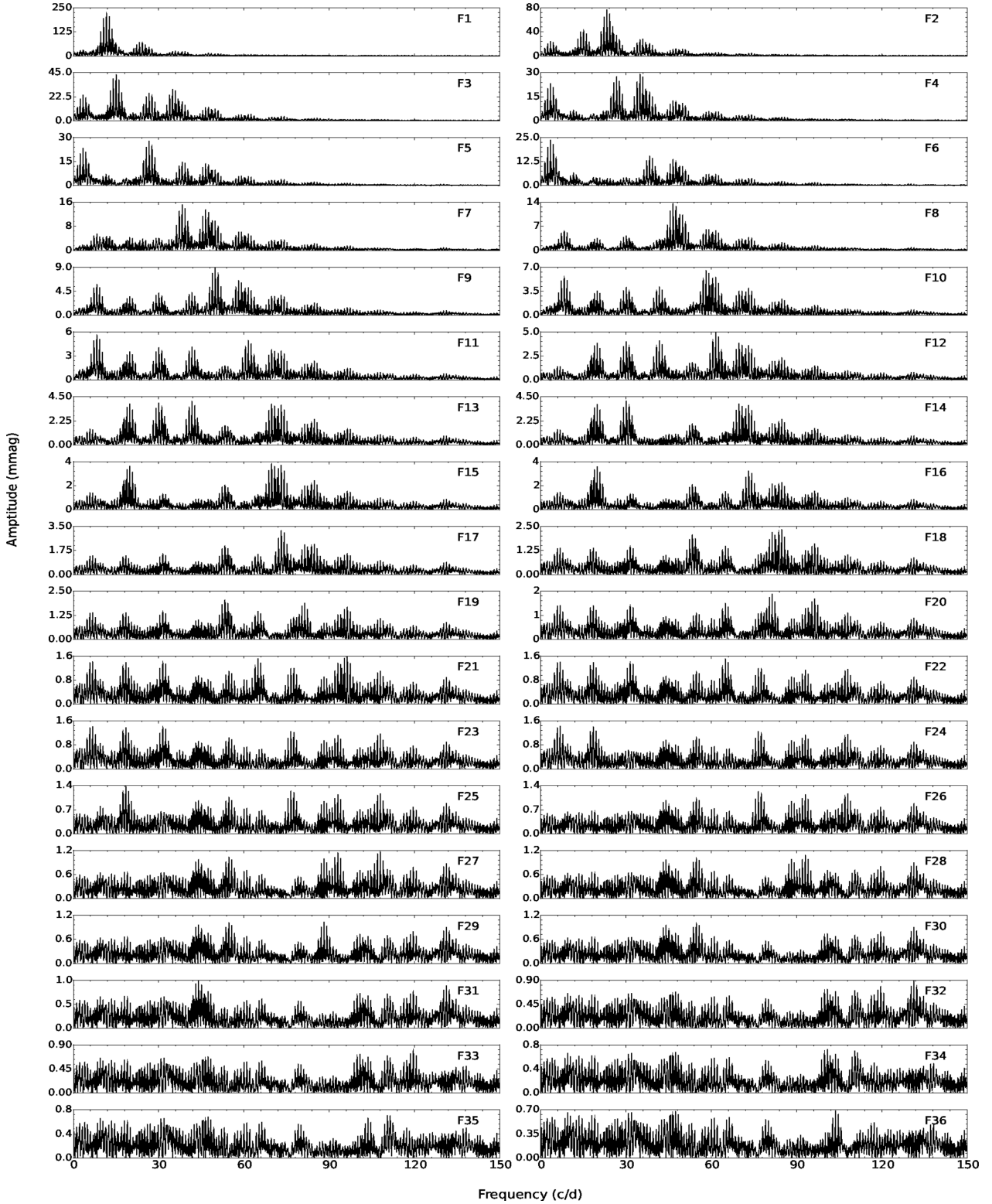
Figure 5. Amplitude spectrum of the light curves in *V* for AE UMa collected in 2009, and the amplitude spectra of the frequency pre-whitening process. Note that the *y*-axis scales are optimized concerning the highest peaks in the panels.

to the relation between the P_1/P_0 ratio and the [Fe/H] value for dwarf Cepheids, which was derived from Hintz et al. (1997a). They got the [Fe/H] values ranging from −0.4 to −0.1. We listed the parameters of AE UMa from Rodriguez et al. (1992) and Hintz et al.

(1997b) in Table 8. The atmospheric parameters derived from our spectrum are in good agreement with the above values, in particular, for the metal ratio [Fe/H] (comparison of Table 3 to 11). We note that in order to perform a search for the best-fitting model in a wide

Table 5. Frequencies and amplitudes of AE UMa for different segments of observations, including the data sets of Zhou (2001) and our data. (The data of 1981–1987 have not been used due to their large scatters.)

Years	f_0	f_1	A_0	A_1
1974–1977	11.625 57	15.030 97	216.9	34.1
⋆1981–1987	11.622 90	15.072 59	219.6	29.4
1996–1998	11.625 60	15.031 22	210.9	36.8
2000–2001	11.625 61	15.031 19	207.0	38.6
2009–2012	11.625 60	15.031 23	219.0	45.1
Mean	11.625 60	15.031 20	213.5	38.7
σ	0.000 015	0.000 123	5.5	4.7

Table 6. Newly determined times of maximum light of AE UMa. T_{max} is in HJD $-$ 2450000. σ is the estimated uncertainty of the times of maximum light in days.

T_{max}	σ	T_{max}	σ
4897.018 76	0.000 09	5621.110 32	0.000 17
4897.106 88	0.000 08	5621.198 60	0.000 19
4897.188 28	0.000 04	5937.398 14	0.000 12
4898.048 97	0.000 10	5961.305 07	0.000 04
4898.133 12	0.000 15	5961.390 70	0.000 10
4898.993 05	0.000 13	5964.314 79	0.000 14
4899.083 69	0.000 23	5964.407 28	0.000 19
4899.170 58	0.000 13	5966.213 31	0.000 07
4900.031 82	0.000 10	5966.294 16	0.000 05
4900.112 85	0.000 08	5966.379 65	0.000 08
4900.197 79	0.000 14	5967.331 06	0.00 009
4901.057 55	0.000 27	5967.415 92	0.000 07
4970.043 14	0.000 08	5968.277 34	0.000 07
4972.107 76	0.000 24	5968.358 17	0.000 04
5230.245 53	0.000 09	5969.303 81	0.000 07
5230.337 88	0.000 10	5969.395 94	0.000 14
5230.420 07	0.000 08	5997.008 00	0.000 08
5231.281 78	0.000 08	5997.090 64	0.000 04
5231.363 52	0.000 06	5997.172 95	0.000 04
5583.431 32	0.000 12	5997.263 91	0.000 10
5584.378 69	0.000 18	5998.033 73	0.000 08
5585.413 21	0.000 08	5998.122 09	0.000 14
5587.394 57	0.000 09	5998.211 92	0.000 08
5588.420 08	0.000 08	5998.292 74	0.000 06
5607.952 82	0.000 18	5998.980 78	0.000 09
5608.034 84	0.000 11	5999.072 67	0.000 09
5608.118 00	0.000 11	5999.154 66	0.000 05
5608.209 86	0.000 22	5999.237 46	0.000 05
5608.295 35	0.000 12	6000.016 12	0.000 05
5608.376 32	0.000 11	6000.097 80	0.000 04
5610.359 12	0.000 10	6000.187 42	0.000 09
5611.387 74	0.000 16	6000.276 18	0.000 06
5612.246 92	0.000 14	6001.045 94	0.000 06
5612.339 17	0.000 22	6001.136 82	0.000 06
5613.197 99	0.000 21	6001.218 5 7	0.000 03
5616.980 03	0.000 11	6001.302 28	0.000 06
5617.070 53	0.000 08	6062.031 20	0.000 05
5617.151 98	0.000 05	6063.069 10	0.000 15
5617.235 83	0.000 06	6064.013 67	0.000 08
5617.328 10	0.000 10	6064.094 79	0.000 08
5620.077 17	0.000 10	6065.041 89	0.000 09
5620.160 24	0.000 17	6068.057 99	0.000 21

parametric range, we used 3σ as the intervals of constraints for our theoretical calculation as follows.

5.2 Constraints from f_0 and f_1

MESA is a suite of open-source, robust, efficient, thread-safe libraries for a wide range of applications in computational stellar astrophysics (Paxton et al. 2011, 2013). The 1D stellar evolution module, MESA star, combines many of the numerical and physics modules for simulations of a wide range of stellar evolution scenarios ranging from very low mass to massive stars, including advanced evolutionary phases. The '*astero*' extension to the MESA star implements an integrated approach that passes results automatically between the MESA star and the new MESA module based on the adiabatic code ADIPLS (Christensen-Dalsgaard 2008).

In MESA version 6208, the *astero* extension enables the calculation of selected pulsation frequencies by the MESA star during the evolution of the model. This allows fitting to the observations that can include spectroscopic constraints (e.g. [Fe/H], $\log g$ and T_{eff}), asteroseismic constraints, a large frequency separation ($\Delta \nu$) and the frequency of maximum power (ν_{max}), and even individual frequencies observed. For the automated χ^2 minimization, *astero* will evolve a pre-MS model from a user-defined starting point, and find the best match along that single evolutionary track. The code then recalculates the track, again initiated at the pre-MS, with different initial parameters such as mass, chemical composition, mixing-length parameter and overshooting, and repeats until the minimum χ^2 is found.

We used the scan-grid mode to minimize the χ^2 for each model, which helps to compact the intervals of the physical parameters.

Every model of evolution starts with creating a pre-MS model by specifying the mass, M, at a uniform composition. The equation-of-state tables are constructed from the 2005 update of the OPAL EOS (Rogers & Nayfonov 2002) and SCVH tables (Saumon, Chabrier & van Horn 1995). The MESA opacity tables, which are derived from Type 1 and 2 OPAL tables (Iglesias & Rogers 1993, 1996), and tables from OP (Seaton 2005; Ferguson et al. 2005), cover a large range of $2.7 \leq \log T \leq 10.3$ and $-8 \leq \log R \leq 8$. The hydrogen burning reaction rates in the calculations are from Bahcall (1997, 2002).

The MESA star treats convective mixing as a time-dependent, diffusive process with a diffusion coefficient D_{OV} defined as

$$D_{OV} = D_{conv,0} \exp \left(-\frac{2z}{f \lambda_{P,0}} \right), \qquad (5)$$

where $\lambda_{P,0}$ is the pressure scaleheight at that location, z is the distance in the radiative layer away from that location and f is an adjustable parameter (Herwig 2000).

In all our subsequent calculations, the used opacity and EOS tables are $eos\_file\_prefix = mesa$, $kappa\_file\_prefix = gs98$ and $kappa\_lowT\_prefix = lowT\_Freedman11$. The atmosphere model is the $which\_atm\_option = photosphere\_tables$ photosphere.

The mixing-length parameter α_{MLT} was chosen as 1.89, since the choice has actually a very small effect on our models (Yang et al. 2012). The convective overshooting parameter $f_{ov} = 0.015$ was the initial value of MESA (version 6208). The effects of rotation on the evolutionary period changes are disregarded, concerning AE UMa as an HADS with very slow rotation (Breger 2000). Table 9 lists the parameters of the grid of model to search for f_0 and f_1 of AE UMa. The diffusion effects were not taken into account because of its negligible results on the models with mass in the range of

Table 7. Times of maximum light and O − C values of AE UMa. T_{max} is the observed times of maximum light in HJD − 2400000. *E*: cycle number. O − C is in days. Det: detector (pg = photograph, vis = visual, and pe = photoelectric photometer). S: source [(1) Tsesevich (1973); (2) Filatov (1960); (3) Pócs & Szeidl (2001); (4) Broglia & Conconi (1975); (5) Braune, Huebscher & Mundry (1979); (6) Braune & Mundry (1982); (7) Huebscher, Lichtenknecker & Mundry (1985); (8) Rodriguez et al. (1992); (9) Hübscher, Agerer & Wunder (1992); (10) Hintz et al. (1997b); (11) Agerer, Dahm & Hubscher (1999b); (12) Agerer et al. (1999a); (13) Pejcha et al. (2001); (14) Zhou (2001); (15) Agerer & Hubscher (2003); (16) Hubscher (2005); (17) Hubscher et al. (2005); (18) Klingenberg et al. (2006); (19) Hubscher et al. (2006); (20) Hubscher & Walter (2007); (21) Samolyk (2010); (22) Hubscher (2007); (23) Hubscher et al. (2009); (24) Hubscher et al. (2010); (25) Huebscher & Monninger (2011); and (26) this work.]. Points not used in the O − C analysis are marked with an asterisk.

NO.	T_{max}	E	O − C	Det	S	NO.	T_{max}	E	O − C	Det	S
1	28 632.398	−156 133	–	pg	(1)*	58	43 162.5708	12 788	0.002 457	pe	(3)
2	31 875.122	−118 434	–	pg	(2)*	59	44 633.4626	29 888	0.002 451	pe	(3)
3	33 379.256	−100 948	–	pg	(2)*	60	44 633.5440	29 889	−0.002 166	pe	(3)
4	35 601.188	−75 117	–	pg	(2)*	61	44 633.6309	29 890	−0.001 283	pe	(3)
5	35 604.337	−75 080	–	vis	(1)*	62	44 634.4046	29 899	−0.001 737	pe	(3)
6	35 607.173	−75 047	–	pg	(2)*	63	44 634.4902	29 900	−0.002 154	pe	(3)
7	35 981.202	−70 699	–	pg	(2)*	64	44 634.5810	29 901	0.002 629	pe	(3)
8	38 106.402	−45 992	–	vis	(1)*	65	44 692.4709	30 574	0.003 043	pe	(3)
9	41 059.368	−11 662	–	vis	(1)*	66	44 696.343	30 619	–	vis	(6)*
10	41 773.223	−3363	–	vis	(1)*	67	44 696.426	30 620	–	vis	(6)*
11	42 062.5832	0	0.001 039	pe	(3)	68	44 696.520	30 621	–	vis	(6)*
12	42 065.5959	35	0.003 142	pe	(4)	69	45 355.4902	38 282	0.002 786	pe	(3)
13	42 065.6778	36	−0.000 975	pe	(4)	70	45 355.5727	38 283	−0.000 731	pe	(3)
14	42 068.3432	67	−0.002 104	pe	(4)	71	45 382.3228	38 594	−0.001 939	pe	(3)
15	42 068.4302	68	−0.001 121	pe	(4)	72	45 382.4104	38 595	−0.000 356	pe	(3)
16	42 068.5203	69	0.002 962	pe	(4)	73	45 382.4997	38 596	0.002 927	pe	(3)
17	42 068.6029	70	−0.000 455	pe	(4)	74	45 382.5807	38 597	−0.002 090	pe	(3)
18	42 068.6871	71	−0.002 272	pe	(4)	75	46 114.332	47 104	–	vis	(7)*
19	42 069.3808	79	0.003 292	pe	(4)	76	46 468.4601	51 221	−0.002 180	pe	(3)
20	42 069.4651	80	0.001 574	pe	(4)	77	46 468.5468	51 222	−0.001 497	pe	(3)
21	42 069.5473	81	−0.002 243	pe	(4)	78	46 855.6279	55 722	0.002 780	pe	(8)
22	42 069.6363	82	0.000 740	pe	(4)	79	46 856.5729	55 733	0.001 592	pe	(8)
23	42 086.4965	278	0.001 597	pe	(4)	80	46 856.6561	55 734	−0.001 225	pe	(8)
24	42 086.5787	279	−0.002 221	pe	(4)	81	46 857.6017	55 745	−0.001 812	pe	(8)
25	42 087.4390	289	−0.002 091	pe	(4)	82	46 857.6925	55 746	0.002 970	pe	(8)
26	42 087.5263	290	−0.000 808	pe	(4)	83	46 858.6382	55 757	0.002 483	pe	(8)
27	42 087.6155	291	0.002 375	pe	(4)	84	46 859.6666	55 769	−0.001 322	pe	(8)
28	42 095.5298	383	0.003 105	pe	(3)	85	46 878.4181	55 987	−0.001 544	pe	(8)
29	42 095.6123	384	−0.000 412	pe	(3)	86	46 878.5064	55 988	0.000 739	pe	(8)
30	42 103.3513	474	−0.002 947	pe	(4)	87	46 878.5946	55 989	0.002 922	pe	(8)
31	42 106.4523	510	0.001 439	pe	(3)	88	46 884.5262	56 058	−0.000 656	pe	(8)
32	42 119.5252	662	−0.000 255	pe	(3)	89	46 884.6117	56 059	−0.001 173	pe	(8)
33	42 121.5025	685	−0.001 347	pe	(3)	90	46 886.5907	56 082	−0.000 566	pe	(8)
34	42 122.3628	695	−0.001 218	pe	(4)	91	48 683.317	76 970	–	vis	(9)*
35	42 122.4484	696	−0.001 635	pe	(4)	92	50 151.4564	94 038	0.000 981	pe	(3)
36	42 128.2968	764	−0.002 395	pe	(3)	93	50 151.5384	94 039	−0.003 036	pe	(3)
37	42 128.3872	765	0.001 988	pe	(3)	94	50 152.3170	94 048	0.001 411	pe	(3)
38	42 128.4727	766	0.001 471	pe	(3)	95	50 152.4862	94 050	−0.001 424	pe	(3)
39	42 128.5557	767	−0.001 546	pe	(3)	96	50 152.5756	94 051	0.001 959	pe	(3)
40	42 133.4627	824	0.002 482	pe	(3)	97	50 458.8815	97 612	0.001 034	CCD	(10)
41	42 133.5442	825	−0.002 035	pe	(3)	98	50 458.9636	97 613	−0.002 883	CCD	(10)
42	42 134.4055	835	−0.000 906	pe	(3)	99	50 459.8240	97 623	−0.002 654	CCD	(10)
43	42 147.3933	986	−0.001 682	pe	(3)	100	50 459.9113	97 624	−0.001 371	CCD	(10)
44	42 148.4295	998	0.002 313	pe	(3)	101	50 467.7388	97 715	−0.001 425	CCD	(10)
45	42 148.5117	999	−0.001 504	pe	(3)	102	50 467.8236	97 716	−0.002 642	CCD	(10)
46	42 159.4365	1126	−0.000 871	pe	(3)	103	50 490.3607	97 978	−0.002 018	pe	(3)
47	42 161.4145	1149	−0.001 263	pe	(3)	104	50 505.6697	98 156	−0.004 058	CCD	(10)
48	42 453.5306	4545	0.000 899	pe	(3)	105	50 505.7595	98 157	−0.000 275	CCD	(10)
49	42 453.6137	4546	−0.002 018	pe	(3)	106	50 505.8461	98 158	0.000 308	CCD	(10)
50	42 460.4989	4626	0.001 817	pe	(3)	107	50 516.7676	98 285	−0.002 362	CCD	(10)
51	42 532.407	5462	–	vis	(5)*	108	50 554.4432	98723	−0.002 243	pe	(3)
52	42 830.6280	8929	−0.000 499	pe	(3)	109	50 813.3550	101 733	−0.001 860	pe	(3)
53	42 837.5120	9009	0.002 136	pe	(3)	110	50 813.4408	101 734	−0.002 077	pe	(3)
54	42 838.4591	9020	0.003 049	pe	(3)	111	50 813.6151	101 736	0.000 189	pe	(3)
55	42 866.496	9346	–	vis	(5)*	112	50 813.6985	101 737	−0.002 428	pe	(3)
56	42 869.3377	9379	0.001 523	pe	(3)	113	50 848.4540	102 141	0.002 170	pe	(3)
57	42 869.4205	9380	−0.001 694	pe	(3)	114	50 848.5391	102 142	0.001 253	pe	(3)

Table 7 – *continued*

NO.	T_{max}	E	O − C	Det	S	NO.	T_{max}	E	O − C	Det	S
115	50 848.6212	102 143	−0.002 664	pe	(3)	179	51 942.2473	114 858	0.002 234	CCD	(14)
116	50 849.4815	102 153	−0.002 535	pe	(3)	180	51 942.3311	114 859	0.000 017	CCD	(14)
117	50 849.5688	102 154	−0.001 252	pe	(3)	181	51 942.4141	119 265	−0.003 000	CCD	(15)
118	50 862.3840	102 303	−0.002 597	CCD	(13)	182	52 321.4089	119 846	0.000 521	CCD	(15)
119	50 862.3840	102 418	−0.002 597	pe	(3)	183	52 371.3836	123 496	−0.000 706	CCD	(15)
120	50 872.2809	102 419	0.002 339	pe	(3)	184	52 685.3460	123 497	−0.000 673	CCD	(15)
121	50 872.3634	102 420	−0.001 178	pe	(3)	185	52 685.4369	124 020	0.004 210	CCD	(15)
122	50 872.4481	102 421	−0.002 496	pe	(3)	186	52 730.4187	124 124	−0.000 926	CCD	(15)
123	50 872.5394	102 733	0.002 787	pe	(3)	187	52 739.3617	124 195	−0.003 703	CCD	(16)
124	50 899.3729	102 734	−0.001 042	pe	(3)	188	52 745.4702	126 928	−0.002 416	CCD	(17)
125	50 899.4570	102 767	−0.002 959	pe	(3)	189	52 980.5608	126 929	0.003 484	CCD	(17)
126	50 902.2976	102 768	−0.000 923	pe	(3)	190	52 980.6421	126 930	−0.001 233	CCD	(17)
127	50 902.3819	102 779	−0.002 640	pe	(3)	191	52 980.7279	127 195	−0.001 451	CCD	(16)
128	50 903.3321	102 780	0.001 372	pe	(3)	192	53 003.5231	127 483	−0.000 779	CCD	(16)
129	50 903.4192	102 781	0.002 455	pe	(3)	193	53028.2942	127 484	−0.002 600	CCD	(16)
130	50 903.5009	107 036	−0.001 862	CCD	(13)	194	53028.3871	127 485	0.004 283	CCD	(16)
131	51 269.5080	107 198	0.002 550	CCD	(13)	195	53028.4705	127 486	0.001 666	CCD	(16)
132	51 283.4410	107 199	0.000 782	CCD	(13)	196	53028.5522	127 487	−0.002 651	CCD	(16)
133	51 283.5250	107 200	−0.001 235	CCD	(13)	197	53028.6420	127 961	0.001 132	CCD	(16)
134	51 283.6090	107 604	−0.003252	CCD	(13)	198	53069.4119	127 962	−0.001 068	CCD	(16)
135	5 1318.3630	107 605	−0.000154	CCD	(13)	199	53069.5029	127 973	0.003 915	CCD	(16)
136	51 318.4460	110 972	−0.003 171	CCD	(14)	200	53070.4493	127 974	0.004 127	CCD	(16)
137	51 608.0716	110 973	0.002 908	CCD	(14)	201	53 070.5320	128 205	0.000 810	CCD	(16)
138	51 608.1577	110 974	0.002 991	CCD	(14)	202	53 090.4053	128 251	0.004 162	CCD	(16)
139	51 608.2395	110 975	−0.00 1226	CCD	(14)	203	53 094.3575	128 437	−0.000 424	CCD	(19)
140	51 608.3264	110 983	−0.000 343	CCD	(14)	204	53 110.3619	131 915	0.004 798	CCD	(18)
141	51 609.0186	110 984	0.003 720	CCD	(14)	205	53 409.5286	131 916	0.004 064	CCD	(18)
142	51 609.1006	110 985	−0.000 297	CCD	(14)	206	53 409.6108	131 917	0.000 247	CCD	(18)
143	51 609.1865	110 986	−0.000 414	CCD	(14)	207	53 409.6940	132 122	−0.002 570	CCD	(19)
144	51 609.2770	110 987	0.004 069	CCD	(14)	208	53 427.3272	132 123	−0.002 873	CCD	(19)
145	51 609.3583	110 995	−0.000 648	CCD	(14)	209	53 427.4181	132 124	0.002 010	CCD	(19)
146	51 610.0450	111 006	−0.002 085	CCD	(14)	210	53 427.5031	132 402	0.000 993	CCD	(17)
147	51 610.9969	111 007	0.003 627	CCD	(14)	211	53 451.4136	132 403	−0.00 1258	CCD	(17)
148	51 611.0821	111 008	0.002 810	CCD	(14)	212	53 451.5042	132 785	0.003 325	CCD	(17)
149	51 611.1627	111 018	−0.002 607	CCD	(14)	213	53 484.3616	136 052	0.002 197	CCD	(20)
150	51 612.0246	111 019	−0.000 878	CCD	(14)	214	53 765.3803	136 053	0.003 066	CCD	(20)
151	51 612.1090	111 020	−0.002 495	CCD	(14)	215	53 765.4660	136 054	0.002 749	CCD	(20)
152	51 612.2010	111 021	0.003 488	CCD	(14)	216	53 765.5462	136 063	−0.003 068	CCD	(20)
153	51 612.2846	111 022	0.001 071	CCD	(14)	217	53 766.3278	136 064	0.004 378	CCD	(20)
154	51 612.3704	111 029	0.000 854	CCD	(14)	218	53 766.4079	136 065	−0.001 539	CCD	(20)
155	51 612.9692	111 030	−0.002 466	CCD	(14)	219	53 766.4943	136 066	−0.001 156	CCD	(20)
156	51 613.0609	111 031	0.003 217	CCD	(14)	220	53766.5849	136 389	0.003 427	CCD	(18)
157	51 613.1453	111 032	0.001 600	CCD	(14)	221	53 794.3619	136 400	−0.003 093	CCD	(18)
158	51 613.2276	111 033	−0.002 117	CCD	(14)	222	53 795.3115	136 401	0.000 319	CCD	(18)
159	51 613.3156	111 053	−0.000 134	CCD	(14)	223	53 795.3998	136 776	0.002 602	CCD	(18)
160	51 615.0341	111 054	−0.001 976	CCD	(14)	224	53 827.6570	139 707	0.003 393	CCD	(21)
161	51 615.1260	111 055	0.003 907	CCD	(14)	225	54 079.7666	139 708	−0.003 098	CCD	(21)
162	51 615.2098	111 056	0.001 690	CCD	(14)	226	54 079.8580	139 709	0.002 285	CCD	(21)
163	51 615.2919	111 064	−0.002 227	CCD	(14)	227	54 079.9437	139 973	0.001 967	CCD	(21)
164	51 615.9855	111 065	0.003 236	CCD	(14)	228	54 102.6471	139 974	−0.003 144	CCD	(21)
165	51 616.0705	111 066	0.002 219	CCD	(14)	229	54 102.7365	139 975	0.000 238	CCD	(21)
166	51 616.1526	111 067	−0.001 698	CCD	(14)	230	54 102.8254	139 985	0.003 121	CCD	(21)
167	51 616.2389	114 706	−0.001 415	CCD	(14)	231	54 103.6849	139 986	0.002 450	CCD	(21)
168	51 929.2556	114 707	−0.000 886	CCD	(14)	232	54 103.7677	139 997	−0.000 767	CCD	(21)
169	51 929.3464	114 717	0.003 897	CCD	(14)	233	54 104.7117	140 031	−0.002 955	CCD	(21)
170	51 930.2058	114 718	0.003 126	CCD	(14)	234	54 107.6358	140 032	−0.003 436	CCD	(21)
171	51 930.2885	114 719	−0.000 191	CCD	(14)	235	54 107.7251	140 033	−0.000 153	CCD	(21)
172	51 930.3721	114 729	−0.002 608	CCD	(14)	236	54 107.8138	140 034	0.002 530	CCD	(21)
173	51 931.2315	114 730	−0.003 379	CCD	(14)	237	54 107.8944	140 067	−0.002 887	CCD	(21)
174	51 931.3203	114 845	−0.000 596	CCD	(14)	238	54 110.7388	140 068	0.002 949	CCD	(21)
175	51 941.2102	114 846	−0.002 661	CCD	(14)	239	54 110.8207	140 069	−0.001 168	CCD	(21)
176	51 941.2979	114 847	−0.000 978	CCD	(14)	240	54 110.9051	140 070	−0.002 785	CCD	(21)
177	51 941.3881	114 856	0.003 205	CCD	(14)	241	54 110.9977	140 241	0.003 798	CCD	(21)
178	51 942.1562	114 857	−0.002 849	CCD	(14)	242	54 125.7056	140 242	0.002 775	CCD	(21)

Table 7 – *continued*

NO.	T_{max}	E	O − C	Det	S	NO.	T_{max}	E	O − C	Det	S
243	54 125.7883	140 243	−0.000 542	CCD	(21)	307	54 770.8336	147 741	0.002 589	CCD	(21)
244	54 125.8716	140 244	−0.003 259	CCD	(21)	308	54 770.9152	147 742	−0.001 828	CCD	(21)
245	54 125.9649	140 309	0.004 024	CCD	(21)	309	54 781.8384	147 869	−0.002 798	CCD	(21)
246	54 131.5550	140 310	0.003 013	CCD	(21)	310	54 781.9301	147 870	0.002 884	CCD	(21)
247	54 131.6392	140 311	0.001 196	CCD	(21)	311	54 788.8080	147 950	−0.000 583	CCD	(21)
248	54 131.7212	140 312	−0.002 821	CCD	(21)	312	54 788.8912	147 951	−0.003 400	CCD	(21)
249	54 131.8106	140 313	0.000 562	CCD	(21)	313	54 788.9833	147 952	0.002 683	CCD	(21)
250	54 131.8989	140 367	0.002 845	CCD	(21)	314	54 791.7333	147 984	0.000 136	CCD	(21)
251	54 136.5446	140 368	0.003 622	CCD	(21)	315	54 791.8157	147 985	−0.003 481	CCD	(21)
252	54 136.6275	140 369	0.000 505	CCD	(21)	316	54 791.9080	147 986	0.002 802	CCD	(21)
253	54 136.7104	140 370	−0.002 612	CCD	(21)	317	54 791.9938	147 987	0.002 585	CCD	(21)
254	54 136.7998	140 371	0.000 771	CCD	(21)	318	54 807.8222	148 171	0.003 840	CCD	(21)
255	54 136.8882	140 372	0.003 154	CCD	(21)	319	54807.9032	148 172	−0.001 177	CCD	(21)
256	54 136.9697	140 380	−0.001 364	CCD	(21)	320	54 807.9866	148 173	−0.003 795	CCD	(21)
257	54 137.6581	140 381	−0.001 100	CCD	(21)	321	54 816.6793	148 274	0.001 179	CCD	(21)
258	54 137.7491	140 382	0.003 883	CCD	(21)	322	54 816.7612	148 275	−0.002 938	CCD	(21)
259	54 137.8311	140 404	−0.000 134	CCD	(21)	323	54 816.8501	148 276	−0.000 055	CCD	(21)
260	54 139.7226	140 405	−0.001 010	CCD	(21)	324	54 816.9399	148 277	0.003 728	CCD	(21)
261	54 139.8124	140 406	0.002 772	CCD	(21)	325	54 837.6637	148 518	−0.002 591	CCD	(21)
262	54 139.8942	140 428	−0.001 445	CCD	(21)	326	54 837.7565	14 8519	0.004 191	CCD	(21)
263	54 141.7876	140 429	−0.000 421	CCD	(21)	327	54 843.6886	148 588	0.001 112	CCD	(21)
264	54 141.8768	140 430	0.002 762	CCD	(21)	328	54 843.7704	148 589	−0.003 105	CCD	(21)
265	54 141.9575	140 554	−0.002 555	CCD	(21)	329	54 843.8567	148 590	−0.002 822	CCD	(21)
266	54 152.6241	140 565	−0.002 074	CCD	(21)	330	54 843.9494	148 591	0.003 861	CCD	(21)
267	54 153.5746	140 578	0.002 238	CCD	(21)	331	54 846.6137	148 622	0.001 631	CCD	(21)
268	54 154.6883	140 579	−0.002 284	CCD	(21)	332	54 846.6960	148 623	−0.002 086	CCD	(21)
269	54 154.7800	140 580	0.003 399	CCD	(21)	333	54 847.7336	148 635	0.003 309	CCD	(21)
270	54 154.8618	140 773	−0.000 818	CCD	(22)	334	54 847.8164	148 636	0.000 092	CCD	(21)
271	54 171.4664	140 808	0.002 483	CCD	(22)	335	54 847.8988	148 637	−0.003 525	CCD	(21)
272	54 175.4206	140 819	−0.000 103	CCD	(22)	336	54 855.6469	148 727	0.003 036	CCD	(21)
273	54 196.4976	141 064	0.00 2710	CCD	(22)	337	54 855.7316	148 728	0.001 719	CCD	(21)
274	54 197.3590	141 074	0.003 939	CCD	(22)	338	54 855.8119	148 729	−0.003 998	CCD	(21)
275	54 197.4402	141 075	−0.000 878	CCD	(22)	339	54 855.9023	148 730	0.000 385	CCD	(21)
276	54 198.3850	141 086	−0.002 266	CCD	(22)	340	54 864.5873	148 831	−0.002 341	CCD	(21)
277	54 198.4741	141 087	0.000 817	CCD	(22)	341	54 864.6724	148 832	−0.003 258	CCD	(21)
278	54 202.4288	141 133	−0.00 1270	CCD	(22)	342	54 864.7649	148 833	0.003 224	CCD	(21)
279	54 414.8939	143 603	0.00 1615	CCD	(21)	343	54 864.8477	148 834	0.000 007	CCD	(21)
280	54 414.9804	143 604	0.002 098	CCD	(21)	344	54 864.9296	148 835	−0.004 110	CCD	(21)
281	54 417.7271	143 636	−0.003 749	CCD	(21)	345	54 868.6346	148 878	0.002 155	CCD	(21)
282	54 417.9058	143 638	0.002 917	CCD	(21)	346	54 868.7166	148 879	−0.001 862	CCD	(21)
283	54 417.9856	143 639	−0.003 300	CCD	(21)	347	54868.8033	148 880	−0.001 179	CCD	(21)
284	54 440.6958	143 903	−0.001 612	CCD	(21)	348	54 868.8941	148 881	0.003 604	CCD	(21)
285	54 442.7619	143 927	0.000 078	CCD	(21)	349	54 878.6935	148 995	−0.002 945	CCD	(21)
286	54 442.8516	143 928	0.003761	CCD	(21)	350	54 878.7811	148 996	−0.001 362	CCD	(21)
287	54 442.9342	143 929	0.000 344	CCD	(21)	351	54 878.8721	148 997	0.003 621	CCD	(21)
288	54 451.6243	144 030	0.002 717	CCD	(21)	352	54894.4412	149 178	0.003 628	CCD	(24)
289	54 460.6513	144 135	−0.002 077	CCD	(21)	353	54894.5227	149 179	−0.000 890	CCD	(24)
290	54 460.7433	144 136	0.003 906	CCD	(21)	354	54 894.6071	149 180	−0.002 507	CCD	(24)
291	54 460.8247	144 137	−0.000 712	CCD	(21)	355	54 897.0188	149 208	0.000 058	CCD	(26)
292	54 460.9089	144 138	−0.002 529	CCD	(21)	356	54 897.1069	149 209	0.004 345	CCD	(26)
293	54 467.7955	144 218	0.002 704	CCD	(21)	357	54 897.1883	149 210	−0.000 972	CCD	(26)
294	54 468.7392	144 229	0.000 216	CCD	(21)	358	54 898.0490	149 220	−0.003 829	CCD	(26)
295	54 468.8220	144 230	−0.003 001	CCD	(21)	359	54 898.1331	149 221	0.004 153	CCD	(26)
296	54 468.9120	144 231	0.000 982	CCD	(21)	360	54 898.3084	149 223	−0.001 064	CCD	(24)
297	54 469.6815	144 240	−0.003 672	CCD	(21)	361	54 898.9930	149 231	−0.003 252	CCD	(26)
298	54 469.7701	144 241	−0.001 089	CCD	(21)	362	54 899.0837	149 232	0.003 172	CCD	(26)
299	54 469.8603	144 242	0.003 094	CCD	(21)	363	54 899.1706	149 233	−0.000 545	CCD	(26)
300	54 469.9414	144 243	−0.001 823	CCD	(21)	364	54 900.0318	149 243	0.002 679	CCD	(26)
301	54 506.5887	144 669	0.002 196	CCD	(23)	365	54 900.1128	149 244	0.002 702	CCD	(26)
302	54 512.5199	144 738	−0.001 784	CCD	(23)	366	54 900.1978	149 245	−0.002 250	CCD	(26)
303	54 513.4650	144 749	−0.002 872	CCD	(23)	367	54 901.0575	149 255	0.004 333	CCD	(26)
304	54 513.5559	144 750	0.002 011	CCD	(23)	368	54904.4199	149 294	0.001 172	CCD	(24)
305	54 524.4815	144 877	0.003 441	CCD	(23)	369	54 904.5006	149 295	−0.003 733	CCD	(24)
306	54 769.8859	147 730	0.001 077	CCD	(21)	370	54 909.3147	149 351	0.000 862	CCD	(24)

Table 7 – *continued*

NO.	T_{max}	E	O − C	Det	S	NO.	T_{max}	E	O − C	Det	S
371	54 909.4087	149 352	−0.003 555	CCD	(24)	417	55 617.3281	157 582	0.002 874	CCD	(26)
372	54 909.4895	149 353	−0.002 426	CCD	(24)	418	55 620.0772	157 614	−0.000 573	CCD	(26)
373	54 910.4335	149 364	−0.003 443	CCD	(24)	419	55 620.1602	157 615	−0.003 590	CCD	(26)
374	54 912.3323	149 386	0.000 770	CCD	(24)	420	55 621.1103	157 626	0.000 322	CCD	(26)
375	54 912.4146	149 387	−0.003 835	CCD	(24)	421	55 621.1986	157 627	0.002 604	CCD	(26)
376	54 924.3742	149 526	0.003 777	CCD	(24)	422	55 937.3981	161 303	0.003 264	CCD	(26)
377	54 970.0431	150 057	0.000 360	CCD	(26)	423	55 961.3051	161 581	−0.002 489	CCD	(26)
378	54 972.1078	150 081	0.000 715	CCD	(26)	424	55 961.3907	161 582	−0.002 906	CCD	(26)
379	55 230.2455	153 082	0.002 798	CCD	(26)	425	55 964.3148	161 616	−0.003 387	CCD	(26)
380	55 230.3379	153 083	−0.001 819	CCD	(26)	426	55 964.4073	161 617	0.003 096	CCD	(26)
381	55230.4201	153 084	−0.001 290	CCD	(26)	427	55 966.2133	161 638	0.002 737	CCD	(26)
382	55 231.2818	153 094	−0.003 207	CCD	(26)	428	55 966.2942	161 639	−0.002 380	CCD	(26)
383	55 231.3635	153 095	−0.003 478	CCD	(26)	429	55 966.3797	161 640	−0.002 897	CCD	(26)
384	55 259.4108	153 421	0.001 205	CCD	(25)	430	55 967.3311	161 651	0.002 315	CCD	(26)
385	55 293.3826	153 816	0.002 087	CCD	(25)	431	55 967.4159	161 652	0.001 098	CCD	(26)
386	55 293.4752	153 817	0.003 117	CCD	(25)	432	55 968.2773	161 662	0.002 327	CCD	(26)
387	55302.3318	153 920	−0.001901	CCD	(25)	433	55 968.3582	161 663	−0.002 790	CCD	(26)
388	55303.3591	153 932	−0.002 918	CCD\	(25)	434	55 969.3038	161 674	−0.003 379	CCD	(26)
389	55304.3959	153 944	−0.003 389	CCD	(25)	435	55 969.3959	161 675	0.002 704	CCD	(26)
390	55304.4775	153 945	−0.003 497	CCD	(25)	436	55 997.0080	161 996	0.003 317	CCD	(26)
391	55305.3388	153 955	−0.003 207	CCD	(25)	437	55 997.0906	161 997	−0.000 100	CCD	(26)
392	55305.4238	153 956	−0.002 804	CCD	(25)	438	55 997.1730	161 998	−0.003 717	CCD	(26)
393	55 309.3848	154 002	0.003 579	CCD	(25)	439	55 997.2639	161 999	0.001 166	CCD	(26)
394	55 310.4124	154 014	−0.000 238	CCD	(25)	440	55 998.0337	162 008	−0.003 188	CCD	(26)
395	55 311.3662	154 025	0.001 291	CCD	(25)	441	55 998.1221	162 009	−0.000 805	CCD	(26)
396	55 311.4488	154 026	−0.003 026	CCD	(25)	442	55 998.2119	162 010	0.002 977	CCD	(26)
397	55 583.4313	157 188	−0.003 191	CCD	(26)	443	55 998.2927	162 011	−0.00 2240	CCD	(26)
398	55 584.3787	157 199	−0.001 979	CCD	(26)	444	55 998.9808	162 019	−0.002 276	CCD	(26)
399	55 585.4132	157 211	0.000 316	CCD	(26)	445	55 999.0727	162 020	0.003 606	CCD	(26)
400	55 587.3946	157 234	0.003 323	CCD	(26)	446	55 999.1547	162 021	−0.000 411	CCD	(26)
401	55 588.4201	157 246	−0.003 383	CCD	(26)	447	55 999.2375	162 022	−0.003 628	CCD	(26)
402	55 607.9528	157 473	0.003 437	CCD	(26)	448	56 000.0161	162 031	0.000 818	CCD	(26)
403	55 608.0348	157 474	−0.000 580	CCD	(26)	449	56 000.0978	162 032	−0.003 499	CCD	(26)
404	55 608.1180	157 475	−0.003 397	CCD	(26)	450	56 000.1874	162 033	0.000 084	CCD	(26)
405	55 608.2099	157 476	0.002 486	CCD	(26)	451	56 000.2762	162 034	0.002 867	CCD	(26)
406	55 608.2954	157 477	0.001 969	CCD	(26)	452	56001.0459	162 043	−0.001 587	CCD	(26)
407	55 608.3763	157 478	−0.003 148	CCD	(26)	453	56 001.1368	162 044	0.003 296	CCD	(26)
408	55 610.3591	157 501	0.001 258	CCD	(26)	454	56 001.2186	162 045	−0.000 921	CCD	(26)
409	55 611.3877	157 513	−0.002347	CCD	(26)	455	56 001.3023	162 046	−0.003 238	CCD	(26)
410	55 612.2469	157 523	−0.003 318	CCD	(26)	456	56 062.0312	162 752	−0.002 407	CCD	(26)
411	55 612.3392	157 524	0.002 965	CCD	(26)	457	56 063.0691	162 764	0.003 287	CCD	(26)
412	55 613.1980	157 534	0.001 594	CCD	(26)	458	56 064.0137	162 775	0.001 699	CCD	(26)
413	55616.9800	157 578	−0.001 158	CCD	(26)	459	56 064.0948	162 776	−0.003 218	CCD	(26)
414	55 617.0705	157 579	0.003 325	CCD	(26)	460	56 065.0419	162 787	−0.002 306	CCD	(26)
415	55 617.1520	157 580	−0.001 192	CCD	(26)	461	56 068.0580	162 822	0.003 196	CCD	(26)
416	55 617.2358	157 581	−0.003 409	CCD	(26)						

1.30–2.70 M$_\odot$ after the MS and the post-MS (before the red giant phase).

As a result, we got the models that included the frequencies f_0 and f_1 along with the stellar evolution tracks. These tracks provided the relevant intervals of the parameters for subsequent calculations, as listed in Table 10.

With the observations and the method used, one can believe that [Fe/H] and log g values have good reliability (Strömgren 1956; Crawford & Mander 1966). So, we decide to take the value [Fe/H] = −0.3 in our calculation.

We used the formula (with the solar metallicity $X_\odot = 0.7381$, $Y_\odot = 0.2485$ and $Z_\odot = 0.0134$ from Asplund et al. 2009)

$$[Fe/H] = \log\left(\frac{Z}{X}\right) - \log\left(\frac{Z_\odot}{X_\odot}\right) \tag{6}$$

and the formula

$$X + Y + Z = 1 \tag{7}$$

to calculate the initial Z. In Girardi et al. (2000), a model was calculated with a couple of values $(Y, Z) = (0.25, 0.008)$, which are in accord with the values in our previous calculation (derived using MESA *astero* with the value of [Fe/H]).

At last, by integrating all the information about the value of (Y, Z), we decide to choose $(Y, Z) = (0.25, 0.008\,521)$ as the unique initial value for the subsequent calculation.

5.3 Constraints from the period variation

Unlike the solar-like stars for which many frequencies are detected, most HADS are observed with only the fundamental and
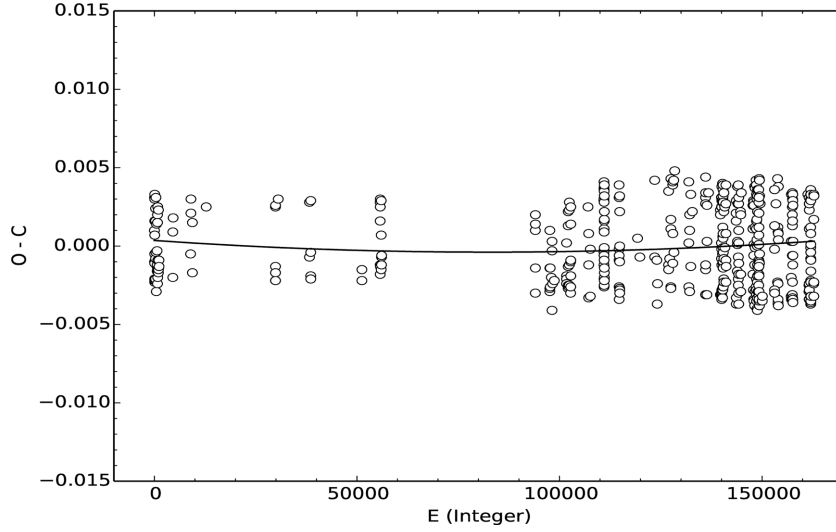
Figure 6. O − C diagram of AE UMa. The O − C values are in days. *E* is the cycle number. The solid curve shows the fit concerning a continuous increasing period change.

Table 8. Physical parameters of AE UMa from Rodriguez et al. (1992) and Hintz et al. (1997b). The $\log(L/L_{\odot})$ value was derived based on $\log(L/L_{\odot}) = 0.4(M_{bol_{\odot}} - M_{bol})$.

Parameters	Mean value	Intervals	3σ
[Fe/H]	−0.3	[−0.4, −0.1]	–
T_{eff} (K)	7569	[7150, 8320]	[5980, 9490]
$\log g$	3.90	[3.77, 4.16]	[3.38, 4.55]
M_{bol}	–	[1.53, 1.93]	[1.33, 2.13]
$M(M_{\odot})$	–	[1.75, 1.95]	–
$\log(L/L_{\odot})$	–	[1.16, 1.32]	[1.08, 1.40]

Table 9. The parameters of the grid of model to search for f_0 and f_1. Since the values of M_{bol} and $\log(L/L_{\odot})$ in Table 6 were calculated from the stellar models of Rodriguez et al. (1992), and from observations, which depended on the models they used, we did not use these values as the constraints during our calculation.

Parameters	Maximum	Minimum	Step
[Fe/H]	−0.1	−0.4	0.05
Initial Y	0.33	0.23	0.02
Mass	2.7	1.3	0.02
$\log T_{eff}$	3.977	3.777	–
$\log g$	4.55	3.38	–

Table 10. The parameters determined with the constraints from f_0 and f_1. The grid was constructed also within the parameter intervals of T_{eff} and $\log g$ listed in Table 6. In order to show an obvious comparison of the evolutionary tracks, we calculated the tracks with the stellar mass from 1.30 to 2.30 M$_{\odot}$.

Parameters	Maximum	Minimum
[Fe/H]	− 0.2	− 0.4
Initial Y	0.27	0.23
Mass	2.26	1.32

Table 11. Physical parameters of AE UMa obtained from our calculation.

Parameter	Value	Uncertainty (per cent)
Mass (M$_{\odot}$)	1.805 ± 0.055	3.04
Age (10^9 yr)	1.055 ± 0.095	9.00
$\log T_{eff}$	3.922 ± 0.01	0.25
Radius (10^{11} cm)	1.647 ± 0.032	1.94
$\log g$	3.9543 ± 0.0044	0.11
$\log L$	1.381 ± 0.048	3.51

the first overtone modes in general (e.g. Balona et al. 2012; Ulusoy et al. 2013). As a result, the period variation becomes a very important constraint on the model calculation of these stars. High-precision detection of period variation may offer strong constraints on AE UMa. We used two independent ways to calculate the period variations of AE UMa theoretically.

5.3.1 Calculation from stellar evolutionary effect

The variation rate of the fundamental period derived from the long time-scale of observations of AE UMa shows a positive period change. From the theoretical point of view, the period changes caused by stellar evolution in and across the lower instability strip permit an observational test of stellar evolution theory (Breger & Pamyatnykh 1998).

The period–luminosity–colour relation can be expressed as (Breger & Pamyatnykh 1998)

$$\log P = -0.3M_{bol} - 3\log T_{eff} - 0.5\log M + \log Q + \text{constant},$$
(8)

where *P* is the period of a radial mode of pulsation, M_{bol} is the bolometric absolute magnitude, T_{eff} is the effective temperature, *M* is the stellar mass in solar mass and *Q* is the pulsation constant in days. For δ Scuti stars with radial pulsation, the constant is 12.708. For individual stars, the evolutionary period changes over long
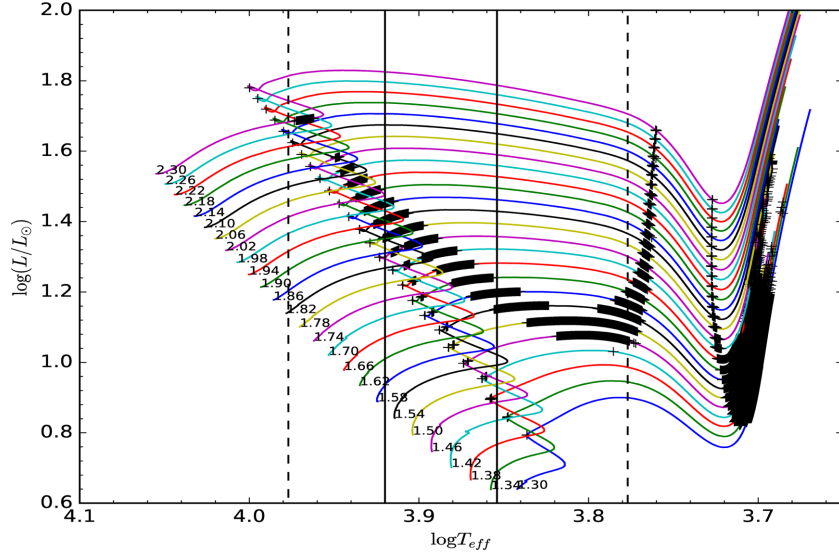
Figure 7. Evolutionary tracks of models with mass from 1.30 to 2.30 $M_\odot$ for $(Y, Z) = (0.25, 0.008521)$. The solid and dashed vertical lines on the Hertzsprung–Russell diagram are determined from the observed T_{eff} in 1σ and 3σ, respectively. The marks on the tracks indicate the models with the values of the evolutionary period changes of $(1/P_0)(dP_0/dt)$ inside the interval $(3.5210 \times 10^{-9}, 7.2448 \times 10^{-9})$ in units of yr^{-1}. Note that the tracks are shown in the diagram with the mass interval of $0.04\,M_\odot$.

time-scales. An evolutionary change in T_{eff}, M_{bol} and M leads to a period change of

$$\frac{1}{P}\frac{dP}{dt} = -0.69\frac{dM_{bol}}{dt} - \frac{3}{T_{eff}} - 0.5\frac{1}{M}\frac{dM}{dt} + \frac{1}{Q}\frac{dQ}{dt}. \quad (9)$$

Assuming that the stellar mass $M = $ constant for δ Scuti stars during the observation interval with mass in the range of 1.30–2.30 $M_\odot$ and that the variation of pulsation constant is negligible, Yang et al. (2012) got

$$\frac{1}{P}\frac{dP}{dt} \approx -0.69\frac{dM_{bol}}{dt} - \frac{3}{T_{eff}}\frac{dT_{eff}}{dt}. \quad (10)$$

As indicated by Rodríguez & Breger (2001), the HADS locate on or near the MS of the Hertzsprung–Russell diagram. Consequently, the evolutionary models are constructed from the pre-MS Hayashi phase to the end of the MS. The effect of rotation was not considered here for mainly two reasons: (1) The HADS typically have slow rotation, and most have a projected rotational velocity, $V\sin i$, of around 20 km s^{-1} (see, e.g. Solano & Fernley 1997). (2) The effects of rotation with a speed of $V\sin i = 18$ km s^{-1} in HADS are very similar to those in the absence of rotation (Casas et al. 2006).

The evolutionary tracks constructed from 1.30 to 2.30 $M_\odot$ are shown in Fig. 7, and the corresponding variation rates of the period are marked.

As shown in Fig. 7, the states whose values of period changes are consistent with the observed ones determined from the O − C analysis lie just after the second turn-offs leaving the MSs on the evolutionary tracks.

5.3.2 Calculation from ADIPLS

ADIPLS (the Aarhus adiabatic oscillation package) is a program for the calculation of adiabatic oscillations of stellar models (Christensen-Dalsgaard 2008). We used it to calculate the frequencies of the eigenmodes of the model at each step of our evolutionary state. As a result, we got the frequencies of the model of F_0 and F_1 and

then deduced the variation of those frequencies. In the calculation, the input frequencies F_0 and F_1 are the fundamental and first over-tone frequencies with quantum numbers of $l = 0$ and $n = 1, 2$, respectively.

We calculated the evolutionary tracks from 1.30 to 2.30 $M_\odot$, and got the frequency values on each tracks, as shown in Fig. 8. Figs 8(a) and (b) show that the models with appropriate frequencies for AE UMa could appear (i) just before the first turn-offs, (ii) after the first and before the second turn-offs and (iii) just after the second turn-offs. We integrated the constraints from f_0 and f_1 and got the results shown in Fig. 8(c).

In addition, we also calculated the variations of the frequencies of the eigenmodes of the models by using ADIPLS. Adding the constraints from $(1/P_0)(dP_0/dt)$, which are thought to be due to the evolutionary effects, we got the results in Fig. 9.

One can find that this result is almost consistent with the result from Fig. 7 just after the second turn-off. The differences arise from the fact that we did not consider the variation of the stellar mass and the pulsation constant along the evolutionary tracks in Fig. 7.

Finally, we combined the constraints from f_0, f_1 and $(1/P_0)(dP_0/dt)$, and got the results shown in Fig. 10. One concludes that AE UMa should locate after the second turn-offs of the evolutionary tracks leaving the MS. Hence, one finds that the period variations of the fundamental mode of AE UMa are caused by the evolutionary effect. The rate of variation is consistent with the theoretically predicted value by Breger & Pamyatnykh (1998).

With the discussion above and constraints from the physical parameters, one can conclude that the mass of AE UMa ranges from 1.75 to 1.86 $M_\odot$ and the age from 0.96×10^9 to 1.15×10^9 yr.
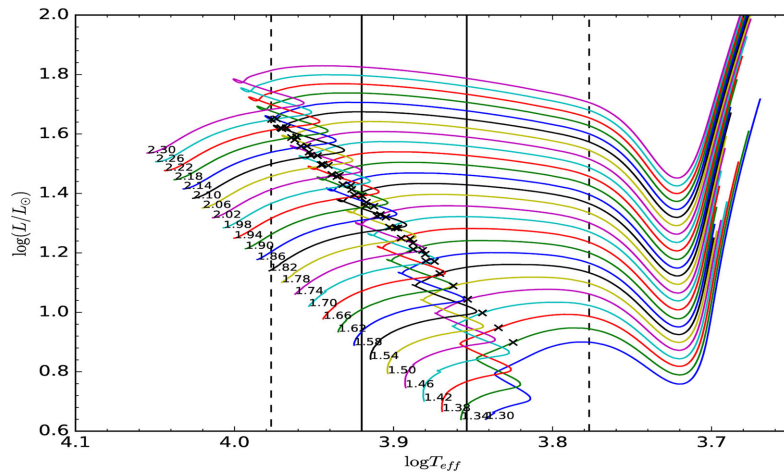
We chose 1.80 $M_\odot$ as a sample to study the evolutionary state and the interior of the models that we gained. More details of the parameters we got from calculations are listed in Table 11. Fig. 11 shows the distribution of H, He^3 and He^4 versus the stellar radius.
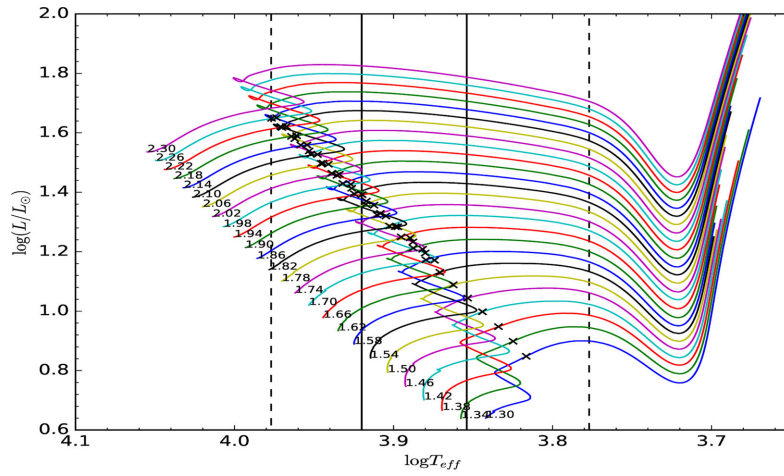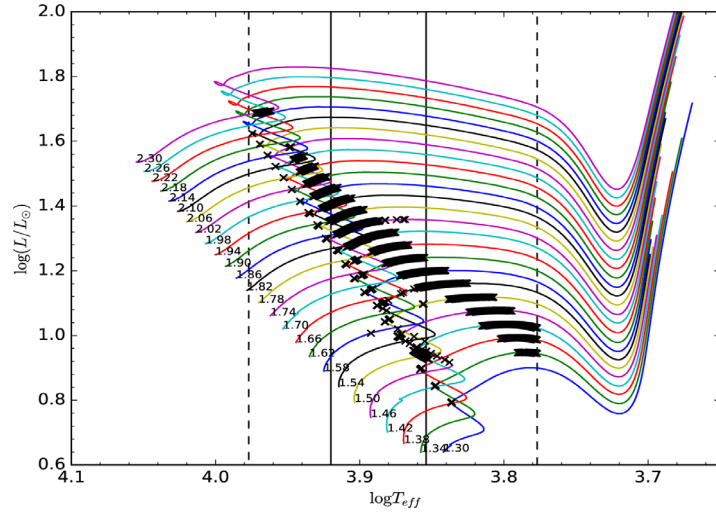
(a)
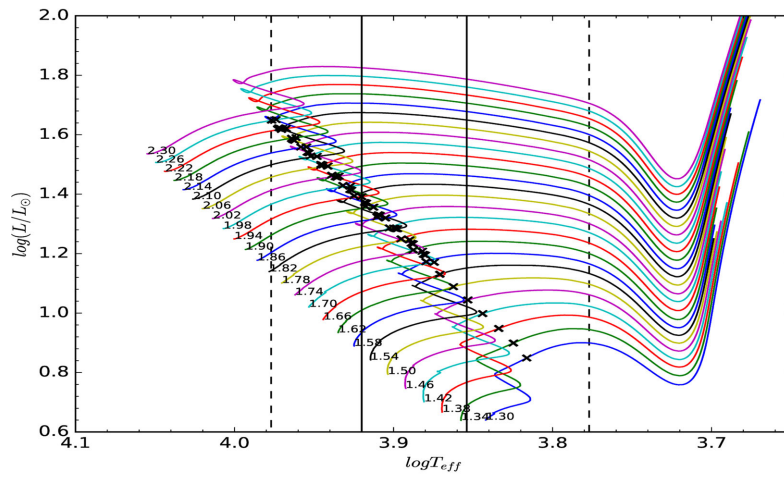
(b)

(c)

Figure 8. Models with the values of F_0 and F_1 calculated from ADIPLS, consistent with the observed ones ($F_0 \in [f_0 - 3\sigma, f_0 + 3\sigma]$ and $F_1 \in [f_1 - 3\sigma, f_1 + 3\sigma]$) are marked on the evolutionary tracks. (a) For $F_0 \in [f_0 - 3\sigma, f_0 + 3\sigma]$; (b) for $F_1 \in [f_1 - 3\sigma, f_1 + 3\sigma]$; and (c) for both $F_0 \in [f_0 - 3\sigma, f_0 + 3\sigma]$ and $F_1 \in [f_1 - 3\sigma, f_1 + 3\sigma]$.
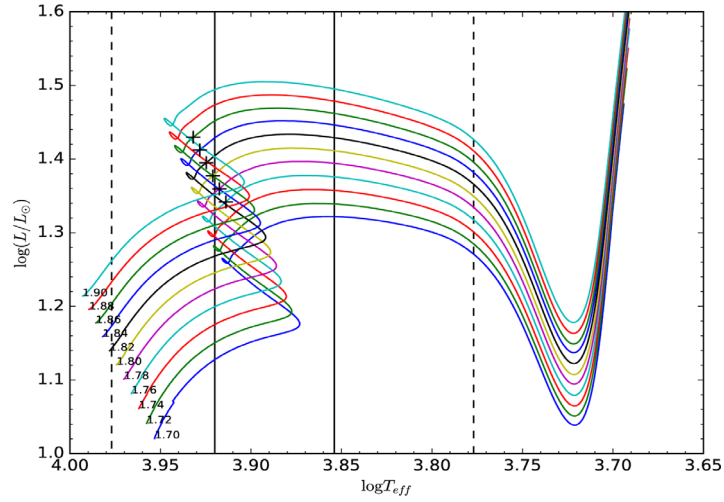
Figure 9. The models for which the period variations of the fundamental mode $(1/P_0)(dP_0/dt)$ calculated with ADIPLS agree with the observed values of $5.3829(\pm1.8619) \times 10^{-9}\,\mathrm{yr}^{-1}$ are marked on the evolutionary tracks.
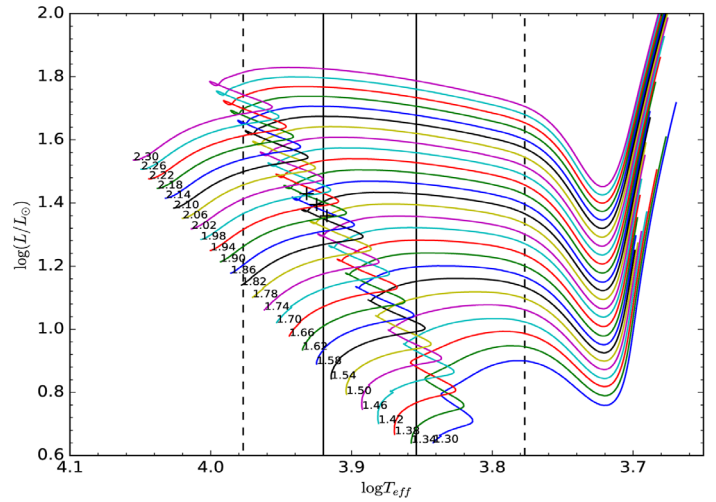
(a)

(b)

Figure 10. Evolutionary tracks of star models. (a) Marks on the tracks indicate the models with constraints from f_0, f_1 and $(1/P_0)(dP_0/dt)$. (b) A zoom-in of (a).
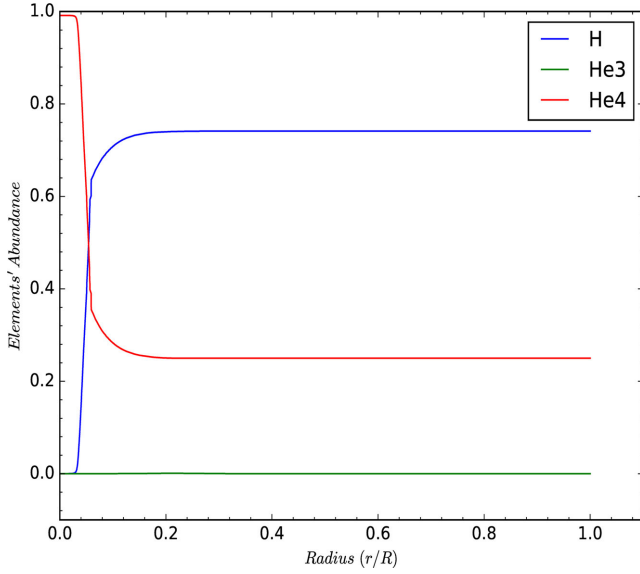
Figure 11. Elements' abundance distribution of H, He^3 and He^4 inside the star for the model with the star mass of $1.80\,M_\odot$.

Fig. 12 presents the energy distribution inside the star. From Figs 11 and 12, one may find that the star should have a helium core and a hydrogen-burning shell.

We also calculated models with different values of Y, Z and $\alpha_{\rm ov}$ by using different grids. The result showed that the states were not different significantly. All the results pointed out that AE UMa should lie just after the second turn-off with a helium core and a hydrogen-burning shell.

6 CONCLUSIONS

We analyse the photometric data gathered on AE UMa over 40 nights spanning from 2009 to 2012 and detect 37 frequencies above the so-called 4σ detection threshold, among which 25 frequencies are newly detected. All these frequencies are linked to either harmonics or linear combinations of the two main frequencies $f_0 = 11.625\,60\,{\rm c\,d^{-1}}$ and $f_1 = 15.031\,23\,{\rm c\,d^{-1}}$, corresponding to the fundamental and the first overtone radial pulsation modes, respectively. No frequencies of the other pulsation modes were detected from the observed data.

An $O - C$ diagram is constructed from a combination of the 84 times of maximum light determined from our new observations and 360 times listed in the literature, leading to the updated value of period $P_0 = 0.086\,017\,0781$ d. A new ephemeris with a quadratic solution suggests that the period change rate of the fundamental mode of AE UMa is of $(1/P_0)(\mathrm{d}P_0/\mathrm{d}t) = 5.4(\pm1.9) \times 10^{-9}\,{\rm yr^{-1}}$. The value is different from the result obtained by Zhou (2001) and needs to be confirmed with more data that will be collected from observations in the near future, both from ground and space (e.g. *TESS*; Ricker et al. 2014). Because the large values of the derivative of $(1/P_1)(\mathrm{d}P_1/\mathrm{d}t)$ were obtained from the standard $O - C$ method, we did not use this value as a constraint in the model calculation.

With the spectroscopic observation data, we got the low-resolution spectrum and used the automated 1D parametrization pipeline LASP to obtain the stellar atmospheric parameters of AE UMa. These parameters (especially the [Fe/H] value of -0.32) certify that AE UMa is a Population I δ Scuti star rather than a Population II SX Phe star.

We then calculated models of stars with masses between 1.30 and $2.70\,M_\odot$. With the constraints of the values of f_0, f_1 and $(1/P_0)(\mathrm{d}P_0/\mathrm{d}t)$, we conclude that AE UMa lies just after the second turn-offs of the evolutionary tracks leaving the MS. The
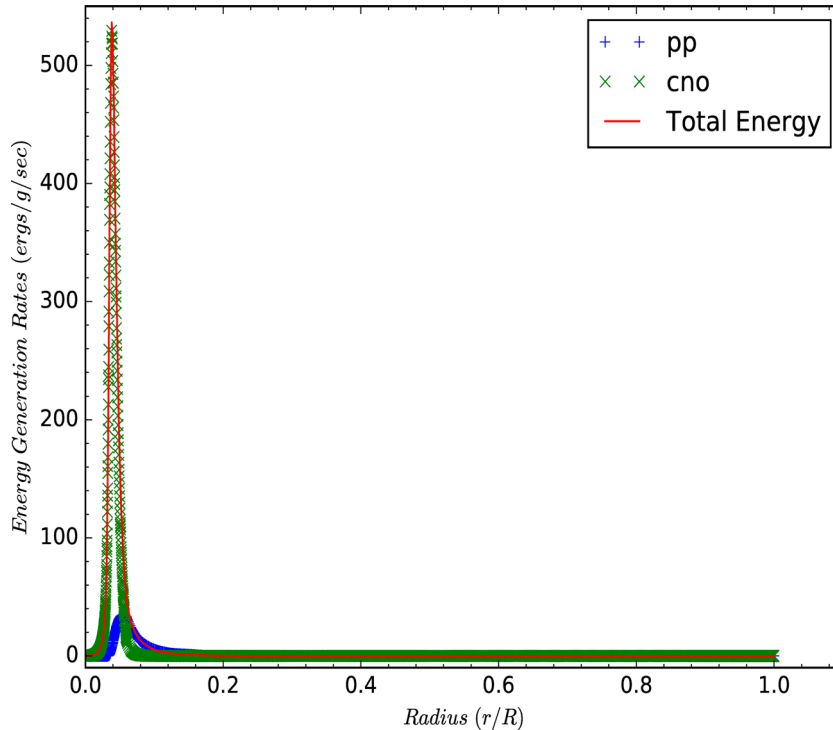
Figure 12. Energy generation rate distribution inside the star for the model with the star mass of $1.80\,M_\odot$.

corresponding mass should be $1.805 \pm 0.055\,\mathrm{M_\odot}$ and the age $1.055 \pm 0.095 \times 10^9$ yr. At this evolutionary phase, the star should have a helium core and a hydrogen-burning shell.

Moreover, according to the concrete observational evidence, we provide an example of the HADS whose evolutionary stage is on the post-MS. This gives a direct support to the general consensus that δ Scuti stars are probably normal stars evolving in the MS or the immediate post-MS stages.

ACKNOWLEDGEMENTS

REFERENCES

Agerer F., Hubscher J., 2003, Inf. Bull. Var. Stars, 5485, 1
Agerer F., Dahm M., Hubscher J., 1999a, Inf. Bull. Var. Stars, 4712, 1
Agerer F., Dahm M., Hubscher J., 1999b, Inf. Bull. Var. Stars, 4712, 1
Asplund M., Grevesse N., Sauval A. J., Scott P., 2009, ARA&A, 47, 481
Baglin A., Breger M., Chevalier C., Hauck B., Le Contel J. M., Sareyan J. P., Valtier J. C., 1973, A&A, 23, 221
Bahcall J. N., 1997, Phys. Rev. C, 56, 3391
Bahcall J. N., 2002, Phys. Rev. C, 65, 025801
Balona L. A. et al., 2012, MNRAS, 419, 3028
Braune W., Mundry E., 1982, BAV Mitt. Nr., 34
Braune W., Huebscher J., Mundry E., 1979, Astron. Nachr., 300, 165
Breger M., 1979, PASP, 91, 5
Breger M., 1980, ApJ, 235, 153
Breger M., 2000, in Breger M., Montgomery M., eds, ASP Conf. Ser. Vol. 210, Delta Scuti and Related Stars. Astron. Soc. Pac., San Francisco, p. 3
Breger M., Pamyatnykh A. A., 1998, A&A, 332, 958
Breger M. et al., 1993, A&A, 271, 482
Broglia P., Conconi P., 1975, A&AS, 22, 243
Casas R., Suárez J. C., Moya A., Garrido R., 2006, A&A, 455, 1019
Christensen-Dalsgaard J., 2008, Ap&SS, 316, 113
Claret A., Rodriguez E., Rolland A., Lopez de Coca P., 1990, in Cacciari C., Clementini G., eds, ASP Conf. Ser. Vol. 11, Confrontation Between Stellar Pulsation and Evolution. Astron. Soc. Pac., San Francisco, p. 481
Crawford D. L., Mander J., 1966, AJ, 71, 114
Ferguson J. W., Alexander D. R., Allard F., Barman T., Bodnarik J. G., Hauschildt P. H., Heffner-Wong A., Tamanai A., 2005, ApJ, 623, 585
Filatov G. S., 1960, Astron. Nachr., 215, 20
Fu J. N. et al., 2008b, AJ, 135, 1958
Fu J.-N., Zhang C., Marak K., Boonyarak C., Khokhuntod P., Jiang S.-Y., 2008a, Chinese J. Astron. Astrophys., 8, 237
Garcia J. R. et al., 1995, A&AS, 109, 201
Geyer E., Kippenhahn R., Strohmeier W., 1955, Kleine Veröff, Bamberg, No. 11
Girardi L., Bressan A., Bertelli G., Chiosi C., 2000, A&AS, 141, 371
Götz W., Wenzel W., 1961, Mitt. Veränd. Sterne, No. 571
Herwig F., 2000, A&A, 360, 952
Hintz E. G., Joner M. D., McNamara D. H., Nelson K. A., Moody J. W., Kim C., 1997a, PASP, 109, 15
Hintz E., Hintz M. L., Joner M. D., 1997b, PASP, 109, 1073
Hubscher J., 2005, Inf. Bull. Var. Stars, 5643, 1
Hubscher J., 2007, Inf. Bull. Var. Stars, 5802, 1
Hubscher J., Walter F., 2007, Inf. Bull. Var. Stars, 5761, 1
Hübscher J., Agerer F., Wunder E., 1992, BAV Mitt., Nr., 60
Hubscher J., Paschke A., Walter F., 2005, Inf. Bull. Var. Stars, 5657, 1
Hubscher J., Paschke A., Walter F., 2006, Inf. Bull. Var. Stars, 5731, 1
Hubscher J., Steinbach H.-M., Walter F., 2009, Inf. Bull. Var. Stars, 5874, 1
Hubscher J., Lehmann P. B., Monninger G., Steinbach H.-M., Walter F., 2010, Inf. Bull. Var. Stars, 5918, 1
Huebscher J., Monninger G., 2011, BAV Mitt., 214, 1
Huebscher J., Lichtenknecker D., Mundry E., 1985, BAV Mitt., Nr., 39
Iglesias C. A., Rogers F. J., 1993, ApJ, 412, 752
Iglesias C. A., Rogers F. J., 1996, ApJ, 464, 943
Kepler S. O., Castanheira B. G., Saraiva M. F. O., Nitta A., Kleinman S. J., Mullally F., Winget D. E., Eisenstein D. J., 2005, A&A, 442, 629
Klingenberg G., Dvorak S. W., Robertson C. W., 2006, Inf. Bull. Var. Stars, 5701, 1
Lenz P., Breger M., 2005, Commun. Asteroseismol., 146, 53
Niu J.-S., Fu J.-N., Zong W.-K., 2013, Res. Astron. Astrophys., 13, 1181
Paxton B., Bildsten L., Dotter A., Herwig F., Lesaffre P., Timmes F., 2011, ApJS, 192, 3
Paxton B. et al., 2013, A&AS, 208, 4
Pejcha O., Havlik T., Kral L., 2001, Inf. Bull. Var. Stars, 5080, 1
Petersen J. O., Christensen-Dalsgaard J., 1996, A&A, 312, 463
Pócs M. D., Szeidl B., 2001, A&A, 368, 880
Poretti E., 2003, A&A, 409, 1031
Pringle J. E., 1975, MNRAS, 170, 633
Ricker G. R. et al., 2014, in Oschmann J. M. Jr., Clampin M., Fazio G. G., MacEwen H. A., Proc. SPIE Conf. Ser. Vol. 9143, Space Telescopes and Instrumentation 2014: Optical, Infrared, and Millimeter Wave. SPIE, Bellingham, p. 914320
Rodríguez E., Breger M., 2001, A&A, 366, 178
Rodríguez E., López-González M. J., 2000, A&A, 359, 597
Rodriguez E., Rolland A., Lopez de Coca P., Garcia-Lobo E., Sedano J. L., 1992, A&AS, 93, 189
Rogers F. J., Nayfonov A., 2002, ApJ, 576, 1064
Samolyk G., 2010, J. Am. Assoc. Var. Star Obs., 38, 12
Saumon D., Chabrier G., van Horn H. M., 1995, ApJS, 99, 713
Seaton M. J., 2005, MNRAS, 362, L1
Solano E., Fernley J., 1997, A&AS, 122
Strömgren B., 1956, Vistas Astron., 2, 1336
Szeidl B., 1974, Inf. Bull. Var. Stars, 903, 1
Tsesevich V. P., 1973, Astronomicheskij Tsirkulyar, 775, 2
Ulusoy C. et al., 2013, MNRAS, 433, 394
Wenger M. et al., 2000, A&AS, 143, 9
Wu Y. et al., 2011, Res. Astron. Astrophys., 11, 924
Yang X. H., Fu J. N., Zha Q., 2012, AJ, 144, 92
Zhou A.-Y., 2001, A&A, 374, 235
Zhou A.-Y., Jiang X.-J., Zhang Y.-P., Wei J.-Y., 2009, Res. Astron. Astrophys., 9, 349
Zong W. et al., 2015, AJ, 149, 84

This paper has been typeset from a TeX/LaTeX file prepared by the author.

LAMOST Spectroscopic Survey of the Galactic Anticentre (LSS-GAC): the second release of value-added catalogues

M.-S. Xiang,[1]★† X.-W. Liu,[2,3]★ H.-B. Yuan,[4] Z.-Y. Huo,[1] Y. Huang,[2]† C. Wang,[2]
B.-Q. Chen,[2]† J.-J. Ren,[2]† H.-W. Zhang,[2] Z.-J. Tian,[2]† Y. Yang,[2,4] J.-R. Shi,[1]
J.-K. Zhao,[1] J. Li,[5] Y.-H. Zhao,[1] X.-Q. Cui,[6] G.-P. Li,[6] Y.-H. Hou,[6] Y. Zhang,[6]
W. Zhang,[1] J.-L. Wang,[1] Y.-Z. Wu,[1] Z.-H. Cao,[1] H.-L. Yan,[1] T.-S. Yan,[1] A.-L. Luo,[1]
H.-T. Zhang,[1] Z.-R. Bai,[1] H.-L. Yuan,[1] Y.-Q. Dong,[1] Y.-J. Lei[1] and G.-W. Li[1]

[1]*Key Laboratory of Optical Astronomy, National Astronomical Observatories, Chinese Academy of Sciences, Beijing 100012, China*
[2]*Department of Astronomy, Peking University, Beijing 100871, China*
[3]*Kavli Institute for Astronomy and Astrophysics, Peking University, Beijing 100871, China*
[4]*Department of Astronomy, Beijing Normal University, Beijing 100875, China*
[5]*Department of Space Science and Astronomy, Hebei Normal University, Shijiazhuang 050024, China*
[6]*Nanjing Institute of Astronomical Optics and Technology, National Astronomical Observatories, Chinese Academy of Sciences, Nanjing 210042, China*

ABSTRACT

We present the second release of value-added catalogues of the LAMOST Spectroscopic Survey of the Galactic Anticentre (LSS-GAC DR2). The catalogues present values of radial velocity V_r, atmospheric parameters – effective temperature T_{eff}, surface gravity log g, metallicity [Fe/H], α-element to iron (metal) abundance ratio [α/Fe] ([α/M]), elemental abundances [C/H] and [N/H] and absolute magnitudes M_V and M_{K_s} deduced from 1.8 million spectra of 1.4 million unique stars targeted by the LSS-GAC since 2011 September until 2014 June. The catalogues also give values of interstellar reddening, distance and orbital parameters determined with a variety of techniques, as well as proper motions and multiband photometry from the far-UV to the mid-IR collected from the literature and various surveys. Accuracies of radial velocities reach 5 km s^{-1} for the late-type stars, and those of distance estimates range between 10 and 30 per cent, depending on the spectral signal-to-noise ratios. Precisions of [Fe/H], [C/H] and [N/H] estimates reach 0.1 dex, and those of [α/Fe] and [α/M] reach 0.05 dex. The large number of stars, the contiguous sky coverage, the simple yet non-trivial target selection function and the robust estimates of stellar radial velocities and atmospheric parameters, distances and elemental abundances make the catalogues a valuable data set to study the structure and evolution of the Galaxy, especially the solar-neighbourhood and the outer disc.

Key words: techniques: spectroscopic – Galaxy: abundance – Galaxy: disc – Galaxy: evolution – Galaxy: formation.

1 INTRODUCTION

Better understanding the structure, stellar populations and the chemical and dynamic evolution of the Milky Way is both a challenge and an opportunity of modern galactic astronomy. The Milky Way is the only galaxy whose distribution of stellar populations can be mapped out in full dimensionality – three-dimensional position

and velocity, age, as well as photospheric elemental abundances. However, owing to our location inside the Milky Way disc, the hundreds of billions of Galactic stars are distributed over the whole sky, and our views in the Galactic disc are seriously limited by the interstellar dust extinction. Obtaining the full dimensional distribution of a complete stellar sample is thus a great challenge. It is only recently that comprehensive surveys of Galactic stars become feasible, thanks to the implementation of a number of large-scale photometric and spectroscopic surveys, such as the Sloan Digital Sky Survey (SDSS; York et al. 2000), the Two Micron All Sky Survey (2MASS; Skrutskie et al. 2006), the Apache Point Observatory

★ E-mail: msxiang@nao.cas.cn (M-SX); x.liu@pku.edu.cn (X-WL)
† LAMOST Fellow

Galactic Evolution Experiment (APOGEE; Majewski et al. 2010), the LAMOST Experiment for Galactic Understanding and Exploration (LEGUE; Deng et al. 2012; Zhao et al. 2012) and the *Gaia* astrometric survey (Perryman et al. 2001; Gaia Collaboration et al. 2016).

As a major component of the LEGUE project, the LAMOST Spectroscopic Survey of the Galactic Anticentre (LSS-GAC; Liu et al. 2014; Yuan et al. 2015) is being carried out with the aim to obtain a statistically complete stellar spectroscopic sample in a contiguous sky area around the Galactic anticentre, taking full advantage of the large number of fibers (4000) and field of view (20 deg^2) offered by LAMOST (Cui et al. 2012). The survey will allow us to acquire a deeper and more comprehensive understanding of the structure, origin and evolution of the Galactic disc and halo, as well as the transition region between them. The main scientific goals of LSS-GAC include: (1) to characterize the stellar populations, chemical composition, kinematics and structure of the thin and thick discs and their interface with the halo, (2) to understand the temporal and secular evolution of the disc(s), (3) to probe the gravitational potential and dark matter distribution, (4) to identify star aggregates and substructures in the multidimensional phase space, (5) to map the interstellar extinction as a function of distance, (6) to search for and study rare objects (e.g. stars of peculiar chemical composition or hypervelocities) and (7) to study variable stars and binaries with multi-epoch spectroscopy.

LSS-GAC plans to collect low-resolution ($R \sim 1800$) optical spectra ($\lambda\lambda 3700$–$9000\,\text{Å}$) of more than 3 million stars down to a limiting magnitude of $r \sim 17.8$ mag (to 18.5 mag for selected fields) in a contiguous sky area of over 3400 deg^2 centred on the Galactic anticentre ($|b| \leq 30°$, $150° \leq l \leq 210°$), and deliver spectral classifications, stellar parameters (radial velocity V_r, effective temperature T_{eff}, surface gravity log g, metallicity [Fe/H], α-element to iron abundance ratio [α/Fe] and individual elemental abundances), as well as values of interstellar extinction and distance of the surveyed stars, so as to build up an unprecedented, statistically representative multidimensional data base for the Galactic (disc) studies. The targets of LSS-GAC are selected uniformly in the planes of ($g - r$, r) and ($r - i$, r) Hess diagrams and in the (RA, Dec.) space with a Monte Carlo method, based on the Xuyi Schmidt Telescope Photometric Survey of the Galactic Anticentre (XSTPS-GAC; Zhang et al. 2013, 2014; Liu et al. 2014; Yuan et al. 2015), a CCD imaging photometric survey of ~ 7000 deg^2 with the Xuyi 1.04-/1.20-m Schmidt Telescope. Stars of all colours are sampled by LSS-GAC. The sampling rates are higher for stars of rare colours, without losing the representation of bulk stars, given the high sampling density ($\gtrsim 1000$ stars per deg^2). This simple yet non-trivial target selection strategy allows for a statistically meaningful study of the underlying stellar populations for a wide range of object class, from white dwarfs (e.g. Rebassa-Mansergas et al. 2015), main-sequence turn-off stars (e.g. Xiang et al. 2015a) to red clump giants (e.g. Huang et al. 2015a), after the selection function has been properly taken into account.

As an extension, LSS-GAC also surveys objects in a contiguous area of a few hundred deg^2 around M31 and M33. The targets include background quasars, planetary nebulae (PNe), H II regions, globular clusters, supergiant stars, as well as foreground Galactic stars. In addition, to make full use of all available observing time, LSS-GAC targets very bright (VB) stars of $r < 14$ mag in sky areas accessible to LAMOST ($-10° \leq$ Dec. $\leq 60°$) in poor observing conditions (bright/grey lunar nights, or nights of poor transparency). Those VB stars comprise an excellent sample supplementary to the main one. Given their relatively low surface densities, at least for the

areas outside the disc, LSS-GAC has achieved a very high sampling completeness (50 per cent) for those VB stars, making the sample a gold mine to study the solar-neighbourhood.

Radial velocities and atmospheric parameters (effective temperature T_{eff}, surface gravity log g, metallicity [Fe/H]) have been deduced from the LSS-GAC spectra for A/F/G/K-type stars using both the official LAMOST Stellar parameter Pipeline (LASP; Wu et al. 2011, 2014) and the LAMOST Stellar Parameter Pipeline at Peking University (LSP3; Xiang et al. 2015b). Typical precisions of the results, depending on the spectral signal-to-noise ratio (SNR) and the spectral type, are a few km s^{-1} for radial velocity V_r, 100–200 K for T_{eff}, 0.1–0.3 dex for log g, 0.1–0.2 dex for [Fe/H] (Gao et al. 2015; Luo et al. 2015; Xiang et al. 2015b; Ren et al. 2016; Wang et al. 2016b). Values of α-element to iron abundance ratio [α/Fe], as well as abundances of individual elements (e.g. [C/H] and [N/H]), have also been derived with LSP3 (Li et al. 2016; Xiang et al. 2017), with precisions similar to those achieved by the APOGEE survey for giant stars (Xiang et al. 2017). Efforts have also been made to derive stellar parameters from LAMOST spectra with other pipelines, such as the SEGUE Stellar Parameter Pipeline (SSPP; Lee et al. 2015) and the Cannon (Ho et al. 2016). Liu et al. (2015) estimate log g using a support vector regression model based on *Kepler* asteroseismic measurements of giant stars. Stellar extinction and distances have been deduced for LSS-GAC sample stars using a variety of methods (Chen et al. 2014; Carlin et al. 2015; Yuan et al. 2015; Wang et al. 2016a), with typical uncertainties of E_{B-V} of about 0.04 mag, and of distance between 10 and 30 per cent, depending on the stellar spectral type (Yuan et al. 2015).

Following a year-long Pilot Survey, LSS-GAC was initiated in 2012 October, and is expected to be complete in the summer of 2017. The LSS-GAC data collected up to the end of the first year of the Regular Survey are public available from two formal official data releases, namely the early (LAMOST EDR; Luo et al. 2012) and first (LAMOST DR1; Luo et al. 2015) data release.[1] The LAMOST EDR includes spectra and stellar parameters derived with the LASP for stars observed during the Pilot Survey, while the LAMOST DR1 includes stars observed by 2013 June. In addition, there is a public release of LSS-GAC value-added catalogues for stars observed by 2013 June, i.e. the LSS-GAC DR1[2] (Yuan et al. 2015). LSS-GAC DR1 presents stellar parameters derived with LSP3, values of interstellar extinction and stellar distance deduced with a variety of methods, as well as magnitudes of broad-band photometry compiled from various photometric catalogues [(e.g. *Galaxy Evolution Explorer* (*GALEX*), SDSS, XSTPS-GAC, UCAC4, 2MASS and *Wide-field Infrared Survey Explorer* (*WISE*)], and values of proper motions from the UCAC4 and PPMXL catalogues and those derived by combing the XSTPS-GAC and 2MASS astrometric measurements, and, finally, stellar orbital parameters (e.g. eccentricity) computed assuming specific Galactic potentials.

This paper presents the second release of value-added catalogues of LSS-GAC (LSS-GAC DR2). LSS-GAC DR2 presents the aforementioned multidimensional parameters deduced from 1796 819 spectra of 1408 737 unique stars observed by 2014 June. Compared to LSS-GAC DR1, in addition to a significant increase in stellar number, several improvements to the data reduction and stellar parameter determinations have been implemented, including: (1) an upgraded LAMOST two-dimensional pipeline has been used

---

[1] http://dr1.lamost.org

[2] http://lamost973.pku.edu.cn/site/data

Table 1. Numbers of spectra and unique stars (in parentheses) observed by LSS-GAC till 2014 June.

	LSS-GAC main survey	M31/M33 survey	VB survey
All SNRs	1332 812 (948 361)	305 226 (171 259)	1944 525 (1431 219)
SNR (4650 Å) >10	510 531 (423 503)	91 921 (65 841)	1194 367 (922 935)
SNR (7450 Å) >10	688 459 (572 438)	68 380 (58 197)	1358 618 (1050 143)
SNR (4650 Å) >10 or SNR(7450) >10	763 723 (618 924)	113 597 (80 452)	1397 538 (1075 677)

to process the spectra; (2) the spectral template library used by LSP3 has been updated, adding more than 200 new templates. The atmospheric parameters for all template stars have also been re-determined/calibrated; (3) values of α-element to iron abundance ratio [α/Fe] have been estimated with LSP3; (4) accurate values of stellar atmospheric parameters ($T_{\rm eff}$, log g, [Fe/H], [α/Fe]), absolute magnitudes M_V and $M_{K_{\rm s}}$, as well as elemental abundances [C/H] and [N/H], have also been estimated from the spectra using a multivariate regression method based on kernel-based principal component analysis (KPCA).

The paper is organized as follows. Section 2 describes the observations of LSS-GAC DR2, including a brief review of the target selection algorithm and the observational footprint. Section 3 introduces the data reduction briefly. Section 4 presents a detailed description of the improvements in stellar parameter determinations incorporated in LSS-GAC DR2. Section 5 briefly discusses the duplicate observations, which accounts for nearly 30 per cent of all observations. Section 6 introduces the determinations of extinction and distance. Section 7 presents the proper motions and derivation of stellar orbital parameters. The format of value-added catalogues is described in Section 8, followed by a summary in Section 9.

2 OBSERVATIONS

To make good use of observing time of different qualities as well as to avoid fibre cross-talking, LSS-GAC stars are targeted by four types of survey plates defined based on *r*-band magnitude (Liu et al. 2014; Yuan et al. 2015). Stars of $r < 14.0$ mag are targeted by the VB plates, and observed in grey/lunar nights, with typical exposure time of $(2–3) \times 600$ s. Stars of $14.0 < r \lesssim 16.3$ mag are targeted by bright (B) plates, and observed in grey/dark nights, with a typical exposure time of 2×1200 s, whereas stars of $16.3 \lesssim r \lesssim 17.8$ mag, and of $17.8 \lesssim r < 18.5$ mag are targeted, respectively, by medium-bright (M) and faint (F) plates, and observed in dark nights of excellent observing conditions (in term of seeing and transparency), with a typical exposure time of 3×1800 s.

By 2014 June, 314 plates (194 B + 103 M + 17 F) for the LSS-GAC main survey, 59 plates (38 B + 17 M + 4 F) for the M31/M33 survey and 682 plates for the VB survey have been observed. Note that the spectra of a few plates could not be successfully processed with the two-dimensional pipeline and are therefore not included in the above statistics. During the survey, some observing time, on the level of one or two grey nights per month, has been reserved for monitoring the instrument performance (e.g. throughput and accuracy of fibre positioning; Liu et al. 2014; Yuan et al. 2015). Some of those reserved nights have been used to target some of the LSS-GAC plates, yielding another 94 observed plates (79 B/M/F + 15 V). Finally, 43 B or M or F LSS-GAC plates were observed from 2011 September to October, when the LAMOST was being commissioned before the start of Pilot Survey. For those 43 plates, the magnitude limits of assigning stars in B/M/F plates are not exactly the same as those adopted during the Pilot and Formal surveys. For convenience, all plates observed using reserved time

as well as those collected during the commissioning phase have been grouped into, as appropriately, the LSS-GAC main, M31/M33 and VB survey, respectively, leading to a total of 395 plates for the LSS-GAC main, 100 plates for the M31/M33 and 697 plates of the VB survey, respectively.

The total numbers of spectra collected and unique stars targeted by those plates are listed in Table 1. Table 1 also lists the numbers of spectra and unique stars that are successfully observed, defined by a spectral SNR of higher than 10 either in the blue (~4650 Å) or the (~7450 Å) part of the spectrum (Liu et al. 2014). The numbers of spectra and stars have increased significantly compared to those of LSS-GAC DR1 that contains, for example, 225 522 spectra of 189 042 unique stars of SNR(4650 Å) >10 for the main survey, and 457 906 spectra of 385 672 unique stars of SNR(4650 Å) >10 for the VB survey (cf. Yuan et al. 2015). Due to the overlapping of LAMOST fields of view of adjacent plates, and the repeating of observations failing to meet the quality control, there is a considerable fraction of stars that have been repeatedly targeted several times. For LSS-GAC DR2, amongst the 948 361 unique stars targeted by the main survey, 71.0, 20.6, 6.0, 1.7, 0.5 and 0.1 per cent of the stars are observed by one to six times, respectively. The corresponding fractions for the M31/M33 survey are 60.1, 20.4, 10.1, 4.4, 2.5 and 1.3 per cent, and those for the VB survey are 73.5, 20.5, 3.7, 1.7, 0.3 and 0.2 per cent. For those unique stars with SNR(4650 Å) >10, the corresponding fractions are 83.6, 13.2, 2.4, 0.6, 0.1 and 0.03 per cent for the LSS-GAC main survey, 72.6, 19.2, 5.6, 1.7, 0.7 and 0.2 per cent for the M31/M33 survey, and 78.3, 17.3, 2.9, 1.2, 0.2 and 0.1 per cent for the VB survey. Note that there are also a small fraction (~0.8 per cent) of stars that are targeted by both the LSS-GAC main (or M31/M33) survey and the VB survey. These duplicates were not considered when calculating the above percentage numbers.

Fig. 1 plots the footprints of the main and M31/M33 surveys, while Fig. 2 plots the footprints of the VB survey. For the main survey, the strategy is to extend the observations of a stripe of Dec. ~29° to both higher and lower declinations (Yuan et al. 2015). Compared to LSS-GAC DR1, LSS-GAC DR2 has completed two more stripes for B and M plates, namely those of Dec. ~34° and ~24°, respectively. A few B and M plates of Galactic latitude $b > 35°$ were observed using either the reserved time or during the commissioning phase. For the M31/M33 survey, seven B and nine M plates were collected in the second year of the Regular Survey (2013 September–2014 June), leading to a much larger sky coverage compared to LSS-GAC DR1. Significant progress in the observation of VB plates is seen in LSS-GAC DR2, in term of both the area and continuity of the sky coverage.

Figs 3–5 plot the density distributions of stars targeted, as well as those successfully observed (i.e. with a spectral SNR higher than 10, either in the blue or red), in the colour–magnitude diagrams (CMDs) for the main, M31/M33 and VB surveys, respectively. For the main and M31/M33 surveys, the diagrams are for colour–magnitude combinations ($g − r$, r) and ($r − i$, r) used to select targets (Yuan et al. 2015). Magnitudes of g, r, i bands are from
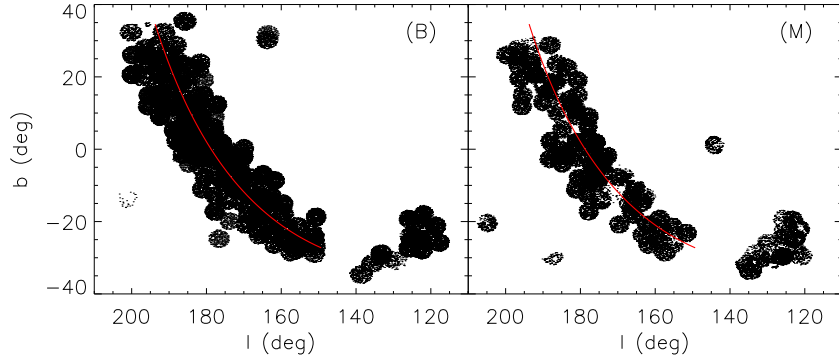
Figure 1. LSS-GAC DR2 footprints in a Galactic coordinate system of stars observed, respectively, with bright (B; left-hand panel) and medium (M; right-hand panel) plates. The red line denotes a constant declination of 30°. To reduce the figure file size, only 1 in 10 observed stars is plotted.
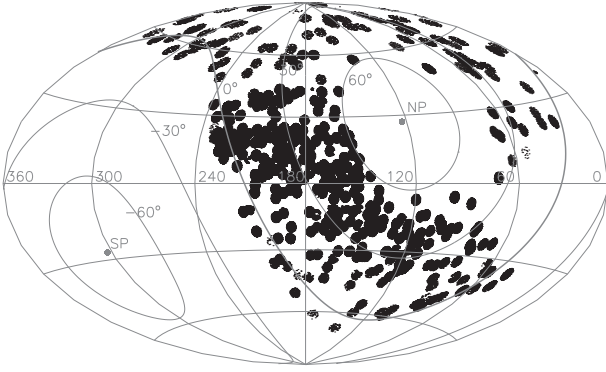
Figure 2. LSS-GAC DR2 footprint for the VB plates. To reduce the figure file size, only 1 in 10 observed stars is plotted.

the XSTPS-GAC survey, except for a few plates of high Galactic latitudes, for which magnitudes from the SDSS photometric survey are used. The figures show that, as planned, stars of all colours have been observed. Figs 3–5 also show that the distributions of stars that have either a blue or red spectral SNR higher than 10, as plotted in the middle panels of those three figures, are quite similar to those targeted, plotted in the top panels of the three figures, except for faint ones ($r > 17.8$ mag). Note that for the main and M31/M33 surveys, some stars of either $r > 18.5$ or $r < 14.0$ mag were observed during the commissioning phase. In contrast, the distributions of stars of SNR(4650 Å) > 10 are quite different – there are fewer faint stars of red colours. This is caused by a combination of the effects of low intrinsic fluxes in the blue of red stars and the lower throughputs of the spectrographs in the blue compared to those in the red (Cui et al. 2012). For the VB survey, ($g - r$, r) and ($J - K_s$, J) diagrams are plotted. The g, r, i magnitudes are taken from the AAVSO Photometric All-Sky Survey (APASS; Munari et al. 2014), which have a bright limiting magnitude of about 10 mag and a faint limiting magnitude (10σ) of about 16.5 mag in g, r, i bands. For stars of $r > 14.0$ mag, magnitudes from the XSTPS-GAC or SDSS surveys are adopted if available. A comparison of stars common to XSTPS-GAC and APASS surveys shows good agreement in both magnitudes and colours for stars of $14.0 < r < 15.0$ mag, with differences of just a few (<5) per cent. Due to the heterogeneous input catalogues and magnitude cut criteria used for the VB survey (Yuan et al. 2015), the morphologies of CMD distributions of VB plates are more complicated than those of the main and M31/M33 plates. Nevertheless, due to the high sampling rates of the VB stars (e.g. Xiang et al. 2015a), and the fact that stars of all colours have
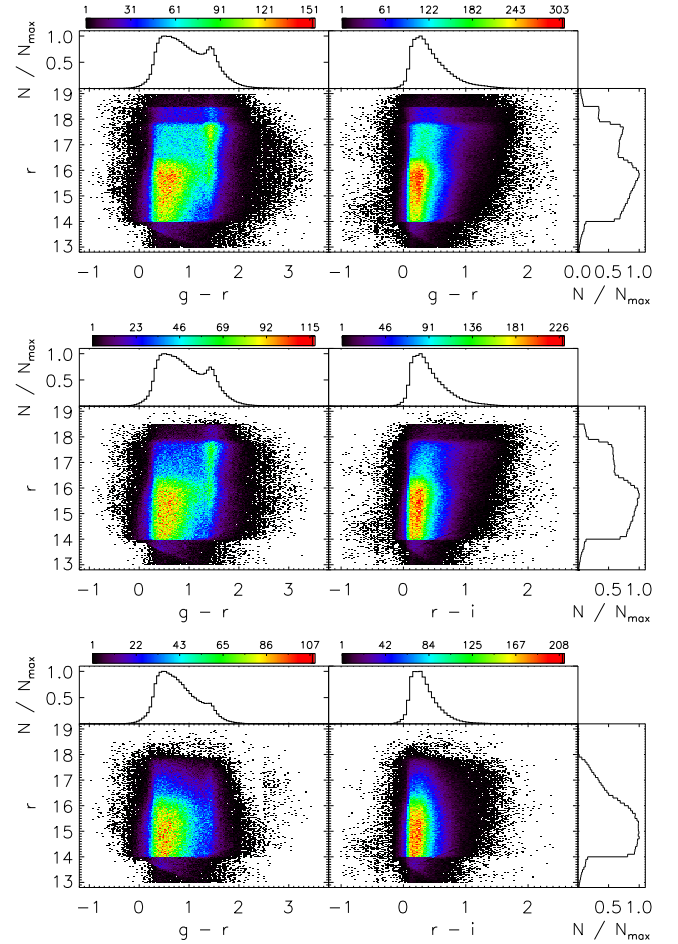
Figure 3. Colour-coded stellar density distributions in the colour–magnitude ($g - r$, r) and ($r - i$, r) diagrams for the LSS-GAC main survey. The upper panels show all observed stars, while the middle panels show those with either SNR(4650 Å) > 10 or SNR(7450 Å) > 10, and the lower panels show those with SNR(4650 Å) >10. The histograms show the one-dimensional distributions of stars in colours ($g - r$) and ($r - i$) or in magnitude r, respectively, normalized to the maximum value.

been observed without a strong colour bias, the selection function can still be well accounted for with some effort and care, if not straightforward. Fig. 6 plots the SNR distribution of spectra for the main, M31/M33 and VB surveys, as well as those of the whole sample for dwarf and giant stars. Only spectra with either SNR
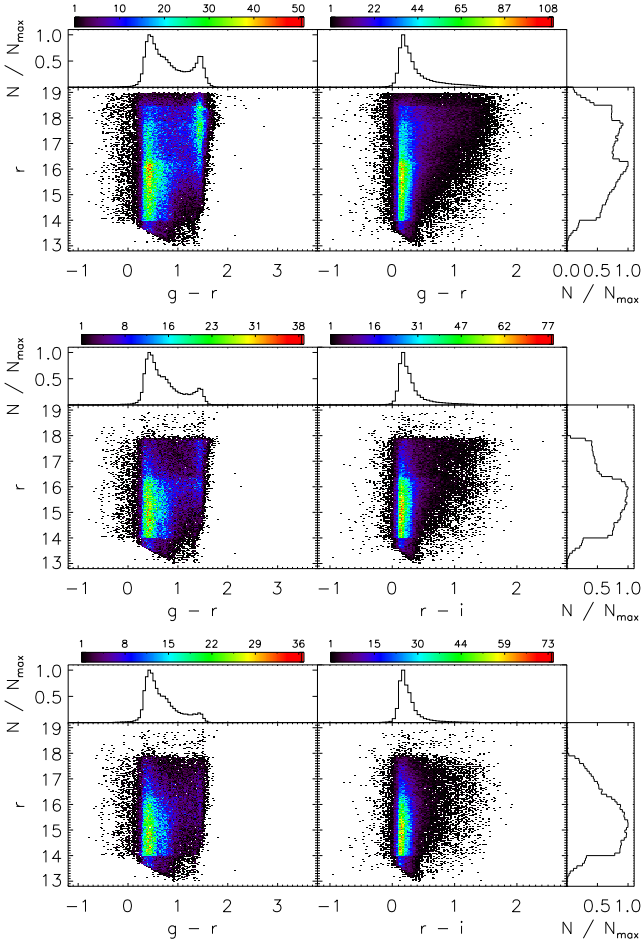
Figure 4. Same as Fig. 3 but for the M31/M33 survey.

Figure 5. Same as Fig. 3 but for the VB survey. CMDs of $(g - r, r)$ and $(J - K_s, J)$ are shown.

(4650 Å) or SNR (7450 Å) higher than 10 are plotted. The number of spectra in logarithmic scale decreases approximately linearly with increasing SNR. SNRs of the red part of the spectra are generally higher than those of the blue part. Also, spectra of the VB survey have generally higher SNRs than those of the main and M31/M33 surveys. Distribution of SNRs for the giants are similar to those of the dwarfs. Here the classification of dwarfs and giants is based on the results of LSP3 (cf. Section 4). For the whole sample, about 36, 57 and 73 per cent of the spectra have an SNR higher than 50, 30 and 20, respectively, in the blue part of the spectrum.

3 DATA REDUCTION

The raw spectra of LSS-GAC used to generate the value-added catalogues were processed at Peking University with the LAMOST two-dimensional reduction pipeline (Luo et al. 2012, 2015) to extract the one-dimensional spectra. This process includes several basic reduction steps, including bias subtraction, fibre tracing, fibre flat-fielding, wavelength calibration and sky subtraction. Both fibre tracing and flat-fielding were first carried out using twilight flat-fields. The results were further revised using sky emission lines when processing the object spectra to account for the potential shifts of fibre traces and the variations in fibre throughput. Typical precision of fibre flat-fielding, as indicated by the dispersions of flat-fields acquired in different days, is better than 1 per cent. Wavelength calibration was carried out using exposures of a Cd–Hg arc lamp for the blue-arm spectra and an Ar–Ne arc lamp for the red-arm spectra.

Figure 6. Distribution of spectral SNRs for the main (top left-hand panel), M31/M33 (top right-hand panel) and VB (bottom left-hand panel) surveys. Blue and red lines represent spectral SNR at 4650 and 7450 Å, respectively. The bottom right-hand panel plots SNR (4650 Å) for the whole sample that have a spectral SNR (4650 Å) higher than 10 for dwarfs (solid line) and giants (dashed line), respectively.

Typically, the residuals of wavelength calibration for the individual arc lines have a mean value close to zero and a standard deviation of ~0.02 Å, which corresponds to ~1 km s^{-1} in velocity space. When processing the object spectra, sky emission lines are used to adjust the wavelengths to account for any residual systematic errors in the wavelength calibration and/or potential wavelength drifts between the arc-lamp and object spectra. A comparison of stellar radial velocities with the APOGEE measurements for LAMOST-APOGEE common stars yields an offset of −3 to −4 km s^{-1} (Luo et al. 2015; Xiang et al. 2015b), and the offset is found to be stable in the past few years, with typical night-to-night variations of about 2 km s^{-1}. For each of the 16 spectrographs, about 20 fibres are typically assigned to target sky background for sky subtraction. The numbers of sky fibres allocated for sky measurement are higher for plates of low source surface density, e.g. VB plates of $|b| > 10°$. To subtract the sky background, the two-dimensional pipeline creates a supersky by the B-spline fitting of fluxes measured by the individual sky fibres. The measured fluxes of sky emission lines in the object spectra are normalized to those of the super-sky spectrum to correct for potential differences of throughputs of fibres used to measure the sky and the objects. The correction assumes that the strengths of the sky emission lines are constant across the sky area covered by a given spectrograph, which is about 1 deg^2, and any differences in sky emission-line fluxes, as measured by the sky and object fibres, are caused by errors in flat-fielding. The correction also assumes that for the sky background, the continuum scales with emission-line flux.

The resultant one-dimensional spectra were then processed with the flux calibration pipeline developed specifically for LSS-GAC to deal with fields of low Galactic latitudes that may suffer from substantial interstellar extinction. The pipeline generates flux-calibrated spectra as well as co-adds the individual exposures of a given plate (Xiang et al. 2015c; Yuan et al. 2015). To deal with the interstellar extinction, the pipeline calibrates the spectra in an iterative way, using F-type stars selected based on the stellar atmospheric parameters yielded by LSP3 as flux standards. The theoretical synthetic spectra from Munari et al. (2005) of the same atmospheric parameters are adopted as the intrinsic spectral energy distributions (SEDs) of the standards. Typical (relative) uncertainties of the spectral response curves thus derived are about 10 per cent for the wavelength range of 4000–9000 Å (Xiang et al. 2015c).

Compared to the pipelines used to generate LSS-GAC DR1, a few improvements have been implemented: (1) Several fibres of Spectrograph #4 are found to be misidentified before 2013 June (Luo, private communication). As a result, the coordinates, magnitudes, spectra and stellar parameters of stars targeted by those fibres were wrongly assigned in LAMOST DR1 (Luo et al. 2015) as well as LSS-GAC DR1 (Yuan et al. 2015). The fibres are: #76 (87), 87 (79), 79 (95), 95 (84), 84 (76), 44 (31), 31 (46), 46 (26) and 26 (44), where the numbers in the brackets are the correct ones. The errors have been corrected; (2) The values of interstellar reddening of flux standard stars are now derived with the star-pair method (Yuan et al. 2015), replacing those deduced by comparing the observed and synthetic colours, as adopted in LSS-GAC DR1. The change is based on the consideration that the star-pair method for extinction determination is model-free, and yields, in general, more robust results than the method adopted for LSS-GAC DR1 (Yuan et al. 2015); (3) For the flux calibration of VB plates, *g*, *r*, *i* magnitudes from the APASS survey (Munari et al. 2014) are combined with 2MASS *J*, *H*, *K*$_s$ magnitudes to derive values of extinction of flux calibration standard stars. In LSS-GAC DR1, only 2MASS *J*, *H*, *K*$_s$ magnitudes were used. The change should significantly

improve the accuracy of extinction estimates for standards used to flux-calibrate VB plates.

Considering that the SNR alone does not give a fully description of the quality of a spectrum, a few flags are now added to the image header of a processed spectrum. The first flag is the ratio of (sky-subtracted) stellar flux to the flux of (super-) sky adopted for sky-subtraction. Due to the uncertainties in sky-subtraction, the spectra of some stars, especially those observed under bright lunar conditions, may have artificially high SNRs, yet this ratio can be, in fact, quite small for those spectra. The flag is denoted by 'OBJECT_SKY_RATIO' in the value-added catalogues. A second flag is used to mark fibres that maybe potentially affected by the nearby saturated fibres. Saturation occurs for the VB stars. When a fibre saturates, spectra of nearby fibres, especially those of faint stars, can be seriously contaminated by flux crosstalk, leading to incorrect SNRs and wrongly estimated stellar parameters. When a fibre saturates, stars observed by the adjacent 50 fibers (±25) are now marked by flag 'SATFLAG' in the value-added catalogues. Even when a fibre is not saturated, crosstalk may still occur if the flux of that fibre is very high. To account for such situation, a third flag is introduced. If the spectrum from a given fibre has an SNR higher than 300, then the adjacent 4 (±2) fibres are assigned a 'BRIGHTFLAG' value of 1; otherwise, the flag has a value of 0. For each fibre, the value of maximum SNR of the nearest five fibres (the adjacent four plus the fibre of concern itself) is also listed as 'BRIGHTSNR' in the value-added catalogues. Finally, a flag has been created to mark bad fibres. Among the 4000 fibres of LAMOST, some have very low throughputs or suffer from serious positioning errors. Spectra yielded by those 'bad' fibers cannot be trusted. The number of bad fibres continuously increases with time, and reaches about 200 by 2014 June. Those fibers are marked by 'BADFIBRE' in the value-added catalogues. In addition to those newly created flags, information of observing conditions with regard to the moon (phase, angular distance), the airmass and the pointing position of the telescope are now also included in LSS-GAC DR2.

4 STELLAR PARAMETER DETERMINATION: IMPROVEMENTS OF LSP3

LSS-GAC DR1 presents values of radial velocity V_r and stellar atmospheric parameters (effective temperature T_{eff}, surface gravity log *g*, metallicity [Fe/H]) derived from LSS-GAC spectra with LSP3. Since then, a few improvements of LSP3 have been implemented and are included in LSS-GAC DR2, including: (1) A number of new spectral templates have been added to the MILES library, and atmospheric parameters of the template stars have been re-determined/calibrated; (2) Several flags are now assigned to describe the best-matching templates that have the characteristics of a, for example, variable star, binary, double/multiple star or supergiant, etc., of a given target spectrum; (3) Values of α-element to iron abundance ratio [α/Fe] have been estimated by template matching with a synthetic spectral library; (4) A multivariate regression method based on KPCA has been used to obtain an independent set of estimates of stellar atmospheric parameters, including T_{eff}, log *g*, [M/H], [Fe/H], [α/M], [α/Fe], absolute magnitudes M_V and M_{K_s} as well as individual elemental abundances including [C/H] and [N/H].

4.1 Updates to the MILES library

The original MILES spectral library contains medium-to-low resolution (full width at half-maximum, FWHM ~2.5 Å) long-slit

spectra of the wavelength range of 3525–7410 Å for 985 stars that have robust stellar parameter estimates in the literature, mostly determined with high-resolution spectroscopy (Sánchez-Blázquez et al. 2006; Falcón-Barroso et al. 2011). The MILES library is adopted by LSP3 as templates for estimation of atmospheric parameters from LAMOST spectra. Compared to other template libraries available in the literature, MILES has two advantages. First, the MILES spectra have robust flux calibration and the spectral resolution matches well that of the LAMOST spectra. Secondly, the template stars cover a large volume of parameter space ($3000 < T_{eff} < 40, 000$ K, $0 < \log g < 5$ dex and $-3.0 < $ [Fe/H] < 0.5 dex).

Still, for the purpose of accurate stellar atmospheric parameter estimation, the MILES library has a few defects in need of improvement. One is the limited spectral wavelength coverage. LAMOST spectra cover the full optical wavelength range of 3700–9000 Å, whereas MILES spectra stop at 7410 Å in the red. As a result, LAMOST spectra in the 7400–9000 Å wavelength range have hitherto not been utilized for parameter estimation. There are a few prominent features in this wavelength range that are sensitive abundance indicators, including, e.g. the Ca II λλ8498, 8542, 8664 triplet and the Na I λλ8193, 8197 doublet. In addition, since LSS-GAC targets stars of all colours, especially those in the disc, about 30 per cent spectra collected have poor SNRs in the blue but good SNRs in the red. Those stars are either intrinsically red or suffer from heavy interstellar extinction. Stellar parameters for those stars have currently not been derived from LAMOST spectra, by either LSP3 or LASP, due to the fact that both the MILES and ELODIE (adopted by LASP) libraries do not have wavelength coverage long enough in the red. Another defect of the MILES library is the inhomogeneous coverage of stars in the parameter space. As shown in Xiang et al. (2015b), there are holes and clusters in the distribution of MILES stars in the parameter space, leading to some significant artefacts in the resultant parameters. Finally, stellar atmospheric parameters of the original MILES library are collected from various sources in the literature, which thus suffer from systematic errors. Although Cenarro et al. (2007) have taken the effort to homogenize the parameters in order to account for the systematics amongst the values from the different sources, the homogenization was carried out for only a limited temperature range of $4000 < T_{eff} < 6300$ K. With more data available, there is a room for considerable improvement.

To deal with the limited wavelength coverage of the MILES spectra and to improve the coverage and distribution of template stars in the parameter space, an observational campaign is being carried out to observe additional template stars that fill the holes in parameter space, to enlarge the coverage of parameter space, as well as to extend the spectral wavelength coverage to 9200 Å, using the NAOC 2.16-m telescope and the YAO 2.4-m telescope (Wang et al., in preparation). The project plans to obtain long-slit spectra covering 3600–9200 Å for some 900 template stars newly selected from the PASTEL catalogue (Soubiran et al. 2010), which is a compilation of stars with robust stellar parameters, mostly inferred from high-resolution spectroscopy. The project will also extend the wavelength coverage of all the original MILES spectra to 9200 Å. In this work, 267 new template spectra obtained by the campaign till 2015 October have been added to the MILES library to generate parameter estimates presented in LSS-GAC DR2. In addition, to reduce systematic and random errors of the atmospheric parameters of the template stars, Huang et al. (in preparation) have re-calibrated/determined the atmospheric parameters of all template stars, both old and newly selected. In doing so, the recent determi-
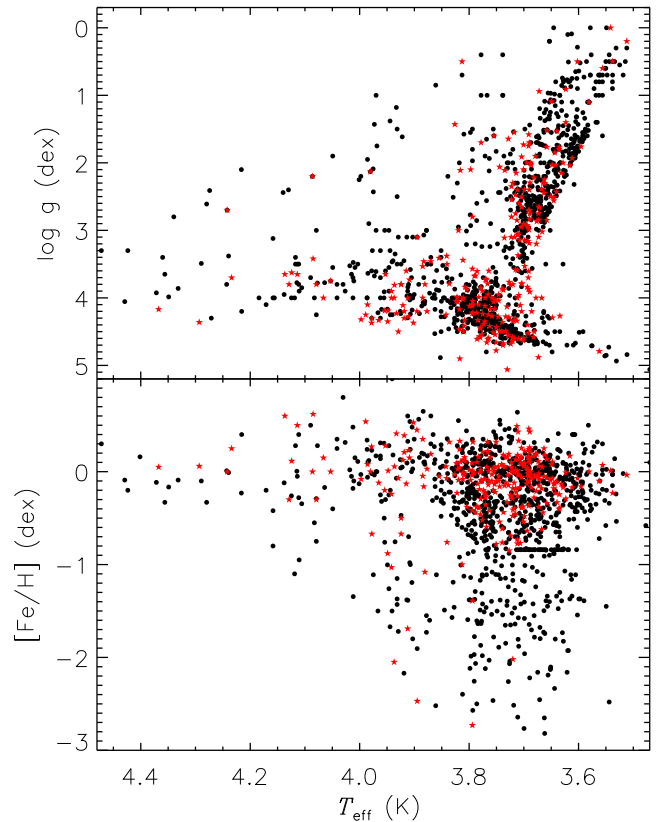
Figure 7. Distributions of template stars used by LSP3 in the T_{eff}–$\log g$ and T_{eff}–[Fe/H] planes. Black dots represent stars in the original MILES library, while red dots represent 267 newly observed templates employed in the generation of LSS-GAC DR2 (see the text).

nations of parameters of template stars available from the PASTEL catalogues have been adopted, replacing the older values used by the original MILES library. The updated values of metallicity are then used to calculate effective temperatures using the newly published metallicity-dependent colour–temperature relations of Huang et al. (2015c), deduced from more than two hundred nearby stars with direct, interferometric angular size measurements and *Hipparcos* parallaxes. Values of surface gravity are re-determined using *Hipparcos* parallaxes (Perryman et al. 1997; Anderson & Francis 2012) and stellar isochrones from the Dartmouth Stellar Evolution Database (Dotter et al. 2008). Values of [Fe/H] are then re-calibrated to the standard scale of *Gaia*-ESO survey (Jofré et al. 2015). Fig. 7 plots the newly calibrated/determined parameters of the template stars in the T_{eff}–$\log g$ and T_{eff}–[Fe/H] planes. Note that in generating LSS-GAC DR1, 85 of the original MILES stars were abandoned because there were no complete parameter estimates in the literatures. Those stars are now included in the library as their parameters have been re-determined. Also, with the newly selected and observed templates added to the library, we have now discarded the 400 interpolated spectra used when generating LSS-GAC DR1.

4.2 [α/Fe] estimation by matching with synthetic spectra

α-element to iron abundance ratio [α/Fe] is a good indicator of the Galactic chemical enrichment history (e.g. Lee et al. 2011), and thus valuable to derive. To estimate [α/Fe] from LAMOST spectra, a method of template matching based on χ^2-fitting with synthetic spectra is developed for LSP3. Details about the

Table 2. Grids of KURUCZ synthetic spectra for [α/Fe] estimation.

Parameter	Range	Step
T_{eff}	[4000, 8000] K	100 K
log g	[0.0, 5.0] dex	0.25 dex
[Fe/H]	[−4.0, 0.5] dex	0.2 dex for [Fe/H] < −1.0 dex
		0.1 dex for [Fe/H] > −1.0 dex
[α/Fe]	[−0.4, 1.0] dex	0.1 dex

method and robustness tests of the deduced [α/Fe] values are described in Li et al. (2016). Here we briefly summarize the method and point out a few improvements that may lead to better results.

The synthetic library used to estimate [α/Fe] was generated with the SPECTRUM code (Gray 1999) of version 2.76, utilizing the Kurucz stellar model atmospheres of Castelli & Kurucz (2004). The solar [α/Fe] ratio is set to zero, and the α-enhanced grids are generated by scaling the elemental abundances of O, Mg, Si, S, Ca and Ti, and those of C and N abundances are also enhanced by the amount of α-elements. Lines from more than 15 diatomic molecule species, including H_2, CH, NH, OH, MgH, AlH, SiH, CaH, C_2, CN, CO, AlO, SiO, TiO and ZrO, are taken into account in the calculation of the opacity. Isotope lines are also taken into account. In total, 320 000 synthetic spectra are generated. Table 2 lists the parameter ranges and steps of the grids. Note that the grids adopted here have a step of 0.1 dex in [α/Fe], half of the value used in Li et al. (2016). All the computed synthetic spectra have a resolution of 2.5 Å FWHM, and is invariant with wavelength.

For a target spectrum with atmospheric parameters T_{eff}, log g and [Fe/H] yielded by LSP3, the synthetic spectra are interpolated to generate a set of spectra that have the same atmospheric parameters as the target for all grid values of [α/Fe]. Values of χ^2 between the target and the individual interpolated synthetic spectra are then calculated. A Gaussian plus a second-order polynomial is then used to fit the deduced χ^2 as a function of [α/Fe]. The value of [α/Fe] that yields minimum χ^2 is taken to be the [α/Fe] ratio of the target spectrum. To compute χ^2, Li et al. (2016) use spectral segments 4400–4600 and 5000–5300 Å. The 4400–4600 Å segment contains mainly Ti features, while that of 5000–5300 Å contains mainly Mg I features, as well as a few features of Ca, Ti and Si. Note that given the low resolution as well as limited SNRs of LAMOST spectra, Ca, Ti and Si features within those two spectral segments contribute, in fact, only a small fraction of the calculated values of χ^2, and are therefore not very useful for the determination of [α/Fe]. In metal-rich stars, the Mg I b features are, in general, prominent enough for a robust determination of [α/Fe]. However, in metal-poor ([Fe/H] < −1.0 dex) stars, the Mg I b lines become less prominent so that the [α/Fe] have larger uncertainties. In this work, in order to improve precision of [α/Fe] estimates, especially for metal-poor stars, we have opted to include the 3910–3980 Å spectral segment that contains the Ca II HK lines in the calculation of χ^2 values. Meanwhile, as an option, we also provide results yielded using the exactly same spectral segments as Li et al. (2016). This is useful considering that the strong Ca II HK lines in model spectra for metal-rich stars are maybe not accurately synthesized.

The resolution of LAMOST spectra from individual fibers varies from one to another, as well as with wavelength (Xiang et al. 2015b). To account for this in template matching, the synthetic spectra are degraded in resolution to match that of the target spectrum. The

latter is derived utilizing the arc spectrum. The deduced resolution as a function of wavelength is further scaled to match the resolution yielded by sky emission lines detected in the target spectrum in order to account for systematic variations of spectral resolution between the arc and target exposures. Typically, for a given spectrograph, fibre-to-fibre variations of spectral resolution amount to 0.3 Å, rising to 0.5–1.0 Å among the different spectrographs. Systematic variations of spectral resolution between the arc and target exposures are found to be typically 0.2 Å.

In addition, in order to allow for possible uncertainties in the input atmospheric parameters T_{eff}, log g and [Fe/H] yielded by LSP3 as well as any possible mismatch between the LSP3 atmospheric parameters and those of the Kurucz stellar model atmospheres, in this work, we have opted not to fix the input values of T_{eff}, log g and [Fe/H] as yielded by LSP3, but allow them to vary in limited ranges around the initial values. The ranges are set to 2σ uncertainties of the parameters concerned, with lower limits of 500 K, 0.5 and 0.5 dex, and upper limits of 1000 K, 1.0 and 1.0 dex for T_{eff}, log g and [Fe/H], respectively. For each grid value of [α/Fe], the synthetic spectrum that has atmospheric parameters T_{eff}, log g and [Fe/H] within the above ranges and fits the target spectrum best (i.e. yielding the smallest χ^2) is taken as the choice of synthetic spectrum when fitting and deriving [α/Fe] using the technique described in Li et al. (2016).

Values of [α/Fe] are derived with the above algorithm for all LSS-GAC DR2 stars of a spectral SNR higher than 15. The left-hand panel in the third row of Fig. 9 plots the density distribution of LSS-GAC DR2 dwarf stars in the [Fe/H]–[α/Fe] plane. Here, the [α/Fe] are those derived using spectra including the 3910–3980 Å segments. The figure shows an [α/Fe] plateau for metal-poor ([Fe/H] < −1.0 dex) stars, at a median value about 0.4 dex. For more metal-rich stars, [α/Fe] decreases with increasing [Fe/H], reaching a median value of zero near the solar metallicity, which means that the zero-point offset, i.e. deviations of [α/Fe] values from zero at solar metallicity, is small, which is in contrast to Li et al. (2016) who find a zero-point offset of −0.12 dex. However, we indeed find a zero-point offset of about −0.1 dex for [α/Fe] derived using only the 4400–4600 and 5000–5300 Å segments, which is basically consistent with Li et al. (2016). The offset is found to be mainly contributed by the 4400–4600 Å segment. The causes of this difference are not fully understood yet. We suspect there may be some unrealistic inputs in either the atmosphere model or the atomic and molecular data used to generate the synthetic spectra. Note that here we opt not to introduce any external corrections on the estimated [α/Fe]. Random errors of [α/Fe] induced by spectral noises, as estimated by comparing the results deduced from duplicate observations, are a function of spectral SNR and atmospheric parameters T_{eff}, log g and [Fe/H], and have typical values that decrease from ∼0.1 to ∼0.05 dex as the spectral SNR increases from 20 to a value higher than 50. To provide a realistic error estimate for [α/Fe], the random error induced by spectral noises is combined with the method error, which is assumed to have a constant value of 0.09 dex, estimated by a comparison with high-resolution measurements (cf. Li et al. 2016).

For giant stars, [α/Fe] estimated with the above algorithm exhibits a zero-point offset between 0.1 and 0.2 dex, probably caused by inadequacies of the synthetic spectra for giant stars. In this work, no corrections for those offsets are applied. Note that for giant stars, [α/Fe] values are also estimated with the KPCA regression method using the LAMOST-APOGEE common stars as the training data set (cf. Section 4.3), and the resultant values are presented as the recommended ones (cf. Section 4.6).

4.3 Stellar atmospheric parameters estimated with the KPCA method

The LSP3 version used to generate LSS-GAC DR1 estimates stellar atmospheric parameters T_{eff}, $\log g$ and [Fe/H] with a χ^2-based weighted-mean algorithm. The algorithm achieves a high precision in the sense that random errors of the deduced parameters induced by spectral noises are well controlled, even for stars of SNRs as low as 10. Nevertheless, parameters estimated with the weighted-mean algorithm suffer from several artefacts. One is the so-called suppression effect – values of the derived $\log g$ are narrowed down to an artificially small range. This is partly caused by the fact that χ^2 calculated from a LAMOST spectrum with respect to a template spectrum is only moderately sensitive to $\log g$, thus the sets of templates used to calculate the weighted-mean values of $\log g$ for the individual target sources often have similar distributions in $\log g$. Another artefact is the so-called boundary effect – parameters of stars with true parameters that pass or are close to the boundary of parameter space covered by the templates are often either underestimated or overestimated systematically by the weighted-mean algorithm. This effect is especially serious for [Fe/H] and $\log g$ estimation. Finally, due to the inhomogeneous distribution of templates in the parameter space, moderate clustering effect is also seen in the deduced parameter values.

To overcome the above defects of the weighted-mean algorithm, a regression method based on the KPCA has recently been incorporated into LSP3 (Xiang et al. 2017). The method is implemented in a machine learning scheme. A training data set is first defined to extract non-linear principal components (PCs, and the loading vectors) as well as to build up regression relations between the PCs and the target parameters. Four training data sets are defined for the determination of specific sets of parameters of specific types of stars. They are: (1) the MILES library for the estimation of T_{eff} and [Fe/H] of A/F/G/K stars, and for the estimation of $\log g$ of stars that have $\log g$ values larger than 3.0 dex, as given by the weighted-mean algorithm. The latter stars are mainly dwarfs and sub-giants; (2) a sample of LAMOST-*Hipparcos* common stars with accurate parallax (thus, distance and absolute magnitude) measurements for the estimation of absolute magnitudes (M_V and M_{K_s}) directly from LAMOST spectra; (3) a sample of LAMOST-*Kepler* common stars with accurate asteroseismic $\log g$ measurements for the estimation of $\log g$ of giant stars; and (4) a sample of LAMOST-APOGEE common stars for the estimation of metal abundance [M/H], α-element to iron (metal) abundance ratio [α/Fe] ([α/M]) and of individual elemental abundances including [Fe/H], [C/H] and [N/H] for giant stars. A detailed description of the implementation and test of the method is presented in Xiang et al. (2017). Here we note two updates of the implementation with respect to those of Xiang et al. (2017). One is that a unified number of PCs of 100 is adopted except for the estimation of absolute magnitudes with the LAMOST-*Hipparcos* training set, for which both 100 and 300 PCs are adopted. Another modification is that additional training stars have been added to the LAMOST-*Kepler* and LAMOST-APOGEE training sets as a result that more common stars become available as the surveys progress. Both training sets now contain (exactly) 3000 stars.

Compared to the weighted-mean results, $\log g$ and [Fe/H] derived with the KPCA regression method using the MILES training set have been found to suffer from less systematics, and thus better for statistical analyses. A comparison with asteroseismic measurements shows that for stars of $T_{eff} < 6000$ K and [Fe/H] $> −1.5$ dex, uncertainties of KPCA $\log g$ estimates can be as small as 0.1 dex for spectral SNRs higher than 50. The uncertainties increase sub-

stantially as the SNR deteriorates, reaching ~ 0.2 dex at an SNR of 20 (Xiang et al. 2017). Similarly, comparisons with [Fe/H] determinations from high-resolution spectroscopy show that uncertainties of KPCA [Fe/H] estimates are ~ 0.1 dex for good SNRs. For metal-poor ([Fe/H] $< −1.5$ dex) or hot ($T_{eff} > 8000$ K) stars, KPCA estimates of both $\log g$ and [Fe/H] become less reliable, and should be used with caution. Systematic differences between KPCA and weighted-mean estimates of T_{eff} exist for stars hotter than ~ 6500 K, with deviations reach as much as ~ 300 K for stars of $T_{eff} \sim 7500$ K. More studies are needed to understand the cause of deviations. For the time being, we recommend weighted-mean T_{eff} values as they are estimated in a straightforward way and well validated (Xiang et al. 2015b). However, note that weighted-mean estimates of T_{eff} suffer from clustering effect so that they may weakly clump in the parameter space on the scale of a few tens of Kelvin, while the KPCA estimates of T_{eff} do not have such problem.

Surface gravities of giant stars of $T_{eff} < 5600$ and $\log g < 3.8$ dex are estimated with the KPCA method using the LAMOST-*Kepler* training set. Here, the cuts of T_{eff} and $\log g$ are based on values yielded by the weighted-mean method. The KPCA estimate of $\log g$ is likely to be accurate to 0.1 dex, given a spectral SNR higher than 50. The uncertainty increases to ~ 0.2 dex at an SNR of 20 (Huang et al. 2015b; Xiang et al. 2017).

Absolute magnitudes M_V and M_{K_s} of all stars with a weighted-mean effective temperature lower than 12 000 K are estimated directly from LAMOST spectra using the LAMOST-*Hipparcos* training set. Two sets of absolute magnitudes are given, corresponding to, respectively, 100 and 300 PCs adopted for parameter estimation. For absolute magnitudes estimated using 100 PCs, typical uncertainties are 0.3–0.4 mag in both M_V and M_{K_s} for a spectral SNR higher than 50, and the values increase to ~ 0.6 mag at an SNR of 20. For absolute magnitudes estimated using 300 PCs, uncertainties are only 0.2–0.3 mag for a spectral SNR higher than 50, but the results are more sensitive to the SNR, with a typical uncertainty of ~ 0.7 mag at an SNR of 20. A significant advantage of estimating absolute magnitudes directly from the observed spectra is that the magnitudes as well as the resultant distance moduli are model independent. Fig. 8 plots a comparison of the estimates of M_{K_s} for 300 PCs as well as the distances, thus estimated with results inferred from the *Gaia* TGAS parallaxes (Lindegren et al. 2016) for a sample of 50 000 LAMOST-TGAS common stars that have a TGAS-based magnitude error smaller than 0.2 mag. Here the TGAS distances and M_{K_s} values are derived using values of interstellar extinction derived with the star-pair method (cf. Section 6.1). The figure shows very good agreement between our estimates and the TGAS results. Systematics in both M_{K_s} and distance estimates are negligible, and the dispersion is only 0.26 mag for M_{K_s}, 12 per cent for distance. A similar comparison of results yielded using 100 PCs yields a mean difference of 0.04 mag and a dispersion of 0.29 mag in M_{K_s}, and a mean difference of $−2$ per cent and a dispersion of 13 per cent in distance estimates. Of course, spectral SNRs for the LAMOST-TGAS common stars are very high, which have a median value of 150, as the stars are very bright. Note that Fig. 8 also shows a positive non-Gaussian tail in the difference of M_{K_s}, with a corresponding negative tail in the difference of distance. This non-Gaussian tail is likely caused by binary stars, for which the estimates of absolute magnitudes from LAMOST spectra are only marginally affected, whereas the photometric magnitudes are underestimated with respect to those assuming single stars. Note that not all the LAMOST-TGAS stars used for the comparison can be found in the LSS-GAC value-added catalogues, as many of them are targeted by other survey projects of LAMOST. The spectra of
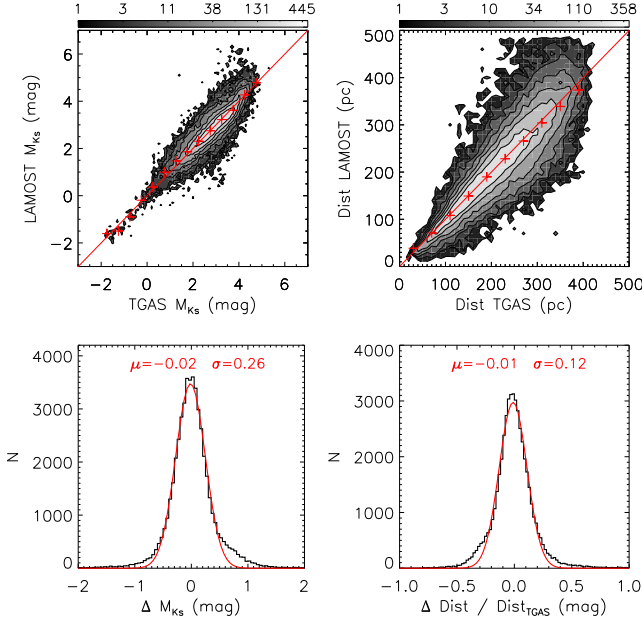
Figure 8. Comparison of absolute magnitudes and distances with those inferred from *Gaia* TGAS parallax for 50 000 LAMOST-TGAS common stars that have a TGAS-based magnitude error smaller than 0.2 mag. The upper panels shows colour-coded contours of stellar number density in logarithmic scale. Crosses in red are median values of our estimates calculated in bins of the TGAS-based values. The lower panels plot the distribution of differences of magnitudes and distances between our estimates and the TGAS-based values. Red lines are Gaussian fits to the distribution, with the mean and dispersion of the Gaussian marked in the plot.

those stars have been processed with LSP3 and the data are only internally available for the moment.

Metal (iron) abundance [M/H] ([Fe/H]), α-element to metal (iron) abundance ratio [α/M] ([α/Fe]), as well as abundances of carbon and nitrogen, [C/H] and [N/H], are estimated using the LAMOST-APOGEE training set. Xiang et al. (2017) have demonstrated that the results have a precision comparable to those deduced from APOGEE spectra with the ASPCAP pipeline (García Pérez et al. 2016; Holtzman et al. 2015). Specifically, estimates of [M/H], [Fe/H], [C/H] and [N/H] have a precision better than 0.1 dex, given a spectral SNR high than 30, and ~0.15 dex for a SNR of 20. We note, however, since the APOGEE stellar parameters are not externally calibrated except for [M/H], any systematics in the APOGEE results propagated into ours through the training set. As pointed out by Holtzman et al. (2015), APOGEE estimates of elemental abundances may suffer from systematic biases of about 0.1–0.2 dex. For [M/H], the APOGEE values are calibrated to [Fe/H] measurements of star clusters for [Fe/H] range [−2.5, 0.5] dex. Nevertheless, it is found that [Fe/H] ([M/H]) estimated with the LAMOST-APOGEE training set are systematically 0.1 dex higher than those estimated with the MILES library. Such an overestimation is also confirmed by examining common stars with high-resolution spectroscopic [Fe/H] measurements available from the PASTEL catalogue. The discrepancy is likely due to an offset in absolute value between the APOGEE and MILES (PASTEL) metallicities. The estimated [α/M] ([α/Fe]) values have a typical precision of 0.03–0.06 dex, given a spectral SNR higher than 20. Xiang et al. (2017) have demonstrated that as a consequence of such a high precision, a clear distinction between the sequences of thick and thin disc stars is seen in the [M/H] ([Fe/H])–[α/M] ([α/Fe]) plane, quite similar to that revealed

by results from high-resolution spectroscopy. Note, however, that for stars with [α/M] higher than 0.30 dex or lower than 0.0 dex, the KPCA values are probably systematically underestimated or overestimated due to a lack of training stars of such abundance ratios. In addition, given that APOGEE [α/M] ([α/Fe]) values are not externally calibrated, there may also be some systematics hidden in our results.

4.4 Estimation of parameter errors

Errors of the deduced stellar parameters are estimated in a statistical way. Parameter errors contributed by both spectral noises and inadequacies of the method are taken into account. For $T_{\rm eff}$, log g and [Fe/H] estimated by the weighted-mean algorithm, or those by the KPCA method using the MILES training set, as well as M_V and $M_{K_{\rm s}}$ estimated by the KPCA method using the LAMOST-*Hipparcos* training set, parameter errors induced by spectral noises and those by the method are estimated separately. Errors induced by spectral noises, as in the case of LSS-GAC DR1, are estimated by comparing results derived from duplicate observations made in different nights, and are estimated separately for giants (log g < 3.5 dex) and dwarfs (log g > 3.5 dex). The results are fitted with a second-order polynomial function of SNR, $T_{\rm eff}$ and [Fe/H],

$$\sigma = c_0 + c_1 \times {\rm SNR} + c_2 \times T_{\rm eff} + c_3 \times {\rm [Fe/H]} + c_4 \times {\rm SNR}^2$$
$$+ c_5 \times T_{\rm eff}^2 + c_6 \times {\rm [Fe/H]}^2 + c_7 \times {\rm SNR} \times T_{\rm eff}$$
$$+ c_8 \times {\rm SNR} \times {\rm [Fe/H]} + c_9 \times T_{\rm eff} \times {\rm [Fe/H]}. \quad (1)$$

Here, log g, estimated with the weighted-mean algorithm, is used to group stars into giants and dwarfs. Generally, the errors decrease significantly with increasing SNR, and hot or metal-poor stars have larger errors than cool or metal-rich ones.

The method errors are deduced from the residuals obtained by applying the method to spectra of the template library or the training sets themselves. Both the mean and dispersion of the residuals are calculated and fitted as functions of $T_{\rm eff}$ and [Fe/H], for dwarfs and giants separately. The mean reflects the bias induced by the method, and is thus corrected for all target stars. While the dispersion is combined with the error induced by the spectral noises to yield the final value of error of the estimated parameter of concern. In doing so, a grid of method errors (mean and dispersion) is first created in the $T_{\rm eff}$–[Fe/H] plane, and for a given set of atmospheric parameters of a target star, the corresponding value of method error is interpolated from the grid.

For log g estimated with the KPCA method using the LAMOST-*Kepler* training set, as well as metal/elemental abundances ([M/H], [Fe/H], [C/H], [N/H], [α/M], [α/Fe]) estimated using the LAMOST-APOGEE training set, since there are sufficiently large number of stars in common with the *Kepler* and APOGEE surveys that have not been included in the training samples, they can be used as the test samples (Xiang et al. 2017) to directly estimate the parameter errors. Given that no obvious trends with $T_{\rm eff}$, log g and [Fe/H] are seen, the errors are estimated as a function of spectral SNR only.

4.5 Specific flags

Specific flags are assigned to each star to better describe the quality of estimated parameters. A flag is assigned to describe the type of the best-matching template star. Based on the SIMBAD data base (Wenger et al. 2000), LSP3 template stars are divided into 38 groups, as listed in Table 3. While the majority template stars are normal (single) stars of A/F/G/K/M spectral types, there are also

Table 3. Types of template stars.

Flag	Type	N
1	Normal star (single; AFGKM)	757
2	Pre-main-sequence star	1
3	L/T-type star	9
4	O/B-type star	19
5	S star	6
6	Carbon star	5
7	Blue supergiant star	6
8	Red supergiant star	3
9	Evolved supergiant star	1
10	Horizontal branch (HB) star (not including RCs)	27
11	Asymptotic giant branch (AGB) Star	6
12	Post-AGB star (proto-PN)	4
13	Planetary nebula (PN)	1
14	Star in nebula	3
15	Emission-line star	2
16	Pulsating variable star	5
17	Semiregular pulsating star	22
18	Classical Cepheid (delta Cep type)	10
19	Variable star of beta Cep type	4
20	Variable star of RR Lyr type	5
21	Variable star of BY Dra type	28
22	Variable star of RS CVn type	12
23	Variable star of alpha2 CVn type	23
24	Variable star of delta Sct type	21
25	Variable star of RV Tau type	1
26	Rotationally variable star	4
27	T Tau-type star	1
28	Flare star	10
29	Peculiar star	4
30	Long-period variable star	13
31	Spectroscopic binary	80
32	Eclipsing binary of Algol type (detached)	7
33	Eclipsing binary of beta Lyr type (semidetached)	2
34	Symbiotic star	2
35	Star with envelope of CH type	7
36	Variable star (unclassfied)	78
37	Double or multiple star	79
38	WD (DA)	3

considerable numbers of spectroscopic binaries, double or multiple stars, variable stars, as well as of other rare types. The flag is set to help identify stars of specific type, although a careful analysis is essential to validate the results. The flag is an integer of value from 1 to 38, and is labelled, respectively, 'TYPEFLAG_CHI2' and 'TYPEFLAG_CORR' for results based on the minimum χ^2 and correlation matching algorithms (Xiang et al. 2015b).

The second flag describes the correlation coefficient for radial velocity estimation. Although LSS-GAC intends to target stars that are identified as point sources in the photometry catalogues, there are still some contaminations from extragalactic sources (e.g. galaxies, QSOs), for which LSP3 gives problematic radial velocities because the pipeline treats all input spectra as stellar. In addition, radial velocity estimates can be problematic for stars of unusual spectra (e.g. of emission-line stars) or defective spectra (e.g. those seriously affected by cosmic rays and/or scatter light). In such cases, it is found that the peak correlation coefficient for radial velocity estimation is small compared to those of bulk stars. To mark those objects, a flag is assigned to each star in a way similar to the third flag in Xiang et al. (2015b), with the only difference that the current flag is set to be a positive float number, with negative ones replaced by 0.0. Experience suggests that one should treat the radial velocity cau-

tiously if the flag has a value larger than 6.0. The flag is denoted by 'VR_FLAG' in the value-added catalogues. The peak correlation coefficient is also given by flag 'PEAK_CORR_COEFF'.

Similar to the second flag of Xiang et al. (2015b), a flag is used to describe anomalies in the minimum χ^2 of the best-matching spectral template. This flag is designed for parameters estimated with the weighted-mean algorithm. Again, the current flag is set to be a positive float, with negative values replaced by 0.0. The flag is denoted by 'CHI2_FLAG'. The minimum χ^2 of the best-matching template is presented as 'MIN_CHI2'.

Another flag is assigned to indicate the quality of parameters estimated with the KPCA method. It is defined as the maximum value of the kernel function, d_g, which reflects the minimum distance between the target and training spectra (Xiang et al. 2017). The flag is a float of value between 0.0 and 1.0, with larger values indicating better parameter estimates. All KPCA estimates that have a d_g value smaller than 0.2 are not provided in the value-added catalogues due to their low reliability. The flag is labelled, respectively, 'DG_MILES_TM', 'DG_MILES_G', 'DG_HIP', 'DG_KEP' and 'DG_APO', for parameters estimated with the aforementioned different training sets, (cf. Table 5).

4.6 Recommended parameter values

Since different methods have been employed to deduce parameters T_{eff}, log g, [Fe/H] and [α/Fe], one needs to choose between parameter values yielded by different methods for the specific problems that she/he may want to address. For this purpose, it is necessary to get to know both the advantages and limits of the individual methods employed.

For atmospheric parameters estimated with the weighted-mean algorithm, the advantage is that the results are found to be relatively insensitive to spectral SNR compared to results yielded by other methods. This implies that for low SNRs (e.g. <20), results from the weighted-mean method are more robust and should be preferred. A disadvantage of the method is that the resultant parameters suffer from some systematics, as described above. The advantage of parameters estimated with the KPCA method is that they are much less affected by systematics, and thus more accurate than the weighted-mean values, given sufficiently high spectral SNRs. A limitation is that they are available for limited ranges of parameters only, and, in addition, suffer from relatively large random errors at low SNRs.

We provide a recommended set of parameters {T_{eff}, log g, M_V, M_{K_s}, [Fe/H], [α/Fe]} based on the above considerations. Table 4 lists the adopted methods for the recommended parameters and their effective parameter ranges. We emphasize that the recommended parameters are not necessarily the most accurate/precise ones. For example, although [Fe/H] values estimated with the KPCA method using the MILES library are adopted as the recommended values, those estimated using the LAMOST-APOGEE training set are, in fact, more precise. Values of T_{eff} derived with the weighted-mean method are robust, but suffer from clustering effect, and are thus weakly clumped in the parameter space on the scale of a few tens of Kelvin. For [α/Fe], considering that there are systematic differences between the template matching and KPCA results (Xiang et al. 2017), our recommendation will lead to some level of inconsistency between the results for giants and dwarfs. For M_V and M_{K_s}, absolute magnitudes yielded using 300 PCs are adopted as the recommend values, but if the targets of interest are mainly composed of stars with low spectral SNRs (<30), one would better use the results from 100 PCs. In addition, because a cut of 0.2 is set for the maximum value of the kernel function, d_g, to safeguard robust

Table 4. Adopted methods and their effective parameter ranges for stellar parameter determinations.

Parameter	Method	Effective range
Effective temperature		
$T_{\rm eff}\_1$	Weighted-mean template matching	All
$T_{\rm eff}\_2$	KPCA with the MILES training set	$T_{\rm eff}\_1 < 10\,000$ K
$T_{\rm eff}$ (recommended)	$T_{\rm eff}\_1$	All
Surface gravity		
Logg_1	Weighted-mean template matching	All
Logg_2	KPCA with the MILES training set	$T_{\rm eff}\_1 < 10\,000$ K, Logg_1 > 3.0 dex
Logg_3	KPCA with the LAMOST-*Kepler* training set	$T_{\rm eff}\_1 < 5600$ K, Logg_1 < 3.8 dex or Logg_2 < 3.8 dex
Logg (recommended)	Logg_1	$T_{\rm eff}\_1 > 10\,000$ K
	Logg_3	$T_{\rm eff}\_1 < 5600$ K, Logg_1 < 3.8 dex or Logg_2 < 3.8 dex
	Logg_2	Otherwise
Metallicity		
[Fe/H]_1	Weighted-mean template matching	All
[Fe/H]_2	KPCA with the MILES training set	$T_{\rm eff}\_1 < 10\,000$ K
[Fe/H]_3	KPCA with the LAMOST-APOGEE training set	$T_{\rm eff}\_1 < 5600$ K, Logg_1 < 3.8 dex or Logg_2 < 3.8 dex
[Fe/H] (recommended)	[Fe/H]_1	$T_{\rm eff}\_1 > 10\,000$ K
	[Fe/H]_2	Otherwise
α-element to iron abundance ratio		
[α/Fe]_1	Template matching using spectra of 3900–3980, 4400–4600 and 5000–5300 Å	$4000 < T_{\rm eff}\_1 < 8000$ K
[α/Fe]_2	Template matching using spectra of 4400–4600 and 5000–5300 Å	$4000 < T_{\rm eff}\_1 < 8000$ K
[α/Fe]_3	KPCA with the LAMOST-APOGEE training set	$T_{\rm eff}\_1 < 5600$ K, Logg_1 < 3.8 dex or Logg_2 < 3.8 dex
[α/Fe] (recommended)	[α/Fe]_3	$T_{\rm eff}\_1 < 5600$ K, Logg_1 < 3.8 dex or Logg_2 < 3.8 dex
	[α/Fe]_1	Otherwise
Other elemental abundances		
[M/H]		
[α/M]	KPCA with the LAMOST-APOGEE training set	$T_{\rm eff}\_1 < 5600$ K, Logg_1 < 3.8 dex or Logg_2 < 3.8 dex
[C/H]		
[N/H]		
Absolute magnitudes		
M_V_1	KPCA with the LAMOST-*Hipparcos* training set	
$M_{K_{\rm s}}\_1$	using 300 PCs	$T_{\rm eff}\_1 < 12\,000$ K
M_V_2	KPCA with the LAMOST-*Hipparcos* training set	
$M_{K_{\rm s}}\_2$	using 100 PCs	$T_{\rm eff}\_1 < 12\,000$ K
M_V (recommended)	M_V_1	
$M_{K_{\rm s}}$ (recommended)	$M_{K_{\rm s}}\_1$	$T_{\rm eff}\_1 < 12\,000$ K

parameter estimates with the KPCA method (Xiang et al. 2017), about 18 per cent of the sample stars (mostly with very low SNRs) have no parameter estimates with the KPCA method. For those stars, the recommended parameters are not available. Rather than adopting the recommended values, we encourage users to make their own choice based on their specific problems under consideration.

For [M/H], [α/M], [C/H] and [N/H], since at the moment there is only one set of measurements, i.e. those with the KPCA method, they are simply adopted as the recommended values. Note that [M/H], [α/M], [C/H] and [N/H] are available only for stars of $T_{\rm eff} < 5600$ K and log $g < 3.8$ dex. Here $T_{\rm eff}$ refers to that estimated with the weighted-mean method, while log g is either estimated with the weighted-mean method or by the KPCA method using the MILES stars as the training set.

Fig. 9 plots the stellar number density distributions in various planes of recommended parameters. In the $T_{\rm eff}$–log g and $T_{\rm eff}$–M_V planes, the stars show two prominent clumps: one composed of FGK dwarfs and another of red clump stars. The compact contours of red clump stars indicate a high precision of the estimated parameters. Trajectories of stars in those planes are well consistent with the theoretical isochrones. Stars of [Fe/H] > -1.0 dex

dominate the sample, indicating that most of the stars belong to the Galactic disc. The fraction of stars with [Fe/H] < -1.0 dex is only 1.8 per cent. Given the large difference between the numbers of metal-rich and metal-poor stars, even a small fraction of those metal-rich stars whose [Fe/H] estimates may have suffered large uncertainties could seriously contaminate the sample of metal-poor stars. This seems to have led to the appearance of a kinematically cold but metal-poor population in the [Fe/H]–V_r plane. One thus needs to be very careful when studying the metal-poor populations using this disc-star dominant sample. Comparison of [Fe/H] values derived with the weighted-mean and KPCA methods may help identify potential contaminators. Exercise shows that one excludes stars whose KPCA [Fe/H] estimates are smaller than the weighted-mean values by 0.3 dex, or replaces the estimates by the latter values; the artificial populations of cold, metal-poor stars in the [Fe/H]–V_r plane is largely disappeared.

Fig. 9 also shows that more metal-poor stars generally have higher [α/Fe] values. This is true for both dwarfs and giants, which is a natural consequence of the Galactic chemical evolution. For both dwarfs and giants, [α/Fe] values for stars of solar metallicity are close to zero. Nevertheless, [α/Fe] values of dwarfs and giants show
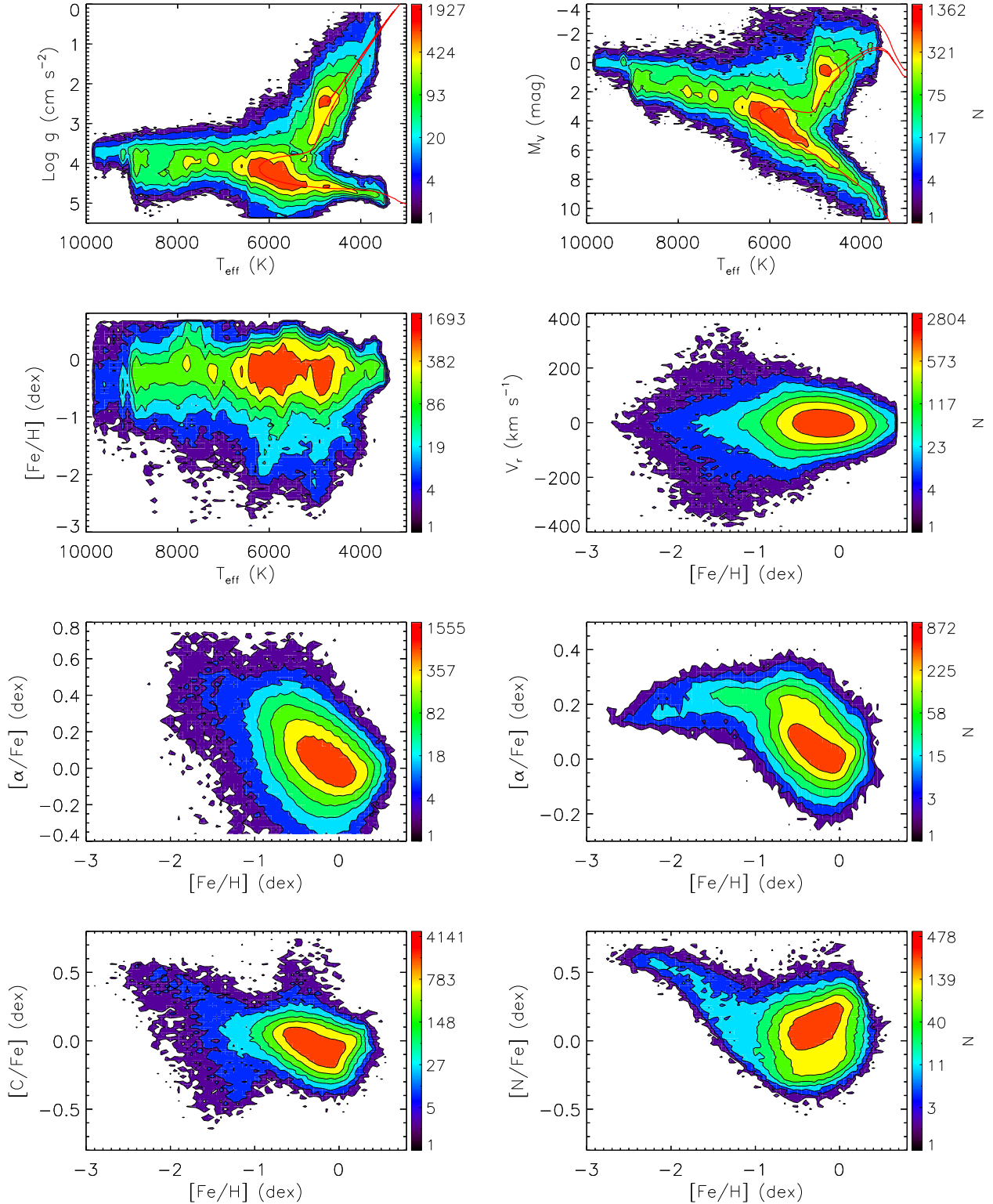
Figure 9. Contours of colour-coded stellar number density distributions in various planes of recommended parameters for the whole sample of stars in the value-added catalogues. Stellar isochrones in the $T_{\rm eff}$–log g and $T_{\rm eff}$–M_V plots are from Rosenfield et al. (2016) and have a solar metallicity and an age of 4.5 Gyr. The left-hand and right-hand panels of third row are [Fe/H]–[α/Fe] plots showing the results for dwarfs and giants, respectively.

different patterns. Dwarfs cover a wider range of [α/Fe] values than giants. There are very few giant stars of [α/Fe] < −0.2 dex or [α/Fe] > 0.3 dex. In contrast, there are quite a number of dwarfs of [α/Fe] < −0.3 dex or [α/Fe] > 0.4 dex. Moreover, besides the

dominant thin disc sequence in the [α/Fe]–[Fe/H] plane, giants also exhibit an extra, weaker sequence of thick disc stars of a [α/Fe] value of ∼0.2 dex. This thick disc sequence is not seen in dwarfs. The larger random errors (Fig. 13) of [α/Fe] estimates for dwarfs are
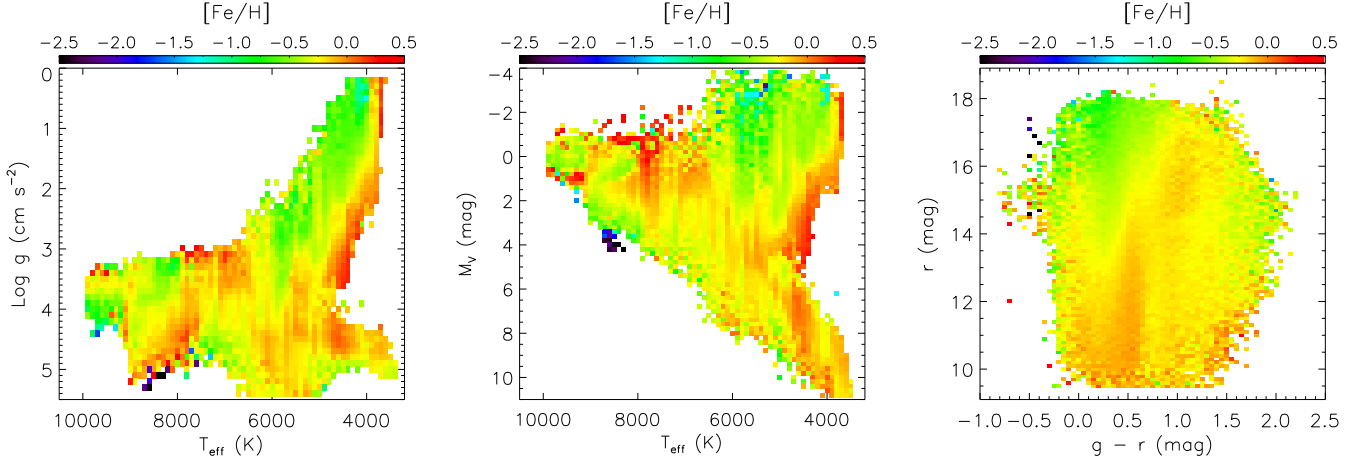
Figure 10. Distributions of sample stars in T_{eff}–log g, T_{eff}–M_V and ($g - r$, r) diagrams colour-coded by median metallicity, defined as the median value of stars in bins of 100 K × 0.1 dex in T_{eff}–log g, 100 K × 0.2 mag in T_{eff}–M_V and 0.05 × 0.1 mag in ($g - r$, r) plane, respectively, for the three panels from left to right.
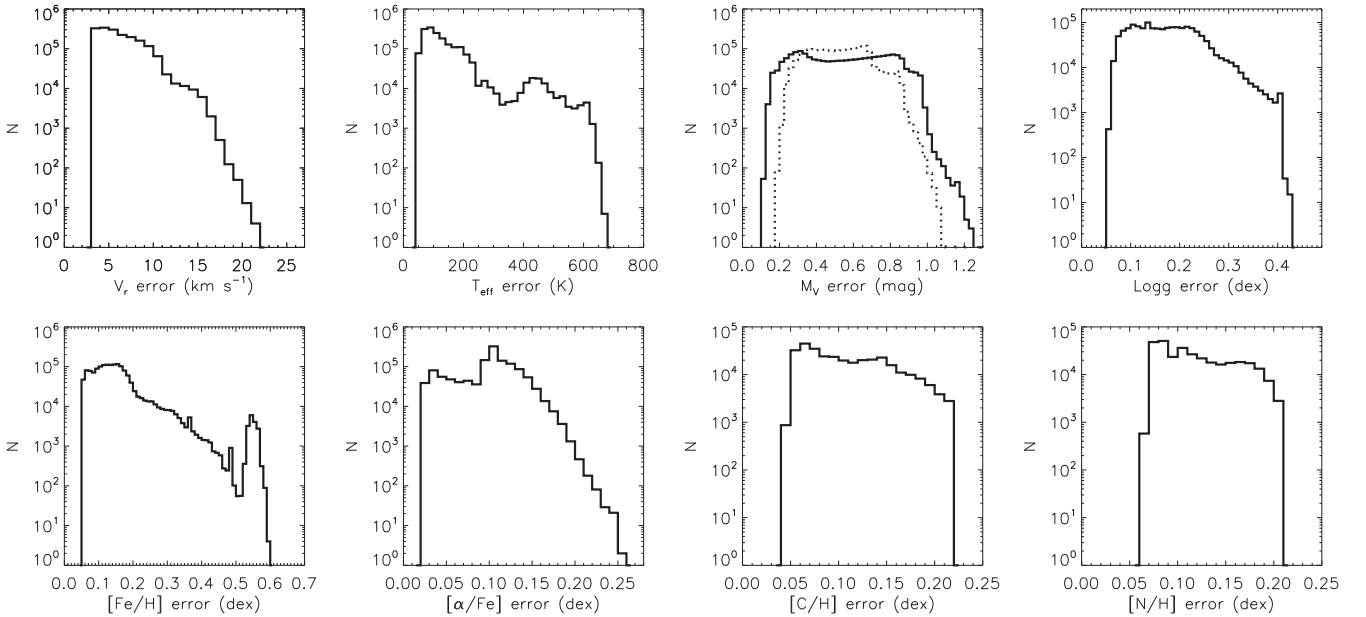
Figure 11. Error distributions of recommended parameter estimates. For M_V, error distribution of the other set of M_V estimates deduced using 100 PCs is shown by a dotted line.

definitively an important reason for the absence of this sequence. Also, giants probe a larger volume than dwarfs as they are brighter. Thus, the giant sample contains more thick disc stars, whereas the dwarf sample is dominated by the local thin disc stars and young, hotter stars in the outer thin disc. In addition, and maybe more importantly, since different algorithms, spectral templates and wavelength ranges are used for [α/Fe] estimation for dwarfs and giants, and the results have not been calibrated externally using the data, for example, from high-resolution spectroscopy, systematic differences and errors may well be hidden in the [α/Fe] estimates of dwarfs and/or giants. A calibration of [α/Fe] estimates is an essential and urgent task for the future.

Fig. 10 plots distributions of stars in the T_{eff} – log g, T_{eff} – M_V and ($g - r$, r) planes, colour-coded by [Fe/H]. The figure shows that amongst the cool stars, as expected, metal-rich ones generally have lower temperatures than those metal-poor ones. However, for hot stars, the derived metallicities show some strange patterns in

the T_{eff}–log g plane, which are not fully understood yet. A possible cause could be the inadequacy of parameter coverage of the MILES spectral library at higher temperatures. A further, detailed examination of log g estimates utilizing LAMOST-TGAS common stars, in particular for hot stars, is underway. On the whole, the trends of [Fe/H] seen in the T_{eff}–M_V and the ($g - r$, r) planes seem to be reasonable. The brighter side of the ($g - r$, r) diagram is dominated by metal-rich stars as they represent a local, thin disc sample. On the other hand, at the fainter side of the diagram, one sees that metal-rich stars are, in general, redder, while the metal-poor ones are bluer. Again, this is what one would expect.

Fig. 11 plots error distributions of recommended parameter estimates. Spectral SNR is the main factor that determines the amount of parameter error, and stars of different spectral types have also different parameter errors. A detailed analysis of how the parameter errors depends on spectral SNR and stellar parameters can be found in Xiang et al. (2015b, 2017). Most of the stars have a radial
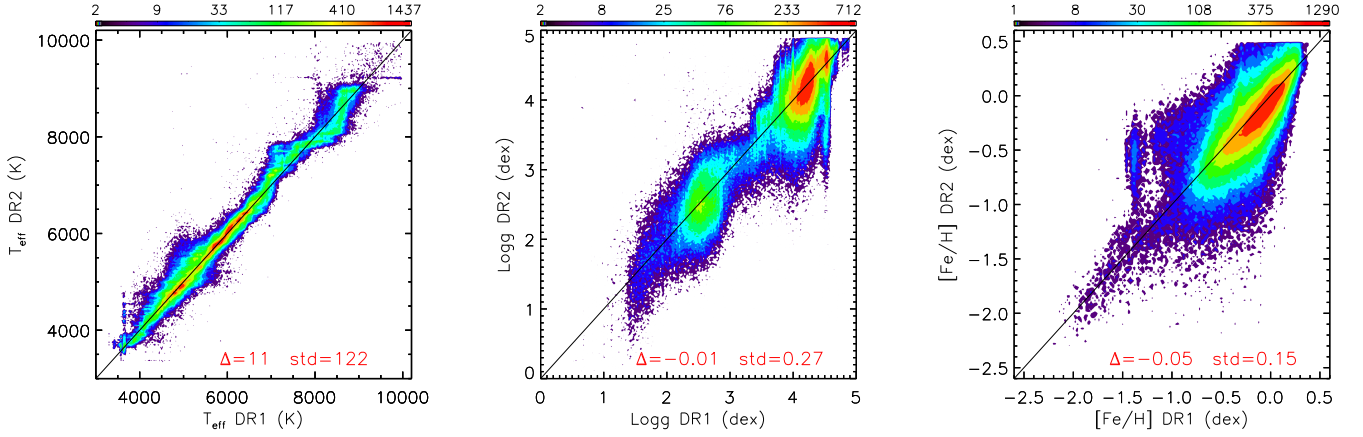
Figure 12. Comparison of the new recommended stellar atmospheric parameters with those of LSS-GAC DR1. Mean and standard deviations of the parameter differences between DR2 and DR1 are marked in the plot.

velocity error of a few km s^{-1}. However, some of them, mostly hot stars of low SNRs, have errors reaching 20 km s^{-1}. Temperature errors are around 100 K for most stars, but those of hot ones reach 400–600 K. The large temperature errors for hot stars are mainly caused by the small number and large parameter uncertainties of hot stars in the MILES library. Similar trend is seen in [Fe/H] errors, where most stars have an error between 0.1 and 0.2 dex. However, the error distribution exhibits a second peak at 0.5–0.6 dex, mainly contributed by hot stars. Errors of log g typically have values of 0.1–0.2 dex, with a small fraction reaching 0.3–0.4 dex. Errors of M_V can be as small as 0.2 mag at high spectral SNRs, but reach 0.8–1.0 mag at low SNRs ($\sim$10). M_V values estimated using 100 PCs have larger errors compared to those deduced using 300 PCs, but they are less sensitive to SNR, and have errors of 0.6–0.8 mag at low SNRs ($\sim$10). Errors of M_{K_s} have similar trends. Errors in [α/Fe] show two populations. The lower one is of giants, which has values of 0.02–0.09 dex. The higher one is of dwarfs, and has values of 0.09–0.25 dex, peaking around 0.1 dex. Note that as discussed above, since the results are not calibrated by independent, external data sets, there could be systematic uncertainties in [α/Fe] estimates that have not been included in the current error estimates. This is particularly true for giant stars, for which the quoted errors are very small. Errors of [C/H] and [N/H] estimates range from 0.05 to 0.20 dex, with most of them smaller than 0.15 dex.

A comparison of recommended stellar atmospheric parameters with LSS-GAC DR1 for the whole LSS-GAC DR1 sample is shown in Fig. 12. The figure shows that $T_{\rm eff}$ estimates from the two data releases are quite consistent. For log g, the plot shows significant patterns. Similar patterns are seen by comparing LSS-GAC DR1 log g estimates with asteroseismic measurements (Ren et al. 2016). The causes of such patterns are discussed in Xiang et al. (2017), and are essentially due to the inadequacies of log g estimates in LSS-GAC DR1 ones. On the whole, new [Fe/H] estimates show good correlation with those of LSS-GAC DR1. The standard deviation of the two sets of [Fe/H] estimates of the whole sample is 0.15 dex. However, the current estimates are systematically 0.05 dex lower than LSS-GAC DR1. There is also a group of stars whose new [Fe/H] values are significantly higher than those of LSS-GAC DR1. In addition, the sharp boundary seen in the LSS-GAC DR1 results now disappears. Again, the causes of these differences are discussed in Xiang et al. (2017), and are mainly due to the inadequacies of [Fe/H] estimates in LSS-GAC DR1.
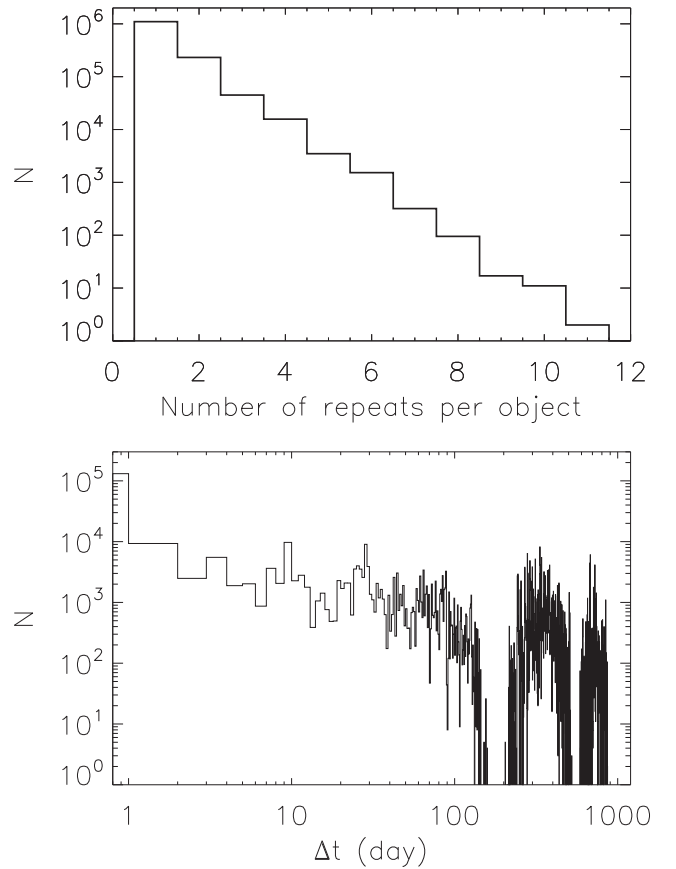
Figure 13. Upper panel: stellar numbers as a function of number of repeat observations per object. Lower panel: distribution of time separation for repeat observations.

5 REPEAT OBSERVATIONS

About 28 per cent of stars in the value-added catalogues have repeat observations. The repeat observations are valuable for various purposes, including (1) time-domain spectroscopy, (2) robustness check of parameter estimates, (3) improvement of stellar parameter estimates by averaging repeat measurements, etc. Fig. 13 plots the distribution of number of stars as a function of number of repeat observations per object, as well as the distribution of time separations
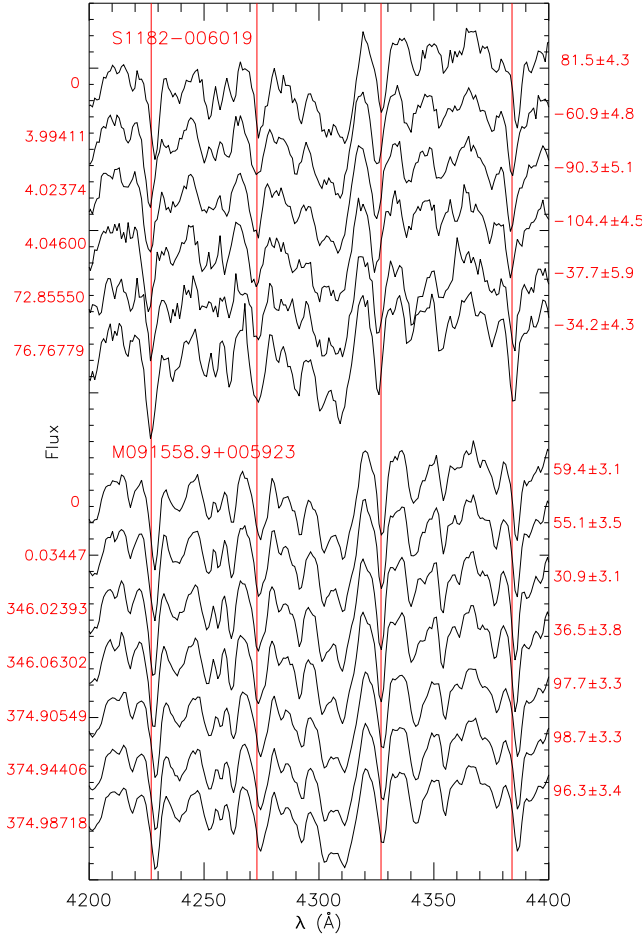
Figure 14. Examples of spectra of wavelength range of 4200–4400 Å of two stars with repeat observations. Numbers on the left are JD offsets with respect to the first observation, while numbers on the right are radial velocity measurements. Object ID from the input catalogues are marked on the plot.

of repeat observations. Stellar number decreases approximately linearly with the increasing number of repeat observations. There are 95 350 unique stars that are observed three times or more, and 5460 unique stars that are observed five times or more. Time separation covers a range from a few hours to nearly 1000 d. Most repeat observations occurred in the same night, when different plates that shared the same central bright stars or adjacent plates that had overlapping fields of views were observed. Note that, to better present the data, the horizontal axis of the figure has been chosen to artificially start from 0.8 d, but the real time separation in the first bin was smaller than 4 h due to hour angle limitations of LAMOST (Cui et al. 2012). Note also that here repeat observations refer to those taken with different plates. In fact, each plate observed usually has two to three exposures. The current analysis is based on co-added spectra of those adjacent individual exposures. Further, independent treatment of the individual exposures of each plate observed in the future will significantly increase the repeat observation rate in the sense that every star targeted has at least one repeat observation, separated by tens of minutes.

Some systematic studies utilizing repeat observations are underway. As an example, Fig. 14 shows the spectra in the 3900–4400 Å wavelength range of two stars with repeat observations. The data clearly show shifts of spectral line positions, thus radial velocity variations. The first example has an amplitude of radial velocity

variations larger than 180 km s^{-1}. The offsets of repeat observations from the first one are, respectively, 3.994 11, 4.023 74, 4.046 00 72.855 50 and 76.767 793 d. Effective temperatures estimated from the six observations are, respectively, 4931, 5192, 5150, 5182, 5507 and 4953 K, M_V absolute magnitudes are 6.10, 5.89, 5.82, 5.43, 5.42 and 6.56 mag, and [Fe/H] metallicities are −0.22, −0.33, −0.24, −0.34, −0.15 and −0.07 dex. The second example star has a radial velocity variation amplitude larger than 60 km s^{-1}. The offsets of repeat observations from the first one are, respectively, 0.034 47, 346.023 93, 346.063 02, 374.905 49, 374.944 06 and 374.987 18 d. T_{eff} estimates from the seven observations are, respectively, 5349, 5340, 5046, 5258, 5512, 5512 and 5526 K, the M_V absolute magnitudes are 4.47, 4.29, 4.62, 4.49, 4.74, 4.79 and 4.76 mag, and [Fe/H] metallicities are −0.11, −0.05, 0.03, 0.00, −0.04, −0.03 and −0.04 dex. It seems that in addition to the radial velocity variations, the two stars also exhibit significant variations in effective temperature and absolute magnitude. Further analyses are, however, required to reveal the nature of the variations.

A detailed robustness examination on the LSP3 stellar parameters using repeat observations can be found in Xiang et al. (2015b) for radial velocity measurements and atmospheric parameter determinations with the weighted-mean method, and in Xiang et al. (2017) for atmospheric parameters estimated with the KPCA method. Fig. 15 plots the dispersions of differences of recommended parameters deduced from repeat observations that have comparable SNRs (20 per cent) as a function of SNR. The dispersions represent random errors of the parameters induced by spectral noises. For this purpose, values of dispersions shown in the figure have been divided by square root of 2. Results for giants, hot ($T_{eff} > 7000$ K) and cool ($T_{eff} < 7000$ K) dwarfs are shown separately. Generally, hot dwarfs have larger random errors in V_r, T_{eff}, [Fe/H] and [α/Fe] estimates. For all parameters, the random errors are quite sensitive to SNR. Given an SNR higher than 100, random errors of radial velocities induced by spectral noises for cool stars can be as small as 1–2 km s^{-1}, and the values are 3–4 km s^{-1} for hot stars. For an SNR of 10, the errors increase to 5–10 km s^{-1} for cool stars, and 20 km s^{-1} for hot stars. Note that the final error estimates of V_r have been set to a minimum value of 3 km s^{-1} to account for the potential systematic uncertainties, which is ∼2 km s^{-1}, as estimated via external examinations using the LAMOST-APOGEE common stars. As introduced in Section 4.4, for all stellar parameters, these random errors and their trends of variations with spectral SNR, T_{eff} and [Fe/H] have been incorporated into the final error estimates, which also include uncertainties induced by the inadequacies of the parameter estimation methods for both giants and dwarfs.

6 EXTINCTION AND DISTANCE

6.1 Extinction

Similar to LSS-GAC DR1 (Yuan et al. 2015), various techniques are employed to estimate the interstellar reddening towards the individual stars. The methods include the star-pair technique, comparing observed colours with synthetic ones from stellar model atmospheres, as well as a method based on the stellar colour loci.

The star-pair method assumes that stars with identical stellar atmospheric parameters (T_{eff}, log g, [Fe/H]) have the same intrinsic colours. Thus, for a reddened star, its intrinsic colours can be inferred from its pairs/counterparts with either nil or well-known extinction (Yuan et al. 2015). The method is straightforward, and, moreover, free from stellar model atmospheres. To derive extinction
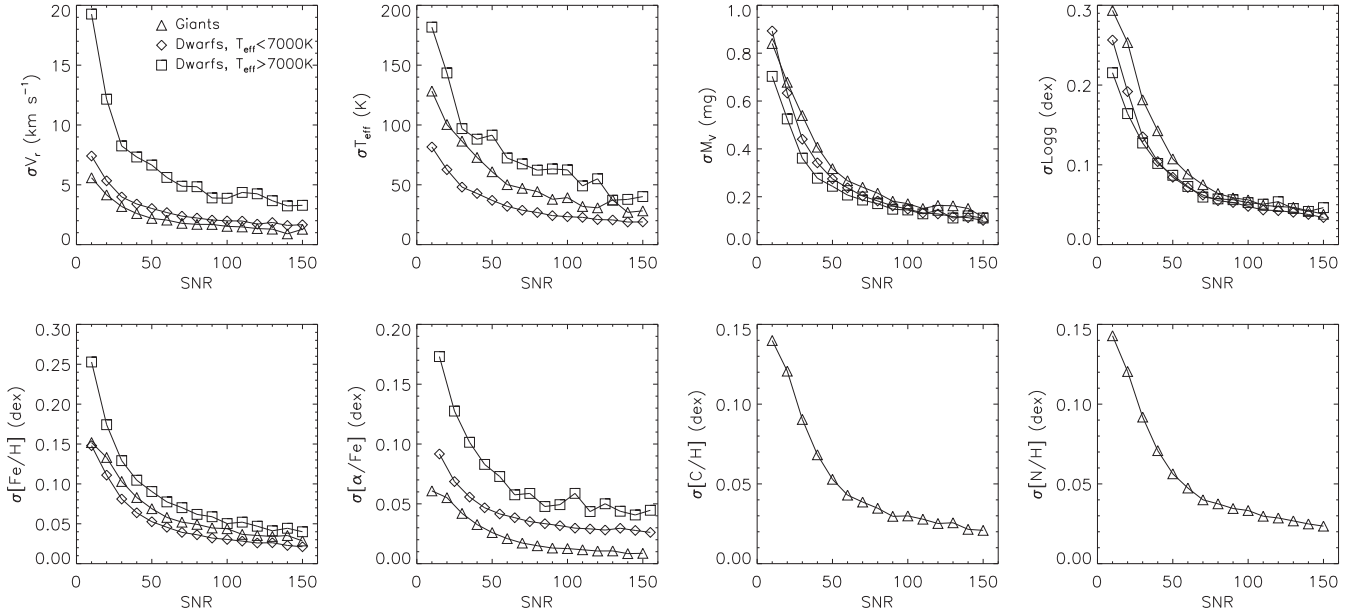
Figure 15. Random errors of recommend parameters as a function of spectral SNR as deduced by comparing results from repeat observations. Results for giants, hot and cool dwarfs are shown separately.

with this method, a control sample with nil or well-known extinction is inherited from LSS-GAC DR1. The control sample contains low-extinction stars whose $E(B-V)$ values can be well approximated by the reddening map of Schlegel, Finkbeiner & Davis (1998, hereafter SFD98). For a given target star, the $E(B-V)$ is then derived by fitting $g-r, r-i, i-J, J-H$ and $H-K_s$ optical to the infrared colours simultaneously by the corresponding values of the pair stars in the control sample, assuming the universal extinction coefficients of Yuan, Liu & Xiang (2013). When available, g-, r-, i-band magnitudes from the XSTPS-GAC survey (Zhang et al. 2013, 2014; Liu et al. 2014) are used, otherwise they are taken from the APASS survey (Munari et al. 2014) or from the SDSS survey (DR8; Aihara et al. 2011) for a few B/M/F plates of high Galactic latitudes. J, H, K_s magnitudes are from the 2MASS survey (Skrutskie et al. 2006). There are a few ($\sim$3–5 per cent) stars for which different colours yield quite different reddenings. For those stars, either the photometry or the stellar atmospheric parameters or both are problematic. It is found that in such cases, $E(B-V)$ is often overestimated by a significant amount. To account for this, if $g-r$ and $r-i$ colours of a given star yield reddening of different signs and yield values differed by more than 0.2 mag, the resultant $E(B-V)$ estimate is discarded. The corresponding entry in the value-added catalogues are set to -9. Comparison with the SFD98 reddening map for high Galactic latitude regions of low extinction illustrates a typical uncertainty of 0.036 mag for $E(B-V)$ thus estimated (Fig. 16), which is similar to that of LSS-GAC DR1. Note that we use the recommended atmospheric parameters for reddening estimation. Different results are expected if different sets of atmospheric parameters are adopted. Nevertheless, given the good precision of the current parameter estimates, the differences are small. For example, $E(B-V)$ values derived using atmospheric parameters estimated with the weighted-mean algorithm differ from the default results by a dispersion of only $\sim$0.01 mag. $E(B-V)$ thus estimated is denoted by 'EBV_SP' in the value-added catalogues.

$E(B-V)$ values have also been determined by comparing photometric colours with synthetic ones. In doing so, a grid of synthetic colours is first constructed by convolving the synthetic spectra of
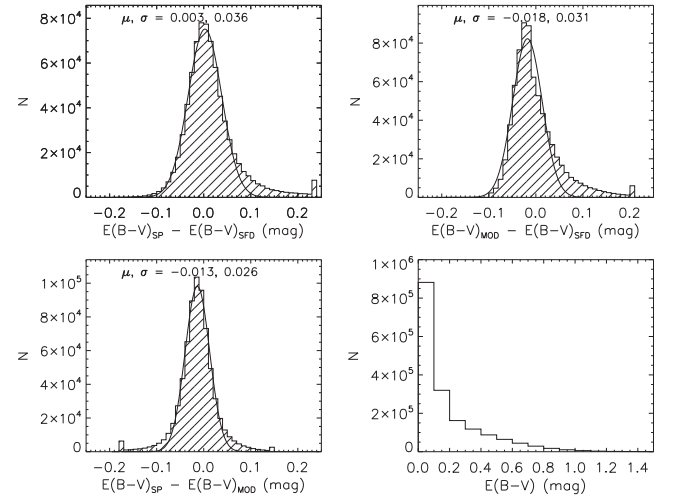
Figure 16. Distributions of differences of $E(B-V)$ estimated by different methods or from the SFD98 map except for the bottom right-hand panel where the distribution is for the adopted values of $E(B-V)$ for all stars in LSS-GAC DR2. $E(B-V)_{SP}$ and $E(B-V)_{MOD}$ denote, respectively, the values derived from the star-pair and stellar model atmosphere methods, whereas $E(B-V)_{SFD}$ refers to values extracted from the two-dimensional reddening map of SFD98. The comparisons are for stars of $|b| > 15°$ and $E(B-V)_{SFD} < 0.3$ mag only.

Castelli & Kurucz (2004) with the transmission curves of filters for the photometric systems of SDSS[3] (Gunn et al. 1998; Doi et al. 2010) and 2MASS[4] (Milligan, Cranton & Skrutskie 1996). Synthetic colours for a star of given atmospheric parameters T_{eff}, log g and [Fe/H] are then deduced by linearly interpolating the grid. $E(B-V)$ is then estimated as the weighted mean of values inferred from the individual colours, weighted by the reddening coefficients

[3] http://classic.sdss.org/dr7/instruments/imager/index.html#filters
[4] http://www.ipac.caltech.edu/2mass/releases/second/doc/sec3_1b1.html

of Yuan et al. (2013). As Fig. 16 shows, $E(B − V)$ values thus derived have a precision of about 0.03 mag, but are found to be systematically lower than the values given by either the star-pair method or by the SFD98 map, by 0.01–0.02 mag. The underestimation is likely to be caused by the slight different temperature scales between the LSP3 and Kurucz atmospheric models. As pointed out above, LSP3 temperatures are calibrated to the metallicity-dependent colour–temperature relations of Huang et al. (2015c), constructed using a sample of stars with T_{eff} estimated directly from angular diameters measured with interferometry and the trigonometric parallaxes from the *Hipparcos Satellite*. It is found that the relations of Huang et al. (2015c) yield temperatures generally ∼100 K lower than earlier results in the literature. $E(B − V)$ estimated with this method is denoted 'EBV_MOD' in the catalogues.

Finally, extinction values deduced from multiband photometry by fitting the stellar colour loci (Chen et al. 2014) are also included in the catalogues. Results from this method are currently available only for stars within the footprint and magnitude range of XSTPS-GAC, i.e. for stars targeted by the LSS-GAC main and M31/M33 surveys. As shown by Yuan et al. (2015), the method yields an $E(B − V)$ precision of about 0.07 mag and works best for dwarf stars. $E(B − V)$ thus estimated is denoted by 'EBV_PHOT' in the catalogues.

Considering that the star-pair method is model free, and often achieves a better precision compared to other methods, $E(B − V)$ yielded by the method ('EBV_SP') are generally adopted as the recommended values. Considering that there are few hot stars in the control sample used by the star-pair method, 'E(B-V)_MOD' is adopted as the recommended for stars hotter than 9000 K. Since the SFD98 map is a two-dimensional one, it provides an upper limit of $E(B − V)$ for reddening towards the individual Galactic stars. Based on this consideration, if the $E(B − V)$ value of a star deduced from the star-pair method or from the method based on model atmospheres excess the SFD98 value by 0.1 mag (∼3σ), the latter is adopted as the recommended value. The distribution of adopted $E(B − V)$ values for all stars in LSS-GAC DR2 are shown in the bottom right-hand panel of Fig. 16. With $E(B − V)$ determined, values of interstellar extinction in the individual photometric bands can be easily computed using the extinction coefficients available from, for example, Yuan et al. (2013).
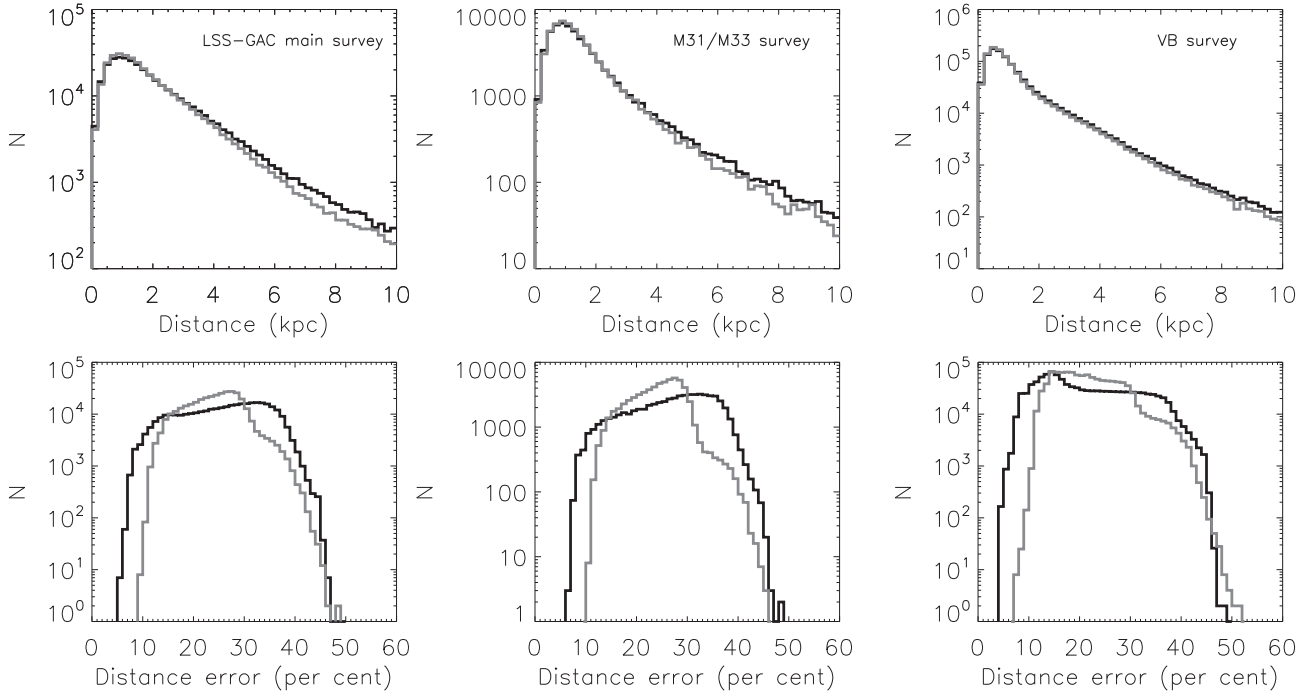
6.2 Distance

Distance to individual stars are also estimated with a variety of methods. One is to infer from the absolute magnitudes derived directly from the LAMOST spectra with the KPCA method using the LAMOST-*Hipparcos* training set. In doing so, if photometric magnitudes of all g, r and K_s bands have an error smaller than 0.1 mag, and are not saturated, then both M_V and M_{K_s} are used to calculate a weighted-mean distance by taking the inverse squared magnitude errors as weights, otherwise only bands with good photometry are utilized to infer the distance. Generally, K_s band contributes a larger weight as it suffers from much less severe extinction than V band. The V-band photometry is transformed from g and r magnitudes using the equation of Jester et al. (2005). Errors of absolute magnitudes, extinction and photometry are all incorporated in the estimation of distance errors. Note that it is found that the estimated M_V and M_{K_s} are not independent quantities but largely correlated with each other, so that when estimating errors for the weighted-mean distance, we simply adopt the weighted-mean distance errors in the individuals bands rather than inferring from the reduced variance as done for the independent measurements. This may have over-

estimated the distance errors to some extent. Distance estimated with this method is denoted as 'DIST_SP1' and 'DIST_SP2' in the value-added catalogues for results inferred from absolute magnitudes using 300 and 100 PCs, respectively.

Another method to estimate stellar distance is based on empirical relations between the absolute magnitudes and stellar atmospheric parameters constructed utilizing the MILES stars. A detailed description of the derivation of the empirical relations is presented in (Yuan et al. 2015). Here, since the atmospheric parameters of MILES stars have been re-determined/calibrated (cf. Section 4.1), the relations are updated accordingly. The new relations have much smaller residuals – with dispersions of g- (and r-) band absolute magnitudes of only about 0.08, 0.13, 0.15 and 0.20 mag for OBA stars, FGK dwarfs, KM dwarfs and GKM giants, respectively. The corresponding residuals in the 2MASS infrared bands are about 0.15, 0.26, 0.06 and 0.26 mag. The small residuals suggest that the method is robust. Errors of absolute magnitudes thus derived for the individual LSS-GAC stars are mainly contributed by uncertainties of the stellar atmospheric parameters. Here, both the recommended atmospheric parameters and atmospheric parameters yielded by the weighted-mean algorithm are used to estimate absolute magnitudes. To obtain realistic error estimates of absolute magnitudes, we adopt a Monte Carlo strategy to propagate the errors of stellar atmospheric parameters. The distance errors are then estimated taking into account contributions by errors in absolute magnitudes, extinction and photometry. Distances estimated with this method using the recommended parameters are denoted as 'DIST_EM1' in the value-added catalogues, and those using the weighted-mean atmospheric parameters are denoted as 'DIST_EM2'. In addition, stellar distances derived from photometry by Chen et al. (2014) via fitting stellar colour loci, if available, are also presented in the value-added catalogues, and are denoted by 'DIST_PHOT'.

Estimating distance using absolute magnitudes derived directly from the LAMOST spectra does not depend on stellar model atmospheres and stellar atmospheric parameters, and thus are expected to suffer from minimal systematics. Comparison with distances inferred from the *Gaia* TGAS parallaxes (Fig. 8) demonstrates that the overall systematic errors in our inferred distances are negligible, and the random errors can be as small as ∼10 per cent, given high enough spectral SNRs. Uncertainties in absolute magnitude thus distance estimates are sensitive to spectral SNRs. For an SNR of 10, the uncertainty increases to 30–40 per cent. Fig. 17 further shows that distance estimates from absolute magnitudes derived using both 300 and 100 PCs have essentially negligible (1–2 per cent) systematic errors at all T_{eff} in the range of 5000–9000 K. Note that to incorporate stars in a wide temperature range for the comparison, especially for the high-temperature end, here we have adopted an error cut of 0.3 mag for the TGAS-based magnitudes instead of 0.2 mag as adopted for Fig. 8. As a result, the dispersion become 14 per cent, which is larger than 12 per cent shown in Fig. 8. While for stars cooler than 5000 K, our distances seem to be underestimated by 5–10 per cent. The figure also shows that distances yielded by the empirical relations using the recommended parameters are systematically underestimated by about 11 per cent, and the systematics show moderate dependence on T_{eff}. Such an underestimation is probably caused by either hidden systematic errors in the stellar atmospheric parameters, especially log g, or by systematic errors in the empirical relations. Note that although the current parameter estimates achieved high precisions, potential systematic errors could be existed, which are probably a few tens of Kelvin in T_{eff}, a few per cent to 0.1 dex in log g and a few per cent to 0.1 dex in [Fe/H]. Potential systematic errors for metal-poor stars ([Fe/H] < −1.0 dex)

Figure 17. Distributions of distances and errors of stars targeted by the LSS-GAC main (left-hand panel), M31/M33 (middle panel) and VB (right-hand panel) surveys. Black and grey lines represent distances inferred from absolute magnitudes derived from LAMOST spectra with the KPCA method using 300 and 100 PCs, respectively.

are likely larger and should be treated cautiously. Distances yielded by the empirical relations using the weighted-mean parameters are systematically overestimated by 6 per cent, and there are strong patterns.

Distances inferred from absolute magnitudes directly determined from the LAMOST spectra using 300 PCs ('DIST_SP1') are currently adopted as the recommended values. It is emphasized that users should choose a proper set according to their own problems of interest. Fig. 18 plots the distributions of distances and error estimates for 'DIST_SP1' and 'DIST_SP2' for LSS-GAC DR2 stars of the main, M31/M33 and VB surveys, respectively. The distances peak at about 1 kpc, but with a few beyond 10 kpc. For the whole sample, 22, 5 and 2 per cent of the stars have a distance larger than 2, 5 and 10 kpc, respectively. The quoted errors have a wide distribution from ~7 to >40 per cent. For 'DIST_SP1', about 11.5, 25.5, 63.0 and 98.8 per cent of the stars have a quoted error smaller than 15, 20, 30 and 40 per cent, respectively. The numbers are, respectively, 4.6, 22.9, 87.8 and 99.7 per cent for distances inferred from absolute magnitudes derived using 100 PCs. Finally, note that as mentioned in Section 4, there are about 18 per cent of stars that the KPCA method has failed to provide reliable estimates of absolute magnitudes due to low spectral SNRs. For those stars, the recommend distances are not available, while as a compromise, one may use the distance derived with the empirical relations utilizing the weighted-mean atmospheric parameters.

Fig. 19 plots the density distributions of LSS-GAC DR2 stars in the Galactic X–Y and X–Z planes for the main, M31/M33 and VB surveys, separately. Here, the X, Y and Z are calculated assuming $R_{\odot} = 8.0$ kpc and $Z_{\odot} = 0$ kpc, and the recommended distances are used for the calculation. The figure shows that the main survey samples the outer disc well, while the VB survey samples the

local disc very well. Some stars are located beyond 20 kpc in the anticentre direction and some are beyond 10 kpc in the vertical direction.

7 MULTIBAND PHOTOMETRY, PROPER MOTION AND ORBITAL PARAMETERS

Multiband photometry from the far-UV to the mid-IR, including magnitudes in *FUV* and *NUV* bands from the *GALEX* (Martin et al. 2005), g, r, i bands from the XSTPS-GAC, SDSS and APASS, J, H, $K_{\rm s}$ bands from the 2MASS, and w_1, w_2, w_3, w_4 bands from the *WISE* (Wright et al. 2010), are included in the value-added catalogues using with a 3 arcsecond match radius for source cross-identifications.

Proper motions for LSS-GAC stars from UCAC4 (Zacharias et al. 2013) and PPMXL (Roeser, Demleitner & Schilbach 2010), as well as those derived by combing the XSTPS-GAC and 2MASS catalogues (Yuan et al. 2015), are also included in the value-added catalogues.

Given celestial position, distance, radial velocity and proper motions, the stellar orbital parameters, including eccentricity, epicentre and pericentre radii, minimum and maximum vertical distances from the disc are computed assuming a simple, axisymmetric Galactic potential as presented in table 1 of Gardner & Flynn (2010). The Sun is assumed to be located at $(X, Y, Z) = (-8, 0, 0)$ kpc, and the local standard of rest has values $(U_{\odot}, V_{\odot}, W_{\odot}) = (7.01, 10.13, 4.95)$ km s^{-1} (Huang et al. 2015b). When calculating the orbital parameters, systematic trends in proper motions with celestial positions are corrected for using the relations presented in Carlin et al. (2013) and in Huang et al. (2015b) for PPMXL and UCAC4 proper motions, respectively. Note that the systematics in proper motions have also been found to correlate with colour and magnitudes (e.g.
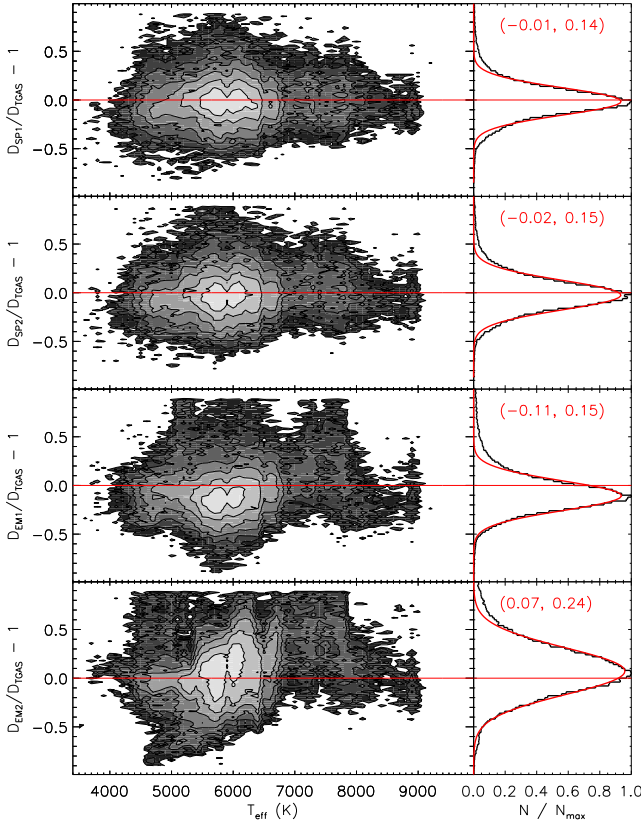
Figure 18. Percentage differences of distances between our estimates and those inferred from *Gaia* TGAS parallax as a function of the recommended $T_{\rm eff}$ for a sample of 100 000 common stars. For up to low, the four panels show results for our distance estimates inferred from absolute magnitudes derived from LAMOST spectra using 300 PCs (first panel), 100 PCs (second panel) and from absolute magnitudes estimated using empirical relations utilizing the recommended parameters (third panel) and the weighted-mean parameters (fourth panel). An error cut of 0.3 mag in the TGAS-based magnitudes is applied.

Sun et al. 2015; Yuan et al. 2015). Such systematics have not been accounted for in the current treatment. Fig. 20 shows the eccentricity distribution of the sample stars.

8 FORMAT OF THE VALUE-ADDED CATALOGUES

Similar to LSS-GAC DR1, this second release of value-added catalogues are stored in three binary tables in FITS format. The filenames are 'lss-gac_dr2_GAC.fits', 'lss-gac_dr2_M31.fits' and 'lss-gac_dr2_VB.fits', corresponding to the LSS-GAC main, M31/M33 and VB surveys, respectively. The value-added catalogues include information of the LAMOST observations, stellar parameters and error estimates, interstellar reddening, distance, multiband photometry, as well as proper motions and orbital parameters for 1790 633 observations of 1393 844 unique stars that have a spectral SNR(4650 Å) higher than 10. A detailed description of the catalogue content is presented in Table 5. Note that compared to LSS-GAC DR1, more information about the observations and stellar parameter estimates is provided for a better description of the data. This includes, for example, information of Julian date at the start of the first exposure, airmass, lunar distance, as well as tele-

scope altitude and so on. Stellar type of the best-matching template is also provided, which should be helpful for identifying stars of special interest (cf. Section 4.5). The catalogues are accessible from http://lamost973.pku.edu.cn/site/data along with a descriptive readme.txt file.

9 SUMMARY

This work describes the second release (DR2) of value-added catalogues of LSS-GAC, which contain observational information, multiband photometry, radial velocity, stellar atmospheric parameters, elemental abundances, absolute magnitudes, extinction, distance, proper motions and orbital parameters for 1790 633 LAMOST spectroscopic observations of 1393 844 unique stars targeted by the LSS-GAC main, M31/M33 and VB surveys between 2011 September and 2014 June that have a spectral SNR (4650 Å) higher than 10.

Spectra used to deliver LSS-GAC DR2 are processed at Peking University with the LAMOST two-dimensional pipeline and a spectral flux calibration pipeline specifically developed for LSS-GAC, as well as with the LSP3. Compared to LSS-GAC DR1, several improvements in stellar parameter determinations have been carried out, including: (1) More than 260 new spectral templates observed with the YAO 2.4-m and NAOC 2.16-m telescopes have been added to the MILES library used by LSP3; (2) Atmospheric parameters of LSP3 template stars have been re-determined/calibrated to reduce the systematic and random errors; (3) Stellar atmospheric parameters $T_{\rm eff}$, $\log g$, [Fe/H], [M/H], [α/Fe], [α/M], absolute magnitudes M_V, $M_{K_{\rm s}}$ and elemental abundances [C/H] and [N/H] are deduced from LAMOST spectra with a KPCA-based multivariate regression method. The method yields robust results for spectra of good SNRs (>50) – estimates of $\log g$ are found to be accurate to 0.1 dex for giants and late-type dwarfs, and estimates of M_V and $M_{K_{\rm s}}$ are accurate to 0.3 mag, corresponding to a distance accuracy of about 15 per cent. Distances inferred from absolute magnitudes determined directly from LAMOST spectra using the LAMOST-*Hipparcos* training set are free from stellar model atmospheres and stellar atmospheric parameters and are thus expected to have minimal systematics. Estimates of [M/H], [Fe/H], [C/H] and [N/H] for giant stars are shown to have a precision better than 0.1 dex, and those of [α/Fe] and [α/M] better than 0.05 dex; (4) Estimates of [α/Fe] by template matching with the KURUCZ synthetic spectra are also provided for both dwarfs and giants; (5) More descriptive critical flags and information about the observations and stellar parameter determination are provided to help better understand the data and find, for instance, stars of special interest, or to mask stars with poorly determined parameters; (6) Realistic errors are estimated for atmospheric parameters, distance and other inferred quantities (e.g. three-dimensional positions and velocities). Parameter errors are estimated in detail by taking into account of contributions from all identified sources, including spectral noise, inadequacy of the methods and templates adopted for the analysis, and errors propagated from other relevant parameters. Errors are assigned to the individual determinations for each star based on the spectral SNR and stellar atmospheric parameters.

Besides the large number of stars, the data sets cover a large and almost contiguous volume of the Galactic disc and halo, and have a relatively simple target selection function. They are thus expected to serve as a unique and valuable asset to study the structure and evolution of the Galaxy, especially the disc and the solar-neighbourhood. In addition, about 28 per cent measurements in the
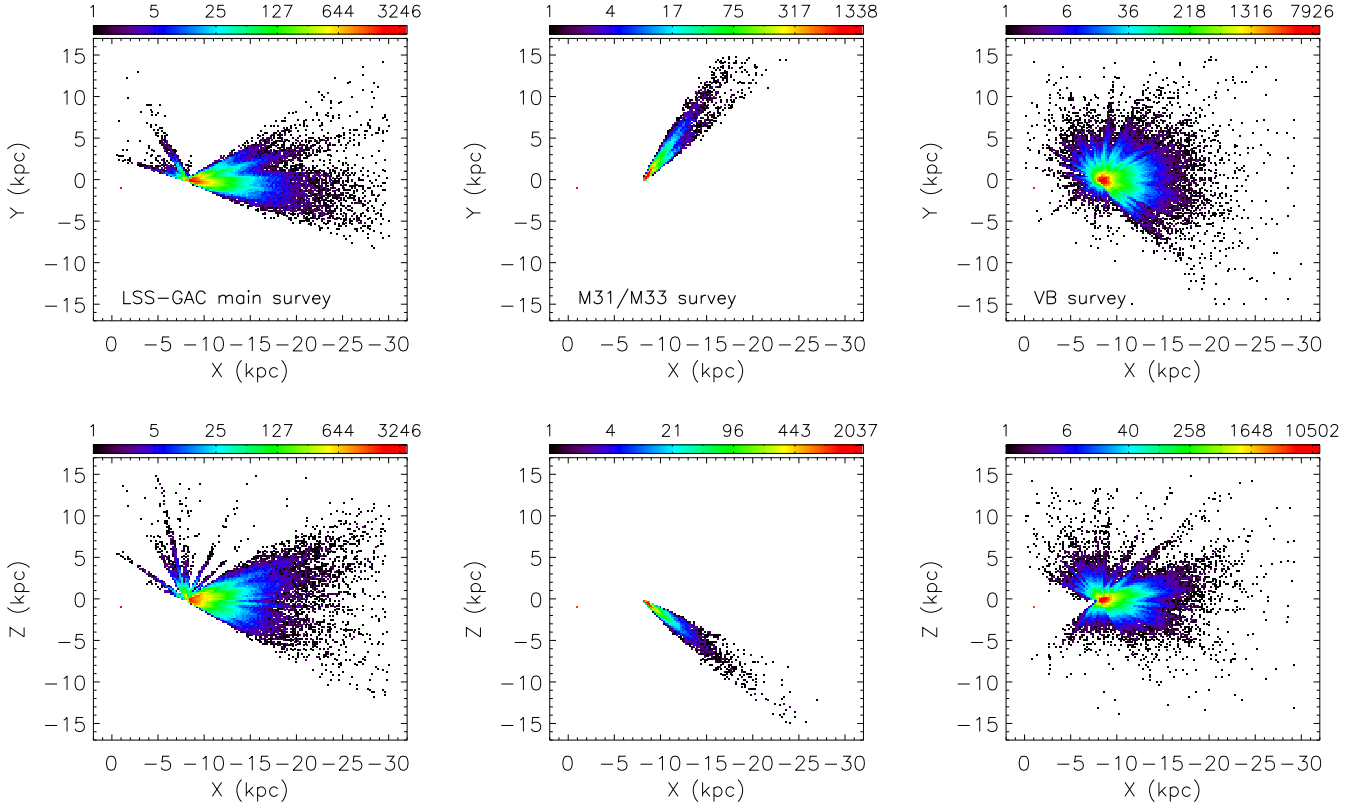
Figure 19. Colour-coded stellar density distributions in the Galactic *X–Y* and *X–Z* planes for stars targeted by the LSS-GAC main (left-hand panel), M31/M33 (middle panel) and VB (right-hand panel) surveys.
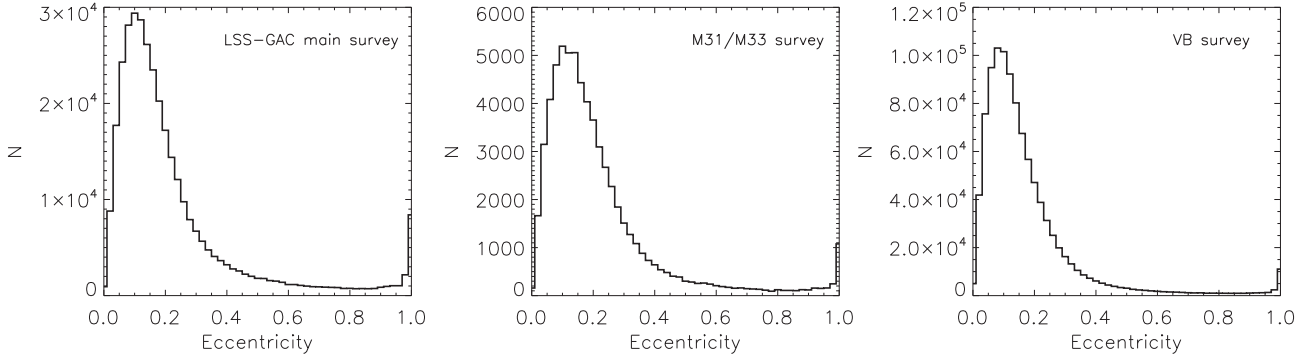
Figure 20. Distributions of orbital eccentricities for stars targeted by the LSS-GAC main (left-hand panel), M31/M33 (middle panel) and the VB (right-hand panel) surveys.

value-added catalogues are duplicate results of the same targets. The data sets are therefore also useful for time-domain spectroscopic studies.

Table 5. Description of the second release of LSS-GAC value-added catalogues.

Col.	Name	Description
1	spec_id	LAMOST unique spectral ID, in format of date-plateid-spectrographid-fibreid
2	date	Date of observation
3	plate	LAMOST plate ID, not necessarily unique
4	sp_id	LAMOST spectrograph ID, ranging from 1 to 16
5	fibre_id	LAMOST fibre ID for a given spectrograph, ranging from 1 to 250
6	objid	Object ID in the input catalogues
7	objtype	Initial object type from the survey input catalogues
8	ra	Right ascension of J2000.0 (°)
9	dec	Declination of J2000.0 (°)
10	l	Galactic longitude (°)
11	b	Galactic latitude (°)
12	jd	Julian days at the middle time of the first exposure
13	moonphase	Moon phase at the middle time of the first exposure
14	monodis	Moon distance at the middle time of the first exposure
15	airmass	Airmass at the middle time of the first exposure
16	alt	Altitude (in degrees) of the telescope at the middle time of the first exposure
17	az	Azimuth angle (in degrees) of the telescope at the middle time of the first exposure
18	ha	Hour angle (in degrees) of the telescope at the middle time of the first exposure
19	badfiber	Is it a bad fibre? (yes – 1, no – 0)
20	satflag	Is the spectrum saturated? (yes – 1, no – 0)
21	brightflag	Are there bright stars (snr_b > 300) in the nearby five fibres (yes – 1, no – 0)
22	brightsnr	Largest snr_b in the nearby five fibres
23	object_sky_ratio	Object to sky flux ratio
24	snr_b	S/N(4650 Å) per pixel
25	snr_r	S/N(7450 Å) per pixel
26	uqflag	Uniqueness flag. If the target has been observed n times, then uqflag runs from 1 to n, with 1 denoting the spectrum of the highest snr_b
27	vr	Radial velocity yielded by LSP3, after corrected for a systematic offset of -3.1 km s^{-1} (km s^{-1})
28	err_vr	Error of radial velocity yielded by LSP3 (km s^{-1})
29	teff	Recommended $T_{\rm eff}$ (K)
30	err_teff	Error of the recommended $T_{\rm eff}$
31	teff_from	Which method is the recommended $T_{\rm eff}$ adopted
32	logg	Recommended log g (cm s^{-2})
33	err_logg	Error of the recommended log g
34	logg_from	Which method is the recommended log g adopted
35	mv	Recommended absolute magnitude in V band
36	err_mv	Error of M_V
37	mv_from	Which method is the recommended M_V adopted
38	mk	Recommended absolute magnitude in $K_{\rm s}$ band
39	err_mk	Error of $M_{K_{\rm s}}$
40	mk_from	Which method is the recommended $M_{K_{\rm s}}$ adopted
41	feh	Recommended [Fe/H] (dex)
42	err_feh	Error of the recommended [Fe/H]
43	feh_from	Which method is the recommended [Fe/H] adopted
44	afe	Recommended [α/Fe] (dex)
45	err_afe	Error of the recommended [α/Fe]
46	afe_from	Which method is the recommended [α/Fe] adopted
47	am	α-element to metal abundance ratio [α/M] estimated by training the LAMOST-APOGEE stars (dex)
48	err_am	Error of [α/M]
49	mh	Metal abundance [M/H] estimated by training the LAMOST-APOGEE stars (dex)
50	err_mh	Error of [M/H]
51	ch	Carbon abundance [C/H] estimated by training the LAMOST-APOGEE stars (dex)
52	err_mh	Error of [C/H]
53	nh	Nitrogen abundance [N/H] estimated by training the LAMOST-APOGEE stars (dex)
54	err_nh	Error of [N/H]
55	ebv	Recommended $E(B - V)$
56	dist	Recommended distance (pc)
57	err_dist	Error of the recommended distance
58	dist_from	Which method is the recommended distance adopted
59	vr_peak_corr_coeff	Peak correlation coefficient for radial velocity estimation
60	vr_flag	Flag to describe value of 'vr_peak_corr_coeff', n means the vr_peak_corr_coeff is smaller than the median value of the sample stars with the same snr_b by $n \times$MAD
61	teff1	$T_{\rm eff}$ estimated with the weighted-mean algorithm (K)
62	err_teff1	Error of teff1

Table 5 – *continued*

Col.	Name	Description
63	teff2	T_{eff} estimated with the KPCA method (K)
64	err_teff2	Error of teff2
65	logg1	Log g estimated with the weighted-mean algorithm (cm s^{-2})
66	err_logg1	Error of logg1
67	logg2	Log g estimated with the KPCA method using MILES stars as training set (cm s^{-2})
68	err_logg2	Error of logg2
69	logg3	Log g estimated with the KPCA method using LAMOST-*Kepler* stars as training set (cm s^{-2})
70	err_logg3	Error of logg3
71	mv1	M_V estimated with the KPCA method taking LAMOST-*Hipparcos* stars as training set using 300 PCs (mag)
72	err_mv1	Error of mv1
73	mv2	M_V estimated with the KPCA method taking LAMOST-*Hipparcos* stars as training set using 100 PCs (mag)
74	err_mv2	Error of mv2
75	mk1	M_{K_s} estimated with the KPCA method taking LAMOST-*Hipparcos* stars as training set using 300 PCs (mag)
76	err_mk1	Error of mk1
77	mk2	M_{K_s} estimated with the KPCA method taking LAMOST-*Hipparcos* stars as training set using 100 PCs (mag)
78	err_mk2	Error of mk2
79	feh1	[Fe/H] estimated with the LSP3 weighted mean algorithm (dex)
80	err_feh1	Error of feh1
81	feh2	[Fe/H] estimated with the LSP3 KPCA method by training the MILES stars (dex)
82	err_feh2	Error of feh2
83	feh3	[Fe/H] estimated with the LSP3 KPCA method by training the LAMOST-APOGEE stars (dex)
84	err_feh3	Error of feh3
85	afe1	[α/Fe] estimated by template matching with synthetic spectra using spectral segments of 3900–3980, 4400–4600 and 5000–5300 Å (dex)
86	err_afe1	Error of afe1
87	afe2	[α/Fe] estimated by template matching with synthetic spectra using spectral segments of 4400–4600 and 5000 – 5300 Å (dex)
88	err_afe2	Error of afe2
89	afe3	[α/Fe] estimated with the LSP3 KPCA method using the LAMOST-APOGEE training set (dex)
90	err_afe3	Error of afe3
91	besttemp_chi2	Name of the best-matching template star with χ^2 algorithm
92	besttemp_corr	Name of the best-matching template star with correlation algorithm
93	typeflag_chi2	Stellar types of the best-matching template star with χ^2 algorithm
94	typeflag_corr	Stellar types of the best-matching template star with correlation algorithm
95	min_chi2	Minimum χ^2 yielded by LSP3 from template matching with the MILES library
96	chi2_flag	The 'min_chi2' is smaller than the median value of the sample stars in the same SNR and atmospheric parameter bin by $n \times$MAD
97	dg_miles_tm	Maximum value of the kernel function for estimation of T_{eff} and [Fe/H] with KPCA method via training the MILES stars
98	dg_miles_g	Maximum value of the kernel function for estimation of log g with KPCA method via training the MILES stars
99	dg_lm_kep	Maximum value of the kernel function for estimation of log g with KPCA method via training the LAMOST-*Kepler* stars
100	dg_lm_hip	Maximum value of the kernel function for estimation of absolute magnitudes with KPCA method via training the LAMOST-*Hipparcos* stars
101	dg_lm_apo	Maximum value of the kernel function for estimation of abundances with KPCA method via training the LAMOST-APOGEE stars
102	fuv	*GALEX FUV*-band magnitude (mag)
103	err_fuv	Error of fuv
104	nuv	*GALEX NUV*-band magnitude (mag)
105	err_nuv	Error of nuv
106	g	XSTPS-GAC *g*-band magnitude (mag)
107	err_g	Error of *g*
108	r	XSTPS-GAC *r*-band magnitude (mag)
109	err_r	Error of *r*
110	i	XSTPS-GAC *i*-band magnitude (mag)
111	err_i	Error of *i*
112	J	2MASS *J*-band magnitude (mag)
113	err_J	Error of *J*
114	H	2MASS *H*-band magnitude (mag)
115	err_H	Error of *H*
116	Ks	2MASS *Ks*-band magnitude (mag)
117	err_Ks	Error of *Ks*

Table 5 – *continued*

Col.	Name	Description
118	w1	*WISE W*1-band magnitude (mag)
119	err_w1	Error of $w1$
120	w2	*WISE W*2-band magnitude (mag)
121	err_w2	Error of $w2$
122	w3	*WISE W*3-band magnitude (mag)
123	err_w3	Error of $w3$
124	w4	*WISE W*4-band magnitude (mag)
125	err_w4	Error of $w3$
126	ph_qual_2mass	2MASS photometric quality flag
127	ph_qual_wise	*WISE* photometric quality flag
128	var_flag_wise	*WISE* variability flag
129	ext_flag_wise	*WISE* extended source flag
130	cc_flag_wise	*WISE* contamination and confusion flag
131	ebv_sfd	$E(B - V)$ from the SFD extinction map (mag)
132	ebv_sp	$E(B - V)$ derived from the star pair method (mag)
133	err_ebv_sp	Error of ebv_sp
134	ebv_mod	$E(B - V)$ derived by comparing the observed and synthetic model atmosphere colours (mag)
135	ebv_phot	$E(B - V)$ derived by fitting multiband photometry to the empirical stellar loci (Chen et al. 2014) (mag)
136	dist_em1	Distance derived using the empirical relations of absolute magnitudes as a function of stellar atmospheric parameters as yielded by the MILES stars using the recommended atmospheric parameters
137	err_dist_em1	Error of dist_em1
138	dist_em2	Distance derived using the empirical relations of absolute magnitudes as a function of stellar atmospheric parameters as yielded by the MILES stars using the weighted-mean atmospheric parameters
139	err_dist_em2	Error of dist_em2
140	dist_sp1	Distance inferred from absolute magnitudes estimated with KPCA method using 300 PCs (pc)
141	err_dist_sp1	Error of dist_sp1
142	dist_sp2	Distance inferred from absolute magnitudes estimated with KPCA method using 100 PCs (pc)
143	err_dist_sp2	Error of dist_sp2
144	dist_phot	Distance derived from the photometric parallax method (Chen et al. 2014) (pc)
145	err_dist_phot	Error of dist_phot
146	pmra_ppmxl	Proper motion in RA from the PPMXL catalogues (mas yr^{-1})
147	epmra_ppmxl	Error of pmra_ppmxl
148	pmdec_ppmxl	Proper motion in Dec. from the PPMXL catalogues (mas yr^{-1})
149	epmdec_ppmxl	Error of pmdec_ppmxl
150	pmra_ucac4	Proper motion in RA from the UCAC4 catalogues (mas yr^{-1})
151	epmra_ucac4	Error of pmra_ucac4
152	pmdec_ucac4	Proper motion in Dec. from the UCAC4 catalogues (mas yr^{-1})
153	epmdec_ucac4	Error of pmdec_ucac4
154	pmra_xuyi2mass	Proper motion in RA derived by comparing the XSTPS-GAC and 2MASS positions (mas yr^{-1})
155	pmdec_xuyi2mass	Proper motion in Dec. derived by comparing the XSTPS-GAC and 2MASS positions (mas yr^{-1})
156	x	x-coordinate in a Galactocentric Cartesian reference system, positive towards the Galactic Centre (kpc)
157	err_x	Error of x
158	y	y-coordinate in a Galactocentric Cartesian reference system, positive in the direction of disc rotation (kpc)
159	err_y	Error of y
160	z	z-coordinate in a Galactocentric Cartesian reference system, positive towards the North Galactic Pole (kpc)
161	err_z	Error of z
162	u[2]	Galactic space velocities in the x-direction computed from dist_em and the corrected PPMXL and UCAC4 proper motions, respectively, positive towards the Galactic Centre (km s^{-1})
163	err_u[2]	Error of u[2]
164	v[2]	Galactic space velocities in the y-direction computed from dist_em and the corrected PPMXL and UCAC4 proper motions, respectively, positive in the direction of Galactic rotation (km s^{-1})
165	err_v[2]	Error of v[2]
166	w[2]	Galactic space velocities in the z-direction computed from dist_em and the corrected PPMXL and UCAC4 proper motions, respectively, positive towards the north Galactic pole (km s^{-1})
167	err_w[2]	Error of w[2]
168	v_r[2]	Galactic space velocities in the r-direction in a Galactocentric cylindrical polar coordinate system, computed from dist_em and the corrected PPMXL and UCAC4 proper motions, respectively (km s^{-1})
169	err_v_r[2]	Error of v_r[2]
170	v_phi[2]	Galactic space velocities in the Φ-direction in a Galactocentric cylindrical polar coordinate system, computed from dist_em and the corrected PPMXL and UCAC4 proper motions, respectively, positive in the direction of counter disc rotation (km s^{-1})
171	err_v_phi[2]	Error of v_phi[2]

Table 5 – *continued*

Col.	Name	Description
172	v_z[2]	Galactic space velocities in the *z*-direction in a Galactocentric cylindrical polar coordinate system, computed from dist_em and the corrected PPMXL and UCAC4 proper motions, respectively, positive towards the north Galactic pole (km s^{-1})
173	err_v_z[2]	Error of v_z[2]
174	e[2]	Orbital eccentricities computed from dist_em and the corrected PPMXL and UCAC4 proper motions, respectively
175	Rapo[2]	Maximum Galactic radii reached by the orbits computed with PPMXL and UCAC4 proper motions, respectively (kpc)
176	Rperi[2]	Minimum Galactic radii reached by the orbits computed with PPMXL and UCAC4 proper motions, respectively (kpc)
177	zmin[2]	Minimum height reached by the orbits computed with PPMXL and UCAC4 proper motions, respectively (kpc)
178	zmax[2]	Maximum height reached by the orbits computed with PPMXL and UCAC4 proper motions, respectively (kpc)

REFERENCES

Aihara H. et al., 2011, ApJS, 193, 29
Anderson E., Francis C., 2012, Astron. Lett., 38, 331
Carlin J. L. et al., 2013, ApJ, 777, L5
Carlin J. L. et al., 2015, AJ, 150, 4
Castelli F., Kurucz R. L., 2004, preprint (astro-ph/0405087)
Cenarro A. J. et al., 2007, MNRAS, 374, 664
Chen B.-Q. et al., 2014, MNRAS, 443, 1192
Cui X.-Q. et al., 2012, Res. Astron. Astrophys., 12, 1197
Deng L.-C. et al., 2012, Res. Astron. Astrophys., 12, 735
Doi M. et al., 2010, AJ, 139, 1628
Dotter A., Chaboyer B., Jevremović D., Kostov V., Baron E., Ferguson J. W., 2008, ApJS, 178, 89
Falcón-Barroso J., Sánchez-Blázquez P., Vazdekis A., Ricciardelli E., Cardiel N., Cenarro A. J., Gorgas J., Peletier R. F., 2011, A&A, 532, A95
Gaia Collaboration et al., 2016, A&A, 595, A1
Gao H. et al., 2015, Res. Astron. Astrophys., 15, 2204
García Pérez A. E. et al., 2016, AJ, 151, 144
Gardner E., Flynn C., 2010, MNRAS, 405, 545
Gray R. O., 1999, Astrophysics Source Code Library, record ascl: 9910.002
Gunn J. E. et al., 1998, AJ, 116, 3040
Ho A. Y. Q. et al., 2016, preprint (arXiv:1602.00303)
Holtzman J. A. et al., 2015, AJ, 150, 148
Huang Y. et al., 2015a, Res. Astron. Astrophys., 15, 1240
Huang Y., Liu X.-W., Yuan H.-B., Xiang M.-S., Huo Z.-Y., Chen B.-Q., Zhang Y., Hou Y.-H., 2015b, MNRAS, 449, 162
Huang Y., Liu X.-W., Yuan H.-B., Xiang M.-S., Chen B.-Q., Zhang H.-W., 2015c, MNRAS, 454, 2863
Jester S. et al., 2005, AJ, 130, 873
Jofré P. et al., 2015, A&A, 582, A81
Lee Y. S. et al., 2011, AJ, 141, 90
Lee Y. S. et al., 2015, AJ, 150, 187
Li J. et al., 2016, Res. Astron. Astrophys., 16, 110
Lindegren L. et al., 2016, A&A, 595, 4
Liu C. et al., 2015, ApJ, 807, 4
Liu X.-W. et al., 2014, in Feltzing S., Zhao G., Walton N. A., Whitelock P., eds, Proc. IAU Symp. 298, Setting the Scene for Gaia and LAMOST. Kluwer, Dordrecht, p. 310
Luo A.-L. et al., 2012, Res. Astron. Astrophys., 12, 1243
Luo A.-L. et al., 2015, Res. Astron. Astrophys., 15, 1095
Majewski S. R., Wilson J. C., Hearty F., Schiavon R. R., Skrutskie M. F., 2010, in Cunha K., Spite M., Barbuy B., eds, Proc. IAU Symp. 265, Chemical Abundances in the Universe: Connecting First Stars to Planets. Kluwer, Dordrecht, p. 480

Martin D. C. et al., 2005, ApJ, 619, L1
Milligan S., Cranton B. W., Skrutskie M. F., 1996, in Fischer R. E., Smith W. J., eds, Proc. SPIEConf. Ser. Vol. 2863, Current Developments in Optical Design and Engineering VI. SPIE, Bellingham, p. 2
Munari U., Sordo R., Castelli F., Zwitter T., 2005, A&A, 442, 1127
Munari U. et al., 2014, AJ, 148, 81
Perryman M. A. C. et al., 1997, A&A, 323, L49
Perryman M. A. C. et al., 2001, A&A, 369, 339
Rebassa-Mansergas A. et al., 2015, MNRAS, 450, 743
Ren J.-J. et al., 2016, Res. Astron. Astrophys, 16, 45
Roeser S., Demleitner M., Schilbach E., 2010, AJ, 139, 2440
Rosenfield P., Marigo P., Girardi L., Dalcanton J. J., Bressan A., Williams B. F., Dolphin A., 2016, ApJ, 822, 73
Sánchez-Blázquez P. et al., 2006, MNRAS, 371, 703
Schlegel D. J., Finkbeiner D. P., Davis M., 1998, ApJ, 500, 525 (SFD98)
Skrutskie M. F. et al., 2006, AJ, 131, 1163
Soubiran C., Le Campion J.-F., Cayrel de Strobel G., Caillo A., 2010, A&A, 515, A111
Sun N.-C. et al., 2015, Res. Astron. Astrophys., 15, 1342
Wang J. et al., 2016a, MNRAS, 456, 672
Wang L. et al., 2016b, AJ, 152, 6
Wenger M. et al., 2000, A&AS, 143, 9
Wright E. L. et al., 2010, AJ, 140, 1868
Wu Y. et al., 2011, Res. Astron. Astrophys., 11, 924
Wu Y., Du B., Luo A., Zhao Y., Yuan H., 2014, in Heavens A., Starck J.-L., Krone-Martins A., eds, Proc. IAU Symp. 306, Statistical Challenges in 21st Century Cosmology. SPIE, Bellingham, p. 340
Xiang M.-S. et al., 2015a, Res. Astron. Astrophys., 15, 1209
Xiang M. S. et al., 2015b, MNRAS, 448, 822
Xiang M. S. et al., 2015c, MNRAS, 448, 90
Xiang M.-S. et al., 2017, MNRAS, 464, 3657
York D. G. et al., 2000, AJ, 120, 1579
Yuan H. B., Liu X. W., Xiang M. S., 2013, MNRAS, 430, 2188
Yuan H.-B. et al., 2015, MNRAS, 448, 855
Zacharias N., Finch C. T., Girard T. M., Henden A., Bartlett J. L., Monet D. G., Zacharias M. I., 2013, AJ, 145, 44
Zhang H.-H., Liu X.-W., Yuan H.-B., Zhao H.-B., Yao J.-S., Zhang H.-W., Xiang M.-S., 2013, Res. Astron. Astrophys., 13, 490
Zhang H.-H., Liu X.-W., Yuan H.-B., Zhao H.-B., Yao J.-S., Zhang H.-W., Xiang M.-S., Huang Y., 2014, Res. Astron. Astrophys., 14, 456
Zhao G., Zhao Y.-H., Chu Y.-Q., Jing Y.-P., Deng L.-C., 2012, Res. Astron. Astrophys., 12, 723

This paper has been typeset from a TEX/LATEX file prepared by the author.

Molecular Gas and Star-formation in Low Surface Brightness Galaxies

Tian-Wen Cao[1,2,3] ⓘ, Hong Wu[1,2], Wei Du[1] ⓘ, Feng-Jie Lei[1,2], Ming Zhu[1], Jan Wouterloot[4] ⓘ, Harriet Parsons[4] ⓘ,
Yi-Nan Zhu[1] ⓘ, Chao-Jian Wu[1] ⓘ, Fan Yang[1], Chen Cao[5], Zhi-Min Zhou[1] ⓘ, Min He[1,2], Jun-Jie Jin[1,2], and James E. Wicker[1]

[1] Key Laboratory of Optical Astronomy, National Astronomical Observatories, Chinese Academy of Sciences, Beijing 100012, P.R. China; twcao@bao.ac.cn
[2] School of Astronomy and Space Science, University of Chinese Academy of Sciences, Beijing, P.R. China; hwu@bao.ac.cn
[3] Chinese Academy of Sciences South America Center for Astronomy, China-Chile Joint Center for Astronomy,
Camino El Observatorio 1515, Las Condes, Santiago, Chile
[4] East Asian Observatory, 660 N. Aohōkū Place, University Park, Hilo, HI 96720, USA
[5] School of Space Science and Physics, Shandong University at Weihai, Weihai, Shandong 264209, China
Received 2017 April 15; revised 2017 July 23; accepted 2017 August 3; published 2017 August 30

Abstract

We have obtained CO($J = 2-1$) spectra of nine face-on low surface brightness galaxies using the JCMT 15 m telescope and observed Hα images using the 2.16 m telescope of NAOC. As no CO has been detected, only upper limits on the H$_2$ masses are given. The upper limits of total molecular hydrogen masses are about $(1.2–82.4) \times 10^7 M_\odot$. Their star-formation rates are mainly lower than $0.4 M_\odot \, \mathrm{yr}^{-1}$ and star-formation efficiencies are lower than $1.364 \times 10^{-10} \, \mathrm{yr}^{-1}$. Our results show that the absence of molecular gas content is the direct reason for the low star-formation rate. The low star-formation efficiency probably resulted from the low efficiency of H I gas transforming to H$_2$ gas.

Key words: galaxies: evolution – galaxies: star formation – ISM: molecules

1. Introduction

Low surface brightness galaxies (LSBGs, Impey & Bothun 1997) are important for investigating the evolution of our universe. The origin and evolution of these LSBGs are still mysterious. They have significantly different chemical enrichment histories from normal galaxies (Peebles 2001; Pustilnik et al. 2011). LSBGs are usually optically faint and blue (de Blok et al. 1995; Impey & Bothun 1997). The stellar disks of most LSBGs are diffuse. They usually have low metallicities ($Z < 1/3 \, Z_\odot$ McGaugh 1994), low column densities ($N_{\mathrm{H\,I}} \sim 10^{20} \, \mathrm{cm}^{-2}$ de Blok et al. 1996), and low dust masses (Matthews & Wood 2001). The star-formation rates (SFRs) of LSBGs are lower than those of normal galaxies (Gerritsen & de Blok 1999; Boissier et al. 2008; Wyder et al. 2009).

According to pervious works, the H I content of most LSBGs is rich, compared with normal star-forming (SF) galaxies (McGaugh 1994). The H I gas disk extends well beyond the stellar disk (McGaugh & de Blok 1997; Gerritsen & de Blok 1999; Matthews et al. 2001; O'Neil et al. 2004) and is about double the size of the optical disk (de Blok et al. 1996; Pickering et al. 1997; Das et al. 2007).

Although the original material involved in star formation is H I, the star formation is indirectly related to H I. Generally, the star formation arises out of molecular clouds. The low star-formation rates in LSBGs may be related to the absence of molecular gas content. The optical peculiarities of LSBGs have been discussed in some works (van der Hulst et al. 1993; McGaugh 1994; McGaugh & Bothun 1994; de Blok et al. 1995; Impey & Bothun 1997; Jimenez et al. 1998); however, the cold molecular gas in these galaxies is far from well understood. Molecular gas is vital for studying the star-formation process. There are some previous works that try to detect the CO content in LSBGs (Schombert et al. 1990; Knezek 1993; de Blok & van der Hulst 1998b; Braine et al. 2000). Most works just give upper limits on CO content, and only a few LSBGs have detected molecular gas (Matthews & Gao 2001; O'Neil et al. 2003; Matthews et al. 2005; Das et al.

2010; Haynes et al. 2011). This may indicate a shortage of molecular gas in LSBGs.

To explore the low star-formation efficiency (SFE) of LSBGs, we need to know which phase is dominant during star formation. There are two phases in the formation of a star: first, the H I gas transforms into molecular gas, then molecular gas forms a star. The CO($J = 2-1$) emission line is used to trace molecular hydrogen gas in this work. We observe the CO ($J = 2-1$) emission line by JCMT, Hα images by the 2.16 m telescope of NAOC and also combine with NUV data from *GALEX* and H I data from Arecibo.

In this paper, the sample and observations of LSBGs are presented in Section 2. Results and an analysis are given in Section 3. Discussion and summary are provided in Section 4 and Section 5.

2. The Sample and Observation of LSBGs

2.1. Sample

The Arecibo Legacy Fast ALFA (ALFALFA) survey (Giovanelli et al. 2005), which covers 7000 deg^2 of high Galactic latitude sky, provides a 21 cm H I emission line spectral database with redshifts from 1600 to 18,000 km s^{-1} and a velocity resolution of 5 km s^{-1}. The α.40 catalog is the first released catalog that covers 40% of the area of the ALFALFA survey and contains 15,855 objects (Haynes et al. 2011). About 78% of sources have optical counterparts from the Sloan Digital Sky Survey (SDSS, Haynes et al. 2011).

Based on the α.40 catalog, Du et al. (2015) selects a sample of LSBGs that contains 1129 LSBGs with surface brightnesses $\mu_{\mathrm{B(0)obs}}$ larger than 22.5 mag arcsec^{-2}. We selected nine LSBGs from this sample. They all have face-on disks and their H I masses are about $(0.52–19.9) \times 10^9 \, M_\odot$, and are expected to have higher fluxes of CO($J = 2-1$) emission lines than others in the 1129 LSBGs sample. The redshifts in our sample are between 0.0029 and 0.0339. Generally, the size of the CO disk is about half the size of the optical disk (Young & Knezek 1989) and the optical sizes of nine targets are about
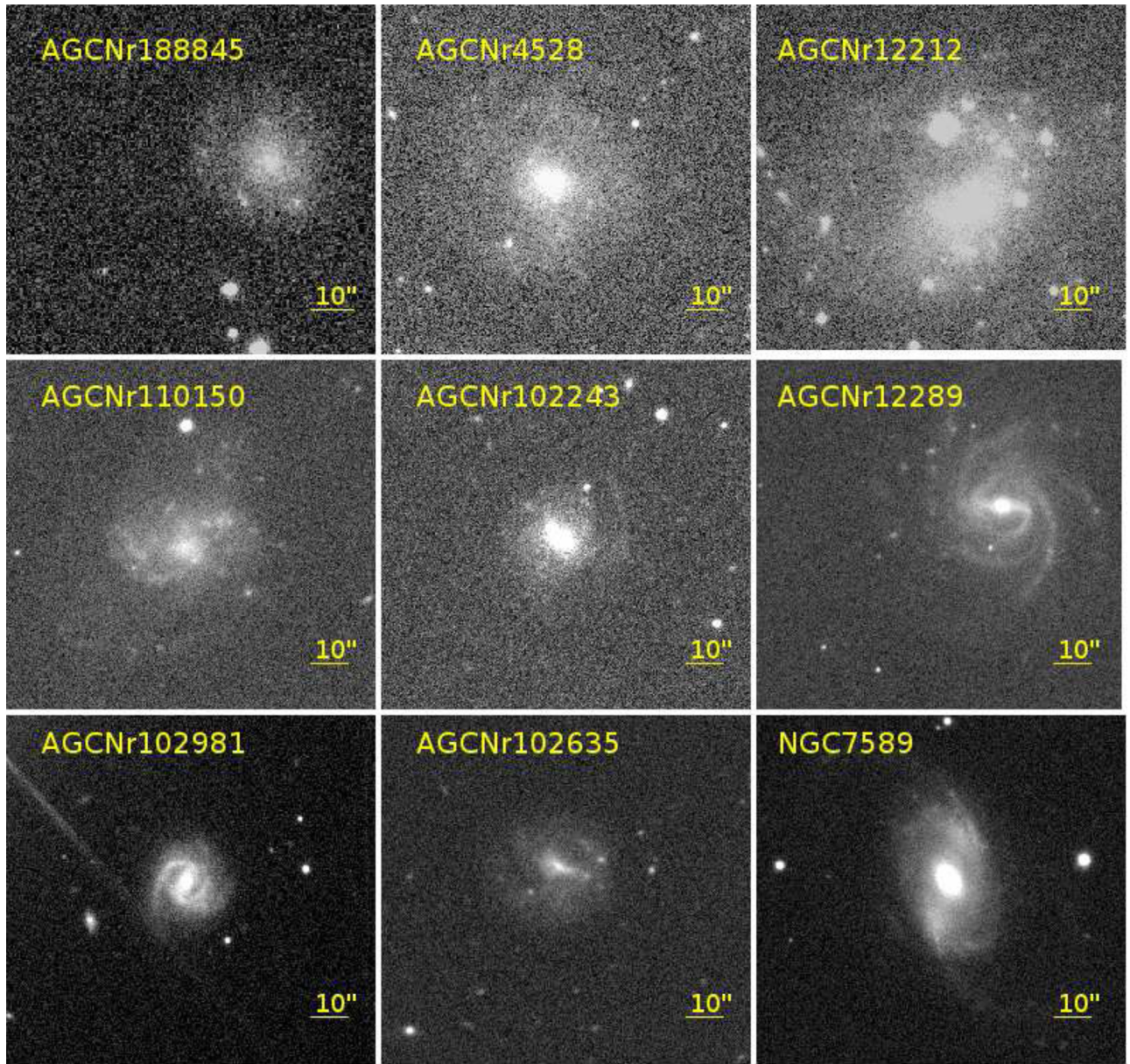
Figure 1. SDSS r-band images of our LSBGs.

30–80 arcsec. Figure 1 shows r-band images of our nine LSBGs from SDSS DR12. More details about properties of the galaxies are shown in Table 1.

2.2. CO(J = 2−1) Emission

We obtained CO($J = 2−1$) spectra of nine targets using the $R \times A3$ receiver with ACSIS as the backend, mounted on the JCMT 15 m telescope near the peak of Mauna Kea, Hawaii. The half power beam width is about $20''$ at 230 GHz. The frequency coverage of the $A3$ receiver ranges from 211.5 to 276.5 GHz and the CO($J = 2−1$) spectra of our objects shift from 222.99 to 229.86 GHz. The A3 receiver gives 1936 channels over a bandwidth of 1 GHz with a channel separation of 0.516 MHz, and the velocity resolution is 0.674 km s^{-1} (one channel).

The targets are finally observed under band 4 weather[6] in March and band 5 weather in August of 2015. In band 4

weather, the atmospheric zenith opacity at 225 GHz, as measured with the Water Vapour Monitor (measured in the direction in which the telescope is observing), or the CSO tau meter (measuring in a fixed direction), is between 0.12 and 0.20. In band 5 weather, the zenith opacity is between 0.20 and 0.32. The on-source intergration time per scan was 400 s and one such scan took 13 minutes. The observation mode was "double beam switching"[7] over 60 arcsec (to both sides with respect to the source). The total integration time of each object is about two hours and eight hours for band 4 weather and band 5 weather, respectively. The data are calibrated by ORAC-DR (Hirst & Cavanagh 2005) data-reduction pipeline[8] using STARLINK software. In Table 2, columns 2–6 show details about the observations of the CO($J = 2−1$) emission line.

---

[6] http://www.eaobservatory.org/jcmt/observing/weather-bands/

[7] http://www.eaobservatory.org/jcmt/instrumentation/heterodyne/observing-modes/

[8] http://starlink.eao.hawaii.edu/devdocs/sun260.htx/sun260.html

Table 1
Parameters of Low Surface Brightness Galaxies

Name	R.A. (J2000)	Decl. (J2000)	$V_{He\,I}$ (km s^{-1})	$u_{B(0)obs}$ (mag arcsec^{-2})	W_{50}[a] (km s^{-1})	$\log M_{H\,I}$ ($M_\odot$)	D (Mpc)	Major-axis (arcsec)	z	NUV$_{AB}$ (mag)	r_{SDSS} (mag)	$W1$[b] (mag)	$W3$[c] (mag)
AGCNr188845	08:01:13.02	+11:37:24.48	4935	23.056	79	8.99	72.5	54	0.0164	...	16.30 ±0.02	13.923 ±0.044	...
AGCNr4528	08:40:58.60	+16:11:00.14	4288	22.900	88	9.40	63.6	66	0.0143	17.56 ±0.02	15.90 ±0.01	13.335 ±0.028	...
AGCNr12212	22:50:30.26	+29:08:19.52	894	23.040	99	9.34	24.3	62	0.0029	...	15.02 ±0.00	...	...
AGCNr110150	01:14:45.56	+27:08:11.10	3617	22.760	108	9.49	49.5	80	0.0120	17.52 ±0.03	16.01 ±0.01	...	...
AGCNr102243	00:05:05.06	+23:58:14.09	6575	22.500	139	9.78	89.0	52	0.0219	...	20.59 ±0.04	13.494 ±0.019	10.83 ±0.336
AGCNr12289	22:59:41.52	+24:04:29.77	10165	22.650	217	10.3	140.2	35	0.0339	...	14.60 ±0.00	11.658 ±0.007	8.64 ±0.034
AGCNr102981	00:02:55.56	+28:16:38.78	4583	22.540	65	8.72	66.2	46	0.0152	...	15.41 ±0.00	12.615 ±0.012	9.74 ±0.117
AGCNr102635	00:16:12.22	+24:50:59.04	9491	22.573	94	9.65	138.7	46	0.0316	18.34 ±0.04	16.66 ±0.01	13.551 ±0.026	10.98 ±0.261
NGC 7589	23:18:15.60	+00:15:40.00	8938	25.000[d]	345	10.01	120.7	76	0.0298	17.53 ±0.01	14.08 ±0.00	11.084 ±0.009	8.26 ±0.024

Notes.
[a] W_{50} is the full width at half maximum (FWHM) of the H I emission line.
[b] $W1$ is 3.4 μm band of the *WISE*.
[c] $W3$ is 12 μm band of the *WISE*.
[d] For NGC 7589, its surface brightness is from de Vaucouleurs et al. (1991).

Name	Receiver	Weather Band	Frequency (GHZ)	Integration Time (hr)	Rms Noise (mk)	Facility	Hα Filter[a] (Å)	$\mathrm{Exp_{H\alpha}}$ (s)	$\mathrm{Exp_{Rband}}$ (s)
AGCNr188845	RxA3/JCMT	4	226.91	1.63	2.7	BFOSC/2.16	6660.0	1800	600
AGCNr4528	RxA3/JCMT	4	227.29	2.62	2.0	BFOSC/2.16	6660.0	1800	600
AGCNr12212	RxA3/JCMT	5	229.86	7.8	2.1	…	…	…	…
AGCNr110150	RxA3/JCMT	5	227.67	7.4	2.8	BFOSC/2.16	6660.0	1800	600
AGCNr102243	RxA3/JCMT	5	225.60	7.8	2.6	BFOSC/2.16	6710.0	1800	600
AGCNr12289	RxA3/JCMT	5	222.99	7.6	3.3	BFOSC/2.16	6760.0	1800	600
AGCNr102981	RxA3/JCMT	5	227.06	7.8	2.0	BFOSC/2.16	6660.0	1800	600
AGCNr102635	RxA3/JCMT	5	223.47	8.3	3.1	BFOSC/2.16	6760.0	1800	600
NGC 7589	RxA3/JCMT	5	223.87	7.8	2.1	…	…	…	…

Note.
[a] The central wavelength of Hα filter.

2.3. Hα Images

The Hα images of NGC 7589 and AGCNr12212 have been observed by van Zee (2000), Epinat et al. (2008), and Subramanian et al. (2016). The Hα images of other seven LSBGs were observed by the 2.16 m telescope at Xinglong Observatory, administered by the National Astronomical Observatories, Chinese Academy of Sciences (NAOC). This facility houses the BAO Faint Object Spectrograph and Camera (BFOSC; Fan et al. 2016) with a 1272 × 1152 E2V CCD. The field of view is about 9.46 arcmin × 8.77 arcmin. The pixel size is 0.″475 and the gain is 1.08 e/ADU. Each target was observed with a broadband R filter and one narrowband Hα filter. The center wavelength of the R-band filter is 6407 Å and the full width at half maximum (FWHM) is 1580 Å. According to the different redshifts of objects, we employed Hα filters with different central wavelengths of 6660 Å, 6710 Å, and 6760 Å and an FWHM of 70 Å. The exposure times are about 600 s and 1800 s for the R band and Hα narrowbands, respectively.

The image reduction is performed by using IRAF software and the sky background subtraction applied the more accurate method by Zheng et al. (1999), Wu et al. (2002), and Du et al. (2015). The stellar continuum of each Ha image is removed by substracting the scaled R-band image. Finally, we measured the Ha fluxes of these LSBGs, using the ellipse photometry of IRAF. In Table 2, columns 7–10 list the details of observations of Hα images. AGCNr102981 is affected by light pollution from a nearby bright star.

3. Results and Analysis

3.1. H₂ Masses

To enhance signal-to-noise, we binned the CO($J = 2-1$) spectral channels. The final CO($J = 2-1$) spectral have been smoothed to 15 km s^{-1} as shown in Figure 2. Apparently, None of nine targets are detected CO($J = 2-1$) content.

To estimate the molecular hydrogen masses, we adopted W_{50} as the linewidth. Here, W_{50} is the FWHM of H I emission line. The W_{50} of our targets is about 65–345 km s^{-1}. The aperture efficiency η_a is 0.61 at 225 GHz, and the conversion from T_A in kelvin to flux density in Jansky is $S(\mathrm{Jy}) = 15.6 \times T_A(\mathrm{K})/\eta_a$, for JCMT. In this work, the T_A is replaced by the $3\sigma/\sqrt{n}$, where the σ is the rms noise at native resolution and n is the number of channels to smooth velocity resolution to 15 km s^{-1}. Hence, flux densities in Jansky are calculated according to

equation: $S_{\mathrm{CO}(J=2-1)}(\mathrm{Jy}) = 15.6 \times 3 \times \sigma/\sqrt{n}/\eta_a$. Here we adopt the $R_{21} = \mathrm{CO}(J = 2-1)/\mathrm{CO}(J = 1\text{-}0) = 0.7$ (Leroy et al. 2009; Schruba et al. 2012).

The CO-to-H₂ conversion equation is as follows.

$$M_{\mathrm{H_2}} = \alpha_{\mathrm{CO}} \times L_{\mathrm{CO}} \tag{1}$$

$$L_{\mathrm{CO}} = 3.25 \times 10^7 \times S'_{\mathrm{CO}} \times \nu_{\mathrm{obs}}^{-2} \times D^2 \times (1+z)^{-3}. \tag{2}$$

In Equation(1), M_{H2} is molecular hydrogen mass in $M_\odot$ and L_{CO} is CO luminosity in K km s^{-1} pc^2. In Equation(2), S'_{CO} is integrated CO flux density in Jy km s^{-1}. We adopt linewidth W_{50} and the resolution 15 km s^{-1}, such as $S'_{\mathrm{CO}(J=1-0)} = S_{\mathrm{CO}(J=1-0)} \times W_{50}/15$. ν_{obs} is observation frequency in GHz, D is distance in Mpc, and z is redshift.

In different environments, the X_{CO} factor is different. Considering that the conversion factor of CO-to-H₂ increases with decreasing metallicity, X_{CO} is chosen to be 3.162×10^{20} cm^{-2}/ (K km s^{-1}) ($X_{\mathrm{CO}} = \alpha_{\mathrm{CO}} \times 6.3 \times 10^{19}$ pc^2 cm^{-2} $M_\odot^{-1}$, α_{CO} simply is a mass-to-light ratio in $M_\odot$ (K km s^{-1} pc^2)$^{-1}$ Bolatto et al. 2013), which is also the same as previous works (Matthews & Gao 2001; Matthews et al. 2005). From Equation (1), we can calculate upper limits of molecular hydrogen masses per beam, which are about $(0.68-31.6) \times 10^7 M_\odot$.

To compare with previous works, we correct the beam size to the CO disk size of our LSBGs. We estimate the upper limits of total molecular hydrogen masses of our sample. The beam filling factors are defined as the ratios between the area of beam and the total area of the CO disk, which is generally half of the optical disk (Young & Knezek 1989), and listed in Table 3. The major-axis of optical disks are given by R-band images and listed in the Table 1. The size of NGC 7589 is from Lauberts & Valentijn (1989). The upper limits of total molecular hydrogen masses are about $(1.2-82.4) \times 10^7 M_\odot$, which are listed in Table 3. Since the H I disk is more extended in LSBGs, the CO disk may be larger than half of optical disk. The total molecular hydrogen masses may be underestimated in Table 3. In the following parts of this paper, $M_{\mathrm{H_2}}$ represents the total molecular hydrogen mass.

In Figure 3, we plot the $M_{\mathrm{H\,I}}$ versus $M_{\mathrm{H_2}}$ including our sample and LSBGs from some previous works. We have calculated the average molecular mass with bin size in $10^{0.5} M_\odot$. The average of $M_{\mathrm{H_2}}$ of LSBGs is smaller than those in SF galaxies for a given H I mass. We can see that upper limits of $M_{\mathrm{H_2}}$ in our work are consistent with previous works. LSBGs are deficient of the molecular gas compared with these SF galaxies.
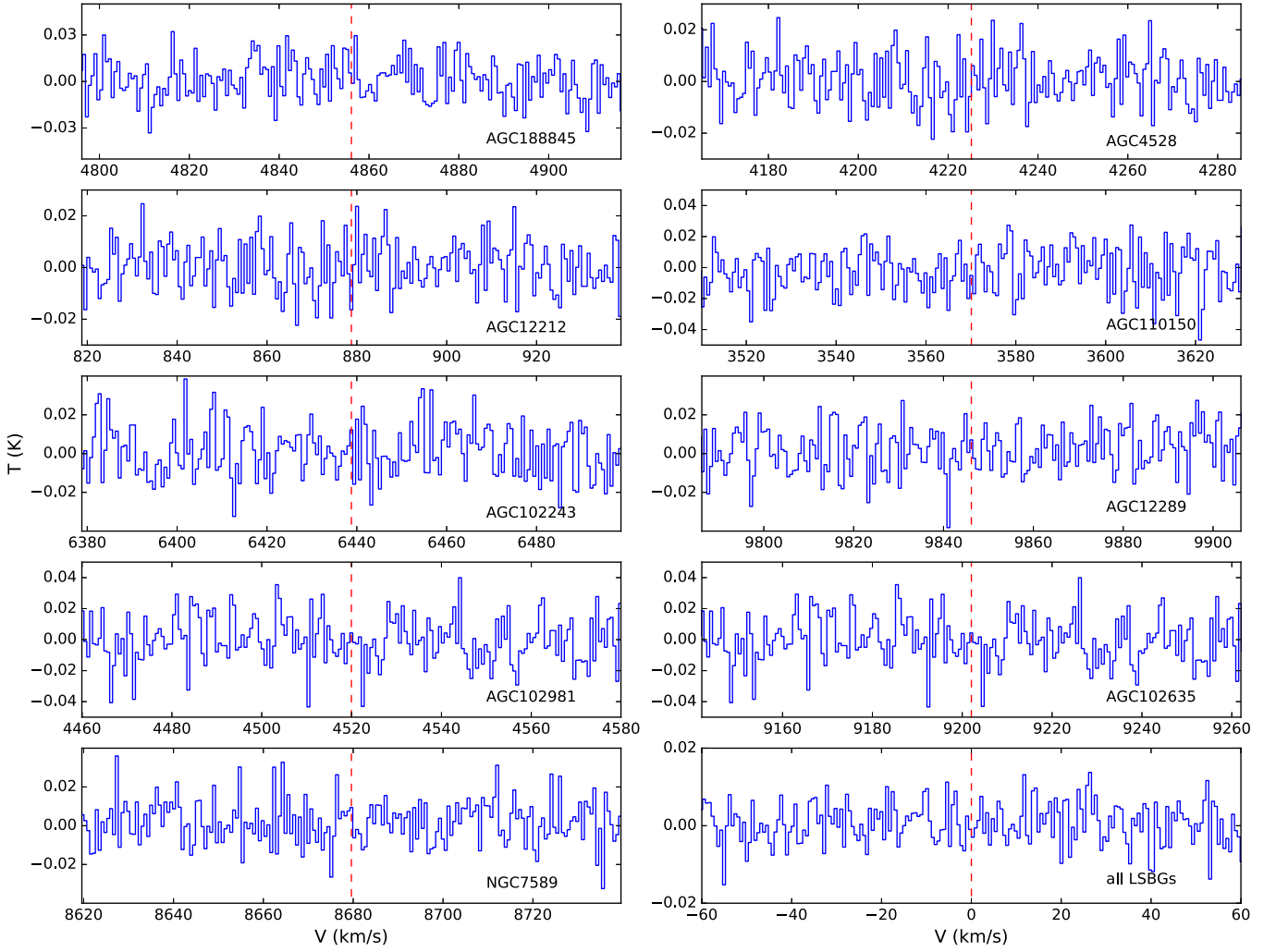
Figure 2. Nine individual and combined CO($J = 2-1$) spectra of LSBGs. The red dashed line marks the position of the emission line of the redshifted CO($J = 2-1$).

Table 3
Upper limits of H$_2$ Masses in the Beam Size

Name	SFR$_{H\alpha}$ ($M_\odot$ yr^{-1})	log(SFE)$_{H\alpha}$ (yr^{-1})	SFR$_{NUV}$ ($M_\odot$ yr^{-1})	log (SFE)$_{NUV}$ (yr^{-1})	logL_{CO} (K km s^{-1}pc^2)	Beam Filling Factor	log$M_{H2Total}$ ($M_\odot$)	$M_{H2Total}/M_{HI}$	log$L_{3.4}$ ($L_\odot$)	logM_* ($M_\odot$)
AGCNr188845	0.097	−10.012	⋯	⋯	<6.71	1.35	<7.635	<0.044	7.316	8.154
AGCNr4528	0.079	−10.500	0.232	−10.037	<6.50	1.65	<7.643	<0.017	7.437	8.290
AGCNr12212[a]	0.111	−10.300			<5.747	1.55	<7.612	<0.0201	⋯	⋯
	0.056	−10.599	⋯	⋯	⋯	⋯	⋯	⋯	⋯	⋯
AGCNr110150	0.108	−10.457	0.146	−10.327	<6.52	2.07	<7.827	<0.022	⋯	⋯
AGCNr102243	0.829	−9.865	⋯	⋯	<7.10	1.35	<8.017	<0.017	7.665	8.545
AGCNr12289[b]	0.339	−10.776	⋯	⋯	<7.79	1.00	<8.615	<0.020	8.795	9.810
AGCNr102981[c]	NAN	⋯	⋯	⋯	<6.411	1.76	<7.07	<0.018	7.760	8.651
AGCNr102635	0.367	−10.085	0.539	−9.930	<7.39	1.76	<8.336	<0.048	8.029	8.952
NGC 7589[d]	0.173	−10.782	1.003	−10.018	<7.66	1.90	<8.960	<0.0806	8.894	9.922

Notes.
[a] For AGCNr12212, the two different SFR$_{H\alpha}$ results are from the works of van Zee (2000) and Epinat et al. (2008). We did not derive its Hα flux from our observation.
[b] The result with the observations of JCMT. The CO content of AGCNr12289 was detected by O'Neil et al. (2003) with the IRAM and the ratio of M_{H_2}/M_{HI} is 0.008.
[c] For AGCNr102981, we did not derive its Hα flux from our observation.
[d] For NGC 7589, the SFR$_{H\alpha}$ is calculated by SDSS spectra (Subramanian et al. 2016).

32 nearby gas-rich SF galaxies in Figure 3 are from Jiang et al. (2015) and observed with the Sub-millimeter Telescope. Their H I masses are from the ALFALFA catalog. These SF galaxies are intermediate-mass galaxies ($<10^{10}\ M_\odot$). The intermediate-mass galaxies were found to be more gas rich (Blanton & Moustakas 2009). These galaxies present the low-mass end of
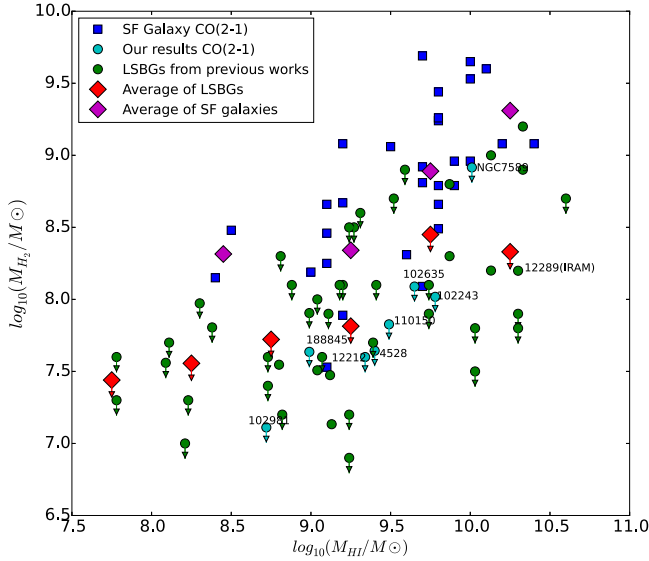
Figure 3. H I mass vs. H$_2$ mass. The cyan dots are LSBGs from this survey, the green dots are LSBGs from previous works (Schombert et al. 1990; de Blok & van der Hulst 1998a; Braine et al. 2000; O'Neil et al. 2000, 2003). Blue squares are SF galaxies from Jiang et al. (2015). The red and purple diamonds present the average molecular mass of LSBGs and SF galaxies, respectively. The arrows indicate the upper limits.

main-sequence SF galaxies. Both the molecular mass of our sample and the SF galaxies sample are calculated by the CO ($J = 2-1$) emission line, so the SF galaxies are selected as a comparison sample.

Some reasons could explain the lack of molecular gas in LSBGs. First, metallicity can affect the cooling efficiency of the interstellar medium (ISM), which may impact the formation of giant molecular clouds (GMCs). Second, dust grains where H$_2$ forms (Savage & Mathis 1979) can shield molecular gas from photodissociation. The low ISM densities make it hard for molecular clouds to form and be maintained.

The low metallicities and low ISM densities in LSBGs can make it either difficult to form H$_2$ or easy to destroy H$_2$.

3.2. Star-formation Rates

We adopt Hα luminosity to calculate the SFR of our sample. As the dust in LSBGs is usually less, few targets can be detected in the 22 μm (*WISE W4*) band, so we ignore the dust extinction in our sample.

The SFR of AGCNr12212 has been found to be 0.111 $M_\odot$ yr^{-1} in the work of van Zee (2000) and 0.056 $M_\odot$ yr^{-1} in the work of Epinat et al. (2008). Six Hα fluxes of LSBGs are available from our observation. We transform Hα fluxes to luminosity using the relation: $L = 4 \times \pi \times D^2 \times F$, where D is distance in centimeters and F is Hα flux in erg s^{-1} cm^2. We employ the following equation to calculate SFR (Kennicutt 1998).

$$\text{SFR}_{\text{H}\alpha}(M_\odot \text{ yr}^{-1}) = 7.9 \times 10^{-42} \times L_{\text{H}\alpha} \text{ erg s}^{-1}. \quad (3)$$

The derived SFRs are from 0.056 to 0.829 $M_\odot$ yr^{-1}.

We also use the NUV-band luminosity to calculate SFR of four sources (AGCNr4528, 110150, 102635, and NGC 7589), which have NUV data from *GALEX*. We adopt the following equation (Kennicutt 1998).

$$\text{SFR}_{\text{UV}}(M_\odot \text{ yr}^{-1}) = 1.4 \times 10^{-28} \times L_\nu(\text{erg s}^{-1} \text{ Hz}^{-1}). \quad (4)$$

The NUV-based SFRs are 0.146 $\sim$ 1.003 $M_\odot$ yr^{-1}, which are systematically larger than those calculated from Hα luminosity. The UV emission is also contaminated by older stars, so this would lead to deriving higher SFR from UV than that from the Hα. All these values are listed in the Table 3.

In Figure 4, we show SFR versus H I mass for our sample and black lines connect the same target. We also show another sample of LSBGs in green dots from Boissier et al. (2008) whose SFRs are estimated by NUV luminosity. The figure shows an increase of the SFR with H I mass. SFR in LSBGs is about 0.2 $M_\odot$ yr^{-1} in the model calculations of McGaugh & Bothun (1994) and 0.17–0.36 $M_\odot$ yr^{-1} by Hα (Burkholder et al. 2001), they are lower than that of SF galaxies. The low SFRs of our sample are consistent with previous results. The low SFR in LSBGs agrees with the low molecular hydrogen mass.

3.3. Star-formation Efficiency

SFE (Leroy et al. 2008) is the ratio of star-formation rate to total mass of gas (SFE = SFR / M_{gas}). M_{gas} is the total gas mass that can be estimated by H$_2$ mass and H I mass ($M_{\text{H}_2} + M_{\text{H I}}$).

The SFR and M_{H_2} of our sample have been calculated in Sections 3.1 and 3.2. $M_{\text{H I}}$ is from the ALFALFA catalog listed in Table 2. Since M_{H_2} is far smaller than $M_{\text{H I}}$, we adopt $M_{\text{H I}}$ to replace M_{gas}. SFE can be calculated by SFR$_{\text{H}\alpha}$ and SFR$_{\text{UV}}$, respectively. SFEs of our LSBGs are (0.165 $\sim$ 1.364) $\times$ 10^{-10} yr^{-1} by SFR$_{\text{H}\alpha}$ and (0.471 $\sim$ 1.174) $\times$ 10^{-10} yr^{-1} by SFR$_{\text{UV}}$, respectively. The results are shown in Table 3.

SFEs of LSBGs are lower than 1.364 $\times$ 10^{-10} yr^{-1} and are far lower than 5.25 $\times$ 10^{-10} yr^{-1} observed in normal spiral galaxies (Leroy et al. 2008). Generally, molecular gas is directly related to star formation, so SFE can reflect the efficiency of transforming the hydrogen atom to molecular hydrogen. Low SFE may hint that atomic hydrogen produces molecular hydrogen at a low speed. In short, the low SFR and SFE imply a lack of molecular hydrogen gas in LSBGs and this will be discussed in Section 4.

4. Discussion

4.1. Comment of Individual Galaxies

AGCNr12289 is a late-type spiral galaxy with a optical disk size of about 35$''$ and has a potential AGN/LINER core (Schombert 1998). There is a supernova (SN2002en) in AGCNr12289. O'Neil et al. (2003) has detected CO($J = 1-0$, $J = 2-1$) content in AGCNr12289 using the IRAM 30 m telescope. The M_{H_2} of AGCNr12289 is about 15.8 $\times$ 10^7 $M_\odot$ using CO($J = 2-1$) observed by IRAM, which is lower than our upper limit of 41.2 $\times$ 10^7 $M_\odot$. The ratio of $M_{\text{H}_2}/M_{\text{H I}}$ is 0.008 for AGCNr12289.

AGCNr188845, *AGCNr102243, AGCNr102635*, and *AGCNr102981*: For these galaxies, the optical sizes are about 54$''$, 52$''$, 46$''$, and 46$''$. From our calculations, the $M_{\text{H}_2}/M_{\text{H I}}$ are lower than 0.044, 0.017, 0.048, and 0.018, respectively. The metallicity of AGCNr188845 is 0.01 and one-half of solar metallicity. AGCNr102981 is a typical late-type spiral galaxy and the spiral structures are shown in Figure 1.

AGCNr4528, AGCNr12212, and AGCNr110150: The optical sizes of these three galaxies are about 66$''$, 62$''$, and 80$''$, respectively, which indicate that JCMT's beam size is not enough to cover their total CO content. The metallicity of AGCNr4528 is 0.02 and same to solar metallicity. The $M_{\text{H}_2}/M_{\text{H I}}$ for these three LSBGs are lower than 0.018, 0.0201, and 0.022 respectively.
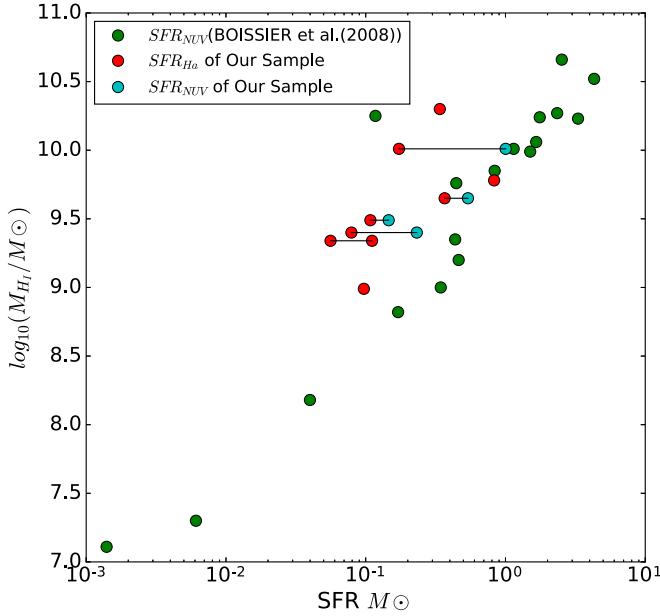
Figure 4. H I mass vs. SFR. The red dots are SFRs calculated by Hα and the blue dots are SFRs calculated by NUV luminosity. The black line connects the same target. The green dots are the sample of LSBGs from Boissier et al. (2008).

NGC 7589: The optical size of NGC 7589 is 76″. It is a Seyfert-1 galaxy. The SFR from NUV band is 1.003 $M_{\odot}$ yr^{-1} and its metallicity is 0.04 and twice the solar metallicity. There are some works investigating this galaxy. It is a typical giant LSBG and has type 1 XUV-disk galaxy (Boissier et al. 2008). The upper limit of M_{H2} is $8.25 \times 10^8\,M_{\odot}$ and the ratio of $M_{H_2}/M_{H\,I}$ is lower than 0.081.

4.2. M_{H_2} versus $L_{12\mu m}$

The 12 μm (*WISE W3*) band is an effective probe of star formation (Donoso et al. 2012) and has a good linear relationship with molecular hydrogen mass for SF galaxies (Jiang et al. 2015). In this section, we try to explore the relation between molecular gas and 12 μm emission in LSBGs.

Five sources in our sample have 12 μm emission data provided by the *WISE* ALL-sky Survey. Figure 5 shows $L_{12\mu m}$ versus M_{H_2}. The blue line in Figure 5 is the relationship between M_{H_2} (CO$_{J=2-1}$) and luminosity of 12 μm for SF galaxies (Jiang et al. 2015).

AGCNr12289 and NGC 7589 have higher luminosities of 12 μm in Figure 5. AGNCr12289 has a potential AGN/LINER core and NGC 7589 is a Seyfert-1 galaxy that may cause them to be different from other LSBGs in our sample. The LSBGs show low luminosities of 12 μm and it may mean less dust in LSBGs. For SF galaxies, they always have larger 12 μm luminosities compared with LSBGs.

4.3. The Stellar Mass and Gas Content

Six LSBGs of our sample have 3.4 μm (*WISE W1*) band data. Using the method in Wen et al. (2013) by following Equation (5), we adopt 3.4 μm data to calculate the stellar mass:

$$\log_{10}(M_*/M_{\odot}) = (-0.040 \pm 0.001) + (1.120 \pm 0.001)$$
$$\times \log_{10}(\nu L_{\nu}(3.4\,\mu m)/L_{\odot}).$$
$$(5)$$

As the redshifts of our sample are small, we ignore the *k*-correction. Their stellar masses are about (1.41–83.17) × 10$^8\,M_{\odot}$.
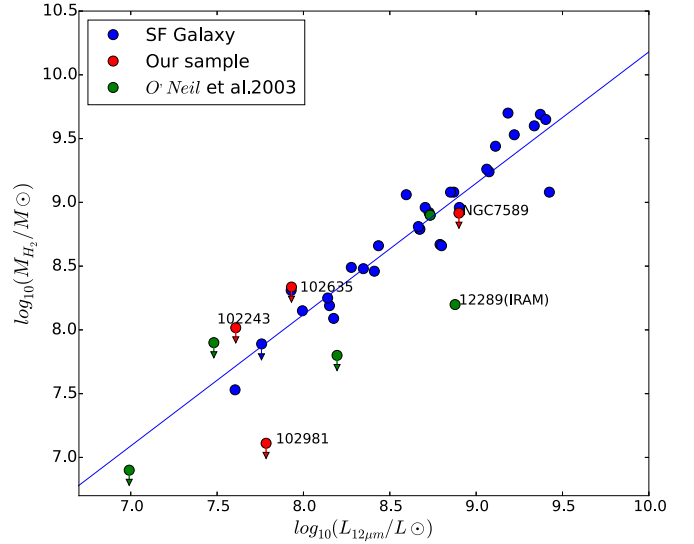
Figure 5. Luminosity of 12 μm vs. M_{H_2}. The red dots are LSBGs from this work, green dots are from O'Neil et al. (2003) and the blue dots are SF galaxies from Jiang et al. (2015). The arrows indicate the upper limits.
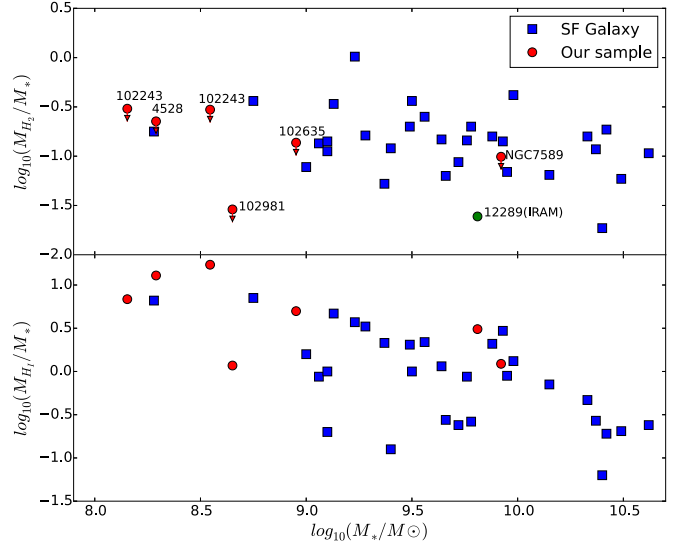
Figure 6. Stellar mass (M_*) vs. the ratio of M_{H_2}/M_* (upper) and $M_{H\,I}/M_*$ (lower). The red dots are LSBGs from this work and the blue squares are SF galaxies (Jiang et al. 2015). The arrows indicate the upper limits.

LSBGs usually have low masses. The stellar masses of our sample are shown in Table 3.

The stellar masses of SF galaxies have a different relation with molecular gas and atomic gas. The ratios of M_{H_2}/M_* are almost constant (Jiang et al. 2015). We are more interested in the relation between stellar mass and gas content of LSBGs.

Figure 6 shows the relation between stellar mass M_* and gas content in SF galaxies and our LSBG sample. The M_{H_2}/M_* shows a flat trend within the considerable scatter and $M_{H\,I}/M_*$ shows an obvious decline with increasing stellar mass. It seems that the molecular gas fraction (M_{H_2}/M_*) is similar in LSBGs and in SF galaxies, though our results provide upper limits, except for the AGCNr12289. Compared with SF galaxies, the stellar mass of our sample is mainly lower than $10^9\,M_{\odot}$, excluding the two special galaxies (AGCNr12289

121
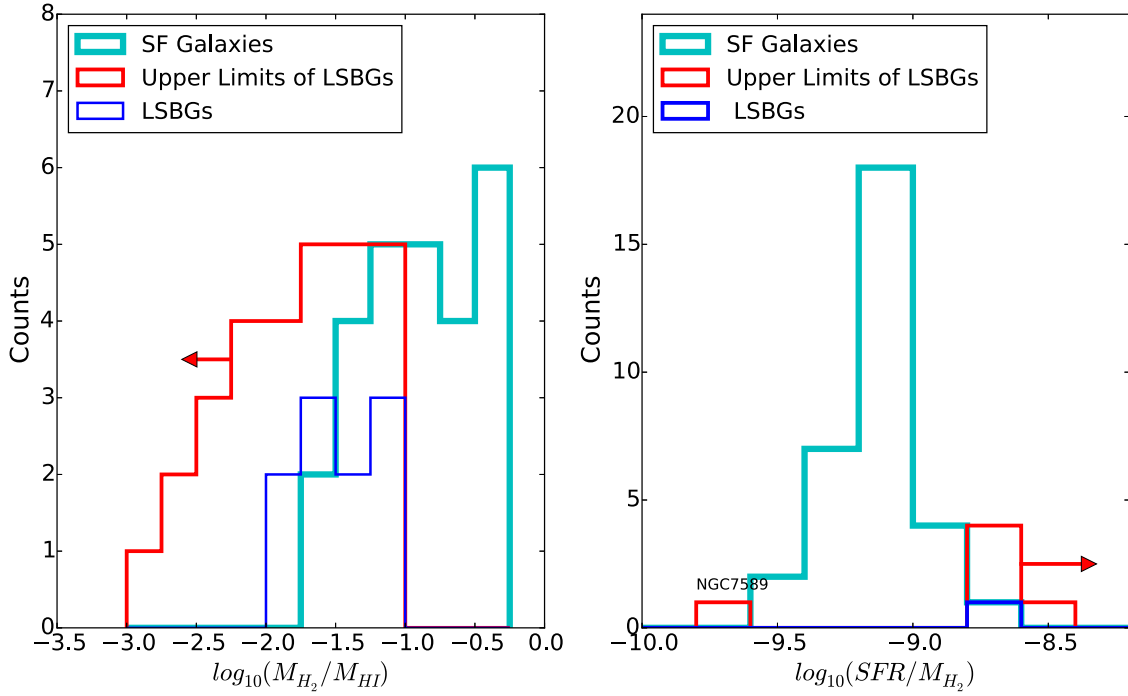
Figure 7. Left panel: the distribution of M_{H_2}/M_{HI}. Right panel: the distribution of SFR/M_{H_2}. The red histogram represents upper limits of LSBGs and the blue histogram represents those detected molecular LSBGs. All LSBG data are from our sample and previous works (Schombert et al. 1990; de Blok & van der Hulst 1998a; Braine et al. 2000; O'Neil et al. 2000, 2003). The cyan histogram represents SF galaxies (Jiang et al. 2015). The arrows represent upper limits.

and NGC 7589). Stellar masses of AGCNr12289 and NGC 7589 may be overestimated by the central AGN.

4.4. M_{H_2}/M_{HI} and SFR/M_{H_2}

H I gas is the original material involved in star formation, and star formation is directly related to molecular gas. The M_{H_2}/M_{HI} ratio should be different for different galaxies. The gas content could change along the main sequence of SF galaixes. Other factors, such as metallicity and environment could affect the ratio. Even for the same galaxy, its gas fraction would also change during its different evolutionary phase. In our nine LSBGs, the M_{H_2}/M_{HI} ratios are less than 0.02. In typically brighter Sd–Sm spirals (Young & Knezek 1989), the M_{H_2}/M_{HI} ratio is about 0.2.

In the Section 3.1, we have discussed the M_{HI} and M_{H_2} in SF galaxies and LSBGs. The M_{H_2} in LSBGs is lower than that in SF galaxies. In this section, we compare M_{H_2}/M_{HI} and SFR/M_{H_2} in those LSBGs and SF galaxies.

Figure 7 shows the distribution of M_{H_2}/M_{HI} on the left and SFR/M_{H_2} on the right. In the right panel, NGC 7589 has completely different values of SFR/M_{H_2} from the other LSBGs because of AGN influence. Due to the dispersed distribution, the difference in SFR/M_{H_2} between SF galaxies and LSBGs is not quite obvious.

We can see that the ratios of M_{H_2}/M_{HI} in LSBGs are less than those in SF galaxies. The rate of transforming atomic hydrogen to molecular hydrogen in LSBGs is lower than that in SF galaxies. In Section 3.1, we have also discussed the shortage of molecular gas in the special environment of LSBGs. However, CO is more easily photodissociated than H_2 in a metal-poor environment (Wolfire et al. 2010; Shetty et al. 2011). Thus, the conversion factor of CO-to-H_2 is usually higher than that in SF galaxies. In this work, we adopt the factor of $3.162 \times$

10^{20} cm^{-2}/(K km s^{-1}) to be consistent with previous works. According to the work of Narayanan et al. (2012), the factor may be larger than 3.16×10^{20} cm^{-2}/(K km s^{-1}) and up to 15×10^{20} cm^{-2}/(K km s^{-1}). So, the M_{H_2} of our sample may be underestimated. Although, due to the lack of detected CO content, it is still possible that M_{H_2} is underestimated in LSBGs.

5. Summary

We observed CO($J=2-1$) emission lines in nine LSBGs with JCMT and Hα images with the 2.16 m telescope administered by NAOC. As no CO has been detected, only upper limits on the H_2 masses are given. The upper limits of hydrogen molecular masses are about $(1.2–82.4) \times 10^7 M_\odot$. Their star-formation rates are about 0.056–0.83 $M_\odot$ yr^{-1} and 0.146–1.003 $M_\odot$ yr^{-1} estimated by Hα and NUV luminosities, respectively. The steller masses are about $(0.14–8.31) \times 10^9 M_\odot$, estimated by the *WISE* 3.4 μm band. From our results, the M_{H_2} and stellar mass in LSBGs are lower than those in SF galaxies. Low SFRs in LSBGs may be related to low molecular hydrogen mass, which may indicate low productivity of atomic hydrogen transforming into molecular hydrogen. More direct detection of molecular gas of LSBG is the key to answering the question in the future.

ORCID iDs

Tian-Wen Cao ⓘ https://orcid.org/0000-0002-1335-6212
Wei Du ⓘ https://orcid.org/0000-0003-4546-8216
Jan Wouterloot ⓘ https://orcid.org/0000-0002-4694-6905
Harriet Parsons ⓘ https://orcid.org/0000-0002-6327-3423
Yi-Nan Zhu ⓘ https://orcid.org/0000-0002-2798-2783
Chao-Jian Wu ⓘ https://orcid.org/0000-0003-3514-6619
Zhi-Min Zhou ⓘ https://orcid.org/0000-0002-4135-0977

References

Blanton, M. R., & Moustakas, J. 2009, ARA&A, 47, 159
Boissier, S., Gil de Paz, A., & Boselli, A. 2008, ApJ, 681, 244
Bolatto, A. D., Wolfire, M., & Leroy, A. K. 2013, ARA&A, 51, 207
Braine, J., Herpin, F., & Radford, S. J. E. 2000, A&A, 358, 494
Burkholder, V., Impey, C., & Sprayberry, D. 2001, AJ, 122, 2318
Das, M., Boone, F., & Viallefond, F. 2010, A&A, 523, A63
Das, M., Kantharia, N., Ramya, S., et al. 2007, MNRAS, 379, 11
de Blok, W. J. G., McGaugh, S. S., & van der Hulst, J. M. 1996, MNRAS, 283, 18
de Blok, W. J. G., & van der Hulst, J. M. 1998a, A&A, 335, 421
de Blok, W. J. G., & van der Hulst, J. M. 1998b, A&A, 336, 49
de Blok, W. J. G., van der Hulst, J. M., & Bothun, G. D. 1995, MNRAS, 274, 235
de Vaucouleurs, G., de Vaucouleurs, A., Corwin, H. G., Jr., et al. 1991, in Third Reference Catalogue of Bright Galaxies. Volume I: Explanations and References. Volume II: Data for Galaxies Between 0h and 12h. Volume III: Data for Galaxies Between 12h and 24h (New York: Springer)
Donoso, E., Yan, L., Tsai, C., et al. 2012, ApJ, 748, 80
Du, W., Wu, H., Lam, M. I., et al. 2015, AJ, 149, 199
Epinat, B., Amram, P., & Marcelin, M. 2008, MNRAS, 390, 466
Fan, Z., Wang, H., & Jiang, X. 2016, PASP, 128, 115005
Gerritsen, J. P. E., & de Blok, W. J. G. 1999, A&A, 342, 655
Giovanelli, R., Haynes, M. P., & Kent, B. R. 2005, AJ, 130, 2598
Haynes, M. P., Giovanelli, R., & Martin, A. M. 2011, AJ, 142, 170
Hirst, P., & Cavanagh, B. 2005, StaUN, 236
Impey, C., & Bothun, G. 1997, ARA&A, 35, 267
Jiang, X.-J., Wang, Z., Gu, Q., Wang, J., & Zhang, Z.-Y. 2015, ApJ, 799, 92
Jimenez, R., Padoan, P., Matteucci, F., & Heavens, A. F. 1998, MNRAS, 299, 123
Kennicutt, R. C., Jr. 1998, ARA&A, 36, 189
Knezek, P. M. 1993, PhD thesis, Massachusetts Univ., Amherst
Lauberts, A., & Valentijn, E. A. 1989, The Surface Photometry Catalogue of the ESO-Uppsala Galaxies (Garching: ESO)
Leroy, A. K., Walter, F., & Bigiel, F. 2009, AJ, 137, 4670
Leroy, A. K., Walter, F., & Brinks, E. 2008, AJ, 136, 2782
Matthews, L. D., & Gao, Y. 2001, ApJL, 549, L191
Matthews, L. D., Gao, Y., Uson, J. M., & Combes, F. 2005, AJ, 129, 1849
Matthews, L. D., van Driel, W., & Monnier-Ragaigne, D. 2001, A&A, 365, 1
Matthews, L. D., & Wood, K. 2001, ApJ, 548, 150
McGaugh, S. S. 1994, ApJ, 426, 135
McGaugh, S. S., & Bothun, G. D. 1994, AJ, 107, 530
McGaugh, S. S., & de Blok, W. J. G. 1997, ApJ, 481, 689
Narayanan, D., Krumholz, M. R., Ostriker, E. C., & Hernquist, L. 2012, MNRAS, 421, 3127
O'Neil, K., Bothun, G., van Driel, W., & Monnier Ragaigne, D. 2004, A&A, 428, 823
O'Neil, K., Hofner, P., & Schinnerer, E. 2000, ApJL, 545, L99
O'Neil, K., Schinnerer, E., & Hofner, P. 2003, ApJ, 588, 230
Peebles, P. J. E. 2001, ApJ, 557, 495
Pickering, T. E., Impey, C. D., van Gorkom, J. H., & Bothun, G. D. 1997, AJ, 114, 1858
Pustilnik, S. A., Martin, J.-M., Tepliakova, A. L., & Kniazev, A. Y. 2011, MNRAS, 417, 1335
Savage, B. D., & Mathis, J. S. 1979, ARA&A, 17, 73
Schombert, J. 1998, AJ, 116, 1650
Schombert, J. M., Bothun, G. D., Impey, C. D., & Mundy, L. G. 1990, AJ, 100, 1523
Schruba, A., Leroy, A. K., & Walter, F. 2012, AJ, 143, 138
Shetty, R., Glover, S. C., Dullemond, C. P., & Klessen, R. S. 2011, MNRAS, 412, 1686
Subramanian, S., Ramya, S., Das, M., et al. 2016, MNRAS, 455, 3148
van der Hulst, J. M., Skillman, E. D., Smith, T. R., et al. 1993, AJ, 106, 548
van Zee, L. 2000, AJ, 119, 2757
Wen, X.-Q., Wu, H., & Zhu, Y.-N. 2013, MNRAS, 433, 2946
Wolfire, M. G., Hollenbach, D., & McKee, C. F. 2010, ApJ, 716, 1191
Wu, H., Burstein, D., & Deng, Z. 2002, AJ, 123, 1364
Wyder, T. K., Martin, D. C., & Barlow, T. A. 2009, ApJ, 696, 1834
Young, J. S., & Knezek, P. M. 1989, ApJL, 347, L55
Zheng, Z., Shang, Z., & Su, H. 1999, AJ, 117, 2757

Revisiting the Lick Observatory Supernova Search Volume-limited Sample: Updated Classifications and Revised Stripped-envelope Supernova Fractions

Isaac Shivvers[1], Maryam Modjaz[2], WeiKang Zheng[1], Yuqian Liu[2], Alexei V. Filippenko[1], Jeffrey M. Silverman[3],
Thomas Matheson[4], Andrea Pastorello[5], Or Graur[2,6,7,12], Ryan J. Foley[8], Ryan Chornock[9], Nathan Smith[10],
Jesse Leaman[11], and Stefano Benetti[5]

[1] Department of Astronomy, University of California, Berkeley, CA 94720-3411, USA; ishivvers@berkeley.edu
[2] Center for Cosmology and Particle Physics, New York University, NY 10003, USA
[3] Department of Astronomy, University of Texas at Austin, Austin, TX 78712, USA
[4] National Optical Astronomy Observatory, Tucson, AZ 85719, USA
[5] INAF-Osservatorio Astronomico di Padova, Vicolo dell'Osservatorio 5, I-35122 Padova, Italy
[6] Harvard-Smithsonian Center for Astrophysics, 60 Garden Street, Cambridge, MA 02138, USA
[7] Department of Astrophysics, American Museum of Natural History, New York, NY 10024-5192, USA
[8] Department of Astronomy and Astrophysics, University of California, Santa Cruz, CA 95064, USA
[9] Department of Physics and Astronomy, Ohio University, Athens, OH 45701, USA
[10] Steward Observatory, University of Arizona, 933 N. Cherry Avenue, Tucson, AZ 85721, USA
[11] Advanced Robotics and Automation Lab, Department of Computer Science and Engineering, University of Nevada, Reno, NV 89557, USA
Received 2016 September 5; accepted 2016 December 19; published 2017 March 24

Abstract

We re-examine the classifications of supernovae (SNe) presented in the Lick Observatory Supernova Search (LOSS) volume-limited sample with a focus on the stripped-envelope SNe. The LOSS volume-limited sample, presented by Leaman et al. and Li et al., was calibrated to provide meaningful measurements of SN rates in the local universe; the results presented therein continue to be used for comparisons to theoretical and modeling efforts. Many of the objects from the LOSS sample were originally classified based upon only a small subset of the data now available, however, and recent studies have both updated some subtype distinctions and improved our ability to perform robust classifications, especially for stripped-envelope SNe. We re-examine the spectroscopic classifications of all events in the LOSS volume-limited sample (180 SNe and SN impostors) and update them if necessary. We discuss the populations of rare objects in our sample including broad-lined SNe Ic, Ca-rich SNe, SN 1987A-like events (we identify SN 2005io as SN 1987A-like here for the first time), and peculiar subtypes. The relative fractions of SNe Ia, SNe II, and stripped-envelope SNe in the local universe are not affected, but those of some subtypes are. Most significantly, after discussing the often unclear boundary between SNe Ib and Ic when only noisy spectra are available, we find a higher SN Ib fraction and a lower SN Ic fraction than calculated by Li et al.: spectroscopically normal SNe Ib occur in the local universe 1.7 ± 0.9 times more often than do normal SNe Ic.

Key words: supernovae: general

Online material: color figures, supplementary files

1. Introduction

The Lick Observatory Supernova Search (LOSS) has been a long-running project at the University of California, Berkeley, using the Katzman Automatic Imaging Telescope at Lick Observatory (KAIT; e.g., Li et al. 2000; Filippenko et al. 2001b; Filippenko 2003, 2005), with many spectroscopic follow-up observations obtained with the 3 m Shane telescope at Lick and the 10 m telescopes at Keck Observatory. LOSS/KAIT has been discovering and observing SNe since first light in 1996; these data have contributed to several PhD theses and formed the foundation of many research projects on SNe. A detailed examination of the relative rates of nearby SNe was

one of those projects, and was published as a series of papers in 2011 (Leaman et al. 2011; Li et al. 2011a, 2011b; Maoz et al. 2011; Smith et al. 2011a). The second of these, Li et al. (2011b, L11 hereafter), presents a sample of 180 events that occurred within 80 Mpc (for SNe Ia) or 60 Mpc (for core-collapse SNe), all of which were spectroscopically classified (the classes of SNe are differentiated primarily via spectroscopy; e.g., Filippenko 1997). Most SN classifications from this time period were performed via visual inspection and comparisons with spectra of a few SNe of well-understood types and subtypes.

Over time we have found that a small fraction of the objects in L11 deserve reclassification; in some cases this is because the original classifications were made using only a subset of the

---

1

now-available data on the objects, while in other cases our more modern classification methods are less prone to errors than the methods used at the time of classification. Independent of data quality or cadence, there is a history of debate in the literature over the exact distinction (if any) between SNe Ib and SNe Ic and whether transitional events showing weak helium lines exist (e.g., Filippenko et al. 1990a; Wheeler & Harkness 1990; Wheeler et al. 1994; Clocchiatti et al. 1996; Matheson et al. 2001; Branch et al. 2006).

The results of recent efforts by Liu & Modjaz (2014), Modjaz et al. (2014), and Liu et al. (2016) argue that the distinction between SNe Ib and SNe Ic is useful, and they offer a clearly defined scheme for discriminating between them alongside updated software tools to perform those classifications in a repeatable manner. Modjaz et al. (2014) identify as SNe Ib all events with detections of both the He I $\lambda6678$ and He I $\lambda7065$ lines at phases between maximum light and ~50 days post-maximum, regardless of line strengths (the stronger He I $\lambda5876$ line is also present, but overlaps with Na I). They find that at least one good spectrum observed at these phases is necessary and sufficient to detect the helium lines, which are often absent at pre-maximum and nebular phases even for helium-rich events. Using this classification scheme, they find evidence for a transitional population of "weak helium" SNe Ib (Valenti et al. 2011; Modjaz et al. 2014; Liu et al. 2016).

Clarifying the distinction between SNe Ib and SNe Ic is important given the surprising ratio of population fractions for these subtypes found by LOSS (SNe Ic/SNe Ib $= 14.9^{+4.2}_{-3.8}\%/$ $7.1^{+3.1}_{-2.6}\%$; Smith et al. 2011a), which has proven difficult to reproduce with stellar modeling efforts (e.g., Georgy et al. 2009; Yoon et al. 2010; Yoon 2015), though see also Groh et al. (2013a). Modjaz et al. (2014) show that a subset of the objects originally labeled SNe Ic in their sample in fact do qualify for the SN Ib label according to the definition above, and so they relabel these events as SNe Ib (see their discussion of all such cases, in their Section 4.2).

For some of those SNe, the spectra that were used to classify them and thus announce their types were obtained before the helium lines became prominent; for some, applying proper telluric corrections made the He I $\lambda6678$ or $\lambda7065$ lines more apparent; for others the spectra show clear helium but the exact division between SNe Ib and SNe Ic was under debate in the literature at the time of classification (e.g., SN 1990U; Filippenko & Shields 1990; Filippenko et al. 1990b; Matheson et al. 2001). We explore these issues within the LOSS sample and also find that some events with helium lines were systematically labeled as SNe Ic—we update the classifications for these events and recalculate the relative fractions of core-collapse events.

In this article we re-examine the classifications of the 180 events in the volume-limited sample of L11 and we make public all spectra of them we have been able to locate. This work was performed in conjunction with Graur et al. (2016a, 2016b), who re-examine correlations between SN rates and galaxy properties. Note that much of the spectroscopy discussed herein has already been described in the literature and made publicly available by, for example, Silverman et al. (2012, SNe Ia), Faran et al. (2014a, 2014b, SNe II), Matheson et al. (2001, SNe IIb/Ib/Ic). We collect these spectra, light curves obtained by LOSS, as-yet unpublished spectra from our archives, and as-yet unpublished spectra contributed from other SN research groups' archives, and analyze the complete set.

We present 151 newly published spectra of 71 SNe and 20 rereduced KAIT light curves. In Section 2 we describe these data, in Section 3 we detail our methods for classification, in Section 4 we present all updated classifications and discuss notable events within the sample, in Section 5 we calculate updated core-collapse SN rates in the local universe, in Section 6 we discuss the implications these updates have for our understanding of the progenitors of stripped-envelope SNe, and in Section 7 we conclude.

2. Data

Spectra were collected from our own UC Berkeley Supernova Database (UCB SNDB; Silverman et al. 2012),[13] from the literature, and from WISeREP (the Weizmann Interactive Supernova Data REPository; Yaron & Gal-Yam 2012).[14] We do not include any results from spectropolarimetric or nonoptical observations; we know of no such observations that would help for the few events we cannot robustly classify using optical data. We made an effort to track down as-yet unpublished spectra for all objects with sparse or no spectral data in our database or in the public domain. All objects in this sample were classified in the Central Bureau of Electronic Telegrams (CBETs), and we contacted original authors to request data whenever possible. Contributions were made by the Center for Astrophysics (CfA) SN group (Matheson et al. 2008),[15] the Padova-Asiago SN group (Tomasella et al. 2014),[16] the Carnegie Supernova Project (CSP; Hamuy et al. 2006),[17] and the National Astronomical Observatories, Chinese Academy of Sciences (NAOC) SN group (Qui et al. 1999; Li et al. 1999).

We publish spectra from the following observatories and instruments:

- the Kast double spectrograph (Miller & Stone 1993) mounted on the Shane 3 m telescope at Lick Observatory;

---

[13] The SNDB was updated in 2015 and is available online at http://heracles.astro.berkeley.edu/sndb/.
[14] http://wiserep.weizmann.ac.il/
[15] https://www.cfa.harvard.edu/supernova/
[16] http://sngroup.oapd.inaf.it/
[17] http://csp.obs.carnegiescience.edu/

- the Low Resolution Imaging Spectrometer (LRIS; Oke et al. 1995) and the Echellette Spectrograph and Imager (ESI; Sheinis et al. 2002) on the 10 m Keck I and II telescopes at Keck Observatory;
- the FAST spectrograph (Fabricant et al. 1998) on the Tillinghast 60 inch telescope and the Blue Channel spectrograph (Schmidt et al. 1989) on the 6.5 m Multiple Mirror Telescope (MMT) at the Fred Lawrence Whipple Observatory (FLWO);
- the European Southern Observatory (ESO) Faint Object Spectrograph and Camera (EFOSC; Buzzoni et al. 1984) on the ESO 3.6 m telescope, the Danish Faint Object Spectrograph and Camera (DFOSC, modeled after EFOSC; Andersen et al. 1995) on the Danish 1.54 m telescope, and the ESO Multi-Mode Instrument in medium resolution spectroscopy mode (EMMI; Dekker et al. 1986) on the ESO 3.58 m New Technology Telescope, all at La Silla Observatory;
- the Asiago Faint Object Spectrograph and Camera (AFOSC, modeled after EFOSC) on the 1.82 m Copernico telescope and the Boller and Chivens spectrograph (B&C$_{1.2}$) on the 1.2 m Galileo telescope at Asiago Observatory;
- the Boller and Chivens spectrograph (B&C$_{2.5}$) and the Wide Field Reimaging CCD Camera in long-slit spectroscopy mode (WFCCD, described by Hamuy et al. 2006) on the 2.5 m du Pont telescope and the Low Dispersion Survey Spectrograph (LDSS-2; Allington-Smith et al. 1994) on the 6.5 m *Magellan* Clay telescope at Las Campanas Observatory; and
- the Optomechanics Research, Inc.[18] spectrograph (OMR) mounted on the NAOC 2.16 m telescope at Xinglong Observatory near Beijing, China.

Details of the spectral reduction pipeline used by the UCB team are described by Silverman et al. (2012). Matheson et al. (2008), Blondin et al. (2012), and Modjaz et al. (2014) discuss the reduction process performed on the CfA spectra, and Hamuy et al. (2006) outline the reduction process performed on the CSP spectra. Standard IRAF[19] reduction packages were used by the Padova-Asiago and NAOC groups. Most spectra presented here have resolutions of ~10 Å, were observed at or near the parallactic angle (Filippenko 1982), and were flux calibrated with bright standard stars observed at similar airmasses. Most spectra have also been corrected for wavelength-dependent telluric absorption. Details of the observations and data-reduction methods vary from group to group, and we discuss any possible data-quality issues for the spectra most vital to our classification effort in the text.

All photometry used by L11 and in this effort was observed at Lick Observatory with KAIT or the Nickel 1 m telescope, and all SNe discussed here were discovered by LOSS/KAIT (e.g., Li et al. 2000; Filippenko et al. 2001b). KAIT photometry is generally performed on unfiltered images (the *clear* band), though filtered *BVRI* KAIT images of some events are available. Nickel data are observed through a *BVRI* filter set. Details for both instruments and for our photometry reduction pipeline are given by Ganeshalingam et al. (2010), and we present these light curves as observed, without correcting for Milky Way (MW) or host-galaxy dust absorption, unless otherwise stated. All of the spectra and photometry used in this project will be made public through the UCB SNDB, WiseREP, and the Open Supernova Catalog (Guillochon et al. 2016).[20] See Appendix for logs of the data released publicly here for the first time.

3. Classification Methods

Following Silverman et al. (2012) and Modjaz et al. (2014), we use the SN IDentification code[21] (SNID; Blondin & Tonry 2007) as our primary classification tool. SNID classifies SNe by cross-correlating an input (optical) spectrum against a library of template spectra (Tonry & Davis 1979). Updated sets of template spectra have been released since the original release of SNID—for this study we use the BSNIP v7.0 templates (Silverman et al. 2012) augmented by the Liu & Modjaz (2014) stripped-envelope templates (and following all suggestions from their Table 4). When running SNID, we set the SN redshift with the *forcez* keyword using observed host-galaxy redshifts from the NASA/IPAC Extragalactic Database (NED).[22] For those SNe that SNID alone cannot identify, we incorporate results from two other spectral identification codes, Superfit[23] (Howell et al. 2005) and GELATO[24] (Harutyunyan et al. 2008), and for some stripped-envelope SNe we also compare to the average spectra of Liu et al. (2016).

As shown by (for example) L11, the light curves of SNe Ic, Ib, and IIb are similar to each other, but are generally distinguishable from those of SNe Ia and hydrogen-rich core-collapse SNe. We incorporate light-curve information in our classifications when it proves useful, comparing the light curves of individual objects to the *clear*-band templates from L11 and providing constraints on the phases of spectra. Recent studies have advanced our understanding of stripped-envelope SN light-curve evolution (e.g., Drout et al. 2011; Cano 2013; Bianco et al. 2014; Taddia et al. 2015; Lyman et al. 2016; Prentice et al. 2016). Drout et al. (2011) present template SN Ib/c light curves in the *R* and *V* bands assembled from 25

---

[18] http://www.echellespectrographs.com/about.htm
[19] http://iraf.noao.edu/

[20] https://sne.space/
[21] http://people.lam.fr/blondin.stephane/software/snid/index.html
[22] https://ned.ipac.caltech.edu/
[23] http://www.dahowell.com/superfit.html
[24] https://gelato.tng.iac.es/

3

events and Lyman et al. (2016) give template bolometric light curves assembled from 38 events, while L11 produce four template light curves for stripped-envelope SNe: "Ibc.fast," "Ibc.ave," "Ibc.slow," and "IIb." The Ibc.ave template is very similar to the R-band SN Ibc template of Drout et al. (2011) and the SN Ib and SN Ic templates of Lyman et al. (2016). The SN IIb templates from L11 and Lyman et al. (2016) are also in good agreement, and both show cooling envelope emission followed by a dip and a rise to a second radioactively powered peak, with a post-peak evolution basically indistinguishable from that of SNe Ib/c. L11 do not produce a template for broad-lined SNe Ic (labeled SNe Ic-BL here), but other authors show that SN Ic-BL light curves are quite similar to those of other SNe Ib/c though trending toward higher absolute luminosities (e.g., Drout et al. 2011; Taddia et al. 2015; Prentice et al. 2016).

Several recent large-scale SN data releases have relied on SNID classifications using relatively stringent requirements for a robust identification, requiring a high $rlap$ value for the top match ($rlap$ is a quality parameter used by SNID—a higher value corresponds to a more trustworthy classification) and that the first few matches be of the same subtype (e.g., Silverman et al. 2012; Graur & Maoz 2013; Modjaz et al. 2014; Graur et al. 2015). We follow these methods whenever possible, and for most of the SNe in our sample they clearly indicate a single type and subtype.

All of the SNe Ia in this sample have been examined in detail by other authors (e.g., Blondin et al. 2012; Silverman et al. 2012; Folatelli et al. 2013). We follow the methods of Silverman et al. (2012) to determine SN Ia subtypes, and we do not attempt to identify subpopulations within the normal SNe Ia—i.e., high-velocity events (Wang et al. 2009a) or the subgroups defined by Benetti et al. (2005). We discuss the more peculiar SNe Ia from this sample in Section 4.3.

We do not attempt to sort the hydrogen-rich SNe II into the IIP and IIL subtypes. SNe II have long been sorted into those that exhibit a clear plateau phase and those that decline linearly in magnitudes (IIP and IIL, respectively; e.g., Barbon et al. 1979; Filippenko 1997). L11 used spectra to identify H-rich SNe, and then labeled as Type IIL those that decline more than 0.5 mag in the R band during the first 50 days after explosion and the rest as IIP, but recent work has shown that the issue may be more complex. While Arcavi et al. (2012) find there to be distinct SN IIP and SN IIL subclasses among the R-band light curves of 21 H-rich noninteracting SNe II, Anderson et al. (2014) show that their sample of V-band light curves for 116 SNe II indicate that there is a continuous distribution of properties for these events. Rubin et al. (2016) present an analysis of the early light curve rise for 57 events finding only a weak correlation between rise times and decline rates, Sanders et al. (2015) and Valenti et al. (2016) argue that there exists a continuous distribution of properties for SNe II and that there is no evidence for separate SNe IIP and SNe IIL subclasses,

while Rubin & Gal-Yam (2016) argue for a type II subclassification system based upon both the rise and the fall of the light curves and Faran et al. (2014a) argue that a simple subclass definition based upon the light curve decline alone remains reasonable. Throughout this article, we group the SN IIP-like and SN IIL-like events under the label "SNe II," but when comparing to data from other sources we preserve the SN IIP/SN IIL labels if given by the original authors.

Though we do not differentiate between SNe IIL and SNe IIP, we do identify other H-rich subclasses. We identify the H-rich SNe with narrow spectral emission lines indicative of interaction with dense circumstellar material (SNe IIn; e.g., Schlegel 1990; Chugai 1991; Filippenko 1991) and the SN impostors, thought to be nonterminal ejections or explosions from the surface of massive stars (labeled "IIni" in L11; e.g., Van Dyk et al. 2000; Maund et al. 2006; Smith et al. 2011b). We also identify three slow-rising (SN 1987A-like) SNe II in our sample (e.g., Arnett et al. 1989; McCray 1993).

Our main focus is on the stripped-envelope SNe. We divide this class into those with some hydrogen features (SNe IIb), those without hydrogen features (or with only very weak hydrogen features; Liu et al. 2016) but with clear helium features (SNe Ib), and those exhibiting neither clear hydrogen nor clear helium features (SNe Ic). The exact distinction between SNe Ib and Ic has been an issue of some debate in the literature; we follow Modjaz et al. (2014) and Liu et al. (2016) to define the differences between these subclasses. We differentiate between SNe Ic and SNe Ic-BL (see Modjaz et al. 2015), and we identify the "calcium-rich" SNe separately (included in the Ibc-pec category by L11, this class of events has been described by, e.g., Filippenko et al. 2003; Perets et al. 2010; Kasliwal et al. 2012).

For events with spectra that match both the SN Ib and SN Ic SNID templates equally well, we discuss the available data in detail and assign the label "Ib/Ic" (i.e., unsure) if we remain unable to determine a single best classification. Figure 1 shows that this classification scheme tends to move events that were previously labeled SNe Ic into the Ib or Ib/Ic categories (there are no SNe Ib that we reclassify as SNe Ic in this work).
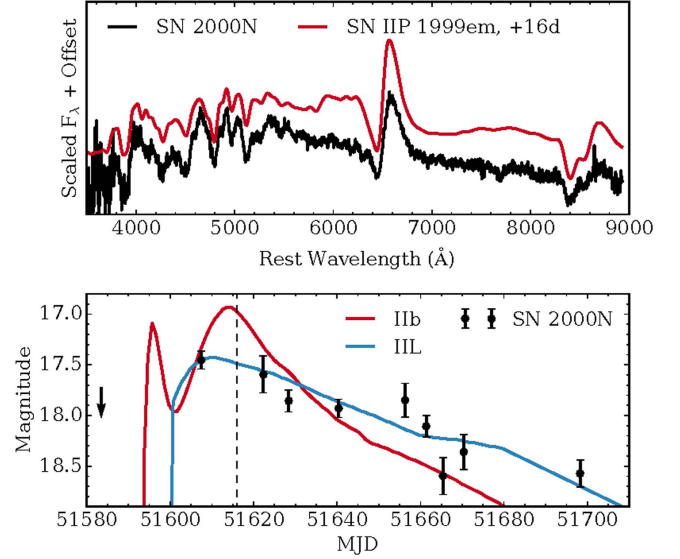
We follow Smith et al. (2011a) and group the SNe IIb with other stripped-envelope SNe in our sample, although L11 included them with the SNe II. SNe IIb show a strong Hα line at early times, as do normal SNe II, but then the hydrogen fades and the later spectra of SNe IIb resemble those of SNe Ib (e.g., Filippenko 1988, 1997; Filippenko et al. 1993; Pastorello et al. 2008; Chornock et al. 2011; Milisavljevic et al. 2013). Several authors have claimed the detection of weak high-velocity hydrogen features in SNe Ib and Ic (e.g., Branch et al. 2006; Parrent et al. 2007, 2016; Liu et al. 2016). However, Liu et al. (2016) argue that the putative weak Hα absorption line often present in SNe Ib is, at all phases, weaker than the Hα line in SNe IIb, and that SNID capably distinguishes between SNe Ib and SNe IIb even after the
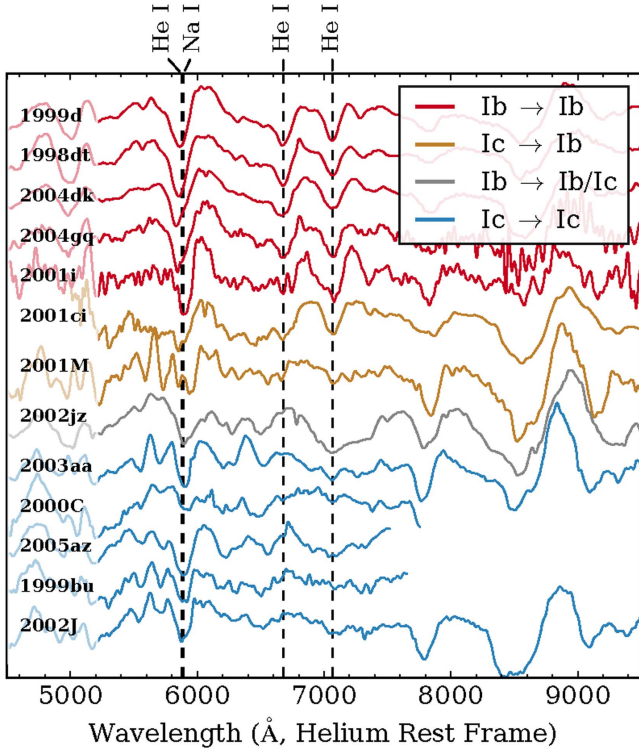
Figure 1. Representative sample of spectra of the SNe Ib and Ic in our sample, observed between 5 and 20 days after peak brightness, as well as spectra of three SNe for which we provide updated classifications (SNe 2001M, 2001ci, and 2002jz). We have subtracted a spline continuum from these spectra, smoothed them with a 50 Å Gaussian kernel, and shifted them in velocity space to align their He I features (or Na I $\lambda 5892$ if no helium is detected).
(A color version of this figure is available in the online journal.)


Figure 2. Top: the near-maximum-light spectrum of SN 2000N alongside that of the Type IIP SN 1999em (Leonard et al. 2002a). Bottom: the light curve of SN 2000N, with a vertical line showing the date the spectrum shown was observed, and colored lines showing the template light curves from L11.
(A color version of this figure is available in the online journal.)

strong Hα feature of the SNe IIb has faded, so long as spectra were obtained during the photospheric phase. The nebular spectra of SNe IIb and SNe Ib, on the other hand, are often very similar and are not well separated by SNID. When discriminating between Types IIb and Ib, we trust the SNID result if obtained from spectra of the photospheric phase.

To examine possible biases SNID may introduce when classifying stripped-envelope subtypes, we ran a series of trials introducing wavelength restrictions, noise, and artificial dust reddening to spectra of SNe IIb, Ib, and Ic at two different phases in their evolution (near maximum brightness and 2–4 weeks post-maximum). We classified the degraded spectra with the methods described above and compared the results to those obtained from the original data. We chose events that are not included in the SNID template set and for which we have relatively high signal-to-noise ratio (S/N) spectra (S/N > 30) at these phases covering ~3500–10000 Å: SN IIb 2003ed, SN Ib 1998dt, and SN I-c 2003aa. The spectra used in this study either cover a similar wavelength range or ~3500–7500 Å; we test the efficacy of SNID

using both the full spectra and spectra trimmed to match the smaller wavelength range.

We find that, regardless of subtype or which of the two wavelength ranges is used, SNID capably classifies events in the presence of strong reddening ($E(B-V) \sim 2.0$ mag and $R_V = 3.1$), so long as the spectra exhibit a S/N $\gtrsim$ 1–3. This is to be expected, as SNID divides input spectra by a pseudo-continuum fit and discards the spectral color information before performing cross-correlation (Blondin & Tonry 2007). In contrast, classifications performed via visual comparison may be prone to error when strong reddening is present.

At moderate and high noise levels (S/N $\lesssim$ 3), the post-maximum spectrum of SN Ic 2003aa could be confused with a SN Ib spectrum while the near-maximum-light spectrum is still identified as that of a SN Ic (the He I lines in SNe Ib fade as the event nears the nebular phase; e.g., Modjaz et al. 2014). At extremely high noise levels (S/N $\lesssim$ 1) SNID prefers a SN Ic-BL classification for SN 2003aa, especially when examining the post-maximum spectrum or using spectra covering only the smaller wavelength range, which does not capture the strong Ca II near-infrared (IR) triplet feature.

We also find that, if the SN redshift is uncertain and the S/N is low, SN Ic spectra can be confused with SN Ia spectra (as shown by Blondin & Tonry 2007), and so incorporating an independently measured redshift is helpful. Though SN 2004aw is not in the sample discussed here, it offers a nice illustration of the sometimes-confounding similarities

128
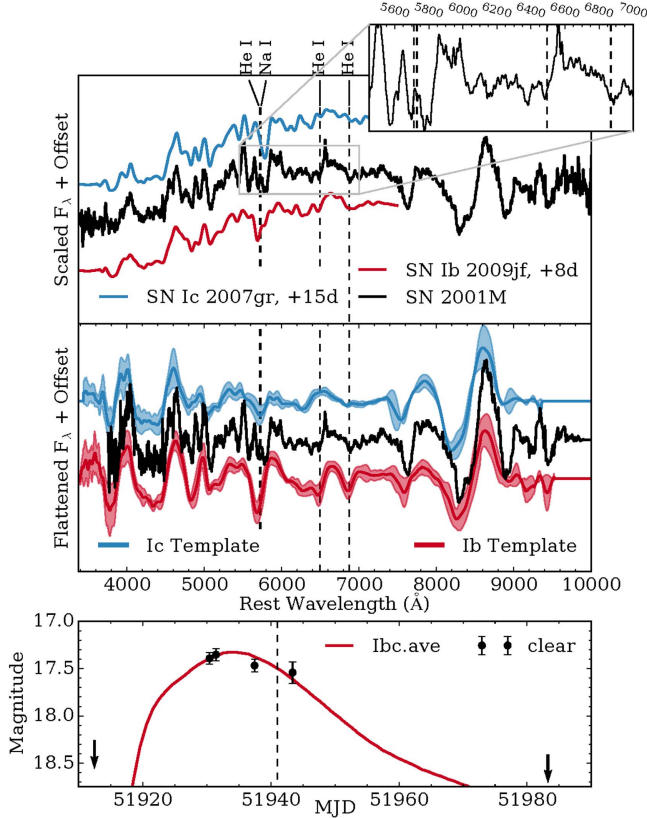
Figure 3. Top: spectrum of SN 2001M smoothed with a 20 Å Gaussian kernel, and with weak helium features identified. We also show spectra of SN Ic 2007gr and SN Ib 2009jf (Modjaz et al. 2014), and the wavelengths of He I and Na I features are marked at $v = 8300$ km s^{-1}. The inset shows the He I lines we identify in the SN 2001M. Middle: the continuum-normalized spectrum of SN 2001M compared to the +10 days average spectra of Ib and Ic SNe from Liu et al. (2016), with the standard deviation shown as shaded regions. Bottom: light curve of SN 2001M compared to the average Ib/c template light curve from L11, with the date of spectrum shown with a dashed line.
(A color version of this figure is available in the online journal.)

between spectra of SNe Ia and Ic (e.g., Benetti et al. 2004; Filippenko et al. 2004; Matheson et al. 2004a).

Examining SN 1998dt, we find that SNID correctly identifies it as a SN Ib at both phases using spectra with S/N $\gtrsim 1$, and though the classification becomes very uncertain using only spectra with S/N $\lesssim 1$ and a restricted wavelength range, SNID never prefers an incorrect label.

SN 2003ed was correctly identified as a SN IIb so long as we examined spectra with S/N $\gtrsim 1$. Unlike SN 1998dt, however, including spectra covering an extended wavelength range did not significantly affect the results even at low S/N, since the He I $\lambda5876$ and Hα features proved the most useful and they are captured by all of our spectra.

Based on the above discussion, we adopt the following guidelines to avoid systematic biases when using SNID for our stripped-envelope classifications. First, it is difficult to

discriminate between SNe Ib and Ic or between SNe IIb and Ib if only noisy (S/N $\lesssim 3$) spectra observed at more than a few weeks post-maximum are available. Second, SNe Ic can be mislabeled as SNe Ic-BL when only low-S/N spectra are available.

4. Updated Classifications

For the bulk of the SNe in the sample, especially the SNe Ia, our methods robustly confirm the L11 classifications.[25] Table 1 lists all SNe in this sample, the type and subtype labels used by L11, and our updated labels. In the ensuing subsections, we discuss each changed classification individually as well as the rare subtypes and the uncertain and peculiar events we find. Many of the comparison spectra used in this section were drawn from the updated SNID template set; citations to the original publications are given.

4.1. Reclassified Objects

4.1.1. SN 2000N (IIb/IIL → II)

SN 2000N was discovered in MCG-02-34-054 (Sato et al. 2000) and classified as a SN II from a spectrum with a low S/N (Jha et al. 2000). However, because the data they had on this object were quite sparse, L11 could not determine if SN 2000N was a Type IIb or a SN II. We were able to obtain the spectrum originally used to classify the SN as well as additional spectra, including one near peak brightness when the spectra of SNe IIb and II are more clearly differentiable (see Figure 2). SNID identifies SN 2000N as a SN II, and our rereduced light curve indicates that the SN IIL template from L11 is a better match than the SN IIb one.

4.1.2. SN 2001M (Ic → Ib)

SN 2001M was discovered in NGC 3240 and classified as a SN Ic (Aazami & Li 2001; Filippenko et al. 2001a; Suntzeff et al. 2001). SNID identifies reasonably good cross-correlations with spectra of both SNe Ib and SNe Ic. We have been able to locate only a single spectrum of this object and our light curve is sparse, so the phase of our spectrum is somewhat uncertain (see Figure 3). Narrow, unresolved Hα emission from the star-forming host galaxy partially obscures the He I $\lambda6678$ absorption line, but we do identify probable weak He I $\lambda6678$ and He I $\lambda7065$ lines at $v \approx 8500$ km s^{-1}. The region around He I $\lambda5876$ is complex, with what must be several overlapping absorption lines; we believe it to be consistent with He I $\lambda5876$ absorption but not dominated by it.

We compare our spectrum to the +10 day average SN Ib and SN Ic spectra of Liu et al. (2016), after estimating a date of peak of 24 January 2001 from the light curve (implying a phase

---

[25] Note that, in a small number of cases, L11 reclassified some events from the original type announced in the CBETs; in this article we only discuss differences relative to the L11 labels.

Table 1
Updated Classifications of SNe in the LOSS Volume-limited Sample

Name	Previous (L11)	This Work	References	Name	Previous (L11)	This Work	References
SN 1998de	Ia-91bg	Ia-91bg	1, 2, 2	SN 1998dh	Ia-norm	Ia-norm	2, 3
SN 1998dk	Ia-norm	Ia-norm	2, 3	SN 1998dm	Ia-norm	Ia-norm	2, 3
SN 1998dt	Ib	Ib	4	SN 1998ef	Ia-norm	Ia-norm	3
SN 1998es[a]	Ia-91T	Ia-99aa	2, 3	SN 1999D	IIP	II	5
SN 1999aa[a]	Ia-91T	Ia-99aa	2, 3, 6	SN 1999ac[a]	Ia-91T	Ia-99aa/Ia-norm	2, 3, 7
SN 1999an	IIP	II	⋯	SN 1999bg	IIP	II	5
SN 1999bh[a]	Ia-02cx	Ia-02es	8, 9	SN 1999br	IIP	II	⋯
SN 1999bu	Ic	Ic	⋯	SN 1999bw	impostor	impostor	10
SN 1999by	Ia-91bg	Ia-91bg	3	SN 1999cd	IIb	IIb	⋯
SN 1999cl	Ia-norm	Ia-norm	2, 3	SN 1999cp	Ia-norm	Ia-norm	3
SN 1999 da	Ia-91bg	Ia-91bg	3	SN 1999dk	Ia-norm	Ia-norm	3
SN 1999dn	Ib	Ib	4	SN 1999dq[a]	Ia-91T	Ia-99aa	2, 3
SN 1999ej	Ia-norm	Ia-norm	2	SN 1999ek	Ia-norm	Ia-norm	3
SN 1999el	IIn	IIn	⋯	SN 1999em	IIP	II	5, 11
SN 1999gd	Ia-norm	Ia-norm	2, 3	SN 1999gi	IIP	II	12
SN 1999go	IIL	II	13	SN 2000C	Ic	Ic	⋯
SN 2000H	IIb	IIb	14	SN 2000L	IIP	II	⋯
SN 2000N	**IIb/IIL**	**II**	⋯	SN 2000cb[b]	IIP	II-87A	15
SN 2000ch	impostor	impostor	10, 16	SN 2000dc	IIL	II	17
SN 2000dm	Ia-norm	Ia-norm	3	SN 2000dr	Ia-norm	Ia-norm	3
SN 2000el	IIP	II	⋯	SN 2000eo	IIn	IIn	⋯
SN 2000ex	IIP	II	⋯	SN 2001E	Ia-norm	Ia-norm	3
SN 2001J	**IIP**	**II/IIb**	⋯	SN 2001K	IIP	II	⋯
SN 2001L	Ia-norm	Ia-norm	3	**SN 2001M**	**Ic**	**Ib**	⋯
SN 2001Q	IIb	IIb	⋯	SN 2001V[a]	Ia-91T	Ia-99aa	2, 3
SN 2001ac	impostor	impostor	10	SN 2001bq	IIP/IIL	II	5
SN 2001ci	**Ic**	**Ib**	⋯	SN 2001cm	IIP	II	5, 18
SN 2001dc	IIP	II	19	SN 2001dn	Ia-norm	Ia-norm	3
SN 2001do	IIL	II	17	SN 2001en	Ia-norm	Ia-norm	3
SN 2001ep	Ia-norm	Ia-norm	3, 20	SN 2001fh	Ia-norm	Ia-norm	3
SN 2001fz	IIP	II	⋯	SN 2001hf	IIL	II	⋯
SN 2001is	Ib	Ib	⋯	SN 2002J	Ic	Ic	⋯
SN 2002an	IIL	II	5	SN 2002ap	Ic-pec	Ic-BL	21
SN 2002bo	Ia-norm	Ia-norm	3	SN 2002bu[c]	IIn	impostor	10
SN 2002bx	IIP	II	5	SN 2002ca	IIP	II	5
SN 2002ce	IIP	II	⋯	SN 2002cf	Ia-91bg	Ia-91bg	3
SN 2002cr	Ia-norm	Ia-norm	3	SN 2002dj	Ia-norm	Ia-norm	3
SN 2002dk	Ia-91bg	Ia-91bg	3	SN 2002do	Ia-norm	Ia-norm	3
SN 2002dq	IIP	II	⋯	SN 2002ds[d]	IIP	II	⋯
SN 2002er	Ia-norm	Ia-norm	3	SN 2002es[a]	Ia-02cx	Ia-02es	22
SN 2002fb	Ia-91bg	Ia-91bg	3	SN 2002fk	Ia-norm	Ia-norm	3
SN 2002gd	IIP	II	5	SN 2002gw	IIP	II	⋯
SN 2002 ha	Ia-norm	Ia-norm	3	SN 2002hh	IIP	II	5
SN 2002hw	Ia-norm	Ia-norm	3	SN 2002jg	Ia-norm	Ia-norm	3
SN 2002jj	**Ic**	**Ic/Ic-BL**	⋯	SN 2002jm	Ia-91bg	Ia-91bg	3
SN 2002jz	**Ic**	**Ib/Ic**	⋯	SN 2002 kg	impostor	impostor	23, 24
SN 2003E	IIP	II	⋯	SN 2003F	Ia-norm	Ia-norm	3
SN 2003G	IIn	IIn	⋯	SN 2003H[e]	Ibc-pec	Ca-rich	25
SN 2003Y	Ia-91bg	Ia-91bg	3	SN 2003Z	IIP	II	5
SN 2003aa	Ic	Ic	⋯	SN 2003ao	IIP	II	⋯
SN 2003bk	IIP	II	⋯	**SN 2003br**	**IIP**	**II/IIb**	⋯
SN 2003bw[d]	**IIP**	**II/IIb**	⋯	SN 2003cg	Ia-norm	Ia-norm	26
SN 2003dr[e]	Ibc-pec	Ca-rich	25	SN 2003du	Ia-norm	Ia-norm	3, 27
SN 2003dv	IIn	IIn	28	SN 2003ed	IIb	IIb	⋯
SN 2003ef	IIP	II	⋯	SN 2003gm	impostor	impostor	23
SN 2003gt	Ia-norm	Ia-norm	3	SN 2003hg	IIP	II	13
SN 2003hl	IIP	II	5	**SN 2003id**	**Ic-pec**	**Ic-pec**	⋯
SN 2003iq	IIP	II	5	SN 2003kf	Ia-norm	Ia-norm	3

7

Table 1
(Continued)

Name	Previous (L11)	This Work	References	Name	Previous (L11)	This Work	References
SN 2003ld	IIP	II	⋯	**SN 2004C**	**Ic**	**IIb**	⋯
SN 2004ab	Ia-norm	Ia-norm	9	**SN 2004al**	**IIb/IIL**	**II**	⋯
SN 2004aq	IIP	II	⋯	SN 2004bd	Ia-norm	Ia-norm	3
SN 2004be	IIb	IIb	⋯	SN 2004bl	Ia-norm	Ia-norm	3
SN 2004bm	**Ibc-pec/IIb**	**IIb/IIb-pec**	⋯	SN 2004bv	Ia-91T	Ia-91T	3
SN 2004ca	Ia-norm	Ia-norm	3	**SN 2004cc**	**Ic**	**Ib/Ic**	13
SN 2004ci	IIP	II	⋯	SN 2004dd	IIP	II	⋯
SN 2004dk	Ib	Ib	⋯	SN 2004er	IIP	II	⋯
SN 2004et	IIP	II	5	SN 2004fc	IIP	II	⋯
SN 2004fx	IIP	II	29	SN 2004gq	Ib	Ib	14
SN 2005A	Ia-norm	Ia-norm	3, 30	SN 2005E[e]	Ibc-pec	Ca-rich	25, 31
SN 2005H	**IIb**	**II/IIb**	13	SN 2005J	IIL	II	⋯
SN 2005U	IIb	IIb	14	SN 2005W	Ia-norm	Ia-norm	3, 30
SN 2005ad	IIP	II	⋯	SN 2005am	Ia-norm	Ia-norm	3, 30
SN 2005an	IIL	II	⋯	SN 2005aq	IIn	IIn	⋯
SN 2005as	Ia-norm	Ia-norm	3	SN 2005ay	IIP	II	5
SN 2005az	Ic	Ic	14	SN 2005bb	IIP	II	⋯
SN 2005bc	Ia-norm	Ia-norm	3	SN 2005bo	Ia-norm	Ia-norm	3, 30
SN 2005cc	Ia-02cx	Ia-02cx	9	SN 2005cf	Ia-norm	Ia-norm	32
SN 2005ci[b]	IIP	II-87A	15	SN 2005de	Ia-norm	Ia-norm	3
SN 2005el	Ia-norm	Ia-norm	3, 30	SN 2005hk	Ia-02cx	Ia-02cx	3, 33, 34
SN 2005io[b]	**IIP**	**II-87A**	⋯	SN 2005kc	Ia-norm	Ia-norm	3, 30
SN 2005ke	Ia-91bg	Ia-91bg	3, 30	**SN 2005lr**	**Ic**	**IIb**	⋯
SN 2005mg	**IIP**	**II/IIb**	⋯	SN 2005mz	Ia-91bg	Ia-91bg	9
SN 2006F	Ib	Ib	⋯	SN 2006T	IIb	IIb	⋯
SN 2006X	Ia-norm	Ia-norm	3, 30	SN 2006ax	Ia-norm	Ia-norm	3, 30
SN 2006be	IIP	II	⋯	SN 2006bp	IIP	II	⋯
SN 2006bv[c,d]	IIn	*impostor*	10	SN 2006ca	IIP	II	⋯
SN 2006cm[a]	Ia-91T	Ia-99aa/Ia-norm	3	SN 2006dy	Ia-norm	Ia-norm	3
SN 2006ef	Ia-norm	Ia-norm	3, 30	**SN 2006eg**	**Ic**	**IIb/Ib/Ic/Ic-BL**	⋯
SN 2006ke	Ia-91bg	Ia-91bg	3	SN 2006le	Ia-norm	Ia-norm	3
SN 2006lf	Ia-norm	Ia-norm	3	SN 2006qr	IIP	II	⋯

Notes. This table lists the previous classifications for all objects in L11 and our confirmed or updated classifications. Notable objects, discussed individually within the text, are printed in boldface. We also list references to the original publishers for all data already in the literature that were used in this effort. When we cannot confim a single clear classification, we list more than one possible type or subtype. See Section 3 for a detailed description of each type and subtype label.
[a] See Section 4.3.
[b] See Section 4.5.
[c] See Section 4.7.
[d] See Section 4.8.
[e] See Section 4.6.

References. [1] Modjaz et al. (2001), [2] Matheson et al. (2008), [3] Silverman et al. (2012), [4] Matheson et al. (2001), [5] Faran et al. (2014b), [6] Garavini et al. (2004), [7] Garavini et al. (2005), [8] Li et al. (2001), [9] Blondin et al. (2012), [10] Smith et al. (2011b), [11] Leonard et al. (2002a), [12] Leonard et al. (2002b), [13] Harutyunyan et al. (2008), [14] Modjaz et al. (2014), [15] Kleiser et al. (2011), [16] Wagner et al. (2004), [17] Faran et al. (2014a), [18] Poznanski et al. (2009), [19] Pastorello et al. (2004), [20], Sauer et al. 2008, (21) Foley et al. (2003), [22] Ganeshalingam et al. (2012), [23] Maund et al. (2006), [24] Van Dyk et al. (2006), [25] Perets et al. (2010), [26] Elias-Rosa et al. (2006), [27] Leonard et al. (2005), [28] Bilinski et al. (2015), [29] Hamuy et al. (2006), [30] Folatelli et al. (2013), [31] Foley et al. (2009), [32] Wang et al. (2009b), [33] Chornock et al. (2006), [34] Phillips et al. (2007).

of +7.5 days for our spectrum). This comparison shows many similarities between SN 2001M and both classes, but reinforces our identifications of the He I lines. Given our detections of both He I λ6678 and He I λ7065, we relabel SN 2001M as a SN Ib, though we note that the helium lines are weak compared to those in most SNe Ib.

4.1.3. SN 2001ci (Ic → Ib)

SN 2001ci was discovered in NGC 3079 (Swift et al. 2001) and announced as a SN Ic heavily obscured by host-galaxy dust absorption (Filippenko & Chornock 2001). A re-examination of the spectrum cited therein (observed UT 2001 May 30; we were not able to locate any other spectra of this object)
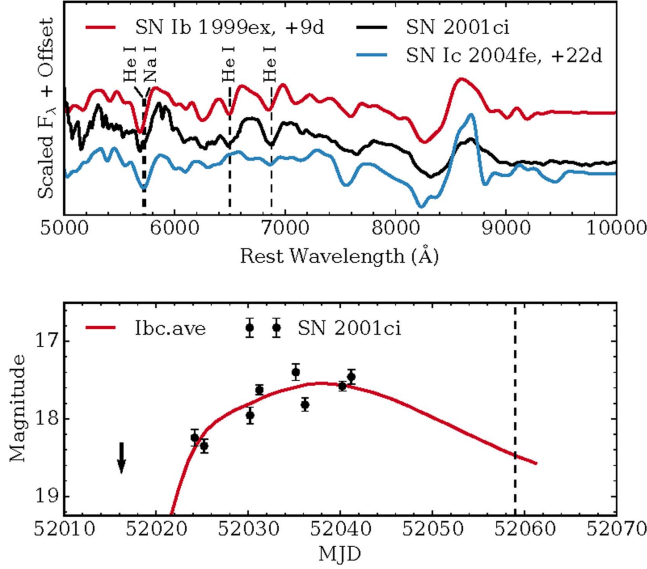
Figure 4. Top: spectrum of SN 2001ci (corrected for a reddening of $E(B-V) = 3.0$ mag and smoothed with a Gaussian kernel 50 Å wide), compared with that of the Type Ib SN 1999ex (Hamuy et al. 2002) and the Type Ic SN 2004fe (Modjaz et al. 2014). Bottom: the light curve compared to a L11 template with the date of the spectrum marked by a vertical line.
(A color version of this figure is available in the online journal.)

confirms that it is heavily reddened by host-galaxy dust. The MW contribution to the reddening is only $E(B-V) = 0.0097$ mag (Schlafly & Finkbeiner 2011, used for all subsequent MW reddening measures), but the spectrum clearly shows narrow Na I absorption features from the host galaxy indicating significant reddening produced by host-galaxy dust. The spectrum is of sufficiently high resolution to resolve both components of the Na I D doublet, but their equivalent widths (EWs) are well outside the range of the empirical relations of Poznanski et al. (2012): $EW_{D1} \approx 2.4$ Å and $EW_{D2} \approx 2.2$ Å. This implies that $E(B-V) \gtrsim 3.0$ mag.

Note that SNID, by construction, is insensitive to color information and to uncertainties in the reddening corrections or flux calibrations (Blondin & Tonry 2007). Throughout this paper we apply (often uncertain) reddening corrections to spectra to facilitate visual comparisons, but they do not appreciably affect the SNID classifications.

Adopting $E(B-V) = 2.0$ mag and a MW-like dust law is good enough to achieve a robust identification: SN 2001ci is a SN Ib, with a spectrum that is most similar to those of SNe Ib with weak helium lines. See Figure 4 for a comparison to the He-weak SN Ib 1999ex (Hamuy et al. 2002). Filippenko & Chornock (2001) drew attention to a similarity with SN 1990U, which was (at the time) classified as a SN Ic, but Modjaz et al. (2014) have subsequently reclassified SN 1990U as a SN Ib.
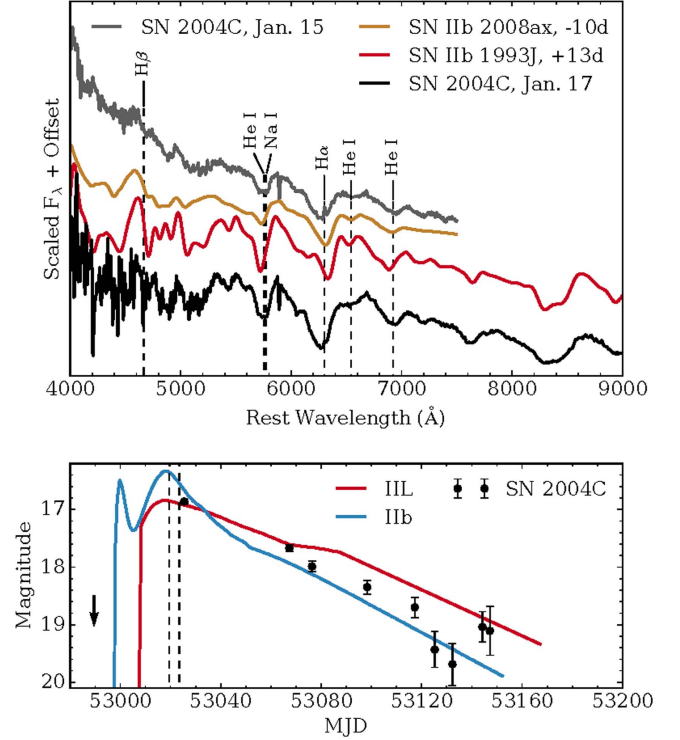
Figure 5. Top: spectra of SN 2004C observed on UT 2004 January 15 and on UT 2004 January 17, alongside a premaximum spectrum of the Type IIb SN 2008ax (Modjaz et al. 2014) and a post-maximum spectrum of the Type IIb SN 1993J (Matheson et al. 2000). Both spectra of SN 2004C have been dereddened by $E(B-V) = 1.0$ mag and smoothed by a 20 Å Gaussian kernel, and galaxy emission lines have been subtracted by hand. Bottom: light curve of SN 2004C compared to templates from L11 with the date of the spectra marked by vertical lines.
(A color version of this figure is available in the online journal.)

4.1.4. SN 2004C (Ic → IIb)

SN 2004C was discovered in NGC 3683 (Dudley & Fischer 2004) and classified as a heavily reddened SN Ic (Matheson et al. 2004b), spectrally similar to SN 1990U (see Section 4.1.3: SN 1990U was a SN Ib). The MW reddening along the line of sight is only $E(B-V) = 0.0133$ mag, but (unresolved) Na I D absorption in our spectra indicates strong host-galaxy obscuration. As with SN 2001ci, the Na I D EW is well beyond the empirical relations of Poznanski et al. (2012), but the spectra do not appear to be as reddened as those of SN 2001ci. Correcting for a total reddening of $E(B-V) = 1.0$ mag produces a reasonable result.

Here we publish several spectra of SN 2004C which indicate that SN 2004C was a SN IIb. Figure 5 shows a comparison between the spectrum announced by Matheson et al. (2004b) and the Type IIb SN 2008ax, as well as a later spectrum with broader wavelength coverage compared to a spectrum of the Type IIb SN 1993J.

9
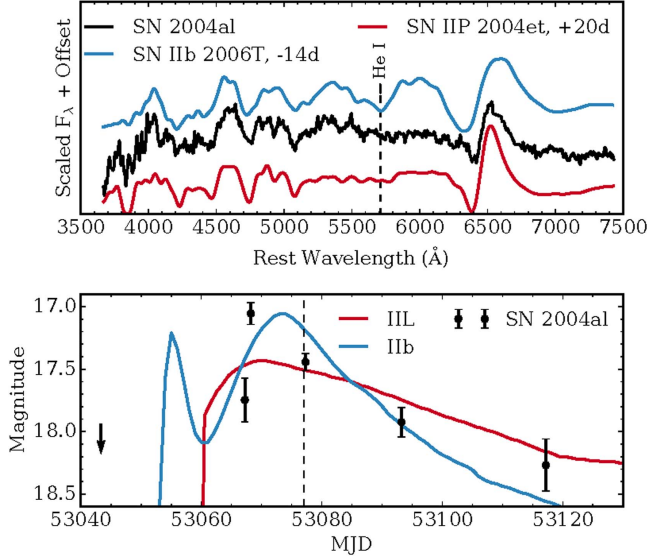
Figure 6. Top: spectrum of SN 2004al smoothed with a 20 Å Gaussian kernel and compared to spectra of the Type IIP SN 2004et a few weeks after maximum (Sahu et al. 2006) and the premaximum SN IIb 2006T (the top non-IIP SNID template, Modjaz et al. 2014). Bottom: the light curve compared to templates from L11 with the date of the spectrum marked by a vertical line. (A color version of this figure is available in the online journal.)

4.1.5. SN 2004al (IIb/IIL → II)

SN 2004al was discovered in ESO 565-G25 (Singer et al. 2004) and classified as a SN II (Matheson et al. 2004c). As L11 show, SN 2004al had a light curve consistent with either a SN IIb or a SN IIL classification, and so they assign it a 50% weight in each class. Although we have no additional spectra to examine, we were able to obtain the classification spectrum and SNID clearly identifies it as a SN II, not a SN IIb, mostly owing to the absence of He I λ5876. Figure 6 shows that our spectrum was observed ∼1 week post-maximum; though He I lines are often weak in young SNe IIb, they become pronounced by maximum light. In good agreement with L11, our rereduced light curve exhibits a relatively rapid decline and is better fit by the SN IIb template; see Figure 6. Despite this tension, we consider the spectroscopic classification robust and we label SN 2004al a Type II event.

4.1.6. SN 2005io (IIP → II-87A)

SN 2005io was discovered in UGC 3361 (Lee et al. 2005) and reported as a young SN II (Filippenko & Foley 2005) based upon a Keck LRIS spectrum. The photometry of SN 2005io shows a peculiar evolution, however—see Figure 7. The light curve initially follows the Type IIP template almost exactly, but after peaking at an absolute magnitude of −15.2 mag SN 2005io goes into a slight decline and then a very slow rise (over ∼100 days) to a second maximum (<−15.75 mag; the peak itself went unobserved). This is similar to the photometric behavior of SN 1987A and other
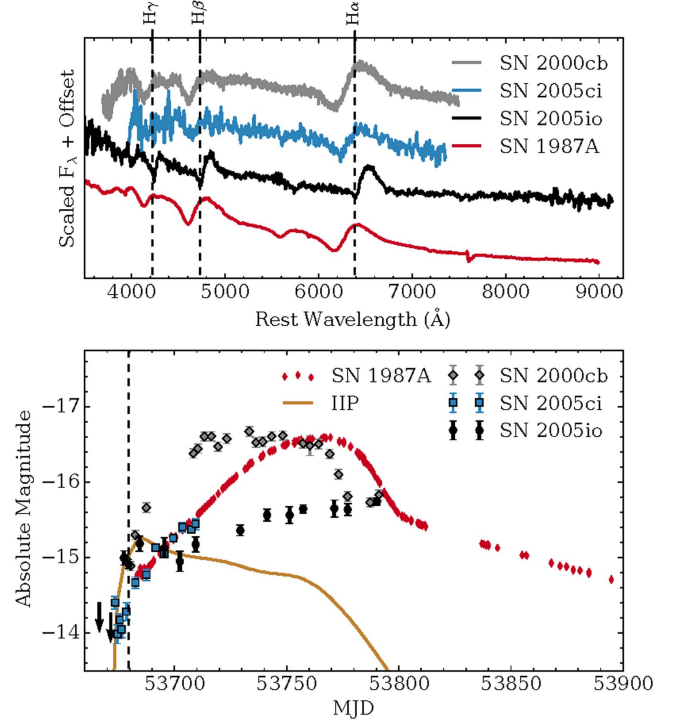
Figure 7. Top: spectrum of SN 2005io compared to spectra of the young SNe 2000cb, 2005ci, and 1987A (SNe 2000cb and 2005ci are also included in the LOSS volume-limited sample; Blanco et al. 1987; Kleiser et al. 2011). The spectra of SNe 2005io and 2005ci have been smoothed by a Gaussian kernel 20 Å wide. We mark prominent hydrogen features at 8000 km s⁻¹. Bottom: light curve of SN 2005io (with a vertical line showing the date the spectrum was observed) compared to the light curves of the other SN 1987A-like events after correcting for distance and MW dust absorption along the line of sight, and then offset in time to align their initial rises (Hamuy & Suntzeff 1990; L11). Also shown is the template Type IIP light curve from L11, offset to match the early evolution of SN 2005io.
(A color version of this figure is available in the online journal.)

related events, though in SN 1987A the early peak was only visible in bluer passbands and the rise to its second, more luminous, peak occurred more rapidly. The spectrum is similar to that of a normal young SN II with hydrogen P-Cygni profiles dominated by the emission component and with an absorption Doppler velocity of ∼8000 km s⁻¹, slower than the velocity found for hydrogen in SN 1987A.

Based primarily upon the light-curve evolution, and noting that the subclass is heterogeneous (Pastorello et al. 2005a, 2012; Kleiser et al. 2011; Taddia et al. 2012, 2016b), we classify SN 2005io as a SN 1987A-like event alongside the two other SN 1987A-like events already identified within the L11 sample (SNe 2000cb and 2005ci; Kleiser et al. 2011). It unfortunately appears that the peculiarity of SN 2005io was not recognized while it was bright: we believe that Figure 7, which shows the classification spectrum and the KAIT photometry, includes all extant observations of the event. Though the

central wavelength of unfiltered KAIT photometry is quite similar to that of the R band, the effective passband is significantly wider (Ganeshalingam et al. 2010). Our early-time spectrum of SN 2005io shows that it was quite blue while young, and it's likely that the rapid rise to the first photometric peak was powered by cooling envelope emission, as was observed in SN 1987A via photometry in bluer passbands.

The second peak of SN 2005io lasts longer than that of SN 1987A, and the fade from peak was not observed. We have upper limits showing that the object had faded to $\gtrsim$19.7 mag (absolute mag -14.2) by September 18, but we have no data obtained between the last detection on February 24 (shown in Figure 7) and then. SN 2005io shares some similarities with SN 2009E (Pastorello et al. 2012), including a slow rise and faint peak compared to the prototypical SN 1987A. The early peak and slow rise to second maximum is also reminiscent of SN 2004ek (Taddia et al. 2016b), although that SN was a great deal more luminous ($R \approx -18.5$ mag) than SN 2005io (clear $\lesssim -15.75$ mag), further illustrating the heterogenous nature of these slow-rising SNe II.

4.1.7. SN 2005lr (Ic → IIb)

SN 2005lr was discovered in ESO 492-G2 (Baek & Li 2005) and was spectroscopically classified as a SN Ic, with spectra similar to those of SN 1990B (Hamuy et al. 2005). We obtained a copy of the classification spectrum for SN 2005lr from the CSP archives (observed 2005 December 18) as well as a second (higher S/N) spectrum taken two days later.

The spectra of SN 2005lr show that this SN was strongly reddened by host-galaxy dust—the Na I D line in these low-resolution spectra exhibits a total EW of $\sim$2.4 Å, just beyond the limits of the relations from Poznanski et al. (2012). We again deredden the spectrum by an arbitrary value of $E(B - V) = 1.0$ mag to facilitate visual inspection.

SNID identifies SN 2005lr as either a SN Ib or IIb, with matches to examples of either class. Distinct He I, O I, and Ca II lines are detected alongside an Hα absorption feature; see Figure 8. Our spectra appear to be taken well after peak brightness (although the light curve is extremely sparse) and the detection of a relatively strong Hα feature at this phase identifies SN 2005lr as a SN IIb.

4.2. Low-certainty Classifications and Peculiar Events

We have made an effort to track down spectra of every object in the volume-limited sample, especially those spectra originally used for classification in the CBETs, and re-examine the classifications of each. Unfortunately, however, there are several objects in our sample for which robust classifications are simply not possible given the peculiarity of the object or the quality of the data.
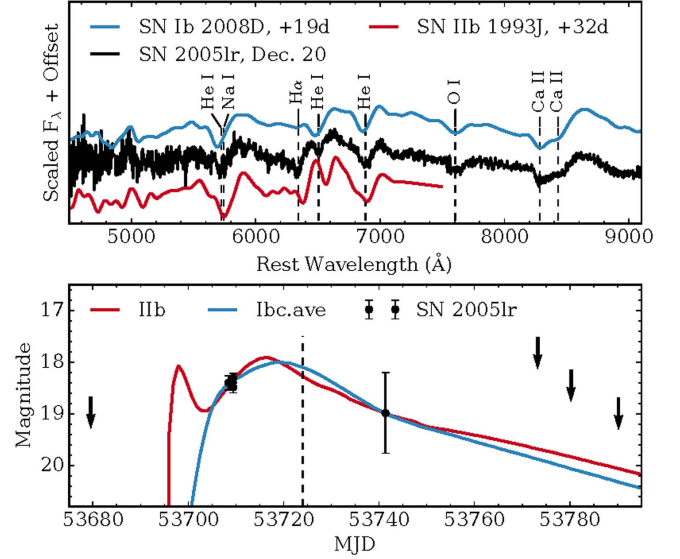
Figure 8. Top: the higher S/N spectrum of SN 2005lr smoothed with a Gaussian kernel 10 Å wide and compared to spectra of the SN Ib 2008D and SN IIb 1993J (Matheson et al. 2000; Modjaz et al. 2009). Bottom: light curve of the SN compared to templates from L11 with date of spectrum shown by a vertical line.

(A color version of this figure is available in the online journal.)

4.2.1. SN 2001J (IIP → II/IIb)

SN 2001J was discovered in UGC 4729 (Beckmann & Li 2001) and classified as a SN II (Jha et al. 2001). SNID identifies the SN 2001J spectrum as that of a young SN IIb, similar to the spectrum of SN 2008ax. L11 list SN 2001J as a SN IIP with poor light-curve coverage, but Figure 9 shows our rereduced KAIT light curve (including nondetection upper limits) indicating there was no bright hydrogen recombination plateau phase. Taking into account both the SNID result and the rapid light-curve decay, we prefer the SN IIb classification, but cannot rule out the possibility that SN 2001J was a hydrogen-rich SN II with a relatively rapid decline rate.

4.2.2. SN 2002jj (Ic → Ic/Ic-BL)

SN 2002jj was discovered in IC 340 (Hutchings & Li 2002) and classified as a SN Ic (Foley & Filippenko 2002), with a spectrum similar to that of SN 1994I. We have three spectra of SN 2002jj, all of moderate quality. SNID prefers a SN Ic-BL classification, as do comparisons with the average spectra of Liu et al. (2016), but the data are not good enough to be sure. The light curve (though it is sparse) indicates that all of our spectra were taken well past peak brightness. SN 2002jj showed a peak absolute magnitude of -17.66 ± 0.23 (L11), a value in the normal range for both SNe Ic and SNe Ic-BL (SNe Ic-BL are, on average, more luminous than other stripped-envelope SNe; e.g.,

11

134
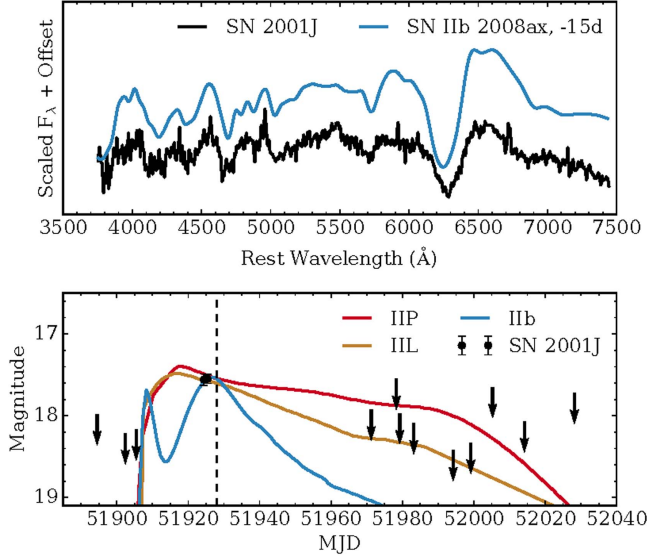
Figure 9. Top: the spectrum of SN 2001J (smoothed by a 20 Å Gaussian kernel) compared to that of the Type IIb SN 2008ax (Modjaz et al. 2014). Bottom: the light curve compared to the Type IIL, IIP, and IIb templates from L11. Upper limits from nondetections are shown as arrows, and the date of the spectrum is marked with a dashed vertical line.
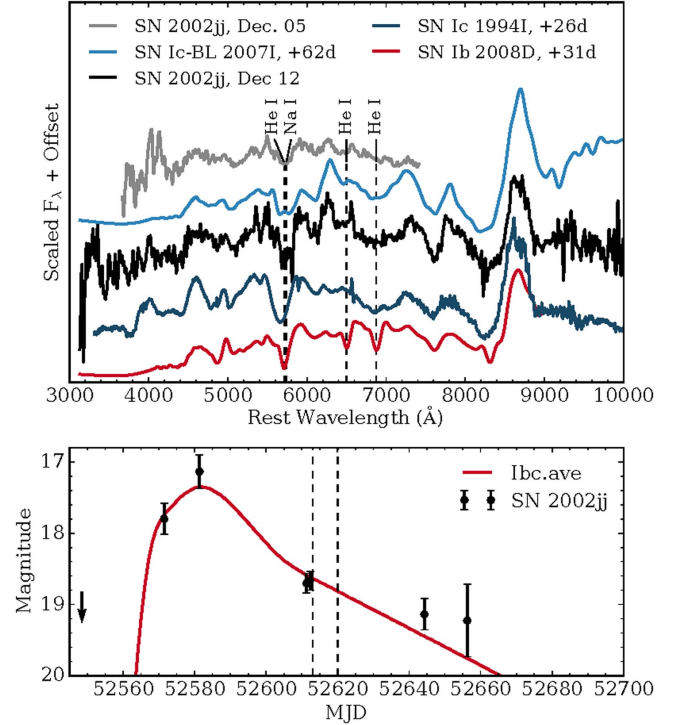(A color version of this figure is available in the online journal.)

Figure 10. Top: spectra of SN 2002jj, smoothed by a 40 Å Gaussian kernel and compared to spectra of the Type Ic-BL SN 2007I (Modjaz et al. 2014), the Type Ic SN 1994I (Filippenko et al. 1995), and the Type Ib SN 2008D (Modjaz et al. 2009). Bottom: light curve of SN 2002jj compared to the average SN Ib/c template from L11, with the dates of the spectra marked by vertical lines.
(A color version of this figure is available in the online journal.)

Drout et al. 2011; Lyman et al. 2016), and so it is not clear whether this SN was a bona-fide SN Ic-BL.

In addition, the He I lines used to distinguish SNe Ic from Ib are most apparent around the time of peak brightness and then fade, in most cases disappearing entirely by ~50–70 days (Modjaz et al. 2014; Liu et al. 2016). The spectroscopic coverage of SN 2002jj did not begin until ~1 month post-peak and we cannot rule out the possibility of weak helium features near peak, but we prefer the SN Ic or SN Ic-BL classification; see Figure 10.

4.2.3. SN 2002jz (Ic → Ib/Ic)

SN 2002jz was discovered in UGC 2984 and classified as a SN Ic with a resemblance to SN 1994I (Puckett et al. 2002). We present three spectra of this object, the most useful of which was observed on UT 2003 January 07. There is significant MW dust reddening along the line of sight ($E(B - V) = 0.4846$ mag), and the unresolved Na I D absorption in our spectra indicates a similar amount of host-galaxy dust obscuration.

SNID weakly prefers a Type Ib label over the Ic label; the best SNID matches are to the spectra of the Type Ib SNe 1995F (reclassified from Ic to Ib by Modjaz et al. 2014) and 1999ex (studied in detail by, e.g., Parrent et al. 2007). However, the He I λ6678 line in SN 2002jz is so weak as to be nearly indiscernible (it is only detected as a notch out of an adjacent P-Cygni emission profile), and the He I λ7065 line is notably

weaker than that of SN 1995F—see Figure 11. We give SN 2002jz equal weights in the Ib and Ic categories.

4.2.4. SN 2003br (II → II/IIb)

SN 2003br was discovered in MCG-05-34-18 (Swift & Li 2003) and was classified as a SN II (Berlind et al. 2003). We present the classification spectrum of SN 2003br, but this alone is not enough to distinguish between a Type II or a Type IIb classification. The MW reddening toward the object is small ($E(B - V) = 0.0822$ mag), but the observed spectral energy distribution (SED) implies that there must be a moderate-to-large degree of host-galaxy reddening. Unfortunately, the spectrum has neither the signal nor the resolution to measure any possible narrow Na I D absorption features. Adopting a correction of $E(B - V) = 1.0$ mag appears to roughly correct the SED, and so we continue with that.

SNID indicates that the best match is with the Type IIb SN 2006T, but the Type IIP SN 1999em also shows a good match. The light curve is more similar to the Type IIL template, and so we prefer a Type II classification but cannot be sure. See Figure 12.

12
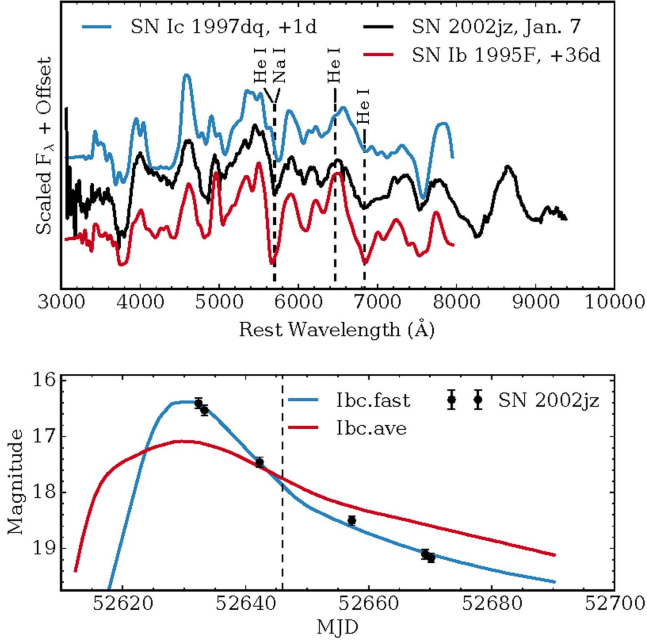
Figure 11. Top: spectrum of SN 2002jz from 2003 January 07 (corrected for a MW reddening of $E(B-V) = 0.4846$ mag) compared with that of SN Ic 1997dq and SN Ib 1995F (Matheson et al. 2001; Modjaz et al. 2014). Bottom: light curve of SN 2002jz compared to the stripped-envelope templates of L11, with the date of the spectrum shown with a vertical line.

(A color version of this figure is available in the online journal.)
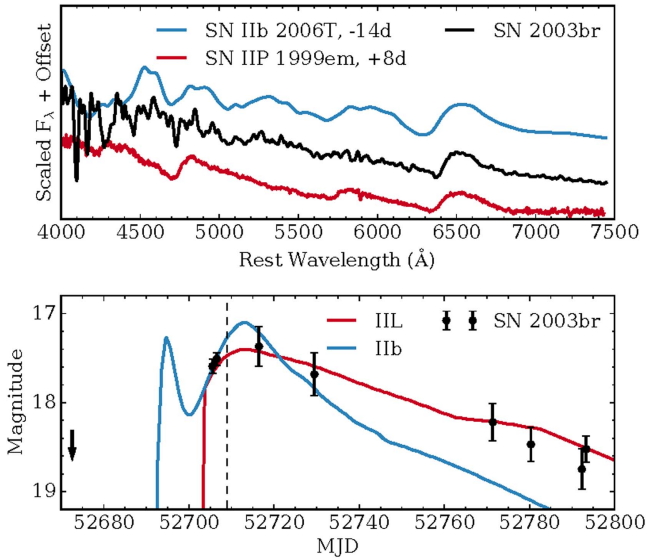
Figure 12. Top: spectrum of SN 2003br (corrected for $E(B-V) = 1.0$ mag and smoothed with a 40 Å Gaussian kernel), compared to that of the Type IIb SN 2006T (Modjaz et al. 2014) and the Type IIP SN 1999em (Leonard et al. 2002a)—both match well. Bottom: the light curve compared to the templates from L11, with the date of the spectrum marked.

(A color version of this figure is available in the online journal.)

4.2.5. SN 2003id (Ic-pec)

SN 2003id was discovered in NGC 895 and classified as a SN Ibc-pec by Hamuy & Roth (2003), who identify several normal SN Ic lines as well as a strong blended feature around 5700 Å. Here we analyze spectra observed on 2003 September 19 and October 23—see Figure 13. Our spectra confirm this to be an odd object with no good matches in the SNID template set, though with many similarities to the peculiar SN Ib 2007uy (Roy et al. 2013; Modjaz et al. 2014).

The strong blended feature around 5700 Å persists and appears to grow stronger over time. We tentatively identify He I $\lambda6678$ at $v \approx 11,000$ km s^{-1}, which implies that the feature at 5700 Å may include some absorption from He I $\lambda5876$ in addition to Na I $\lambda\lambda5890, 5896$; perhaps this feature arises from multiple velocity components of these two ions. However, we find no clear sign of He I $\lambda7065$ absorption in either spectrum. (Note that these spectra have undergone a correction for telluric absorption and none of the features in them is telluric.)

We also identify a feature near 6140 Å that evolves from a strongly blended state into two clearly defined components, the redder of which is plausibly high-velocity Hα at $v \approx 17,500$ km s^{-1}, and we tentatively identify Hβ at $v \approx 17,500$–18,500 km s^{-1} in the spectrum from September 19. The bluer feature may be a second, even higher-velocity Hα line at $v \approx 23,500$ km s^{-1}; the bluemost edge of the Ca II IR triplet absorption implies similar velocities for the calcium in SN 2003id. Several authors have previously identified high-velocity Hα lines in SN Ib/c spectra (e.g., Branch et al. 2006; Elmhamdi et al. 2006; Parrent et al. 2007).

We compare the spectra of SN 2003id to the average spectra of Liu et al. (2016) in the middle panel of Figure 13. We estimate that the date of R-band maximum was 2003 September 30, which means our two spectra were obtained at phases of -11 and $+22$ days; hence, we show the -10 days and $+20$ days average spectra. The peculiarity of SN 2003id is apparent here as well: our spectra deviate significantly from both SNe Ib and SNe Ic spectra at several wavelengths. As above, we find that the putative He I $\lambda6678$ line is SN Ib-like, while the lack of a He I $\lambda7065$ line is SN Ic-like, and the extreme widths of the Ca II and 5700 Å features are unlike both.

The light curves provide an additional wrinkle: SN 2003id distinctly shows a double-peaked evolution, with a rapid decline from the blue first peak followed by a rise to the second maximum a few days later. There is no evidence from the later spectrum that the second peak arises from interaction with dense circumstellar interaction (i.e., we find no narrow emission lines). Most SNe Ib and SNe Ic do not exhibit double-peaked light curves like those of SN 2003id, though similar behavior is often observed in SNe IIb. A very small
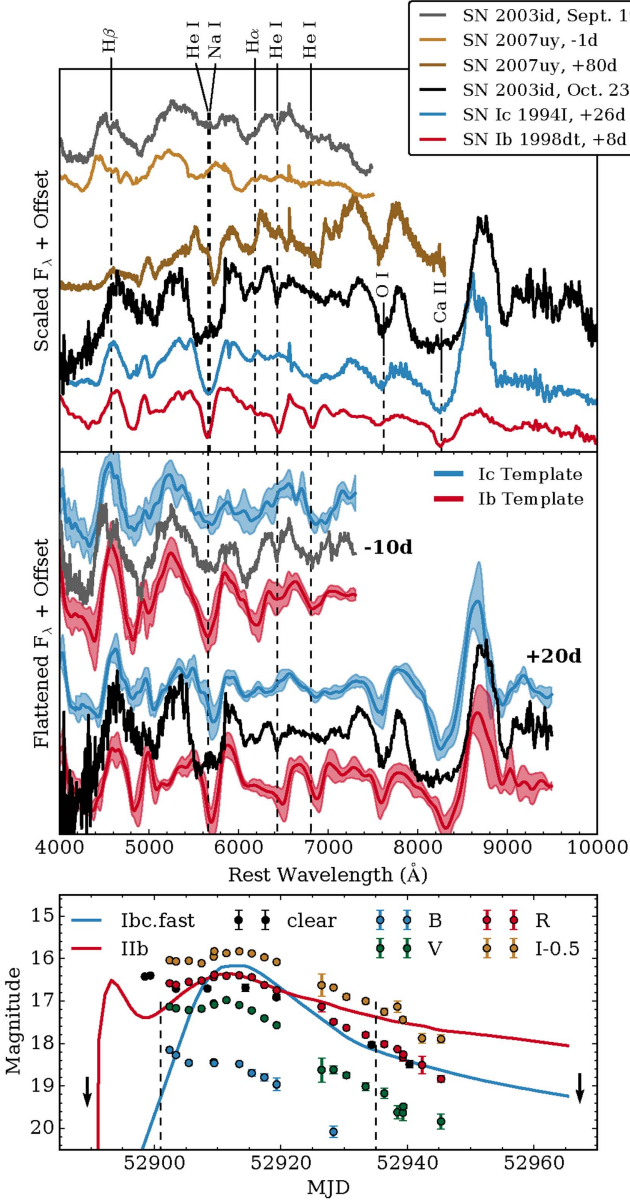
Figure 13. Top: spectra of SN 2003id smoothed with a 20 Å Gaussian kernel and compared to spectra of the peculiar Type Ib SN 2007uy (Modjaz et al. 2014), the normal Type Ic SN 1994I (Filippenko et al. 1995), and the normal Type Ib SN 1998dt (Matheson et al. 2001). Putative hydrogen and helium lines are marked at $v = 17,500$ km s^{-1} and 11,000 km s^{-1}, respectively. Middle: the continuum-normalized spectra of SN 2003id compared to the -10 days and $+20$ days average spectra of SNe Ib and SNe Ic from Liu et al. (2016), with the standard deviation shown as shaded regions and He I lines marked as above. Bottom: filtered light curves of SN 2003id, with phases of spectra marked by the dashed lines. Template SN IIb and "fast" SN Ib/c light curves from L11 are overplotted. (A color version of this figure is available in the online journal.)

number of double-peaked SNe Ib have been discovered (e.g., SNe 2005bf and 2008D; Tominaga et al. 2005; Folatelli et al. 2006; Modjaz et al. 2009), as has one double-peaked SN Ic (Taddia et al. 2016a). However, these events had early peaks
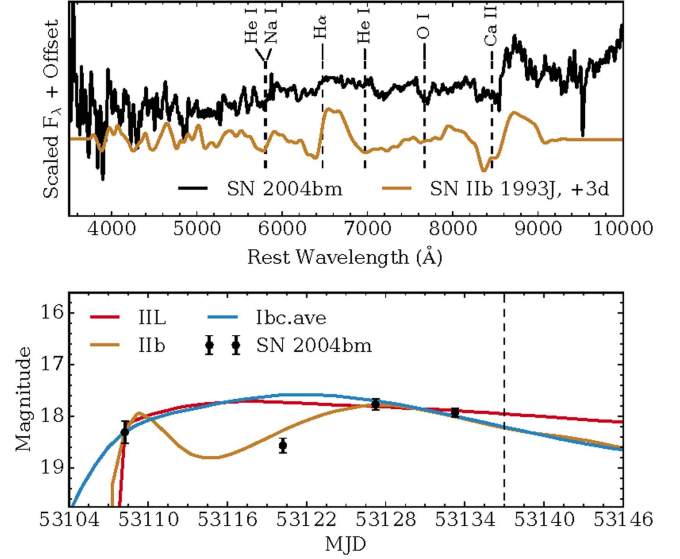
Figure 14. Top: spectrum of SN 2004bm smoothed with a Gaussian kernel 40 Å wide and compared to the near-maximum spectrum of the Type IIb SN 1993J (reddened by $E(B - V) = 0.4$ mag for comparison; Matheson et al. 2000). Bottom: the light curve compared to the Type IIL, IIb, and average Ib/c template light curves from L11. A single data point indicates a light-curve dip and argues for a Type IIb classification. The date of the spectrum is marked by the vertical line.
(A color version of this figure is available in the online journal.)

which were notably less bright than their main peaks, they exhibited a diversity of different peak absolute magnitudes, and none show the peculiar 5700 Å feature of SN 2003id.

Given the lack of He I $\lambda7065$ and the uncertain (and certainly peculiar) He I $\lambda6678$ Å and He I $\lambda5876$ Å lines, we classify SN 2003id as a peculiar and double-peaked SN Ic. We note that this object appears to be different from the other stripped-envelope SNe in this sample.

4.2.6. SN 2004bm (Ibc-pec/IIb → IIb/IIb-pec)

SN 2004bm was discovered in NGC 3437 (Armstrong et al. 2004) and originally classified as a SN Ic (though with some uncertainty; Foley et al. 2004a). L11 note that the light curve shows a dip. Though the data are sparse, the SN occurred near the core of its host galaxy, and this conclusion depends upon only one data point out of four total, our rereduction of the light curve also shows a dip indicated by the second detection—see Figure 14. Similar light-curve behavior has been observed in SNe IIb (e.g., L11; Arcavi et al. 2012), and L11 used the light curve to argue that SN 2004bm was a SN IIb.

The only spectrum we have of this SN is the one used for the original classification and it is of low quality—SNID does not provide a clear classification, but it does indicate that the best cross-correlations are with spectra of SNe IIb and IIP (though

the phases are in disagreement). The spectrum of SN 2004bm does not correlate with spectra of SNe Ic well. Narrow Na I D absorption at the host-galaxy redshift is apparent but unresolved and very noisy, indicating moderate host-galaxy reddening atop the MW contribution of $E(B - V) = 0.0159$ mag. There are few spectral features in our spectrum, though we identify Ca II P-Cygni profiles, faint O I absorption, and a very shallow Hα P-Cygni line—see Figure 14.

Based on the above discussion, we prefer a classification of Type IIb for SN 2004bm, but the Hα line in the spectrum of SN 2004bm is much too weak for a normal SN IIb. We also note that, if we discard the second photometric data point, the light curve of SN 2004bm is well-fit by normal Type II events or by stripped-envelope events.

4.2.7. SN 2004cc (Ic → Ib/Ic)

SN 2004cc was discovered in NGC 4568 (Monard & Li 2004). Matheson et al. (2004d) note the strong reddening toward SN2004cc and classify it as a SN I, though they prefer no subtype, while Foley et al. (2004b) present a SN Ic classification.

There is little MW reddening toward SN 2004cc ($E(B - V) = 0.0279$ mag), but the (unresolved) Na I D lines in our spectra indicate strong host-galaxy dust obscuration. The EW measured from these lines is well outside the relations of Poznanski et al. (2012), and so we only roughly estimate the total reddening, adopting $E(B - V) = 1.0$ mag for visual comparisons.

SNID identifies reasonable correlations between the spectra of SN 2004cc and the spectra of both SNe Ib and SNe Ic, strongly disfavoring all other types and slightly preferring the Ib label over Ic. Unfortunately, we have only a single photometric detection of the SN, so there is little independent information about the phases of these spectra.

Figure 15 shows that the later spectrum of SN 2004cc matches that of SN Ib 1999ex quite well, while the earlier spectrum matches that of SN Ic 1994I. Weak Hα detections have been claimed for both of these events (Branch et al. 2006). Though hydrogen absorption may be present, we trust the SNID result (which prefers a Type Ib or Ic label, rather than a IIb), and we do not consider a Type IIb label for SN 2004cc— see the discussion in Section 3. Note also that, if the identification of the Hα line in Figure 15 is correct, it exhibits a much faster (and unchanging) Doppler velocity ($\sim$17,000 km s^{-1}) than the He I lines (which are at $\sim$15,000 and $\sim$10,000 km s^{-1} on June 13 and June 20, respectively). This behavior is peculiar but not unique for this feature in stripped-envelope SNe (Liu et al. 2016).

The spectra of SN 2004cc present another puzzle. The early-time spectrum appears to show a strong He I λ6678 line (and a strong He I/Na I blend near 5500 Å), but very little He I λ7065 absorption. It is difficult to physically explain a strong
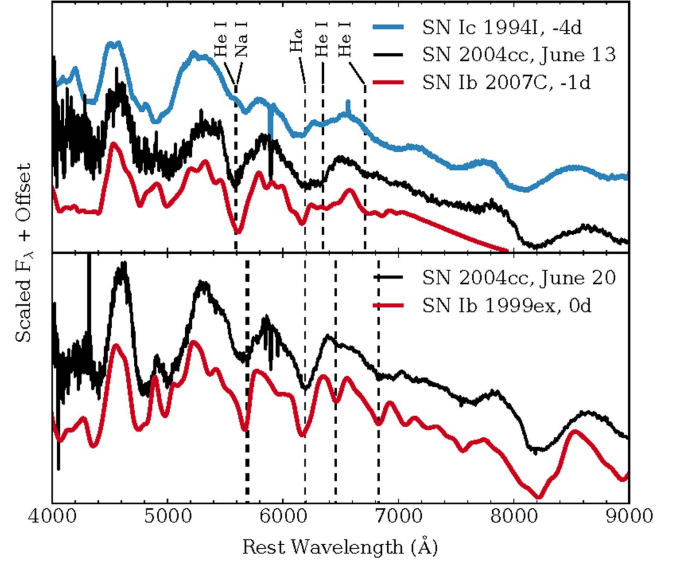

Figure 15. Top: spectrum of SN 2004cc observed on UT 2004 June 13 alongside premaximum spectra of SN Ic 1994I and SN Ib 2007C (Filippenko et al. 1995; Modjaz et al. 2014), and we mark He I lines at a velocity of 15,000 km s^{-1}. Bottom: spectrum of SN 2004cc observed on UT 2004 June 20 and a spectrum of the Type Ib SN 1999ex (Hamuy et al. 2002), with the helium line marked at 10,000 km s^{-1}, a deceleration consistent with the normal evolution of helium-line velocities in SNe Ib (Liu et al. 2016). Both spectra of SN 2004cc have been dereddened by $E(B - V) = 1.0$ mag.
(A color version of this figure is available in the online journal.)

He I λ6678 absorption line without a similarly strong λ7065 line; other ions may be contributing to this feature. Just one week later the He I λ6678 line has disappeared, though the width of the line near 5500 Å implies that He I λ5876 is still present. Given the above uncertainties and the weakness of the He I λ7065 line, we assign SN 2004cc the Ib/Ic label. Interestingly, Wellons et al. (2012) present a variable and long-lasting radio light curve, indicating the presence of a complex circumstellar medium near this object.

4.2.8. SN 2005H (II → II/IIb)

SN 2005H was discovered in NGC 838 (Graham et al. 2005) and classified as a SN II based upon a noisy spectrum (Pastorello et al. 2005b). Very few data exist on SN 2005H, and most of the spectra are entirely dominated by host-galaxy light. However, we were able to obtain the original classification spectrum (Harutyunyan et al. 2008) and we find clear detections of Hα absorption and P-Cygni profiles of Hβ and Na I on an otherwise smooth blue continuum; see Figure 16.

SNID shows this spectrum to be more similar to spectra of young SNe II than SNe IIb. We have very little information on the light-curve evolution of this object—the SN was discovered very near the bright ($R \approx 12 - 14$ mag) core of the host and our data are badly contaminated by galaxy light. Other than the
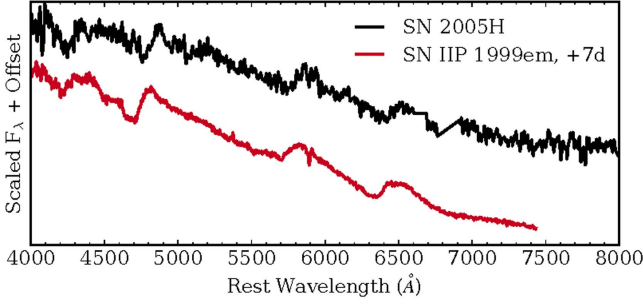
Figure 16. Spectrum of SN 2005H alongside a spectrum of the Type IIP SN 1999em (Leonard et al. 2002a).

(A color version of this figure is available in the online journal.)

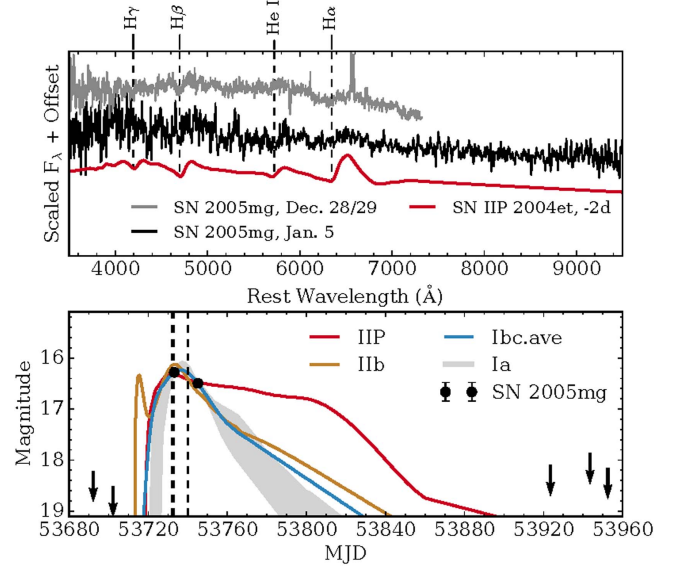discovery image we have no clear detections, only uninformative upper limits.

4.2.9. SN 2005mg (II → II/IIb)

SN 2005mg was discovered in UGC 155 (Newton & Puckett 2005) and classified as a heavily reddened young SN II, with detections of Hα and Hβ in the noisy spectrum (Modjaz et al. 2005). We have a spectrum obtained one week later, but unfortunately we were unable to locate a digital copy of the spectrum cited above. We did, however, locate plots of both the classification spectrum and another one obtained the night prior, both in image form.[26] Using an online tool,[27] we traced the spectra from these plots and consider the results in our analysis.

All three spectra exhibit extremely low S/N and SNID identifies no good matches. The KAIT light curve is similarly uninformative with only two detections and is consistent with template light curves of all types; see Figure 17. However, the spectra do appear to corroborate the Modjaz et al. (2005) classification of SN 2005mg as a SN II, with plausible detections of weak Hα and Hβ lines showing broad P-Cygni profiles. We therefore consider the original classification robust though we cannot determine whether SN 2005mg was a Type IIb or a normal SN II, and so we label it as II/IIb (unsure).

4.2.10. SN 2006eg (Ic → IIb/Ib/Ic/Ic-BL)

SN 2006eg was discovered in an anonymous galaxy (Madison & Li 2006) and classified as a SN Ib/c (Foley et al. 2006). SNID, GELATO, and Superfit identify no good matches, but the best cross-correlations are with spectra of SNe Ic-norm and SNe Ic-BL. The MW reddening toward SN 2006eg is small ($E(B - V) = 0.0933$ mag), and though the spectrum of SN 2006eg is noisy it does not appear that there could be more than a modest degree of host-galaxy

---

[26] https://www.cfa.harvard.edu/supernova/spectra/
[27] http://arohatgi.info/WebPlotDigitizer/app/

Figure 17. Top: spectra of SN 2005mg alongside a spectrum of the Type IIP SN 2004et (Sahu et al. 2006). In blue we show the co-addition of the traces obtained from plots of the two spectra from 2005 December, while in black we show the full spectrum from 2006 January. Bottom: the light curve compared to template light curves from L11, with the dates of spectra shown with dashed lines.

(A color version of this figure is available in the online journal.)

reddening—we detect no narrow Na I D lines at the host galaxy's redshift. Our sparse and noisy light curve is most similar to that of a SN IIL, but it is also consistent with a stripped-envelope classification.

SN 2006eg had a peak measured magnitude of -14.86 ± 0.23 mag (unfiltered; L11), which makes the event an underluminous outlier from both the SN Ic-BL and normal SN Ib/Ic populations (L11, Drout et al. 2011). However, as Figure 18 shows, the true peak could have occurred before discovery and the event may have been significantly more luminous at the true (unobserved) peak.

Our spectrum of SN 2006eg is not only noisy, it also exhibits a low contrast between the continuum and the SN features—this event occurred near the center of its spiral host galaxy, and it appears that our spectrum suffers from significant host-galaxy contamination (the strong, narrow absorption features are likely badly subtracted host-galaxy emission lines). It has been our experience that SNID sometimes mistakenly prefers a SN Ic-BL classification for low-contrast spectra, and so we are hesitant to assign much belief to that result.

The He I lines that mark the difference between SNe Ib and SNe Ic are, in general, time-dependent: they are most apparent soon after peak and generally fade completely away by ~50–70 days (Modjaz et al. 2014; Liu et al. 2016). These types can be difficult to differentiate at these ages, and SNe Ic, Ib, and IIb all show strong features at the same wavelengths as
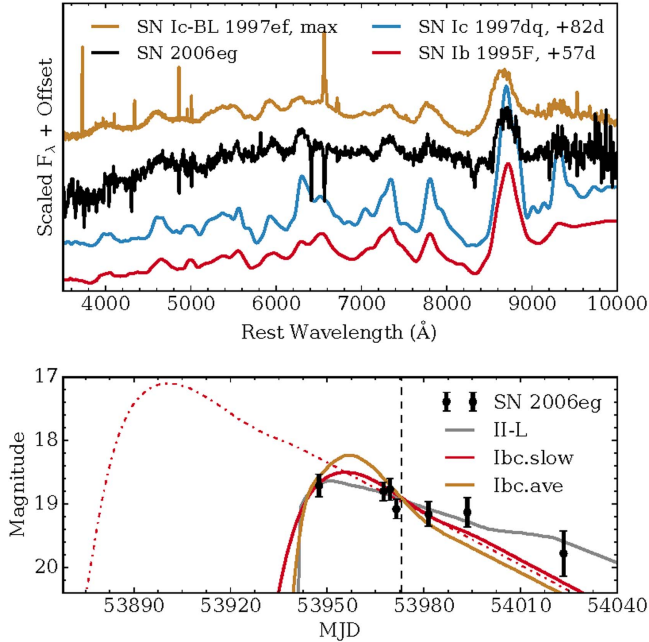
Figure 18. Top: spectrum of SN 2006eg (smoothed with a 20 Å Gaussian kernel) compared to that of the SN Ic-BL 1997ef, SN Ic 1997dq, and SN Ib 1995F (Matheson et al. 2001; Modjaz et al. 2014). Bottom: the light curve, with the date the spectrum was taken marked, alongside template light curves from L11. Our last prediscovery upper limit was 173 days before the first detection; though we show comparison light curves assuming the peak was observed, the true peak could have occurred months before discovery. The red dash-dot line shows the Ibc.slow template of L11 offset by 55 days, illustrating how the peak may have occurred prediscovery.
(A color version of this figure is available in the online journal.)

those in SN 2006eg's spectrum. It is likely that our spectrum of SN 2006eg shows a nearly nebular SN IIb, Ib, or Ic "watered down" by host-galaxy contamination. If SN 2006eg was a mostly normal stripped-envelope SN discovered late, then its light curve was slowly declining, but it was not an extreme outlier from the diverse late-time decline rates observed for these SNe (e.g., Lyman et al. 2016).

Without better data, it is very difficult to firmly label SN 2006eg—our spectrum shows it was not a SN Ia or II, but it could have been a SN IIb, Ib, Ic, or Ic-BL.

4.3. SNe Ia

We follow Silverman et al. (2012) when identifying the subtypes of SNe Ia, and in most cases simply duplicate the classifications from their Table 7. We propose some updated subtype classifications from L11, but no objects appear to be misclassified as SNe Ia, nor does it appear that any events labeled otherwise should be reclassified as SNe Ia.

We update the classifications of SNe 1999bh and 2002es, labeling them with the subtype "Ia-02es" as identified by Ganeshalingam et al. (2012). These events are subluminous and exhibit low expansion velocities, sharing properties with

both the SN Ia-2002cx (i.e., SN Iax; Foley et al. 2013) and SN Ia-1991bg subtypes. Though L11 note that these two events may form their own subtype, they include them with the SNe Iax as the properties of the subtype were only partially understood at the time (subsequent work has furthered our understanding; e.g., Cao et al. 2015; White et al. 2015; Cao et al. 2016). Foley et al. (2013) show that SNe Iax display a wide range of peak luminosities, from the extremely sub-luminous SN 2008 ha ($M_V \approx -14.2$ mag) up into the range of typical SNe Ia ($M_V \approx -18.5$ mag), and the rate calculations of L11 did not account for the low-luminosity members of this class and therefore underestimated the true rate of these events.

We also update several events previously labeled SNe Ia 1991T to the "SN Ia-1999aa" subtype (Garavini et al. 2004), a subclass that falls in between SNe Ia-norm and SNe Ia-1991T and another distinction intentionally not included in L11 (see Li et al. 2001). Three of these events (SNe 1998es, 1999aa, and 1999dq) were previously given a Ia-99aa label by Silverman et al. (2012). The spectral evolution of SN 1999ac was studied in detail by Garavini et al. (2005), who note that early-time spectra are similar to those of SN 1999aa with relatively weak silicon absorption, but SNID identifies both premaximum and postmaximum spectra as SN Ia-norm (Silverman et al. 2012, though Ia-99aa templates also provide reasonable fits) and subtle peculiarities exist throughout this object's evolution. Owing to this peculiarity, we give this event equal weights in the Ia-norm and Ia-99aa subclasses.

SN 2001V is grouped among the "shallow silicon" events by Branch et al. (2009), and the premaximum spectra of SN 2001V published by Blondin et al. (2012) are strongly classified as 99aa-like by SNID. The data on SN 2006cm are somewhat less conclusive and the early evolution is not well constrained. The spectra show strong Na I D absorption features from the host UGC 11723 and they are noticeably reddened by host-galaxy dust (Blondin et al. 2006; Sternberg et al. 2011). SNID prefers a SN Ia-normal classification for SN 2006cm (Silverman et al. 2012), but the spectra also exhibit good matches to those of Ia-99aa objects and the silicon absorption features are weaker than those in the SNID-preferred SN Ia-norm templates. We give SN 2006cm equal weights in the SN Ia-norm and SN Ia-99aa subclasses.

Finally, SN 2004bv is classified as a SN Ia-91T event by SNID, but unfortunately the only existing premaximum spectrum of this SN does not extend to sufficiently blue wavelengths to capture the Ca II H&K lines, which are the strongest indicator of a SN 1991T-like event at young epochs (Silverman et al. 2012, see their Figure 5), and so this classification is somewhat suspect and this event may also have been SN 1999aa-like. These updates indicate that 91T/99aa-like events exhibit a continuum of spectroscopic properties, with normal SNe Ia at one end and SN 1991T-like events at the other extreme; most "shallow silicon" events fall somewhere in between.

17

4.4. SNe Ic-BL

L11 grouped the broad-lined SNe Ic (SN Ic-BL, sometimes associated with gamma-ray bursts; e.g., Woosley & Bloom 2006) into the SN Ic-pec subclass, though they noted in the text that SN 2002ap is a member of that group (e.g., Mazzali et al. 2002). As discussed in Section 4.2, SNe 2002jj and 2006eg may plausibly also be of Type Ic-BL.

4.5. SN 1987A-like SNe

As discussed in Section 4.1.6, SN 2005io was very likely a SN 1987A-like event (for reviews of SN 1987A and related events, see, e.g., Arnett et al. 1989; McCray 1993). The LOSS volume-limited sample also includes the SN 1987A-like SNe 2000cb and 2005ci (Kleiser et al. 2011). All of these objects were grouped with the SNe IIP by L11.

4.6. Ca-rich Transients

There are three examples of the recently identified class of "Ca-rich" SNe in our sample: SNe 2003H, 2003dr, and 2005E (e.g., Filippenko et al. 2003; Perets et al. 2010; Kasliwal et al. 2012; Foley 2015). All three were identified by Perets et al. (2010). Though discussed within the text as Ca-rich events, these three SNe were labeled SN Ibc-pec by L11 and were grouped with the other stripped-envelope SNe in their analysis.

Though the provenance of these events is not fully understood, it now seems likely that they do not arise from the core collapse of massive stars. Removing these three events from the sample of core-collapse SNe slightly reduces the ratio of stripped-envelope SNe relative to SNe II. Figure 19 shows spectra of all three Ca-rich SNe in the sample. We note that the photospheric spectra of these events are extremely similar to those of normal SNe Ib; it is their nebular spectra, their rapid evolution, and their low peak luminosities that primarily differentiate these events.

4.7. Type IIn SNe and SN Impostors

SNe IIn are hydrogen-rich SNe that exhibit narrow lines in their spectrum—indicative of dense circumstellar material surrounding the progenitor at the time of explosion (see, e.g., Filippenko 1989; Schlegel 1990; Chugai 1991; Smith 2014). There were seven SNe IIn in the sample identified by L11, but two of those (SNe 2002bu and 2006bv) were reclassified as SN impostors (luminous but nonterminal outbursts from massive stars) by Smith et al. (2011b). We group SNe 2002bu and 2006bv with the five other SN impostors from the original sample and do not include them when calculating the relative fractions of SNe.

4.8. SNe That Lack Spectra

Every object in the L11 volume-limited sample was originally classified spectroscopically and announced through CBETs, but we have not been able to track down spectra for three events: see Table 2 and Figure 20. One of these
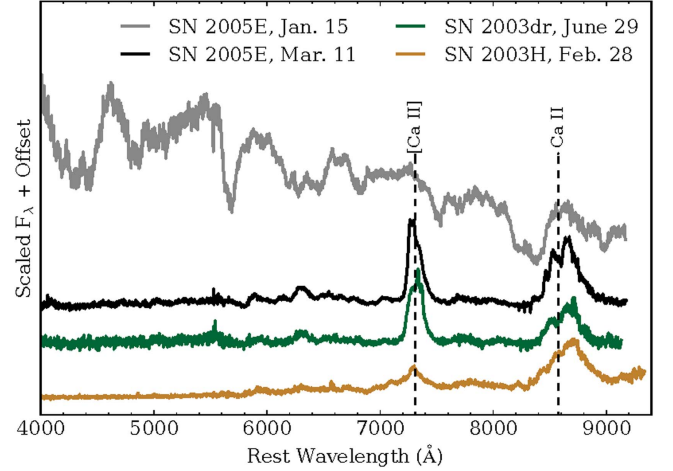
Figure 19. Spectra of the Ca-rich objects in our sample. For SN 2005E we present photospheric and nebular spectra; for the other objects we only have nebular spectra.

(A color version of this figure is available in the online journal.)

Table 2
SNe That Lack Spectra

| Name	Previous (L11)	This Work	References
SN 2002ds	IIP	II	1
SN 2003bw	IIP	II/IIb	2
SN 2006bv	IIn	*impostor*	3, 4

References. [1] Li et al. (2002), [2] Hamuy (2003), [3] Sehgal et al. (2006), [4] Smith et al. (2011b).

(SN 2002ds) exhibits a light curve with a pronounced plateau, which corroborates the original CBET classification of a SN II. The light curve of SN 2003bw, however, does not rule out the possibility that this event was a low-hydrogen SN IIb (assuming that the hydrogen detection announced in the CBET is robust; Hamuy 2003). For SN 2006bv we adopt the SN impostor reclassification of Smith et al. (2011b).

5. Updated Fraction Calculations

Figure 21 and Table 3 summarize our updated fraction calculations. We follow L11 to estimate our uncertainties, running 10^6 Monte Carlo realizations of the sample assuming Poisson statistics and the control-time corrections from L11, Leaman et al. (2011), and Li et al. (2011a). (Note that the stated uncertainties are statistical only.) We do not recalculate the control times for each event after these updated classifications. Almost all of our updates are swaps between stripped-envelope subtypes which show very similar light curves, and so the control-time calculations should change very little. For events with more than one possible classification listed in Table 1 we
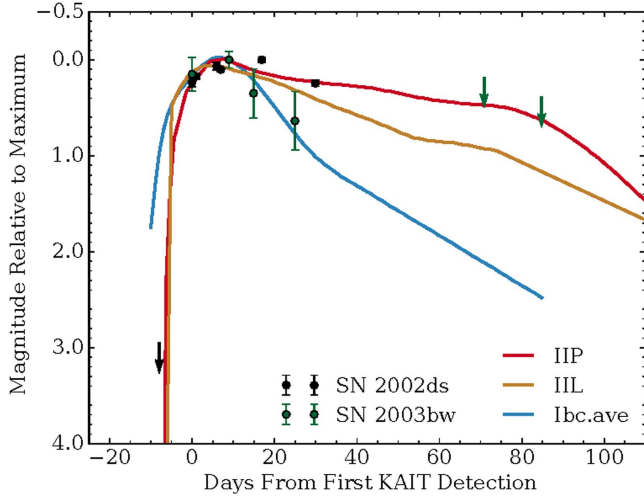
Figure 20. Unfiltered light curves for two SNe for which we have not been able to collect spectra, along with template light curves from L11 for comparison. Upper limits are shown with arrows. For SN 2002ds, the CBET classification of a SN II with a hydrogen-recombination plateau is robustly supported. The light curve of SN 2003bw appears to match the stripped-envelope template from L11 better than the Type II templates, but the data are noisy and are consistent with either classification. SN 2006bv (not shown) was likely a SN impostor; see Smith et al. (2011b).

(A color version of this figure is available in the online journal.)

assign a fractional weight to each given the relative frequencies of the subtypes among the well-classified events.

Many authors, based on both theory and observation, argue for trends in the relative SN rates as a function of metallicity (e.g., Modjaz et al. 2008; Arcavi et al. 2010; Modjaz et al. 2011; Kelly & Kirshner 2012; Yoon 2015). Adopting the metallicity-luminosity relation of Garnett (2002) and noting that the galaxies hosting core-collapse SNe within the LOSS sample cover a range of luminosities of $M_K \approx -22$ to -25 mag, Smith et al. (2011a) estimate metal abundances of $\sim$0.5–2.0 $Z_\odot$ for these galaxies, and our results are therefore applicable to roughly that range. Graur et al. (2016a, 2016b) use the LOSS sample and our updated classifications to examine correlations between SN rates and host galaxy properties in more detail, including the stellar masses, specific star formation rates, and oxygen abundances (i.e., metallicities) of the host galaxies. Several authors have shown that local measures of host-galaxy metallicities are more informative than global ones (e.g., Modjaz et al. 2008; Anderson et al. 2010; Modjaz et al. 2011; Anderson et al. 2016); a study of the explosion-site metallicities of the LOSS sample is a worthy endeavor we leave to future work.

As with L11, our calculations for several of the rarer subtypes suffer from the effects of small-number statistics, but Table 3 and Figure 21 indicate an important update: the percentage of SNe Ic is reduced while the percentage of SNe Ib is increased. Adopting our updated classifications, 83% of our Monte Carlo trials indicate that normal SNe Ib are more

common than normal SNe Ic, while 99% of the trials using the L11 classifications indicate the opposite.

L11 and Smith et al. (2011a) found that SNe Ic are more than twice as common as SNe Ib (grouping the SNe Ic-BL with the SNe Ic, which only affects these rates by a small amount). L11 calculate a ratio of SNe Ic/SNe Ib = $54.2 \pm 9.8\%/21.2^{+8.4}_{-7.7}\% = 2.6 \pm 1.1$, while Smith et al. (2011a, excluding SNe from highly inclined galaxies) calculated SNe Ic/Ib = $14.9^{+4.2}_{-3.8}\%/7.1^{+3.1}_{-2.6}\% = 2.1 \pm 1.1$ (in all cases the errors listed are statistical only, and were derived from Monte Carlo simulations similar to those described above).

We now calculate a ratio of normal SNe Ic to normal SNe Ib of 0.6 ± 0.3 and, if we include the SNe Ic-BL and other peculiar subtypes with the normal SNe Ib and Ic, we find a (SN Ic+Ic-BL+Ic-pec)/SN Ib ratio of 0.8 ± 0.4.

This update to the population fractions is driven by our reclassifications of seven stripped-envelope events. First, we relabeled four events from a Ic subtype to a Ib or IIb subtype (SNe 2001M, 2001ci, 2004C, and 2005lr). In each of these cases, the need for reclassification is easily understood: three of these events had spectra severely reddened by host-galaxy dust and were originally classified by eye without the aid of SNID, and one showed only weak He I lines in the spectrum (SN 2001M). Second, we created the SN Ib/Ic (unsure) category, which includes an additional two events that show weak He I lines with some uncertainty on their identification (SNe 2002jz and 2004cc) and one event with only sparse and noisy observations (SN 2006eg). If we assume that all of the SNe in the latter category deserve the Ic label, our Monte Carlo trials indicate that normal SNe Ib and SNe Ic (excluding peculiar subtypes) occur at similar rates: SNe Ic/Ib = 0.9 ± 0.5. If we rather assume that they are all SNe Ib, we get a ratio of normal SNe Ic/Ib = 0.5 ± 0.3.

These results have implications for our understanding of the progenitors of stripped-envelope SNe, as we discuss below, and may affect other works that use the LOSS rates as input (e.g., Foley & Mandel 2013).

6. Progenitor Constraints on Stripped-envelope SNe

Wolf–Rayet (WR) stars have long been discussed as Galactic analogues of SN Ib/c progenitors (e.g., Meynet & Maeder 2003; Crowther 2007), though many authors have argued that binary stars which undergo mass loss via Roche-lobe overflow before core collapse are likely the most common SN Ib/c progenitor (e.g., Podsiadlowski et al. 1992; Smartt 2009; Smith et al. 2011a; Eldridge et al. 2013). Regardless, stellar modeling efforts have found it difficult to match the SN Ic/Ib fractions presented by L11 and Smith et al. (2011a), which demand more SN Ic progenitors (stars that lose both their hydrogen envelope and a large fraction of their helium envelopes) than Ib progenitors (stars that lose just the hydrogen; e.g., Georgy et al. 2009; Yoon et al. 2010; Yoon 2015), though some

Previous   This Work
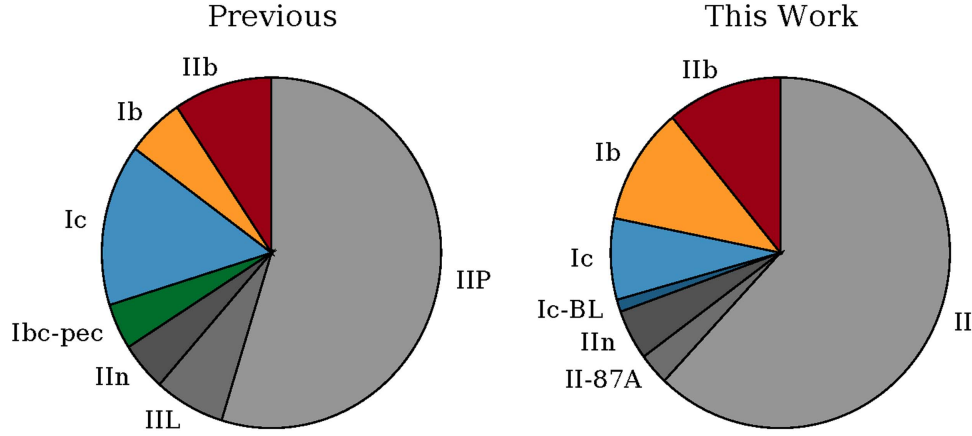
Figure 21. Relative fractions of core-collapse SN types within a volume-limited sample using the original classifications from L11 (left) compared to the updated classifications presented here (right). Subtypes are color-coded along with the other members of their major type, and the "peculiar" subtype labels are grouped with the appropriate "normal" events (except for the SN Ibc-pec group of L11, which included both SNe Ic-BL and Ca-Rich transients). All fractions are listed in Table 3 and any objects listed in Table 1 with more than one possible classification are given a fractional weight in each class, as described in Section 5.
(A color version of this figure is available in the online journal.)

Table 3
Updated Relative SN Fractions in a Volume-limited Survey

Type	Previous	This Work	Difference
	Core Collapse		
II	$68.9^{+6.0}_{-6.0}$	$69.6^{+6.7}_{-6.7}$	...
IIb/Ib/Ic	$31.1^{+4.6}_{-4.6}$	$30.4^{+5.0}_{-4.9}$	...
	Stripped Envelope		
IIb	$27.6^{+9.1}_{-9.1}$	$34.0^{+11.1}_{-11.1}$	+6.3
IIb-pec	...	$2.0^{+1.5}_{-2.0}$	...
Ib	$16.1^{+6.8}_{-6.6}$	$35.6^{+11.4}_{-11.4}$	+19.5
Ib-pec	...	...	...
Ibc-pec[a]	$12.4^{+5.9}_{-5.6}$	...	...
Ic	$41.1^{+11.5}_{-11.4}$	$21.5^{+8.6}_{-8.6}$	−19.6
Ic-pec	$2.8^{+2.6}_{-2.8}$	$3.2^{+3.1}_{-3.2}$	...
Ic-BL	...	$3.7^{+2.9}_{-3.7}$	...
	Hydrogen Rich		
II[b]	$93.2^{+11.5}_{-11.3}$	$89.1^{+10.9}_{-10.9}$	...
II-87A	...	$4.2^{+2.4}_{-2.7}$	...
IIn	$6.8^{+3.0}_{-2.9}$	$6.7^{+3.0}_{-2.9}$	...

Notes. Relative fractions of core-collapse SNe in the LOSS volume-limited sample, within several different subsets, expressed in percentages. In the left column we present the fractions assuming the original classifications used by L11, in the center column we present our updated fractions, and in the right column we highlight the most notable updates.
[a] L11 included SNe Ic-BL and Ca-Rich transients with the Ibc-pec class. In our updated fractions we list the SNe Ic-BL seperately, and we do not group the Ca-Rich events with core-collapse SNe.
[b] Including the II-L and II-P subclasses of L11.

success has been achieved by invoking rapid rotation of the progenitors (e.g., Cao et al. 2013; Groh et al. 2013b).

To address this putative issue, some authors have proposed that some amount of helium in SNe Ic may be "hidden" and remain neutral if the ^{56}Ni (which provides nonthermal excitations via radioactive decay) is insufficiently mixed with the helium-rich ejecta (e.g., Dessart et al. 2011, 2012). Comparisons to observation do not find evidence for large amounts of hidden helium in SNe Ic, however, and it is unclear from the models how much helium could truly be hidden in this way (e.g., Hachinger et al. 2012; Taddia et al. 2015; Liu et al. 2016). Our updated stripped-envelope fractions argue that this problem is less egregious than previously indicated.

Other discrepancies have arisen within the single WR-like progenitor scenario. The observed ejecta masses of normal SNe Ib/c ($M_{ej} \approx 2.0$–$4\,M_\odot$; Drout et al. 2011; Cano 2013; Lyman et al. 2016) are not in good agreement with the estimated masses of WR stars at the time of core collapse ($M \gtrsim 10\,M_\odot$; Meynet & Maeder 2003; Yoon 2015), assuming that most SNe Ib/c produce neutron star remnants rather than black hole remnants. Note that SNe Ic-BL may have larger ejecta masses, and so this reasoning holds for normal SNe Ib/c only (Cano 2013). In addition, the rates of SNe Ib/c compared to those of SNe II are inconsistent with WR star progenitors (the incidence rate of WR stars is too low to explain the high fraction of SNe Ib/c; e.g., Smith et al. 2011a), and the search for SN Ib/c progenitors in pre-explosion images has, in several instances, ruled out normal WR stars (Eldridge et al. 2013, though see also Groh et al. 2013b).

The binary progenitor system scenario for normal SNe Ib/Ic does not suffer from the same problems. The modeled masses at the time of core collapse for post-mass-transfer binary members are generally in agreement with the observed SN Ib/c ejecta masses (Eldridge et al. 2013; Yoon 2015), constraints from SN Ib/c progenitor searches are largely compatible with binary progenitors (Eldridge et al. 2013), and the identified progenitors of some SNe IIb have been shown to be the products of binary evolution (SNe 1993J and 2011dh; e.g., Maund et al. 2004, 2011; Van Dyk et al. 2011; Bersten et al. 2012).

Sana et al. (2012) show that more than 70% of O-type stars (zero-age main sequence $M \gtrsim 15\,M_\odot$) are formed in binary pairs that will undergo significant binary interaction (either mass gain or mass stripping) before core collapse, and so the population of core-collapse SN progenitors must necessarily be dominated by post-binary-interaction stars. We calculate a stripped-envelope fraction of $30 \pm 5\%$ among all core-collapse SNe, similar to fractions found by previous authors. As Smith et al. (2011a) note, this value is in remarkably good agreement with the ~33% of O-type stars in our Galaxy found to experience envelope stripping via binary interaction before their deaths (Sana et al. 2012).

7. Conclusion

We have re-examined every SN classification within the LOSS volume-limited sample published by L11, have discussed the peculiar and rare events within the sample, and have found that several of the stripped-envelope SNe originally labeled as SNe Ic show clear signatures of helium and (in two cases) hydrogen. After relabeling these SNe as Type Ib or IIb appropriately, and discussing the intrinsically peculiar events and those for which we cannot assign a clear classification, we recalculate the implied fractions of these subtypes. We find that the relative fractions of SNe Ia, SNe II, and stripped-envelope SNe are unchanged, but the relative fractions between different stripped-envelope SN subtypes are.

Based on the prior spectral identifications, L11 and Smith et al. (2011a) found that SNe Ic are roughly twice as common as SNe Ib. We show that this measurement was hampered by the above misclassifications and, additionally, that the SN Ib/SN Ic ratio is strongly dependent on exactly where one draws the line between these subclasses. We find that SNe Ib are at least as common as SNe Ic in the local universe and in fact are likely to be more common. We present a best-estimate normal SN Ic/SN Ib ratio of 0.6 ± 0.3—i.e., spectroscopically normal SNe Ib occur in the local universe 1.7 ± 0.9 times more often than do normal SNe Ic.

Other efforts (e.g., Smartt et al. 2009; Eldridge et al. 2013) found SN Ic/SN Ib ratios similar to those of L11, and we believe they may also have been plagued by systematically mislabeled stripped-envelope events. The updated stripped-envelope SN fractions published here should prove important for constraining the elusive progenitors of the various subtypes of stripped-envelope SNe, and we hope the public release of these data will be useful when exploring this valuable sample going forward.

Table 4
Log of Spectra Published Herein

SN Name	UT Date	File Name[a]	Instrument[b]	WL Range (Å)	Resolution[c] (Å)	Source[b]
SN 1999an	1999 Mar 10	sn1999an-19991003.flm	OMR	3610–8580	10	NAOC
SN 1999br	1999 Apr 24.0	sn1999br-19990424-opt.flm	Kast	4300–7000	6/5	UCB
SN 1999bu	1999 Apr 18.21	sn1999bu-19990418.flm	FAST	3720–7540	7	CfA
SN 1999cd	1999 May 15.32	sn1999cd-19990515.flm	FAST	3720–7540	7	CfA
SN 1999cd	1999 May 16.27	sn1999cd-19990516.flm	FAST	3720–7540	7	CfA
SN 1999el	1999 Nov 05.0	sn1999el-19991105-ui.flm	Kast	3380–10,460	6/11	UCB
SN 1999gi	1999 Dec 10.0	sn1999gi-19991210.flm	Kast	3720–7540	6/5	UCB
SN 1999gi	1999 Dec 12.0	sn1999gi-19991212.flm	Kast	3720–7540	6/5	UCB
SN 1999gi	1999 Dec 13.0	sn1999gi-19991213.flm	Kast	3720–7540	6/5	UCB
SN 1999gi	2000 Jan 05.0	sn1999gi-20000105.flm	Kast	3720–7540	6/5	UCB

Notes.
[a] Different groups utilize different naming conventions for their data; we preserve these differences and the original names of these files.
[b] See Section 2 for a description of the instruments and observational efforts listed here.
[c] Listed resolutions are estimates of the average resolution for the instrument (if two resolutions are given, they refer to the blue side and red side of the spectrograph separately).
[d] Traced from image of plot; see Section 4.2.9.
(This table is available in its entirety as supporting data in the online version of this article.)

Table 5
Log of Light Curves Published Herein

SN Name	Telescope	Filters	N Detections	Date Range
SN 2000N	KAIT	clear	9	2000 Mar 04–2000 Jun 03
SN 2001J	KAIT	clear	2	2001 Jan 15–2001 Jan 16
SN 2001M	KAIT	clear	4	2001 Jan 21–2001 Feb 03
SN 2001ci	KAIT	clear	8	2001 Apr 25–2001 May 12
SN 2002ds	KAIT	clear	6	2002 Jun 25–2002 Jul 25
SN 2002jj	KAIT	clear	6	2002 Oct 24–2003 Jan 17
SN 2002jz	KAIT	clear	6	2002 Dec 24–2003 Jan 31
SN 2003bk	KAIT	clear	6	2003 Feb 28–2003 May 31
SN 2003br	KAIT	clear	8	2003 Mar 07–2003 Jun 03
SN 2003bw	KAIT	clear	4	2003 Mar 03–2003 Mar 28

(This table is available in its entirety as supporting data in the online version of this article.)

Appendix
Journal of Data Presented Here

Table 4 lists every spectrum published here for the first time: a total of 151 spectra of 71 SNe. Table 5 lists all light curves rereduced from images and published here, including data for 20 SNe. See Section 2 for a description of the observing and data-acquisition efforts. All data will be made public via the Berkeley SNDB (http://heracles.astro.berkeley.edu/sndb), WiseREP (http://wiserep.weizmann.ac.il), and the Open Supernova Catalog (https://sne.space/).

References

Aazami, A. B., & Li, W. D. 2001, IAUC, 7568
Allington-Smith, J., Breare, M., Ellis, R., et al. 1994, PASP, 106, 983
Andersen, J., Andersen, M. I., Klougart, J., et al. 1995, Msngr, 79, 12
Anderson, J. P., Covarrubias, R. A., James, P. A., Hamuy, M., & Habergham, S. M. 2010, MNRAS, 407, 2660
Anderson, J. P., González-Gaitán, S., Hamuy, M., et al. 2014, ApJ, 786, 67
Anderson, J. P., Gutiérrez, C. P., Dessart, L., et al. 2016, A&A, 589, A110
Arcavi, I., Gal-Yam, A., Cenko, S. B., et al. 2012, ApJL, 756, L30
Arcavi, I., Gal-Yam, A., Kasliwal, M. M., et al. 2010, ApJ, 721, 777
Armstrong, M., Singer, D., Burket, J., & Li, W. 2004, IAUC, 8335, 1
Arnett, W. D., Bahcall, J. N., Kirshner, R. P., & Woosley, S. E. 1989, ARA&A, 27, 629
Baek, M., & Li, W. 2005, IAUC, 8641
Barbon, R., Ciatti, F., & Rosino, L. 1979, A&A, 72, 287
Beckmann, S., & Li, W. D. 2001, IAUC, 7564, 2
Benetti, S., Cappellaro, E., Mazzali, P. A., et al. 2005, ApJ, 623, 1011
Benetti, S., Elias-Rosa, N., Blanc, G., et al. 2004, IAUC, 8312
Berlind, P., Matheson, T., & Calkins, M. 2003, IAUC, 8091, 2
Bersten, M. C., Benvenuto, O. G., Nomoto, K., et al. 2012, ApJ, 757, 31
Bianco, F. B., Modjaz, M., Hicken, M., et al. 2014, ApJS, 213, 19
Bilinski, C., Smith, N., Li, W., et al. 2015, MNRAS, 450, 246
Blanco, V. M., Gregory, B., Hamuy, M., et al. 1987, ApJ, 320, 589
Blondin, S., Matheson, T., Kirshner, R. P., et al. 2012, AJ, 143, 126
Blondin, S., Modjaz, M., Kirshner, R., Challis, P., & Calkins, M. 2006, CBET, 526

145

Blondin, S., & Tonry, J. L. 2007, ApJ, 666, 1024
Branch, D., Dang, L. C., & Baron, E. 2009, PASP, 121, 238
Branch, D., Jeffery, D. J., Young, T. R., & Baron, E. 2006, PASP, 118, 791
Buzzoni, B., Delabre, B., Dekker, H., et al. 1984, Msngr, 38, 9
Cano, Z. 2013, MNRAS, 434, 1098
Cao, Y., Kasliwal, M. M., Arcavi, I., et al. 2013, ApJL, 775, L7
Cao, Y., Kulkarni, S. R., Gal-Yam, A., et al. 2016, ApJ, 832, 86
Cao, Y., Kulkarni, S. R., Howell, D. A., et al. 2015, Natur, 521, 328
Chornock, R., Filippenko, A. V., Branch, D., et al. 2006, PASP, 118, 722
Chornock, R., Filippenko, A. V., Li, W., et al. 2011, ApJ, 739, 41
Chugai, N. N. 1991, MNRAS, 250, 513
Clocchiatti, A., Wheeler, J. C., Brotherton, M. S., et al. 1996, ApJ, 462, 462
Crowther, P. A. 2007, ARA&A, 45, 177
Dekker, H., Delabre, B., & Dodorico, S. 1986, Proc. SPIE, 627, 339
Dessart, L., Hillier, D. J., Li, C., & Woosley, S. 2012, MNRAS, 424, 2139
Dessart, L., Hillier, D. J., Livne, E., et al. 2011, MNRAS, 414, 2985
Drout, M. R., Soderberg, A. M., Gal-Yam, A., et al. 2011, ApJ, 741, 97
Dudley, C. C., & Fischer, J. 2004, CBET, 57, 1
Eldridge, J. J., Fraser, M., Smartt, S. J., Maund, J. R., & Crockett, R. M. 2013, MNRAS, 436, 774
Elias-Rosa, N., Benetti, S., Cappellaro, E., et al. 2006, MNRAS, 369, 1880
Elmhamdi, A., Danziger, I. J., Branch, D., et al. 2006, A&A, 450, 305
Fabricant, D., Cheimets, P., Caldwell, N., & Geary, J. 1998, PASP, 110, 79
Faran, T., Poznanski, D., Filippenko, A. V., et al. 2014a, MNRAS, 445, 554
Faran, T., Poznanski, D., Filippenko, A. V., et al. 2014b, MNRAS, 442, 844
Filippenko, A. V. 1982, PASP, 94, 715
Filippenko, A. V. 1988, AJ, 96, 1941
Filippenko, A. V. 1989, AJ, 97, 726
Filippenko, A. V. 1997, ARA&A, 35, 309
Filippenko, A. V. 2003, in From Twilight to Highlight: The Physics of Supernovae, ed. W. Hillebrandt & B. Leibundgut, 171
Filippenko, A. V. 2005, in ASP Conf. Ser. 332, The Fate of the Most Massive Stars, ed. R. Humphreys & K. Stanek (San Francisco, CA: ASP), 34
Filippenko, A. V. 1991, in European Southern Observatory Conf. and Workshop Proc. 37, ed. I. J. Danziger & K. Kjaer, 343
Filippenko, A. V., Barth, A. J., Matheson, T., et al. 1995, ApJL, 450, L11
Filippenko, A. V., & Chornock, R. 2001, IAUC, 7638, 1
Filippenko, A. V., Chornock, R., & Modjaz, M. 2001a, IAUC, 7579, 2
Filippenko, A. V., Chornock, R., Swift, B., et al. 2003, IAUC, 8159
Filippenko, A. V., Desroches, L., Ganeshalingam, M., Chornock, R., & Serduke, F. J. D. 2004, IAUC, 8331
Filippenko, A. V., & Foley, R. J. 2005, CBET, 274, 1
Filippenko, A. V., Li, W. D., Treffers, R. R., & Modjaz, M. 2001b, in ASP Conf. Ser. 246, IAU Coll. 183: Small Telescope Astronomy on Global Scales, ed. B. Paczynski, W.-P. Chen, & C. Lemme (San Francisco, CA: ASP), 121
Filippenko, A. V., Matheson, T., & Ho, L. C. 1993, ApJL, 415, L103
Filippenko, A. V., Porter, A. C., & Sargent, W. L. W. 1990a, AJ, 100, 1575
Filippenko, A. V., & Shields, J. C. 1990, IAUC, 5111
Filippenko, A. V., Shields, J. C., & Richmond, M. W. 1990b, IAUC, 5069
Folatelli, G., Contreras, C., Phillips, M. M., et al. 2006, ApJ, 641, 1039
Folatelli, G., Morrell, N., Phillips, M. M., et al. 2013, ApJ, 773, 53
Foley, R. J. 2015, MNRAS, 452, 2463
Foley, R. J., Challis, P. J., Chornock, R., et al. 2013, ApJ, 767, 57
Foley, R. J., Chornock, R., Filippenko, A. V., et al. 2009, AJ, 138, 376
Foley, R. J., & Filippenko, A. V. 2002, IAUC, 8031, 4
Foley, R. J., & Mandel, K. 2013, ApJ, 778, 167
Foley, R. J., Papenkova, M. S., Swift, B. J., et al. 2003, PASP, 115, 1220
Foley, R. J., Silverman, J. M., Moore, M., & Filippenko, A. V. 2006, CBET, 604, 1
Foley, R. J., Wong, D. S., Ganeshalingam, M., Filippenko, A. V., & Chornock, R. 2004a, IAUC, 8339, 2
Foley, R. J., Wong, D. S., Moore, M., & Filippenko, A. V. 2004b, IAUC, 8353, 3
Ganeshalingam, M., Li, W., Filippenko, A. V., et al. 2010, ApJS, 190, 418
Ganeshalingam, M., Li, W., Filippenko, A. V., et al. 2012, ApJ, 751, 142
Garavini, G., Aldering, G., Amadon, A., et al. 2005, AJ, 130, 2278
Garavini, G., Folatelli, G., Goobar, A., et al. 2004, AJ, 128, 387
Garnett, D. R. 2002, ApJ, 581, 1019

Georgy, C., Meynet, G., Walder, R., Folini, D., & Maeder, A. 2009, A&A, 502, 611
Graham, J., Li, W., (Loss/Kait), Trondal, O., & Schwartz, M. 2005, IAUC, 8467, 1
Graur, O., Bianco, F. B., Huang, S., et al. 2016a, arXiv:1609.02921
Graur, O., Bianco, F. B., & Modjaz, M. 2015, MNRAS, 450, 905
Graur, O., Bianco, F. B., Modjaz, M., et al. 2016b, arXiv:1609.02923
Graur, O., & Maoz, D. 2013, MNRAS, 430, 1746
Groh, J. H., Georgy, C., & Ekström, S. 2013a, A&A, 558, L1
Groh, J. H., Meynet, G., Georgy, C., & Ekström, S. 2013b, A&A, 558, A131
Guillochon, J., Parrent, J., & Margutti, R. 2016, arXiv
Hachinger, S., Mazzali, P. A., Taubenberger, S., et al. 2012, MNRAS, 422, 70
Hamuy, M. 2003, IAUC, 8103, 2
Hamuy, M., Folatelli, G., Morrell, N. I., et al. 2006, PASP, 118, 2
Hamuy, M., Maza, J., & Morrell, N. 2005, CBET, 321, 1
Hamuy, M., Maza, J., Pinto, P. A., et al. 2002, AJ, 124, 417
Hamuy, M., & Roth, M. 2003, IAUC, 8228, 2
Hamuy, M., & Suntzeff, N. B. 1990, AJ, 99, 1146
Harutyunyan, A. H., Pfahler, P., Pastorello, A., et al. 2008, A&A, 488, 383
Howell, D. A., Sullivan, M., Perrett, K., et al. 2005, ApJ, 634, 1190
Hutchings, D., & Li, W. 2002, IAUC, 8026, 1
Jha, S., Challis, P., Kirshner, R., et al. 2000, IAUC, 7377, 2
Jha, S., Matheson, T., Challis, P., Kirshner, R., & Calkins, M. 2001, IAUC, 7566, 2
Kasliwal, M. M., Kulkarni, S. R., Gal-Yam, A., et al. 2012, ApJ, 755, 161
Kelly, P. L., & Kirshner, R. P. 2012, ApJ, 759, 107
Kleiser, I. K. W., Poznanski, D., Kasen, D., et al. 2011, MNRAS, 415, 372
Leaman, J., Li, W., Chornock, R., & Filippenko, A. V. 2011, MNRAS, 412, 1419
Lee, E., Li, W., Boles, T., et al. 2005, IAUC, 8628, 1
Leonard, D. C., Filippenko, A. V., Gates, E. L., et al. 2002a, PASP, 114, 35
Leonard, D. C., Filippenko, A. V., Li, W., et al. 2002b, AJ, 124, 2490
Leonard, D. C., Li, W., Filippenko, A. V., Foley, R. J., & Chornock, R. 2005, ApJ, 632, 450
Li, W., Chornock, R., Leaman, J., et al. 2011a, MNRAS, 412, 1473
Li, W., Filippenko, A. V., Treffers, R. R., et al. 2001, ApJ, 546, 734
Li, W., Leaman, J., Chornock, R., et al. 2011b, MNRAS, 412, 1441
Li, W., Qui, Y., Qiao, Q., Hu, J., & Li, Q. 1999, ScChA, 42, 1075
Li, W. D., Chornock, R., Filippenko, A. V., & Phillips, M. M. 2002, IAUC, 7929, 3
Li, W. D., Filippenko, A. V., Treffers, R. R., et al. 2000, in AIP Conf. Ser. 522, ed. S. S. Holt & W. W. Zhang, 103
Liu, Y., & Modjaz, M. 2014, arXiv:1405.1437
Liu, Y.-Q., Modjaz, M., Bianco, F. B., & Graur, O. 2016, ApJ, 827, 90
Lyman, J. D., Bersier, D., James, P. A., et al. 2016, MNRAS, 457, 328
Madison, D. R., & Li, W. 2006, CBET, 600, 1
Maoz, D., Mannucci, F., Li, W., et al. 2011, MNRAS, 412, 1508
Matheson, T., Challis, P., Kirshner, R., & Berlind, P. 2004a, IAUC, 8311
Matheson, T., Challis, P., Kirshner, R., & Berlind, P. 2004b, CBET, 57, 2
Matheson, T., Challis, P., Kirshner, R., & Berlind, P. 2004c, IAUC, 8303, 1
Matheson, T., Challis, P., Kirshner, R., & Penev, K. 2004d, IAUC, 8353, 2
Matheson, T., Filippenko, A. V., Barth, A. J., et al. 2000, AJ, 120, 1487
Matheson, T., Filippenko, A. V., Li, W., Leonard, D. C., & Shields, J. C. 2001, AJ, 121, 1648
Matheson, T., Kirshner, R. P., Challis, P., et al. 2008, AJ, 135, 1598
Maund, J. R., Fraser, M., Ergon, M., et al. 2011, ApJL, 739, L37
Maund, J. R., Smartt, S. J., Kudritzki, R.-P., et al. 2006, MNRAS, 369, 390
Maund, J. R., Smartt, S. J., Kudritzki, R. P., Podsiadlowski, P., & Gilmore, G. F. 2004, Natur, 427, 129
Mazzali, P. A., Deng, J., Maeda, K., et al. 2002, ApJL, 572, L61
McCray, R. 1993, ARA&A, 31, 175
Meynet, G., & Maeder, A. 2003, A&A, 404, 975
Milisavljevic, D., Margutti, R., Soderberg, A. M., et al. 2013, ApJ, 767, 71
Miller, J., & Stone, R. 1993, Lick Observatory Tech. Rep. 66
Modjaz, M., Blondin, S., Kirshner, R. P., et al. 2014, AJ, 147, 99
Modjaz, M., Kewley, L., Bloom, J. S., et al. 2011, ApJL, 731, L4
Modjaz, M., Kewley, L., Kirshner, R. P., et al. 2008, AJ, 135, 1136
Modjaz, M., Kirshner, R., Challis, P., Blondin, S., & Berlind, P. 2005, CBET, 342, 1
Modjaz, M., Li, W., Butler, N., et al. 2009, ApJ, 702, 226

146

Modjaz, M., Li, W., Filippenko, A. V., et al. 2001, PASP, 113, 308
Modjaz, M., Liu, Y. Q., Bianco, F. B., & Graur, O. 2015, arXiv:1509.07124
Monard, L. A. G., & Li, W. 2004, IAUC, 8350, 2
Newton, J., & Puckett, T. 2005, CBET, 336
Oke, J. B., Cohen, J. G., Carr, M., et al. 1995, PASP, 107, 375
Parrent, J., Branch, D., Troxel, M. A., et al. 2007, PASP, 119, 135
Parrent, J. T., Milisavljevic, D., Soderberg, A. M., & Parthasarathy, M. 2016,
    ApJ, 820, 75
Pastorello, A., Baron, E., Branch, D., et al. 2005a, MNRAS, 360, 950
Pastorello, A., Kasliwal, M. M., Crockett, R. M., et al. 2008, MNRAS,
    389, 955
Pastorello, A., Pumo, M. L., Navasardyan, H., et al. 2012, A&A, 537,
    A141
Pastorello, A., Taubenberger, S., Patat, F., et al. 2005b, IAUC, 8467, 2
Pastorello, A., Zampieri, L., Turatto, M., et al. 2004, MNRAS, 347, 74
Perets, H. B., Gal-Yam, A., Mazzali, P. A., et al. 2010, Natur, 465, 322
Phillips, M. M., Li, W., Frieman, J. A., et al. 2007, PASP, 119, 360
Podsiadlowski, P., Joss, P. C., & Hsu, J. J. L. 1992, ApJ, 391, 246
Poznanski, D., Butler, N., Filippenko, A. V., et al. 2009, ApJ, 694, 1067
Poznanski, D., Prochaska, J. X., & Bloom, J. S. 2012, MNRAS, 426, 1465
Prentice, S. J., Mazzali, P. A., Pian, E., et al. 2016, MNRAS, 458, 2973
Puckett, T., Tigner, D., & Sehgal, A. 2002, IAUC, 8037, 1
Qui, Y., Li, W., Zhao, Z., et al. 1999, ScChA, 42, 220
Roy, R., Kumar, B., Maund, J. R., et al. 2013, MNRAS, 434, 2032
Rubin, A., & Gal-Yam, A. 2016, ApJ, 828, 111
Rubin, A., Gal-Yam, A., De Cia, A., et al. 2016, ApJ, 820, 33
Sahu, D. K., Anupama, G. C., Srividya, S., & Muneer, S. 2006, MNRAS,
    372, 1315
Sana, H., de Mink, S. E., de Koter, A., et al. 2012, Sci, 337, 444
Sanders, N. E., Soderberg, A. M., Gezari, S., et al. 2015, ApJ, 799, 208
Sato, Y., Li, W. D., & Puckett, T. 2000, IAUC, 7374, 1
Sehgal, A., Gagliano, R., & Puckett, T. 2006, CBET, 493, 1
Schlafly, E. F., & Finkbeiner, D. P. 2011, ApJ, 737, 103
Schlegel, E. M. 1990, MNRAS, 244, 269
Schmidt, G. D., Weymann, R. J., & Foltz, C. B. 1989, PASP, 101, 713
Sheinis, A. I., Bolte, M., Epps, H. W., et al. 2002, PASP, 114, 851
Silverman, J. M., Foley, R. J., Filippenko, A. V., et al. 2012, MNRAS,
    425, 1789

Singer, D., Pugh, H., & Li, W. 2004, IAUC, 8297, 2
Smartt, S. J. 2009, ARA&A, 47, 63
Smartt, S. J., Eldridge, J. J., Crockett, R. M., & Maund, J. R. 2009, MNRAS,
    395, 1409
Smith, N. 2014, ARA&A, 52, 487
Smith, N., Li, W., Filippenko, A. V., & Chornock, R. 2011a, MNRAS,
    412, 1522
Smith, N., Li, W., Silverman, J. M., Ganeshalingam, M., & Filippenko, A. V.
    2011b, MNRAS, 415, 773
Sternberg, A., Gal-Yam, A., Simon, J. D., et al. 2011, Sci, 333, 856
Suntzeff, N., Colianni, J., Gokas, T., et al. 2001, IAUC, 7576, 5
Swift, B., & Li, W. 2003, IAUC, 8090, 1
Swift, B., Li, W. D., & Filippenko, A. V. 2001, IAUC, 7618, 1
Taddia, F., Fremling, C., Sollerman, J., et al. 2016a, A&A, 592, A89
Taddia, F., Sollerman, J., Fremling, C., et al. 2016b, A&A, 588, A5
Taddia, F., Sollerman, J., Leloudas, G., et al. 2015, A&A, 574, A60
Taddia, F., Stritzinger, M. D., Sollerman, J., et al. 2012, A&A, 537, A140
Tomasella, L., Benetti, S., Cappellaro, E., et al. 2014, AN, 335, 841
Tominaga, N., Tanaka, M., Nomoto, K., et al. 2005, ApJL, 633, L97
Tonry, J., & Davis, M. 1979, AJ, 84, 1511
Valenti, S., et al. 2016, MNRAS
Valenti, S., Fraser, M., Benetti, S., et al. 2011, MNRAS, 416, 3138
Van Dyk, S. D., Li, W., Cenko, S. B., et al. 2011, ApJL, 741, L28
Van Dyk, S. D., Li, W., Filippenko, A. V., et al. 2006, arXiv:astro-ph/0603025
Van Dyk, S. D., Peng, C. Y., King, J. Y., et al. 2000, PASP, 112, 1532
Wagner, R. M., Vrba, F. J., Henden, A. A., et al. 2004, PASP, 116, 326
Wang, X., Filippenko, A. V., Ganeshalingam, M., et al. 2009a, ApJL,
    699, L139
Wang, X., Li, W., Filippenko, A. V., et al. 2009b, ApJ, 697, 380
Wellons, S., Soderberg, A. M., & Chevalier, R. A. 2012, ApJ, 752, 17
Wheeler, J. C., & Harkness, R. P. 1990, RPPh, 53, 1467
Wheeler, J. C., Harkness, R. P., Clocchiatti, A., et al. 1994, ApJL, 436,
    L135
White, C. J., Kasliwal, M. M., Nugent, P. E., et al. 2015, ApJ, 799, 52
Woosley, S. E., & Bloom, J. S. 2006, ARA&A, 44, 507
Yaron, O., & Gal-Yam, A. 2012, PASP, 124, 668
Yoon, S.-C. 2015, PASA, 32, e015
Yoon, S.-C., Woosley, S. E., & Langer, N. 2010, ApJ, 725, 940

147

The Nature of EU Peg: an Algol-type Binary with a δ Scuti-type Component

Yuangui Yang[1], Huiyu, Yuan[1*], Haifeng Dai[1], Xiliang Zhang[2]

[1]Information College/School of Physics and Electronic Information, Huaibei Normal University, Huaibei 235000, Anhui Province, China

[2]Yunnan Observatories, Chinese Academy of Sciences, 396 Yangfangwang, Guandu District, Kunming 650216 China

*E-mail: yuanhy@chnu.edu.cn (Huiyu Yuan; corresponding author); yygcn@163.com

Abstract

The comprehensive photometry and spectroscopy for the neglected eclipsing binary EU Peg are presented. We determine its spectral type to be A3V. With the W-D program, the photometric solution was deduced from the four-color light curves. The results imply that EU Peg is a detached binary with a mass ratio of $q = 0.3105(\pm 0.0011)$, whose components nearly fills theirs Roche lobes. The low-amplitude pulsation occurs around the secondary eclipse, which may be attributed to the more massive component. Three frequencies are preliminarily explored by the Fourier analysis. The pulsating frequency at $f_1 = 34.1$ c/d is a *p*-mode pulsation. The orbital period may be undergoing a secular decrease, superimposed by a cyclic variation. The period decreases at a rate of $dP/dt = -7.34 \pm 1.06$ d yr^{-1}, which may be attributed to mass loss from system due to stellar wind. The cyclic oscillation, with $P_{mod} = 31.0 \pm 1.4$ yr and $A = 0.0054 \pm 0.0010$ day, may be interpreted by the light-time effect due to the assumed third body. With its evolution, the pulsating binary EU Peg will evolve from the detached configuration to semi-detached case.

Key words: stars: binaries: eclipsing; star: variables: delta Scuti; stars: individuals (EU Peg)

1 Introduction

Pulsations in eclipsing binaries are of particular interest for the theories of stellar formation, structure and evolution because binarity may provide accurate physical parameters of both components. It may tell us about the internal structure for the pulsating star, especially for our Sun (Gough 2000). Therefore, it is important for us to probe such pulsations in helioseismology of eclipsing binaries (Aerts 2007; Huber 2015), which will help us to identify pulsating modes and compare the results from stellar theory. The pulsations of eclipsing binaries have not yet been adequately investigated, since the δ Scuti-type pulsations in AB Cas was first discovered by Tempesti (1971). In the detached and semi-detached binaries, mass transfer, accretion and gas envelopes may influence pulsation (Mkrtichian et al. 2005). Although the dozens of observed sample binaries (Liakos et al.

2012; Zhang et al. 2013; Yang et al. 2014), the problem of mode identification and shortcomings in the stellar models are majors difficulties (Pamyatnykh et al. 1998). The pulsation modes have been detected and their frequencies determined by many authors. Zhang et al. (2013) and Cakirli & İbanoğlu (2016) derived the correction between orbital and dominant pulsation periods. The threshold orbital period of ~ 13 day may be an apparent limit, beyond which the intrinsic pulsations for the δ Sct stars may not affected by the binarity (Liakos & Niarchos 2015). Liakos & Niarchos (2017) published the catalogue and properties of 118 δ Scuti stars in binaries. The pulsating binaries with less than 0.7 days are only two stars, i.e., VV UMa ($P = 0.6874$ day; Kim et al. 2005) and V1464 Aql ($P = 0.6978$ day; Dal & Sipahi 2013). Therefore, searching the short-period eclipsing binaries with pulsations is helpful for us to understand

their pulsating mechanisms.

EU Peg (=*2MASS* J23012519+2720211) is an Algol-type eclipsing binary with EA-type light curves (Budding et al. 2004). Malkov al. (2006) then classified it to be in "semi-detached status" and assigned its spectral type to be (A8)+[G2IV]. The visual magnitude ranges from 12.20 mag to 12.80 mag (Kukarkin et al. 1971). The orbital period of EU Peg is 0.7211 days, which is refined to be 0.721113 days (Keriner 2004). No determinations for this binary have been made of the physical properties, and the system then has generally neglected except for the measurements of the times of eclipse made up to now.

In this paper, we found a δ Scuti component in the EU Peg binary system, which is the third short-period pulsating binary. In Section 2, the photometry and spectroscopy for this binary are first presented. On the basis of two spectrograms, we determined the spectral type. Section 3 is devoted to study possible period variations. Modeling four-band light curves and pulsation analysis are given in Section 4, in which we obtained photometric elements and pulsating frequencies. Finally, we discussed the evolutionary state and causes of period changes.

2 Data and Their Reduction

2.1 Spectroscopy

Two low-resolution spectrograms for EU Peg were observed by using the *OMR* of the 2.16-m telescope at the Xinglong station (XLs) of National Astronomical Observatories of China (NAOC) on 2016 Oct 8, and the *BFOSC* of the 2.4-m telescope at the Lijiang station of Yunnan Astronomical Observatory (YNAO) on 2016 Oct 23, respectively. For the 2.16-m telescope, we chose the slit width of $1.''8$ and the *Grism-14* with a wavelength ranging from 3200 Å to 7500 Å (Fan et al. 2015). Its exposure time is 10 minutes. For the 2.4-m telescope, meanwhile, we used the grating of 1200 lines/mm, which results in the wavelength coverage ~ 1380 Å (Fan et al. 2016). The exposure time is 15 minutes. Reduction of the spectra was performed by using IRAF packages [3], including bias subtraction, flat-fielding and cosmic-ray removal. Finally, the one-dimension spectrum was extracted. With the *winmk* software [4], two normalized spectra are displayed in Fig.1. The spectra of standard stars, HD 122408 and HD 002857 [5], are also plotted in both panels. The spectrum of Fig.1(a) is large noisy although the double lines for *Na* and *H*α line are evident. Due to lack of short wavelength, we re-observed this binary using the 2.4-m telescope and obtained the spectrum shown in Fig.1(b). On the basis of the stellar spectral classification (Gray & Corbally
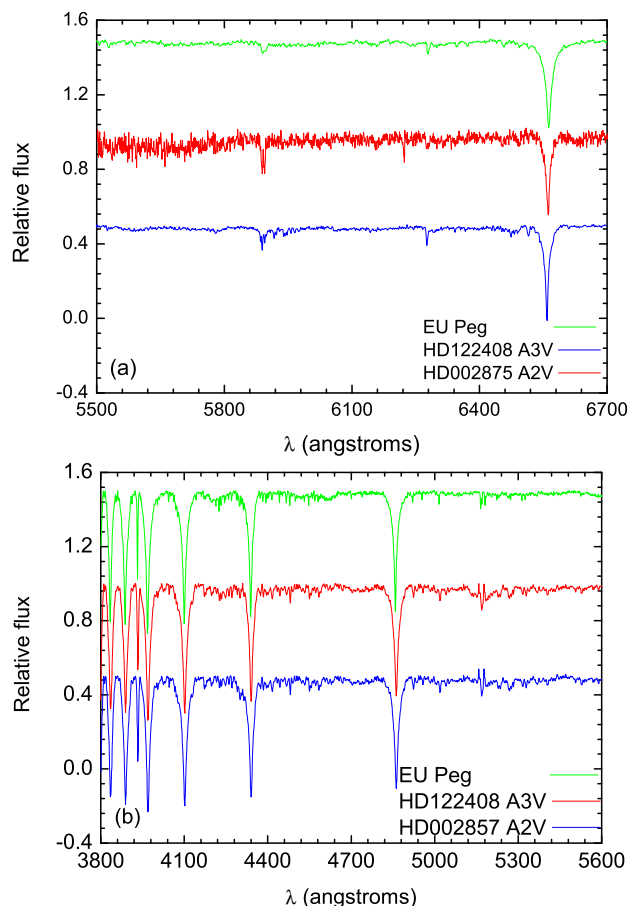
Fig. 1. Normalized spectra of the eclipsing binary EU Peg, which were observed on 2016 October 8 (a) and October 23 (b), respectively. The spectrum data are added the displacements of "+0.5" for HD 002857 and "-0.5" for HD 122408.

2009), we determined its spectral type to be A3V, which differs from the estimated spectral type of (A8)+[G2IV] (Malkov al. 2006).
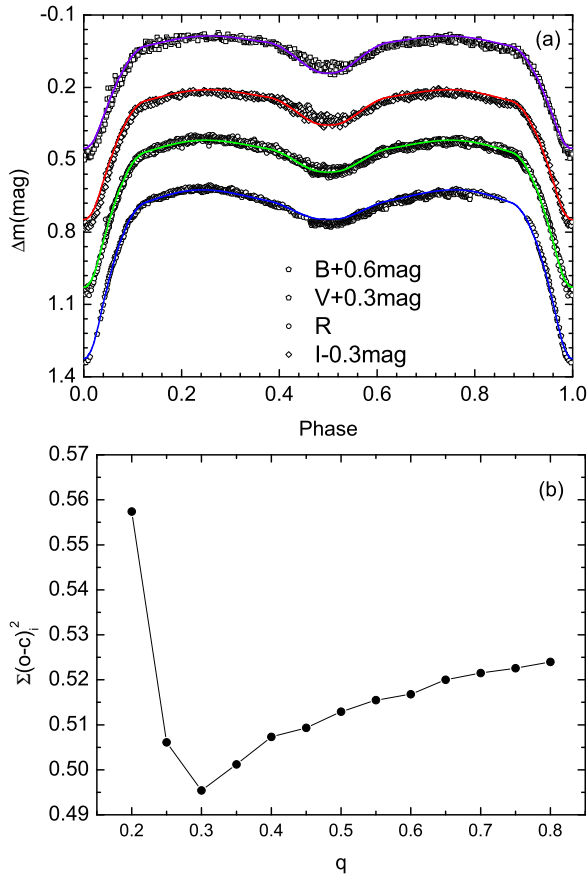
2.2 CCD Photometry

The comprehensive photometry for EU Peg was carried out from 2013 September 25 to November 11 with the 85-cm telescope (Zhou et al. 2009) and the 60-cm telescope (Yang et al. 2010) at XLs of NAOC. The standard Johnson-Cousin-Bessel $UBVR_cI_c$ systems are mounted on two small telescopes. Photometric effective images were reduced by using the IMRED and APPHOT packages in IRAF, after we preformed bias and dark subtraction, and flat-field correction. We then obtained the differential magnitudes between the variable and the comparison star.

In the observing process, TYC 2243-709-1 (*B=11.88, V=11.22*) and TYC 2243-1242-1 (*B=11.98, V=11.09*) are chosen to be the comparison and check stars, respectively. Typical exposure times were generally set to be 50s for B, 40 s for V,

---

[3] IRAF is supported by the National Optical Astronomy Observatories (NOAO) in Tucson, Arizona from http://iraf.noao.edu/iraf/web/iraf-homepage.html.

[4] http://www.appstate.edu/ grayro/MK/winmk.htm
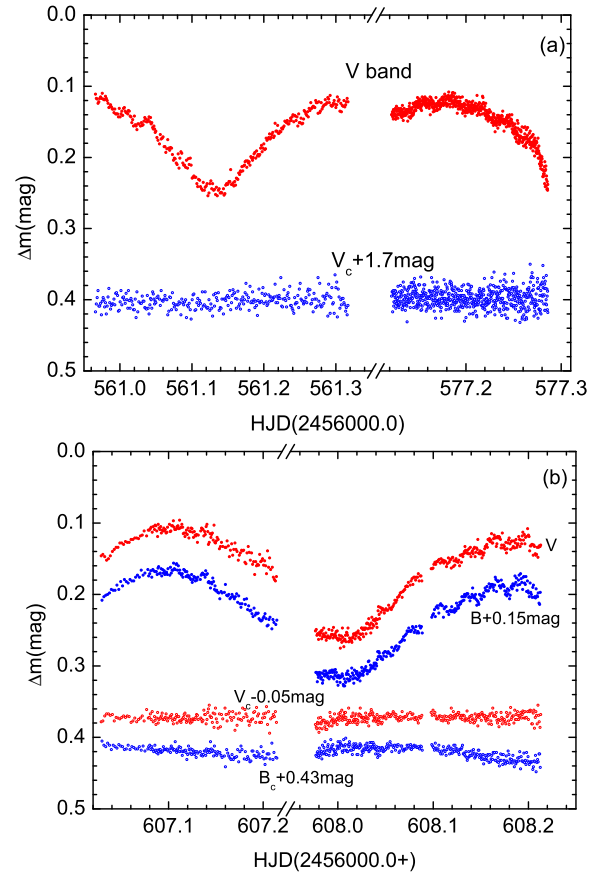
[5] http://www.ast.obs-mip.fr/users/leborgne/stelib/stars.html

Fig. 2. BVR_cI_c-band light curves of EU Peg (a). The solid color lines are depicted by photometric solution (see from Table 5). The resulting $\Sigma(q)$ curve (b) is deduced from all photometric data.

Fig. 3. Pulsating light variations with low amplitudes around secondary minima for EU Peg, observed by using the 85-cm telescope (a) and the 60-cm telescope (b) at XLs of NAOC in 2013. In low part of both panels, "Bc" and "Vc" values are in the sense of *Comparison-Check* with magnitude displacements.

30 s for R_c and 25 s for I_c band, which depends on the weather condition. Most useful observations were obtained on 9 nights. In total, we obtained 4565 effective CCD images. Table 1 lists heliocentric Julian dates (HJDs) *versus* differential magnitudes with respect to the comparison star. The $Comparison-Check$ magnitude differences, i.e., *rms* scatters, are 0.007 mag in B and 0.006 mag in V band for the 60-cm telescope, and 0.013 mag in V, 0.014 mag in R_c, and 0.022 in I_c band for the 85-cm telescope, respectively. The complete light curves are shown in Fig.2(a), in which phases are computed by the new linear ephemeris in Eq.(1) in Sect.3. From this figure, the brightness fluctuations, especially in B and V bands, occur during the secondary minima and disappear near the central phase of the primary minima, which is similar to another previously studied star FR Ori (Yang et al. 2014). The low-amplitude pulsations in BV light curves are displayed in Fig.3, which are obtained only at the fine nights. The pulsations occurring at the secondary eclipses imply that the more massive component in the EU Peg binary may be a δ Scuti-type star.

3 Orbital Period Variations

From our new data, we determined four light minimum times, listed in Table 2. From the *O-C* gateway [6], a total of 34 eclipse times (i.e., 11 photographic, 3 photoelectric and 20 CCD ones) was compiled to study the period changes. Table 3 give those data with their errors and measured methods. For all eclipsing times, individual weights are assigned inversely proportional to their standard errors. However, the uncertainties for some timings did not be given. Therefore, we assumed the errors of ±0.001 day for 11 photographic data, and ±0.0005 day for 2 photoelectric ones (Hübscher et al. 1994), respectively. Based on all times of minimum light, a weight least-squares method yields a new linear ephemeris as follows,

$$\text{Min. I} = \text{HJD } 2456562.2086(11) + 0.72111515(8) \times \text{E}, \quad (1)$$

in which the number in brackets are listed the errors in the last decimal place. Initial timing residuals with respect to Eq.(1), $(O-C)_i$, are listed in Table 3 and displayed in Fig.4(a). From

[6] http://var2.astro.cz/ocgate/

this figure, the orbital period of EU Peg clearly displays a secular decrease with some irregular oscillations, although a 36-year gap exists between HJD 2435401.078 (Kaho 1952) and HJD 2448465.538 (Hübscher et al. 1995). Therefore we assumed that the $(O-C)_i$ curve may be described by a downward parabola with a sinusoidal curve, whose is similar to the case occurring in the binary SX Dra (Soydugan & Kaçar 2013). By using a nonlinear least-squares method with weights, the following equation was used to represent the cyclic variation and parabola of the $(O-C)$ data,

$$\text{Min. I} = T_0 + P \times E + Q \times E^2 + A_{mod} \times \sin[\frac{2\pi}{P_{mod}}(E - T_s)], (2)$$

where A_{mod}, P_{mod} and T_s are the amplitude, period and moment of the minimum of sinusoidal variation, while T_0, P, Q and E are the epoch , orbital period of the binary system, the coefficient of quadratic term and epoch number, respectively. The fitting parameters are listed in Table 4. From Eq.(2), we obtained the computed values, $(O-C)_{parab}$ and $(O-C)_c$, for all eclipsing times, which are listed in Table 3. From the coefficient of quadratic term, Q, we determined a period decrease rate of $dP/dt = -7.34(\pm1.06) \times 10^{-7}$ day/yr. As shown in Fig.4(a), the solid and dotted lines are plotted by Eq.(2) and only its parabolic part, respectively.

After removed from $(O-C)_i$ by the best parabolic fit of Eq.(2), the $(O-C)_c$ residuals are displayed in Fig.4(b). The cyclic change is plotted as a solid line only by the sinusoidal term of Eq.(2). The period of this oscillation is $P_{mod} = 31.0(\pm1.4)$ yr. From the fit including both quadratic and sinusoidal terms, we obtained the final residuals $(O-C)_f$, which are listed in Table 3 and shown in Fig.4(c). From this figure, no regularity is found. Therefore, Eq.(2) is acceptable for us to fit all data, although a large gap exists. In the future observation, more eclipsing times are needed to check the behavior of the orbital period variations.

4 Analyzing Light Curves

From the light curves of Fig.2(a), EU Peg is identified to be an Algol-type eclipsing binary. The photometric elements are deduced from four-color light curves, including 912 data in B band, 2729 in V band, 806 in R_c band and 741 in I_c band. After the binary solution was removed from the observations (i.e., the light-curve residuals), a Fourier analysis was performed on the residuals in order to study the pulsation behavior of the primary component.

4.1 Photometric Solution

Theoretical light curves of EU Peg were simultaneously computed by the 2015-version W-D Program (Wilson & Devinney
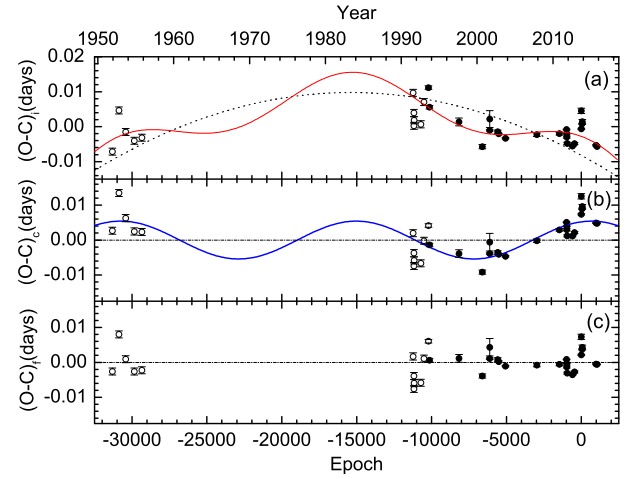
Fig. 4. The residual diagrams: $(O-C)_i$ (a), $(O-C)_c$ (b), and $(O-C)_f$ (c). The open and filled circles represent photographic measurements, and photoelectric/CCD ones, respectively. In the panel (a), the solid and dotted lines are computed by Eq.(2) and only its parabolic part, respectively. Meanwhile, the continuous curve in the panel (b) is plotted by the sinusoidal term of Eq.(2).

1971; Wilson & Van Hamme 2014) [7]. The limb darkening coefficients are generated with the LC and DC programs. In the calculating process, we fixed $LD_1 = LD_2 = -2$ for the bolometric logarithmic limb darkening law (van Hamme & Wilson 2007), and MREF=2 for the detailed reflect model (Wilson 1979). Assumed the spectral type of A3V with an uncertainty of a subtype for EU Peg, the mean effective temperature for Star 1 may be estimated to be $T_1 = 8730(\pm270)$ K, which are based on the calibration of *MK* spectral types (Cox 2000). The gravity darking exponents and bolometric albedo coefficients are fixed to be $g_1 = 1.0$ (von Zeipel 1924) and $g_2 = 0.32$ (Lucy 1967), $A_1 = 1.0$ and $A_2 = 0.5$ (Rucinski 1973), respectively. As usual, other adjustable parameters are T_0, P_0, T_2, i, q, Ω_1, Ω_2 and ℓ_3 in solving light curves.

In order to search a mass ratio, we performed a q-search process from all data. The tried solutions imply that EU Peg has a detached configuration, rather than a semi-detached one (Budding et al. 2004). The relation between q and Σ is shown in Fig.2(b), in which a minimum value of Σ arrives around a mass ratio of 0.3. The mass ratio q and third light ℓ_3 are then considered to be free parameters. The final photometric elements are listed in Table 5. The fill-out factor is computed by $f = <r>/r_{cr}$, in which r_{cr} is an equivalent relative radius of Roche lobe (Eggleton 1983). The values for both components are $f_p = 86.7(\pm0.6)\%$ and $f_s = 92.6(\pm0.1\%)$. The computed light curves are plotted as solid lines in Fig.2(a). From this figure, R_c and I_c light curves may be not fitted well, which may be contributed the different filters. The contributions to the total light, ℓ_3, are 0.25%, 0.39% and 0.68% in B, V, R_c and I_c

---

[7] FTP site: //ftp.astro.ufl.edu/pub/wilson/lcdc2015.
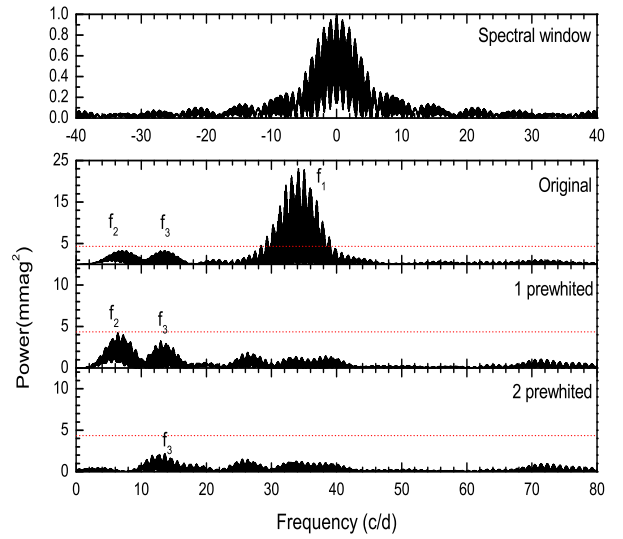
bands, respectively.
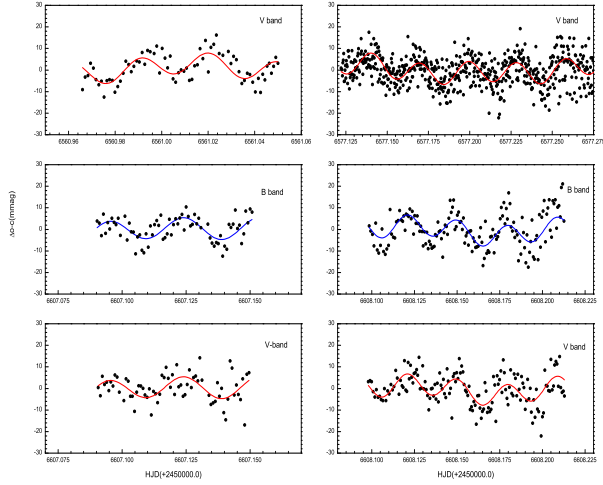
Fig. 5. Residual light curves with pulsations, observed by using the 85-cm telescope (*top*), and the 60-cm telescope (*middle* and *bottom*). The solid lines are plotted by three fitted frequencies from Table 6.

Fig. 6. Spectral window, power spectra and significance limit (as dotted line), which are derived from all pulsating data in B and V.

4.2 Pulsating Frequency Analysis

To explore pulsating frequencies, small-amplitude pulsations were analyzed after removed by the binary solution from light curves. From Fig.3, the pulsations occur around both light maxima, which may result from the more massive component, possibly in the instability strip of H-R diagram. This kind of pulsations occur in other short-period ($P < 1$ days) detached Algol-type binary HZ Dra (Liakos et al. 2012). After the eclipses and proximity effects of the binary were removed by theoretical light curves, we obtained 5.9 hr in V band (from the 85 telescope), and 4.2 hr in B, V bands (from the 60-cm telescope) residual data. Due to only 10.1-hour pulsations (i.e., 225 in B band and 917 in V band), searching pulsation frequencies is then preliminary. As shown in Fig.5, a total of 1142 residual observations were analyzed by using Period04 software [8] (Lenz 2004; Lenz & Breger 2005), which is based on the classical discrete Fourier transform and multiple-least-squares algorithms.

When we calculate frequencies, the residual light curves were subsequently pre-whitened one by one. The signal/noise amplitude ratio is $S/N \sim 4.0$ as a good criterion to distinguish between peaks due to pulsation and noise (Breger et al. 1993). The analyses were preformed for B data, V data, and all data together, respectively. The detected frequencies are listed in Table 6, in which the uncertainties of parameters are computed by the formulae from Montgomery & O'donoghue (1999). The observed noises are $\sigma(m)_B = 0.0071$ mag, $\sigma(m)_V = 0.0113$ mag and $\sigma(m)_{B+V} = 0.0106$ mag, respectively. From Table 5, three frequencies from V data approximately agree with those

[8] Period04 is available at the web site of http://www.univie.ac.at/tops/.

from all data. For 225 data in B band, the only reliable result may be the frequency of f_1. So we accept the results derived from the data in B and V bands. The spectral window and amplitude spectra are displayed in Fig.6, although three peaks are not prominent due to pulsating observations with a short duration of 10.1 hours. Using the estimated parameters in Table 4, the mean density of the primary can be computed to be $\rho_1/\rho_\odot = \frac{M_1}{M_\odot}/(\frac{R_1}{R_\odot})^3 = 0.2685(\pm 0.0370)$. Following the formula of $Q = P_{pul}(\rho/\rho_\odot)$, we can calculate the pulsating constant for each frequency. The theoretical curves are plotted in Fig.5 as solid lines by using the equation of $m(t) = a_0 + \sum a_i \sin[2\pi(f_i t + \phi_i)]$ ($i = 1, 2, 3$), where $m(t)$, a_0, a_i, ϕ_i and f_i are calculated magnitude, zero point, semi-amplitude, phase and frequency of the i-th frequency. The dominant frequency of $f_1 = 34.119$ c/d (i.e., $P_{puls} \simeq 42.2$ minutes) with an amplitude of $4.82(\pm 0.44)$ mmag may be a reliable pulsating frequency. The value of Q for low-radial-order press mode (i.e., p-mode) oscillation of a δ-Scuti star is shorter than 0.04 day or less (Handler & Shobbrook 2002), which serves as a criterion to perform a rough-mode identification. In order to further identify the pulsation mode, we estimated phase shift and amplitude ratio between B and V bands. For the frequency of f_1 from Table 5, the observed phase shift is $+4.6°$ for B-V, which means its radial pulsation according to the diagrams of Watson (1988) and Garrido et al. (1996). The amplitude ratio of B/V of 1.47 may be a typical value compared with those for radial mode δ Scuti stars (Rodríguez et al. 1996). Therefore, the detected frequency of f_1 may be a p-mode pulsator.

Based on the eclipsing binaries with δ Scuti type primaries, Soydugan et al. (2006) and Soydugan & Kaçar (2013) successively derived two relations of $P_{puls} - P_{orb}$ (see Fig.7a) and $\log P_{plus} - \log F$ (see Fig.7b), where F is the gravitational pull

exerted to per gram of the matter on the surface of the primaries by the secondary companions. The primary pulsation of EU Peg (i.e., $P_{\mathrm{plus}} = 0.029$ days) is also plotted as a solid circle in Fig.7. From both panels, the observed main pulsation of EU Peg identifies the two relations (Soydugan et al. 2006; Soydugan & Kaçar 2013). For the short-period Algol-type binary EU Peg, the large gravitational force exerted from the secondary component, F, results in the short pulsating period. Figure 7 implies that when the orbital period decreases, the separation between two components decreases. This will cause the gravitational force applied by the secondary companion onto the pulsating primary star to increase. Finally, the pulsating period will also decrease. According to the criterion given Breger et al. (1993), two frequencies f_2 and f_3 are below the significance limit and maybe are not meaningful. This case occurs in the pulsating binary SX Dra (Soydugan & Kaçar 2013). Therefore, f_2, and f_3 with low amplitudes are needed to further identify in the future.
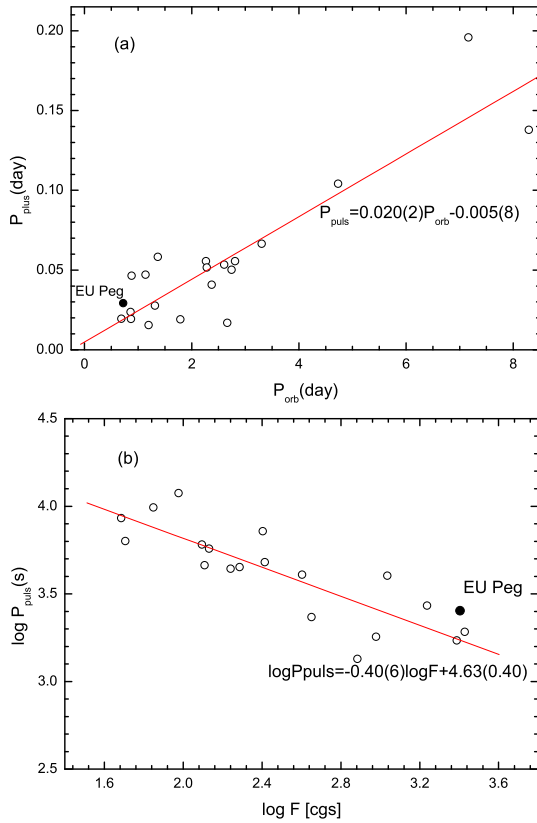

Fig. 7. (a)The relation between P_{orb} and P_{puls} taken from Soydugan et al. (2006), where the open circles represent 20 systems. (b) The relation between P_{orb} and P_{puls} taken from Soydugan & Kaçar (2013), in which the open circles refer to 19 binaries. The solid circle refers to the binary EU Peg in both panels.

5 Discussions

From the previous analysis, EU Peg is a detached binary with a δ Sculti component, whose mass ratio is $q = 0.3105(\pm0.0011)$. The fill-out factors for both components are $f_p = 86.7(\pm0.6)\%$ and $f_s = 92.6(\pm0.1)\%$, respectively. The light curves process small pulsations, The dominant pulsating frequency of $f_1 = 34.12$ c/d is a *p*-mode pulsation. In order to reliable frequency values, more data are needed in the future observation. Due to the lack of spectroscopic elements (i.e., the semi-amplitudes of radial velocity curves, K_1 and K_2), the absolute parameters are estimated by using Kepler's third law, $M_1 + M_2 = 0.134a^3/P^2$, in which $M_{1,2}$, a and P are in units of $M_\odot$, $R_\odot$ and day respectively.

Based on the spectral type of A3V assuming with a subtype error, we adopted a mass of $M_1 = 2.60(\pm0.30)$ $M_\odot$ (Cox 2000). Using the Kepler's third law and photometric solution, we determined other absolute parameters, listed in Table 5. In Both components are shown in Fig.8. *ZAMS, TAMS*, evolutionary tracks and isochrones for solar chemical compositions are taken from Girardi et al. (2000). The primary component between ZAMS and TAMS lines, is close to ~ 2.0 $M_\odot$ in an isochrone of ~ 0.47 Gyr, whose low luminosity and temperature with respect to its mass may result from the single-star evolutionary model. Meanwhile, the secondary component is near to the evolutionary track of 0.8 $M_\odot$, and is far from the isochrone line. This may result form the binary interactive, which may represent its true evolutionary state.
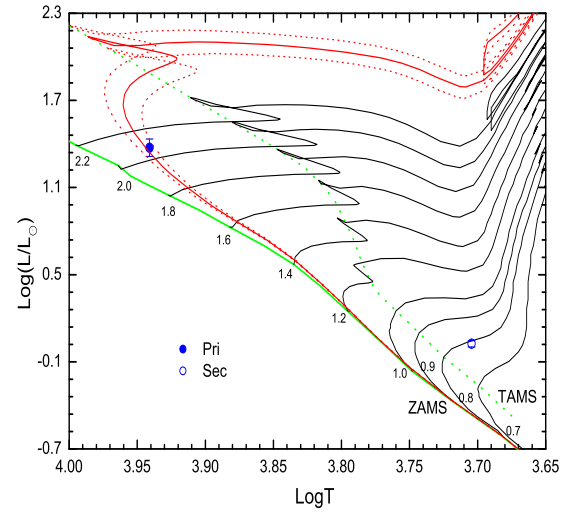
Fig. 8. The evolutionary locations of both components for the detached binary EU Peg.

From the period analysis, the $(O - C)$ curve possibly includes a cyclic variation. For the close binaries, this kind of changes may be attributed to either cyclic magnetic activity (Applegate 1992) or light-time effect (Irwin 1952). For the early-type binary EU Peg, the less massive component may be

an active star. The observed amplitude of sinusoidal term in Eq.(2) may result from the change of gravitational quadrupole moment, which can be computed by Lanza & Rodonò (2002)'s equation as follows,

$$-9\frac{R}{a}\frac{\Delta Q}{MR^2} = \frac{\Delta P}{P} \simeq \frac{2\pi A_{mod}}{P_{mod}}, \tag{3}$$

where a, R, M are taken from Table 5, A and P_{mod} from Eq.(2), respectively. The value of $\Delta Q_2 = 6.71(\pm 1.24) \times 10^{-49}$ g cm^2 is much smaller than the typical order of $10^{-51} - 10^{-52}$ g cm^2 (Lanza & Rodonò 1999). Therefore, we could remove the magnetic active, which may not work out in the secondary. On the other hand, another mechanism is light-time effect due to the assumed third companion. From Eq.(2), we can easily obtain the value of $a_{12}\sin i' = A_{mod} \times c$, in which c and i' are light velocity and orbital inclination. Then we can compute the mass function of the additional companion, $f(m)$, with the help of the following equation,

$$f(m) = \frac{4\pi^2}{GP_{mod}^2} \times (a_{12}\sin i')^3 = \frac{(M_3 \sin i')^3}{(M_1 + M_2 + M_3)^2}. \tag{4}$$

By the iteration method, we can determine the mass and radius for some an orbital inclination i'. The minimum mass for the suggested third companion (i.e., $i' = 90$ deg) is $M_3 = 0.23(\pm 0.04)$ M$_\odot$ at a radius of $14.2(\pm 5.1)$ AU. It may be a red dwarf with low luminosity (i.e., $\ell_3 \leq 1.0\%$), which is difficult to explore by spectroscopy.

In the non-conservative evolution for a close binary, the secular period changes should be the result of a net effect of mass transfer, mass loss, and angular momentum loss (Tout & Hall 1991). Due to the detached configuration for EU Peg, both components do not fill the Roche lobes, respectively. Assuming that the mass loss due to stellar wind is proportional to its total mass of system (i.e., $\dot{M} = \dot{M}_2 M/M_2$) and the escape radius is equal to the separation between both components (i.e., $R_{es} \simeq a$), we can obtain a simplified formula as follows (see Yang et al. 2013),

$$\frac{1}{P}\frac{dP}{dt} = \frac{5q^2 - q + 2}{q}\frac{\dot{M}}{M}, \tag{5}$$

where P, q, M are orbital period, mass ratio and total mass, respectively. Inserting dP/dt and other parameters of the binary, we can determine a mass loss rate of $dM/dt = -4.96(\pm 0.72) \times 10^{-8}$ M$_\odot$/yr. Moreover, the possible additional companion in the EU Peg binary may extract angular momentum from the central system. Mass loss and angular loss result in the period decreasing. This will cause the orbit of binary to shrink. Due to two components nearly filling their limiting Roche lobes, EU Peg finally may evolve from the detached configuration into the semi-detached one. More high-precision spectroscopy and photometry for EU Peg are necessitated to determine the absolute parameters more reliably, to explore the pulsating frequencies and to search any signature of the presence of a third component.

References

Aerts, C., 2006, IAUS, 240, 432

Agerer, F., & Hübscher, J., 1999, Inf. Bull. Var. Stars, 4712, 1

Agerer, F., & Hübscher, J., 2003, Inf. Bull. Var. Stars, 5484, 1

Applegate, J. H., 1992, ApJ, 385, 621

Breger, M., Stich, J., Garrido, R., et al., 1993, A&A, 271, 482

Budding, E., Erdem, A., Çiçek, C., et al., 2004, A&A, 417, 263

Cakirli, Ö., & İbanoğlu, C., 2016, New Astron., 45, 36

Cox, A. N. 2000, Allen's Astrophysical Quantities, 4th ed. (New York: Springer)

Diethelm, R., 2000, BBSAG Bull, 123, 1

Diethelm, R., 2003, Inf. Bull. Var. Stars, 5438, 1

Diethelm, R., 2011, Inf. Bull. Var. Stars, 5960, 1

Diethelm, R., 2012, Inf. Bull. Var. Stars, 6011, 1

Diethelm, R., 2013, Inf. Bull. Var. Stars, 6042, 1

Dal, H. A., & Sipahi, E., PASA, 30, 16

Dvorak, S. W., 2003, Inf. Bull. Var. Stars, 5378, 1

Eggleton, P. P., 1983, ApJ, 268, 368

Fan, Yu-Feng, Bai, Jin-Ming, Zhang, Ju-Jia, et al., 2015, RAA, 15, 918

Fan, Zhou, Wang, Huijuan, Jiang, Xiaojun, et al., 2016, PASP, 128, 115005(15pp)

Garrido, R., Garcia-Lobo, E., & Rodríguez, E., 1990, A&A, 234, 262

Girardi, L., Bressan, A., Bertelli, G., & Chiosi, C., 2000, A&AS, 141, 371

Gray, R. O., & Corbally, C. J., 2009, Stellar spectral classification, Princeton Univ. Press (New Jersey: Princeton)

Gough, D., 2000, ASPC, 203, 529

Handler, G., & Shobbrook, R. R., 2002, MNRAS, 333, 251

Hübscher, J., 2005, Inf. Bull. Var. Stars, 5643, 1

Hübscher, J., 2014, Inf. Bull. Var. Stars, 6118, 1

Huber, D., 2015, Astrophysics and Space Science Library, 408, 169

Hübscher, J., Agerer, F., & Wunder, E., 1992, BAV Mitt., 60, 1

Hübscher, J., Agerer, F., & Wunder, E., 1993, BAV Mitt., 62, 1

Hübscher, J., Agerer, F., & Wunder, E., 1994, BAV Mitt., 68, 1

Hübscher, J., Agerer, F., & Wunder, E., 1995, BAV Mitt., 79, 1

Hübscher, J., Agerer, F., & Wunder, E., 1996, BAV Mitt., 93, 1

Irwin, J. B., 1952, ApJ, 116, 211

Juryšek, J. Hoňková, K., Šmelcer, L., et al., 2017, Open Eur. J. Var. Stars, 179, 1

Kaho, S., 1952, Tokyo Bull. Sec. Ser., 30, 217

Kim, S.-L., Lee, J. W., Lee, C.-U., et al., 2005, Inf. Bull. Var. Stars, 5598, 1

Kreiner, J. M., 2004, Acta Astron., 54, 207

Kreiner, J. M., 2011, private communciation

Kukarkin, B. V., Kholopov, P. N., Pskovsky, Y. P., et al., 1971, General Catalogue of Variable Stars, 3rd ed.

Liakos, A., & Niarchos, P., 2015, in Rucinski, S. M., Torres, G., Zejda, M., eds, ASP Conf. Ser., Vol. 496, Living Together: Planets, Host Stars and Binaries, Astron. Soc. Pac. San Francisco, p.195

Liakos, A., & Niarchos, P., 2017, MNRAS, 465, 1181

Lanza, A. F., & Rodonò, M., 1999, A&A, 349, 887

Lanza, A. F., & Rodonò, M., 2002, Astron. Notes, 323, 424

Lenz, P., 2004, Comm. in Asteroseismology, 144, 41

Lenz, P., & Breger, M., 2005, Comm. in Asteroseismology, 146, 1

Liakos, A., Niarchos, P., Soydugan, E., & Zasche, P., 2012, MNRAS, 422, 1250

Lucy, L. B., 1967, ZA, 65, 89

Malkov, Y. O., Oblak, E., Snegireva, E. A., & Torra, J., 2006, A&A, 446, 785

Montgomery, M. H., & O'donoghue, D., 1999, Delta Scuti Star Newsletter, 13, 28

Mkrtichian, D. E., Rodríguez, E., Olson, E. C., et al., 2005, ASPC, 333, 197

Nagai, K., 2008, Var. Star Bull. Japan, 46, 1

Pickles, A., & Depagne, E., 2010, PASP, 122, 1437

Pamyatnykh, A. A., Dziembowski, W. A., Handler, G., & Pikall, H., 1998, A&A, 331, 141

Rodríguez, E., Rolland, A., López de Coca, P., & Martín, S., 1996, A&A, 307, 539

Rucinski, S. M., 1973, Astron. Acta, 23, 79

Soydugan, E., İbanoğlu, C., Soydugan, F., et al., 2006, MNRAS, 366, 1289

Soydugan, E., & Kaçar, Y., 2013, AJ, 145, 87 (8pp)

Tempesti, P., 1971, Inf. Bull. Var. Stars, 596, 1

Tout, C. A., & Hall, D. S., 1991, MNRAS, 253, 9

van Hamme, W., & Wilson, R. E. 2007, ApJ, 661, 1129

von Zeipel, H., 1924, MNRAS, 84, 655

Watson, R. D., 1988, Ap&SS, 140, 255

Wilson, R. E., 1979, ApJ, 234, 1054

Wilson, R. E., & Devinney, E. J. 1971, ApJ, 166, 605

Wilson, R. E., & Van Hamme, W. 2014, ApJ, 780, 151

Yang, Y.-G., Dai, H.-F., & Yin, X.-G., 2010, New Astron., 15, 392

Yang, Y.-G., Qian, S.-B., & Dai, H.-F., 2013, AJ, 145, 60

Yang, Y.-G., Wei, J.-Y., & Li, H.-L., 2014, AJ, 147, 35

Zejda, M., 2004, Inf. Bull. Var. Stars, 5583, 1

Zhang, X.-B., Luo, C.-Q., & Fu, J.-N., 2013, ApJ, 777, 77

Zhou, A.-Y., Jiang, X.-J., Zhang, Y.-P., & Wei, J.-Y., 2009, Res. Astron. Astrophys., 9, 349

Table 1. Multicolor Photometric Observations for EU Peg

60-cm telescope				85-cm telescope					
B band		*V* band		*V* band		R_c band		I_c band	
JD(Hel.)	Δm	JD(Hel.)	Δm	JD(Hel.)	Δm	JD(Hel.)	Δm	JD(Hel.)	Δm
601.98744	+0.053	576.15711	+0.126	560.96598	+0.111	560.96656	+0.214	561.05232	+0.330
601.98868	+0.051	576.15750	+0.126	560.96715	+0.117	560.96773	+0.218	561.05362	+0.324
601.98992	+0.044	576.15790	+0.125	560.96831	+0.118	560.96890	+0.219	561.05558	+0.327
601.99116	+0.050	576.15829	+0.121	560.96948	+0.124	560.97006	+0.224	561.05689	+0.348
601.99258	+0.046	576.15869	+0.133	560.97065	+0.122	560.97123	+0.221	561.05819	+0.339
601.99405	+0.048	576.15908	+0.130	560.97181	+0.117	560.97238	+0.216	561.05949	+0.343
601.99552	+0.056	576.15948	+0.127	560.97297	+0.115	560.97355	+0.214	561.06079	+0.352
601.99699	+0.048	576.15987	+0.138	560.97413	+0.117	560.97472	+0.220	561.06209	+0.342
601.99847	+0.043	576.16026	+0.129	560.97530	+0.110	560.97588	+0.213	561.06339	+0.341
601.99997	+0.048	576.16066	+0.124	560.97647	+0.118	560.97705	+0.222	561.06468	+0.354
602.00148	+0.036	576.16105	+0.127	560.97763	+0.119	560.97822	+0.217	561.06599	+0.338
602.00300	+0.044	576.16145	+0.124	560.97880	+0.119	560.97938	+0.221	561.06729	+0.352

Notice: All individual data are available only on the web journal of *PASJ*.

Table 2. New Observed Eclipsing Times for EU Peg

JD(Hel.)	Error	Filter	Min.	Telescopes
2456561.13335	±0.00065	*V*	II	85-cm
2456561.13790	±0.00100	R_c	II	85-cm
2456561.13238	±0.00066	I_c	II	85-cm
2456562.21142	±0.00023	*V*	I	85-cm
2456562.20989	±0.00019	R_c	I	85-cm
2456562.21184	±0.00023	I_c	I	85-cm
2456604.03722	±0.00019	*B*	I	60-cm
2456606.20108	±0.00057	*B*	I	60-cm
2456606.20121	±0.00069	*V*	I	60-cm

Table 3. All Available Times of Light Minima for EU Peg

JD(Hel.)	Error	Epoch	Method	$(O-C)_i$ (days)	$(O-C)_{\mathrm{parab}}$ (days)	$(O-C)_c$ (days)	$(O-C)_f$ (days)	References
2433981.919[a]	±0.001	−31313.0	pg	−0.0109	−0.0136	+0.0053	−0.0026	Kaho (1952)
2434302.106[a]	±0.001	−30869.0	pg	+0.0009	−0.0125	+0.0054	+0.0080	Kaho (1952)
2434628.044[a]	±0.001	−30417.0	pg	−0.0051	−0.0114	+0.0054	+0.0009	Kaho (1952)
2435044.125[a]	±0.001	−29840.0	pg	−0.0076	−0.0100	+0.0051	−0.0026	Kaho (1952)
2435401.078[a]	±0.001	−29345.0	pg	−0.0066	−0.0089	+0.0046	−0.0022	Kaho (1952)
2448465.538[a]	±0.001	−11228.0	pg	+0.0103	+0.0083	+0.0003	+0.0017	Hübscher et al. (1995)
2448499.421[a]	±0.001	−11181.0	pg	+0.0009	+0.0083	+0.0002	−0.0076	Hübscher et al. (1992)
2448501.588[a]	±0.001	−11178.0	pg	+0.0045	+0.0083	+0.0002	−0.0039	Hübscher et al. (1992)
2448514.566[a]	±0.001	−11160.0	pg	+0.0024	+0.0083	+0.0001	−0.0060	Hübscher et al. (1992)
2448840.509[a]	±0.001	−10708.0	pg	+0.0014	+0.0081	−0.0008	−0.0058	Hübscher et al. (1996)
2448988.344[a]	±0.001	−10503.0	pg	+0.0078	+0.0080	−0.0013	+0.0011	Hübscher & Agerer (1993)
2449202.5194[b]	±0.0005	−10206.0	pe	+0.0120	+0.0078	−0.0019	+0.0060	Hübscher et al. (1994)
2449249.3863[b]	±0.0005	−10141.0	pe	+0.0064	+0.0078	−0.0020	+0.0006	Hübscher et al. (1994)
2450671.4216	±0.0011	−8169.0	CCD	+0.0026	+0.0065	−0.0050	+0.0011	Agerer & Hübscher (1999)
2451796.3545	±0.0006	−6609.0	CCD	−0.0041	+0.0051	−0.0053	−0.0039	Diethelm (2000)
2452147.5456	±0.0024	−6122.0	CCD	+0.0039	+0.0045	−0.0049	+0.0043	Zejda (2004)
2452150.4268	±0.0002	−6118.0	CCD	+0.0007	+0.0045	−0.0049	+0.0011	Agerer & Hübscher (2003)
2452535.5020	±0.0005	−5584.0	CCD	+0.0004	+0.0039	−0.0044	+0.0008	Diethelm (2003)
2452581.6528	±0.0002	−5520.0	CCD	−0.0002	+0.0038	−0.0043	+0.0002	Dvorak (2003)
2452913.3646	±0.0002	−5060.0	CCD	−0.0014	+0.0033	−0.0036	−0.0011	Hübscher (2005)
2454421.9390	±0.0005	−2968.0	CCD	+0.0001	+0.0003	+0.0006	−0.0008	Nagai (2008)
2455500.7279	±0.0004	−1472.0	CCD	+0.0008	−0.0022	+0.0035	−0.0006	Diethelm (2011)
2455854.7967	±0.0001	−981.0	CCD	+0.0020	−0.0031	+0.0042	+0.0008	Kreiner (2011)
2455862.7278	±0.0001	−970.0	CCD	+0.0009	−0.0031	+0.0043	−0.0003	Kreiner (2011)
2455863.8085	±0.0003	−968.5	CCD	−0.0001	−0.0031	+0.0043	−0.0013	Kreiner (2011)
2455875.7051	±0.0003	−952.0	CCD	−0.0019	−0.0031	+0.0043	−0.0031	Diethelm (2012)
2456132.4214	±0.0002	−596.0	pe	−0.0026	−0.0038	+0.0047	−0.0035	Hübscher (2014)
2456232.6571	±0.0003	−457.0	CCD	−0.0019	−0.0040	+0.0049	−0.0027	Diethelm (2013)
2456561.1345	±0.0008	−1.5	CCD	+0.0076	−0.0049	+0.0052	+0.0073	Present paper
2456562.2111	±0.0002	+0.0	CCD	+0.0024	−0.0049	+0.0052	+0.0022	Present paper
2456604.0372	±0.0002	+58.0	CCD	+0.0039	−0.0051	+0.0052	+0.0037	Present paper
2456606.2012	±0.0006	+61.0	CCD	+0.0045	−0.0051	+0.0052	+0.0043	Present paper
2457267.4572	±0.0002	+978.0	CCD	−0.0021	−0.0070	+0.0054	−0.0005	Juryšek et al. (2017)
2457324.4250	±0.0001	+1057.0	CCD	−0.0023	−0.0071	+0.0054	−0.0006	Juryšek et al. (2017)

Notice: [a]For 11 photographic data, we assumed their observed errors to be ±0.001 day.

[b]For two photoelectric data (Hübscher et al. 1995), their uncertainties are given to be ±0.0005 day.

Table 4. New ephemeris of EU Peg

Quadratic plus sinusoidal fitting
Min.I (HJD)=$T_0 + E \times P + Q \times E^2 + A \times \sin[\frac{2\pi}{P_{mod}}(E - T_s)]$
T_0=HJD 2456562.2037($\pm$0.0008)
P=0.72111515($\pm$0.00000028) d
Q=$-7.24(\pm1.05) \times 10^{-11}$ d
A_{mod}=0.0054($\pm$0.0010) d
$P_{mod} = 11327(\pm570)$ days=31.0($\pm$1.4) years
$T_s = 12470(\pm400)$ epochs

Table 5. Geometrical and Physical Parameters for EU Peg

Parameter	Primary	Secondary
T (K)	8730 ± 270^a	5064 ± 12
T_0(HJD)	2456562.2117($\pm$0.0002)	
P_0(day)	0.72113316($\pm$0.00000192)	
i (deg)	81.3 ± 0.8	
$q = M_2/M_1$	0.3105 ± 0.0011	
$\Omega_{1,2}$	2.8713 ± 0.0031	2.5938 ± 0.0041
$L_i/(L_1 + L_2)_B$	0.9829 ± 0.0055	0.0171
$L_i/(L_1 + L_2)_V$	0.9650 ± 0.0057	0.0350
$L_i/(L_1 + L_2)_{R_c}$	0.9474 ± 0.0065	0.0526
$L_i/(L_1 + L_2)_{I_c}$	0.9269 ± 0.0087	0.0731
$\ell_{3B}(\%)$	0.25 ± 0.04	
$\ell_{3V}(\%)$	0.39 ± 0.04	
$\ell_{3R_c}(\%)$	0.68 ± 0.05	
$\ell_{3I_c}(\%)$	1.02 ± 0.07	
r(pole)	0.3954 ± 0.0022	0.2429 ± 0.0018
r(point)	0.4398 ± 0.0035	0.2875 ± 0.0087
r(side)	0.4134 ± 0.0034	0.2506 ± 0.0020
r(back)	0.4256 ± 0.0025	0.2714 ± 0.0023
$< r >^b$	0.4185 ± 0.0032	0.2631 ± 0.0037
a ($R_\odot$)	5.09 ± 0.20	
M ($M_\odot$)	2.60 ± 0.30^c	0.81 ± 0.10
R ($R_\odot$)	2.13 ± 0.02	1.34 ± 0.02
L ($L_\odot$)	23.65 ± 0.36	1.06 ± 0.03

Notice: [a]The mean effective temperature for the more massive component is fixed from the spectral type of A3V with an uncertainty of a subtype.

[b]Bracket indicates the equal-volume radius.

[c]Based on A3V with a subtype error, the mass for the primary component (i.e., star 1) was estimated (Cox 2000).

158

Table 6. Results of the Multiple-Frequency Analysis

Band	Frequency	Amplitude	Phase	S/N	Q
	(c/d)	(mmag)	(rad)		$(\times 10^{-2}$ days)
B	$f_1 = 34.125436(3)^a$	6.55 ± 0.67	0.9784 ± 0.1025	7.927	1.52
	$f_2 = 11.182094(9)$	1.74 ± 0.67	0.5956 ± 0.3860	4.152	4.63
	$f_1 = 34.183144(3)$	4.47 ± 0.53	0.8968 ± 0.1176	13.365	1.52
V	$f_2 = 6.455440(5)$	2.17 ± 0.53	0.9837 ± 0.2423	12.436	8.03
	$f_3 = 12.904531(7)$	1.54 ± 0.53	0.4752 ± 0.3414	6.154	4.01
	$f_1 = 34.118590(1)$	4.82 ± 0.44	0.4875 ± 0.0918	9.264	1.52
B+V	$f_2 = 6.393003(3)$	1.97 ± 0.44	0.6553 ± 0.2246	8.378	8.11
	$f_3 = 13.645320(4)$	1.42 ± 0.44	0.1436 ± 0.3116	5.979	3.80

Notice: [a]The number in brackets are the errors in the last decimal place.

Optical flare events on the RS Canum Venaticorum star UX Arietis

Dong-Tao Cao and Sheng-Hong Gu

Yunnan Observatories, Chinese Academy of Sciences, Kunming 650216, China; *dtcao@ynao.ac.cn, shenghonggu@ynao.ac.cn*
Key Laboratory for the Structure and Evolution of Celestial Objects, Chinese Academy of Sciences, Kunming 650216, China
University of Chinese Academy of Sciences, Beijing 100049, China

Abstract Based on long-term high-resolution spectroscopic observations obtained during five observing runs from 2001 to 2004, we study optical flare events and chromospheric activity variability of the very active RS CVn star UX Ari. By means of the spectral subtraction technique, several optical chromospheric activity indicators (including the He I D_3, Na I D_1, D_2 doublet, Hα and Ca II IRT lines) covered in our echelle spectra were analyzed. Four large optical flare events were detected on UX Ari during our observations, which show prominent He I D_3 line emission together with great enhancement in emission of the Hα and Ca II IRT lines and strong filled-in or emission reversal features in the Na I D_1, D_2 doublet lines. The newly detected flares are much more energetic than previous discoveries, especially for the flare identified during the 2002 December observing run. Optical flare events on UX Ari are more likely to be observed around two quadratures of the system, except for our optical flares detected during the 2004 November observing run. Moreover, we have found rotational modulation of chromospheric activity in the Hα and Ca II IRT lines, which suggests the presence of chromospherically active longitudes over the surface of UX Ari. The change in chromospherically active longitudes among our observing runs, as well as the variation in chromospheric activity level from 2001 to 2004, indicates a long-term evolution of active regions.

Key words: stars: activity — stars: chromospheres — stars: binaries: spectroscopic — stars: flare — stars: individual (UX Ari)

1 INTRODUCTION

A broad range of solar-type active phenomena, such as starspots, plages, prominences and flares, has been widely observed in cool stars. It is believed that all of these phenomena arise from a powerful magnetic dynamo process generated by the coupling between convection and differential rotation. Among these active phenomena, flares are very violent and abrupt events in the atmosphere, which are generally thought to result from the release of massive magnetic energy stored in the corona through reconnection (Haisch et al. 1991; Schrijver & Zwaan 2000). Flares have been observed in many types of cool stars at almost all wavelengths (Pettersen 1989; Garcia Alvarez 2000; Schrijver &

Zwaan 2000), including both young and evolved stars, singles and members of close binary systems.

UX Ari (HD 21242, BD+28°532) is a non-eclipsing spectroscopic system, consisting of a K0 IV primary and a G5 V secondary, in an almost circular orbit with a period of about 6.44 d (Carlos & Popper 1971). According to previously published radial velocities together with their highly accurate ones, however, Duemmler & Aarum (2001) concluded that a third star just happens to lie in the same line of sight and therefore contributes a set of weak lines in the spectra of UX Ari. Due to the brightness of the system ($V = 6.37$, Ducati 2002) and the K0 IV component showing a very high level of magnetic activity, UX Ari has attracted much attention in nearly all wavelength regions during recent years.

160

As a member of RS CVn-type stars, UX Ari always shows significant photometric variability caused by starspot activity (e.g. Raveendran & Mohin 1995; Aarum Ulvås & Henry 2003; Rosario et al. 2007, 2008; Ekmekci 2010). Long-term photometric observations have been analyzed by Aarum Ulvås & Henry (2003), Rosario et al. (2007) and Ekmekci (2010). Using a Doppler imaging technique, Vogt & Hatzes (1991) and Gu et al. (2004, 2005) derived the spot distribution on the surface of UX Ari and discussed possible spot evolution.

Strong chromospheric activity of UX Ari has been exhibited by continuous Hα line emission above the continuum, as well as Ca II H and K and Ca II IRT line core emission in the optical spectral range (Carlos & Popper 1971; Bopp & Talcott 1978; Nations & Ramsey 1986; Huenemoerder et al. 1989; Frasca & Catalano 1994; Raveendran & Mohin 1995; Montes et al. 1995a,b,c, 1996, 2000; Gu et al. 2002; Aarum Ulvås & Engvold 2003). It is well accepted that the chromospheric emission is mainly attributed to the K0 IV primary star of the system. Bopp & Talcott (1978) found that the equivalent width (EW) of Hα was correlated to the orbital phase. Moreover, an orbital phase modulation of chromospheric emission in the Hα and Ca II IRT lines was also found by Gu et al. (2002). Aarum Ulvås & Engvold (2003) applied a technique for separation of individual components in composite spectra of UX Ari, and concluded that the active longitudes seem to be separated by about 180° on the surface of the primary star and the secondary is also subject to some chromospheric activity. A small amount of chromospheric activity from the G5 V secondary was also found by Huenemoerder et al. (1989).

Flares on UX Ari have been reported several times over a wide range of wavelength regions from X-ray to radio wavelengths (e.g. Simon et al. 1980; Elias et al. 1995; Montes et al. 1996; Franciosini et al. 2001; Gu et al. 2002; Richards et al. 2003; Aarum Ulvås & Engvold 2003; Catalano et al. 2003). According to *International Ultraviolet Explorer* (*IUE*) spectra, for example, Simon et al. (1980) found a very large ultraviolet (UV) flare on UX Ari and proposed a scenario to explain activity in major long-lived RS CVn flares. In the optical spectral lines, Montes et al. (1996) detected a strong flare through the presence of prominent He I D$_3$ line emission together with a great enhancement of the Hα line emission and larger filled-in cores of the Na I D$_1$, D$_2$ doublet lines. Another flare-like event was observed with several frequently used optical chromospheric activity indicators (including the He I D$_3$, Na I D$_1$, D$_2$ doublet, Hα and Ca II IRT lines) by Gu et al. (2002), which happened at a very similar orbital phase as the flare detected by Montes et al. (1996). Aarum Ulvås & Engvold (2003) attributed stronger core emission in the Ca II λ8662 line to an optical flare-like event. Moreover, a simultaneous Hα and radio flare on UX Ari was reported by Catalano et al. (2003).

In this paper, we present the study of optical flares and the variation of chromospheric activity on UX Ari, based on long-term high-resolution spectroscopic observations of the Ca II IRT, Hα, Na I D$_1$, D$_2$ doublet and He I D$_3$ lines from 2001 to 2004. The details of our observations and data reduction are given in Section 2, and the procedure for the spectral subtraction of chromospheric activity indicators and results are described in Section 3. In Section 4, optical flares detected during our observations and the variation of chromospheric activity are discussed in detail. Finally, we give a summary of the present study in Section 5.

2 OBSERVATIONS AND DATA REDUCTION

The observations of UX Ari were carried out with the Coudé echelle spectrograph (Zhao & Li 2001) mounted on the 2.16-m telescope at Xinglong Station, administered by National Astronomical Observatories, Chinese Academy of Sciences, during five observing runs from 2001 to 2004. The echelle spectra were recorded on a 1024×1024-pixel Tektronix CCD detector, and the spectrograph has a resolving power of about 37 000. The reciprocal dispersions are 0.082 Å/pixel for the Na I D$_1$, D$_2$ doublet and He I D$_3$ spectral region, 0.091 Å/pixel for the Hα spectral region, 0.119 Å/pixel for the Ca II λλ8498, 8542 spectral region and 0.120 Å/pixel for the Ca II λ8662 spectral region. The corresponding spectral resolution determined as the full width at half-maximum (FWHM) of the arc comparison lines is 0.152, 0.167, 0.211 and 0.216 Å, respectively. We acquired a total of 51 spectra of UX Ari during our observations. As well as the target star, some rapidly rotating early-type stars and slowly rotating inactive stars with the same spectral type and luminosity class as each component of UX Ari were also observed. The spectra of early-type stars were used as telluric templates whereas the inactive stars were used as reference stars in the spectral subtraction technique.

We give the observing log of UX Ari in Table 1, which includes observing date, heliocentric Julian date (HJD), orbital phase and exposure time. The orbital phases are calculated with the ephemeris

$$\text{HJD} = 2\,450\,640.39272 + 6.4372703^{\text{d}} \times E, \quad (1)$$

from Duemmler & Aarum (2001), where the epoch corresponds to a conjunction with the K0 IV primary component in front.

Table 1 Observing Log of UX Ari

Date	HJD	Phase	Exp.time	Date	HJD	Phase	Exp.time
	(2 455 000+)		(s)		(2 455 000+)		(s)
2001 Nov 23	2237.0773	0.0375	1800	2004 Feb 06	3042.0838	0.0915	900
2001 Nov 24	2238.0644	0.1909	2700	2004 Feb 06	3042.0946	0.0932	900
2001 Nov 24	2238.0988	0.1962	2700	2004 Feb 07	3043.1082	0.2507	900
2001 Nov 25	2239.0654	0.3464	2700	2004 Feb 07	3043.1189	0.2523	900
2001 Nov 25	2239.2790	0.3796	2700	2004 Feb 08	3044.0566	0.3980	900
2001 Nov 26	2240.0352	0.4970	2400	2004 Feb 08	3044.0675	0.3997	900
2001 Nov 26	2240.2705	0.5336	2400	2004 Feb 09	3045.0710	0.5556	900
2001 Nov 27	2241.0063	0.6479	1800	2004 Feb 09	3045.0817	0.5572	900
2001 Nov 29	2243.0426	0.9642	2400	2004 Nov 20	3330.2108	0.8507	1200
2001 Dec 01	2245.0311	0.2731	1800	2004 Nov 20	3330.2257	0.8530	1200
2002 Dec 13	2622.1013	0.8492	1800	2004 Nov 21	3331.1819	0.0016	1500
2002 Dec 16	2625.0445	0.3064	1800	2004 Nov 21	3331.2004	0.0045	1500
2002 Dec 16	2625.0659	0.3097	1800	2004 Nov 22	3332.3545	0.1837	1800
2002 Dec 16	2625.1328	0.3201	3600	2004 Nov 23	3333.2037	0.3157	1800
2002 Dec 17	2626.0605	0.4643	2400	2004 Nov 23	3333.2260	0.3191	1800
2002 Dec 17	2626.2233	0.4895	1800	2004 Nov 25	3335.0840	0.6078	2400
2003 Nov 08	2952.1339	0.1182	1200	2004 Nov 25	3335.1200	0.6134	3600
2003 Nov 08	2952.1481	0.1204	1200	2004 Nov 25	3335.1633	0.6201	3600
2003 Nov 10	2954.2356	0.4447	1200	2004 Nov 26	3336.1836	0.7786	1800
2003 Nov 10	2954.2500	0.4470	1200	2004 Nov 26	3336.2049	0.7819	1800
2004 Feb 03	3039.0619	0.6221	1200	2004 Nov 27	3337.1856	0.9342	1200
2004 Feb 03	3039.0768	0.6244	1200	2004 Nov 27	3337.1985	0.9362	900
2004 Feb 04	3040.0937	0.7824	1800	2004 Nov 27	3337.2095	0.9379	900
2004 Feb 04	3040.1165	0.7859	1800	2004 Nov 28	3338.1798	0.0887	2400
2004 Feb 05	3041.0544	0.9316	900	2004 Nov 29	3339.2381	0.2531	2400
2004 Feb 05	3041.0678	0.9337	900				

The spectral reduction was performed with the IRAF[1] package following the standard procedures (see Cao & Gu 2015). The wavelength calibration was obtained using the spectra of a Th-Ar lamp, and all spectra were normalized using a low-order polynomial fit to the observed continuum. Finally, for some of our observations, we eliminated the telluric lines in the wavelength regions of interest with the spectra of two rapidly rotating early-type stars, HR 8858 (B5 V, $v \sin i = 332 \, \text{km s}^{-1}$) and HR 1051 (B8 V, $v \sin i = 334 \, \text{km s}^{-1}$). Examples of removing the telluric lines in different spectral regions can be found in Gu et al. (2002). In Figure 1, we display examples of the normalized Ca II IRT, Hα, Na I D$_1$, D$_2$ doublet and He I D$_3$ line profiles of UX Ari obtained during our observations. The orbital phase and observing date are also marked in the figure.

---

[1] IRAF is distributed by the National Optical Astronomy Observatories, which is operated by the Association of Universities for Research in Astronomy (AURA), Inc., under cooperative agreement with the National Science Foundation.

3 SPECTRAL SUBTRACTION AND RESULTS

Chromospheric activity indicators Ca II IRT, Hα, Na I D$_1$, D$_2$ doublet and He I D$_3$ lines, formed at different atmospheric heights, were covered in our echelle spectra. As shown in Figure 1, clear central emission features appear in the cores of the Ca II IRT absorption line profiles. The similar behavior in the Ca II IRT lines has also been found in several other stars with chromospheric activity (Berdyugina et al. 1999; Montes et al. 2000; López-Santiago et al. 2003; Cao & Gu 2014, 2015). Moreover, we can see that the Hα line is in emission above the continuum, similar to very active RS CVn stars II Peg (Gu & Tan 2003; Frasca et al. 2008a) and V711 Tau (García-Alvarez et al. 2003; Cao & Gu 2015). The Na I D$_1$, D$_2$ doublet lines are characterized by deep absorption, and exhibit self-reversal emission in the line core for some of our observations when the usual optical chromospheric flare diagnostic He I D$_3$ line shows strong emission features, such as the observations at phases 0.3064, 0.3097

and 0.3201 on 2002 December 16 (see Fig. 4). The He I D_3 line emission means that there might be strong optical flare events during our observations.

We obtain the chromospheric contribution in these activity indicators with the spectral subtraction technique by using the popular program STARMOD (Barden 1985; Montes et al. 1995c, 1997, 2000). This technique has been widely and successfully used for chromospheric activity studies (e.g., Gunn & Doyle 1997; Gunn et al. 1997; Montes et al. 1995c, 1997, 2000; Gu et al. 2002; Frasca et al. 2008a; Zhang & Gu 2008; Cao & Gu 2012, 2014, 2015; Zhang et al. 2016). Although a spectral line from the third star has been found in the UX Ari spectrum, the contribution of the lines is very weak. Thus, we use two stars, HR 3351 (K0 IV) and HR 3309 (G5 V), as reference stars for the primary and secondary of the system respectively in construction of the synthesized spectrum. The rotational velocity ($v \sin i$) values of $39\,\mathrm{km\,s^{-1}}$ for the primary and $7.5\,\mathrm{km\,s^{-1}}$ for the secondary are taken from Duemmler & Aarum (2001), and the adopted intensity weight ratios, derived from high S/N spectra at phases where the two components were well separated, are 0.69/0.31 for the Na I D_1, D_2 doublet and He I D_3 spectral region, 0.74/0.26 for the Hα spectral region, 0.76/0.24 for the Ca II $\lambda\lambda8498$, 8542 spectral region and 0.77/0.23 for the Ca II $\lambda8662$ spectral region. Consequently, the synthesized spectra are constructed by broadening and weighting the reference spectra to the above values, and shifting along the radial-velocity axis. Finally, the subtracted spectra are calculated for UX Ari. Examples of spectral subtraction in the Ca II IRT, Hα, Na I D_1, D_2 doublet and He I D_3 line regions are also presented in Figure 1. The synthesized spectra match the observational ones quite well, except for the Na I D_1, D_2 doublet lines. Because the Na I D_1, D_2 doublet lines are more sensitive to the effective temperature, a slight temperature difference between the UX Ari components and reference stars can produce significant changes in the wings of the line profiles (see Montes et al. 1997).

After applying the spectral subtraction technique, we can see that the Ca II IRT, Hα and Na I D_1, D_2 doublet lines show strong excess emission in the subtraction and the emission is mainly associated with the primary star of the system, which supports earlier results that the K0 IV star is very active in the UX Ari system. Moreover, it is also seen that some evidence of very weak emission from the G5 V star is present in the Ca II IRT subtraction and a small bump associated with the secondary is superimposed on the wing of the main Hα excess emission profile, at phases where the two components are well separated, which suggests that the secondary is also ac-

tive, but less active than the primary star. This is consistent with the weak emission of the G5 V star in the Ca II H line found by Huenemoerder et al. (1989) and in the Ca II K line derived by Aarum Ulvås & Engvold (2003). Moreover, the activity of the G5 V star is also in good agreement with the existence of starspots on this component found by Ekmekci (2010) and the results of *IUE* observations derived by Ekmekçi (2010). Unlike optical chromospheric activity lines, Ekmekçi (2010) found that the activity contribution of the G5 V star in the UV Mg II h and k lines can be up to 20% of the system.

The EWs of the excess emission in the He I D_3, Hα and Ca II IRT lines are measured for the subtracted spectra with the IRAF/SPLOT task, following the methods described in our previous papers (Cao & Gu 2014, 2015), and are listed in Table 2 along with their errors.

In Table 2, we also give the ratio of excess emission, $\mathrm{EW_{8542}/EW_{8498}}$. The ratios are in the range of 1–2, which indicate that Ca II IRT emission arises from plage-like regions, consistent with the values found for several other chromospherically active stars (e.g., Montes et al. 2000; Gu et al. 2002; López-Santiago et al. 2003; Zhang & Gu 2008; Gálvez et al. 2009; Cao & Gu 2014, 2015; Zhang et al. 2016).

Finally, the observations of each observing run are grouped together to analyze the possible rotational modulation of chromospheric activity in UX Ari. We plot the EWs of Hα and Ca II IRT excess emission as a function of orbital phase in Figure 2.

4 DISCUSSION

4.1 Optical Flares

4.1.1 The behavior of chromospheric activity indicators during flares

Four optical flare events were detected during our long-term observations from 2001 to 2004, which suggest that UX Ari is a star with a high flaring rate. When flares happen, the He I D_3 line shows an obvious emission feature above the continuum due to its very high excitation potential, which is very important evidence in support of the occurrence of an optical flare in the Sun (Zirin 1988) and in very active stars, such as RS CVn-type systems II Peg (Huenemoerder & Ramsey 1987; Montes et al. 1997; Berdyugina et al. 1999; Gu & Tan 2003; Frasca et al. 2008a), V711 Tau (García-Alvarez et al. 2003; Cao & Gu 2015), DM UMa (Zhang et al. 2016) and SZ Psc (Cao et al., paper in preparation), and young single active stars LQ Hya (Montes et al. 1999) and PW And (López-Santiago et al. 2003). For UX Ari, the He I D_3 line has

Table 2 Measurements for Excess Emission of the He I D$_3$, Hα and Ca II IRT Lines in the Subtracted Spectra

| Phase	EW$_{\text{He I D}_3}$ (Å)	EW$_{\text{H}\alpha}$ (Å)	EW$_{\lambda 8498}$ (Å)	EW$_{\lambda 8542}$ (Å)	EW$_{\lambda 8662}$ (Å)	EW$_{8542}$/EW$_{8498}$
			2001 Nov–Dec			
0.0375		1.544±0.005	0.667±0.011	1.083±0.018	0.910±0.007	1.624
0.1909		3.570±0.018	0.830±0.005	1.379±0.003	1.147±0.012	1.661
0.1962		3.463±0.016	0.833±0.012	1.360±0.011	1.142±0.013	1.633
0.3464		1.401±0.004	0.761±0.003	1.176±0.004	1.099±0.016	1.545
0.3796		1.309±0.014	0.734±0.010	1.197±0.010	1.103±0.013	1.631
0.4970		1.305±0.009	0.716±0.008	1.109±0.014	0.964±0.004	1.549
0.5336		1.426±0.013	0.756±0.012	1.223±0.011	1.032±0.016	1.618
0.6479		1.573±0.016	0.721±0.007	1.054±0.021	0.971±0.003	1.462
0.9642		1.628±0.010	0.664±0.011	1.039±0.010	0.924±0.017	1.565
0.2731	0.034±0.007	2.509±0.008	0.873±0.010	1.343±0.014	1.149±0.016	1.538
			2002 Dec			
0.8492		2.333±0.016	0.670±0.001	1.156±0.012	1.085±0.010	1.725
0.3064	0.116±0.004	4.509±0.017	1.186±0.014	1.734±0.017	1.612±0.007	1.462
0.3097	0.115±0.006	4.294±0.008	1.164±0.019	1.727±0.015	1.590±0.016	1.484
0.3201	0.110±0.010	4.253±0.007	1.147±0.016	1.729±0.010	1.575±0.010	1.507
0.4643		2.717±0.008	0.887±0.018	1.348±0.009	1.193±0.013	1.520
0.4895		2.781±0.009	0.880±0.007	1.373±0.013	1.205±0.009	1.560
			2003 Nov			
0.1182		2.020±0.014	0.686±0.010	1.123±0.015	1.106±0.010	1.637
0.1204		2.016±0.010	0.697±0.011	1.119±0.007	1.106±0.016	1.605
0.4447		2.230±0.012	0.798±0.014	1.324±0.020	1.270±0.020	1.659
0.4470		2.219±0.007	0.802±0.006	1.321±0.011	1.243±0.016	1.647
			2004 Feb			
0.6221		2.455±0.008	0.752±0.008	1.399±0.015	1.159±0.015	1.860
0.6244		2.428±0.009	0.744±0.008	1.362±0.008	1.155±0.008	1.831
0.7824		1.905±0.004	0.639±0.010	1.176±0.014	0.991±0.014	1.840
0.7859		1.859±0.012	0.646±0.005	1.167±0.011	0.997±0.011	1.807
0.9316		1.596±0.010	0.574±0.011	1.057±0.016	0.931±0.016	1.841
0.9337		1.601±0.011	0.574±0.003	1.059±0.018	0.940±0.018	1.845
0.0915		1.654±0.003	0.588±0.008	1.055±0.007	0.977±0.007	1.794
0.0932		1.673±0.003	0.592±0.006	1.038±0.010	0.985±0.010	1.753
0.2507		1.688±0.011	0.708±0.018	1.162±0.005	1.029±0.005	1.641
0.2523		1.662±0.013	0.691±0.008	1.195±0.010	1.000±0.010	1.729
0.3980		1.480±0.009	0.742±0.003	1.217±0.017	1.106±0.017	1.640
0.3997		1.481±0.005	0.754±0.002	1.192±0.007	1.127±0.007	1.581
0.5556		2.503±0.010	0.796±0.010	1.335±0.005	1.217±0.005	1.677
0.5572		2.495±0.010	0.804±0.011	1.338±0.011	1.257±0.011	1.664
			2004 Nov			
0.8507		2.398±0.006	0.788±0.004	1.305±0.010	1.202±0.010	1.656
0.8530		2.286±0.013	0.805±0.004	1.310±0.011	1.120±0.011	1.627
0.0016		2.148±0.013	0.724±0.012	1.252±0.023	1.091±0.023	1.729
0.0045		2.117±0.011	0.746±0.005	1.260±0.015	1.117±0.015	1.689
0.1837		1.623±0.006	0.710±0.009	1.232±0.012	1.076±0.012	1.735
0.3157		2.017±0.007	0.782±0.013	1.309±0.015	1.150±0.015	1.674
0.3191		2.027±0.003	0.778±0.008	1.315±0.007	1.128±0.007	1.690
0.6078	0.058±0.010	2.653±0.008	0.800±0.011	1.323±0.013	1.187±0.013	1.654
0.6134	0.055±0.011	2.633±0.018	0.812±0.010	1.319±0.012	1.244±0.012	1.624
0.6201	0.041±0.009	2.632±0.018	0.808±0.006	1.320±0.011	1.225±0.011	1.634
0.7786		2.268±0.010	0.806±0.012	1.316±0.018	1.100±0.018	1.633
0.7819		2.246±0.006	0.811±0.005	1.312±0.012	1.140±0.012	1.618
0.9342	0.083±0.006	2.643±0.015	0.875±0.004	1.414±0.006	1.366±0.006	1.616
0.9362	0.081±0.013	2.677±0.007	0.876±0.011	1.413±0.015	1.336±0.015	1.613
0.9379	0.086±0.009	2.652±0.011	0.872±0.009	1.416±0.008	1.355±0.008	1.624
0.0887		1.976±0.003	0.751±0.010	1.214±0.010	1.139±0.010	1.617
0.2531		2.214±0.005	0.760±0.008	1.269±0.019	1.173±0.019	1.670
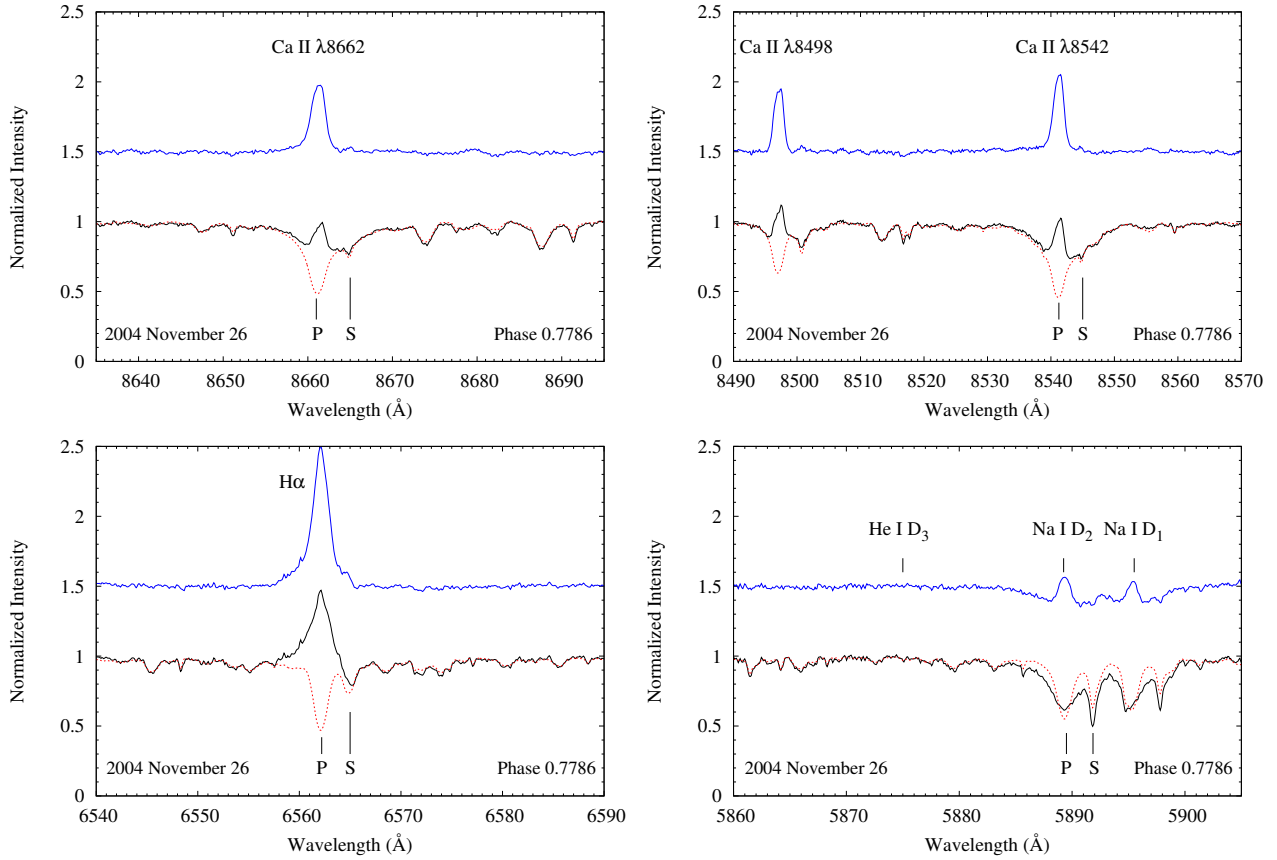
Fig. 1 Examples of the observed, synthesized and subtracted spectra for the Ca II IRT ($\lambda 8662$, $\lambda 8542$ and $\lambda 8498$), Hα, Na I D$_1$, D$_2$ doublet and He I D$_3$ line spectral regions. For each panel, the lower solid line is the observed spectrum, the dotted line represents the synthesized spectrum and the upper spectrum is the subtracted one, shifted for better display. "P" and "S" indicate the primary and secondary components of the system, respectively.

also been observed in emission during flares by Montes et al. (1996) and Gu et al. (2002).

The first optical flare was observed at phase 0.2731 on 2001 December 01. We plot the observed and subtracted Hα, Na I D$_1$, D$_2$ doublet and He I D$_3$ lines obtained on 2001 November 24 and December 01 in Figure 3, where the He I D$_3$ line emission, together with stronger Hα emission and the larger filled-in features of the Na I D$_1$, D$_2$ doublet lines, which support the presence of an optical flare on December 01. The Ca II IRT line excess emission also has a strong increase during the flare (see Table 2). In addition, for observations at close phases 0.1962 and 0.1969 on November 24 (about one orbital cycle before the flare), we find that the Hα lines have broad wings and therefore result in large EWs, and the He I D$_3$ lines also show a very weak emission feature in comparison to the synthesized spectra, which are probably due to a flare precursor (Byrne 1983), such as a preflare brightening, and indicate the presence of a strong nearby active region. Broad wings could be interpreted

as arising from large-scale mass motions produced in the chromosphere.

The second optical flare was detected during our 2002 December observing run. From Figure 4, showing the observed and subtracted Hα, Na I D$_1$, D$_2$ doublet and He I D$_3$ lines during this observing run, it can be found that the Hα lines exhibit a remarkable enhancement in emission on December 16 with respect to the other two night observations, and the He I D$_3$ lines show strong excess emission features during this night and weak emission that is still present on the following night. Moreover, the Na I D$_1$, D$_2$ doublet lines exhibit a very obvious emission reversal feature in the line cores on December 16, similar to the finding during the flare maximum on V711 Tau (García-Alvarez et al. 2003), and the Ca II IRT line excess emission also has a sudden dramatic increase (see Table 2). Therefore, all these related facts indicate that we observed a more energetic optical flare on December 16 and the observations on December 17 were at the gradual decay phase of the flare.
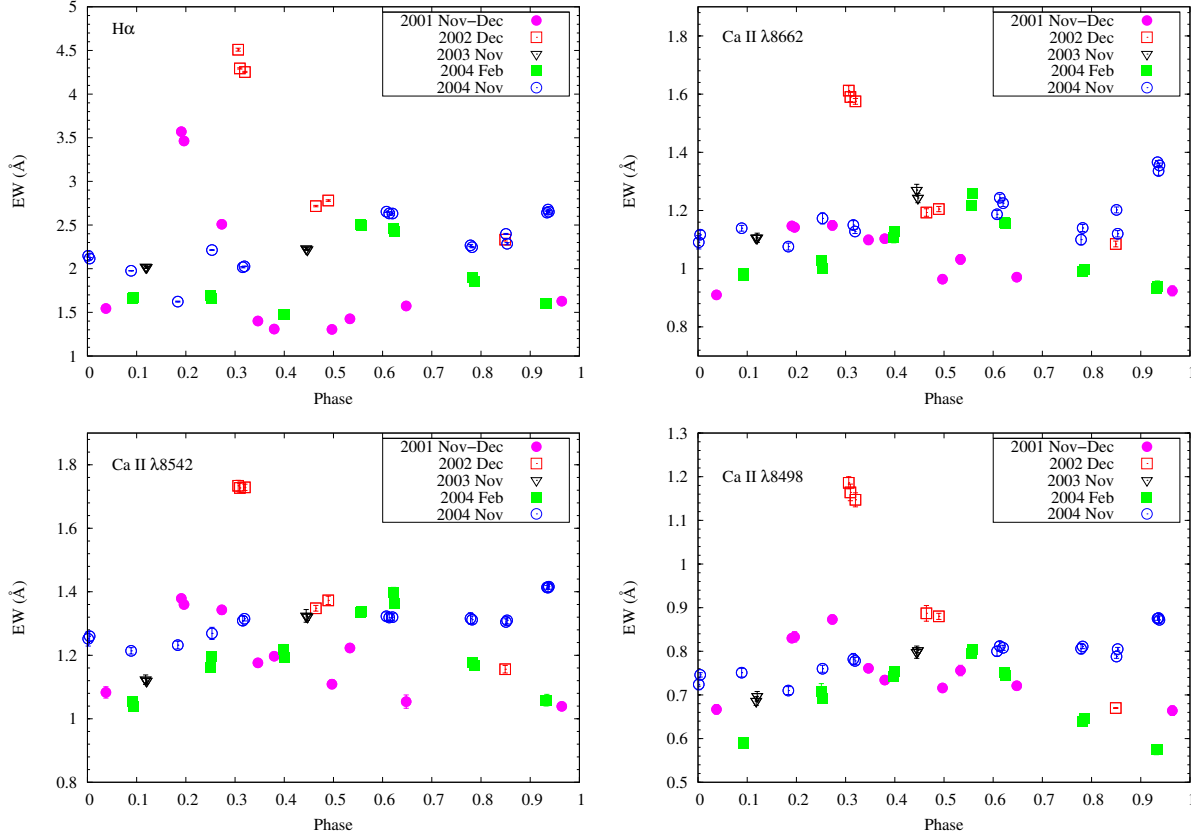
Fig. 2 EWs of the excess emission versus orbital phase for Hα and Ca II IRT lines. The labels identifying each observing run and chromospheric activity indicator are marked in the corresponding plot.

This also means that the flare has a time scale longer than one day (24 h). According to the EWs of the excess emission (see Table 2), the observation at phase 0.3064 on December 16 corresponds to the maximum Hα emission during the flare.

The third optical flare and the fourth one were observed during the 2004 November observing run. From Figure 5, showing the observed and subtracted Hα, Na I D$_1$, D$_2$ doublet and He I D$_3$ lines taken in several consecutive observing nights from 2004 November 23 to 28, we can see that the Hα line emissions are much stronger on November 25 and 27 than the other observations (also see Table 2), and the He I D$_3$ lines show an emission feature during these two observing nights. Correspondingly, strong excess emission in the Na I D$_1$, D$_2$ doublet lines is seen in the subtracted spectra and the emission reversal feature appears in the absorption line core on November 27. The Ca II IRT line excess emission also has a strong increase (see Table 2) during these two observing nights. From these pieces of evidence, therefore, we can infer that two optical flares happened on November 25 and 27, respectively, and the latter was

much more energetic. The observations at phase 0.6078 on November 25 and at phase 0.9362 on November 27 correspond to the Hα maximum emission of two flares (see Table 2).

4.1.2 Flare energy released in the Hα line

Calculating the stellar continuum flux $F_{\text{H}\alpha}$ (erg cm^{-2} s^{-1} Å^{-1}) in the Hα line region as a function of the color index $B - V$ (0.88, Aarum Ulvås & Henry 2003) based on the calibration

$$\log F_{\text{H}\alpha} = [7.538 - 1.081(B - V)] \pm 0.33$$
$$0.0 \leq (B - V) \leq 1.4 \qquad (2)$$

of Hall (1996), and then converting the EWs into the absolute surface flux F_S (erg cm^{-2} s^{-1}) through the relation $F_S = F_{\text{H}\alpha} \times \text{EW}_{\text{H}\alpha}$, we have estimated the flare energy (luminosity) E (erg s^{-1}) in the observed Hα maximum emission using the formula $E = 4\pi R_*^2 F_S$. The radius $R_* = 5.78 \, R_\odot$ of the K0 IV primary component (Duemmler & Aarum 2001) is used for the calculation. Because the K0 IV star is very active in the UX Ari system and the flare enhancements are all associated with
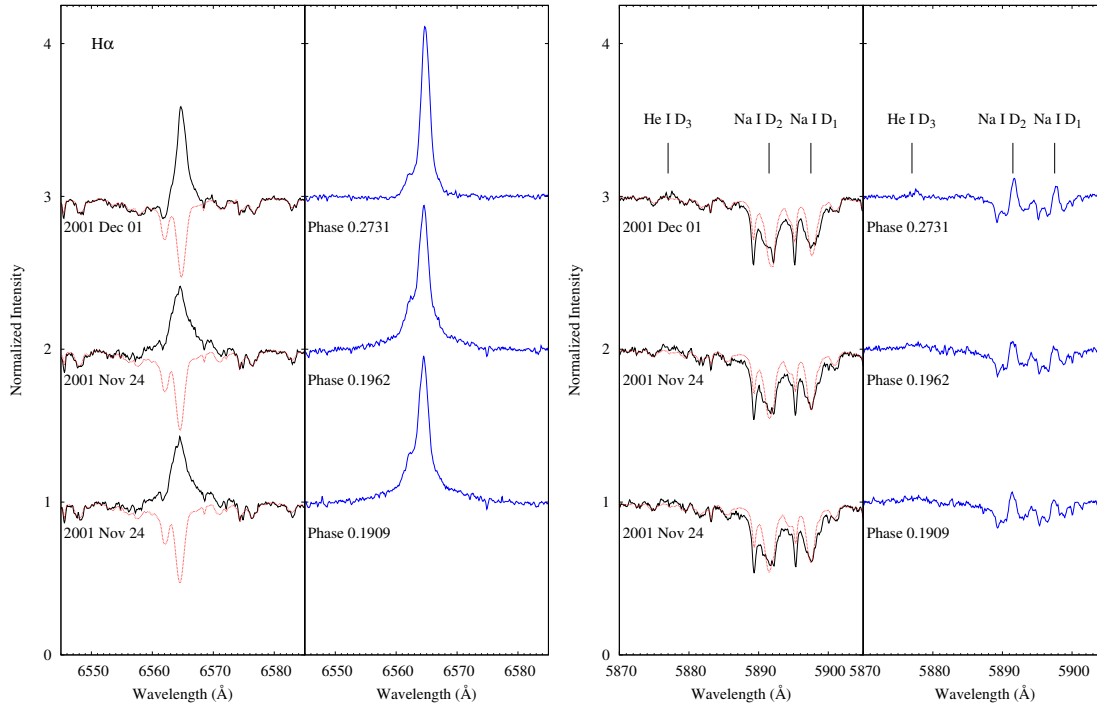
Fig. 3 Hα, Na I D$_1$, D$_2$ doublet and He I D$_3$ lines obtained on 2001 November 24 and December 01. The observed spectra (*solid lines*) and the synthesized ones (*dotted lines*) are plotted in the left part of the panels and the subtracted spectra in the right part. The orbital phase and observing date are also marked in each panel.

this component (see Figs. 3–5), we have assumed that all optical flares happened on the primary star. Moreover, we have corrected the EWs to the total continuum before they are converted to the absolute flux at the stellar surface. The results are $E_1 = 2.66 \times 10^{31}\,\mathrm{erg\,s^{-1}}$ for the first optical flare, $E_2 = 4.78 \times 10^{31}\,\mathrm{erg\,s^{-1}}$ for the second one, $E_3 = 2.81 \times 10^{31}\,\mathrm{erg\,s^{-1}}$ for the third one and $E_4 = 2.84 \times 10^{31}\,\mathrm{erg\,s^{-1}}$ for the fourth one.

The values for energy released in the Hα line during flares have a similar order of magnitude to the ones for UX Ari estimated by Montes et al. (1996) and Gu et al. (2002), and for other RS CVn-type stars such as V711 Tau (García-Alvarez et al. 2003; Cao & Gu 2015) and HK Lac (Catalano & Frasca 1994). Comparing with the values of $1.7 \times 10^{31}\,\mathrm{erg\,s^{-1}}$ derived by Montes et al. (1996) and $2.1 \times 10^{31}\,\mathrm{erg\,s^{-1}}$ by Gu et al. (2002), the newly detected flares are much more energetic, especially for the flare observed during our 2002 December observing run. For our observations, it is difficult to estimate the flare duration from the initial outburst to the end, but we can give a rough time scale of 24 hours for our second optical flare. Thus, total energy emitted in the Hα line can be up to the order of magnitude of 10^{36} erg for this flare, which is much stronger than the largest observed solar flare with energy up to 10^{33} erg (Schrijver

et al. 2012). For RS CVn-type systems, there are observations showing that the flare energy can be up to 10^{38} erg (Doyle et al. 1992; Foing et al. 1994).

4.1.3 Flare location

We have noticed that both optical flare events detected on 2001 December 01 and 2002 December 16 respectively took place at close orbital phases (phases 0.2731 and 0.3064), near the first quadrature of the system. The flare observed by Montes et al. (1996) happened around phase 0.74, near second quadrature, and Gu et al. (2002) found a flare which occurred again at the close phase 0.78. A flare-like event reported by Aarum Ulvås & Engvold (2003) also took place very near the first quadrature of the system. This possibly suggests that optical flares of UX Ari are more likely to be observed around two quadratures of the system. Simon et al. (1980) proposed a speculative scenario of flares for UX Ari in which the component stars of the system have large corotating flux tubes that occasionally interact. The resulting magnetic reconnection leads to flare eruption. According to this magnetic loop model and the He I D$_3$ line formation mechanism in which the line can be seen in emission features when the emitting regions are observed off the
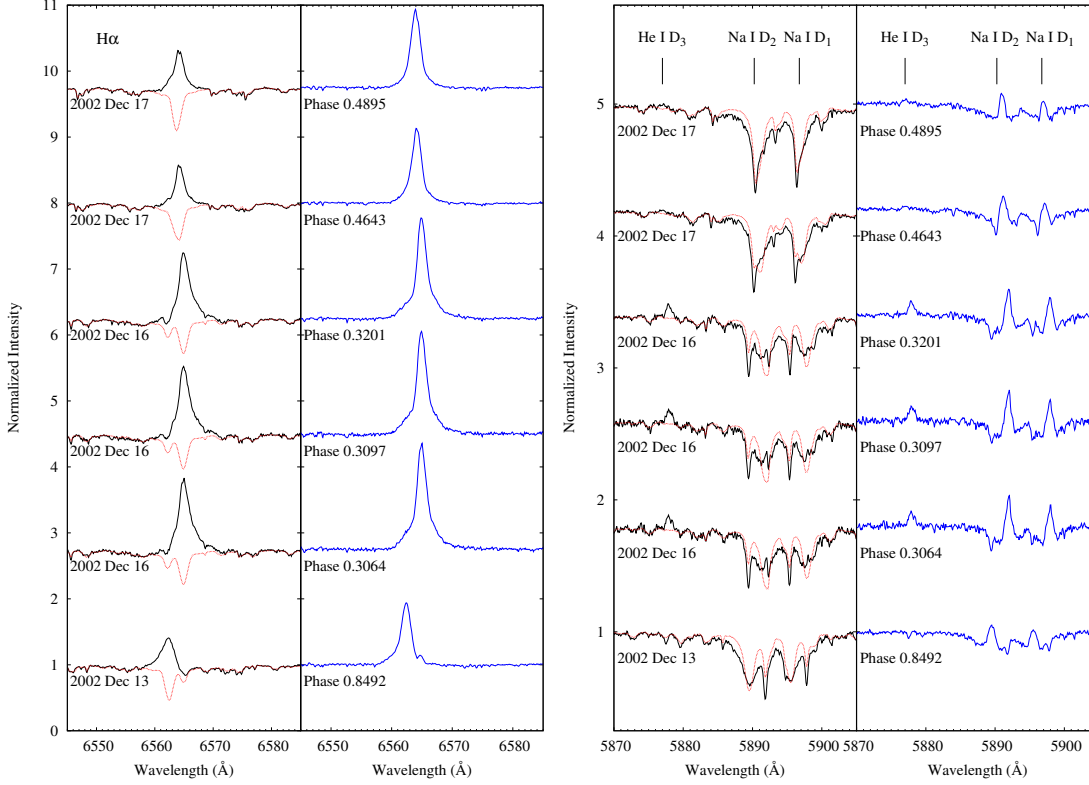
Fig. 4 Same as Fig. 3, but for spectra obtained during the 2002 observing run.

stellar limb, Montes et al. (1996) indicated that the symmetrical positions around two quadratures of the system (phases 0.25 and 0.75) are the most favorable for observing the He I D_3 line in emission due to the flare. Using the same observations of 2001 November to December, moreover, Gu et al. (2005) derived a Doppler imaging map of UX Ari and showed that there is a low-latitude spot region near the phase 0.3. Therefore, our optical flare that occurred on 2001 December 01 is probably associated with this active region in terms of spatial structure.

During the 2004 November observing run, two optical flares took place at phases 0.6078 and 0.9362, which are off the quadratures of the system. In Figure 6, we give a schematic representation of flux tube interaction between two components of UX Ari during flares. Optical flares occurred in the chromosphere near the surface of the K1 IV primary star. Taking into account that the system has an orbital inclination of about 59.2° (Duemmler & Aarum 2001), the flare at phase 0.9362 might have occurred at a high-latitude region through the interaction, otherwise it would be occulted by the K0 IV primary star. However, if the flare happened at a high-latitude region at phase 0.6078, it would be projected on the stellar disk.

Therefore, the flare at phase 0.6078 probably took place at a low-latitude region. We can also infer that both optical flares are unlikely to occur at the same active region, although they happened in the same hemisphere.

Finally, we may propose an alternative magnetic reconnection mechanism for flare eruption on UX Ari. Although the K0 IV primary star of the system does not totally fill its Roche lobe (fills about 80%, Duemmler & Aarum 2001), the mass transfer from Roche lobe overflow of the primary has been discussed by Huenemoerder et al. (1989) and Gu et al. (2002). Therefore, we believe that mass transfer is also a probable reason, which may disturb the flux tubes so as to result in magnetic reconnection, and then produce flares.

4.2 Active Longitudes and Long-Term Activity Variation

During our observations, the observing runs of 2001 November to December, 2004 February and 2004 November had better orbital phase coverage, which are favorable for analyzing the possible rotational modulation of chromospheric activity. Rotational modulation of chromospheric activity indicates that there are active lon-
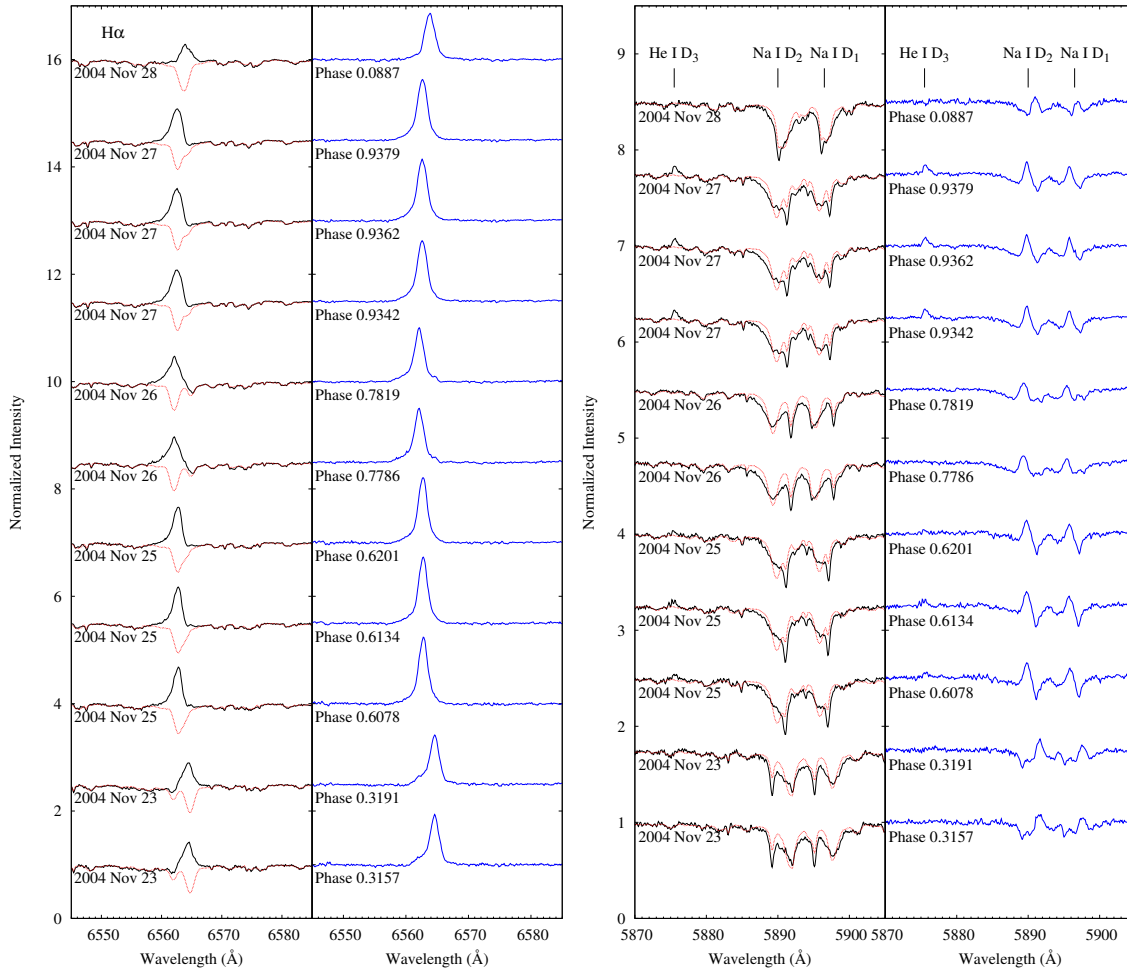
Fig. 5 Same as Fig. 3, but for the spectra obtained during several consecutive observing nights from 2004 November 23 to 28.

gitudes over the stellar surface, and has been found in many active stars based on several chromospheric diagnostics (Berdyugina et al. 1999; Gu et al. 2002; Frasca et al. 2008a,b; Zhang & Gu 2008; Cao & Gu 2014, 2015; Zhang et al. 2016). From Figure 2, it can be seen that the variation of Hα and Ca II IRT excess emission basically correlates and shows rotational modulation. For the 2001 observing run, the observations reveal extreme enhancement in chromospheric emission around the first quadrature, and an optical flare happens near here, which indicates that a strong active longitude exists. At the opposite hemisphere, Gu et al. (2002) found that the level of chromospheric activity is higher around the second quadrature in 2000. Unfortunately, we have an observational gap between phases 0.65 and 0.97. In 2004 February, the activity variation indicates one strong active longitude appears near phase 0.6, similar to what was found by Bopp & Talcott (1978). For the 2004 November observing run, there were two optical flares that occurred

in the second half of the orbital phase, and we find that the flare on November 25 took place at a phase near the chromospheric activity longitude found in the February observing run. In addition, the chromospherically active longitudes display changes among our observing runs, which indicates evolution of active regions.

As seen in Figure 2, the chromospheric activity level (especially for the Hα line) seems to be gradually increasing from 2001 to 2004. From figure 1 of Rosario et al. (2007), showing the differential V magnitudes against the observing date, we can see that the brightness of UX Ari decreased from 2001 to 2004, anti-correlated with the chromospheric activity variation found by us. This suggests that the long-term variation of chromospheric activity is spatially connected with the long-term evolution of photospheric starspot regions. A similar long-term behavior has also been found on V711 Tau (Cao & Gu 2015). An activity cycle with a long period of about 25 years on UX Ari was obtained by

Phase 0.61 Phase 0.94
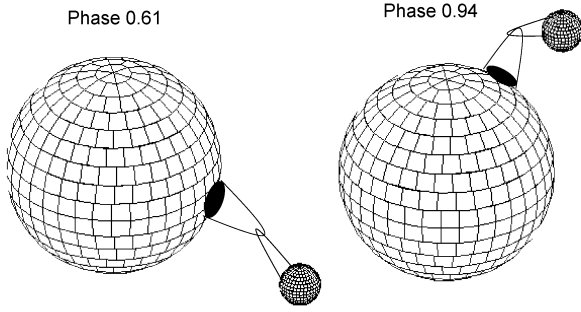
Fig. 6 Schematic representation of flux tube interaction between two components of UX Ari during flares.

Aarum Ulvås & Henry (2003) through an analysis of the long-term photometric observations, but this variation pattern was not confirmed by Rosario et al. (2007). Moreover, Buccino & Mauas (2009) found a possible chromospheric activity cycle with a period of about 7 years based on *IUE* observations from 1975 to 1996. To study the longer chromospheric activity variation in detail and infer its possible activity cycle for UX Ari, therefore, we may require more frequent observations over several years in the future.

5 CONCLUSIONS

From the above analysis of our long-term high-resolution spectroscopic observations of the very active RS CVn-type star UX Ari, the following main results are obtained:

– Strong and variable chromospheric excess emission in the Na I D_1, D_2 doublet, Hα and Ca II IRT lines confirms that UX Ari is a very active system and the chromospheric activity emission is mainly attributed to the K0 IV primary star of the system. The G5 V secondary also shows very weak emission implying less activity.

– UX Ari is a star with a high flaring rate. Four large optical flares were detected in 2001 November to December, 2002 December and 2004 November observing runs, which are demonstrated by the prominent He I D_3 line emission together with the great enhancement in emission of Hα and Ca II IRT lines and strong filled-in or emission reversal features in the Na I D_1, D_2 doublet lines. We have estimated the flare energy released in the Hα maximum emission, which is stronger than the previous discoveries, especially for the flare detected during the 2002 observing run.

– Optical flares on UX Ari are more likely to be observed around two quadratures of the system, except

for our flares detected during the 2004 November observing run. Moreover, both optical flares of 2004 are unlikely to occur at the same active region, although they happened in the same hemisphere (at phases 0.6078 and 0.9362).

– We have found rotational modulation of chromospheric activity in the Hα and Ca II IRT lines, which suggests the presence of chromospherically active longitudes over the surface of UX Ari during our observations. The chromospherically active longitudes display changes among our observing runs, and the chromospheric activity level shows a long-term variation which gradually increases from 2001 to 2004. This indicates a long-term evolution of active regions over the surface of UX Ari.

References

Aarum Ulvås, V., & Engvold, O. 2003, A&A, 402, 1043

Aarum Ulvås, V., & Henry, G. W. 2003, A&A, 402, 1033

Barden, S. C. 1985, ApJ, 295, 162

Berdyugina, S. V., Ilyin, I., & Tuominen, I. 1999, A&A, 349, 863

Bopp, B. W., & Talcott, J. C. 1978, AJ, 83, 1517

Buccino, A. P., & Mauas, P. J. D. 2009, A&A, 495, 287

Byrne, P. B. 1983, in Astrophysics and Space Science Library, 102, IAU Colloq. 71: Activity in Red-Dwarf Stars, eds. P. B. Byrne & M. Rodono, 157

Cao, D.-T., & Gu, S.-H. 2012, A&A, 538, A130

Cao, D.-t., & Gu, S.-h. 2014, AJ, 147, 38

Cao, D., & Gu, S. 2015, MNRAS, 449, 1380

Carlos, R. C., & Popper, D. M. 1971, PASP, 83, 504

Catalano, S., & Frasca, A. 1994, A&A, 287, 575

Catalano, S., Umana, G., Cafra, B., et al. 2003, in Cambridge Workshop on Cool Stars, Stellar Systems, and the Sun, 12,

The Future of Cool-Star Astrophysics, eds. A. Brown, G. M. Harper, & T. R. Ayres, 981

Doyle, J. G., van den Oord, G. H. J., & Kellett, B. J. 1992, A&A, 262, 533

Ducati, J. R. 2002, VizieR Online Data Catalog, 2237

Duemmler, R., & Aarum, V. 2001, A&A, 370, 974

Ekmekçi, F. 2010, PASA, 27, 1

Ekmekci, F. 2010, Publications de l'Observatoire Astronomique de Beograd, 90, 131

Elias, II, N. M., Quirrenbach, A., Witzel, A., et al. 1995, ApJ, 439, 983

Foing, B. H., Char, S., Ayres, T., et al. 1994, A&A, 292, 543

Franciosini, E., Pallavicini, R., & Tagliaferri, G. 2001, A&A, 375, 196

Frasca, A., Biazzo, K., Taş, G., Evren, S., & Lanzafame, A. C. 2008a, A&A, 479, 557

Frasca, A., & Catalano, S. 1994, A&A, 284, 883

Frasca, A., Kovári, Z., Strassmeier, K. G., & Biazzo, K. 2008b, A&A, 481, 229

Gálvez, M. C., Montes, D., Fernández-Figueroa, M. J., De Castro, E., & Cornide, M. 2009, AJ, 137, 3965

Garcia Alvarez, D. 2000, Irish Astronomical Journal, 27

García-Alvarez, D., Foing, B. H., Montes, D., et al. 2003, A&A, 397, 285

Gu, S.-H., Tan, H.-S., Shan, H.-G., & Zhang, F.-H. 2002, A&A, 388, 889

Gu, S., & Tan, H. 2003, in Cambridge Workshop on Cool Stars, Stellar Systems, and the Sun, 12, The Future of Cool-Star Astrophysics, eds. A. Brown, G. M. Harper, & T. R. Ayres, 986

Gu, S., Tan, H., & Shan, H. 2005, in ESA Special Publication, 560, 13th Cambridge Workshop on Cool Stars, Stellar Systems and the Sun, eds. F. Favata, G. A. J. Hussain, & B. Battrick, 599

Gu, S., Tan, H., Wang, X., & Shan, H. 2004, in IAU Symposium, 219, Stars as Suns: Activity, Evolution and Planets, eds. A. K. Dupree & A. O. Benz, 873

Gunn, A. G., & Doyle, J. G. 1997, A&A, 318, 60

Gunn, A. G., Doyle, J. G., & Houdebine, E. R. 1997, A&A, 319, 211

Haisch, B., Strong, K. T., & Rodono, M. 1991, ARA&A, 29, 275

Hall, J. C. 1996, PASP, 108, 313

Huenemoerder, D. P., Buzasi, D. L., & Ramsey, L. W. 1989,

AJ, 98, 1398

Huenemoerder, D. P., & Ramsey, L. W. 1987, ApJ, 319, 392

López-Santiago, J., Montes, D., Fernández-Figueroa, M. J., & Ramsey, L. W. 2003, A&A, 411, 489

Montes, D., de Castro, E., Fernandez-Figueroa, M. J., & Cornide, M. 1995a, A&AS, 114, 287

Montes, D., Fernandez-Figueroa, M. J., de Castro, E., & Cornide, M. 1995b, A&A, 294, 165

Montes, D., Fernandez-Figueroa, M. J., de Castro, E., & Cornide, M. 1995c, A&AS, 109

Montes, D., Fernández-Figueroa, M. J., De Castro, E., et al. 2000, A&AS, 146, 103

Montes, D., Fernandez-Figueroa, M. J., de Castro, E., & Sanz-Forcada, J. 1997, A&AS, 125, 263

Montes, D., Saar, S. H., Collier Cameron, A., & Unruh, Y. C. 1999, MNRAS, 305, 45

Montes, D., Sanz-Forcada, J., Fernandez-Figueroa, M. J., & Lorente, R. 1996, A&A, 310, L29

Nations, H. L., & Ramsey, L. W. 1986, AJ, 92, 1403

Pettersen, B. R. 1989, Sol. Phys., 121, 299

Raveendran, A. V., & Mohin, S. 1995, A&A, 301, 788

Richards, M. T., Waltman, E. B., Ghigo, F. D., & Richards, D. S. P. 2003, ApJS, 147, 337

Rosario, M. J., Mekkaden, M. V., & Raveendran, A. V. 2008, Information Bulletin on Variable Stars, 5836

Rosario, M. J., Raveendran, A. V., & Mekkaden, M. V. 2007, A&A, 474, L41

Schrijver, C. J., & Zwaan, C. 2000, Solar and Stellar Magnetic Activity (Cambridge: Cambridge Univ. Press)

Schrijver, C. J., Beer, J., Baltensperger, U., et al. 2012, Journal of Geophysical Research (Space Physics), 117, A08103

Simon, T., Linsky, J. L., & Schiffer, III, F. H. 1980, ApJ, 239, 911

Vogt, S. S., & Hatzes, A. P. 1991, in Lecture Notes in Physics, Berlin Springer Verlag, 380, IAU Colloq. 130: The Sun and Cool Stars. Activity, Magnetism, Dynamos, eds. I. Tuominen, D. Moss, & G. Rüdiger, 297

Zhang, L., Pi, Q., Han, X. L., Chang, L., & Wang, D. 2016, MNRAS, 459, 854

Zhang, L.-Y., & Gu, S.-H. 2008, A&A, 487, 709

Zhao, G., & Li, H.-B. 2001, ChJAA (Chin. J. Astron. Astrophys.), 1, 555

Zirin, H. 1988, Astrophysics of the Sun (Cambridge: Cambridge Univ. Press)

Long-term photometric behavior of the eclipsing Z Cam-type dwarf nova AY Psc

Zhong-Tao Han[1,2,3], Sheng-Bang Qian[1,2,3], Irina Voloshina[4] and Li-Ying Zhu[1,2,3]

[1] Yunnan Observatories, Chinese Academy of Sciences, Kunming 650216, China; *zhongtaohan@ynao.ac.cn*
[2] Key Laboratory of the Structure and Evolution of Celestial Objects, Chinese Academy of Sciences, Kunming 650216, China
[3] University of Chinese Academy of Sciences, Beijing 100049, China
[4] Sternberg Astronomical Institute, Moscow State University, Universitetskij prospect 13, Moscow 119992, Russia

Abstract New eclipse timings of the Z Cam-type dwarf nova AY Psc were measured and the orbital ephemeris was revised. In addition, based on long-term AAVSO data, the outburst behaviors were also explored. Our analysis suggests that normal outbursts are quasi-periodic, with an amplitude of $\sim 2.5(\pm 0.1)$ mag and a period of $\sim 18.3(\pm 0.7)$ d. The amplitude vs. recurrence-time relation of AY Psc is discussed, and we conclude that this relation may represent general properties of dwarf nova outbursts. The observed standstill ends with an outburst, which is inconsistent with the general picture of Z Cam-type stars. This unusual behavior was considered to be related to mass-transfer outbursts. Moreover, the average luminosity is brighter during standstills than during outburst cycles. The changes in brightness mark variations in $\dot{M}_2$ due to the fact that the disk of AY Psc is nearly steady state. $\dot{M}_2$ value was limited to the range from 6.35×10^{-9} to $1.18 \times 10^{-8} \, M_\odot \, \mathrm{yr}^{-1}$. More detailed examination shows that there are a few small outbursts present during standstills. These events with amplitudes of $\sim 0.5 - 0.9$ mag are very similar to the stunted outbursts reported in some nova-like cataclysmic variables. We discussed several possible mechanisms and suggested that the most reasonable mechanism for these stunted outbursts is a changing mass-transfer rate.

Key words: binaries: close — stars: cataclysmic variables — stars: individual (AY Psc)

1 INTRODUCTION

Z Cam stars are a subtype of dwarf nova-type (DN) cataclysmic variables (CVs) exhibiting protracted standstills about 0.7 mag below maximum brightness, during which the brightness stays constant (Warner 1995). The duration of standstills has a large range from tens of days to years. These stars exhibit U Gem-type outbursts but the standstills are similar to the behavior of nova-like CVs (NLs). Osaki (1974) proposed an interpretation of standstills for the first time in which the accretion disk was in the steady stage. After that, these systems are defined as an intermediate between stable NLs and unstable DNe (Smak 1983). Moreover, a model for the standstills was presented by Meyer & Meyer-Hofmeister (1983). This model suggested that the mass transfer rate in Z Cam stars is close to a critical rate (i.e. $\dot{M}_2 \approx \dot{M}_{\mathrm{crit}}$). A system with $\dot{M}_2 < \dot{M}_{\mathrm{crit}}$ will generate U Gem-type normal outbursts. When $\dot{M}_2 > \dot{M}_{\mathrm{crit}}$, the system enters standstill behaving like NLs. Moderate fluctuation in $\dot{M}_2$ could produce Z Cam-type light curves (Lin et al. 1985; Buat-Ménard et al. 2001). Changes in $\dot{M}_2$ have generally been explained as irradiation effects of the secondary star's surface by the accretion disk (Meyer & Meyer-Hofmeister 1983). As expected, the average brightness in NLs was higher (by ~ 3 mag) than in DNe at the same orbital period (Warner 1995). On long timescales, the average brightness in Z Cam stars is expected to follow changes in $\dot{M}_2$ because their disks are nearly steady state.

AY Psc was classified as a Z Cam star due to its occasional standstills and normal DN outbursts (Mercado & Honeycutt 2002). It was identified as a CV candidate by Green et al. (1982) and first studied in detail by

Szkody et al. (1989) who presented $B-$ and $V-$band light curves showing deep eclipses with an orbital period of 5.13 h. Later, an orbital ephemeris was provided by Diaz & Steiner (1990) who also revised the orbital period to be 5.2 h. The system parameters were derived by Howell & Blanton (1993) through photometric analysis and by Szkody & Howell (1993) using time-resolved spectroscopy. According to Szkody & Howell (1993), AY Psc contains a massive $\sim 1.31\,M_\odot$ white dwarf and a $\sim 0.59\,M_\odot$ companion, for a total system mass of $\sim 1.9\,M_\odot$, which is well in excess of the Chandrasekhar limit ($\sim 1.4\,M_\odot$) and therefore is a ballpark estimate for potential SN Ia progenitors. However, we still know little about its outbursts because of the paucity of long-term photometric data. Fortunately, many V-band data from the American Association of Variable Star Observers (AAVSO) covering a timescale of $\sim 6\,$yr provide a good opportunity to ascertain the outburst properties. Moreover, the deeply eclipsing nature of AY Psc can be used to probe orbital period changes. From an evolutionary perspective, the period analysis can offer some clues concerning the orbital evolution and circumbinary companions. The most common method for determining period variations is to analyze the observed-calculated $(O - C)$ diagram. We have applied this method several times in the past few years to study a few eclipsing CVs such as Z Cha (Dai et al. 2009), OY Car (Han et al. 2015), V2051 Oph (Qian et al. 2015) and GSC 4560-02157 (Han et al. 2016). In this paper, we present new CCD photometric observations of AY Psc and update the orbital ephemeris. Then its outburst properties are analyzed by using the AAVSO data.

2 OBSERVATIONS AND DATA PREPARATION

New CCD photometric observations of AY Psc were carried out by using several different telescopes. They were: the 60 cm and the 1.0 m reflecting telescopes utilizing Andor DW436 2K CCD cameras at Yunnan Observatories (YNO); the 85 cm and the 2.16 m telescopes at Xinglong Station administered by National Astronomical Observatories, Chinese Academy of Sciences (NAOC); and the 2.4 m Thai National Telescope (TNT) administered by National Astronomical Research Institute of Thailand (NARIT). The 85 cm telescope had an Andor DW436 1K CCD camera and the 2.16 m telescope was equipped with a PI 1274×1152 TE CCD. The TNT is a Ritchey-Chrétien with two focuses and an ULTRASPEC fast camera was attached to it. During observations, no filters were used in order to improve the time resolution. The aperture photometry package of IRAF was used to reduce the ob-

served CCD images. Differential photometry was performed, with a nearby non-variable comparison star.

Figure 1 displays four eclipsing profiles observed with different telescopes. As done by Diaz & Steiner (1990), new mid-eclipse times are determined by using a cubic polynomial fitting. The errors are standard deviation values. All mid-eclipse times and errors are listed in Table 1.

To investigate the outburst properties, long-term light curves are required. Figure 2 shows the entire AAVSO light curve of AY Psc in V- and R-band from 2010 August 19−2016 November 29. Here we only used digital photometric data because errors in the visual data are too large ($\sim 0.3 - 0.5\,$mag). The digital photometric observations began in 2010 August and over 1400 observations from 26 observers are included in Figure 2. The errors are estimated to within 0.1 mag for the bright state (during outburst and standstill) and within 0.2 mag for quiescence using the comparison and check stars with known magnitudes in this field by these observers. Due to the fact that AY Psc is an eclipsing system, such data have been prepared by omitting the data during eclipse before the analysis. Although fragmentary data and gaps are present, the standstill is clearly visible in the light curve. The long-term light curve was partitioned into seven data sets by the gaps. The best data occur after JD 2457553, where the density of observations is $1.7\,\mathrm{d}^{-1}$ and every day contains at least one data point. Continuous outbursts in this data set are plotted in Figure 4 and reveal a feature similar to a sine wave. More detailed analysis is given in Section 3.2.

3 RESULTS AND DISCUSSION

3.1 Revised Ephemeris

Mid-eclipse times of AY Psc have been published in the literatures by two authors (e.g. Diaz & Steiner 1990 and Gülsecen et al. 2009). Diaz & Steiner (1990) reported nine mid-eclipse times and showed no sign of any orbital period change. Combining the previous data with our observations, the latest version of the $O - C$ diagram is displayed in Figure 3. The $O - C$ values of all available data are computed with the linear ephemeris given by Diaz & Steiner (1990)

$$\mathrm{Min.I} = \mathrm{HJD}\,2447623.3463 + 0.2173209 \times E, \quad (1)$$

where $\mathrm{HJD}\,2447623.3463$ is the initial epoch and $0.2173209\,$d is the orbital period. The best-fitting linear ephemeris to all the eclipse times of AY Psc is

$$\mathrm{Min.I} = \mathrm{HJD}\,2447623.34628(2) + 0.21732061(1) \times E. \quad (2)$$
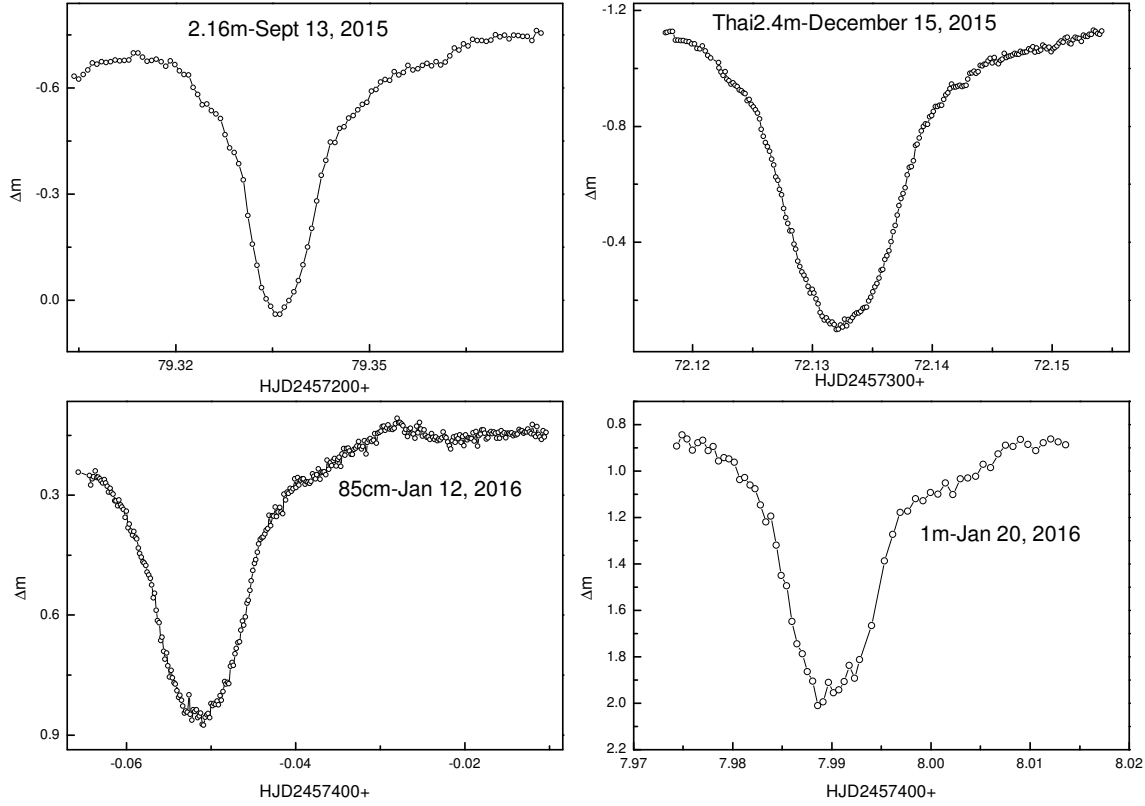
Fig. 1 Four eclipse profiles of AY Psc obtained with four different telescopes in China and in Thailand.

Table 1 New CCD Mid-eclipse Times of AY Psc

Date	Min.(HJD)	E	$O - C$	Error	Filter	Telescope
2012 Dec 13	2456275.09576	39811	–0.01289	0.00011	N	60 cm
2015 Sep 13	2457279.33629	44432	–0.01224	0.00005	N	2.16 m
2015 Sep 24	2457290.20122	44482	–0.01335	0.00019	N	1 m
2015 Dec 15	2457372.13246	44859	–0.01209	0.00003	N	Thai-2.4 m
2016 Jan 12	2457399.94876	44987	–0.01287	0.00003	N	85 cm
2016 Jan 20	2457407.98993	45024	–0.01257	0.00008	N	1 m

The dashed line in Figure 3 represents the revised linear ephemeris. However, the residuals from this ephemeris show some deviations and the orbital period does not seem to be constant. This may be caused by some of the unknowns or a true period change. However, there is still no more evidence to support this change. Therefore, further observations are critically required to ascertain the changes in orbital period of this system.

3.2 Outburst Properties

3.2.1 Normal outbursts and the K-P relation

In Figure 2 we show the long-term AAVSO light curve of AY Psc during 2010 August−2016 November. The data are divided into seven segments because a lot of data are missing. A detailed view of the light curves reveals three main features: normal outburst, standstill and stunted outburst. During normal outburst, the duty cycle of AY Psc approaches 100%. This behavior is thought to be due to $\dot{M}_2 \approx \dot{M}_{\mathrm{crit}}$ (Lin et al. 1985; Warner 1995). The system rises from $V \approx 17.1$ at minimum to $V \approx 14.6$ at maximum in $6 - 8\,\mathrm{d}$, exhibiting a mean outburst amplitude of $\sim 2.5(\pm 0.1)\,\mathrm{mag}$.

Figure 4 displays a best outburst data set for AY Psc covering $169\,\mathrm{d}$ (2016 Jun 14−2016 Nov 29). A sine curve fit was applied to the eight outburst cycles in Figure 4, giving a recurrence time of $\sim 19.03(\pm 0.04)\,\mathrm{d}$. However, the full light curve contains at least four out-
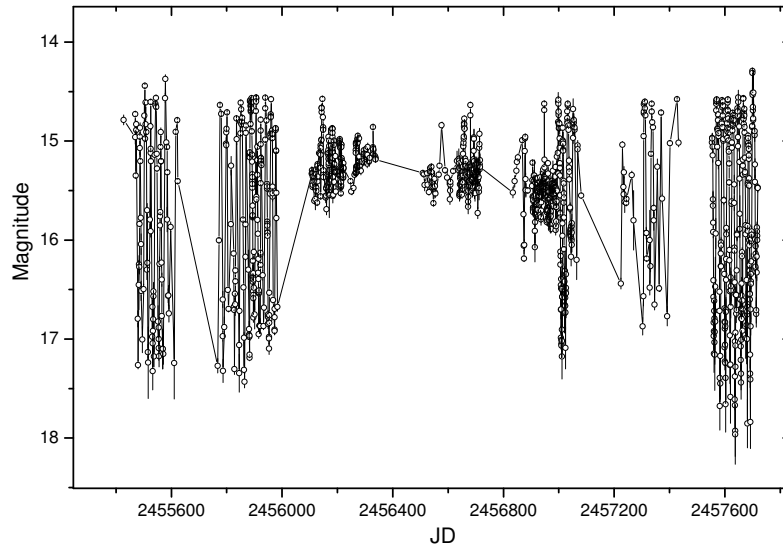
Fig. 2 The long-term light curve of AY Psc from AAVSO observations during 2010 August−2016 November. Note the presence of obvious standstills at $15.3(\pm0.2)$ mag.
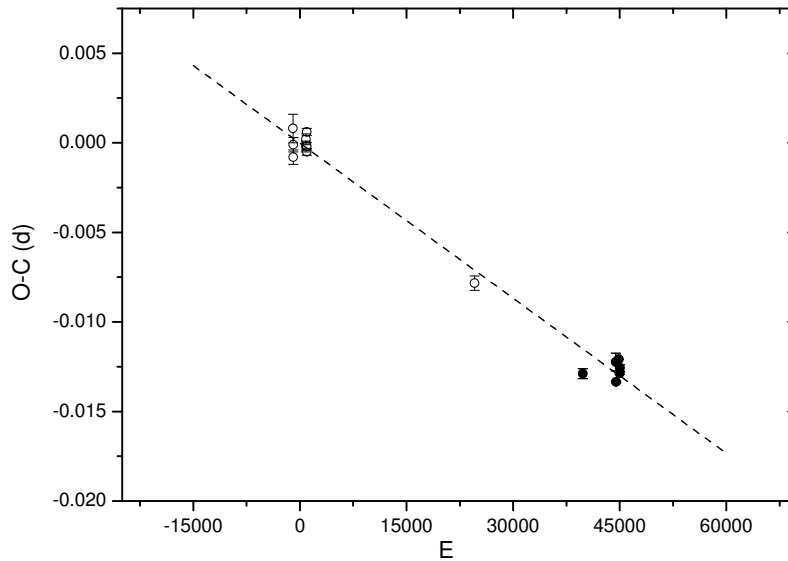

Fig. 3 $O - C$ diagram of AY Psc. The open circles and solid circles denote the data in the literature and our observations, respectively. The dashed line represents the best-fitting linear ephemeris.

burst segments. To verify this result, analysis of all these outburst segments is required.

Figure 5 shows all outburst data sets and their associated power spectrums. The power spectrums correspond to the periods between 17.7 and 18.5 d, which is smaller than the period from the sine fitting (~ 19.03 d). This implies that the outburst in AY Psc is not strictly periodic but rather quasi-periodic.

Kukarkin & Parenago (1934) first noted that there was a relation between the outburst amplitude (A_n) and the outburst recurrence time (T_n) for DNe and recurrent novae. After that, this relation has been revised and improved many times to constrain its application range. Finally, a general correlation was found by analyzing normal outbursts in DNe (van Paradijs 1985). The most
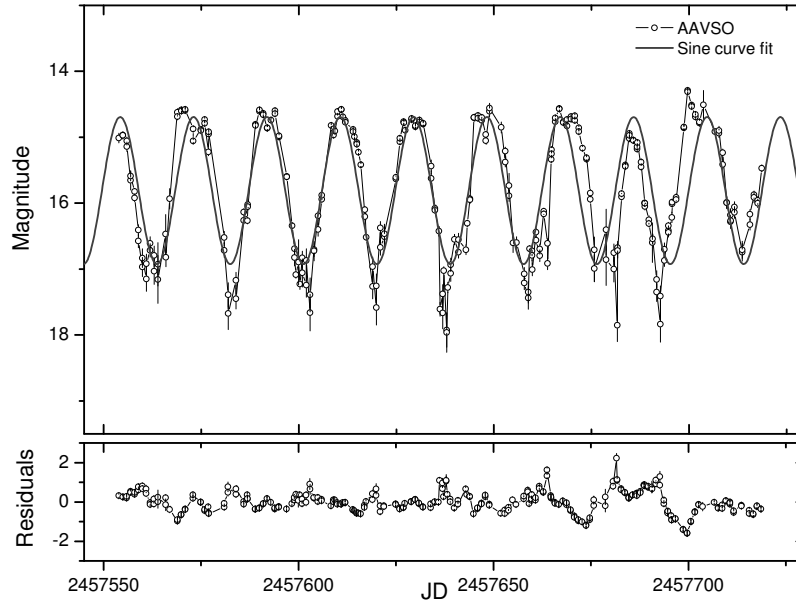
Fig. 4 Continuous outbursts in AY Psc spanning ~ 170 d (2016 Jun 14 − 2016 Sept 27). The sine curve fit was superposed on this outburst segment, which gives a period of $\sim 19.03(\pm 0.04)$ d. The lower panel displays the fitting residuals from the sine wave.

recent version of the Kukarkin-Parenago (K-P) relation from Warner (1995) is as follows

$$A_n = 0.7(\pm 0.43) + 1.9(\pm 0.22) \log T_n. \tag{3}$$

This is an empirical relation. Moreover, to explore if this relation is model-dependent, a theoretical K-P relation was derived by Kotko & Lasota (2012) using the disk instability model

$$A_n = C_1 + 2.5 \log T_n, \tag{4}$$

where the constant term

$$C_1 = 2.5 \log 2\tilde{g} - 2.5 \log t_{\mathrm{dec}} + BC_{\max} - BC_{\min},$$

depends on the properties of the white dwarf and the viscosity parameter α. The outburst parameters of AY Psc and the K-P relation are plotted in Figure 6. The open squares represent statistical data from the AAVSO database, the red solid line refers to the empirical K-P relation and red dashed lines denote its upper and lower uncertainties. However, the observational data were not covered in this relation. Note that this relation is only significant for systems with $A_n > 2.5$ mag (Warner 1995). The lower uncertainty of the empirical relation follows the overall trend of observational data reasonably well because the amplitude of AY Psc falls on the boundary of 2.5 mag. Therefore, the K-P relation for AY Psc will be roughly replaced by the lower limit of the empirical relation

$$A_n = 0.27 + 1.68 \log T_n. \tag{5}$$

Based on those descriptions, we suggest that the K-P relation may represent a common characteristic of DN outbursts.

3.2.2 Standstills and brightness modulation

Figure 7 shows the standstill signal at $15.3(\pm 0.2)$ mag extracted from Figure 2 during the period from 2012 June 29 to 2015 January 1. The upper panel of Figure 8 displays a well-observed transition from standstill to outburst, where we see an unusual characteristic behavior that differs from what is exhibited by most Z Cam stars. This standstill ends with an outburst (see Fig. 8). However, the currently used model of Z Cam stars predicts that a standstill can only be terminated by a decline to quiescence rather than an outburst (Buat-Ménard et al. 2001). Before several of the the unusual Z Cam systems were discovered, only one recorded standstill in the prototype star Z Cam was observed to terminate in a rise to maximum (Warner 1995; Oppenheimer et al. 1998). Recently, this rare behavior was observed in several anomalous Z Cam-type stars such as AH Her, IW And, V513 Cas and ST Cha (Simonsen 2011; Simonsen et al. 2014). A plausible explanation for this behavior was proposed by Hameury & Lasota (2014), who indicated that mass-transfer outbursts can reproduce the observed properties of these unusual systems. This implies that the changes in mass transfer from the secondary star are responsible for changes in brightness on longer timescales.
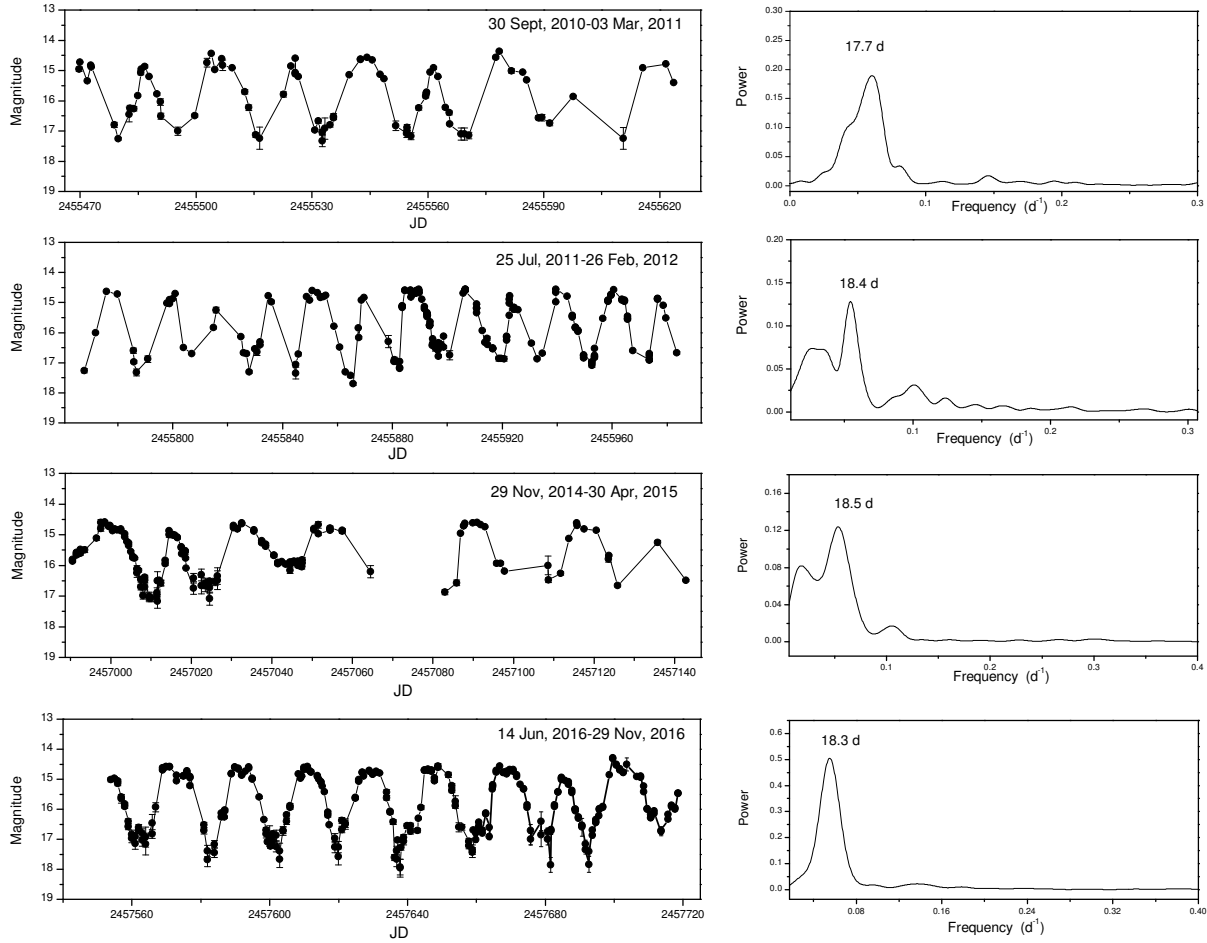
Fig. 5 Four outburst segments and corresponding power spectrums. The power spectrums indicate that the outbursts are quasi-periodic, with periods between 17.7 and 18.5 d.

For Z Cam-type systems, a direct test is to compare the standstill and outburst brightness. In effect, there have been several studies that investigated this aspect (Lortet 1968; Oppenheimer et al. 1998; Honeycutt et al. 1998). To clearly reveal the mass-transfer variations, the mean brightness during standstills and the outbursts were calculated by averaging long-term AAVSO data. In computing the mean magnitude values, only full cycles were averaged. For outbursts, two mean values were measured per outburst cycle, overlapping by one-half cycle. For standstills, means were computed for successive intervals of several tens of days. The mean brightness values of all data are plotted in Figure 9. The red dots in Figure 9 represent the means during standstills and the black dots denote the means during outbursts. Clearly, the average magnitudes during standstills are brighter than during outburst intervals. This result is consistent with previous authors (e.g. Oppenheimer et al. 1998; Honeycutt et al. 1998). Moreover, the trend in Figure 9 also implies there

are changes in $\dot{M}_2$, in agreement with the general picture of standstills. The green solid line marks the transition between outburst cycles and standstills, corresponding to $\dot{M}_{\rm crit}$. Frank et al. (2002) give an expression for $\dot{M}_{\rm crit}$

$$\dot{M}_{\rm crit} \simeq 3 \times 10^{-9} (P_{\rm orb}/3)^2 M_\odot \,{\rm yr}^{-1} \,, \qquad (6)$$

where $P_{\rm orb}$ is in hours. For AY Psc, with $P_{\rm orb} = 5.22\,{\rm h}$, we find $\dot{M}_{\rm crit} \simeq 9.07 \times 10^{-9} \, M_\odot \,{\rm yr}^{-1}$. Buat-Ménard et al. (2001) pointed out that $\dot{M}_2$ will vary by about 30% around $\dot{M}_{\rm crit}$. More specifically, $\dot{M}_2$ in AY Psc should be restricted to the range from 6.35×10^{-9} to $1.18 \times 10^{-8} \, M_\odot \,{\rm yr}^{-1}$.

3.2.3 Stunted outbursts in AY Psc

More detailed inspection of the AAVSO data reveals that there are diverse behaviors during standstill. Note that the brightness of the standstill is not constant, but rather keeps fluctuating. Oscillations with an amplitude

177
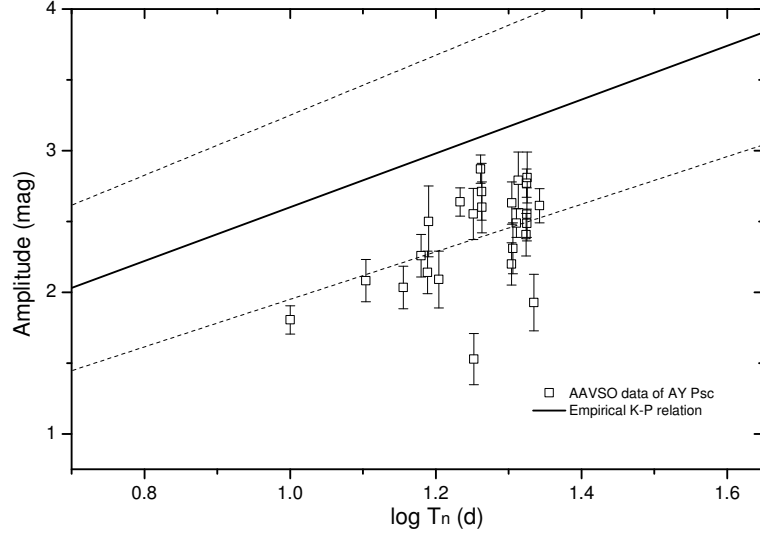
Fig. 6 Comparison of the K-P relation and AAVSO data for AY Psc. The open squares represent statistical data, the red solid line refers to the empirical K-P relation (Warner 1995) and red dashed lines denote its upper and lower uncertainties.
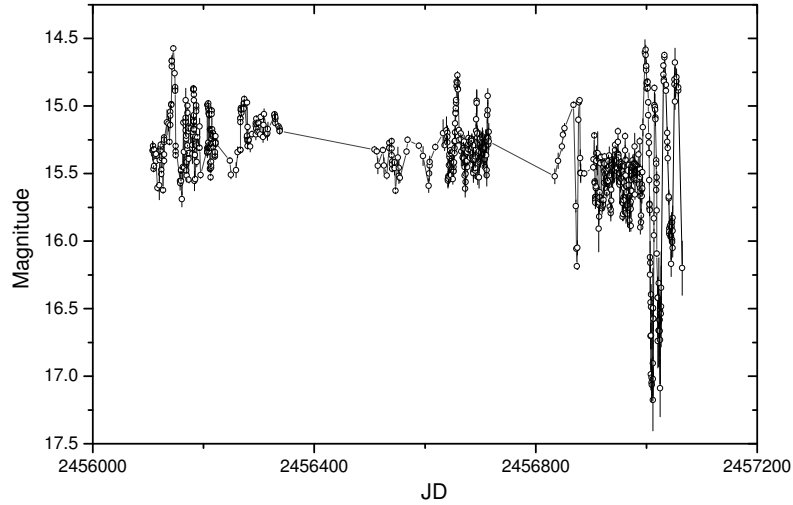

Fig. 7 The standstill data at $15.3(\pm0.2)$ mag extracted from Fig. 2 during the period from 2012 June 29 to 2015 January 1. It is clear that there are small amplitude oscillations present during standstills.

of ~ 0.2 mag can be seen by eye in Figures 7 and 8. Moreover, we find occasional outburst-like events during standstill, as shown in Figure 10. These events are best characterized as small amplitude outbursts, which have properties very similar to the stunted outbursts seen in some NLs (e.g. Honeycutt et al. 1995, 1998; Honeycutt 2001; Honeycutt et al. 2014; Warner 1995; Hoard et al. 2000; Ramsay et al. 2016).

Table 2 summarizes the properties of stunted outbursts in AY Psc. The stunted outbursts in Figure 10 are visible with amplitudes of $\sim 0.5-0.9$ mag and full width

at half maximums (FWHMs) of $\sim 2-14$ d. The rises are slower than the declines, implying that the outbursts are Type B (inside-out). However, to date, the origin of stunted outbursts is still uncertain. Some possible mechanisms are proposed to account for the stunted outbursts, including a disk truncated by the magnetic field of the white dwarf or a very hot white dwarf, DN outbursts being related to the standard disk instability and mass transfer modulations (Honeycutt et al. 1998; Honeycutt 2001; Honeycutt et al. 2014; Ramsay et al. 2016). For AY Psc, a truncated disk mechanism can be ruled out because the
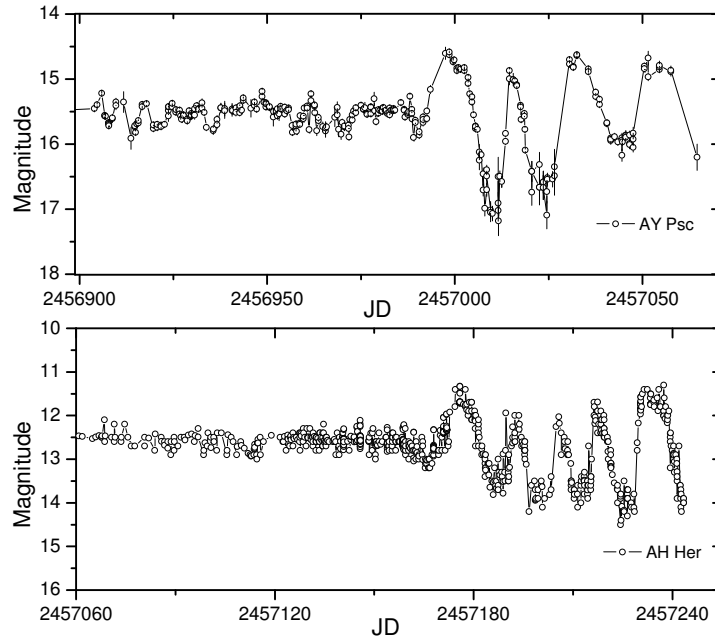
Fig. 8 *Upper panel*: a transition from standstill to outburst interval in AY Psc. *Lower panel*: a transition from standstill to outburst interval in AH Her. The two transitions terminate in an outburst, in disagreement with current theoretical prediction and observations.
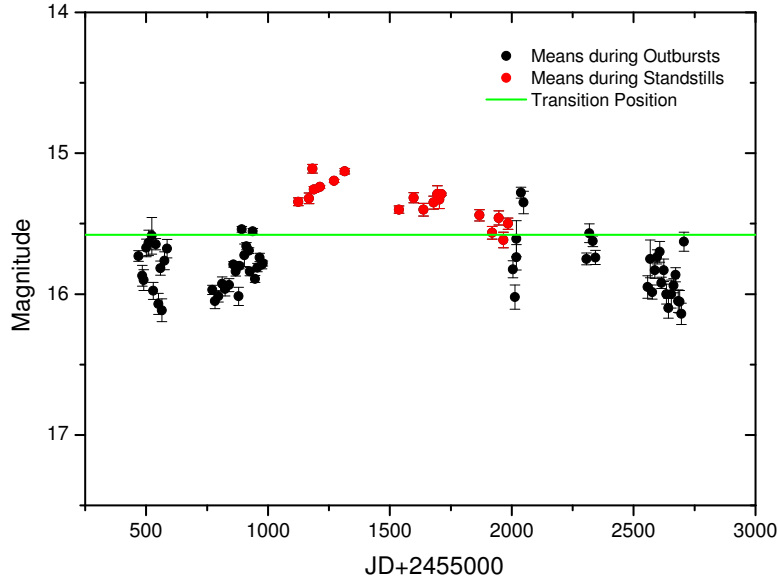

Fig. 9 Comparison of the outburst and standstill mean brightness in AY Psc using all AAVSO data. The red dots are the means during standstills and the black dots denote the means during outburst cycles. The green line represents the transition position.

inside-out outbursts (Type B) in a truncated disk are infrequent (Honeycutt et al. 1998). During standstill, $\dot{M}_2$ from the secondary star exceeds $\dot{M}_{\mathrm{crit}}$, and the disk stays in steady state, without DN outbursts. In addition, Warner (1995) indicated that DN outbursts have faster rise times than decline times by a factor of ~ 2 (i.e. Type A out-

bursts), which is not compatible with the stunted behaviors of AY Psc. Therefore, the disk instability may not be the cause of stunted outbursts. It seems that a changing mass transfer is a reasonable candidate mechanism for these stunted behaviors. First, a steady-state disk allows the brightness to follow changes in mass transfer.

Table 2 Basic Parameters of the Stunted Outbursts in AY Psc

Outburst	JD	Ampl. (mag)	FWHM (d)	τ_{rise} (d)	τ_{fall} (d)
1	2456145	0.89	7.3	21	10
2	2456273	0.53	14.1	15	11
3	2456658	0.68	6.5	8	10
4	2456693	0.56	2.8	3	2
5	2456713	0.59	2.1	2	1
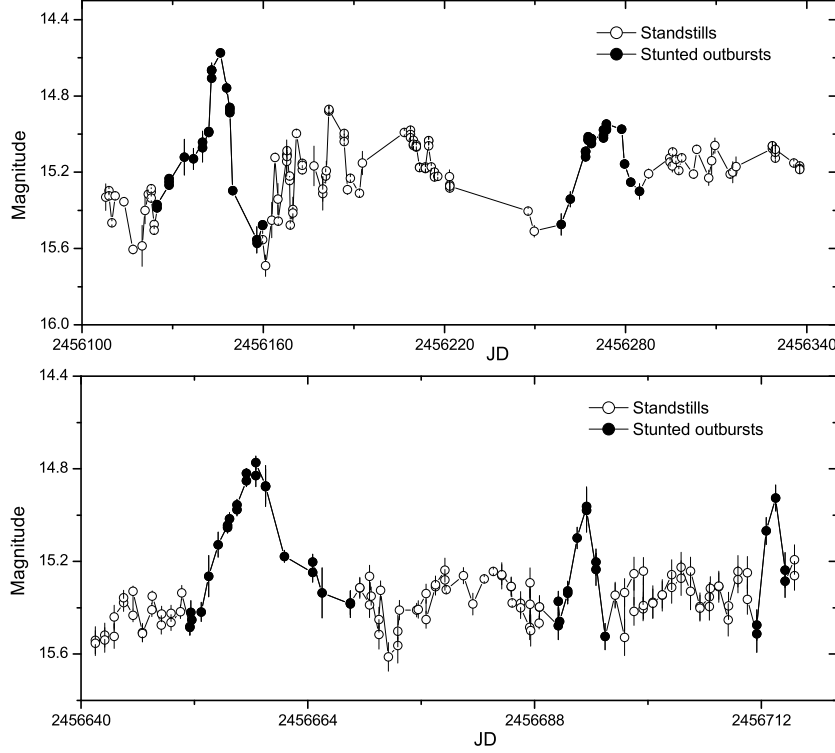
Fig. 10 Five stunted outbursts during standstills showing amplitudes of $\sim 0.5-0.9$ mag. The characteristics of the stunted outbursts are summarized in Table 2.

Second, Hameury & Lasota (2014) studied the disk's response to a mass transfer outburst during standstills and reproduced an outburst with an amplitude of ~ 0.8 mag starting from a steady state disk. Meanwhile, the possible origins of the mass transfer outbursts were also discussed by these authors. Nevertheless, these stunted outbursts are not well understood so far.

4 SUMMARY

We have presented the photometric results of the eclipsing Z Cam-type star AY Psc using our observations together with AAVSO data. Our analysis focuses on the orbital period and outburst properties. The main conclusions of this paper can be summarized as follows.

(i) The orbital period has been revised from 0.2173209 d to 0.21732061 d.

(ii) The duty cycle of AY Psc is close to 100%.

(iii) The observed standstill, extending from 2012 June 29 to 2014 December 1, ended with an outburst rather than a decline to quiescence, which is rarely seen in similar systems.

(iv) During the standstill, several stunted outbursts were present.

180

References

Buat-Ménard, V., Hameury, J.-M., & Lasota, J.-P. 2001, A&A, 366, 612

Dai, Z., Qian, S., & Fernández Lajús, E. 2009, ApJ, 703, 109

Diaz, M. P., & Steiner, J. E. 1990, A&A, 238, 170

Frank, J., King, A., & Raine, D. J. 2002, Accretion Power in Astrophysics: Third Edition (Cambridge: Cambridge University Press), 398

Green, R. F., Ferguson, D. H., Liebert, J., & Schmidt, M. 1982, PASP, 94, 560

Gülsecen, H., Retter, A., Liu, A., & Esenoğlu, H. 2009, New Astron., 14, 330

Hameury, J.-M., & Lasota, J.-P. 2014, A&A, 569, A48

Han, Z.-T., Qian, S.-B., Fernández Lajús, E., Liao, W.-P., & Zhang, J. 2015, New Astron., 34, 1

Han, Z.-T., Qian, S.-B., Voloshina, I., et al. 2016, RAA (Research in Astronomy and Astrophysics), 16, 156

Hoard, D. W., Szkody, P., Honeycutt, R. K., et al. 2000, PASP, 112, 1595

Honeycutt, R. K., Robertson, J. W., & Turner, G. W. 1995, ApJ, 446, 838

Honeycutt, R. K., Robertson, J. W., & Turner, G. W. 1998, AJ, 115, 2527

Honeycutt, R. K. 2001, PASP, 113, 473

Honeycutt, R. K., Kafka, S., & Robertson, J. W. 2014, AJ, 147, 10

Howell, S. B., & Blanton, S. A. 1993, AJ, 106, 311

Kotko, I., & Lasota, J.-P. 2012, A&A, 545, A115

Kukarkin, B. W., & Parenago, P. P., 1934, Var. Star. Bull., 4, 44

Lin, D. N. C., Faulkner, J., & Papaloizou, J. 1985, MNRAS, 212, 105

Lortet, M.-C. 1968, in IAU Colloq. 4, Variable Stars, Nonperiodic Phenomena in Variable Stars, ed. L. Detre (Budapest: Academic Press), 381

Mercado, L., & Honeycutt, R. K. 2002, in Bulletin of the American Astronomical Society, 34, American Astronomical Society Meeting Abstracts, 1162

Meyer, F., & Meyer-Hofmeister, E. 1983, A&A, 121, 29

Oppenheimer, B. D., Kenyon, S. J., & Mattei, J. A. 1998, AJ, 115, 1175

Osaki, Y. 1974, PASJ, 26, 429

Qian, S. B., Han, Z. T., Fernández Lajús, E., et al. 2015, ApJS, 221, 17

Ramsay, G., Hakala, P., Wood, M. A., et al. 2016, MNRAS, 455, 2772

Simonsen, M. 2011, Journal of the American Association of Variable Star Observers (JAAVSO), 39, 66

Simonsen, M., Bohlsen, T., Hambsch, F.-J., & Stubbings, R. 2014, Journal of the American Association of Variable Star Observers (JAAVSO), 42, 199

Smak, J. 1983, ApJ, 272, 234

Szkody, P., & Howell, S. B. 1993, ApJ, 403, 743

Szkody, P., Howell, S. B., Mateo, M., & Kreidl, T. J. 1989, PASP, 101, 899

van Paradijs, J. 1985, A&A, 144, 199

Warner, B. 1995, Cataclysmic Variable Stars (Cambridge Astrophysics Series), 28

ELSEVIER

CrossMark
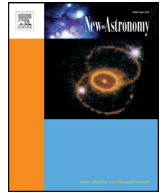
Asteroseismology of the ultramassive ZZ ceti star WD 0246+326☆

Chun Li[a], Jianning Fu[a,*], Lester Fox-Machado[b], Jie Su[a], Fangfang Chen[a]

[a] *Department of Astronomy, Beijing Normal University, Beijing, China*
[b] *Observetorio Astrómico Nacional, Instituto de Astronomia, Universided Nacional Autónoma de México, Ensenada, México*

HIGHLIGHTS

- A bi-site observation campaign were made for ZZ Ceti star WD 0246+326 during in 2014.
- Frequencies were detected and identified as $l = 1$ and $l = 2$ modes.
- Pulsation properties indicates that WD 0246+326 may be a massive ZZ Ceti star.
- Theoretical models were constructed to constrain the stellar parameters.

ARTICLE INFO

ABSTRACT

The internal structures of pulsating white dwarfs can be explored only with asteroseismology. Time series photometric observations were made for the pulsating DA white dwarf (ZZ Ceti star) WD 0246+326 during 9 nights in 2014 with a bi-site observation campaign. Eleven frequencies were detected including 1 triplet, 2 doublets, and 4 single modes, which are identified as either $l = 1$ or $l = 2$ modes with the complementarity of frequencies present in the literature. From the multiplets, the rotation period of WD 0246+326 is derived as 3.78 ± 0.11 days. The average period spacing of the $l = 1$ modes $\Delta P = 29.3 \pm 0.2$ s, implies that WD 0246+326 may be a massive ZZ Ceti star concerning the $\Delta P - M_*$ relationship for the DAVs. Preliminary analysis derives the stellar parameters of $M_* = 0.98 \pm 0.01$ M$_\odot$ and $T_{\mathrm{eff}} = 11700 \pm 100$ K by fitting the theoretical frequencies of the eigen modes to the observed ones.

1. Introduction

As final remains of stellar evolutions of the majority of stars in the Galaxy, white dwarfs offer opportunities of investigations with significant constraints on ages of both the Galactic Disk and the globular clusters (Winget et al., 1987; Winget and Kepler, 2008). They are also nature laboratories for testing physics under extreme conditions. Landolt (1968) discovered the first pulsating white dwarf HL Tau 76. As asteroseismology is a unique and powerful method known to explore the internal structures of stars, the pulsating white dwarfs have been hot targets of asteroseismology particularly due to their relatively simple internal structures compared to the stars at the other phases of evolution. Pulsating DA white dwarfs, also called ZZ Ceti stars, have the lowest temperatures among all four kinds of pulsating white dwarfs (Saio, 2013). The instability strip of ZZ Ceti stars locates at the intersection of the Cepheid instability strip and the evolution track of white

dwarfs. The purity of the instability strip makes ZZ Ceti stars excellent samples to investigate the internal structures of all DA white dwarfs. However, although they compose the biggest group of pulsating white dwarfs with the largest number of confirmed members by far, the properties of low luminosities, low amplitudes and high frequencies enhance the difficulties of making observational investigations on these stars.

Statistical studies show that ZZ Ceti stars with low effective temperatures locate close to the red edge of the instability strip with long periods, high amplitudes and large amplitude modulations, while the ones with high effective temperatures exhibit the opposite properties. Short time scale variations of pulsating parameters (mainly the amplitudes) are reported for multiple ZZ Ceti stars through time series observations (c.f. Bognár et al., 2009; Provencal et al., 2012; Fu et al., 2013).

The variability of the ZZ Ceti star WD 0246+326 (KUV 02464+3239) was discovered by Fontaine et al. (2001), who reported only one pulsating mode with a period of 832 s from the Fourier transform due to the short duration of data (∼ 1 h of observations). Two sets of stellar parameters were given by Bergeron et al. (1995) and Gianninas et al. (2011) respectively,

Table 1
Journal of observations in *V* for WD 0246+326 in October of 2014. XL = Xinglong station of National Astronomical Observatories of China. SPM = San Pédro Martír Observatory of Mexico.

Observatory/Telescope	Date	Frame number	Length (hour)
	24	280	6.4
	25	468	9.5
XL/	26	397	9.2
2.16 m	27	436	9.9
	28	83	1.2
	28	236	3.1
SPM/	29	231	3.0
1.5 m	30	230	2.9
	31	210	2.7

including the effective temperatures T_{eff} and the surface gravities *Log* g.

Bognár et al. (2009) carried out photometric observations from Konkoly Observatory with a 1 m telescope in 2006 and 2007. Light curves of WD 0246+326 during ~ 97 h were obtained and six modes were reported.

We made bi-site time-series photometric observations for WD 0246+326 in 2014. The descriptions of the observations and data reduction is introduced in Section 2. Section 3 presents the process of frequency analysis. In Section 4 we focus on asteroseismological analysis. Our modeling attempt and related results are provided in Section 5. Finally, we make discussion and give conclusions in Section 6.

2. Observations and data reduction

A bi-site observation campaign was carried out in October of 2014. Table 1 lists the journal of observations. The 2.16 m telescope at Xinglong (XL) Station of National Astronomical Observatory of China and the 1.5 m reflector of San Pédro Martír Observatory (SPM) of Mexico were used during the campaign. The instrument BFOSC mounted to the 2.16 m telescope of XL was taken as the detector through the Johnson *V* filter. The data at SPM were acquired with the instrument RATIR (Reionization and Transients Infrared Camera, Butler et al., 2012), which consists of two optical and two infrared channels, simultaneous imaging in six colors, two optical and four near-infrared (http://ratir.astroscu.unam.mx/public/). Only the two optical cameras were used in this campaign. The frames were obtained simultaneously through the Bessel *V* and *I* filters (only frames observed though V filter were employed in further study). The number of images and data lengths during each observation night are listed in the 3rd and 4th columns of Table 1, respectively. The package of IRAF DAOPHOT was used to reduce the data according to the standard data reduction procedure. Light curves of WD 0246+326 are obtained and shown in Fig. 1.

3. Frequency analysis

3.1. Frequencies extracted from light curves

We used the software `Period04` (Lenz and Breger, 2005) to analyze the light curves. Eleven frequencies with signal-to-noise ratios larger than 4.0 (Breger et al., 1993; Kuschnig et al., 1997) were extracted with the pre-whitening procedure and are listed in Table 2. No linear combination or aliasing frequency were detected. Fig. 2 shows the Fourier transforms of the light curves of WD 0246+326 and the residuals after 11 frequencies are extracted. We used the method of Monte–Carlo simulation to estimate the uncertainties of the frequencies and amplitudes. For more details about the Monte–Carlo simulation, we refer to Fu et al. (2013).

Table 2
Frequency solution resolved from the light curves. Note that *f* is the frequency in μHz, *A* the amplitude in mma, S/N the signal-to noise ratio. ID is the name of the frequency.

ID	$f \pm 3\sigma (\mu\text{Hz})$	$A \pm 3\sigma (\text{mma})$	S/N
a7	1049.27 ± 0.22	5.1 ± 1.2	5.9
a1	1122.67 ± 0.07	20.6 ± 1.3	24.2
a3	1131.46 ± 0.20	5.8 ± 1.6	6.8
a2	1174.21 ± 0.22	7.6 ± 1.4	9.0
a10	1179.43 ± 0.27	4.8 ± 1.4	5.7
a11	1181.93 ± 0.32	4.3 ± 1.4	5.1
a5	1211.75 ± 0.27	5.0 ± 1.3	6.0
a9	1213.53 ± 0.54	3.5 ± 1.4	4.2
a6	1259.24 ± 0.16	6.5 ± 1.3	7.8
a8	1304.32 ± 0.24	5.0 ± 1.3	6.1
a4	1616.03 ± 0.19	6.6 ± 1.1	8.1

Table 3
Frequency list of WD 0246+326. *f* is the frequency in μHz, δf the difference between the adjacent frequencies. *P* the corresponding period in *second* and ΔP the period differences. Note that the frequencies in "b" are taken from Bognár et al. No. is the Number of frequency group, ID the name of the frequency. 2009.

No.	ID	$f(\mu\text{Hz})$	$\delta f(\mu\text{Hz})$	$P(s)$	$\Delta P(s)$
	b1	*799.84*		*1250.3*	
			206.97		257.0
G1	b2	*1006.80*		*993.2*	
			42.47		40.2
	a7	1049.27		953.0	
			73.40		62.3
	a1	1122.67		890.7	
G2			8.80		6.9
	a3	1131.46		883.8	
G3	b3	*1154.53*		*866.2*	
			19.68		14.5
	a2	1174.21		851.6	
G4			5.22		3.8
	a10	1179.43		847.9	
			2.50		1.8
	a11	1181.93		846.2	
G5	b4	*1206.73*		*828.7*	
			24.80		17.4
			5.02		3.43
	a5	1211.75		825.3	
G6			1.78		1.2
	a9	1213.53		824.0	
			45.72		29.9
	a6	1259.24		794.1	
G7	b5	*1285.99*		*777.6*	
			26.75		16.5
			18.33		10.9
	a8	1304.32		766.7	
			310.45		147.4
	b6	*1614.77*		*619.3*	
G8			1.27		0.5
	a4	1616.03		618.8	

3.2. Frequency analysis and mode identification

Table 3 lists the 11 frequencies in Table 2 and the 6 frequencies reported in Bognár et al. (2009). The frequency separations between the adjacent frequencies, the corresponding periods, and the period separations are also given in Table 3. The frequencies are separated into different groups for the convenience of discussion.

1. **G6 and G8** Looking at Table 3, one finds, it can be seen from column 3 that there exist two groups of very closely-spaced frequencies, G6 and G8, with frequency separations of 1.78 μHz and 1.26 μHz, respectively. In addition, G2 and G4 have fre-
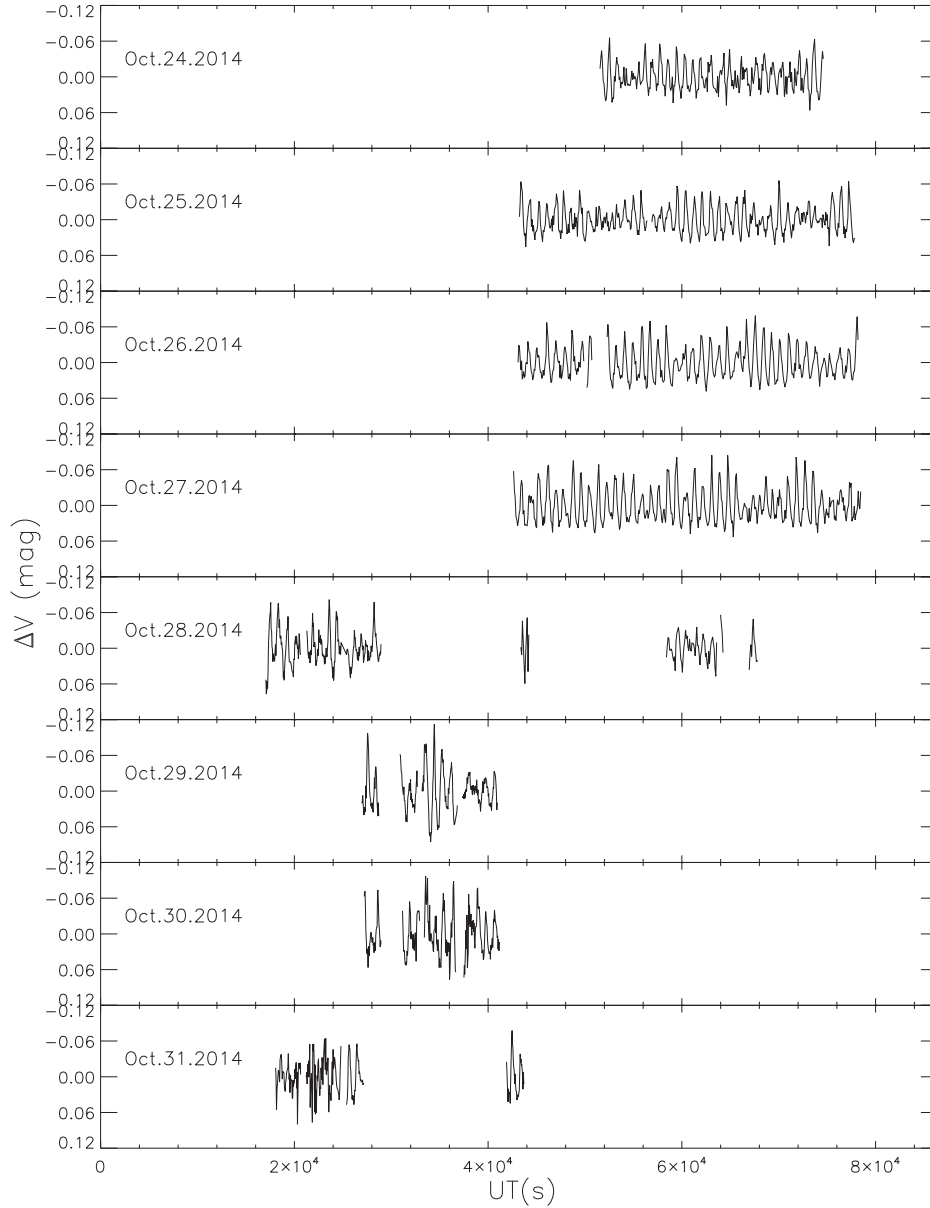
Fig. 1. Light curves of WD 0246+326 in V in 2014.

quency separations equal to or smaller than 8.8 μ Hz. The reason that we do not include b4 into G6 is given in (iv).

2. **G4** The frequency spacings in G4 are 5.2 μ Hz and 2.5 μ Hz, respectively, with the spacing ratio of $\sim$ 2:1. From the spherical symmetry, we suppose that they could be frequencies of the same mode of $l = 2$ with m values of either $+2, +0, -1$ or $+1, -1, -2$.

3. **G4 and G8** According to the equation

$$\sigma_{k,l,m} = \sigma_{k,l} + m \times (1 - C_{k,l})\Omega$$

Where $C_{k,l} = 1/l(l+1)$ in the asymptotic regime (Brickhill, 1975), the rotation splits of the $l = 2$ modes are $\sim$ 1.67 times of the ones of the $l = 1$ modes. Since we identified G4 as $l = 2$, the average frequency split of the $l = 2$ modes is derived as 2.5 μ Hz. Thus, the frequency split of $l = 1$ modes should be $\sim$ 1.5 μ Hz. Since the frequency separation of G2 is as large as 8.8 μ Hz, we interpret them as rotation splits of a $l = 2$ mode rather than a $l = 1$ mode.

4. **G5** The frequency splits of G6 (1.78 μ Hz) and G8 (1.26 μ Hz) are close to the estimated frequency split of the l=1 modes. We thus identify them as $l = 1$ modes. Since the frequency separation of b4-a5 of 5.02 μ Hz is much larger than the average frequency split of $l = 1$ modes, we do not identify b4 as a frequency split of G6.

5. **Period spacing of** $l = 1$**modes** From the asymptotic theory (Unno et al., 1979; Tassoul, 1980), periods of a pulsation mode can be estimated as

$$P_{l,k} \simeq \frac{2\pi^2 k}{\sqrt{l(l+1)}} \left(\int_0^R \frac{N}{r} dr \right)^{-1}$$

Where N is the Brunt–Väisälä frequency, R the stellar radius. The integral part of the right side of the equation is fixed in one ZZ Ceti star. This equation suggests a uniform period spacing for the modes with the same l value and consecutive k values. We notice that the period spacings of a6-a9 as well as a6-a8 are 29.9 s and 27.4 s, respectively, which could be an evidence showing that a8 and a6 are also $l = 1$ modes. A linear
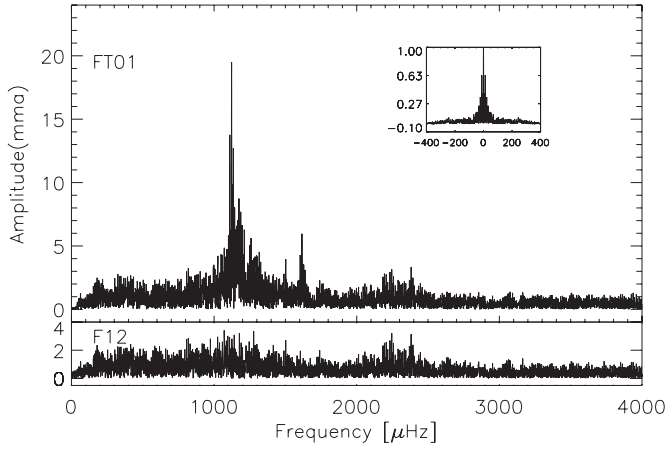
Fig. 2. Fourier transforms of the light curves of WD 0246+326. The upper panel shows the amplitude spectrum of the light curves with the spectral window shown as the insert. The lower panel shows the amplitude spectrum of the residuals with the 11 frequencies extracted through the prewhitening process.
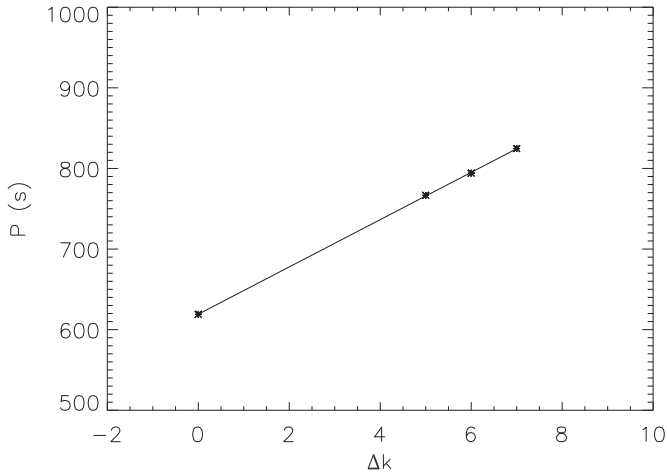
Fig. 3. Linear fitting of the four identified $l = 1$ modes.

fit is made to a9, a6, a8 and b6 with the k values of +7, +6, +5 and 0, respectively concerning the period spacing values between the frequencies. Fig. 3 shows the linear fitting.

6. **Period spacing of $l = 2$ modes** As deduced from the asymptotic theory, the average period spacing of the $l = 1$ modes is $\sim \sqrt{3}$ times as large as that of the $l = 2$ modes. The average period spacing 29.3 ± 0.2 s of $l = 1$ modes is calculated with the four corresponding modes. Hence the average period spacing of the $l = 2$ modes should be ~ 16.9 s. We find that the period spacing between the deduced $m = 0$ modes of the two multiplets a1-a3 and a2-a10-a11 is 39.3 s, not far from twice the average period spacing of the $l = 2$ modes.

7. **The rest frequencies** The l values of the rest other observed frequencies can not be identified directly. We list these frequencies as further signals.

We summarize the mode identification result in Table 4.

4. Asteroseismology

4.1. Frequency splitting and rotational period

From the two doublets which are identified as $l = 1$ modes in Table 4, the average frequency splitting due to rotation is $1.52 \pm 0.13 \mu$ Hz. With the two sets of $l = 2$ modes identified, we notice

Table 4
Mode identifications and further signals. f is the frequency in μHz, δf the frequency separation between the consecutive frequencies in μHz, and P the period in second. The frequencies with IDs given in "b" are from Table 4 of Bognár et al. (2009).

ID	$f(\mu Hz)$	δf	$P(s)$	$\Delta P(s)$	δk	δm
			$l = 1$			
a5	1211.75		825.3			
		1.78				
a9	1213.53		824.0		+7	
				29.9		
a6	1259.24		794.1		+6	
				27.4		
a8	1304.32		766.7		+5	
				147.4		
b6	*1614.77*		*619.3*		0	
		1.27				
a4	1616.03		618.8			
			$l = 2$			
a1	1122.67		890.7			+2?
		8.80			+2	
a3	1131.46		883.8			−2 or −1
				32.2		
a2	1174.21		851.6			+2 or +1
		5.22				
a10	1179.43		847.9		0	0 or −1
		2.50				
a11	1181.93		846.1			−1 or −2
			Further signals			
b1	*799.84*		*1250.3*			
b2	*1006.80*		*993.2*			
a7	1049.27		953.0			
b3	*1154.53*		*866.2*			
b4	*1206.73*		*828.7*			
b5	*1285.99*		*777.6*			

that the frequency separation of a10-a11 is approximately the half of that of a2-a10, suggesting the m values of a2, a10, a11 as either +2, 0, −1 or +1, −1, −2, respectively. The average frequency splitting due to rotation for the $l = 2$ modes are hence derived as 2.51 $\pm 0.01 \mu$ Hz. We do not use G2 to estimate the frequency splitting of the $l = 2$ modes, since the m values of a1 and a3 can not be assigned reliably.

With the average rotation splitting of the $l = 1$ modes of 1.52 $\pm 0.13 \mu$ Hz and that of the $l = 2$ modes of 2.51 $\pm 0.01 \mu$ Hz, we calculate the rotation period of WD 0246+326 as 3.78 ± 0.11 days.
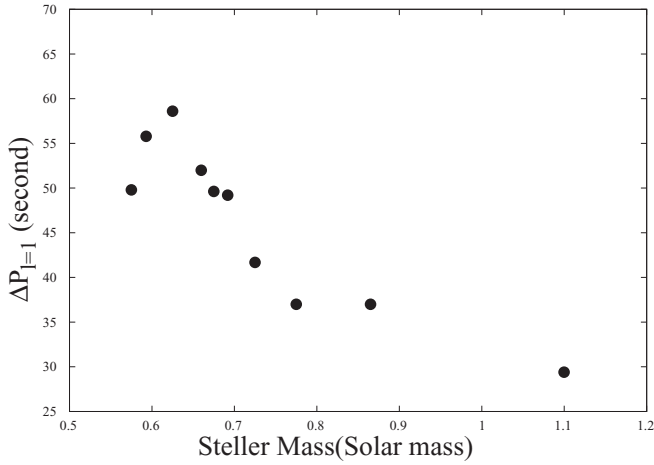
4.2. Average period spacing

As shown in Fig. 3, the four identified $l = 1$ modes are used to make a linear fitting, leading to an average period spacing of 29.3 ± 0.2 s. It is known that the period spacing of pulsating white dwarfs depends sensitively on the total mass of the stars, as shown in Fig. 2 of Kawaler and Bradley (1994) for pulsating PG1159 stars with models of different masses. Brassard et al. (1992) also noted this dependence in their Figure 38 for ZZ Ceti stars from a modeling work.

Table 5 lists the average period spacings of the $l = 1$, $\Delta P_{l=1}$ modes determined from observations and the stellar mass, M_* deduced from the constraints of the theoretical models for 10 ZZ Ceti stars (Kanaan et al., 2005; Li et al., 2015; Fu et al., 2013; Su et al., 2014b; 2014a; Pakštienė, 2013; Pakštienė et al., 2014; Córsico et al., 2012; Pech et al., 2006; Guifang et al., 2015; Bognár et al., 2016). Fig. 4 plots the $\Delta P_{l=1}$ versus M_*. A trend of increasing mass with decreasing average period spacing can be seen from Fig. 4. With an average period spacing of the $l = 1$ modes of 29.3 s, WD 0246+326 would be a massive ZZ Ceti star, with the mass larger than 0.75 solar mass.

Table 5

Summary of average period spacings of the $l = 1$ modes determined from observations and the stellar mass deduced theoretical models for 10 ZZ Ceti stars.

ID	Steller Mass($M_\odot$)	$\Delta P_{l=1}(s)$
GD1212	0.775	37
KUV 08368+4026	0.692	49.2
HS 0507+0434B	0.675	49.63
PG 2303+243	0.66	52.0
G117-B15A	0.593	55.8
HL Tau 76	0.575	49.8
BPM37093	1.1	29.4
G207-9	0.725	41.7
LP 133-144	0.865	37
KUV 11370+4222	0.625	58.6

Fig. 4. Stellar mass versus average period spacing of l = 1 modes for 10 well-studied ZZ Ceti stars.

5. Constraints from theoretical models

5.1. Modeling tool

We calculated theoretical evolutionary models of white dwarf stars with the WDEC codes (originally developed by Schwarzschild and Härm 1965, see Su et al., 2014b for the information of the latest update). Construction of the grid of models is made with the input of four parameters: the stellar mass, the effective temperature, the Hydrogen mass fraction and the Helium mass fraction.

5.2. Stellar parameters

Bergeron et al. (1995) provided for WD 0246+326 the effective temperature T_{eff} of 11290 ± 200 K and the surface gravity $\log g$ of 8.08 ± 0.05. Gianninas et al. (2011) presented with spectroscopic observations $T_{eff} = 11940 \pm 180$ K and $\log g = 8.21 \pm 0.05$. These two sets of parameter are very different to each other and place WD 0246+326 on either the red or the blue edge of the instability strip of ZZ Ceti stars on the H-R diagram. As indicated in Section 4.2, the value of the average period spacing of the $l = 1$ modes determined in present paper suggests that the stellar mass of WD 0246+326 should be larger than 0.75 solar mass. We hence build a coarse grid of models with a wide parameter range and relatively large steps, as listed in Table 6. The Helium mass fraction is fixed as 10^{-2} in the grid calculation because the models are not sensitive to this parameter (Brassard et al., 1992).

Table 6

Parameters of the coarse grid of models. Note that M_H is the ratio of the hydrogen layer mass to the stellar mass M_*, and M_{He} the ratio of the helium layer mass to M_*.

	Coarse grid		Fine grid	
	Range	Step	Range	Step
Mass($M_\odot$)	$0.75 - 1.20$	0.02	$0.9 - 1.02$	0.01
$T_{eff}(K)$	$11000 - 14000$	200	$11400 - 12200$	100
$\log M_H$	$-4.0 - -8.0$	0.5	$-4.5 - -7.0$	0.1
$\log M_{He}$	-2		-2	

Table 7

The best fit model for WD 0246+326. The symbols are the same as in Table 6.

$T_{eff}(K)$	11700 ± 100
$\log g$	8.66 ± 0.02
$M(M_\odot)$	0.98 ± 0.01
$\log M_H$	-5.1 ± 0.1
$\log M_{He}$	-2

5.3. Frequency matching

Firstly, periods of the four $l = 1$ modes, two $l = 2$ modes and other six signals with undetermined l (listed in Table 4) are used to match periods of the eigen modes of the theoretical models on the coarse grid. The χ^2 tests are used to select the best fit models as follows,

$$\chi^2 = \sum_n (P_n^{the} - P_n^{obs})^2$$

where P^{the} denotes the periods of the eigen modes of the theoretical models and P^{obs} the observationally determined periods.

One minimum of χ^2 was found on the coarse grid, which corresponds to the model of stellar parameters: $M = 0.95 \, M_\odot$ and $T_{eff} = 11700$ K. In order to put a better constraint on the model parameters, we build a finer model grid with a narrower range of parameters and smaller steps, as listed in Table 6.

Since we can not determined the m values for the frequencies listed in Table 4, we calculate fore each theoretical mode the frequencies of the multiplets due to rotation splitting derived in Section 4.1. Then we search the whole set of frequency for the best fitted ones with the observationally detected frequencies. Frequencies of all identified $l = 1$ modes are compared with theoretical ones of the $l = 1$modes and their rotation splits, and the same for the $l = 2$ modes. The further signals listed in Table 4 are compared with all $l = 1$ and $l = 2$ modes and their rotation splits. With the minimum χ^2, one best fit model was found in the procedure. We summarize its stellar parameters in Table 7. Fig. 5 displays the distribution of χ^2 test. The three slices are plotted with the hydrogen fraction, the effective temperature and the stellar mass fixed, respectively.

The best fit model provides a set of l, k and m values corresponding to the observationally determined frequencies. Table 8 lists the observed periods and the calculated periods from the best fit model together with the mode identifications.

6. Conclusions

Time series photometric observations were made for WD 0246+326 for eight night during a bi-site observation campaign in October 2014. Analysis of the obtained data leads to 11 frequencies. Combined with the results of Bognár et al. (2009), 17 frequencies, including one triplet, three doublets, and eight single frequencies, are identified as either $l = 1$ and $l = 2$ modes
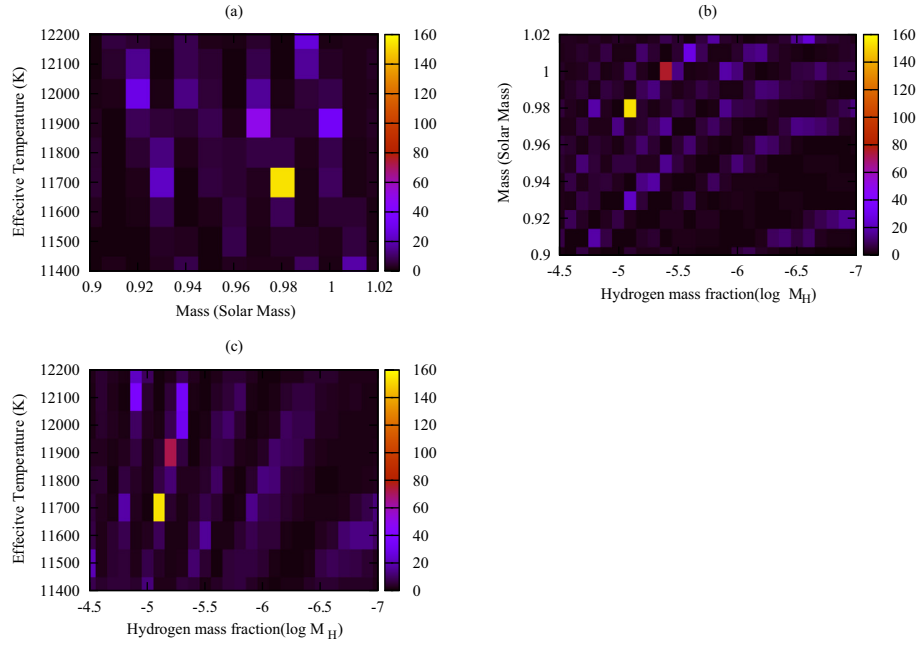
Fig. 5. χ^2 test for the fine grid of model. The grey scales on the right side of each panel represent the inversed χ^2 values. (a) Stellar mass versus effective temperature with a fixed hydrogen mass fraction of $10^{-5.1}$, (b) Stellar mass versus hydrogen mass fraction with a fixed effective temperature of 11700 K, (c) hydrogen mass fraction versus effective temperature with a fixed stellar mass of 0.98 solar mass.

Table 8

Mode identifications for WD 0246+326. P_o is the observed period in seconds, P_c the theoretically calculated period of the best fit models as listed in Table 7.

	$P_o(s)$	$P_c(s)$	(l, k, m)
		$l = 1$	
a4	618.8	619.5	(1,19,−1)
b6	619.3	620.1	(1,19,0)
a8	766.7	766.8	(1,24,0)
a6	794.1	793.5	(1,25,+1)
a9	824.0	824.5	(1,26,0)
a5	825.3	825.5	(1,26,1)
		$l = 2$	
a11	846.9	846.6	(2,47,−2)
a10	847.9	848.4	(2,47,−1)
a2	851.6	852.0	(2,47,+1)
a3	883.6	884.2	(2,49,−1)
a1	890.7	890.2	(2,49,+2)
		Further signal	
b1	1250.3	1248.5	(2,68,0)
b2	993.2	993.2	(1,32,−1)
a7	953.0	954.6	(2,53,−2)
b3	866.2	865.8	(2,48,−1)
b4	828.7	828.2	(2,46,−2)
b5	777.6	777.8	(2,43,0)

or further signals. The rotation split of the $l = 1$ modes is derived as $1.52 \pm 0.05 \mu$ Hz, hence the rotation period is deduced to be 3.78 ± 0.11 days. With the four identified $l = 1$ modes, the average period spacing of the $l = 1$ modes is determined as 29.3 s, which implies that WD 0246+326 could be a massive ZZ Ceti star. Theoretical modeling for this star is then performed. The theoretically calculated frequencies are compared with the observed ones with the χ^2 test. The stellar parameters of the best fit model are $M = 0.98 \pm 0.01 \, M_\odot$, $T_{eff} = 11700 \pm 100$ K and the hydrogen mass fraction $logM_H/M = -5.1 \pm 0.1$. The modes of observed frequencies are hence identified.

Although the number of ZZ Ceti stars is the largest in the four known types of pulsating white dwarfs, the samples with stellar parameters determined precisely through asteroseismology are still very limited (less than a dozen). Our result in determining stel-

lar parameters of WD 0246+326 through asteroseismology shows that WD 0246+326 is a massive ZZ Ceti star. With the mass of WD 0246+326 $0.98 \pm 0.01 M_\odot$ would be a newly-discovered ultra-massive ZZ Ceti star ever known after BPM37093 with $M \approx 1.1 M_\odot$, which could experience core crystallization. The debate about the fraction of the crystallized core of BPM37093 depending on the core chemical composition is still open (Kanaan et al., 2005; Brassard et al., 1992). We also notice that the mass of the DAV GD518 is derived as $1.20 \pm 0.03 M_\odot$ based upon spectroscopic observations (Hermes et al., 2013). However, this mass value is not yet confirmed by means of asteroseismology with existing photometric data. Determination of the stellar mass of WD 0246+326 from this work with $M_* \approx 0.98 \pm 0.01 M_\odot$ provides a new target for study of potential core crystallization of white dwarf stars. Hence, high quality spectroscopic observations and more multi-site photometric campaigns are needed for further study of WD 0246+326 as an interesting ZZ Ceti star.

Acknowledgements

References

Bergeron, P., Wesemael, F., Lamontagne, R., Fontaine, G., Saffer, R.A., Allard, N.F., 1995. Optical and ultraviolet analyses of ZZ ceti stars and study of the atmospheric convective efficiency in DA white dwarfs. ApJ 449, 258. doi:10.1086/176053.

Bognár, Z., Paparó, M., Bradley, P.A., Bischoff-Kim, A., 2009. Characterizing the pulsations of the ZZ ceti star KUV 02464+3239. MNRAS 399, 1954–1963. doi:10.1111/j.1365-2966.2009.15438.x.

Bognár, Z., Paparó, M., Molnár, L., Pápics, P.I., Plachy, E., Verebélyi, E., Sódor, Á., 2016. G 207-9 and LP 133-144: light-curve analysis and asteroseismology of two ZZ ceti stars. MNRAS 461, 4059–4070. doi:10.1093/mnras/stw1597.

Brassard, P., Fontaine, G., Wesemael, F., Tassoul, M., 1992. Adiabatic properties of pulsating DA white dwarfs. IV - an extensive survey of the period structure of evolutionary models. ApJS 81, 747–794. doi:10.1086/191704.

Breger, M., Stich, J., Garrido, R., Martin, B., Jiang, S.Y., Li, Z.P., Hube, D.P., Ostermann, W., Paparo, M., Scheck, M., 1993. Nonradial pulsation of the Delta-Scuti star Bu-Cancri in the praesepe cluster. A&A 271, 482.

Brickhill, A.J., 1975. The gravity oscillations of white dwarfs.. MNRAS 170, 405–421. doi:10.1093/mnras/170.2.405.

Butler, N., Klein, C., Fox, O., Lotkin, G., Bloom, J., Prochaska, J.X., Ramirez-Ruiz, E., de Diego, J.A., Georgiev, L., González, J., Lee, W.H., Richer, M.G., Román, C., Watson, A.M., Gehrels, N., Kutyrev, A., Bernstein, R., Alvarez, L.C., Ceseña, U., Clark, D., Colorado, E., Córdova, A., Farah, A., García, B., Guisa, G., Herrera, J., Lazo, F., López, E., Luna, E., Martínez, B., Murillo, F., Murillo, J.M., Núñez, J.M., Pedrayes, M.H., Quirós, F., Ochoa, J.L., Sierra, G., Moseley, H., Rapchun, D., Robinson, F.D., Samuel, M.V., Sparr, L.M., 2012. First Light with RATIR: An Automated 6-band Optical/NIR Imaging Camera. In: Ground-based and Airborne Instrumentation for Astronomy IV. In: Proc. SPIE, 8446, p. 844610. doi:10.1117/12.926471.

Córsico, A.H., Althaus, L.G., Miller Bertolami, M.M., Romero, A.D., García-Berro, E., Isern, J., Kepler, S.O., 2012. The rate of cooling of the pulsating white dwarf star G117-B15A: a new asteroseismological inference of the axion mass. MNRAS 424, 2792–2799. doi:10.1111/j.1365-2966.2012.21401.x.

Fontaine, G., Bergeron, P., Brassard, P., Billères, M., Charpinet, S., 2001. Discovery of two new pulsating DA (ZZ ceti) white dwarfs. ApJ 557, 792–797. doi:10.1086/321695.

Fu, J.-N., Dolez, N., Vauclair, G., Fox-Machado, L., Kim, S.-L., Li, C., Chen, L., Alvarez, M., Su, J., Charpinet, S., Chevreton, M., Michel, R., Yang, X.H., Li, Y., Zhang, Y.P., Molnar, L., Plachy, E., 2013. Asteroseismology of the ZZ ceti star HS 0507+0434b. MNRAS 429, 1585–1595. doi:10.1093/mnras/sts438.

Gianninas, A., Bergeron, P., Ruiz, M.T., 2011. A spectroscopic survey and analysis of bright, hydrogen-rich white dwarfs. ApJ 743, 138. doi:10.1088/0004-637X/743/2/138.

Guifang, L., Yan, L., Jie, S., 2015. The asteroseismology of ZZ ceti star GD1212. ArXiv:1501.05360.

Hermes, J.J., Kepler, S.O., Castanheira, B.G., Gianninas, A., Winget, D.E., Montgomery, M.H., Brown, W.R., Harrold, S.T., 2013. Discovery of an ultramassive pulsating white dwarf. ApJ 771, L2. doi:10.1088/2041-8205/771/1/L2.

Kanaan, A., Nitta, A., Winget, D.E., Kepler, S.O., Montgomery, M.H., Metcalfe, T.S., Oliveira, H., Fraga, L., da Costa, A.F.M., Costa, J.E.S., Castanheira, B.G., Giovannini, O., Nather, R.E., Mukadam, A., Kawaler, S.D., O'Brien, M.S., Reed, M.D., Kleinman, S.J., Provencal, J.L., Watson, T.K., Kilkenny, D., Sullivan, D.J., Sullivan, T., Shobbrook, B., Jiang, X.J., Ashoka, B.N., Seetha, S., Leibowitz, E., Ibbetson, P., Mendelson, H., Meištas, E.G., Kalytis, R., Ališauskas, D., O'Donoghue, D., Buckley, D., Martinez, P., van Wyk, F., Stobie, R., Marang, F., van Zyl, L., Ogloza, W., Krzesinski, J., Zola, S., Moskalik, P., Breger, M., Stankov, A., Silvotti, R., Piccioni, A., Vauclair, G., Dolez, N., Chevreton, M., Deetjen, J., Dreizler, S., Schuh, S., Gonzalez Perez, J.M., Østensen, R., Ulla, A., Manteiga, M., Suarez, O., Burleigh, M.R., Barstow, M.A., 2005. Whole earth telescope observations of BPM 37093: a seismological test of crystallization theory in white dwarfs. A&A 432, 219–224. doi:10.1051/0004-6361:20041125.

Kawaler, S.D., Bradley, P.A., 1994. Precision asteroseismology of pulsating PG 1159 stars. ApJ 427, 415–428. doi:10.1086/174152.

Kuschnig, R., Weiss, W.W., Gruber, R., Bely, P.Y., Jenkner, H., 1997. Microvariability survey with the hubble space telescope fine guidance sensors. Exploring the instrumental properties. A&A 328, 544–550.

Landolt, A.U., 1968. A new short-Period blue variable. ApJ 153, 151. doi:10.1086/149645.

Lenz, P., Breger, M., 2005. Period04 user guide. Commun. Asteroseismol. 146, 53–136. doi:10.1553/cia146s53.

Li, C., Fu, J.-N., Vauclair, G., Dolez, N., Fox-Machado, L., Michel, R., Chavez, M., Bertone, E., 2015. Asteroseismology of the ZZ ceti star KUV 08368+4026. MNRAS 449, 3360–3369. doi:10.1093/mnras/stv481.

Pakštienė, E., 2013. Identification of PG 2303+243 pulsation modes. In: European Physical Journal Web of Conferences. In: European Physical Journal Web of Conferences, vol. 43, p. 05012. doi:10.1051/epjconf/20134305012.

Pakštienė, E., Laugalys, V., Qvam, J., Boyle, R.P., 2014. New analysis of ZZ Ceti star PG 2303+243. In: Guzik, J.A., Chaplin, W.J., Handler, G., Pigulski, A. (Eds.), Precision Asteroseismology. In: IAU Symposium, vol. 301, pp. 469–470. doi:10.1017/S1743921313015093.

Pech, D., Vauclair, G., Dolez, N., 2006. Asteroseismological constraints on the structure of the ZZ ceti star HL tau 76. A&A 446, 223–235. doi:10.1051/0004-6361:20053150.

Provencal, J.L., Montgomery, M.H., Kanaan, A., Thompson, S.E., Dalessio, J., Shipman, H.L., Childers, D., Clemens, J.C., Rosen, R., Henrique, P., Bischoff-Kim, A., Strickland, W., Chandler, D., Walter, B., Watson, T.K., Castanheira, B., Wang, S., Handler, G., Wood, M., Vennes, S., Nemeth, P., Kepler, S.O., Reed, M., Nitta, A., Kleinman, S.J., Brown, T., Kim, S.-L., Sullivan, D., Chen, W.P., Yang, M., Shih, C.Y., Jiang, X.J., Sergeev, A.V., Maksim, A., Janulis, R., Baliyan, K.S., Vats, H.O., Zola, S., Baran, A., Winiarski, M., Ogloza, W., Paparo, M., Bognar, Z., Papics, P., Kilkenny, D., Sefako, R., Buckley, D., Loaring, N., Kniazev, A., Silvotti, R., Galleti, S., Nagel, T., Vauclair, G., Dolez, N., Fremy, J.R., Perez, J., Almenara, J.M., Fraga, L., 2012. Empirical determination of convection parameters in white dwarfs. I. Whole telescope observations of EC14012-1446. ApJ 751, 91. doi:10.1088/0004-637X/751/2/91.

Saio, H., 2013. Pulsations in white dwarfs: Selected topics. In: European Physical Journal Web of Conferences. In: European Physical Journal Web of Conferences, vol. 43, p. 05005. doi:10.1051/epjconf/20134305005.

Schwarzschild, M., Härm, R., 1965. Thermal instability in non-degenerate stars. The Astrophysical Journal 142, 855. doi:10.1086/148358.

Su, J., Li, Y., Fu, J.-N., 2014a. Preliminary identification of the observed pulsation modes of ZZ ceti star KUV 03442+0719. New A 33, 52–56. doi:10.1016/j.newast.2014.04.006.

Su, J., Li, Y., Fu, J.-N., Li, C., 2014b. Asteroseismology of the ZZ ceti star KUV 11370+4222. MNRAS 437, 2566–2576. doi:10.1093/mnras/stt2069.

Tassoul, M., 1980. Asymptotic approximations for stellar nonradial pulsations. ApJS 43, 469–490. doi:10.1086/190678.

Unno, W., Osaki, Y., Ando, H., Shibahashi, H., 1979. Nonradial Oscillations of Stars.

Winget, D.E., Hansen, C.J., Liebert, J., van Horn, H.M., Fontaine, G., Nather, R.E., Kepler, S.O., Lamb, D.Q., 1987. An independent method for determining the age of the universe. ApJ 315, L77–L81. doi:10.1086/184864.

Winget, D.E., Kepler, S.O., 2008. Pulsating white dwarf stars and precision asteroseismology. ARA&A 46, 157–199. doi:10.1146/annurev.astro.46.060407.145250.

论 文　　　**自适应光学专题**

兴隆2.16 m望远镜自适应光学系统

李常伟[1,2*], 李邦明[1,2], 陆彦婷[1,2], 陆启帅[1,2], 郑兆瑛[1,2], 王地[1,2], 李顺[1,2]

1. 中国科学院国家天文台南京天文光学技术研究所, 南京 210042;
2. 中国科学院天文光学技术重点实验室, 南京 210042

* 联系人, E-mail: cwli@niaot.ac.cn

摘要　　　自适应光学系统是大口径天文望远镜克服大气湍流,提高望远镜成像质量的必备手段之一. 本文针对兴隆2.16 m望远镜及其所在台址的大气视宁度,研制了一套自适应光学系统. 系统的主要部件包括具有109个压电陶瓷驱动器的变形镜,具有100个子孔径的Shack-Hartmann波前传感器,以及基于现场可编程门阵列(Field Programmable Gate Array, FPGA)的高速波前控制平台等. 实验结果表明,该系统可以把大气扰动引起的波前像差的均方根值校正到0.1λ以下,获得接近衍射极限的成像质量.

关键词　　　自适应光学系统,波前重建,波前控制,高速控制平台

PACS: 07.05.Pj, 42.25.Dd, 42.68.Bz, 95.75.Qr

1 引言

大气湍流是影响地基天文望远镜成像质量的主要因素, 为了克服大气湍流的影响, 提高望远镜的分辨率, 许多大口径天文望远镜都装配了自适应光学系统[1–3]. 位于国家天文台兴隆观测站的2.16 m望远镜是国内口径较大的天文光学望远镜之一. 由于兴隆站点视宁度条件的限制, 2.16 m望远镜目前主要进行天文光谱观测. 为了提高望远镜工作效率, 同时便于天文学家进行成像观测, 我们在中国科学院天文台站设备更新及重大仪器设备运行专项资助的支持下研制了一套适用于2.16 m望远镜的小视场自适应光学系统.

望远镜自适应光学系统的设计必须考虑望远镜

站点关于大气湍流的统计数据. 大气湍流的统计数据反映了站点大气湍流扰动的剧烈程度, 其中包括大气的相位结构常数、视宁度、等晕角、相干长度等[4–10]. 其中, 主要反映站点望远镜实际成像质量的统计参数为大气视宁度. 兴隆观测站的大气视宁度大部分时间在2″–3″之间, 平均风速为6 m/s. 与世界上其他天文观测站点相比[11,12], 兴隆站的视宁度条件并不理想. 据兴隆站点的前期统计数据, 大气湍流扰动对兴隆站2.16 m望远镜引入的波前畸变的均方根(Root Mean Square, RMS)值为1.5倍波长, 对应焦面处的斯特列尔比约为0.02. 为了使望远镜能满足清晰成像的观测要求, 所配备的自适应光学系统必须能够将该湍流波前校正至0.2倍波长(RMS)以下, 焦面处的斯特列尔比大于0.2,

将望远镜的斯特列尔比提高至少1个量级. 这意味着, 为2.16 m望远镜配备自适应光学系统不仅技术难度大, 而且需要高性能的元器件. 在预算范围之内, 研制了一套工作在自然导星模式下的单共轭自适应光学系统, 能够在近红外波段提供接近衍射极限的成像质量. 该系统利用Shack-Hartmann (SH)波前传感器和四象限探测器(Quadrant Photodiodes, QD)在可见光波段分别探测大气湍流引起的高阶波前像差和倾斜像差, 并分别利用压电陶瓷变形镜和倾斜镜对这两种波像差进行实时补偿, 经过自适应光学系统补偿的星光经离轴抛物镜汇聚至近红外相机成像. 本文将从光学系统、控制系统、波前控制算法和实验结果几方面对这套自适应光系统进行简要介绍.

2 光学系统

兴隆2.16 m望远镜具有3个光学焦点, 分别是主焦点、卡塞格林(Cassegrain)焦点和折轴(Coude)焦点. 考虑到自适应光学系统的体积以及焦点的稳定性, 此套自适应光学系统设计安装在望远镜的折轴焦点处.

该自适应光学系统的光路结构如图1所示, 来自望远镜折轴焦点的发散光经过离轴抛物镜OAP1准直, 入射到倾斜镜TTM上, 继而入射到变形镜DM上, 经DM反射后的平行光经长通二向色分光棱镜(Dichroic Beam Splitter, DBS)后, 分为两束, 透过二向色分光棱镜的红外波段(>800 nm)的平行光, 经过离轴抛物镜OAP2汇聚到红外CCD (Charge Coupled Device)相机上, 用于成像观测, 经二向色分光棱镜反射的可见光波段(<800 nm)的平行光经可见光分光棱镜BS (Beam Splitter)后分为两束平行光: 一束经离轴抛物镜OAP3和OAP4压缩, 入射到波前传感器(Wavefront Sensor, WFS)上, 用于测量光束的波前像差; 第二束经过透镜汇聚, 入射到四象限探测器(Quadrant Detector, QD)上, 用于传感光束的倾斜.

确定系统的初步结构后, 结合兴隆站点的大气条件采用蒙特卡罗方法对该自适应光学系统进行了详细的结构优化和性能仿真[13,14], 根据仿真结果选择和确定了波前校正器和波前传感器的详细参数. 该自适应光学系统中, 波前校正器包括变形镜和倾斜镜两部分. 其中, 变形镜采用OKO公司制造的109通道压电陶瓷促动器变形镜, 具体技术参数如表1所示. 倾斜镜采

用PI公司制造的压电陶瓷倾斜镜, 技术参数如表2所示. 模拟仿真结果表明所选择变形镜和倾斜镜组合对兴隆站点的大气湍流引起的波前畸变面形拟合误差约为0.06个波长, 能够达到该自适应系统设计的成像目标. SH波前传感器为定制, 其微透镜阵列的子孔径数目为100个, 有效子孔径为64个, 测量精度达到1/100个波长, 技术参数如表3所示.
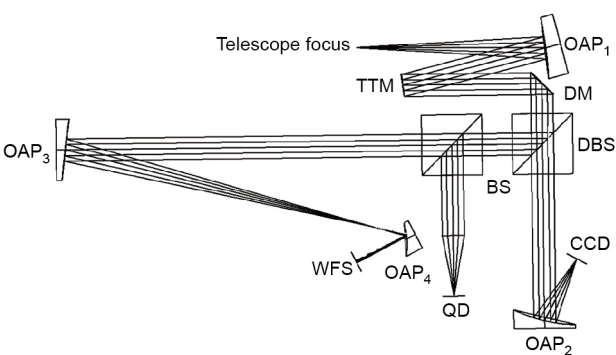

图 1 2.16 m望远镜自适应光学系统光路示意图
Figure 1 Diagram of the adaptive optics (AO) system for the 2.16 m telescope.

表 1 变形镜技术参数
Table 1 Technical parameters for deformable mirror

口径	驱动器数目	初始面形误差RMS	电压范围	最大行程
50 mm	109	<2 μm	0–400 V	8 μm

表 2 倾斜镜技术参数
Table 2 Technical parameters for tip/tilt mirror

口径	校正范围	闭环校正精度
50 mm	2 mrad	0.02 mrad

表 3 SH波前传感器技术参数
Table 3 Technical parameters for SH wavefront sensor

参数	描述
口径	5 mm
像素大小	14 μm
像素个数	256×256
测量精度	$\lambda/100$
微透镜口径	300 μm
微透镜焦距	4.5 mm
工作波段	350–1100 nm
帧频	>1000 fps

3 控制系统

兴隆2.16 m望远镜自适应光学系统控制系统的框图如图2所示, 该控制系统主要包括上位机软件、变形镜控制回路和倾斜镜控制回路3个部分. 其中上位机软件用于提供可视化的人机接口, 通过以太网接口与变形镜和倾斜镜控制回路相连, 方便用户监控系统运行状况, 并进行各种操作. 为提高系统的实时性, 控制系统和上位机通信采用了裸机程序设计方法, 并且设计实现了TCP/IP协议栈, 同时满足了控制系统的实时性和稳定性要求. 变形镜控制回路通过采集SH波前传感器的光斑信号, 经计算转化为变形镜驱动电压, 驱动变形镜校正波前的高阶像差, 该回路的控制频率为1000 Hz. 倾斜镜控制回路通过采集QD的输出信号, 经计算转化为倾斜镜的驱动电压, 驱动倾斜镜校正波前的倾斜像差, 该回路的控制频率为2000 Hz. 变形镜控制回路和倾斜镜控制回路的具体硬件实现介绍如下.

3.1 变形镜控制回路

如图2上半部分所示, 变形镜控制回路以FPGA+DSP作为主处理器, 通过Camera Link接口实时采集SH传感器获得的光斑图, 对光斑图进行波前重建和控制信号计算后得到相应的控制电压, 然后通过12位数模转换器(Digital to Analog Converter, DAC)和高压放大器(High Voltage Amplifier, HVA)输出0–300 V的高压驱动变形镜产生相应的面形.

控制回路主处理器的FPGA部分主要以高速并行

图 2 控制系统框图
Figure 2 Diagram of the control system.

计算的方式对光斑图进行处理, 完成波前重建和波前控制信号计算, 数据处理和相关算法均以硬件描述语言实现. 波前重建和波前控制的算法介绍见第4节. 主处理器的DSP部分主要用于硬件和上位机数据交换和控制变形镜改变面型以补偿大气湍流引起的波前畸变.

3.2 倾斜镜控制回路

如图2下半部分所示, 倾斜镜控制回路以Xilinx公司的Zynq处理器(FPGA+ARM)作为主处理器, 通过16位高精度模数转换器(Analog to Digital Converter, ADC)对QD信号进行实时采集, 将QD信号转化为对应的倾斜量后, 经计算处理得到相应的电压控制量, 继而通过16位DAC和HVA输出0–100 V的高压, 驱动倾斜镜产生相应的倾斜.

Zynq处理器的FPGA部分主要以高速并行计算的方式对QD信号进行数据处理和控制信号计算. 分析了不规则入射光斑情况下QD信号与所测倾斜量的对应关系, 并综合采用自抗扰控制算法和改进的PID算法, 获得了较高的倾斜校正精度[15–17]. Zynq处理器的ARM部分主要用于和上位机通信. 有关Zynq编程开发和基于Zynq的高精度数据采集知识可参阅文献[18,19].

由于压电陶瓷倾斜镜是较大的容性负载, 需要较大的电流驱动, 倾斜控制回路中的HVA为自主设计, 最大输出电流高达8 A, 经测试, 其线性、精度和带宽均优于本控制系统设计指标.

4 波前控制算法

4.1 波前重建

在自适应光学系统中, 波前重建是指由波前传感器得到的光强信息, 重建出湍流波前. 波前重建是自适应光学系统中校正大气湍流的重要环节, 其精度直接决定了系统的性能. 兴隆2.16 m自适应光学系统采用SH波前传感器探测大气湍流像差, 波前重建的过程就是由SH传感器得到的光斑图重建出湍流波前的过程. 本系统采用了基于Zernike多项式的模式法[20]进行波前重建. 该方法首先将波前表示为若干Zernike多项式的线性组合, 然后利用SH波前传感器各子孔径探测到局部波前斜率, 通过最小范数最小二乘法拟合出各项Zernike多项式的系数, 最终求解出的波前系数用于后续的波前校正.
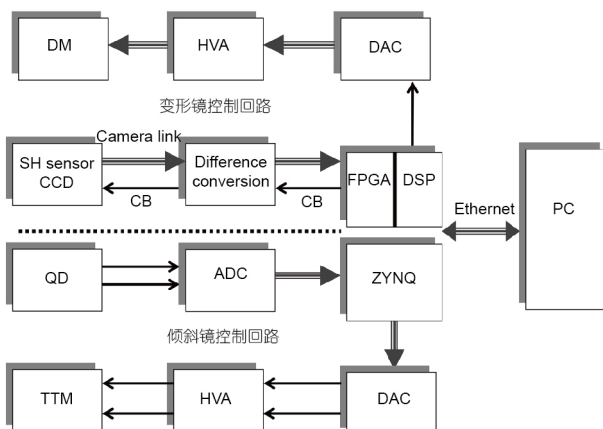
具体说来, 整个波前重建过程分三步完成, 即从光斑图中提取光斑实际质心和参考质心位置、依据质心位置计算局部波前斜率、基于Zernike多项式的波前重建. 这三个步骤中, 精确定位光斑实际质心点与参考质心点是波前重建的关键. 因为在实际天文望远镜工作环境下, 通常没有合适的参考光源用于参考质心定标, 使质心的精确定位比较困难. 针对这一问题, 设计了一种无参考输入光条件下的自适应波前重建算法[21]. 该方法首先采用亮度分层法确定光斑探测窗口, 然后采用自适应阈值法确定实际质心位置, 能够准确定位参考质心和实际质心的位置. 完整的波前重建算法请参阅文献[21], 该算法经FPGA实现后进行了模拟动态大气环境的自适应光学系统校正实验, 验证了该算法的可靠性与实用性.

需要注意的是, 在采用模式法进行波前重建时, 所采用的Zernike多项式的阶数并不是越多越好, 而是要与SH传感器子孔径的个数相匹配. 所选择的Zernike多项式的阶数过小, 就不能够充分发挥波前传感器的性能, 是对传感器性能的浪费; 所选择的多项式阶数过大, 由于波前传感器子孔径数目有限, 会存在采样不足导致重建波前不准确的问题. 因此使用模式法重建波前时必须仔细选择所使用Zernike多项式的阶数.

4.2 波前控制

自适应光学系统可以看作是一个以光学波前为控制对象的自动控制系统. 为了减小对波前传感器动态范围的要求, 克服系统中变形镜本身存在的迟滞、蠕动等非线性效应, 自适应光学系统一般采用闭环负反馈的工作方式. 图3给出了本系统的控制框图, 其中CC为控制计算. 设$\varphi_{tur}(x,y,t)$是入射的大气畸变波前, $\varphi_{dm}(x,y,t)$是变形镜在控制信号下产生的波前, $\varphi_{res}(x,y,t)$是残余波前, 则有$\varphi_{res}(x,y,t)=\varphi_{tur}(x,y,t)-\varphi_{dm}(x,y,t)$, 即波前传感器测量的是变形镜校正后的波前误差. 采用闭环负反馈的工作方式, 要求输出信号$\varphi_{dm}(x,y,t)$能够很好地跟踪输入信号$\varphi_{tur}(x,y,t)$, 从而使$\varphi_{res}(x,y,t)$取得较小值.

为了实现自适应光学系统和大气湍流像差时空特性的最优匹配, 本系统采用模式控制方法滤掉容易引起控制系统不稳定且对像质影响不大的高频像差, 只对大气湍流中对系统像质影响较大的低频像差进行校正. 图4给出了模式控制法的原理结构图, 其基本思想为: 残余波前由SH波前传感器采样并测量, 然后经过波前重建算法, 分解为一系列正交的像差模式, 并把各个模式像差分别输入到控制器中. 控制器根据自适应光学系统对这些模式的响应特性以及大气湍流、噪声等环境对模式的影响程度, 根据设计的控制算法计算出各个模式控制信号的输出, 汇总后驱动变形镜进行工作. 这样就把多输入多输出的自适应光学控制系统分解为多个并行的单输入单输出的控制系统进行处理, 并通过控制算法设计对每个控制通道进行控制. 具体的控制算法可参阅文献[22,23], 实验表明该方法实现了系统和待校正像差模式时空特性的最优匹配, 增加了系统的稳定性.
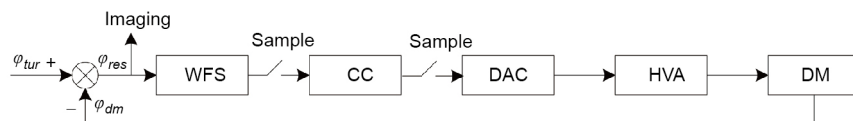

图 3 自适应光学系统控制框图
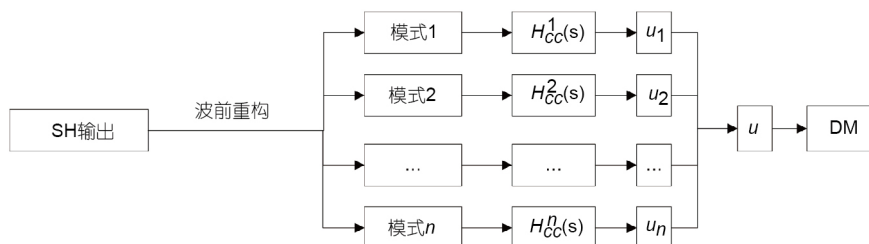**Figure 3** Block-diagram of control system for the AO system.

图 4 模式控制法的原理结构图
Figure 4 Diagram of the scheme of the modal control.

5 系统性能

由于预算有限, 目前系统中的SH传感器的探测器和红外成像相机灵敏度太低, 无法进行星光下的自适应光学校正实验, 只能进行实验室模拟验证.

为了验证系统性能, 采用波长为0.66 μm的激光二极管作为光源, 将二极管发出的激光耦合到单模光纤中. 由于单模光纤的直径很小, 对可见光一般为几个微米, 因此, 单模光纤的输出可以近似看作点光源. 实验中, 以单模光纤的输出作为点光源模拟宇宙中的恒星. 用一块直径为40 mm的双胶合透镜将单模光纤输出的发散光准直成平行光. 为了避免透镜边缘对平行光的影响, 用一个直径为35 mm的光阑将光束变为直径35 mm的平行光束, 模拟来自无穷远处恒星发出的光. 然后, 再利用一块口径为50 mm的双胶合透镜模拟望远镜, 将准直的平行光汇聚到一点, 用该汇聚点模拟望远镜的焦点和自适应光学系统进行对接, 构成完整的望远镜自适应光学系统.

为了能够在系统中引入符合大气湍流扰动规律且动态变化的波前畸变, 加工制作了一块大气湍流相位屏. 该大气湍流相位屏引入的相位分布满足Kolmogorov模型, 而且, 大气相干长度和兴隆站点的大气湍流统计相干长度一致. 关于大气湍流相位屏模拟和加工的详细讨论见参考文献[24]. 加工好的大气湍流相位屏刻蚀在一个直径为150 mm的圆形石英玻璃板上. 当大气湍流相位屏的部分相位分布置于直径为35 mm的平行光束时, 就会在系统中引入一个静态的波前畸变. 如果大气湍流相位屏绕轴旋转, 并且保证在旋转过程中平行光束始终通过大气湍流相位屏

的某一部分, 这样就可以在系统中引入一个动态的波前畸变. 在实验中就是使用旋转的大气湍流相位屏来模拟动态波前畸变的, 其中大气湍流相位屏以8圈/分钟的速度匀速旋转.

在系统中引入动态畸变波前之后, 开启自适应光学系统之前, CCD相机上捕获的长曝光(CCD的曝光时间设置为3.5 s)图像, 即点光源的像十分模糊, 几乎淹没在噪声之中, 并且动态变化. 图5(a)为自适应光学系统开启之前, CCD捕获的一系列动态图像中的一幅. 开启自适应光学系统之后, CCD相机上捕获的长曝光图像变得十分明亮清晰. 图5(b)为自适应光学系统开启之后, CCD捕获的一系列动态图像中的一幅, 和点扩散函数十分接近. 图6为实验时通过SH波前传感器得到的自适应光学校正前后的像差, 其中图6(a)为自适应系统校正前的像差, 图6(b)为自适应系统校正后的残余像差. 校正前像差的RMS值为1.07λ, 校正后像差的RMS为0.07λ. 实验过程中, 观测到经过自适应光学系统校正之后, CCD相机捕获的图像十分稳定, 波前传感器测得残余波像差也稳定在0.1λ (RMS)以下. 通过对比图5(a)和(b)可以发现, 校正前, 点光源像的最大灰度值为14, 信号基本湮灭在背景噪声中, 几乎难以分辨出目标, 经过自适应光学系统校正后, 物体的亮度明显增强, 最大灰度值达到255, 表明校正后光斑能量更集中. 同时, 自适应光学校正前后图像的半高全宽也明显减小, 由原来的95个像素减小到了12个像素, 十分接近理想的点扩散函数; 系统的斯特列尔比提高了18倍多, 成像质量显著提高. 根据系统残差和斯特列尔比的近似关系[8], 系统的残余波像差在0.1λ (RMS)
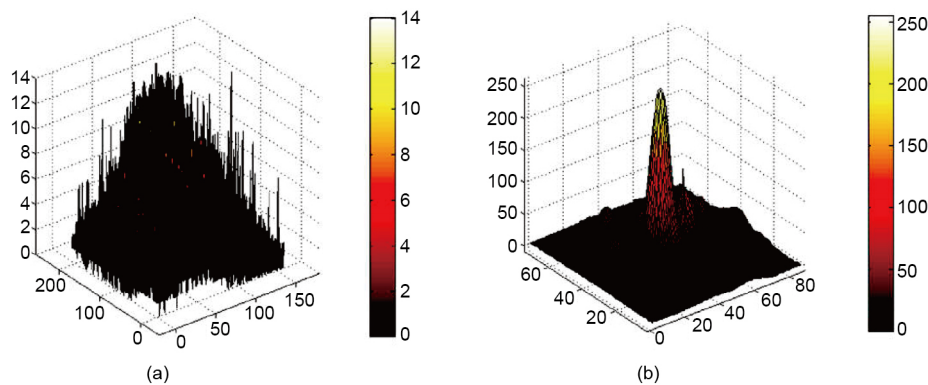

(a)   (b)

图 5 (网络版彩图)自适应光学系统校正前后光斑的三维能量分布图. (a) 校正前光斑的能量分布图; (b) 校正后光斑的能量分布图

Figure 5 (Color online) 3-dimensional intensity profiles before (a) and after (b) correction by the AO system.
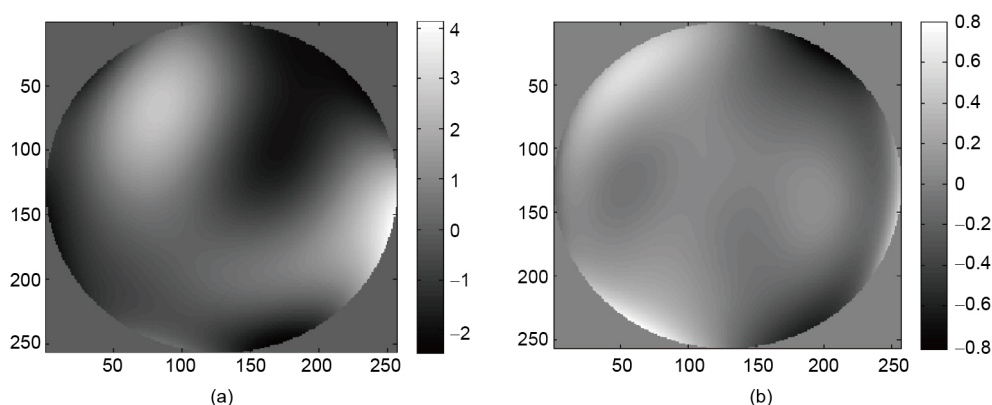
图 6 自适应光学系统校正前后的像差. (a) 校正前的像差; (b) 校正后的残余像差
Figure 6 Aberrations before (a) and after (b) correction by the AO system.

时, 系统的斯特列尔比可以达到0.68. 实验结果表明该自适应光学系统的校正性能超出了设计值, 具有很好的像差校正性能.

6 结论

本文根据2.16 m望远镜及兴隆站点的大气视宁度条件, 研制了一套自适应光学系统. 系统实验结果表明, 研制的自适应光学系统可以将波前像差的均方根值校正到0.1λ以下, 可以获得接近衍射极限的成像质量. 下一步, 将对SH波前传感器的CCD探测器和成像相机进行升级, 与望远镜联调进行星光自适应光学校正实验, 进一步验证系统性能.

参考文献

1　Rousset G, Lacombe F, Puget P, et al. Status of the VLT Nasmyth adaptive optics system (NAOS). SPIE, 2000, 4007: 72–81

2　Sauvage J F, Fusco T, Petit C, et al. SAXO, the extreme adaptive optics system of SPHERE. Overview and calibration procedure. In: Proceedings of Astronomical Telescopes and Instrumentation, Adaptive Optics Systems II. Bellingham: SPIE, 2010

3　Guyon O, Arimoto N, Blain C, et al. Subaru telescope LGSAO: Overview of expected performance. In: Proceedings of Astronomical Telescopes and Instrumentation, Advancements in adaptive Optics. Bellingham: SPIE, 2004. 733–741

4　Tatarski V I. Wave Propagation in a Turbulent Medium. New York: McGrow-Hill, 1961

5　Roddier F. The effects of atmospheric turbulence in optical astronomy. Prog Opt, 1981, 19: 283–376

6　Fried D L. Statistics of a geometric representation of wavefront distortion. J Opt Soc Am, 1965, 55: 1427–1435

7　Fried D L. Anisoplanatism in adaptive optics. J Opt Soc Am, 1982, 72: 52–61

8　Roddier F. Imaging through turbulence. In: Adaptive Optics in Astronomy. Cambridge: Cambridge University Press, 1999. 9–22

9　Noll R J. Zernike polynomials and atmospheric turbulence. J Opt Soc Am, 1976, 66: 207–211

10　Fried D L. Optical resolution through a randomly inhomogeneous medium for very long and very short exposures. J Opt Soc Am, 1966, 56: 1372–1379

11　Rigaut F, Rousset G, Kern P, et al. Adaptive optics on a 3.6-m telescope: Results and performances. Astron Astrophys, 1991, 250: 280–290

12　Roddier F J, Cowie L L, Graves J E, et al. Seeing at Mauna Kea: A joint UH-UN-NOAO-CFHT study. SPIE, 1990, 1236: 485–491

13　Jia P, Zhang S J. Performance modeling of the adaptive optics system on the 2.16 m telescope. Sci China-Phys Mech Astron, 2013, 56: 658–662

14　Li S, Zhang S. Numerical model of the influence function of deformable mirrors based on Bessel Fourier orthogonal functions. Res Astron Astrophys, 2014, 14: 1504–1510

15　Zheng Z Y, Li C W, Zhang S J. Theoretical analyses for the relationship between the performance of quadrant photodetector and the size of incident light spot. In: Proceedings of Astronomical Telescopes and Instrumentation, Adaptive Optics Systems IV. Bellingham: SPIE, 2014

16　Zheng Z Y, Lu Q S, Zhang S J. Active disturbance rejection control for precise position tracking of piezoelectric actuators. High Tech Lett, 2015, 21: 333–338

17　Zheng Z Y, Li C W, Li B M, et al. Analysis and demonstration of PID algorithm based on arranging the transient process for adaptive optics.

Chin Opt Lett, 2013, 11: 110101–110104

18 Lu Q S, Lu Y T, Wang D. Practical Design Guide for Xilinx Zynq Soc Running Embedded Linux (in Chinese). Beijing: Tsinghua University Press, 2014 [陆启帅, 陆彦婷, 王地. Xilinx Zynq SoC与嵌入式Linux设计实战指南. 北京: 清华大学出版社, 2014]

19 Lu Q S. Piezoelectric sesor precision acquisition system based on Zynq (in Chinese). Microcontrol Embed Syst, 2015, 9: 54–56 [陆启帅. 基于Zynq压电陶瓷传感器的高精度采集系统设计. 单片机与嵌入式系统应用, 2015, 9: 54–56]

20 Herrmann J. Cross coupling and aliasing in modal wave-front estimation. J Opt Soc Am, 1981, 71: 989–992

21 Li Z G, Li B M, Li C W, et al. An adaptive algorithm for wavefront reconstruction based on a Shack-Hartmann sensor (in Chinese). Chin J Quantum Electron, 2013, 30: 482–489 [李战国, 李邦明, 李常伟, 等. 一种基于Shack-Hartmann传感器的自适应波前重建算法. 量子电子学报, 2013, 30: 482–489]

22 Li B M, Li C W, Zhang S J. Dynamic optimization method for modal control of adaptive optics system (in Chinese). Acta Opt Sin, 2012, 32: 26–30 [李邦明, 李常伟, 张思炯. 自适应光学系统模式控制动态优化方法. 光学学报, 2012, 32: 26–30]

23 Li B M, Li C W, Jia P, et al. Analysis and experimental demonstration of adaptive optics based on the modal control optimization. In: Proceedings of Astronomical Telescopes and Instrumentation, Adaptive Optics Systems III. Amstrdam: SPIE, 2012

24 Jia P, Zhang S. Simulation and fabrication of the atmospheric turbulence phase screen based on a fractal model. Res Astron Astrophys, 2012, 12: 584–590

Adaptive optics system for the Xinglong 2.16 m telescope

LI ChangWei[1,2*], LI BangMing[1,2], LU YanTing[1,2], LU QiShuai[1,2],
ZHENG ZhaoYing[1,2], WANG Di[1,2] & LI Shun[1,2]

[1] *National Astronomical Observatories Nanjing Institute of Astronomical Optics & Technology, Chinese Academy of Sciences, Nanjing 210042, China;*

[2] *Key Laboratory of Astronomical Optics & Technology, Chinese Academy of Sciences, Nanjing 210042, China*

Adaptive optics (AO) is one of the essential techniques for the large-diameter astronomical telescopes to overcome the wavefront aberrations caused by atmospheric turbulence and improve their imaging qualities. This paper describes an adaptive optics system developed for the 2.16-m telescope at Xinglong. This AO system mainly consists of a piezoelectric deformable mirror with 109 actuators, a Shack-Hartmann wavefront sensor with 100 subapertures, and a high-speed control platform based on field-programmable gate array (FPGA). Experimental results show that this AO system can reduce the root-mean-square (RMS) of the atmospheric wavefront aberrations to, or even smaller than 0.1λ, and then the telescope can obtain a near diffraction limited resolution.

adaptive optics system, wavefront reconstruction, wavefront control, high-speed control platform

084206-7

兴隆观测基地网站二维码　兴隆观测基地微信平台

中国科学院国家天文台兴隆观测基地

Xinglong Observatory
National Astronomical Observatories
Chinese Academy of Sciences
http://www.xinglong-naoc.org